DOT/FAA/AR-xx/xx

Air Traffic Organization
NextGen & Operations Planning
Office of Research and
Technology Development
Washington, DC 20591

The FAA's Center of Excellence for UAS Research
ASSURE
Alliance for System Safety of UAS through Research Excellence

Volume II – UAS Airborne Collision Severity Evaluation – Quadcopter

July 2017

Final Report

This document is available to the U.S. public through the National Technical Information Services (NTIS), Springfield, Virginia 22161.

This document is also available from the Federal Aviation Administration William J. Hughes Technical Center at actlibrary.tc.faa.gov.

U.S. Department of Transportation
Federal Aviation Administration

NOTICE

Technical Report Documentation Page

1. Report No.	2. Government Accession No.	3. Recipient's Catalog No.
DOT/FAA/AR-xx/xx		

4. Title and Subtitle	5. Report Date
Volume II – UAS Airborne Collision Severity Evaluation – Quadcopter Quadcopter projectile development, simulation protocols, target development, testing, and results.	**July 2017**
	6. Performing Organization Code
7. Author(s) **Gerardo Olivares, Luis Gomez, Jaime Espinosa de los Monteros, Russel J. Baldridge, Chandresh Zinzuwadia, and Tom Aldag**	8. Performing Organization Report No.
9. Performing Organization Name and Address National Institute for Aviation Research Wichita State University 1845 Fairmount Wichita, KS 67260-0093	10. Work Unit No. (TRAIS) 11. Contract or Grant No.
12. Sponsoring Agency Name and Address U.S. Department of Transportation Federal Aviation Administration Office of Aviation Research Washington, DC 20591	13. Type of Report and Period Covered 14. Sponsoring Agency Code

15. Supplementary Notes

16. Abstract

17. Key Words	18. Distribution Statement
Crashworthiness, Airborne Collision, UAS, National Institute for Aviation Research, NIAR	This document is available to the U.S. public through the National Technical Information Service (NTIS), Springfield, Virginia 22161. This document is also available from the Federal Aviation Administration William J. Hughes Technical Center at actlibrary.tc.faa.gov.

19. Security Classif. (of this report)	20. Security Classif. (of this page)	21. No. of Pages	22. Price
Unclassified	Unclassified		

Form DOT F 1700.7 (8-72) Reproduction of completed page authorized

REVISION HISTORY

Revision	Description of Modifications	Release Date
-	Initial release	9 Dec 2017
1	- Page 7 – added paragraph to specify the project will not assess already certified products. - Page 44 – added section 2.4.4.5 describing the FE model of the component level test hardware. - Page 48-50/54-56/59-61/65-66/70-72/75-77 – added results summary chart, description of filter used and modified results description. - Page 126 – added figures 180 and 181 with diagram showing materials in both manned aircraft. - Page 125 – added figures 182 and 183 with diagram showing gage thicknesses of main components of both aircraft. - Page 129 – extended explanation of impact velocity selection. - Page 136 – removed paragraph relating level 4 with catastrophic events. - Page 200 – added paragraph to specify the project will not assess already certified products. - Page 203 – removed paragraph relating level 4 with catastrophic events. - Page 213-214 – added recommendation: analyze more velocities and masses to be able to stablish thresholds. - Appendix F – added appendix to describe data processing methods used in physical testing.	18 Jul 2017

ACKNOWLEDGEMENTS

The authors would like to thank all the Federal Aviation Administration (FAA) personnel that have been involved in this research project. In particular, the authors would like to thank Sabrina Saunders-Hodge, Bill Oehlschlager, Paul Rumberger, and Paul Campbell for all their contributions and their valuable input throughout the research.

The authors would also like to thank General Jim Poss and Colonel Stephen P. Luxion from the FAA's Center of Excellence for Unmanned Aircraft Systems (ASSURE) for supporting this research.

Dr. Thomas Lacy and his research team Kalyan Raj Kota, Trent Ricks, and Nimesh Jayakody from Mississippi State University.

The authors also acknowledge the contributions of the graduate research assistants from the National Institute for Aviation Research Computational Mechanics Laboratory Armando Barriga, Hoa Ly, Rodrigo Marco, Sameer Naukudkar, and Nathaniel J. Baum, as well as the researchers from the Crash Dynamics Laboratory Robert Huculak and Andy Mackey. Last, but not least, thanks to all the industry participants that helped throughout the research.

TABLE OF CONTENTS

LIST OF FIGURES

LIST OF TABLES

Table Page

LIST OF ACRONYMS

ABS	Acrylonitrile Butadiene Styrene
ARC	Aviation Rulemaking Committee
CAD	Computer-Aided Design
CFD	Computational Fluid Dynamics
CFR	Code of Federal Regulations
CG	Center of Gravity
DIC	Digital Image Correlation
ELoS	Equivalent Level of Safety
FAA	Federal Aviation Administration
FE	Finite Element
FEA	Finite Element Analysis
FEM	Finite Element Method
FTIR	Fourier Transform Infrared Spectroscopy
JAA	Joint Aviation Authority
LiPo	Lithium-ion Polymer (battery)
MTOW	Maximum Take-Off Weight
NAS	National Airspace System
NIAR	National Institute for Aviation Research
NPRM	Notice of Proposed Rulemaking
NTSB	National Transportation Safety Board
OEM	Original Equipment Manufacturer
PCB	Printed Circuit Board
RTCA	Radio Technical Commission for Aeronautics
SPH	Smoothed-Particle Hydrodynamics
sUAS	Small Unmanned Aircraft System
UAS	Unmanned Aircraft System
WP	Working Package

EXECUTIVE SUMMARY

According to the latest industry forecast studies, the Unmanned Aircraft Systems (UASs) market volume is expected to reach 4.7 million units by 2020 [1]. Nonetheless, safety, regulatory, social, and technical challenges need to be addressed before the sight of an unmanned aircraft in the sky becomes as common and accepted by the public as its manned counterparts. The effect of an airborne collision between an UAS and a manned aircraft is a concern to the public and government officials at all levels. The primary goal of regulating UAS operations into the National Airspace System (NAS) is to ensure an appropriate level of safety. Research is needed to define airborne hazard severity thresholds for collisions between unmanned and manned aircraft, or collisions with people on the ground.

The results presented in this report focus the initial effort on analyzing a small quadcopter UAS configuration impacting on a typical commercial transport jet and a typical business jet aircraft. This research will help determine airworthiness requirements for unmanned aircraft based on their potential hazard severity to other airspace users in the NAS. The resulting severity thresholds will be based on UAS characteristics (kinetic energy, structure, shape, materials, etc.) under credible encounter scenarios and will provide for test criteria used to evaluate applicable operational and airworthiness standards. UAS that meet test criteria based on thresholds for these characteristics may be approved for operations over or near people on the ground and may be certified as airworthy under different criteria than other UAS [19]. Due to the complexity of the problem, full-scale test article availability, time, and budget constraints, it was decided to conduct the R&D effort by using the National Institute for Aviation Research (NIAR) physics based Finite Element (FE) modeling techniques based on the Building Block Approach. Conducting these type of impact studies by analysis provides a better insight into the crashworthiness response of the target and the projectile. Damage evaluation criteria are proposed to quantify aircraft damage to the different impact scenarios summarized in this report.

Studies were conducted to analyze the damage introduced into different areas in the aircraft structure for both the commercial and business jet aircraft configurations. According to the simulations presented in this report, an airborne collision between a commercial transport jet and a 1.2 kg (2.7 lb) quadcopter UAS at 128.6 m/s (250 knots) may result in a damage severity level of medium-high (3-4) in the horizontal and vertical stabilizer, medium (2-3) in the leading edge of the wing and medium-low (2) in the windshield. Equally, an airborne collision between a business jet and a 1.2 kg (2.7 lb) quadcopter UAS may result in a damage severity level of medium-high (3-4) in the horizontal and vertical stabilizer, medium (2-3) in the leading edge of the wing and medium-low (2) in the windshield.

Correspondingly to what was observed in component level physical testing, the simulations carried out in Chapter 4 predicted that most of the damage is produced by relatively dense and stiffer parts (motors, camera, etc.) of the UAS. Additional parametric studies were conducted to analyze the effect of the projectile mass, impact velocity, and UAS architecture.

This research concluded that UAS impacts are likely to cause more damage than bird strikes for an equivalent initial kinetic energy. UAS impacts were generally associated with greater damage levels due to the hard-bodied mechanical construction of the UAS, its components made of dense, rigid, materials. Therefore, a 4lb bird and a 4lb UAS will introduce different levels of damage to the aircraft.

1. INTRODUCTION

Unmanned Aircraft Systems (UASs) is the fastest growing sector of the aviation industry today, according to The Association for Unmanned Vehicles International (AUVSI), the largest trade group around UASs, estimates that by 2019 more than 70,000 jobs will be created in the US with an economic impact of more than $13.6B.[1]. Globally, UAS market volume is expected to reach 4.7 million units by 2020 [1]. Nonetheless, safety, regulatory, social, and technical challenges need to be addressed before the sight of an unmanned aircraft in the sky becomes as common and accepted by the public as its manned counterparts.

The effect of an airborne collision between an UAS and a manned aircraft is a concern to the public and government officials at all levels. The primary goal of regulating UAS operations into the National Airspace System (NAS) is to assure an appropriate level of safety. While the effects of bird impacts on airplanes are well documented, little is known about the effects of more rigid and higher mass UASs on aircraft structures and propulsion systems. This research evaluates the severity of small UAS (sUAS) (under 55 lb, as defined in the Small Unmanned Aircraft Rule (*Part 107*)) collisions on commercial and business jet airframes and propulsion systems.

Findings from this research can be used to help define airborne hazard severity thresholds for collisions between unmanned and manned aircraft. The results presented in this report will focus on small quadcopter configurations impacting on a typical commercial transport aircraft and a typical business jet. A second report will document a fixed wing UAS configuration impacting on the same aircraft structures [2], and the third report will focus on the effects of UAS engine ingestion [3]. Further research will be conducted in the near future to analyze the severity level of UAS airborne collisions with General Aviation (GA) aircraft and rotorcraft.

1.1 BACKGROUND

1.1.1 Unmanned Aircraft Systems Categories

An UAS is an Unmanned Aerial Vehicle (UAV) and the equipment necessary for the safe and efficient operation of that aircraft. An UAV is a component of an UAS. It is defined by statute as an aircraft that is operated without the possibility of direct human intervention from within or on the aircraft [4]. It either can fly autonomously or be piloted remotely.

Currently there is no standard when it comes to the classification of UASs. Defense agencies have their own standard, and civilian agencies worldwide have their ever-evolving categories definitions for UASs. Currently the Federal Aviation Administration (FAA) classifies UASs into the following categories:

- **Small Unmanned Aircraft Rule (*Part 107*) [5]:** The proposed rule does not cover the full spectrum of UAS types or weights. The FAA acknowledges that the rulemaking is an incremental stage of adding UASs into the NAS. The small non-hobby or non-recreational UASs must be operated in accordance with the following limitations:
  - Unmanned aircraft must weigh less than 55 lb (25 kg).
  - Cannot be flown faster than a groundspeed of 87 knots (100 mph).
  - Cannot be flown higher than 400 feet (≈122 m) above ground level (AGL), unless flown within a 400 ft radius of a structure and does not fly higher than 400 ft above the structure's immediate uppermost limit.

  - Minimum visibility, as observed from the location of the CS, may not be less than three statute miles (sm).
  - Minimum distance from clouds being no less than 500 ft (≈152 m) below a cloud and no less than 2000 ft (≈610 m) horizontally from the cloud.
- **Micro-UAS:** The Aviation Rulemaking Committee (ARC) was focused on flight over people, and in furtherance of that goal, identified four sUAS categories, defined primarily by level of risk of injury posed, for operations over people. For each category, the ARC recommends a risk threshold that correlates to either a weight or an impact energy equivalent and, to the extent necessary to minimize the risks associated with that category, additional performance standards and operational restrictions. The following is a summary of the category recommendations [6]:
  - For Category 1, a sUAS may operate over people if the mass (including accessories/payload, *e.g.*, cameras) is 250 g or less.
  - Under Categories 2, 3, and 4, a sUAS may operate over people if it does not exceed the impact energy threshold specified for each category, as certified by the manufacturer using industry consensus test methods, and if its operator complies with operational restrictions specified for each category.

1.1.2 Unmanned Aircraft Systems Market Size

The UAS market is divided into two groups: Hobbyist and Commercial.

1.1.2.1 Hobbyist UAS Forecast

In order to operate in the NAS, the FAA must ensure that aircraft operators are not only aware of the system in which they are operating, but that the agency also has a means to identify owners. One means to accomplish this is through aircraft registration and marking. On December 14, 2015, the FAA issued a rule requiring all UAS weighing more than 0.55 lb (250 g) and less than 55 lb (24.9 kg) to be registered using a new on-line system (UAS weighing more than 55 lb must be registered using the existing Aircraft Registration Process). This registration rule will aid in investigations and allow the FAA to gather data about UAS use.

As of mid-March 2016, there have been over 408,000 registrations. As shown in Table 1, a sales forecast was developed for the sUAS registration rule, which included very small units below the registration size cutoff of 250 g. For this interim final rule, in 2016, the forecast was of 1.9 million potential annual sales, which could increase to 4.3 million units sold annually by 2020. As shown in the first row of Table 1, this would represent the upper bound of the potential number of sUAS operated as model or hobby aircraft [7].

Table 1. Sales forecast summary (million sUAS units) [7]

	2016	2017	2018	2019	2020
Hobbyist (model aircraft)	1.9	2.3	2.9	3.5	4.3
Commercial (non-model aircraft)	0.6	2.5	2.6	2.6	2.7
TOTAL UASs	2.5	4.8	5.5	6.1	7.0

1.1.2.2 Commercial UAS Forecast

In 2015, in support of the sUAS registration rule, a sales forecast for commercial sUASs was developed to derive the potential demand for the new on-line registration system. That forecast represents the high end of the sUAS commercial fleet. As summarized in the second row of Table 1, for 2016, the potential sales of commercial sUAS requiring registration was forecast to be over 600,000, growing to 2.7 million by 2020 [7].

On February 23, 2015, the FAA issued the Operation and Certification of Small Unmanned Aircraft Systems Notice of Proposed Rulemaking (NPRM) proposing to amend its regulations to adopt specific rules for the operation of sUASs in the NAS. More information on the derivation and assumptions behind this forecast will be provided in the Regulatory Impact Assessment accompanying the final rule publication [7].

The FAA is working with the Teal Group Corporation, an industry expert in UAS forecasting, to develop a commercial forecast for sUAS operations described in the NPRM. The civil and commercial UAS market will take time to develop and the size of the market will directly relate to the specific requirements developed along with airspace accessibility. The Teal Group has provided the FAA with a forecast for small commercial unmanned aircraft. This forecast analyzes the market demand for different sectors within the regulatory environment.

As shown Figure 2, it is expected that, once the final small UAS rule is implemented, two different categories of sUAS will emerge. Higher end sUASs will have an average sales price of $40,000 per unit, while lower end units will have an average price of $2,500. Over a five-year period, Teal Group forecasts the sUAS fleet to be approximately 542,500. Of this estimated fleet, it is expected that roughly 90% of the demand will be satisfied by the lower end units. The number of sUASs forecasted is highly uncertain and is dependent on the regulatory structure ultimately adopted. Once a final rule for sUASs is published, they will become more commercially viable than they are today. The total fleet shown in Table 1 is expected to satisfy the market for the top five industries (Figure 1) that will employ the use of sUASs [7].

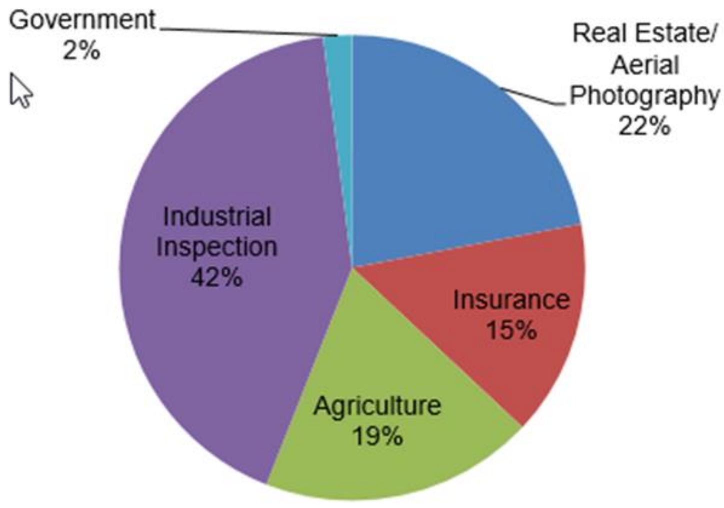

Figure 1. Top five UAS markets [7]

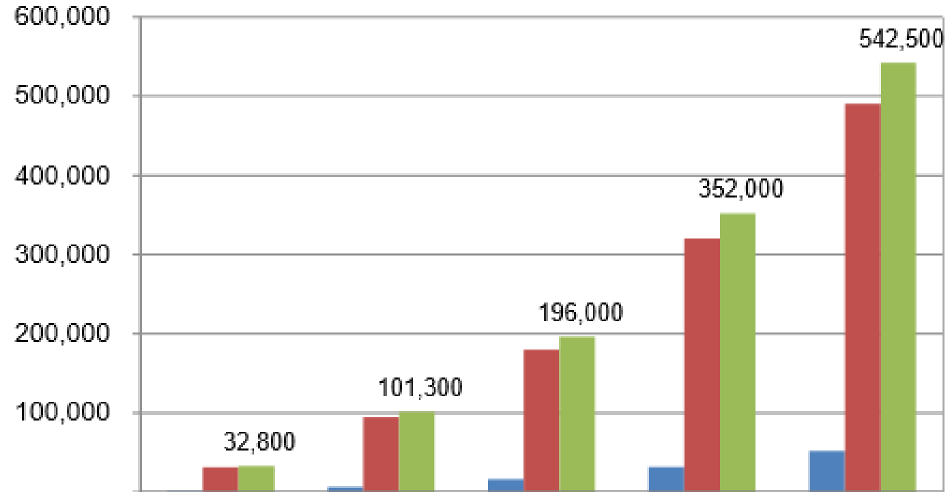

	2016	2017	2018	2019	2020
Higher end UAS	1,300	6,300	16,000	32,000	52,000
Lower end UAS	31,500	95,000	180,000	320,000	490,500
Total Fleet	32,800	101,300	196,000	352,000	542,500

Figure 2. sUAS fleet [7]

1.1.3 Unmanned Aircraft Systems Impact Severity Classification

Conventional *Code of Federal Regulations Title 14 (14 CFR*) system safety analyses include hazards to flight crew and occupants that may not be applicable to unmanned aircraft. However, UAS operations may pose unique hazards to other aircraft and people on the ground. It is necessary to determine hazard severity thresholds for UASs using safety characteristic factors that affect the potential severity of UASs in collisions with other aircraft on the ground or in airborne encounters as well as collisions with people on the ground. The factors that determine the outcome of an airborne collision are numerous and complex and are highly dependent on the structural design and materials used for the construction of the UAS.

1.1.3.1 Unmanned Aircraft Systems Mid-Air Collisions Equivalent Level of Safety

The primary goal of regulating UAS operations in the NAS is to assure an appropriate level of safety. This goal is quantified by national aviation agencies as an “Equivalent Level of Safety” with that of manned aviation. There are major key differences between manned and unmanned aviation that do not only lay in the separation of the pilot from the cockpit and the level of automation introduced but also in the variety of architectures and materials used for the construction of UASs. These differences could introduce new failure modes, and, as a result, increase perceived risk that needs to be evaluated [9].

In order to have an Equivalent Level of Safety, according to the definition of the Range Commanders Council in its guidance on UAS operations it states that any UAS operation or test must show a level of risk to human life no greater than that for an operation or test of a piloted aircraft [10].

Although current manned aviation regulations do not impose limits on fatality rates, a statistical analysis of historical data can provide valuable insight on the collision and fatality rates of manned aviation and could be used to define the basis for the Equivalent Level of Safety for UASs.

In order for an Equivalent Level of Safety to be derived, accident statistics involving mid-air collisions are required. The National Transportation Safety Board (NTSB) has defined two categories of relevant collision accident scenarios; *(i)* in-flight collisions with obstacles such as birds, trees, power lines and *(ii)* mid-air collisions with other aircraft. The later could be used to define the UAS requirements. Data pertaining this approach is presented in reference [9] for NTSB data compiled between 1983-2006. If this approach is used, in the future as a reference metrics to define the Equivalent Level of Safety, it is recommended to conduct further studies that include an updated NTSB data available.

Once the Equivalent Level of Safety is defined based on historical data from manned aviation, the next step is to develop a method to estimate the probability of mid-air collisions between UASs and manned aircraft. Several authors have published methodologies on how to evaluate the risk of mid-air collisions between manned aircraft and UASs [11] [12]; some of the midair collision models are based on a theory originally developed to predict the collision frequency of gas molecules [13]. This theory was similarly applied to air traffic in prior literature [14] [15]. The collision frequency between a single UAS and transient air traffic is a product of the transient aircraft density, the combined frontal areas, and the relative closing velocity between the colliding manned and unmanned aircraft. [11].

The aforementioned metrics provide statistical probabilities of UAS mid-air collisions according to specific parameters defined for the evaluation. It should be noted that not all collisions could lead to catastrophic accidents. The large variability of UAS sizes and the fact that not all the aircraft systems are critical for remaining airborne means that the aircraft involved may survive certain collisions.

The risk assessment to develop an Airborne Collision Unmanned Aircraft Systems Impact Severity Classification can be divided into three elements:

- **Estimation of the probability of mid-air collision** between UASs and manned aircraft. This will be a function of the operating airspace, aircraft operated within the airspace and the UAS configurations operating within the shared airspace. Methods to estimate the probability of impact are presented in references [11] [12].
- **Evaluation of damage potential for typical UASs** (classes based on weight, architecture, operational characteristics [altitude, velocity] mid-air collisions scenarios per manned aircraft class (commercial, general aviation, rotorcraft, etc.) in order to assess the damage severity to manned aircraft. Several groups advocate to use simplified ballistic penetration models [16], similarity principles to existing bird strike requirements or kinetic energy thresholds [17] [18]. The objective of this overcharging project is to evaluate the severity of a typical quadcopter and fixed wing UAS airborne collision, with detailed Finite Element (FE) models of the UASs and the target aircraft. These results will be compared with current proposed penetration mechanics and energy based criteria.
- Once the probability of an airborne collision is determined, **the damage models obtained through the research presented in this study can be combined with the probabilistic collision models to define appropriate Equivalent Level of Safety criteria.**

1.2 PROJECT SCOPE

Research is needed to establish airborne hazard severity thresholds for collisions between unmanned and manned aircraft. This research will help determine airworthiness requirements for unmanned aircraft based on their potential hazard severity to other airspace users in the NAS. The resulting severity thresholds will be based on UAS characteristics (kinetic energy, structure, shape, materials, etc.) under credible encounter scenarios and will provide for test criteria used to evaluate applicable operational and airworthiness standards. UASs that meet test criteria based on thresholds for these characteristics may be approved for operations over or near people on the ground and may be certified as airworthy under different criteria than other UASs [19].

The main research questions being answered through this research are [19]:

- What are the hazard severity criteria for an UAS collision (weight, kinetic energy, etc.)?
- What is the severity of an UAS collision with an aircraft in the air?
- Can an UAS impact be classified similar to a bird strike?
- Will an UAS impacting an engine be similar to a bird engine ingestion?
- What are the characteristics of an UAS where it will not be a risk to an aircraft if a mid-air collision was to happen?
- Can the severity of an UAS mid-air collision with an aircraft be characterized into categories based on the UAS? What would those categories look like?

Using the approved hazard severity characteristics and method(s), comprehensive lists of lethality characteristics thresholds will be developed using data and analysis from proposed methods and UAS safety definitions provided by the Radio Technical Commission for Aeronautics (RTCA) for airborne collision with other UAS and commercial aircraft. Scenarios should involve impacts with representative commercial aircraft structures, control surfaces, propellers and engines, as well as representative sUASs. The scenarios should include analyses similar to bird strike methods of impacts on windshields, as well as an engine ingesting sUASs. The analyses should include minimum characteristic thresholds for which there is no relevant risk of damage from a collision. In order to answer the aforementioned items the National Institute for Aviation Research (NIAR) proposes the following research approach, divided into seven Working Packages (WP):

- WP I – Projectile Definition: definition UAS classes based on: maximum take-off weight (MTOW), speed, altitude, power-plant, material construction, geometry.
- WP II – Target Definition: business and commercial transport jet.
- WP III – UAS Projectile Model Development: Computer-Aided Design (CAD), and FE model.
- WP IV – Aircraft Target Development: CAD, and FE model
- WP V – Safety Evaluation UAS to Aircraft
- WP VI – Aircraft Susceptibility Evaluation: definition surrogate projectile and test condition.
- WP VII – UAS Susceptibility Evaluation: definition UAS crashworthiness evaluation method

This research project will utilize a proven simulation technique, the Building Block Approach (BBA) to analyze the outcome and severity of typical impact scenarios. The numerical models will be validated with experimental data at the coupon, and component levels in order to predict the full-scale UAS, system level response under impact. Due to the high level of concern related to this topic, initial simulation analyses were focused on providing a rough order of magnitude severity evaluation of a quadcopter and fixed wing UAS with commercial and business jet airframes.

It is important to emphasize that the intent of this research project was not to do an assessment of already certified products (e.g. Part 33/23/25/27/29). The investigation was focused on understanding the physics of airborne collisions between UASs and manned aircraft, and identifying characteristics of the UAS that may influence post-impact damage on the manned aircraft.

2. QUADCOPTER UAS PROJECTILE DEFINITION

In this research project, two different UAS FE models were produced, one for a quadcopter and the other for a fixed wing configuration. Mississippi State University was in charge of modeling the latter [2] while Wichita State University – NIAR was in charge of modeling the former. The process of creating the FE model of the quadcopter UAS is presented in this chapter.

Firstly, a brief description is given on which existing UAS was selected. Work that was carried out by Montana State University in WP I of the project [20] to select representative UAS models. Subsequently, as part of WP III, an UAS was purchased and reverse engineered by the NIAR to obtain a detailed CAD model and the constituent materials. Each of the structural parts where discretized, and the Finite Element (FE) model was set up for the explicit dynamics solver LS-DYNA [21]. Finally, the principal components of the UAS were verified through physical testing. Structurally complete quadcopter UAS models will later be used to assess the impact threat posed to business and commercial transport jets. Figure 3 illustrates the procedure that the NIAR has followed to produce the FE model of the quadcopter UAS.

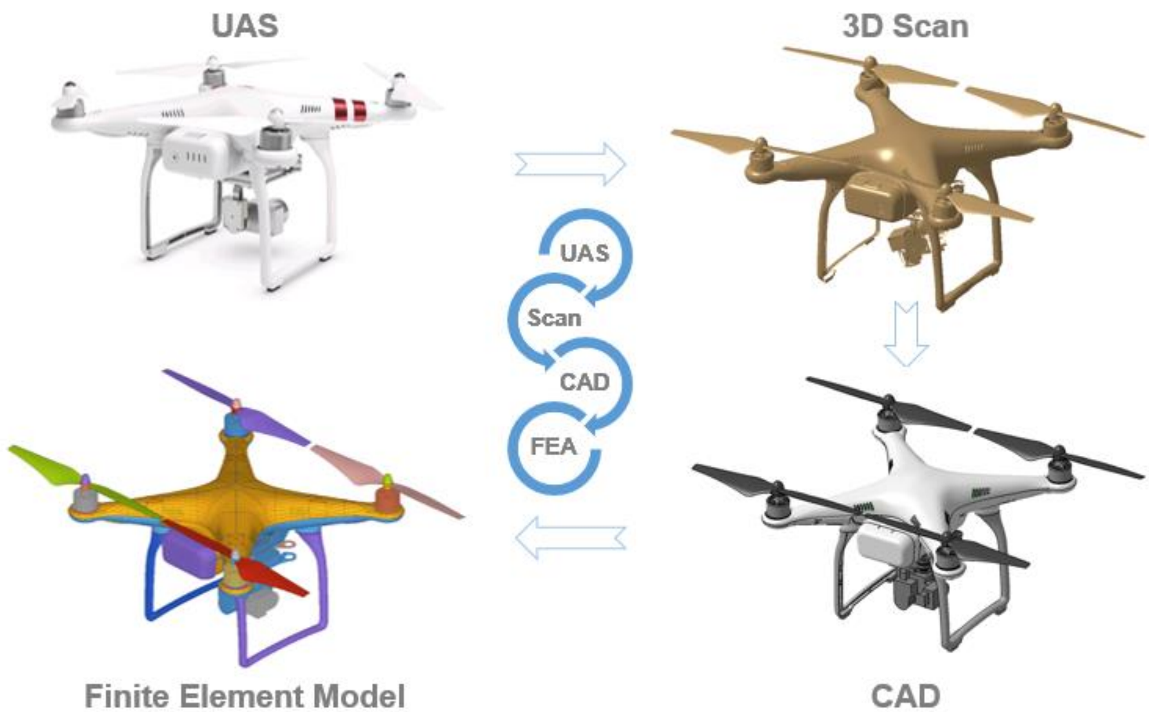

Figure 3. UAS FE modeling process

2.1 UAS GEOMETRY AND SPECIFICATIONS

The investigations of Montana State University [20] concluded that the DJI Phantom family are the most common UAS under 2.3 kg (5 lb), with a presence of more than 61% of the market at the time when this research was being conducted. Consequently, the DJI Phantom 3 Standard edition was selected as baseline to define the quadcopter UAS FE model for the collision study.

The Phantom 3 Standard is a 1.2 kg (2.7 lb) quadcopter intended for recreational and commercial aerial photography and easily accessible to the public. Figure 4 and Table 2 show the basic dimensions and relevant specifications of the selected quadcopter UAS.

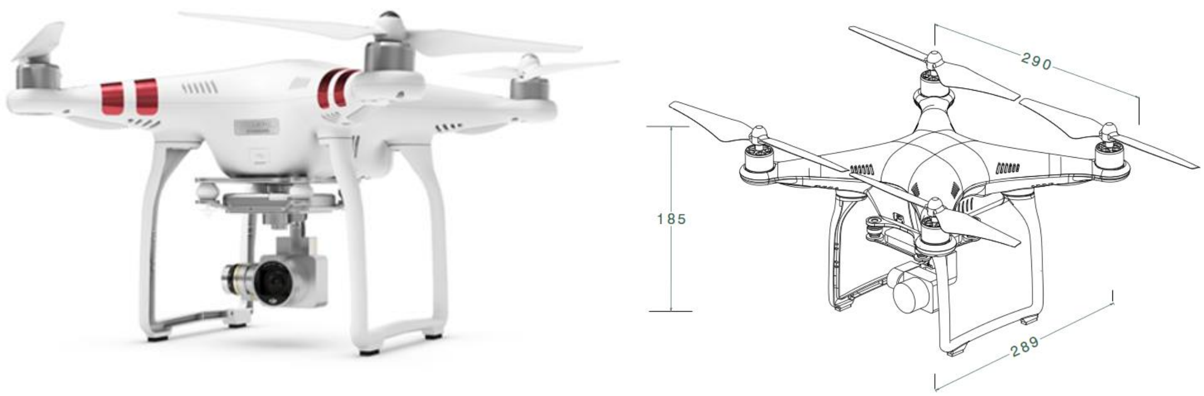

Figure 4. Geometry features of the DJI Phantom 3 (dimensions in mm)

Table 2. Relevant specifications of the DJI Phantom 3

Mass	1,216 g	2.68 lb.
Diagonal	350 mm	13.8 in
Max. Horizontal Speed	16 m/s	31 knot
Max. Service Ceiling	6,000 m	19,685 ft.
Electronic limit above ground	120 m	394 ft.
Max. Motor Speed	1,240 rad/s	11,840 rpm
Motors	4x brushless DC motors; mass: 54 g	
Battery	4x LiPo cells; capacity: 4480 mAh; mass: 363 g	

As a clarification, the maximum service ceiling describes the maximum altitude above mean sea level at which the UAS is capable of operating. Electronic limit above take-off point represents the limit set by the manufacturer. The electronic limit is not necessarily implemented by all the drone manufacturers.

2.2 CAD REVERSE ENGINEERING

Reverse engineering is a technique used to analyze and extract design information from a product and replicate it physically or in the form of a virtual CAD model. The details of the reverse engineering process used for this project are described in the following subsections.

2.2.1 Geometry Data Collection

First, an Absolute Romer Arm equipped with a CMS 108 scanner attachment was used to acquire point cloud data of the geometry of the UAS. The quadcopter was disassembled, the mass of each component was measured and recorded, and the external surface was scanned.

The CMS 108 scanner uses a laser technology called flying dot method that allows the capture of data for a variety of materials without having to adjust exposure settings, unlike traditional line scanners. The scanner achieves an accuracy of 0.003” (76.2 μm), which in this project provided adequate detail for small features present in the UAS body

.

Figure 5. Absolute Romer Arm equipped with a CMS 108 scanner

2.2.2 Cloud Point Generation

After a point cloud had been collected, it was converted to a triangular mesh using Polyworks IMerge workbench. The software was used to align, process, and edit the cloud of points, result of the scan for each of the components. The file was exported in STL format.

2.2.3 CAD Modeling

CATIA was selected as the software to produce the entire CAD modeling and the virtual assembly of the quadcopter's geometry. Once the STL was imported, a local coordinate system was established for each part and any anomalies that may have occurred during scanning were fixed. Each of the components were modeled and assembled in a product. In the assembly, it was ensured that all the parts fit together correctly and parts did not produce any clashing. The origin of the global coordinate system of the CAD model was setup to match approximately the position of the center of gravity of the UAS. Figure 6 shows the steps for generating the UAS CAD model.

Figure 6. CAD model development steps

2.2.4 CAD Sanity Check

The final step in the reverse engineering process was to compare the CAD model back to the original scan to verify that the CAD model was within the specified tolerances. Color maps can be generated inside CATIA to highlight areas of the model that need to be adjusted to better fit the scan. Figure 7 illustrates an example of this verification, in this case applied to the upper body of the quadcopter. The error is plot in a scale from green to red, green being a perfect match.

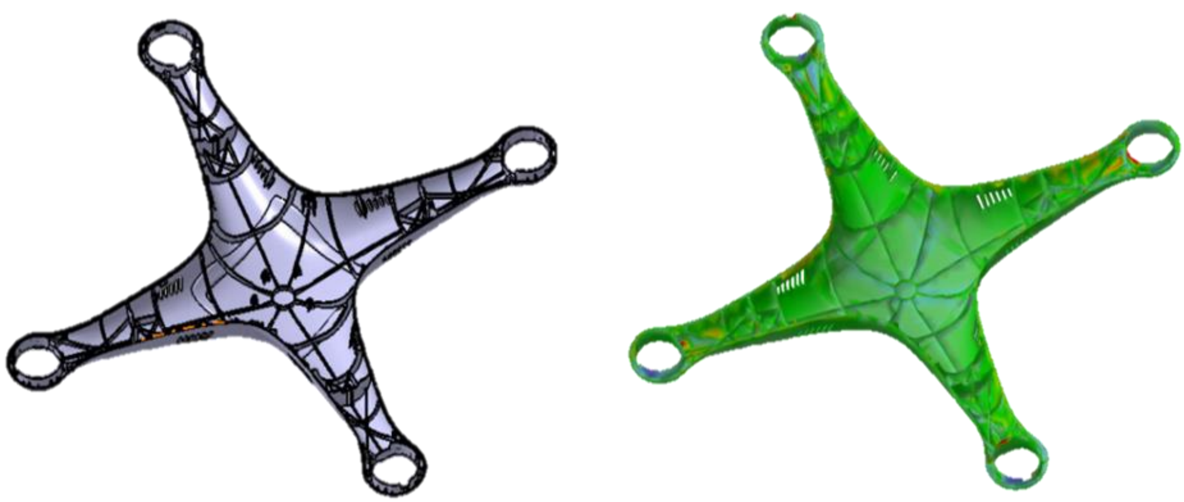

Figure 7. UAS CAD model verification

2.2.5 UAS Geometry Details

Figure 8 shows a general and exploded view of the UAS geometry model illustrating the main components of the quadcopter being considered. A detail view of some of the components is shown later on section 2.3.1 .

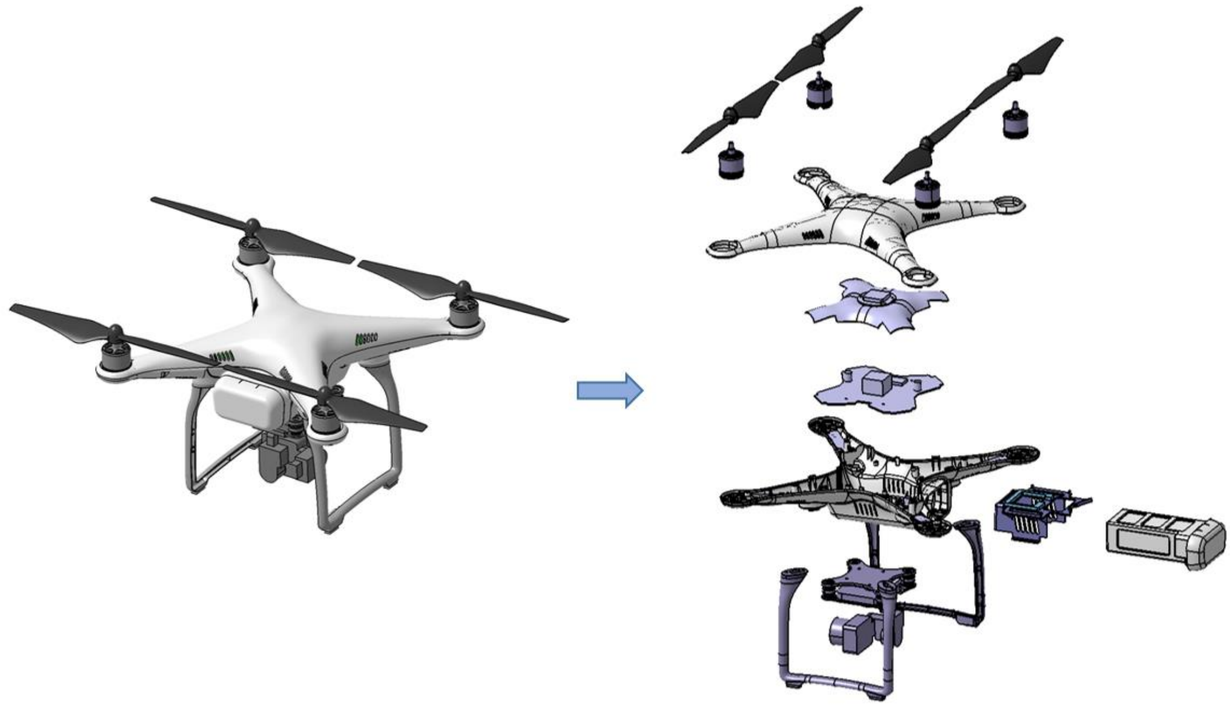

Figure 8. UAS geometry model

2.3 FINITE ELEMENT MODEL

This section describes the process followed to produce the FE model of the small UAS, starting from the CAD described in the previous section and ending with the final mass check. The following procedure was carried out to create the UAS FE model.

- Obtain CAD data (STP format) for each part of the model.
- Clean up geometry and prepare for meshing (*i.e.* split surfaces where symmetric, defeature small elements, etc.).
- Select element type (*e.g.* shell, solid, etc.) for each of the different parts depending on geometry and element size constraints.
- Discretize the geometry (*i.e.* meshing).
- Check quality criteria with NIAR standards.
- Assign section properties: shell thicknesses and beam cross section.
- Assemble meshed parts to create complete FE model.
- Check model for non-desired entities (free-nodes, free-edges, mesh overlap, duplicated elements, non-aligned element normals, etc.).

- Assign corresponding material properties.
- Add non-structural mass to nodes wherever a part is not being modeled.
- Perform mass check, comparing individual components to its physical counterpart.
- Renumber model components (nodes and elements within 50,000,000-50,999,999 and rest of keywords in 10,000-10,999).

2.3.1 Discretization

This section describes the techniques used for meshing the UAS, presents the element types used, and discusses the quality criteria followed to ensure a reliable FE solution with reasonable computation time. The FE model was preprocessed for the solver LS-DYNA [21]. Figures from Figure 9 to Figure 16 show the mesh of the major components in the FE model compared with the respective CAD model. Figure 17 displays a cross section of the complete UAS FE model, showing details of the assembly and internal construction of some of the components.

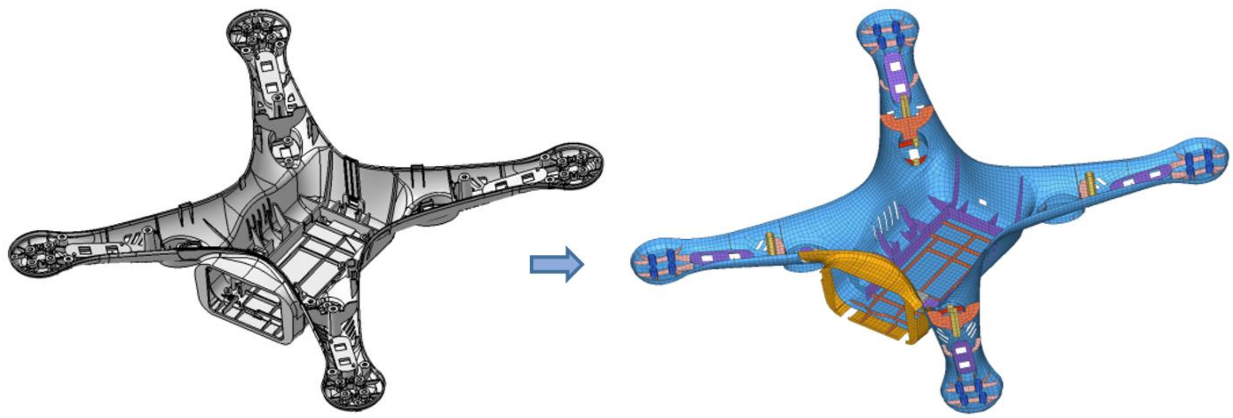

Figure 9. UAS lower body CAD geometry and FE mesh

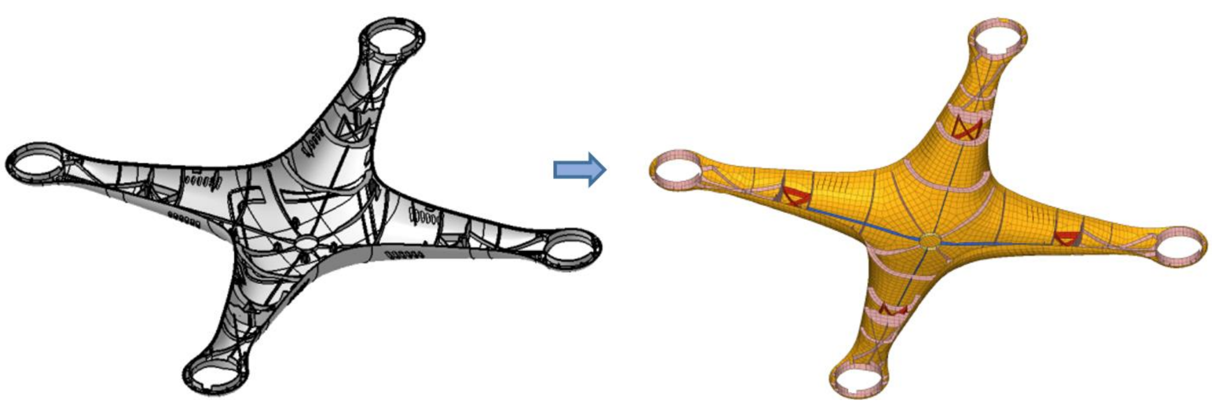

Figure 10. UAS upper body CAD geometry and FE mesh

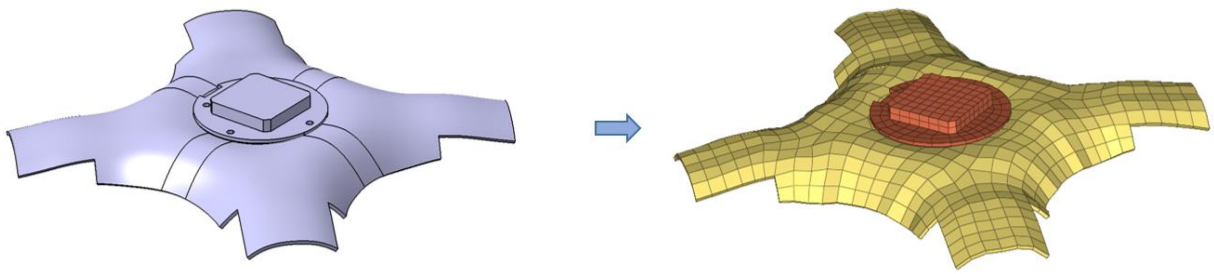

Figure 11. UAS GPS antenna CAD geometry and FE mesh

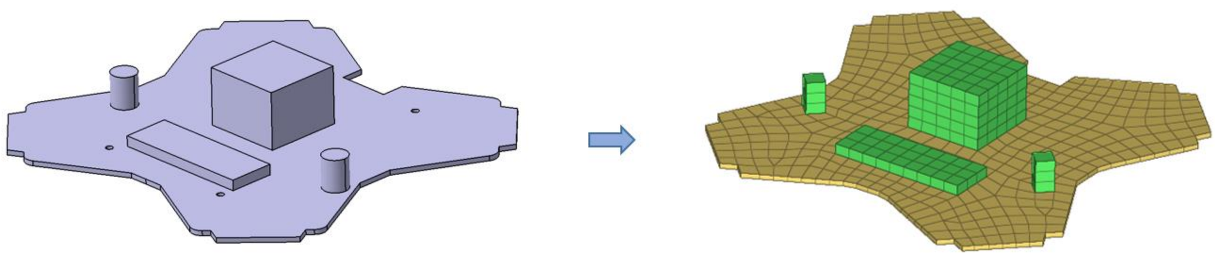

Figure 12. UAS circuit board CAD geometry and FE mesh

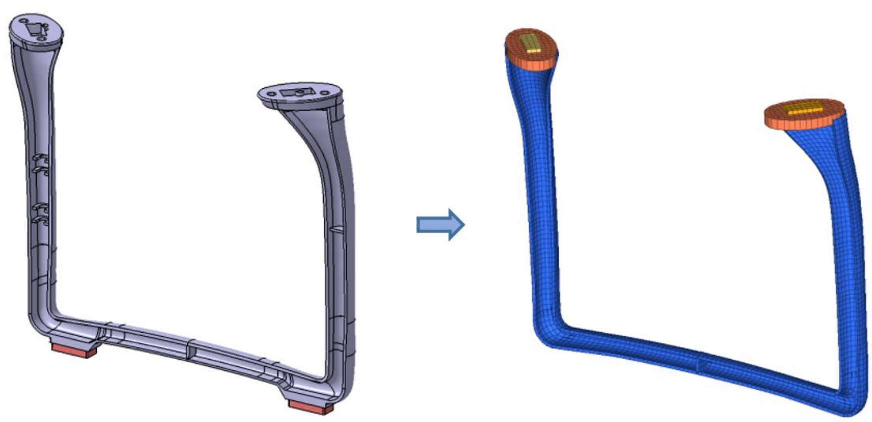

Figure 13. UAS landing frame CAD geometry and FE mesh

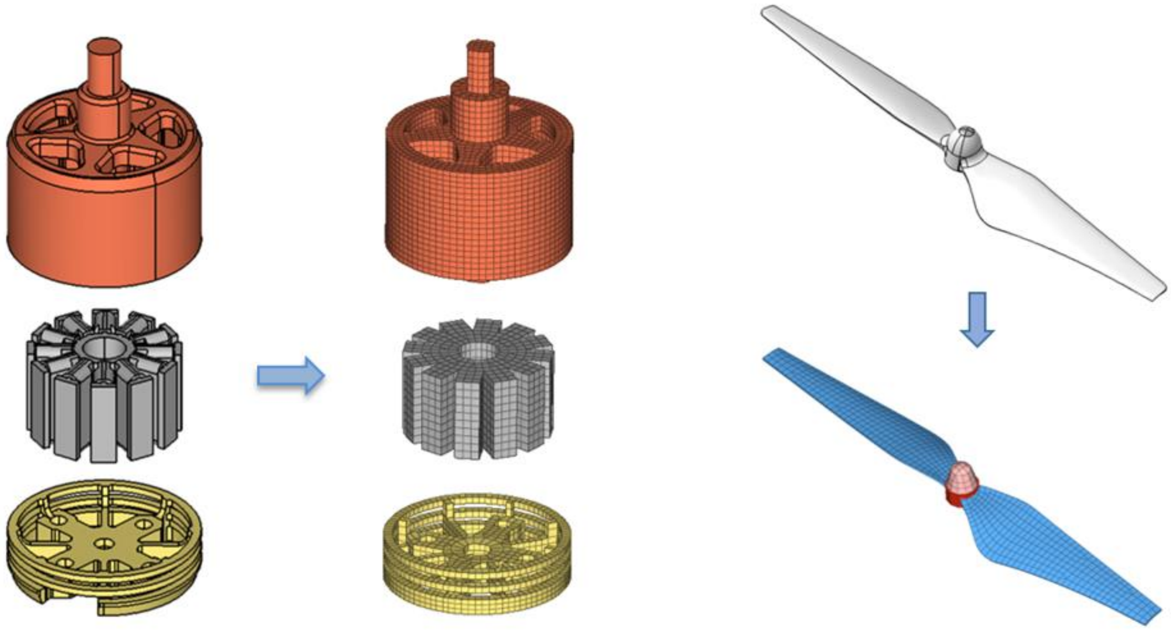

Figure 14. UAS motor and propeller CAD geometry and FE mesh

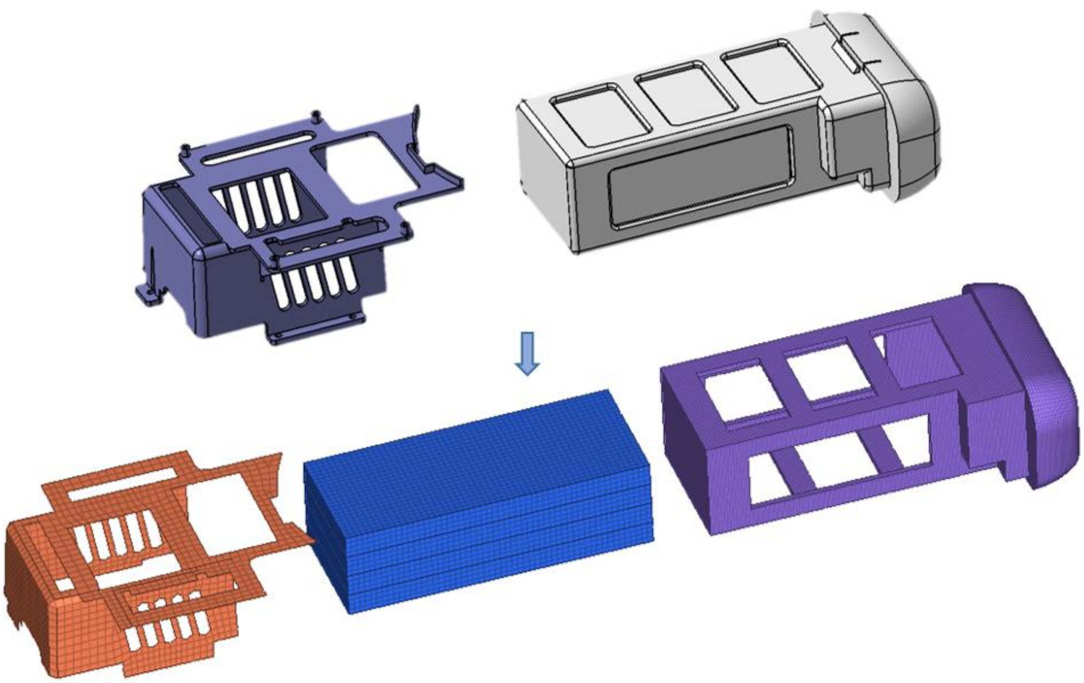

Figure 15. UAS battery CAD geometry and FE mesh

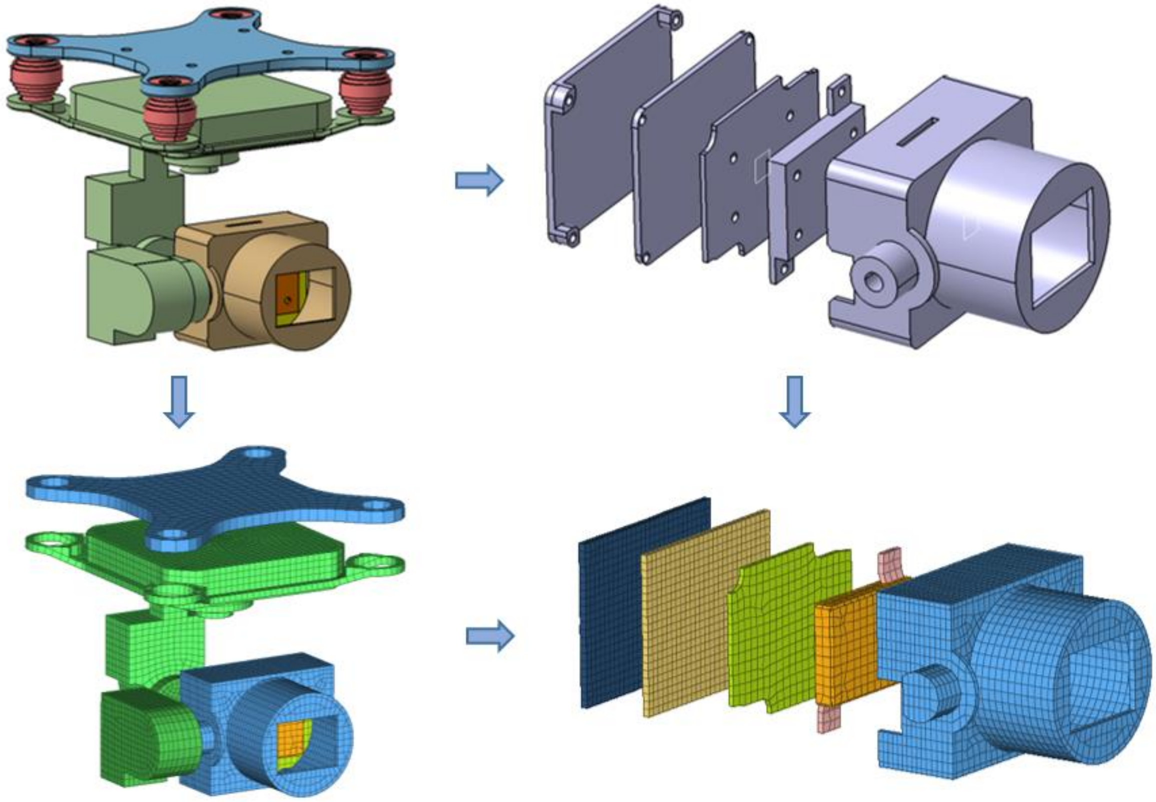

Figure 16. UAS camera and gimbal CAD geometry and FE mesh

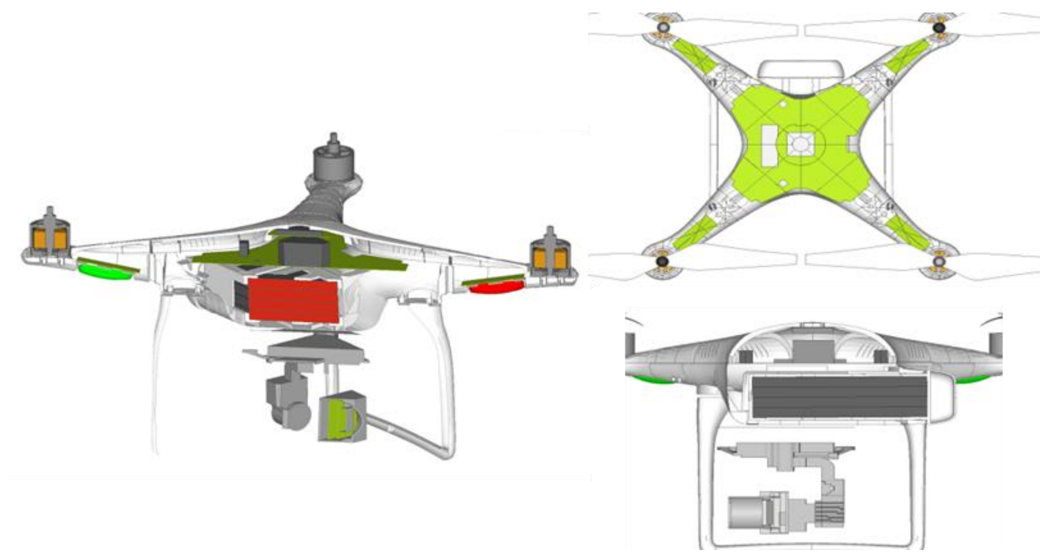

Figure 17. Cross section of full UAS FE model

For the camera/gimbal assembly the major simplifications and assumptions made during the discretization process were:

– The structure, circuit boards, and propellers were modeled with shells (*i.e.* 2D elements).

- Motor winding, gimbal arms, and battery cells were simplified as bulk solids (*i.e.* 3D elements).
- No joints or servomotors were considered for the gimbal mechanism.
- The rubber springs/dampeners that attach the gimbal to the body were modeled with discrete elements (*i.e.* scalar elements).
- The electronic internals were not considered (only its non-structural mass).

Summarizing, the complete FE UAS model is comprised of 137,325 elements and 191,455 nodes. The quality of the mesh was ensured following the criteria presented in the following section.

2.3.1.1 Mesh quality criteria

This section describes the quality criteria used for meshing (See Table 3.) All parameters were strictly checked and registered before approval of the FE mesh for analysis. Some definitions of the parameters are presented below.

Warpage is defined as the angle by which an element or element face (in case of solid elements) deviates from being planar. It only applies to 4-node elements or faces. The procedure to calculate it is by splitting the quad element into four triangular elements along the diagonals, and then the angle formed between the normal of the trias is measured. 15° warpage angle was used as the maximum allowable limit for meshing.

Aspect Ratio is defined as the fraction breadth/height of an element. A maximum of 5:1 is set to avoid instabilities caused by unusual travel of the stress wave through the element.

The *Jacobian* ratio measures the deviation of a given element from an ideally shaped element (*i.e.* all sides equal). It ranges from -1.0 to 1.0, where 1.0 represents the ideal shaped element.

Skew angle is measured as 90 degrees minus the angle formed by two lines joining the mid points of opposite sides of a quad element. It was limited to 60 degrees.

LS-DYNA sets the simulation’s time discretization to the *time-step* required by the element with the smallest time-step of the whole model [21]. Maintaining a numerically stable simulation requires the following equation to be satisfied.

$$\Delta t = \frac{l}{c}$$

Where,

c = elastic wave speed through the material = $(E/\rho)^{1/2}$

l = equivalent length of the element

Therefore, the time-step is a function of each element’s size and the material properties. Consequently, for a given material, a minimum length of the element is required to satisfy the requirement of maintaining the time-step of the simulation above 0.1 microseconds. This value was selected as a limit to make computational times feasible in this project with the available computational power.

Table 3. Mesh quality criteria

Quality Parameter	Allowable Min.	Allowable Max.
Element Size	0.8 mm	5 mm
Aspect Ratio	-	5
Quad Angle	45°	140°
Tria Angle	30°	120°
Warp Angle	-	15°
Jacobian	0.7 (2D Element) 0.5 (3D Element)	-
Time-step	1E-7 s	-

Apart from the quality criteria presented in the previous table, other criteria were followed when meshing in order to generate a good quality mesh for crashworthiness:

- Fillets with a radius of less than 2 mm were defeatured and meshed with sharp-edges.
- Holes with a diameter of 1 mm or less were ignored, and instead a node was placed in the center to allow an aligned connection with the fastener. For bigger holes, at least 6 nodes were placed in the perimeter. Triangular elements (trias) were avoided around the hole.
- A minimum of two elements were kept on flanges to maintain the correct stiffness.
- Whenever possible, at least three elements across thickness were used when meshing with solid elements. If it was not feasible due to the element size constraint, a fully integrated formulation was used instead.
- Triangular elements (or penta in solids) were used for mesh transitions. However, it is important to note that trias exhibit a stiffer behavior than quadrilateral elements (quads). Consequently, the total number of trias in the model was limited to 5%, and any concentration of tria elements was avoided to maintain a homogeneous stress distribution.

2.3.1.2 Element Types

LS-DYNA offers a variety of element formulations for numerical modeling [22]. These elements are categorized as scalar elements, unidimensional (1D), two-dimensional (2D), and three-dimensional (3D). Some properties of the element types selected for the FE model are discussed below.

Scalar Elements

Scalar elements are assigned to individual nodes and are used to represent concentrated masses or spring/damper elements. The different elements of this type used in the UAS FE model were **ELEMENT_MASS* and **ELEMENT_DISCRETE*. The former was used to add non-structural mass (*e.g.* electronics, cables, camera lens, etc.) to a selected node. The latter allows simple modeling of spring-damper systems connecting two nodes.

One-Dimensional Elements

Beam elements are represented in 1-dimension. They can carry axial loads as well as shear forces, bending and torsion moments. A cross section (circular, tube, I-shape, etc.) is required to calculate its area and moments of inertia. Hughes-Liu (*ELFORM* = 1) and Belytschko-Schwer (*ELFORM* = 2) are typically the element formulation theories selected for these elements. This type of elements was used to model bolts and fasteners in the UAS model.

Two-Dimensional Elements

Two-dimensional elements, also known as shell elements, are used to represent thin wall structures. Typically, it is recommended to use shells whenever the thickness is one tenth or less of the equivalent length of the element ($l>10t$). LS-DYNA allows quadrilateral and triangular types of shell elements. Triangular elements show higher (artificial) stiffness than equivalent quadrangular elements, therefore the number of trias was always limited to 5% of the total number of elements in order to ensure minimization of mathematical error.

Belytschko-Tsay (*ELFORM* = 2) was selected as the default under-integrated formulation. For these type of elements, the mass is distributed equally between the nodes, and each node has six degrees of freedom (so it can load in bending). The only input properties required for shell elements are thickness and number of integration points (≥3). A shear correction factor of 0.833 was applied whenever the material was isotropic, as recommended in the Aerospace Working Group (AWG) Guidelines [23]. Under-integrated elements require the control and monitoring of the hourglass energy during the simulation. For some parts (mainly in the UAS body) for which the hourglass energy exceeded the recommended values by the AWG guidelines, the element formulation was upgraded to *fully-integrated* (*ELFOR* = 16), which eliminated any existing hourglass energy. In the UAS FE model, the body, propellers, landing frames, electronic boards and some other minor components were modeled with shell elements.

Three-Dimensional Elements

Tetrahedral (tetra), pentahedral (penta) and hexahedral (hexa) elements are categorized under three-dimensional or solid elements. For them, mass is distributed equally across all the nodes, and can carry tensile, compression and shear loads. The nodes of solid elements have only three degrees of freedom (translational).

Typically, under-integrated element formulation (*ELFORM* = 1) was used to reduce computational cost. However, this formulation requires at least three elements across thickness to properly represent bending stiffness. In some components (*e.g.* motors) this was not possible, so full integrated elements (*ELFORM* = 2 or -1) were considered. The camera, gimbal, motors, and battery were modeled with solid elements to obtain a better behavior of these critical components during impact.

2.3.2 Material Definitions

The process of obtaining material properties and the sources of the information as well as the final material identification are discussed in this section. For the materials for which it was possible, the material was identified with experimental methods. For the rest, the philosophy of selecting a material was identifying materials of similar density, inexpensive and easily available for a consumer product and, in general, that it made engineering sense for the application and consistent with similar products. The description is classified and presented in different subsections depending on the type of material. Figure 19 and Figure 18 show the materials and the material models respectively used for the various components of the UAS.

Code	Material Model	LS-DYNA Model
(blue)	Johnson Cook	*MAT_015
(yellow)	Piecewise Linear Plasticity	*MAT_024
(green)	Enhanced Composite with Damage	*MAT_054
(red)	Crushable Foam	*MAT_063

Figure 18. UAS material models for LS-DYNA solver [24]

Code	Material
(blue)	Polycarbonate
(lime green)	Nylon
(yellow)	Cast Aluminum 520-F
(orange)	Steel 4030
(green)	G-10 Fiberglass (PCB)
(red)	Li-Po Battery Cell
(light blue)	Aluminum Film 1145-O

Figure 19. UAS materials

2.3.2.1 Structural Plastic

The body, main structural components, and propellers of the UAS are constructed of plastic materials. The different polymers were identified performing a Fourier Transform Infrared Spectroscopy (FTIR) test at the facilities of the NIAR. FTIR analysis method uses infrared light to scan test samples for collecting spectral data and then match it with a database of common materials. The results identified the following polymers.

- Polycarbonate. Present in the main body, landing frame, internal structure, and gimbal arms.
- Nylon 6/6. This polymer was present in the propellers.

The plots output from the FTIR test are presented in Figure 20.

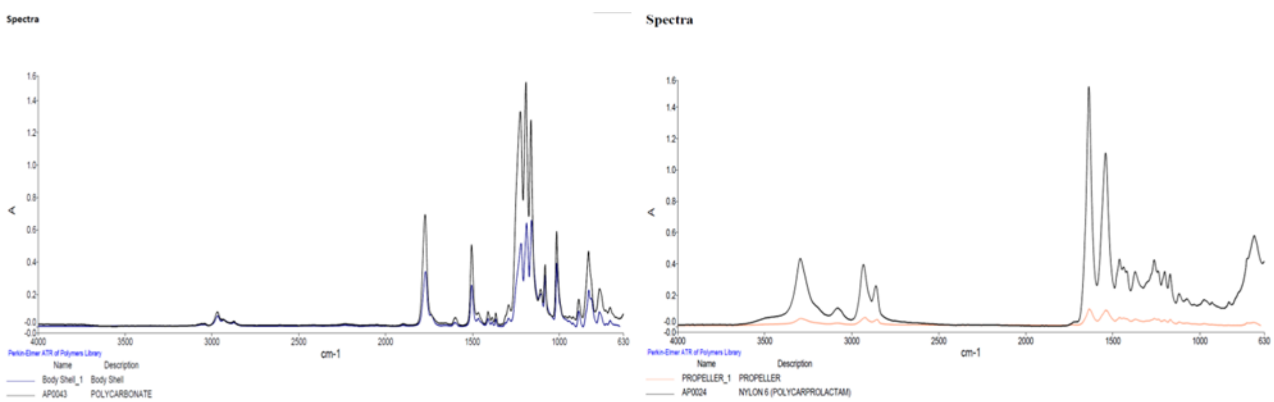

Figure 20. FTIR plots for polycarbonate and nylon 6

The mechanical properties of polycarbonate polymer were obtained from a report of the Army Research Laboratory [25]. This report presented the parameters of a Johnson-Cook constitutive model that was fit to experimental data from tensile and compression tests at different temperatures and strain-rate levels. **MAT_JOHNSON_COOK* was selected as the most appropriate material card from LS-DYNA [24] to represent the polycarbonate, because most of the input parameters were available from the report. This advanced material model is capable of capturing not only elastic and plastic deformation but also strain-rate and temperature effects in the behavior of the material. The parameters are summarized in Table 4.

Table 4. Material properties and Johnson Cook parameters of polycarbonate polymer

Density *(kg/m^3)*	Modulus of Elasticity *(GPa)*	Shear Modulus *(GPa)*	A *(MPa)*	B *(MPa)*	C	m	n	C_v *(KJ/kgK)*	Tmelt *(K)*
1197.8	2.59	0.93	80	75	0.052	0.548	2	1.3	562

The failure criteria was set initially to 70% tensile elongation, and later calibrated with two component level tests conducted in NIAR facilities. This process is presented in Section 2.4

2.3.2.2 Metallic Alloys

Typically, brushless motors for sUAS applications are constructed with an aluminum alloy rotor and a laminated steel core with copper wire winding. Because the FE model was simplified to just capture the aluminum rotor and the steel core stator, only those two materials were needed.

The aluminum body of the motor and camera for this type of applications is typically made of casting alloy A520.0-F, according to a market research performed for this project. The mechanical properties of the alloy were obtained from MMPDS [26] and input to a **MAT_PIECEWISE_LINEAR_PLASTICITY* material card of LS-DYNA [24]. In addition, the steel stator was assumed to be of the alloy AISI 4030. Properties were obtained from MMPDS.

2.3.2.3 Electronic Printed Circuit Board

The electronic boards of the UAS typically consist of a Printed Circuit Board (PCB) to which other electronic components (*e.g.* capacitors, chips, etc.) are connected). In the FE model, only the PCB was modeled as a structural member. It was assumed that the rest of the elements would add little stiffness, and only the mass of was considered and applied as non-structural masses.

It is common that PCBs of the consumer industry are manufactured in a glass fiber-epoxy composite laminate covered with a copper layer. A typical composite laminate for this application is G-10. Ravi-Chandar and Satapathy [27] present the mechanical properties of G-10, which were determined from compression and tension quasi-static tests. The properties presented in the publication are summarized in Table 5.

To model the G-10 composite, a **MAT_ENHANCED_COMPOSITE_DAMAGE* was used from the LS-DYNA material model library [24]. The properties given in the table were input directly to the material card and applied to the PCB components of the FE model.

Table 5. Material properties of G-10 glass-epoxy composite for PCB components

Density *(kg/m^3)*	Young's Modulus *(GPa)*		Compressive Strength *(MPa)*		Tensile Strength *(MPa)*		Shear Modulus *(MPa)*	Shear Strength *(MPa)*	Poisson's Ratio	
	X	Y	X	Y	X	Y			XY	XZ/YZ
1850	18.83	19.26	365	300	233	310	8,275	152	0.136	0.118

2.3.2.4 Battery Cells

The cells of the UAS battery are constructed using lithium-ion polymer (LiPo) technology. Based on the information published by Sahraei, Meier and Wierzbicki [28][29], a **MAT_CRUSHABLE_FOAM* [24] material card was setup to represent bulk behavior of the battery cells. Table 6 shows the parameters specified in the paper and used for the battery cells of the UAS in this research project.

Table 6. Battery cells properties

Young's Modulus *(MPa)*	Poisson's Ratio	Density *(kg/m^3)*
500	0.01	1755

LS-OPT, an optimization software developed by LSTC [30], was used to fit some parameters in the material card to obtain greater correlation between the test and simulation. More details about this study can be found in Section 2.4.1 .

Additionally, the aluminum pouch covering each of the battery cells was modeled with the alloy 1145-O, typical for aluminum foil applications. The mechanical properties of the alloy were obtained from ASM handbook [31] and input to a **MAT_PIECEWISE_LINEAR_PLASTICITY* material card of LS-DYNA [24].

2.3.3 Connections

Several modeling techniques were used in the UAS FE model to represent connections (*e.g.* fasteners, bolts, etc.) between different components. A description of the different methods used is given below.

- Nodal Rigid Body (**CONSTRAINED_NODAL_RIGID_BODY*): connection made by linking the degrees of freedom of a set of nodes to an independent node, typically in the center of the hole (e.g. spider). For this method, the holes must be modeled. See Figure 21.

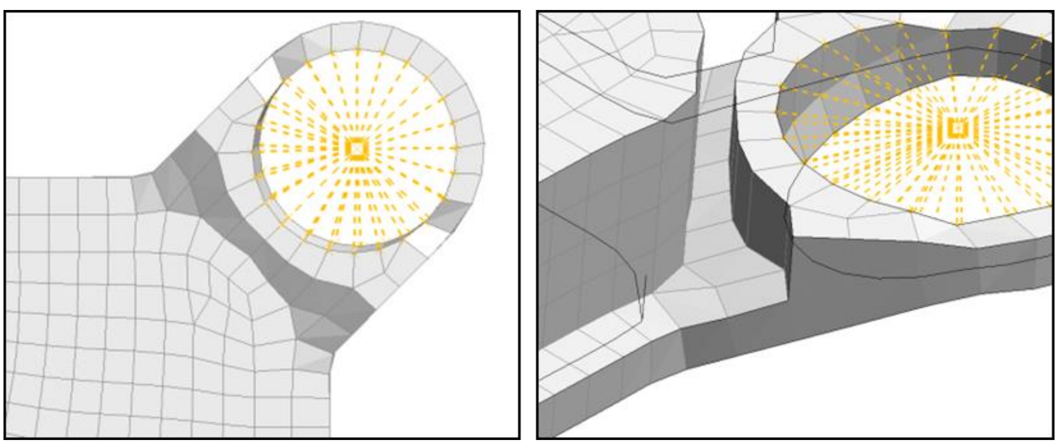

Figure 21. Nodal rigid body connection

- Spot-weld: links the degrees of freedom of two nodes with a rigid bar. In this model, it was used to represents non-critical bolts. The hole can be replaced with a node in the center when discretizing. See Figure 22.

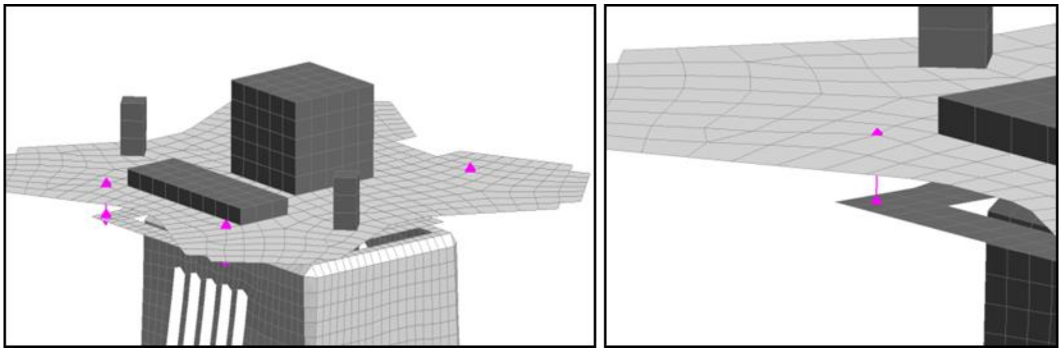

Figure 22. Spot-weld connection

- NRB + Beam element: the first method is used to link the degrees of freedom of each of the holes with the respective extremes of the beam (for the bolt). See Figure 23.

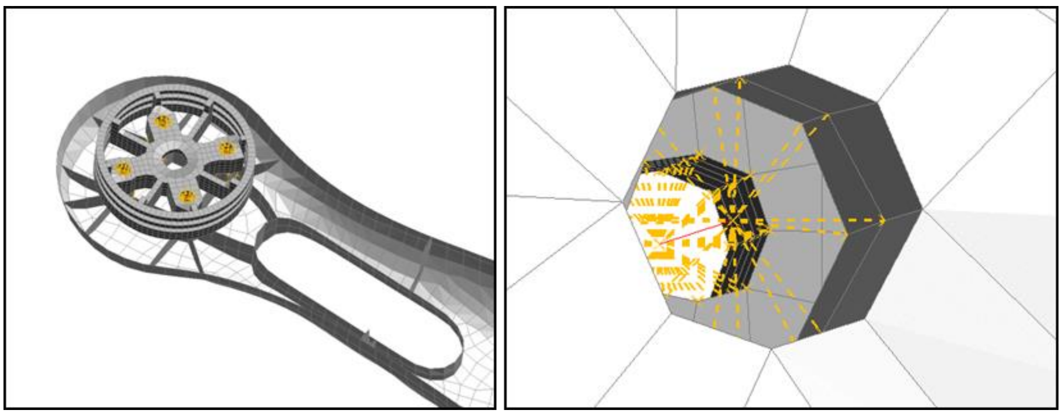

Figure 23. NRB + Beam element connection

- NRB + Element-Spring: Similar to the previous, but the beams are replaced with spring elements. This connection was used to replicate the spring-damper system, which stabilize the camera gimbal against vibrations. See Figure 24.

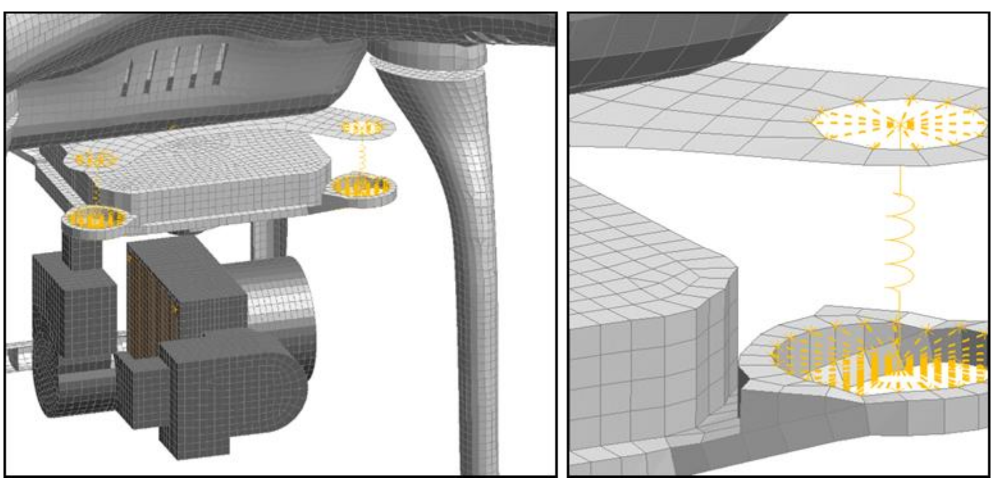

Figure 24. NRB + Element-Spring connection

Figure 25 shows the overall view of the UAS connections, while Table 7 summarizes the amount of each type of connection used in the UAS FE model.

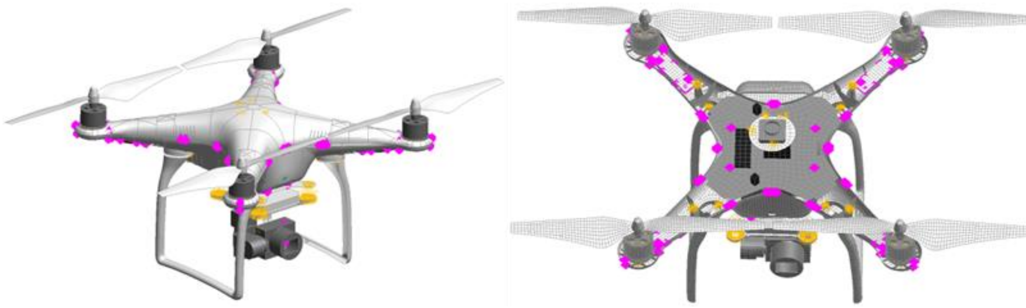

Figure 25. Summary of UAS connections

Table 7. Summary of UAS connections, by type

Spot-weld	**NRB**	**NRB + Beam**	**NRB + Spring**
94	27	16	4

2.3.4 Contact Modeling

Contact modeling is an important aspect in the FE modeling of a dynamic event, such as a mid-air collision. The results of the simulations are highly sensitive to the correct modeling of contact forces and friction energies between different components. The different algorithms offered in LS-DYNA are described the manual [21][22].

In the simulations carried out for this report, the UAS had its own independent contact definition. **CONTACT_AUTOMATIC_SINGLE_SURFACE* was selected as the most appropriate option to keep the contact simple. This contact algorithm automatically detects proximity between elements (either shells or solids) and produces a normal contact force applied at the respective nodes to avoid penetration. This force is proportional to the stiffness of the contact, which is estimated following two different approaches, penalty based and soft constraint approach, which are described below. In addition, because dynamic and static coefficients of friction were considered, a proportional tangential force is created simultaneously.

The penalty-based method is the default in LS-DYNA's contact card for the contact stiffness calculation. The calculation is dependent on the material model and the size of the parts in the contact list. This method is a good option when parts in the contact are constructed of similar materials. If very hard materials, such as metals, are in contact with softer materials, such as foam, then there is a chance of contact failure.

The soft constraint based method is dependent on the global time step and the mass of the nodes in the contact segments. As it is not dependent on material constants, it is a good option for the treatment of contact between materials with dissimilar stiffness properties, as in the UAS FE model. Therefore, this method was selected for the UAS internal contact.

The friction coefficients were defined following common simulation standards and later calibrated with the help of the component level tests conducted, details of which are given in Section 2.4.2 . The thicknesses of shells were considered in the contact by activating the respective parameter in the control card.

2.3.5 UAS Mass Sanity Check

In this section, the mass of the different components of the UAS FE model is compared against the actual physical parts as a sanity check to ensure the FE model is accurate. The total mass of the FE model was calculated as 1215.5 g, that if compared to 1216 g for the actual UAS it represents a 0.04% deviation.

The following figure depicts the CG for the UAS FE model.

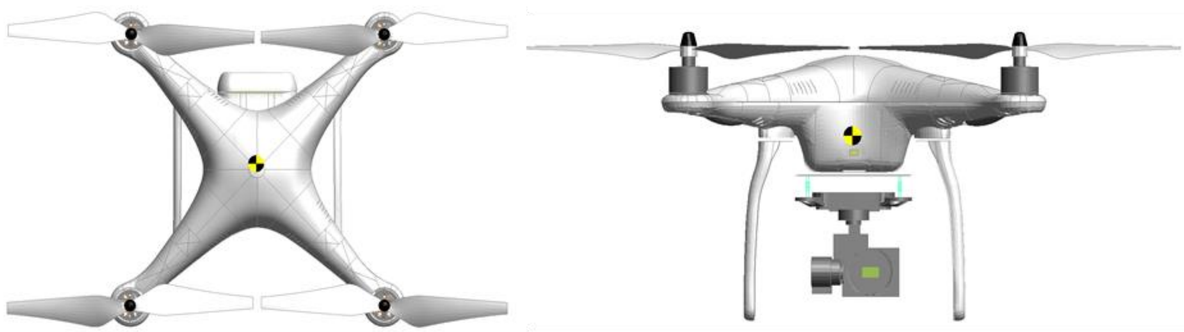

Figure 26. UAS FE model center of gravity

2.4 UAS COMPONENT LEVEL TESTS AND VERIFICATION

This section presents a description of the various component level tests performed and of the procedure followed to verify the FE model by correlation to the physical testing. For each of the tests, a simulation was set up with the same conditions (initial conditions, boundary conditions, etc.) as the physical test and the same parameters were output for comparison and correlation with test results.

2.4.1 Battery Test

The publications by Sahraei, Meier and Wierzbicki [28][29] present the results of mechanical testing performed on LiPo batteries. Battery cells of three sizes were subject to face compression and punch indentation tests. The dimensions specified for the medium size battery cell in this publication were of similar magnitude to the battery of the UAS. For each test, the publication included load displacement time histories. The information available in both publications allowed replicating the tests with FE simulation.

Initially, the parameters for the respective LS-DYNA card suggested in the publication were used: fully integrated solid elements, a crushable foam material model (*MAT_063*) with properties for stress-strain curve, Poisson's ratio, density, and failure. Both lateral compression and punch indentation tests were replicated. The results are presented in sections 2.4.1.1 and 2.4.1.2, respectively.

Finally, some parameters were calibrated using optimization software (LS-OPT), so a much better level of correlation was achieved. The process and results of the fitting is shown in section 2.4.1.3

2.4.1.1 Lateral Compression Test

In order to replicate this test, a simulation was setup with rigid walls on both sides of the battery cell. One of the rigid walls was fixed while the other was assigned a prescribed motion of 3mm/min for the compression. The load was measured as a reaction on the fixed rigid wall. The setup as well as the results of the compression test and simulation are shown in Figure 27.

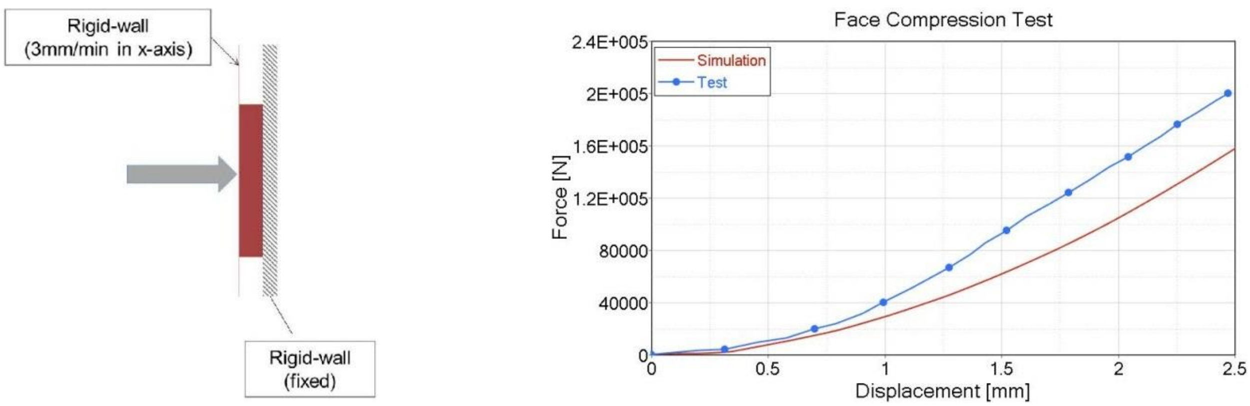

Figure 27. Lateral compression test and simulation setup and results for battery model verification

2.4.1.2 Punch Indentation Test

The same material model was used in this test simulation. A fixed rigid wall was set on the bottom face of the battery cell. On the other side, a rigid sphere of 12.7 mm diameter was set with a prescribed motion of 3 mm/min. The setup and the results for the simulation and test are shown in Figure 28.

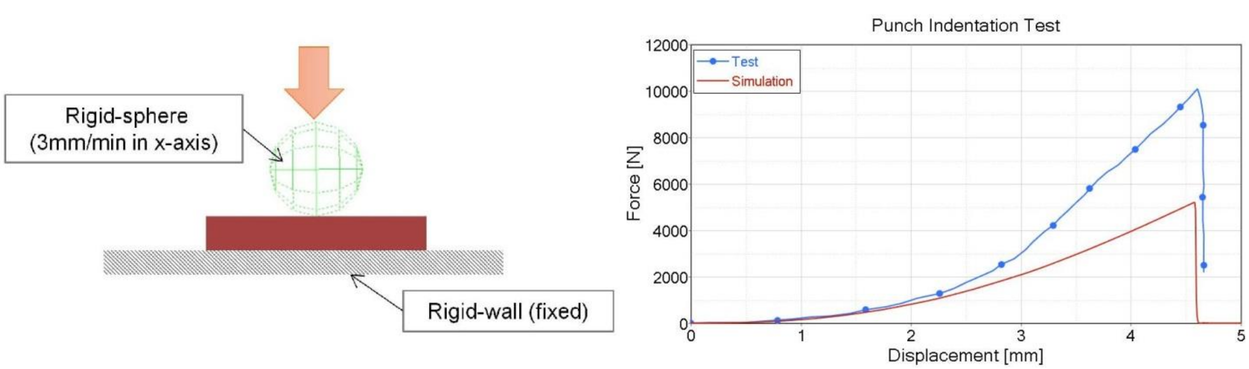

Figure 28. Punch indentation test and simulation setup and results for battery model verification

2.4.1.3 Material fitting with LS-OPT

From the results obtained for both tests, it was observed that the load obtained from the simulation was much lower than the load from the test data from the publication. Consequently, it was decided to calibrate the material card to achieve a better match of the tests by using LS-OPT, which is an optimization software, offered as a part of the LS-DYNA package [30]. For the compression test, a factor multiplying the stiffness curve was used as variable while for the punch indentation test, the failure strain and the tensile cut-off value were selected.

The objective of these two optimizations was to fit the simulation force-displacement curves with the respective data from the tests by calibrating the values of the three input variables. The optimization algorithm utilized a metamodel method with second order polynomial fitting. The approximation was achieved by minimizing the mean square root error between the test and simulation curves.

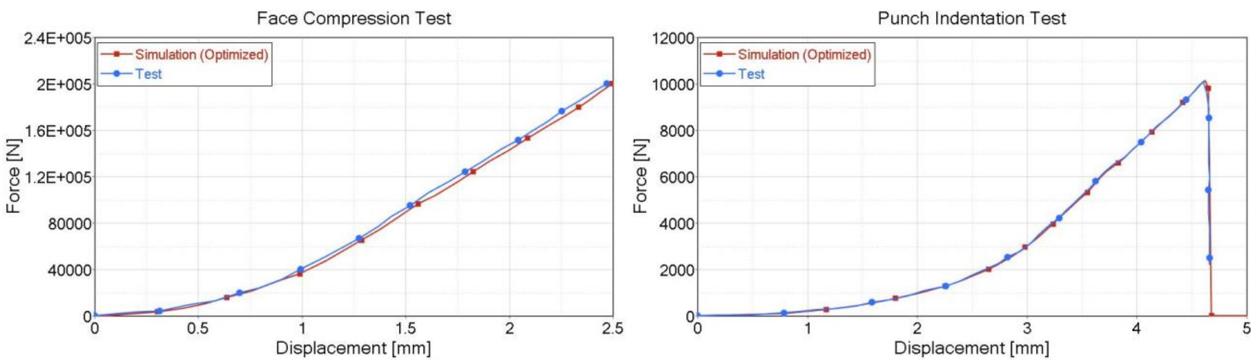

Figure 29. Results after optimization for battery model verification

Figure 29 shows the optimized simulation curve, which shows a much higher level of correlation with the test results, achieving mean square errors of less than 0.5% in both cases. The maximum load peak is perfectly predicted for the punch indentation test. Consequently, the battery FE model was considered verified.

2.4.2 Drop Tower Test

This section provides a brief review of the vertical drop tower test performed on the UAS upper body followed by the verification of the UAS material model. The objective of this test was to verify the FE modeling of the plastic body of the UAS. To achieve this, the test was set up so it would drop an impactor on the UAS body. The upper part of the body was selected to be impacted, as it is more symmetric and therefore simpler to design a setup. The test results obtained were used to replicate the test by simulation, and helped verifying the FE model of the UAS body by correlating the simulation to the test.

2.4.2.1 Test Setup

To maintain the UAS body restrained to the plate, each of the four arms of the UAS were fixed, as shown in the left image of Figure 30, to ensure the arm would not slip along the plate. The right image shows the drop tower equipment used for this test, which integrated both impactor and instrumentation to measure reaction loads and displacements.

The body was aligned so the impactor would contact the center of the UAS body, as it is illustrated in the left image of Figure 31. Two different high-speed cameras were set up as shown in the right image of Figure 31 to capture the kinematics of the event.

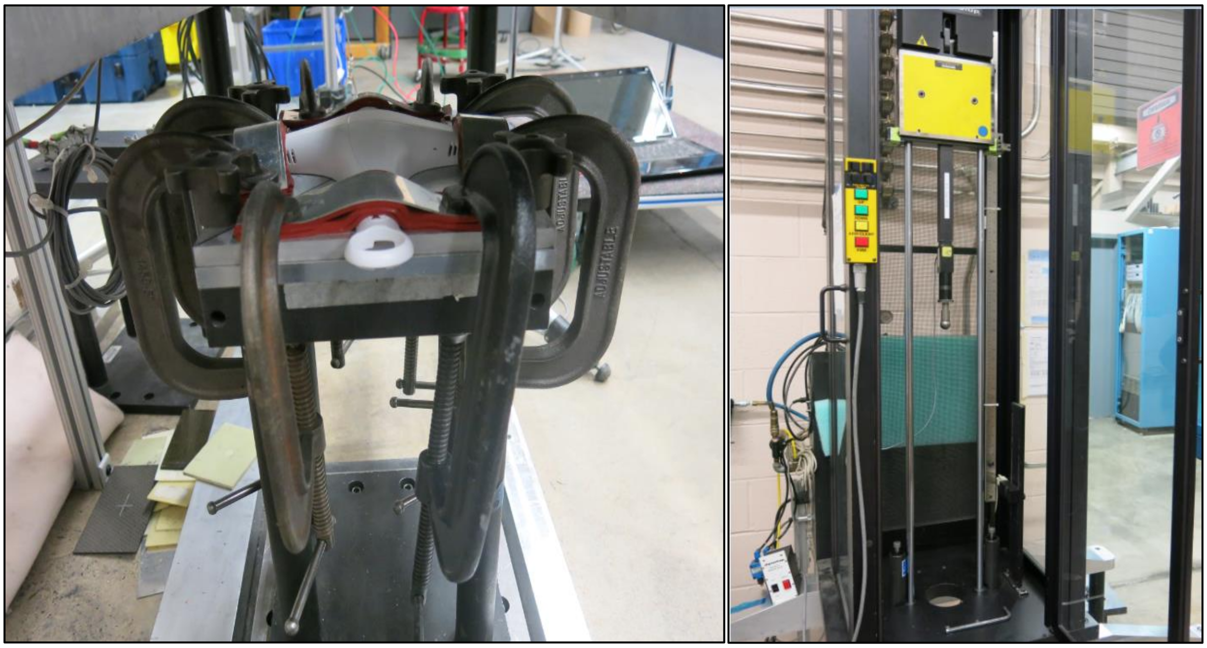

Figure 30. UAS body fixture (left) and test frame (right) for vertical drop tower test

2.4.2.2 Test Equipment

The following equipment was necessary to conduct the test and record the data.

I. Drop tower:

The drop tower is composed of a steel spherical impactor attached to a mass. The drop height along with the preselected mass define the impact energy of the test. Note that the impactor diameter was selected to ensure failure on the plastic, based on the results preliminary simulations. The equipment had embedded instrumentation to measure and register the time history of load reactions and displacements of the impactor at 80 kHz.

The configuration selected for the test conducted is presented in Table 8.

Table 8. Impactor characteristics

Diameter *(mm)*	Mass *(kg)*	Impact energy *(J)*
19	13	110

II. High speed video cameras:

Two high-speed cameras were placed on the side and bottom of the impact location to record the event at 500 frames per second. The right image on Figure 31 shows the positioning of the two cameras.

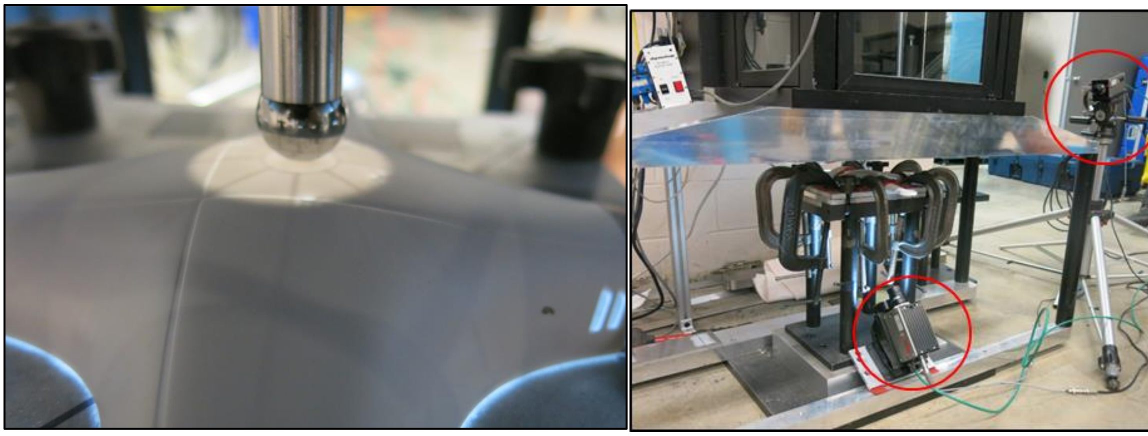

Figure 31. Impactor lined up with the center of UAS body (left) and high speed camera setup for vertical drop tower test (right)

2.4.2.3 Test Results

Failure of the polycarbonate shell occurred after the impact event. As shown in Figure 32, the impactor penetrated and fractured the UAS body. Furthermore, the adapter used for attaching the impactor to the tower also penetrated the body. The force-displacement plots for this test along with the results acquired from the simulation are compared in the following subsection.

Figure 32. Drop tower test results

2.4.2.4 Verification

A simulation was set up with the upper body or the UAS FE model to replicate the test initial and boundary conditions described in the previous section. To achieve so, a plate was modeled using the same dimensions and properties. The UAS body was rigidly connected to the plate using nodal rigid bodies (NRB) to replicate the clamps. The impactor was modeled with the same geometry and mass as used in the test. The initial velocity of the impactor measured in the test was assigned to it as initial condition. The friction coefficient between the impactor and the body was calibrated with the help of an iterative process, and later used for the final UAS model.

Figure 33, Figure 34, Figure 35 and Figure 36 show the comparison between the kinematics of test and simulation. The simulation was able to capture not only the kinematics (and deformations) of the event, but also to predict the failure of the polycarbonate shell at the same instance of time and with a very similar failure mechanism as the physical test.

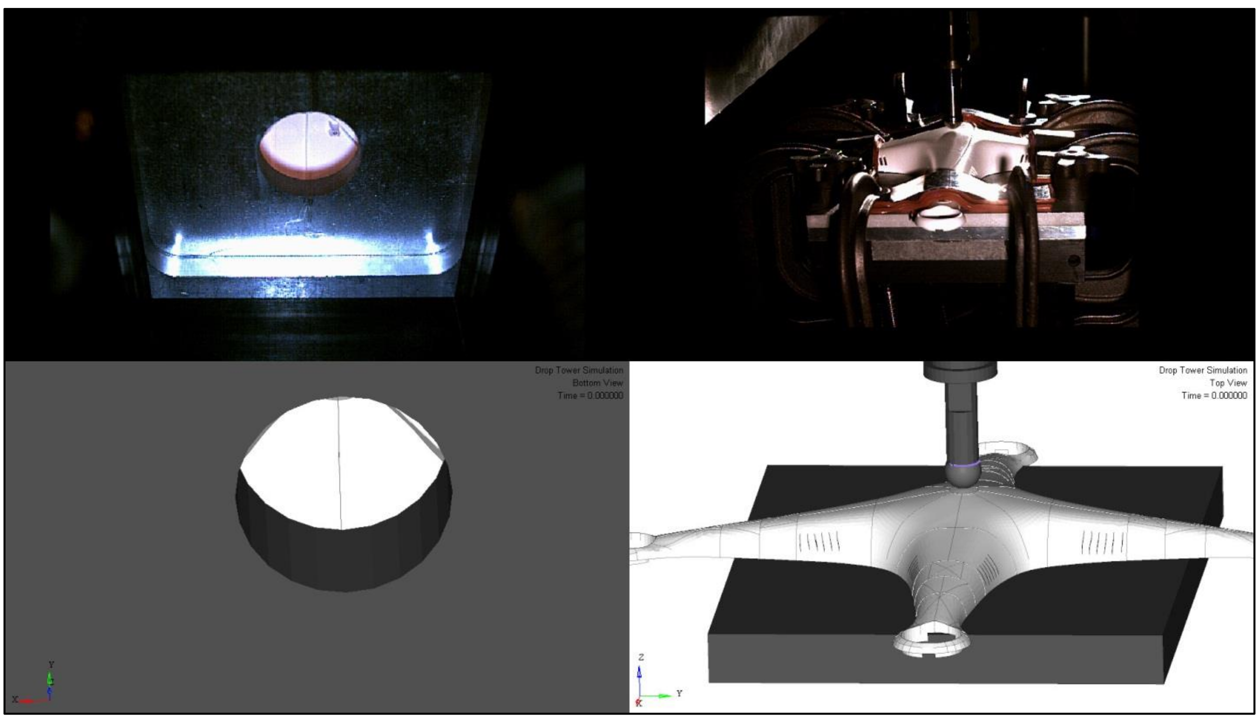

Figure 33. Drop tower test FE model verification - Kinematics comparison at t = 0 ms

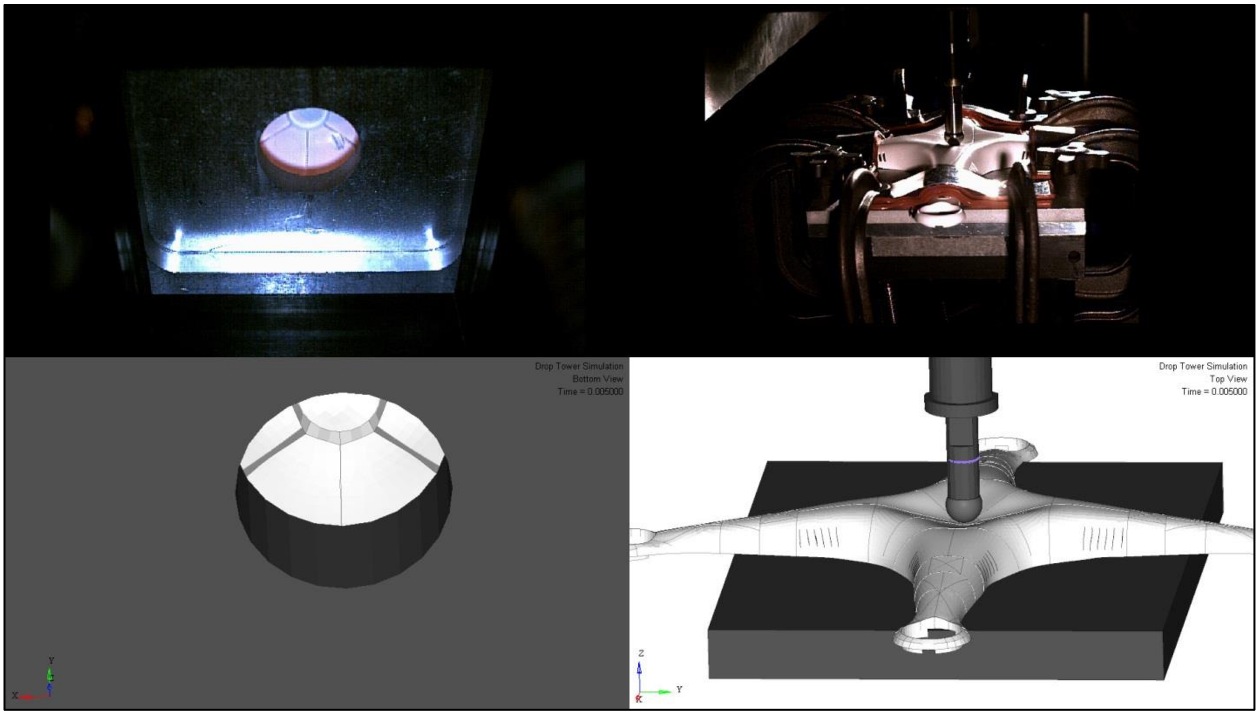

Figure 34. Drop tower test FE model verification - Kinematics comparison at t = 5 ms

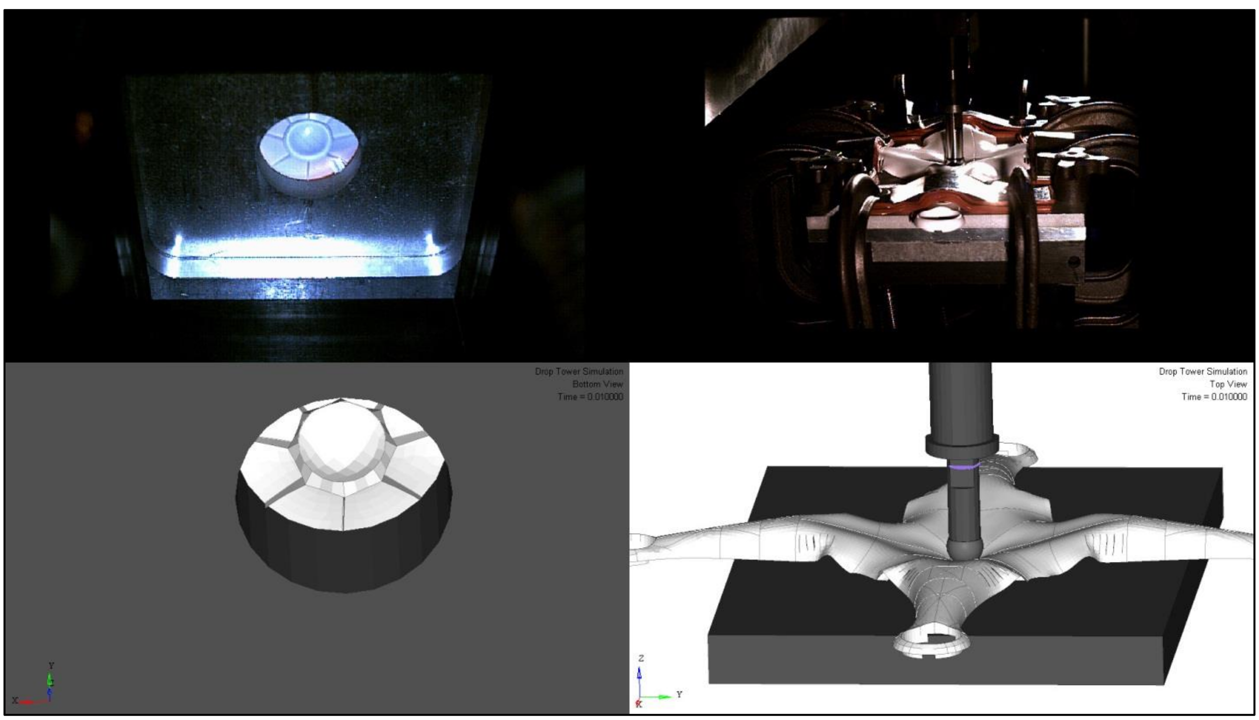

Figure 35. Drop tower test FE model verification - Kinematics comparison at t = 10 ms

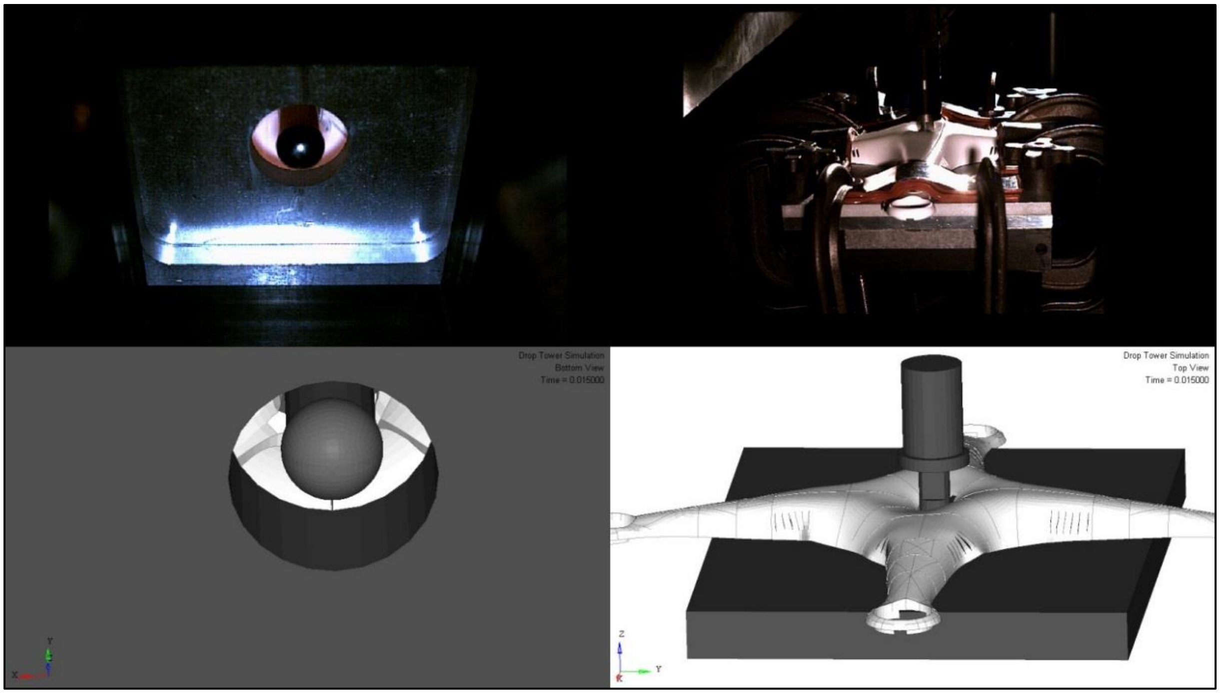

Figure 36. Drop tower test FE model verification - Kinematics comparison at t = 15 ms

Figure 37 presents a comparison of the load cell data recorded in the test and the reaction load measured in the simulation. The impulse was derived from both curves by integrating the respective force time history.

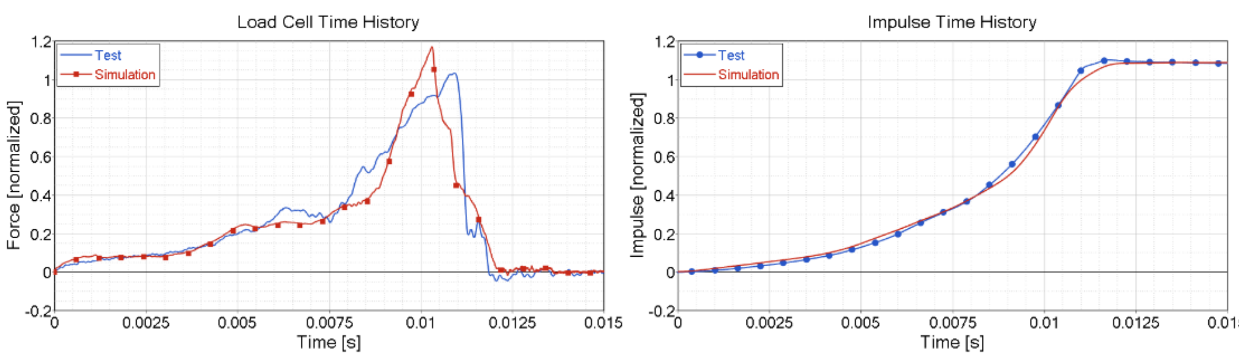

Figure 37. Drop tower test FE model verification - Reaction force and impulse comparison plots

From the comparison between simulation and test results, both in terms of kinematics and instrumented measurements, it can be inferred that there was high correlation between the test and simulation. Consequently, the polycarbonate FE model defined for the UAS can be considered accurate and therefore verified.

2.4.3 Free-fall Drop Test

This section provides a description of the free-fall drop test performed on the UAS followed by the verification of the UAS material model. The objective of this test was to assess the behavior of the full UAS assembly FE model (no battery) under low velocity impact loads by correlation with the physical test. This was achieved by dropping the entire UAS assembly on a rigid plate.

2.4.3.1 Test setup

The battery and camera were removed from the UAS and a lead ballast mass of 1.36 kg (3 lb) was placed in the battery housing to increase the overall weight and force greater damage on the UAS structure. The mass of the UAS structure after adding ballast measured 2.03 kg (4.49 lb). Figure 38 shows the ballast inside the battery compartment.

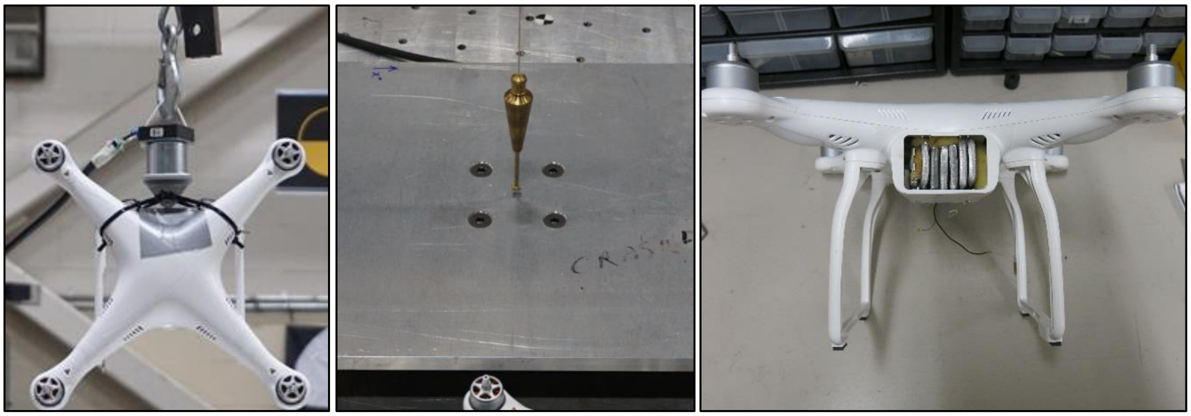

Figure 38. UAS release mechanism (left), alignment with plate (center) and lead ballast (right)

The UAS was suspended and dropped from a height of 5.18 m (17 ft). It was connected to the suspension cable through a magnet that was triggered to release the UAS at the beginning of the test, as shown in the left image of Figure 38. The cable was attached close to the center of gravity of the quadcopter to ensure a proper alignment and avoid rotations during the free-fall. A rigid plate was placed below the UAS with a load cell at the center to capture the reaction forces after impact. It was ensured the UAS was perfectly aligned with the center of the plate, see Figure 38.

2.4.3.2 Test Equipment

The following equipment was necessary to conduct the test and record the data.

I. Load cell force gage of a range of 5000 lbf (22,241 N) and sampling rate of 20 kHz.
II. Three high-speed video cameras placed around the setup to record the event at 500 frames per second. Figure shows the positioning of the three cameras.

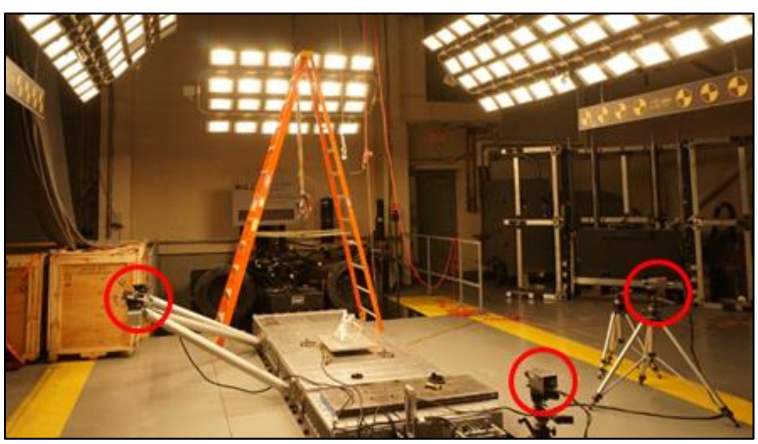

Figure 39. High speed camera setup for free-fall drop test

2.4.3.3 Test results

After being released from a height of 5.18 m (17 ft), the UAS hit the plate and one of the legs experienced failure. The maximum force recorded by the load cells was of 2,833 N (637 lbf). Figure 40 shows the UAS after impact. Mainly the plastic legs sustained permanent deformation. The results for this test are compared with the simulation in the following subsection.

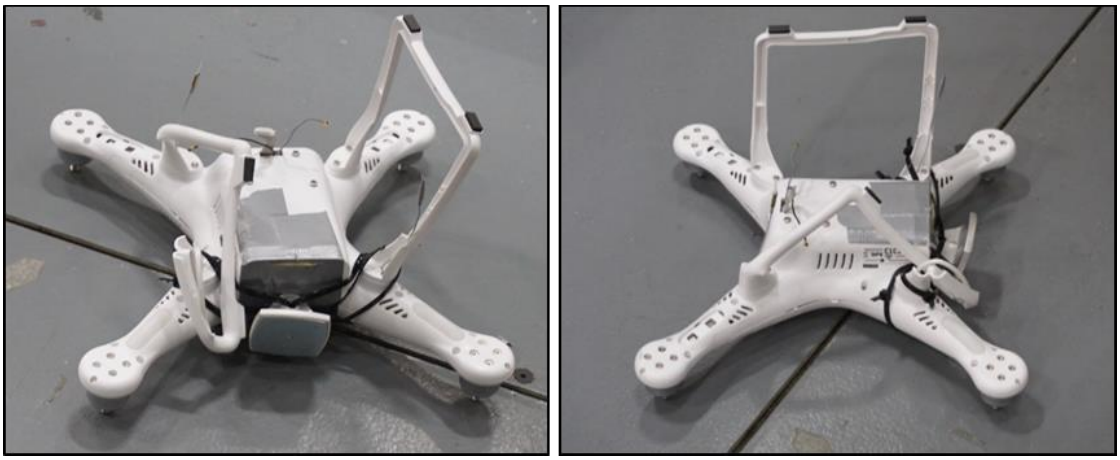

Figure 40. Free-fall drop test results

2.4.3.4 Verification

The FE model of the UAS was subjected to a drop with the same configuration and initial conditions as the physical test for its verification. A lead ballast was modeled in place of the battery cells. Figure 41 to Figure 44 show the comparison between the test and simulation at various instances of the impact.

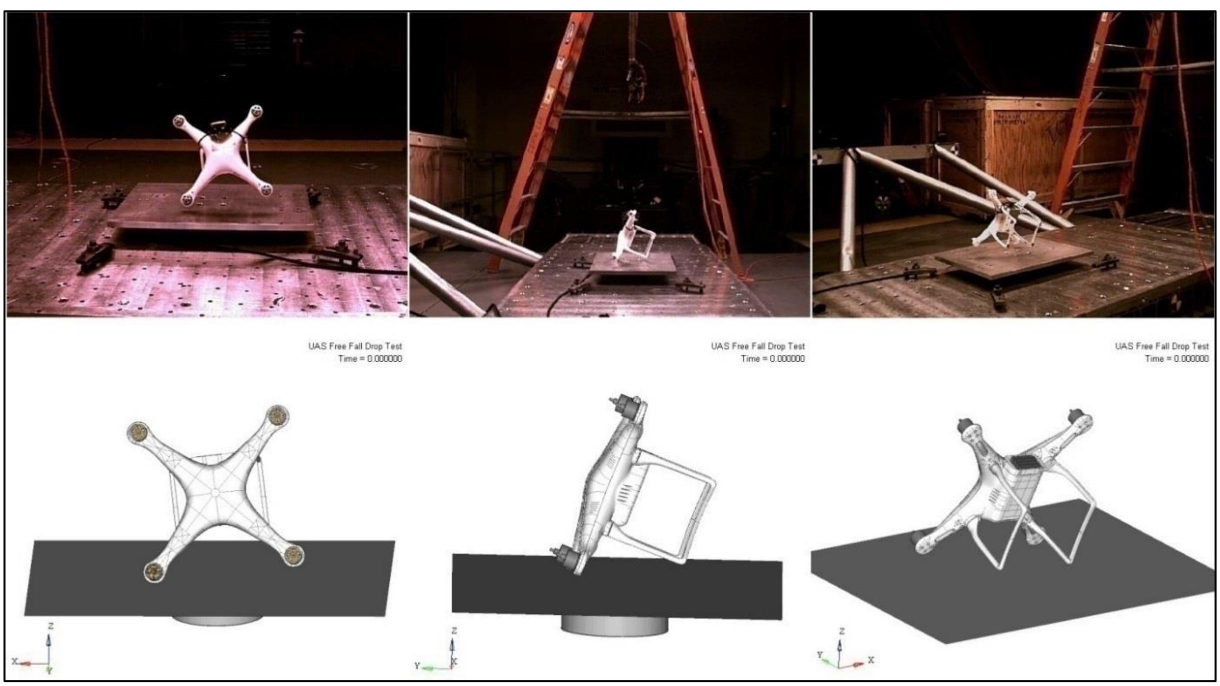

Figure 41. Free-fall drop test FE model verification - Kinematics comparison at t = 0 ms

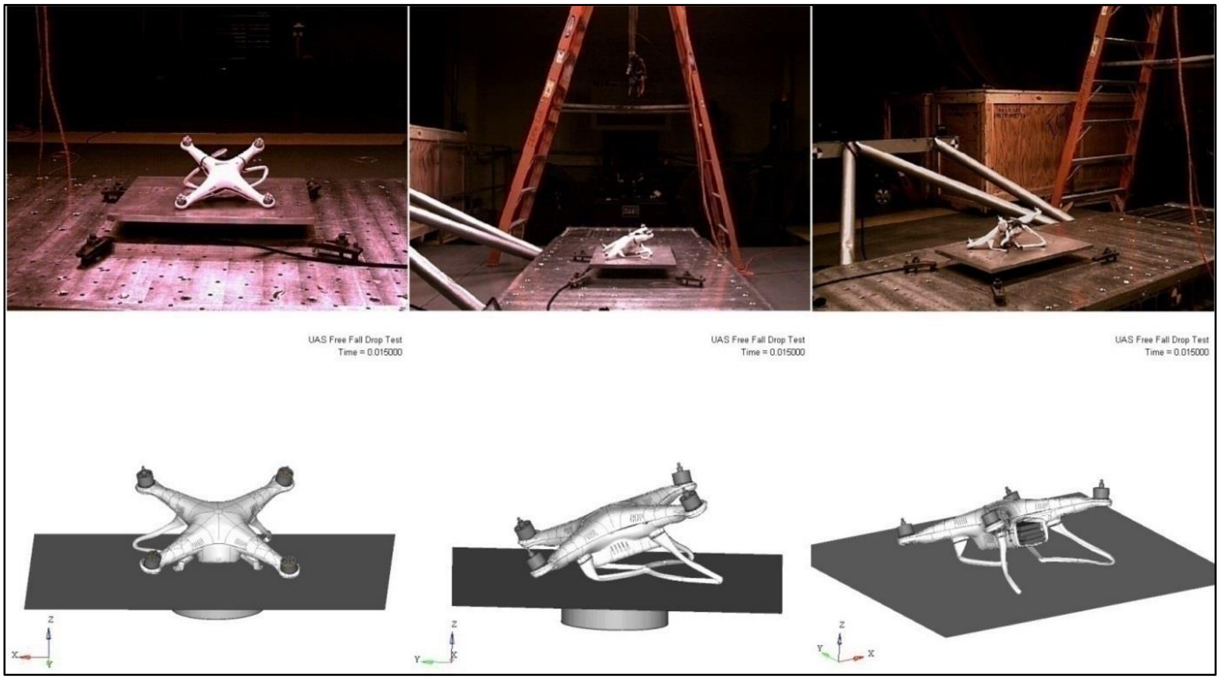

Figure 42. Free-fall drop test FE model verification - Kinematics comparison at t = 15 ms

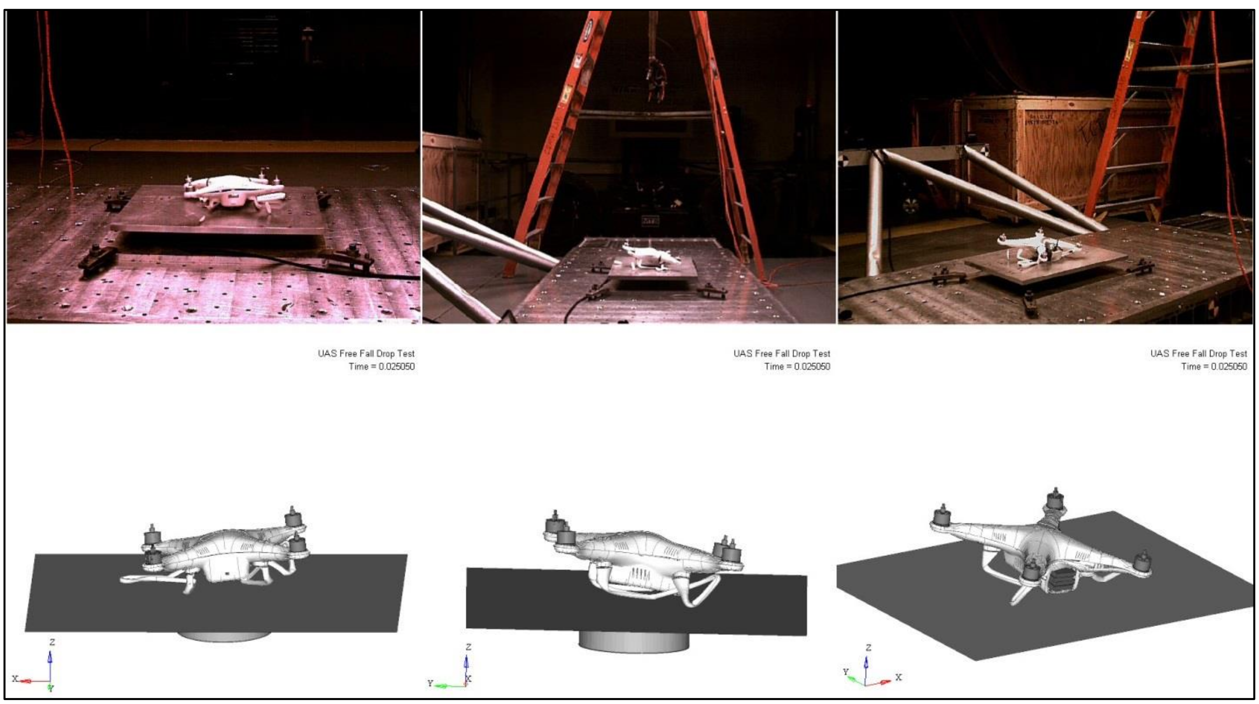

Figure 43. Free-fall drop test FE model verification - Kinematics comparison at t = 25 ms

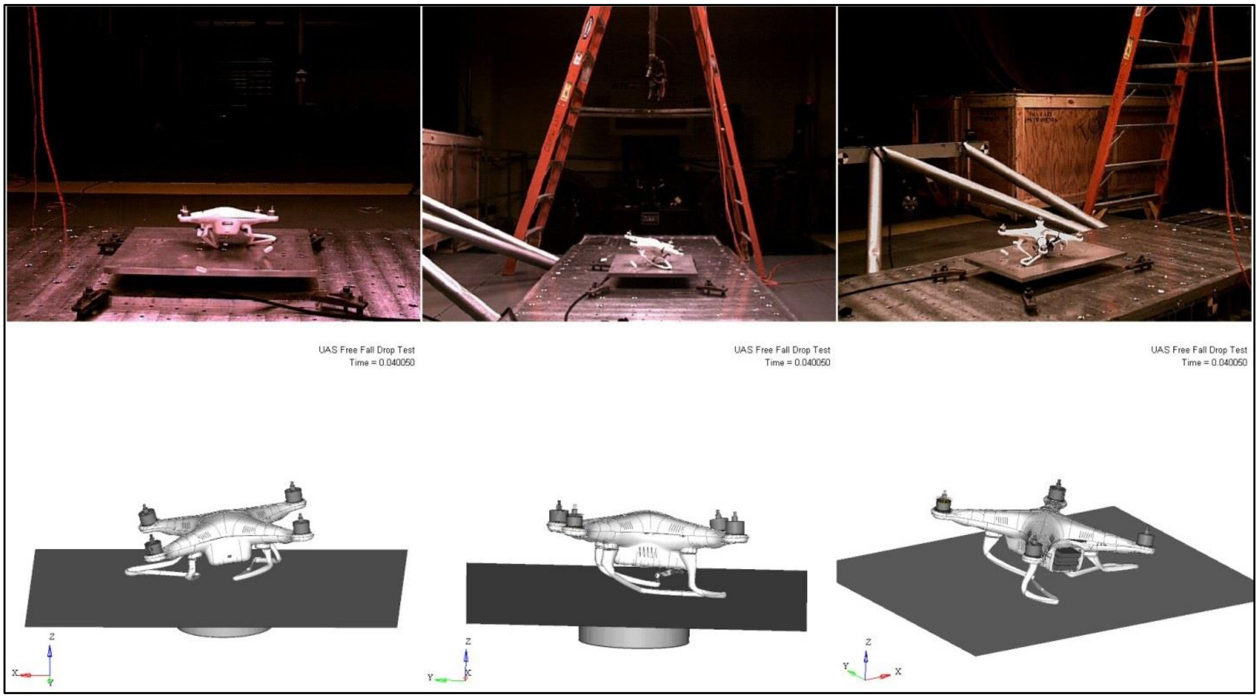

Figure 44. Free-fall drop test FE model verification - Kinematics comparison at t = 40 ms

The comparison between the test and simulation for the load cell data and the impulse is given in Figure 45. Both the test and simulation data have been filtered with a 4000 Hz low pass filter.

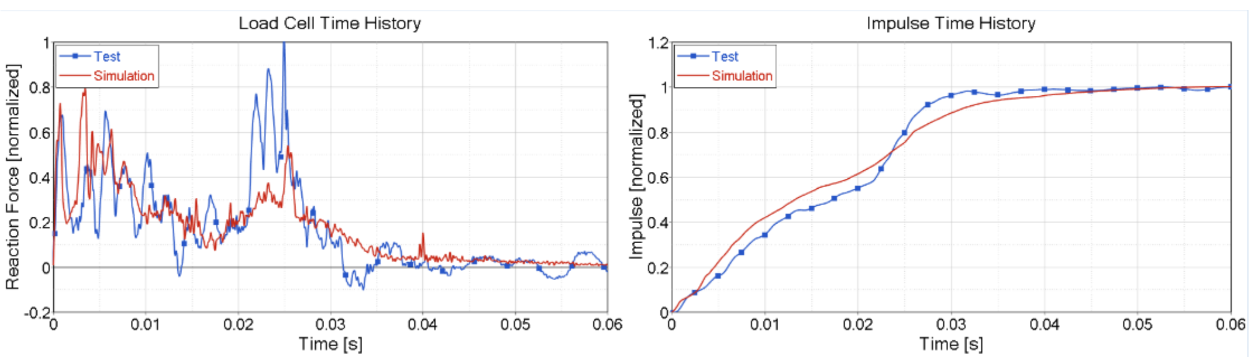

Figure 45. Free fall drop test FE model verification - Reaction force and impulse plots

From the kinematics, it can be perceived that the simulation predicts well general behavior of the quadcopter respect to the test. Complementarily, the reaction force and impulse show good correlation between simulation and test. The shape and major peaks are captured, and the impulse is very similar. Therefore, in conjunction with the drop tower test, it can be stated that the UAS plastic body behaves realistically in the simulations. This test also allowed obtaining some initial verification for ground collision applications.

2.4.4 Ballistic Component Level Tests

Several components of the UAS were subject to ballistic tests in a compressed gas gun system. The objective of this test was to understand the behavior of the most critical components of the

UAS under impact loads and to later use the test results to verify the FE model through correlation. The test conditions were selected as representative of an UAS midair collision similar to the ones being studied in this project.

To accomplish this, three different projectiles (battery, motor and camera) were shot against instrumented aluminum 2024-T3 flat panels of thicknesses of 1.60 mm (0.063″), 3.17 mm (0.125″) and 6.35 mm (0.25″) at velocities of 100 knots and 250 knots (51.4 m/s and 128.6 m/s). The kinematics of the event was recorded, and the reaction loads and strains at different locations of the panel were measured and logged. This data was compared with the results of a set of simulations replicating the test configurations in order to verify the FE model.

The panel thickness of 1.6 mm (0.063″) was selected as a representative for a typical leading edge skin of commercial transport and business jets of similar size than the ones being studied in this project. The purpose of having thicker panels was to have a more rigid panel that could transfer cleaner loads to the instruments in order to verify the projectile models. 250 knots (128.6 m/s) was selected as a representative impact speed for a midair collision event, based on the possible relative velocities of both the aircraft and the UAS. A more detailed explanation can be found in Section 4.1.1 . The reason for selecting 100 knots (51.4 m/s) was to study the impact behavior of the components near aircraft landing velocities.

The aluminum flat panels design was based on previous research conducted by NIAR to characterize and validate the FE numerical model of different bird sizes, as well as gelatin bird substitutes. The FE model of the panel was validated during that project [32].

2.4.4.1 Selection of components for Ballistic Tests

A set of three complementary studies were carried out to understand which factors might influence a midair collision with an UAS. A detailed description of these studies can be found in APPENDIX A.

In the first study, four 1.81 kg (4 lb) projectiles comprised of typical UAS materials (steel, aluminum, plastic, and LiPo battery) were compared with a bird of the same mass. The projectiles were impacted into a flat aluminum plate at 169.8 m/s (330 knots), and the projectile material behavior and the load transfer to the target was compared. It was identified that the components with greater strength and stiffness induced greater damage and higher loads.

In a different study, four spherical 34 g projectiles comprised of the same UAS materials as in the first study were compared with an ice projectile of equivalent mass at velocities ranging from 56.6-180 m/s (110-350 knots). The study's objective was to compare projectile impacts involving UAS materials to hail impacts. Projectiles made of higher strength/stiffness, more dense materials (*e.g.* steel or aluminum), produced aluminum target panel perforations at impact speeds above 102.9 m/s (200 knots), while the projectiles with softer material failed to penetrate the target panels at velocities up to 180 m/s (350 knots). These results suggest that hard UAS components, such as motors, can be particularly damaging during high-speed impacts. This would later prove to be correct with results from physical testing.

Finally, the influence of mass concentration on the damage introduce into a structure during impact was investigated. Impact test results obtained using a single 1.81 kg (4 lb) spherical steel projectile were compared to results obtained using either 2, 4, 6, or 8 independent (not linked between them) spherical projectiles with the same overall mass. Distributing the mass between multiple projectiles increased the internal energy absorbed by the impacted structure and caused the masses to more rapidly decelerate than with a single projectile. Therefore, less damage was introduced into the aluminum panel.

From these three studies, UAS components with a higher mass, stiffness and/or strength pose a greater threat to a given target structure. Therefore, the quadcopter UAS, camera, motors and battery were selected as critical projectiles in component level ballistic testing. Figure 46 presents the three type of components tested.

Figure 46. UAS components for ballistic test – battery (left), motor (center) and camera (right)

2.4.4.2 Test Setup

The target frame for the ballistic impact test consisted of two square steel frames bolted together, sandwiching about a flat aluminum test panel. The frame was bolted in all four corners to the anchor frame, through the load cells. The test frame assembled in the testing rig as well as the positions of the load cells is shown in Figure 47.

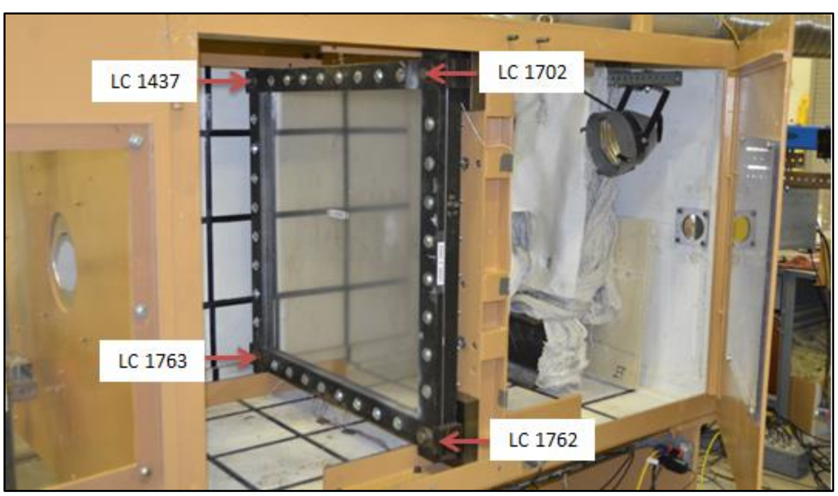

Figure 47. Test frame setup for ballistic component level tests

2.4.4.3 Test Equipment

The following instruments were used to conduct the ballistic tests and record all necessary data.

I. Compressed Gas Gun System:
A compressed gas gun system was used to accelerate the projectiles (UAS motors, batteries, and cameras) up to velocities of 128.6 m/s (250 knots) and impact precisely the center of the panel specimen. Tolerances of 5% in the velocity and 5 degrees deviation in the perpendicularity of the impact were desired.

II. Projectile Sabot:
Custom-designed polyurethane foam, sabot were used to support the projectile in the compressed gas gun and to provide a uniform loading surface during launch and to ensure a proper impact orientation. The types of sabot used are shown in Figure 48.

Figure 48. Projectile sabots for ballistic tests – battery (left), motor (center) and camera (right)

III. Load Cells:
Four uniaxial load cells from PCB Piezotronics were located at the corners of the test specimen mounting frame and were used to record the force transferred to the test fixture base. The load cell force gages had a 266,893 N (60,000 lbf) capacity and had a sampling rate of 1 MHz. All load cells were calibrated to within 1.1% linearity with ±1% of uncertainty. Figure 49 and Figure 47 show the load cell and their positions for the test setup respectively.

Figure 49. PCB load cell used in ballistic component level tests

IV. Strain Gages:

Thirteen linear, ¼ in grid, 350-ohm standard elongation strain gages from Vishay were installed at selected locations on the panel specimens at the NIAR. The data acquisition system sampled results at a rate of 1 MHz. The locations where the uniaxial strain gages were installed on the panel are shown in Figure 50. Specifications in Table 9.

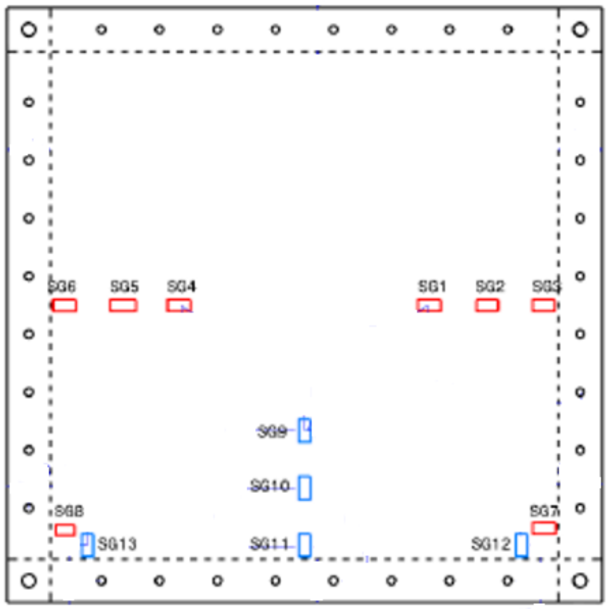

Figure 50. Strain gages on test frame for ballistic component level tests

Table 9. Strain gage specifications for component level tests

Gage ID	K-216.31-2041
Gage Resistance	350 ± 0.3% Ω
Gage Factor	2.02 ± 1.0%
Transverse Sensitivity	0.00%
Adhesive	AE-10
Post Curve	N/A

V. High-Speed Video Cameras:

Three high-speed video cameras were used to record the projectile impacts at 10,000 frames per second from three different viewing angles. Camera 1 was positioned perpendicular to the shot line, camera 2 was positioned in front of the plate at an oblique angle, and camera 3 recorded the impact from the top.

VI. 3D Digital Image Correlation (DIC) system:

A Vision Research high-speed camera capable of data acquisition rate of 10 KHz was used for the digital image correlation setup. A 1x1ft portion at the center on the rear of the panel was painted white and a random black speckle pattern was applied using spray paint. The camera setup was pointed at this speckled patch. The DIC software was able to capture the 3D displacements and in-plane strains induced in the panel during impact.

VII. Projectile Velocity Measurement:
Projectile velocity measurements were obtained using two lasers placed perpendicular to the projectile's trajectory as it exited the barrel. The distance between the lasers was known and allowed for automated velocity calculation based on the time difference from the projectile sequentially interrupting the laser beams.

In addition, digital camera still images of the test setup and the test articles were taken before and after each test.

2.4.4.4 Test Matrix

Ten battery, four motor, and two camera subassembly impact tests were performed. Table 10 shows the full test matrix of the sixteen tests along with the numerical results obtained. For each impact test, the projectile impact velocity and energy, mass, and pitch and yaw angles were determined and logged in the test matrix. The maximum deflections captured with the DIC and peak loads measured in the load cells were also included.

The iteration that showed the least deviation from the nominal velocity as well as the least amount of pitch and yaw was selected for the simulation in LS-DYNA. The projectile in the simulation was assigned equal velocity, pitch, and yaw initial conditions to replicate the test as accurately as possible. The following sections present and compare the test and simulation results of the six tests, which was used for the FE model verification.

Table 10. Component test matrix with results

Test Number	Shot Number	Panel Type	Projectile Type	Projectile Weight (g)	Pitch (Deg.)	Yaw (Deg.)	Impact Velocity (knots)	Impact Velocity (m/s)	Deviation from nominal velocity	Impact Energy (J)	Panel Penetration (Y/N)	Rebound Velocity (m/s)	Residual Velocity (m/s)	Peak Load (N)	Permanent Deformation (mm)	Max Deflection (mm)
BATTERY																
1	5660	0.063" Al	Battery (discharged)	344.28	0.2° D	9.9° L	258.92	133.2	+3.6%	3,054.4	N	n/a	n/a	102,709	32.0	48.5
	5669	0.063" Al	Battery (discharged)	348.86	0.2° D	13.8° L	251.21	129.24	+0.5%	2,913.7	N	n/a	n/a	91,522	30.6	49.5
	5670	0.063" Al	Battery (discharged)	343.07	0.8° D	0.8° L	248.25	127.71	-0.7%	2,798.1	N	n/a	n/a	92,483	34.0	47.8
2	5661	0.25" Al	Battery (discharged)	350.06	1.7° D	2.1° L	255.95	131.67	+2.4%	3,035.1	N	n/a	n/a	123,892	7.2	19.6
	5662	0.25" Al	Battery (charged)	351.62	0.2° U	10.4° L	250.03	128.63	0.0%	2,909.1	N	n/a	n/a	122,184	9.1	20.1
	5671	0.25" Al	Battery (discharged)	344.71	3.5° D	5.7° L	251.81	129.54	+0.7%	2,892.6	N	n/a	n/a	134,719	5.8	19.1
	5672	0.25" Al	Battery (charged + turned on)	343.62	0.4° D	3.8° L	250.62	128.93	+0.2%	2,856.0	N	n/a	n/a	131,521	6.5	19.1
3	5675	0.125" Al	Battery (discharged)	344.1	2.0° U	1.5° L	96.57	49.68	-3.4%	424.7	N	7.62	n/a	48,170	5.5	14.5
	5676	0.125" Al	Battery (discharged)	344.08	17.1° U	11.7° R	90.65	46.63	-9.4%	374.2	N	6.40	n/a	38,829	4.5	12.7
	5679	0.125" Al	Battery (charged)	351.45	2.8° D	10.4° R	99.54	51.21	-0.5%	460.8	N	6.40	n/a	44,424	5.3	15.5
MOTOR																
4	5665	0.063" Al	Motor	50.73	2.8° D	n/a	249.44	128.32	-0.2%	417.7	Y	n/a	29.57	16,160	n/a	n/a
	5668	0.063" Al	Motor	51.10	7.2° U	n/a	263.66	135.64	+5.5%	470.1	Y	n/a	28.96	14,448	n/a	n/a
5	5677	0.25" Al	Motor	51.30	10.5° D	n/a	236.40	121.62	-5.4%	379.4	N	3.66	n/a	55,661	2.3	6.9
	5678	0.25" Al	Motor	50.98	2.1° U	n/a	264.84	136.25	+5.9%	473.2	N	2.13	n/a	58,703	3.3	7.9
CAMERA																
6	5666	0.063" Al	Camera	52.91	2.6° D	18.1° L	255.36	131.37	+2.1%	456.6	N	4.8768	n/a	29,131	13.7	15.2
	5667	0.063" Al	Camera	52.57	1.2° U	8.6° L	251.21	129.24	+0.5%	439.1	N	5.4864	n/a	31,142	16.8	18.5

2.4.4.5 Test Hardware FE Model

Each of the tests was replicated with a FE simulation in LS-DYNA. The results of both were compared to verify the FE models of the different components tested.

The kinematics of the simulation was synchronized with the high-speed videos recorded in the physical testing. The correlation between both was assessed qualitatively. Additionally, each of the thirteen strain gage and of the four load cell channels was compared with measurements in the simulation.

Some preliminary simulations demonstrated that the compliance of the test frame as well as the initial preload of the bolts had a great influence on the load cell results. Therefore, it was decided to model in detail not only the projectile and the aluminum panel, but also the frame and bolts that sandwiched the panel as well as the actual load cells, anchor blocks and the full steel test bench. Figure 51 shows the FE model of the test frame. If compared with Figure 47 it can be seen the level of detail achieved for the simulation models. All the dimensions were based on the CAD geometry and bill of material provided by the test facility.

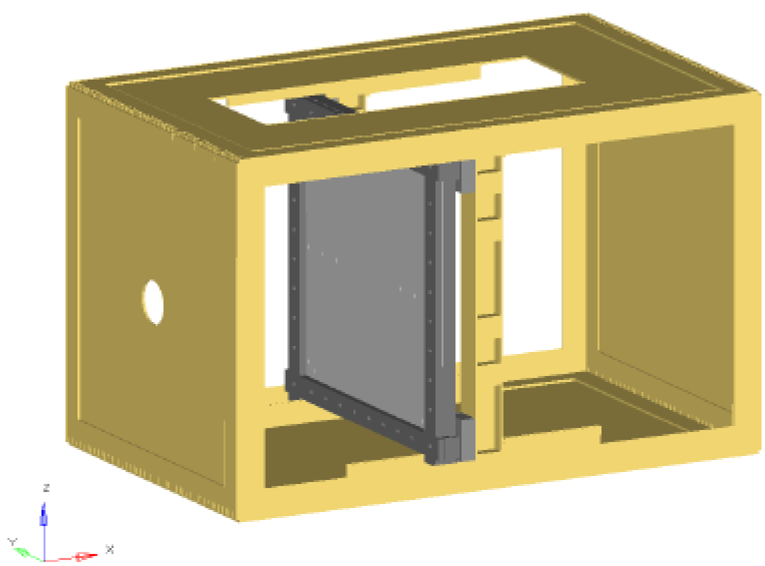

Figure 51. Finite element model of the test frame for ballistic component level tests

The bolts clamping the panel to the anchor block with the load cell in between had a preload defined that matched the 50,000 N recommended by the load cell manufacturer (PCB Piezoelectronics) and used in the physical test. The model was initialized during a dynamic relaxation phase that applied the bolt preloads in a preliminary explicit dynamics simulation. This is executed by LS-DYNA automatically.

All the simulations presented in this section use this baseline FE model, with the thickness of the panel adapted according to the specifications of each test.

2.4.4.6 Test 1 – Component Level Tests Results and Verification

For the test configuration (test 1) in which the battery impacts a 1.6 mm (0.063″) aluminum panel at 128.6 m/s (250 knots), three iterations with designations 5660, 5669 and 5670 were conducted. Out of these three iterations, 5670 had the least deviation from the nominal conditions.

The FE simulation was set up with an initial projectile velocity of 127.7 m/s (248.3 knots), pitch, and yaw angles of 0.8 and 0.8 degrees respectively to match the test conditions from 5670. The non-structural mass of the battery was trimmed to match the 243.1 g measured in the test.

Figure 52, Figure 53, Figure 54 and Figure 55 below show the comparison of the kinematics between the test and simulation at four different instances of the event, starting at the beginning of the contact between the plate and the projectile and finishing at the end of it. These instances were considered of highest interest, and therefore the rest of the simulation and test (rebound) was trimmed out of the kinematics.

All three repetitions of this test ensured that the battery was fully discharged and the control electronics disassembled from the battery itself. The effect of electric charge on the results will be discussed in section 2.4.4.12

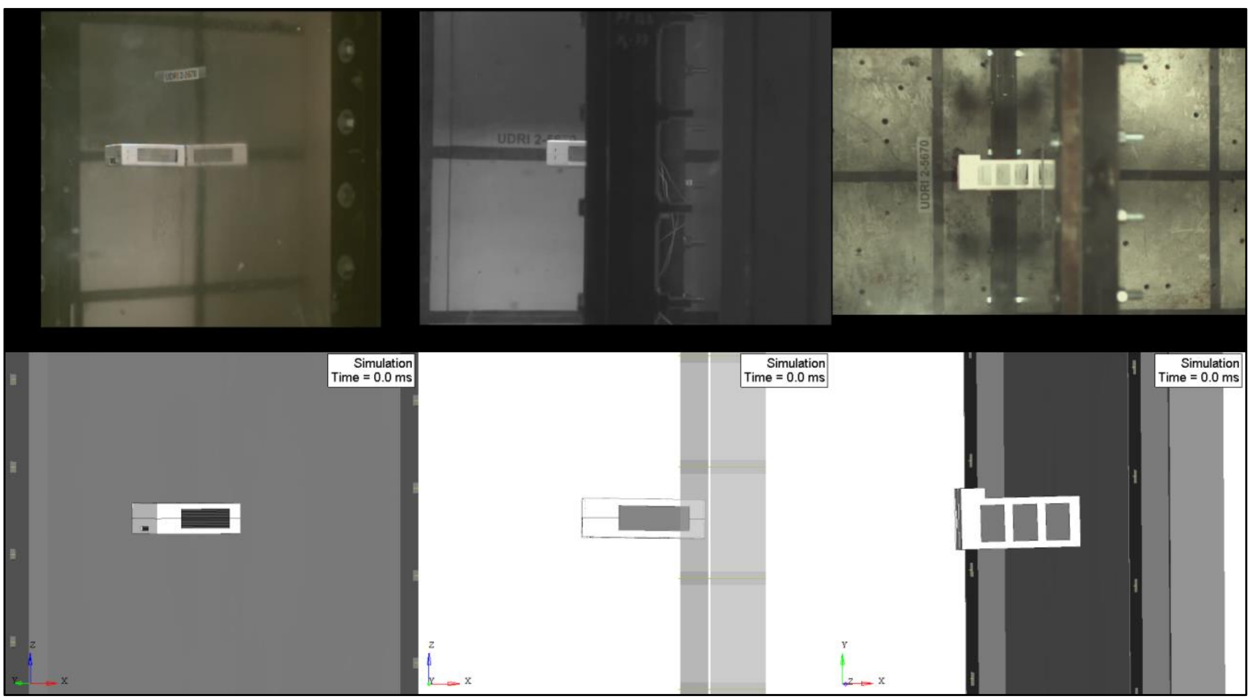

Figure 52. Comparison for battery impact on 1.6 mm (0.063″) thick aluminum panel at 127.7 m/s (248.2 kt) at t = 0 ms (beginning of contact)

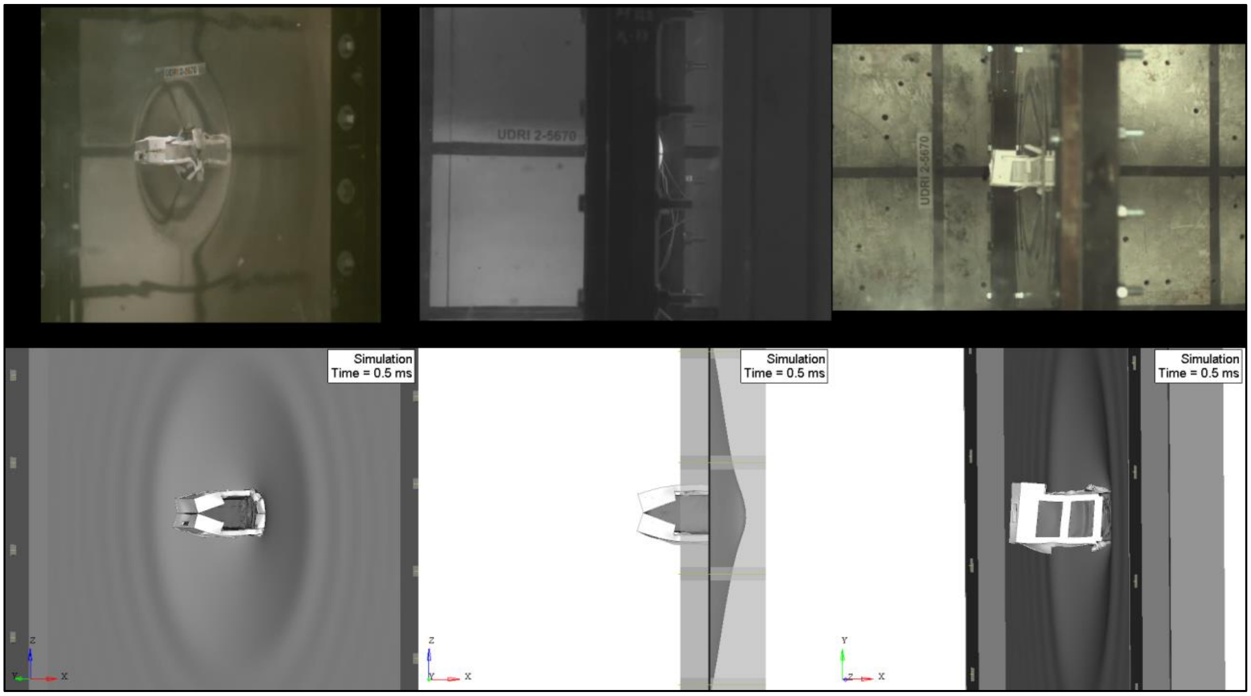

Figure 53. Comparison for battery impact on 1.6 mm (0.063″) thick aluminum panel at 127.7 m/s (248.2 kt) at t = 0.5 ms

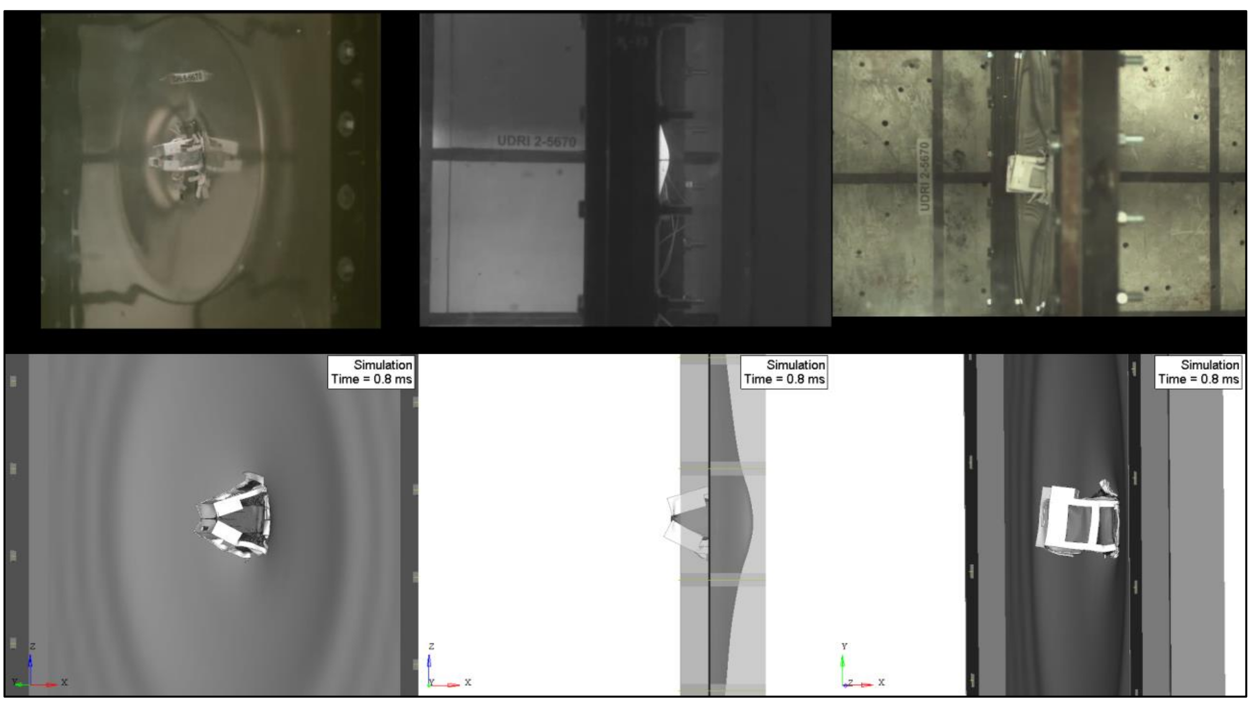

Figure 54. Comparison for battery impact on 1.6 mm (0.063″) thick aluminum panel at 127.7 m/s (248.2 kt) at t = 0.8 ms

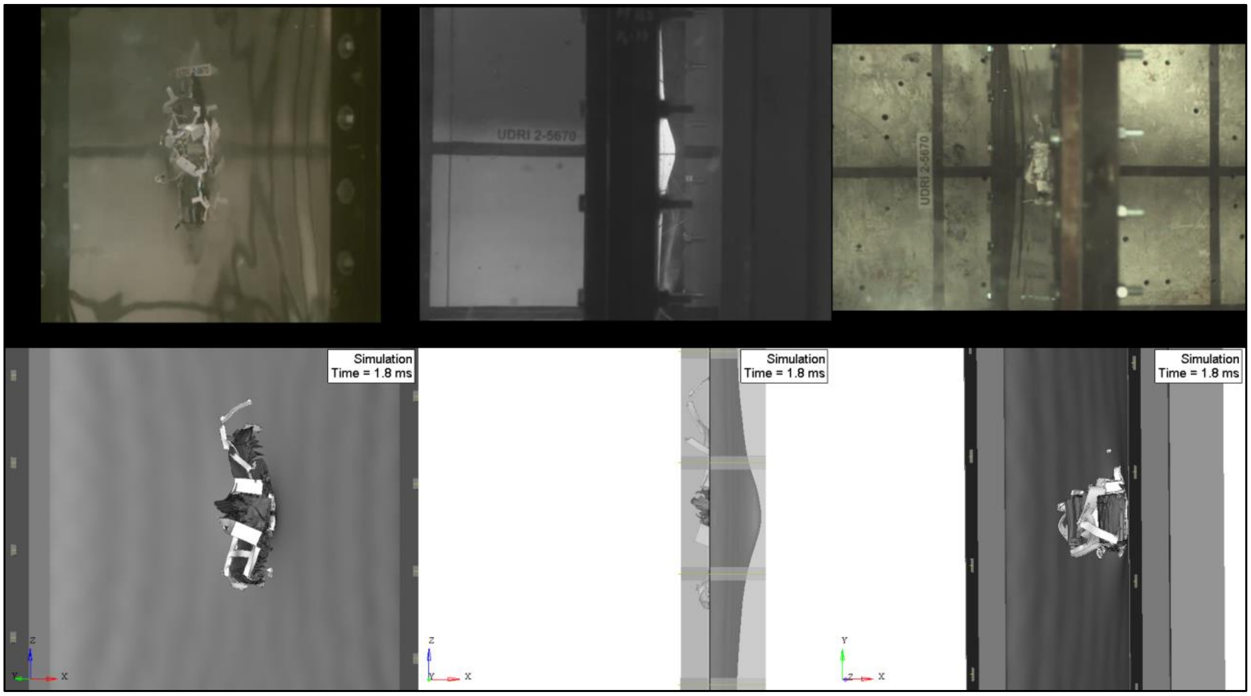

Figure 55. Comparison for battery impact on 1.6 mm (0.063”) thick aluminum panel at 127.7 m/s (248.2 kt) at t = 1.8 ms (end of contact)

Figure 56 shows the comparison of the X (horizontal) and Y (vertical) strains as well as out-of-plane displacements (mm) of the component level test obtained from the DIC data and the equivalent contour plot results of the simulation for the instance with maximum displacement of the aluminum panel.

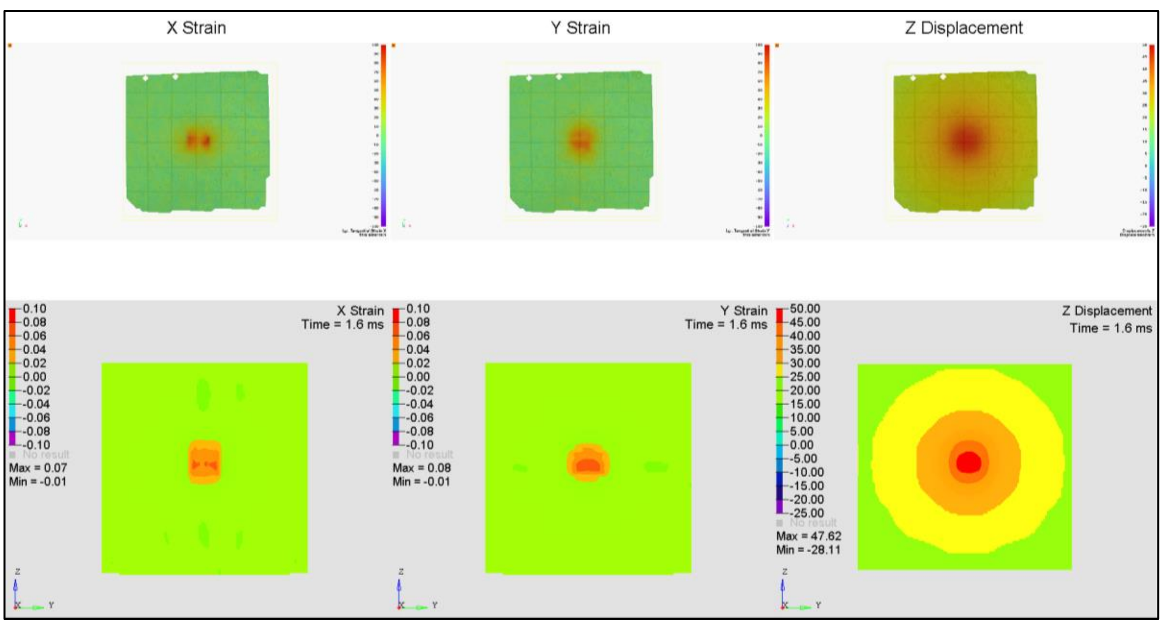

Figure 56. DIC for battery impact on 1.6 mm (0.063”) panel at 128.6 m/s (250 kt) at time of maximum panel deformation (t = 1.8 ms)

The top two images of Figure 57 show the permanent deformation on the panel. In the bottom left image, the remains of the battery after the test can be seen. The battery case is broken and the battery cells have been separated from each other. The bottom right image shows the predicted permanent deformation of the FE simulation, which can be compared with the top images.

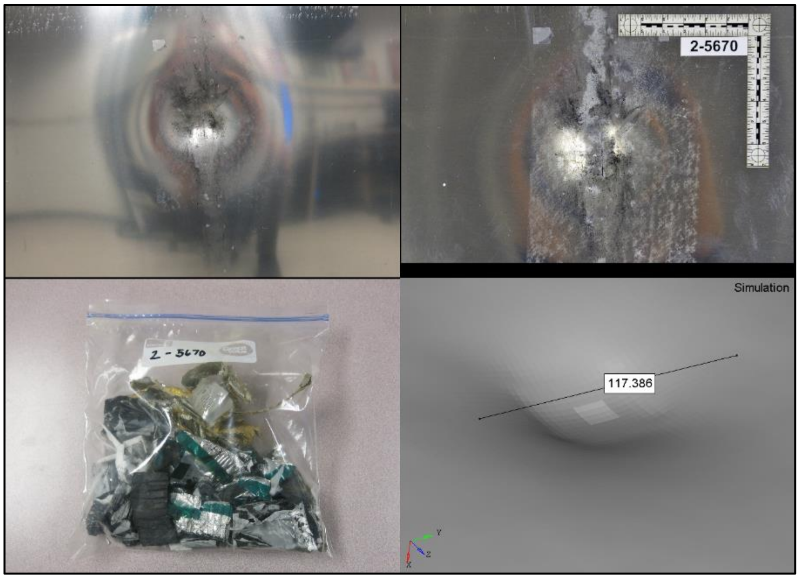

Figure 57. Component level test results for battery impact on 1.6 mm (0.063″) thick aluminum panel at 127.7 m/s (248.2 kt)

Figure 58 shows the displacement of the panel over the test period, obtained from the output of the DIC measurements at the center of the panel.

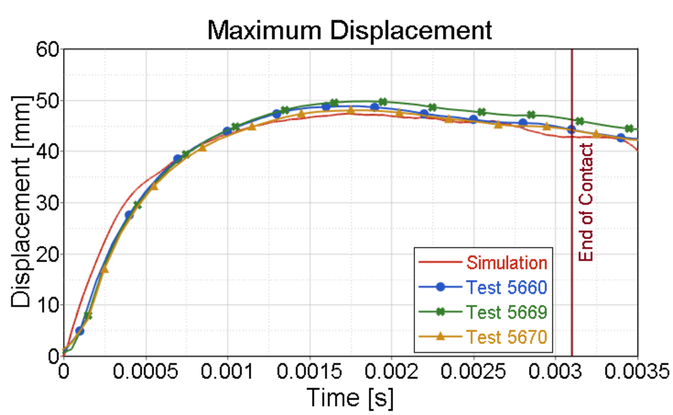

Figure 58. Panel displacement over test period obtained from DIC for battery impact on 1.6 mm (0.063″) panel at 128.6 m/s (250 kt)

Figure 59 and Figure 60 below show the forces and strains for each load cell and the nine channels of strain transducers closest to the impact location respectively in the three test repetitions with the corresponding values obtained from the simulation. All the curves were filtered with a low-pass 15,000 Hz filter. See Appendix F for more details on the data processing methods followed.

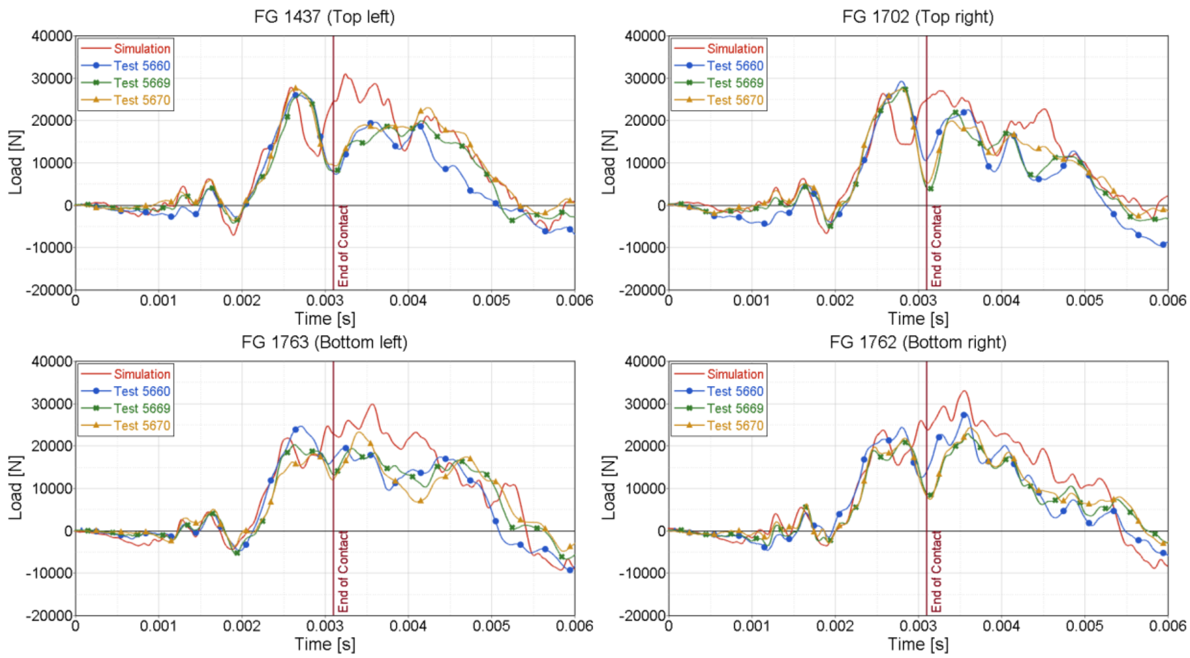

Figure 59. Reaction loads for battery impact on 1.6 mm (0.063″) panel at 128.6 m/s (250 kt)

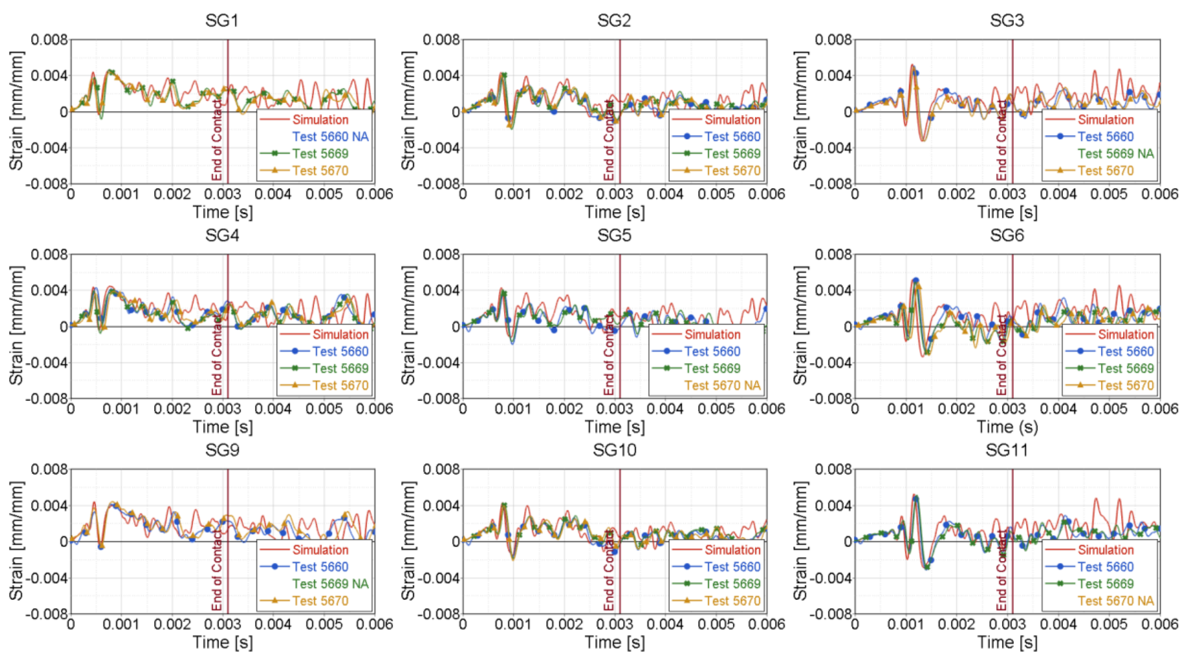

Figure 60. Strains for battery impact on 1.6 mm (0.063″) panel at 128.6 m/s (250 kt)

Figure 61 shows a summary of the most representative test results and impact conditions. An average column and error bar indicate the mean and standard deviation of the test results for each plot. A red bar indicates in each case the value obtained from the simulation. This figure shows that in general, the three repetitions of Test 1 produced small variability, most of it below 10%. This is in spite of having considerable yaw angle deviations of the battery at impact. It can be seen that the magnitude of the peak of displacement and strain for the simulation lies within or close to the variability of the test. However, the peak load is slightly over predicted by the simulation.

From the results presented in this section, it can be observed that the battery FE model produces simulations with high correlation with the respective physical testing. It can be seen in Figure 59 and Figure 60 that from a qualitative perspective, the shape, and overall performance of the simulation was good. Consequently, it was considered verified for the conditions specified for this test (128.6 m/s and 1.6 mm thick aluminum panel).

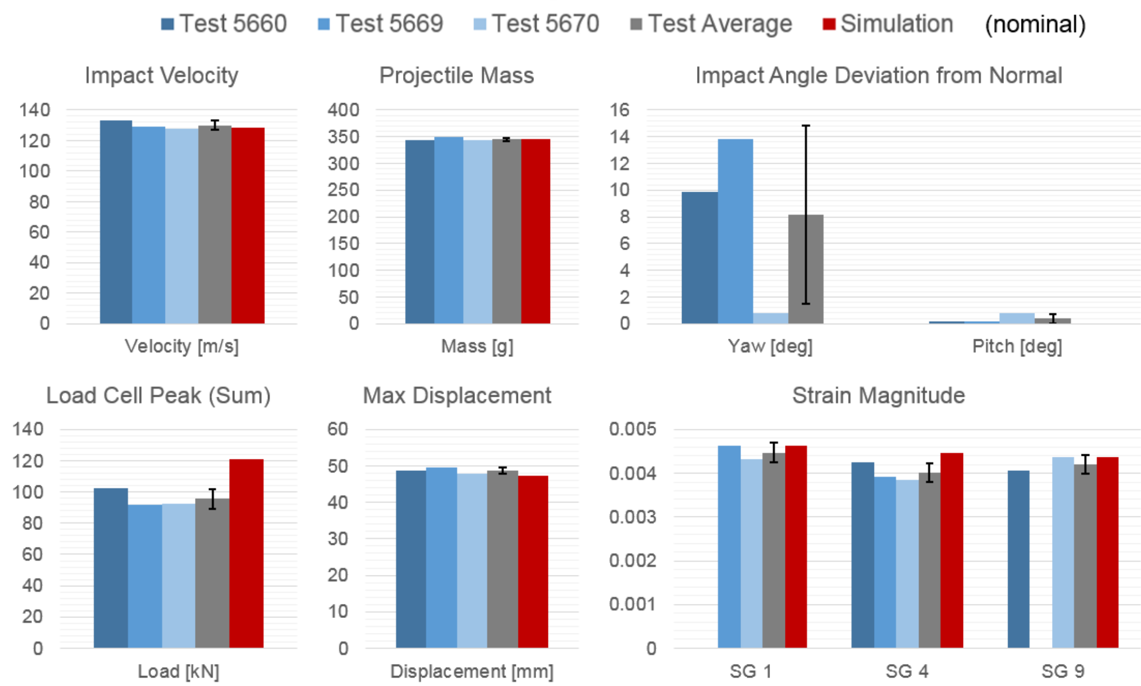

Figure 61. Summary of results for component level test 1, battery impact on 1.6 mm Al panel.

2.4.4.7 Test 2 – Component Level Tests Results and Verification

For the test configuration (test 2) in which the battery impacts a 6.35 mm (0.25″) aluminum panel at 128.6 m/s (250 knots), four iterations with designations 5661, 5662, 5671 and 5672 were conducted. Out of these four iterations, 5661 had the least deviation from the nominal conditions.

The FE simulation was set up with an initial projectile velocity of 131.7 m/s (255.9 knots), pitch of 1.7 degrees and yaw of 2.1 degrees to match the test conditions from 5661. The **ELEMENT_MASS* was adjusted to match the 350.1 g measured in the test.

Figure 62, Figure 63, Figure 64 and Figure 65 below show the comparison of the kinematics between the test and simulation at four different instances of the event, starting at the beginning of the contact between the plate and the projectile and finishing at the end of it.

Repetitions 5661 and 5671 were conducted with the battery completely discharged; repetition 5662 with the battery fully charged, and repetition 5672 charged and with the electronics activated. There was no effect of the battery charge observed in the results from testing. All of the data shows good repeatability and small deviations. A more in depth discussion can be found in section 2.4.4.11.

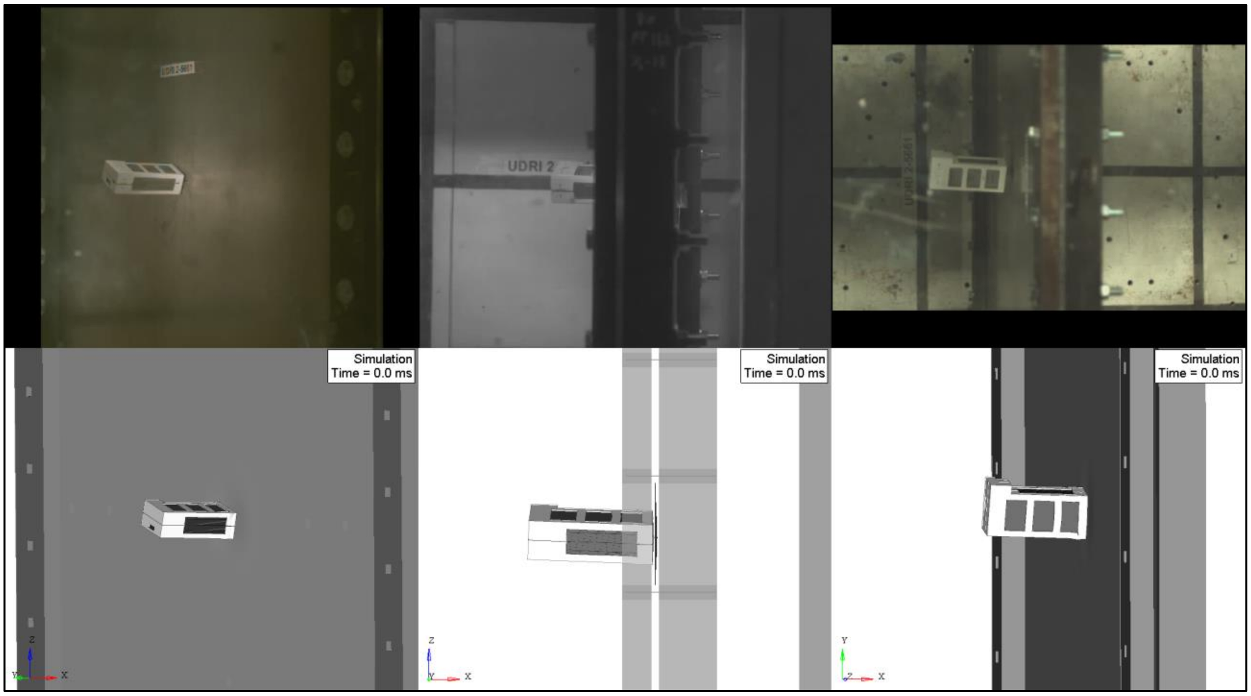

Figure 62. Comparison for battery impact 5661 on 6.35 mm (0.25″) thick aluminum panel at 131.7 m/s (255.9 kt) at t = 0 ms (beginning of contact)

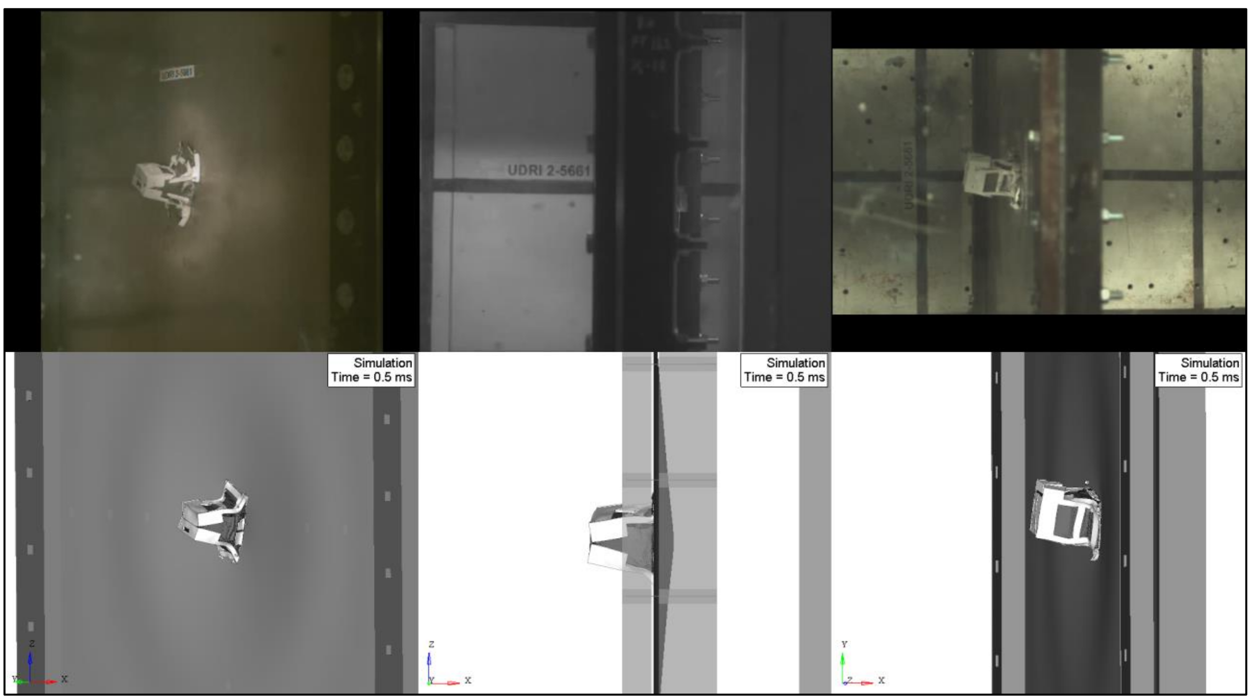

Figure 63. Comparison of battery impact 5661 on 6.35 mm (0.25″) thick aluminum panel at 131.7 m/s (255.9 kt) t = 0.5 ms

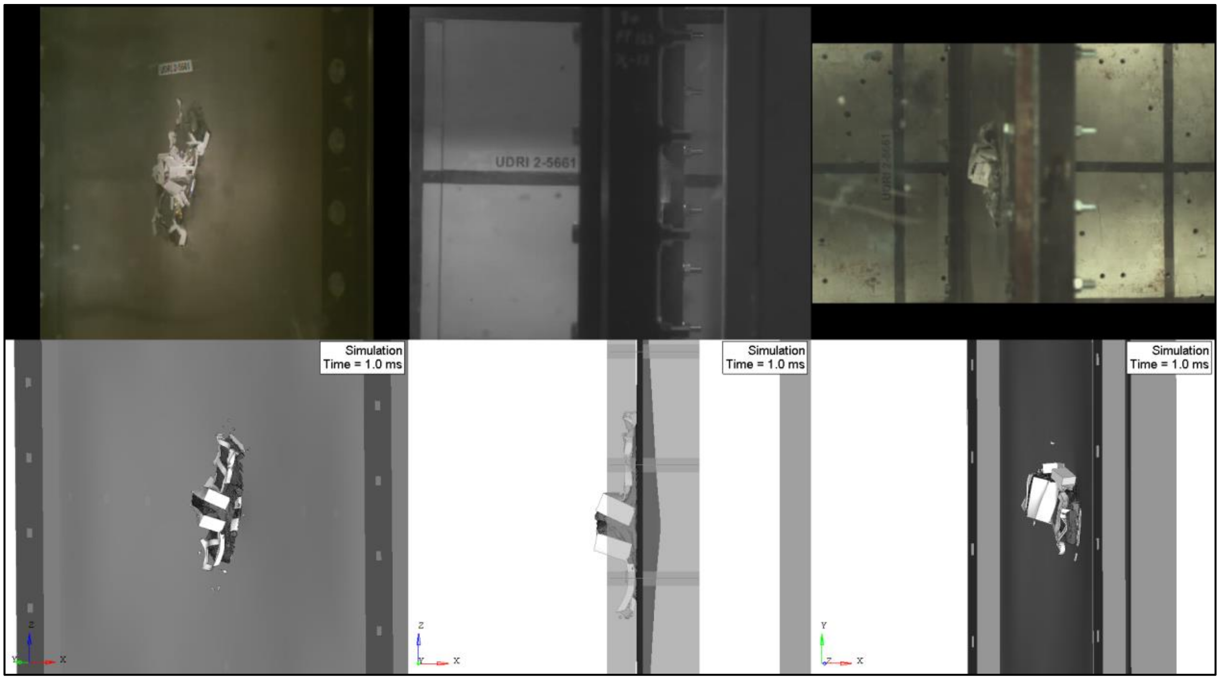

Figure 64. Comparison of battery impact 5661 on 6.35 mm (0.25″) thick aluminum panel at 131.7 m/s (255.9 kt) at t = 1 ms

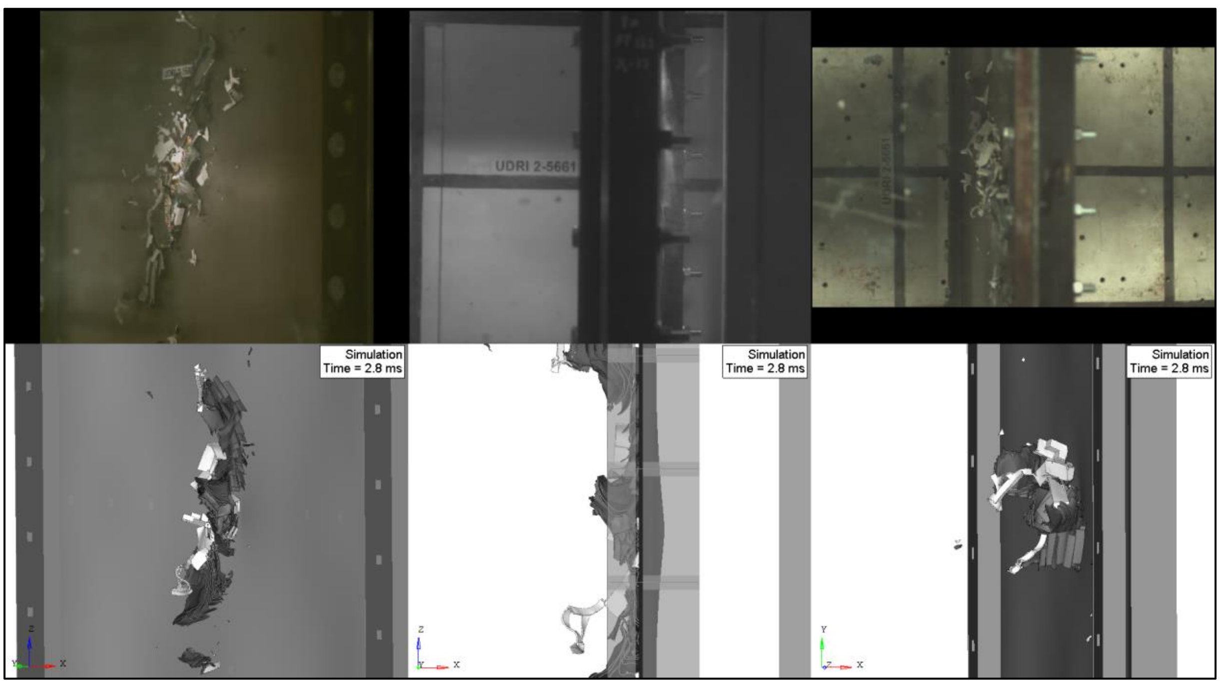

Figure 65. Comparison of battery impact 5661 on 6.35 mm (0.25″) thick aluminum panel at 131.7 m/s (255.9 kt) at t = 2.8 ms (end of contact)

Figure 66 shows the comparison of the X (horizontal) and Y (vertical) strains as well as out-of-plane displacements (mm) of the component level test obtained from the DIC data and the equivalent contour plot results of the simulation for the instance with maximum displacement of the aluminum panel.

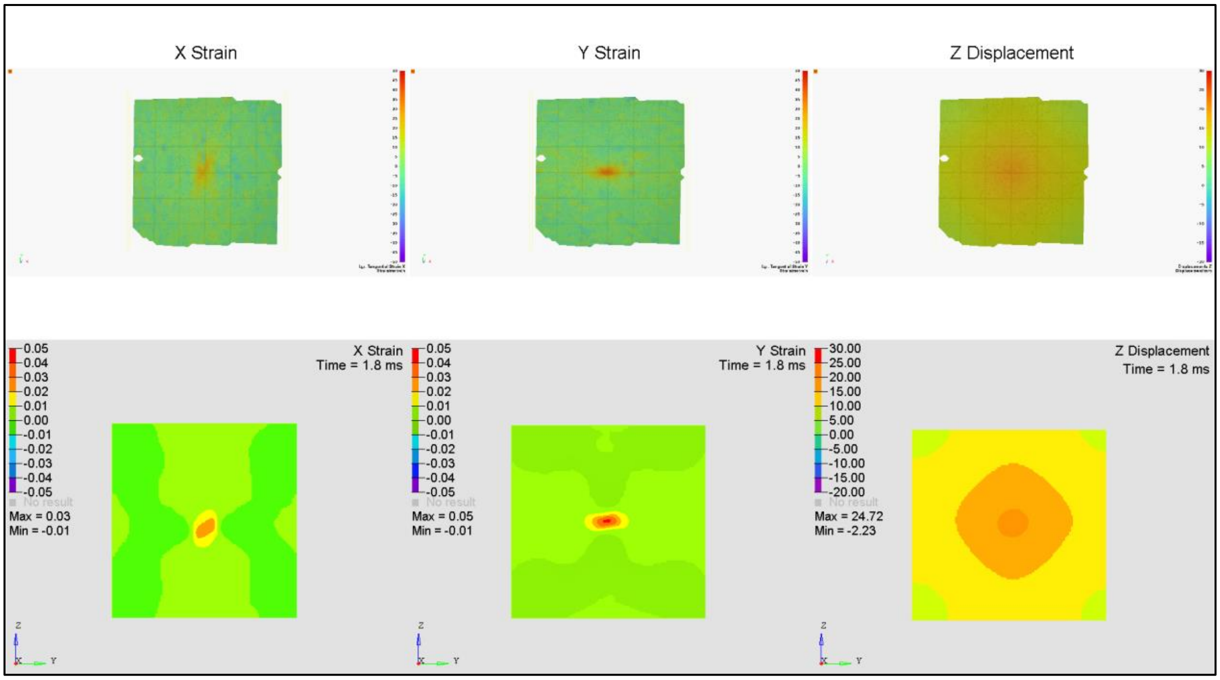

Figure 66. DIC data for battery impact 5661 on 6.35 mm (0.25″) thick aluminum panel at 131.7 m/s (255.9 kts) at time of maximum panel deformation (t = 2.8 ms)

The top two images of Figure 67 show the permanent deformation on the panel. In the bottom left image, the remains of the battery after the test can be seen. The battery shell is broken and the cells have been separated from each other. The bottom right image shows the predicted permanent deformation of the FE simulation, which can be compared with the top images.

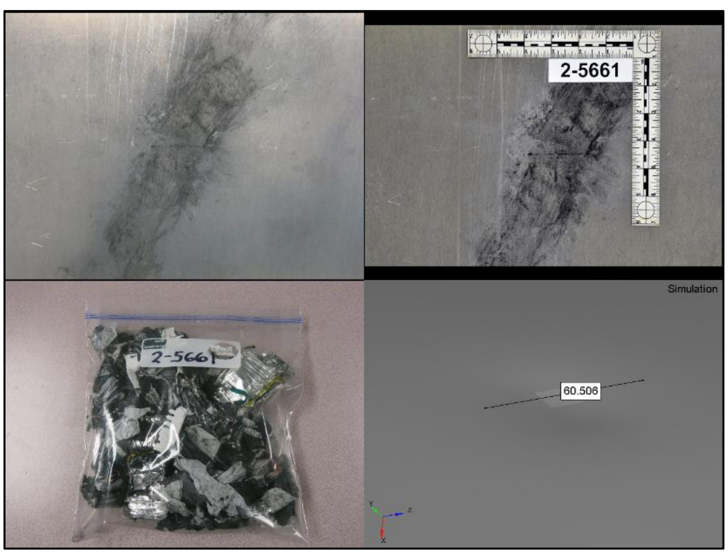

Figure 67. Component level test results for battery impact 5661 on 6.35 mm (0.25″) thick aluminum panel at 131.7 m/s (255.9 kt)

Figure 68 shows the displacement of the panel over the test period. All test repetitions showed great repeatability and the simulation high correlation with the test results.

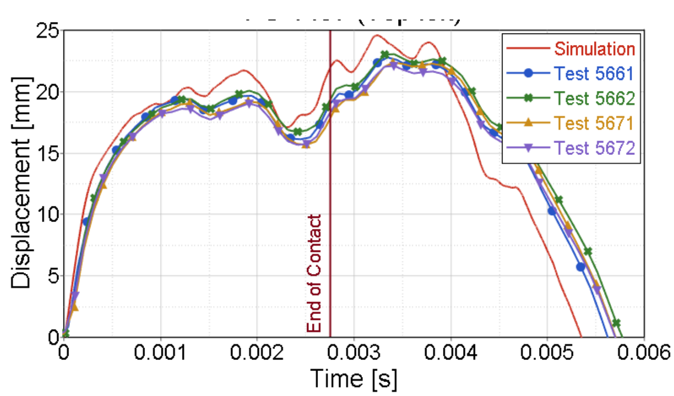

Figure 68. Panel displacement over test period obtained from DIC for battery impact on 6.35 mm (0.25″) panel at 128.6 m/s (250 kt)

Figure 69 and Figure 70 below show the forces and strains for each load cell and the nine channels of strain transducers closest to the impact location respectively in the four test repetitions with the corresponding values obtained from the simulation. All the curves were filtered with a low-pass 15,000 Hz filter. See Appendix F for more details on the data processing methods followed.

Figure 71 shows a summary of the most representative test results and impact conditions. An average column and error bar indicate the mean and standard deviation of the test results. A red bar indicates in each case the value from the simulation.

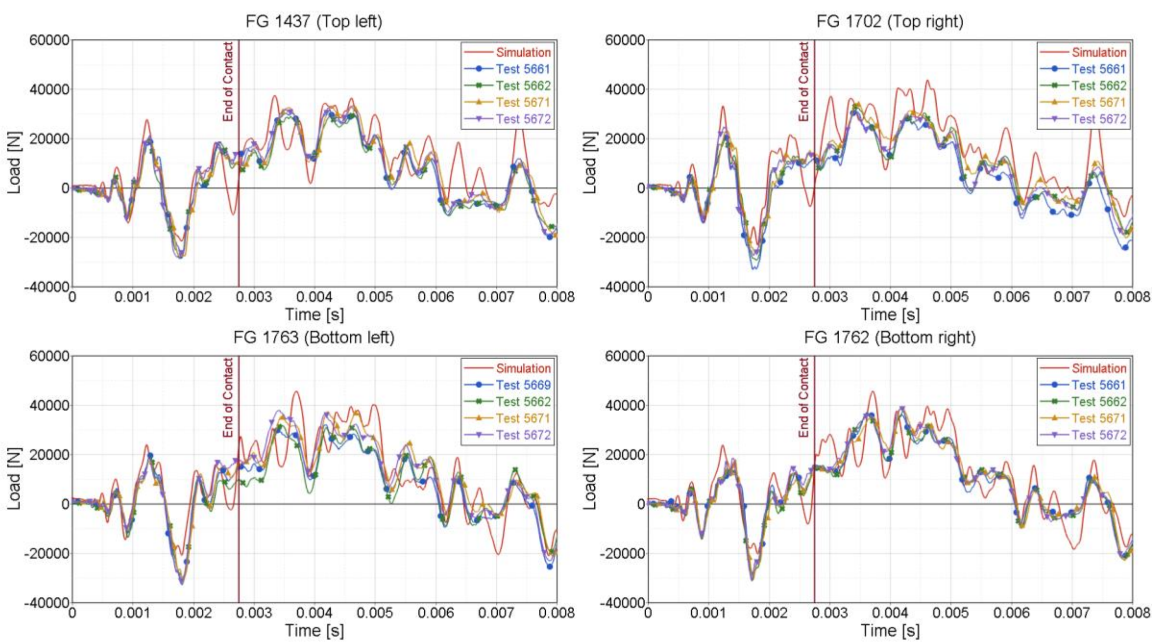

Figure 69. Reaction loads for battery impact on 6.35 mm (0.25″) panel at 128.6 m/s (250 kt)

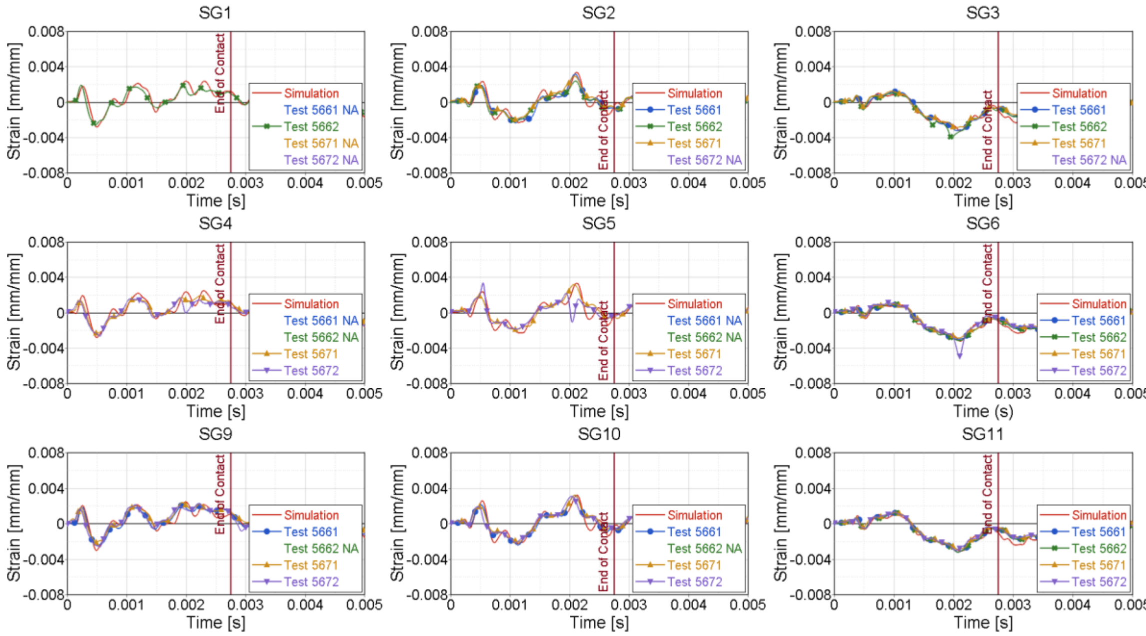

Figure 70. Strains for battery impact on 6.35 mm (0.25″) panel at 128.6 m/s (250 kt)

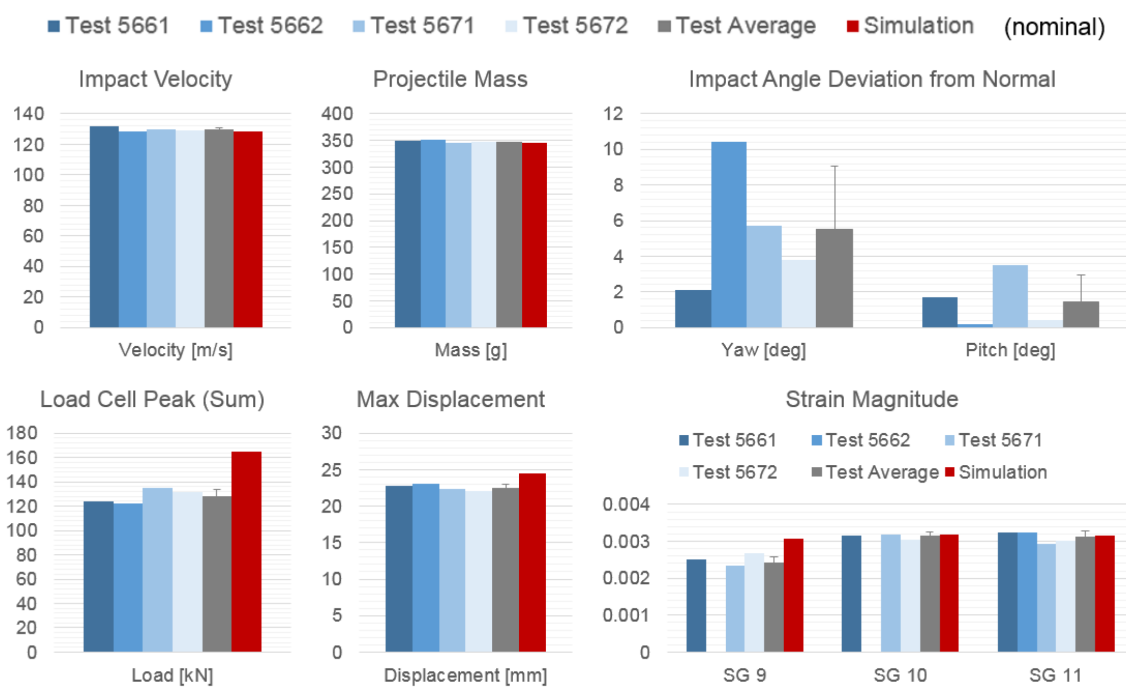

Figure 71. Summary of results for component level test 2, battery impact on 6.35 mm Al panel.

From Figure 71 it can be seen that in general, the four repetitions of test 2 produced small variability, most of it below 10%. This is in spite of having considerable yaw angle deviations of the battery at impact. The magnitude of the peak strain for the simulation lies within or close to the variability of the test. However, the peak displacement and load were slightly over predicted by the simulation. It can be seen in Figure 69 and Figure 70 however that from a qualitative perspective, the shape, and overall performance of the simulation was good.

From the results presented in this section, it can be observed that the battery FE model produces simulations with high correlation with the respective physical testing. Consequently, it was considered verified for the conditions specified for this test (128.6 m/s and 6.35 mm thick panel).

Test 2 involved battery specimens with electric charge. It was observed that no effect was influencing the impact behavior of the battery due to this pre-charge. From the results of tests 1 and 2, it can also be observed that the battery experiences high levels of damage when impacting at high speeds (128.6 m/s) both thin (1.6 mm) and thick (6.35 mm) aluminum panels. This will be important when assessing the risk of fire in the battery cells as it will be introduced in 2.4.4.12 .

2.4.4.8 Test 3 – Component Level Tests Results and Verification

For the test configuration (test 3) in which the battery impacts a 3.18 mm (0.125″) aluminum panel at 51.4 m/s) (100 knots), three iterations with designations 5675, 5676 and 5679 were conducted. Out of these three iterations, 5675 had the least deviation from the nominal conditions. The FE simulation was set up with an initial projectile velocity of 49.7 m/s (96.6 knots), pitch of 2 degrees and yaw of 1.5 degrees to match the test conditions from 5675. The non-structural mass of the battery was adjusted to match the 344.1 g measured in the test.

Figure 72, Figure 73, Figure 74, and Figure 75 show the comparison of the kinematics between the test and simulation at four different instances of the event, starting at the beginning of the contact between the plate and the projectile and finishing at the end of it.

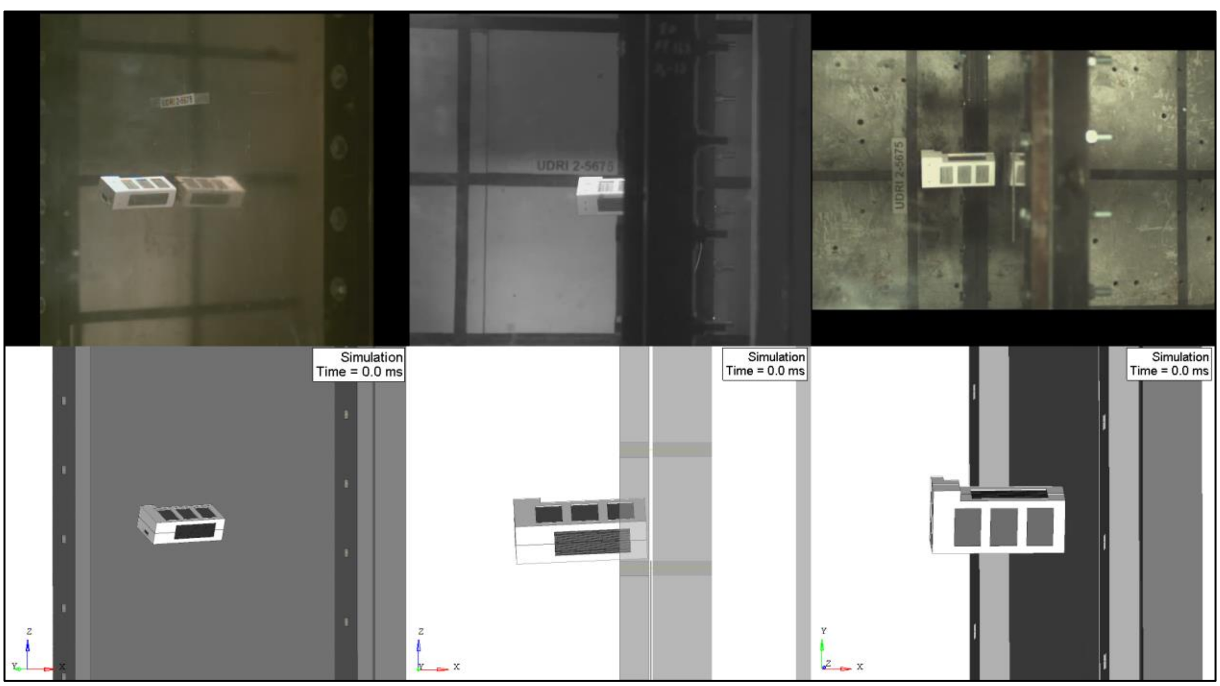

Figure 72. Comparison for battery impact 5675 on 3.18 mm (0.125″) thick aluminum panel at 49.7 m/s (96.6 kt) at t = 0 ms (beginning of contact)

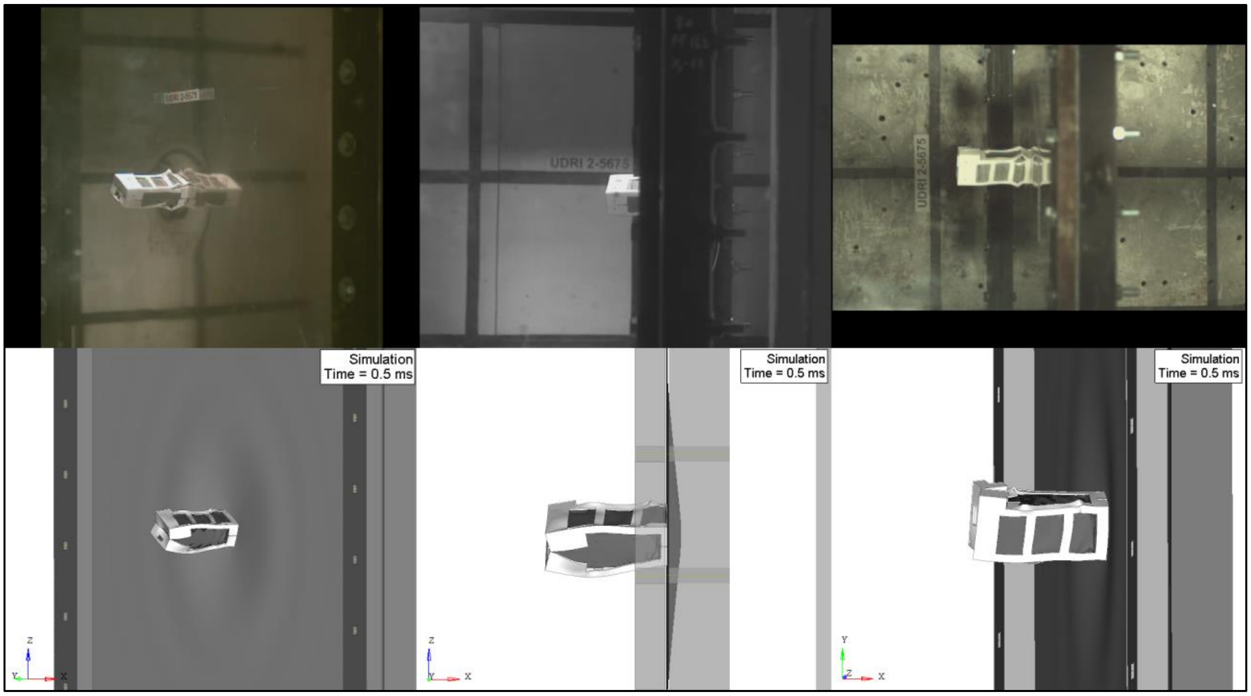

Figure 73. Comparison of battery impact 5675 on 3.18 mm (0.125″) thick aluminum panel at 49.7 m/s (96.6 kt) at t = 0.5 ms

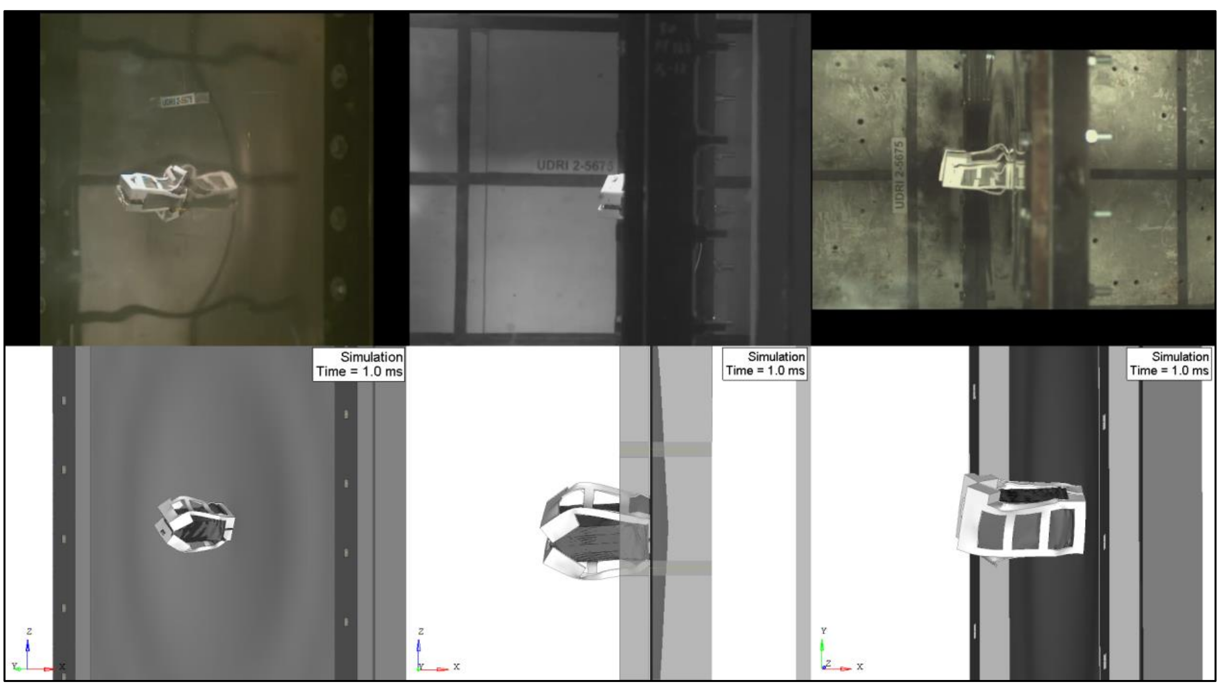

Figure 74. Comparison of battery impact 5675 on 3.18 mm (0.125″) thick aluminum panel at 49.7 m/s (96.6 kt) at t = 1 ms

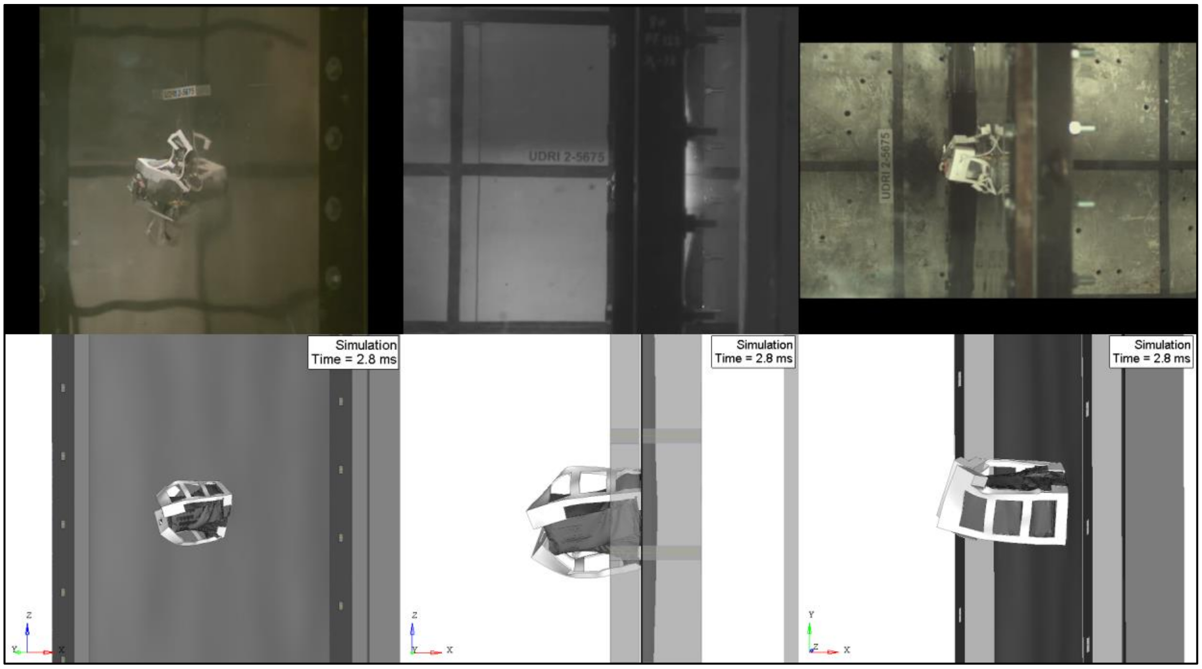

Figure 75. Comparison of battery impact 5675 on 3.18 mm (0.125″) thick aluminum panel at 49.7 m/s (96.6 kt) at t = 2.8 ms (end of contact)

Figure 76 shows the comparison of the X (horizontal) and Y (vertical) strains as well as out-of-plane displacements (mm) of the component level test obtained from the DIC data and the contour plot results of the simulation for the instance of maximum displacement of the panel.

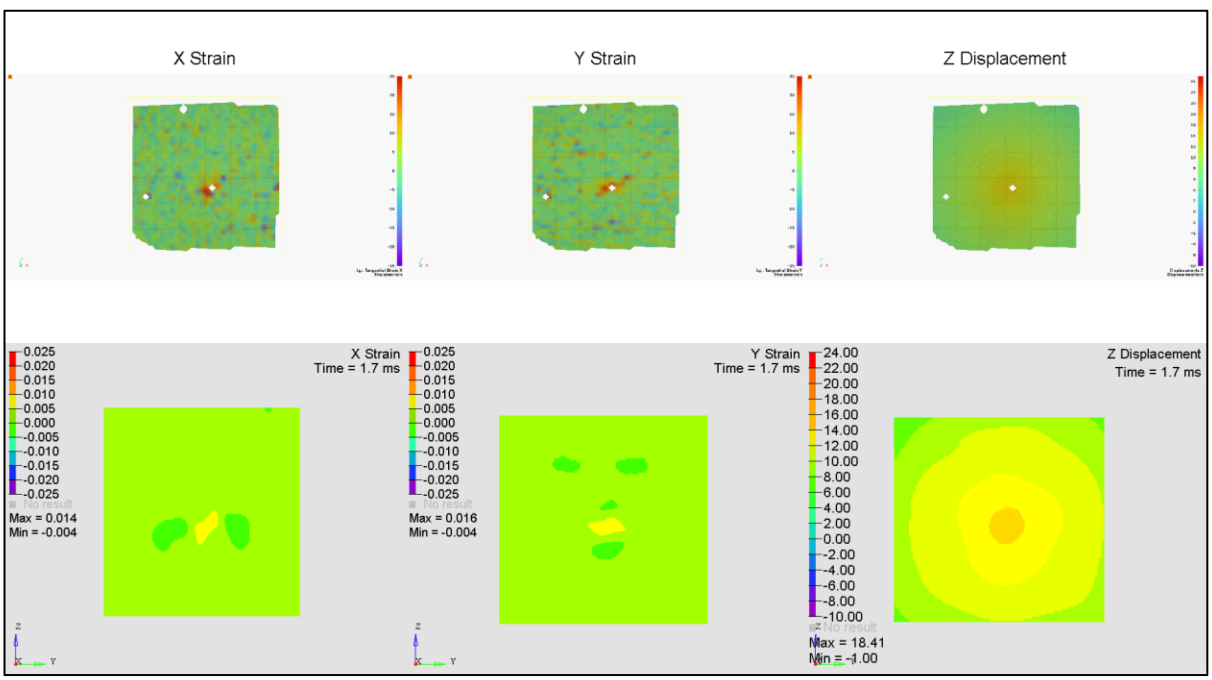

Figure 76. DIC data for battery impact 5675 3.18 mm (0.125″) thick aluminum panel at 49.7 m/s (96.6 kt) at time of maximum panel deformation (t = 1.6 ms)

The top two images of Figure 77 show the permanent deformation on the panel. In the bottom left image, the remains of the battery after the test can be seen. The casing is broken but the battery cells are partly deformed bat not entirely damaged. The bottom right image shows the predicted permanent deformation of the FE simulation, which can be compared with the image above it.

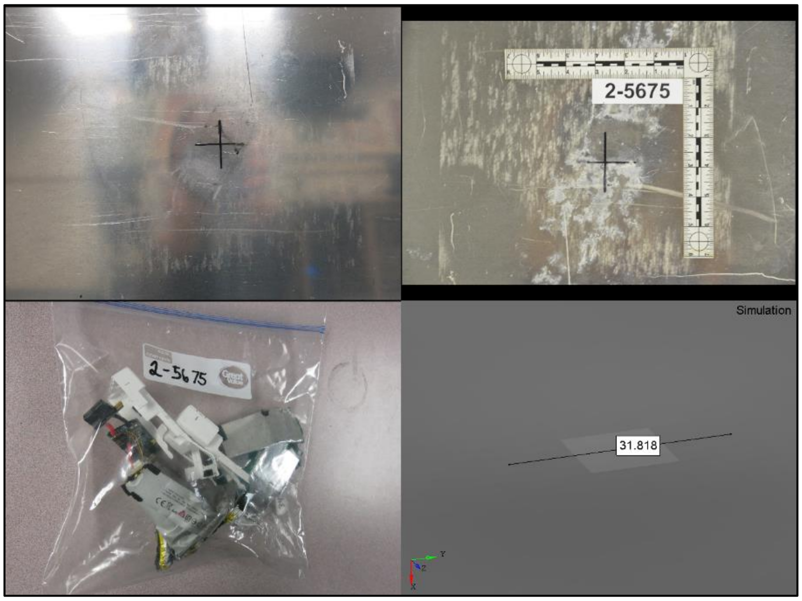

Figure 77. Component level test results for battery impact 5675 on 3.18 mm (0.125″) thick aluminum panel at 49.7 m/s (96.6 kt)

Figure 78 shows the displacement of the panel over the test period. All tests showed great repeatability and the simulation high correlation with the test results.

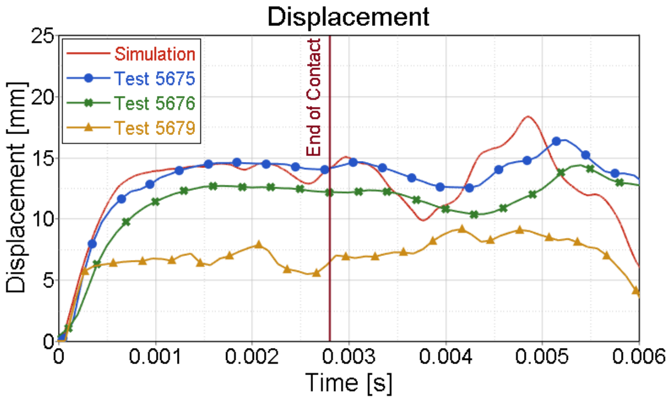

Figure 78. Panel displacement over test period obtained from DIC for battery impact 5675 on 3.18 mm (0.125″) panel at 51.4 m/s (100 kt)

Figure 79 and Figure 80 show the forces and strains for each load cell and the nine channels of strain transducers closest to the impact location respectively in the three test repetitions with the corresponding values obtained from the simulation. All the curves were filtered with a low-pass 15,000 Hz filter. See Appendix F for more details on the data processing methods followed.

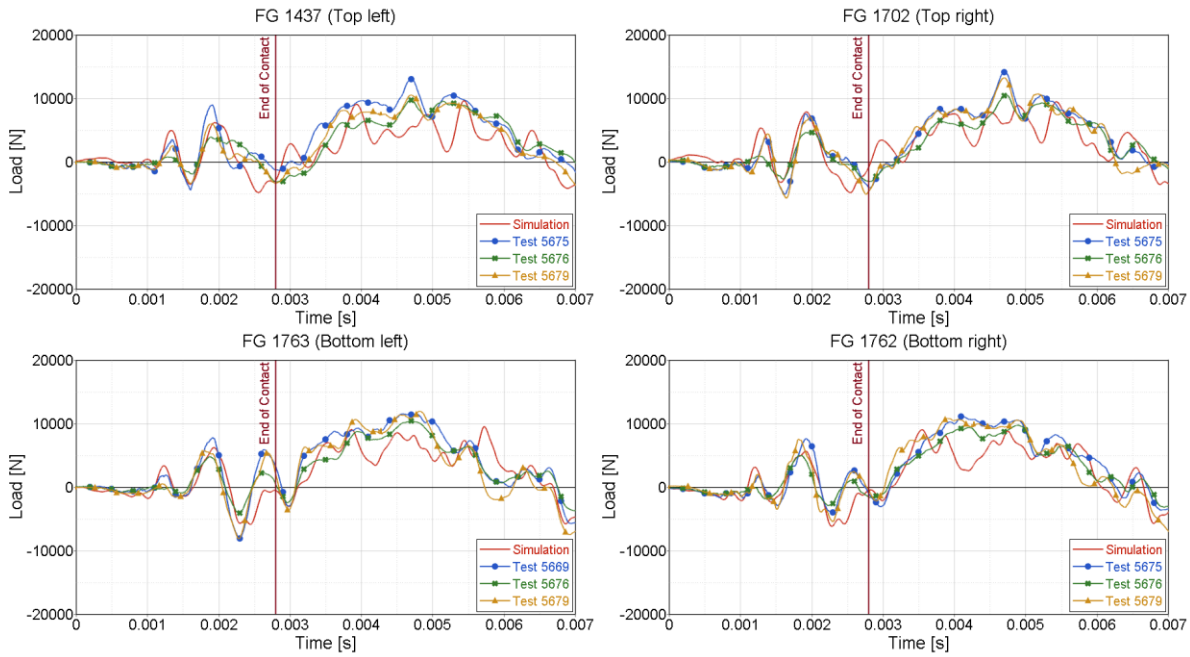

Figure 79. Reaction loads for battery impact 3.18 mm (0.125″) panel at 51.4 m/s (100 kt)

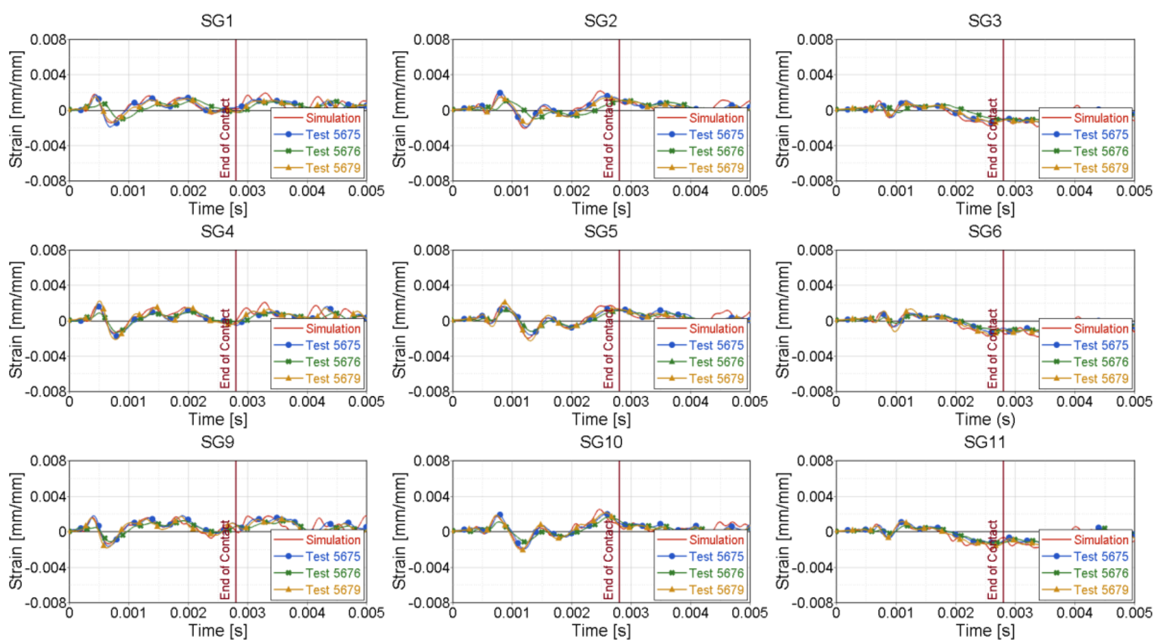

Figure 80. Strains for battery impact 3.18 mm (0.125″) panel at 51.4 m/s (100 kt)

Figure 81 shows a summary of the most representative test results and impact conditions. An average column and error bar indicate the mean and standard deviation of the test results. A red bar indicates in each case the value from the simulation. This figure shows that the three repetitions of test 3 produced a considerable variability, most of it above 10%. It can be seen that test 5679 has the greatest deviation in magnitude values for displacement and strain.

From Figure 81 it can be seen that the magnitude of the peak load displacement and strain for the simulation lies within the variability of the test for all the cases. It can be seen in Figure 79 and Figure 80 that from a qualitative perspective, the shape, and overall performance of the simulation was good, and therefore considered as valid.

From the results presented in this section, it can be observed that the battery FE model produces simulations with high correlation with the respective physical testing. Consequently, it was considered verified for the conditions specified for this test (51.4 m/s and 3.18 mm thick panel).

Test 3 involved battery specimens with electric charge. It was observed that no effect was influencing the impact behavior of the battery due to this pre-charge. It can also be observed that the battery cells experience low levels of damage when impacting at medium speeds (54.1 m/s). This will be important when assessing the risk of fire in the battery cells as it will be introduced in 2.4.4.12 .

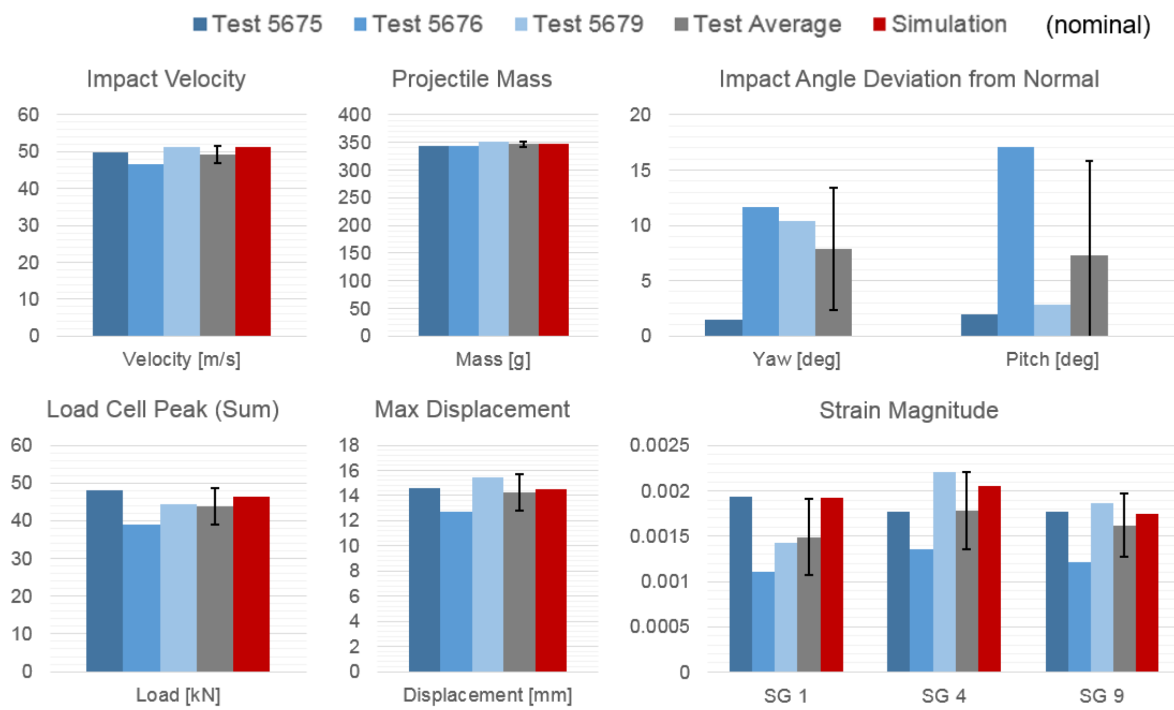

Figure 81. Summary of results for component level test 3, battery impact on 3.2 mm Al panel.

2.4.4.9 Test 4 – Component Level Tests Results and Verification

For the test configuration (test 4) in which the motor impacts a 1.6 mm (0.063″) aluminum panel at 128.6 m/s (250 knots), two iterations with designations 5665 and 5668 and were conducted. Out of these two iterations, 5665 had the least deviation from the nominal conditions.

The FE simulation was set up with an initial projectile velocity of 249.44 knots (128.3 m/s) and pitch of 2.8 degrees to match the test conditions from 5665. The non-structural mass of the motor model was adjusted so the total mass matched the 50.7 g measured in the test.

Figure 82, Figure 83, Figure 84 and Figure 85 below show the comparison of the kinematics between the test and simulation at four different instances of the event, starting at the beginning of the contact between the plate and the projectile and finishing at the end of it.

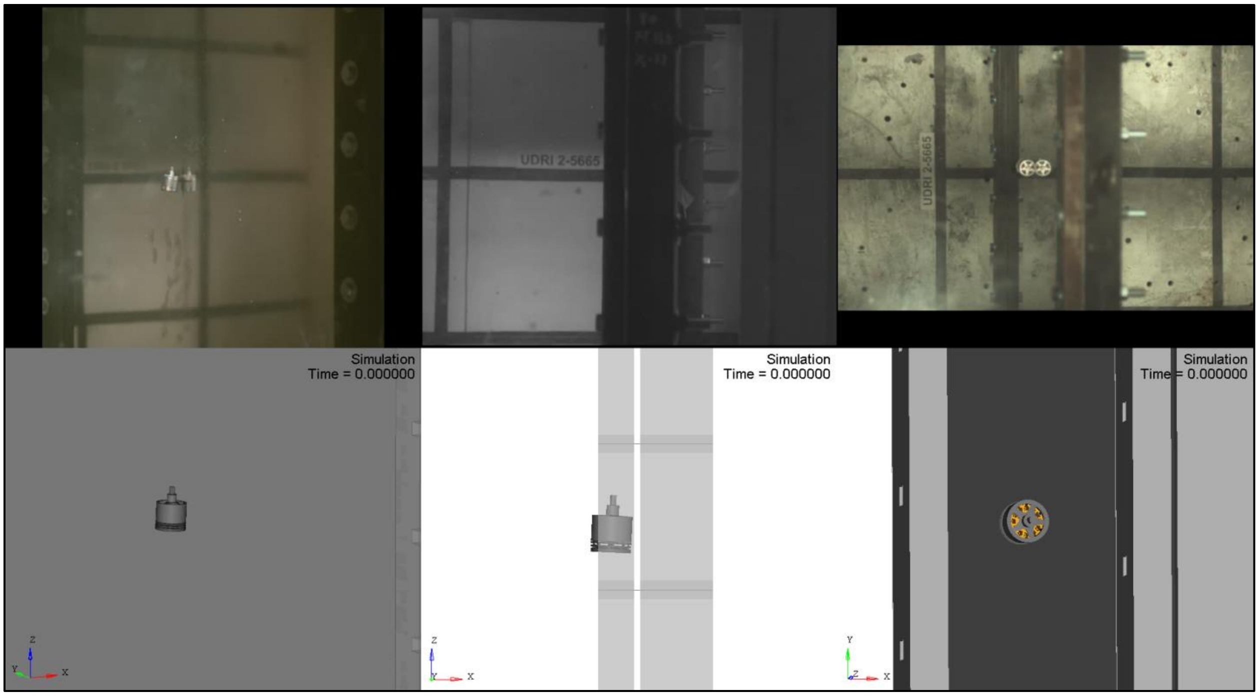

Figure 82. Comparison for motor impact 5665 on 1.6 mm (0.063″) thick aluminum panel at 128.3 m/s (249.4 kt) at t = 0 ms (beginning of contact)

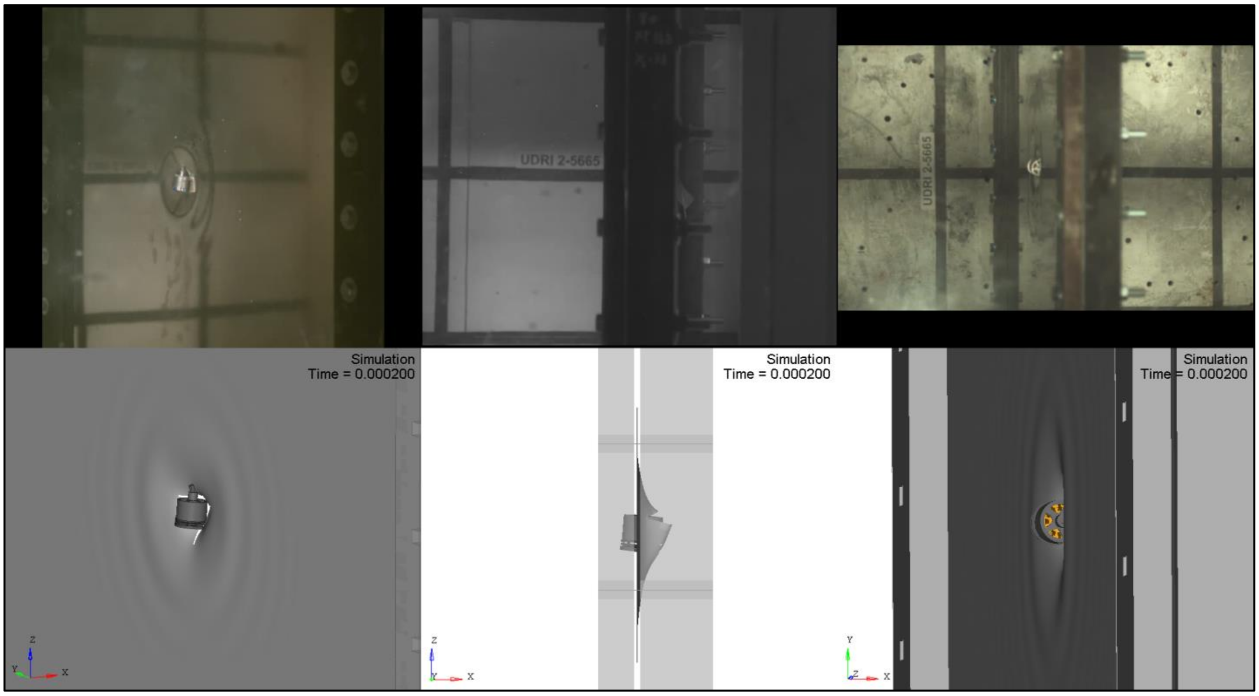

Figure 83. Comparison of motor impact 5665 on 1.6 mm (0.063″) thick aluminum panel at 128.3 m/s (249.4 kt) at t = 0.2 ms

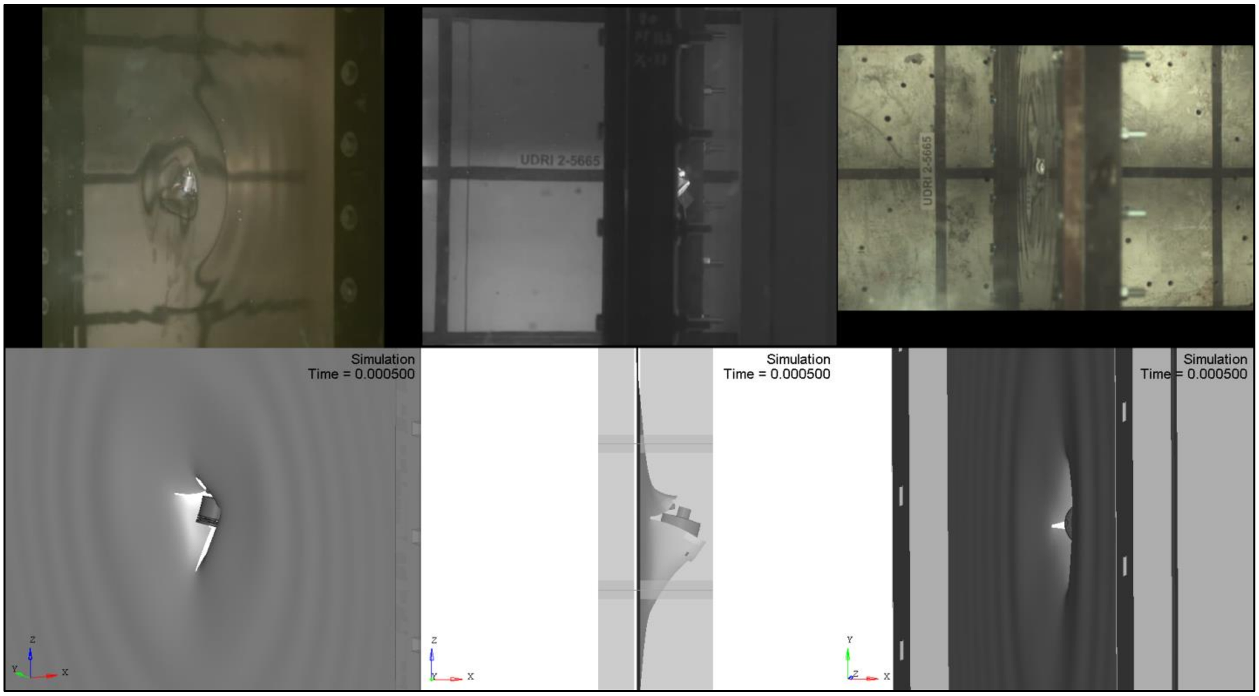

Figure 84. Comparison of motor impact 5665 on 1.6 mm (0.063″) thick aluminum panel at 128.3 m/s (249.4 kt) at t = 0.5 ms

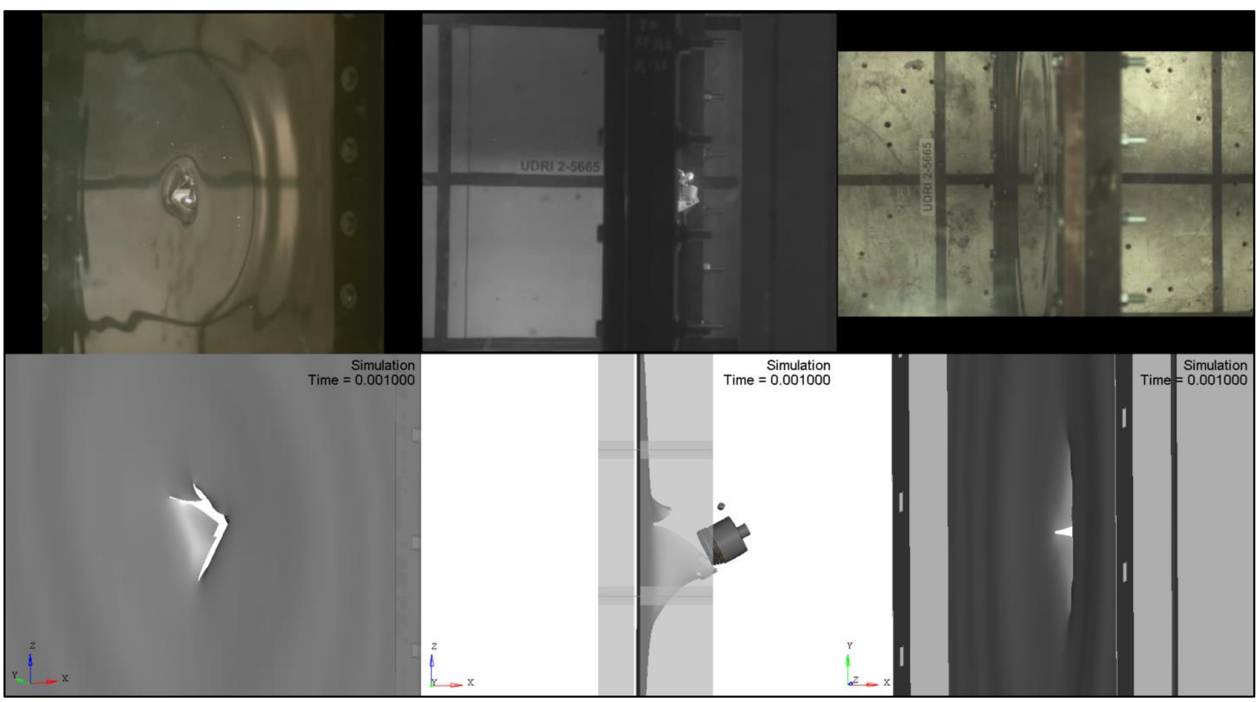

Figure 85. Comparison of motor impact 5665 on 1.6 mm (0.063″) thick aluminum panel at 128.3 m/s (249.4 kt) at t = 1 ms (end of contact)

Figure 86 shows the comparison of the X (horizontal) and Y (vertical) strains as well as out-of-plane displacements (mm) of the component level test obtained from the digital image correlation data and the equivalent contour plot results of the simulation. Figure 87 shows the comparison between the test and simulation for the permanent deformation on the motor and the panel after the impact. Even though the simulation did not predict the separation of the motor into two parts, it captured well the deformations on the body and more importantly, the failure in the panel (see both right images). Both the size and petaling shape were closely captured.

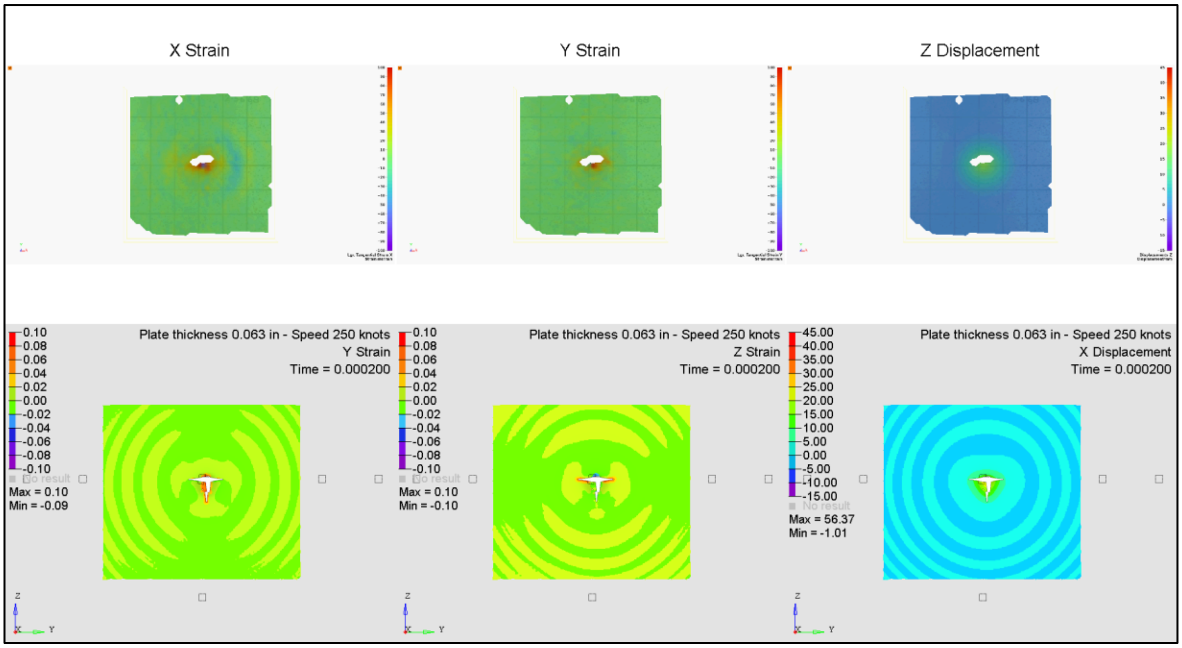

Figure 86. DIC data for motor impact 5665 on 1.6 mm (0.063″) thick aluminum panel at 128.3 m/s (249.4 kts) at the onset of crack initiation (t = 0.2 ms)

Figure 87. Component level test results for motor impact 5665 on 1.6 mm (0.063″) thick aluminum panel at 128.3 m/s (249.4 kts)

Figure 88 and Figure 89 below show the forces and strains for each load cell and the the nine channels of strain transducers closest to the impact location respectively in the two test repetitions with the corresponding values obtained from the simulation. All the curves were filtered with a low-pass 15,000 Hz filter. See Appendix F for more details on the data processing methods followed.

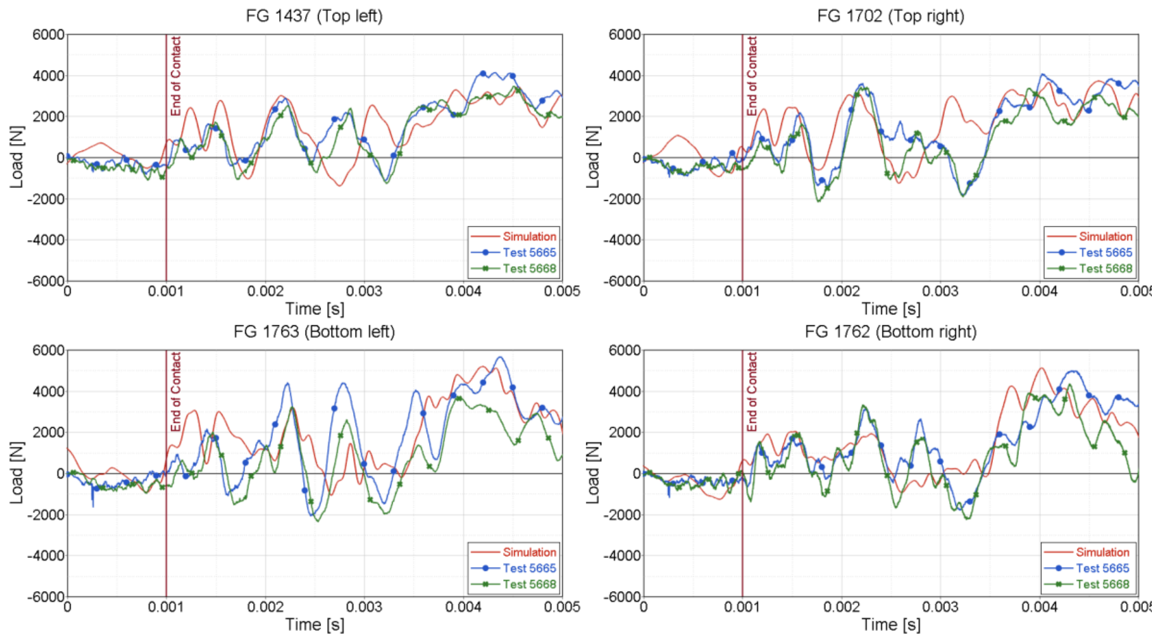

Figure 88. Reaction loads for motor impact on 1.6 mm (0.063″) panel at 128.6 m/s (250 kts)

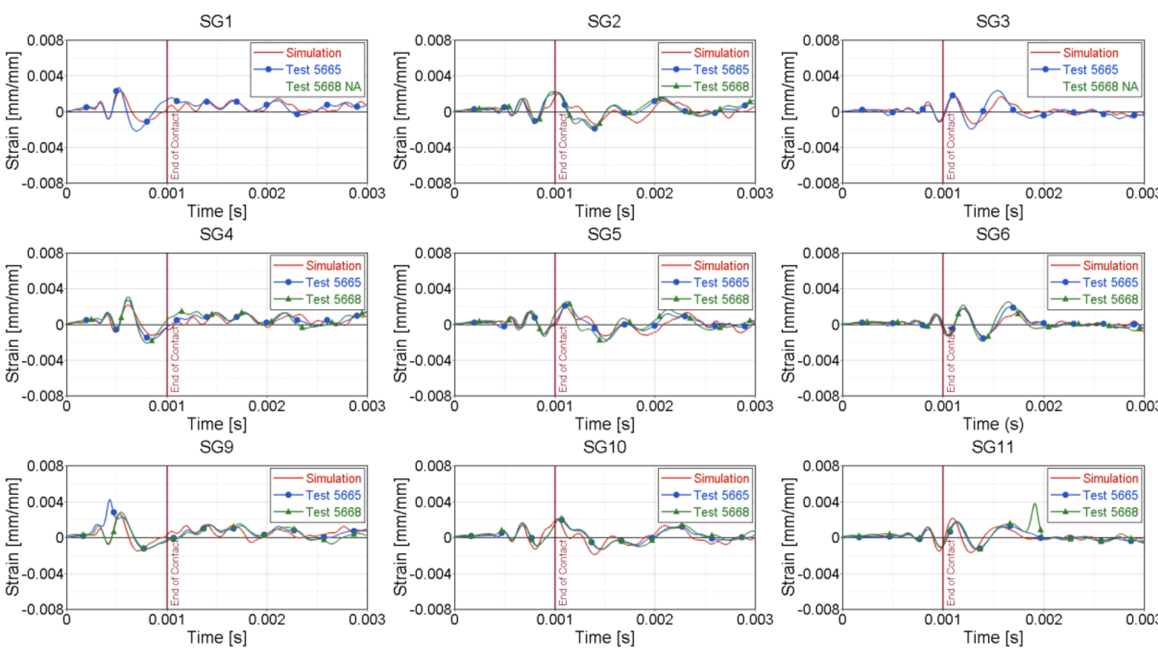

Figure 89. Strains for motor impact on 1.6 mm (0.063″) panel at 128.6 m/s (250 kts)

Figure 90 shows a summary of the most representative test results and impact conditions. An average column and error bar indicate the mean and standard deviation of the test results. A red bar indicates in each case the value from the simulation. This figure shows that the two repetitions of test 4 produced an important level of variability, especially with the load measurements. There is a considerable pitch angle and impact velocity deviations of the motor at impact. It can be seen that the magnitude of the strain for the simulation lies within the variability of the test for most of the cases, while for the load; the value was slightly over predicted.

From the results presented in this section, it can be observed that the motor FE model produces simulations with high correlation with the respective physical testing. It can be seen in Figure 88 and Figure 89 that from a qualitative perspective, the shape, and overall performance of the simulation was good. The plots matched well the initial peaks, and the overall wave shape was captured precisely. In addition, the strain and deformation field measured with the DIC was closely matched with the simulation. Consequently, the motor FE model was considered verified for the conditions specified for this test (128.6 m/s and 1.6 mm thick aluminum panel).

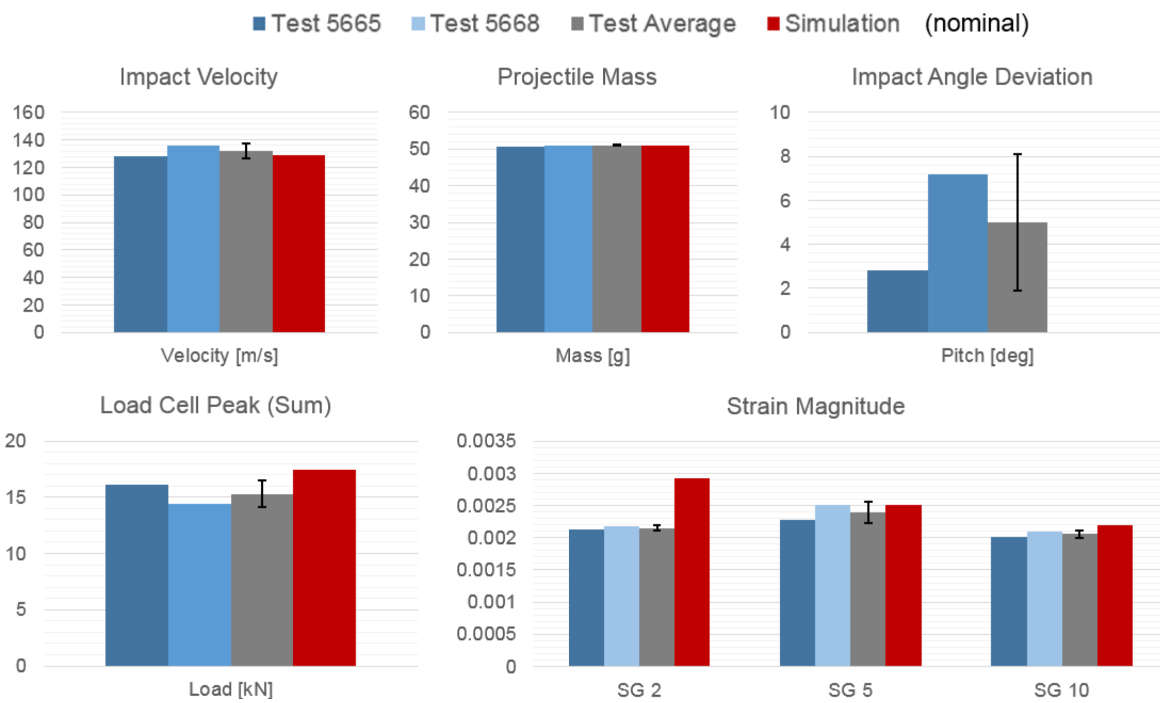

Figure 90. Summary of results for component level test 4, motor impact on 1.6 mm Al panel.

<u>2.4.4.10 Test 5 – Component Level Tests Results and Verification</u>

For the test configuration (test 5) in which the motor impacts a 6.35 mm (0.25″) aluminum panel at 128.6 m/s (250 knots), two iterations with designations 5677 and 5678 were conducted. Out of these two iterations, 5678 had the least deviation from the nominal conditions.

The FE simulation was set up with an initial projectile velocity of 264.84 knots (136.2 m/s) and pitch of 2.1 degrees to match the test conditions from 5678. The non-structural mass of the motor was adjusted to match the 51.0 g measured in the test.

Figure 91, Figure 92, Figure 93 and Figure 94 below show the comparison of the kinematics between the test and simulation at four different instances of the event, starting at the beginning of the contact between the plate and the projectile and finishing at the end of it.

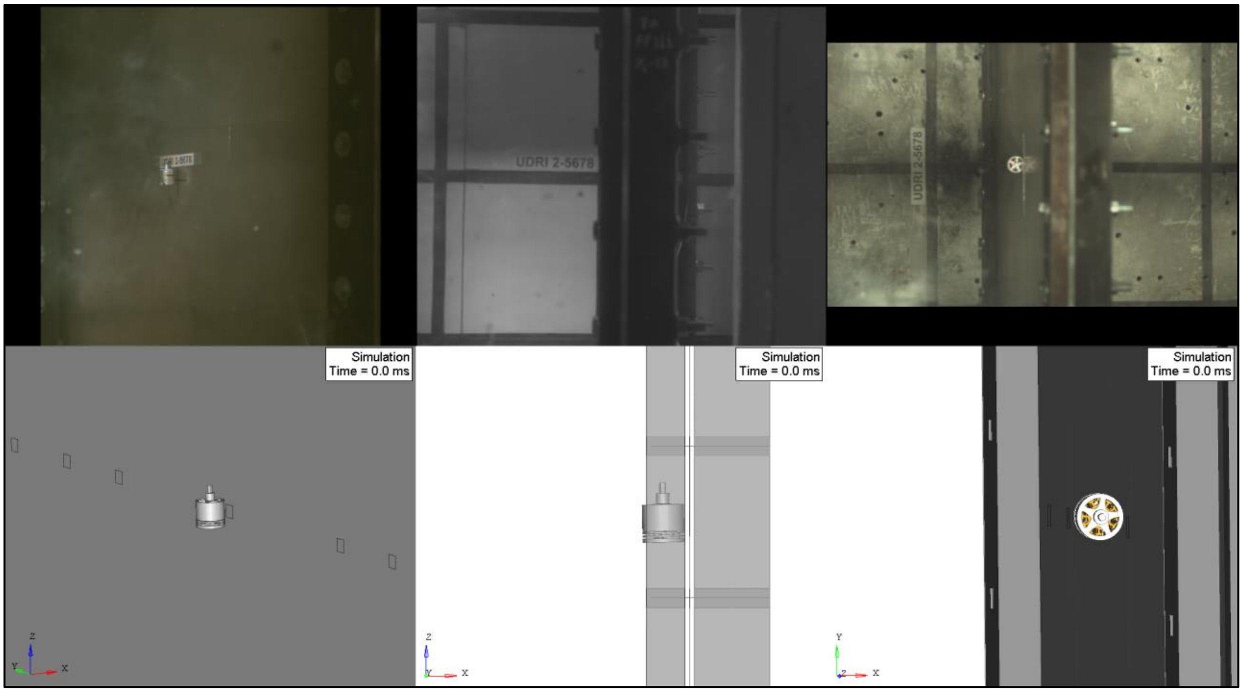

Figure 91. Comparison for motor impact 5678 on 6.35 mm (0.25″) thick aluminum panel at 136.2 m/s (264.8 kt) at t = 0 ms (beginning of contact)

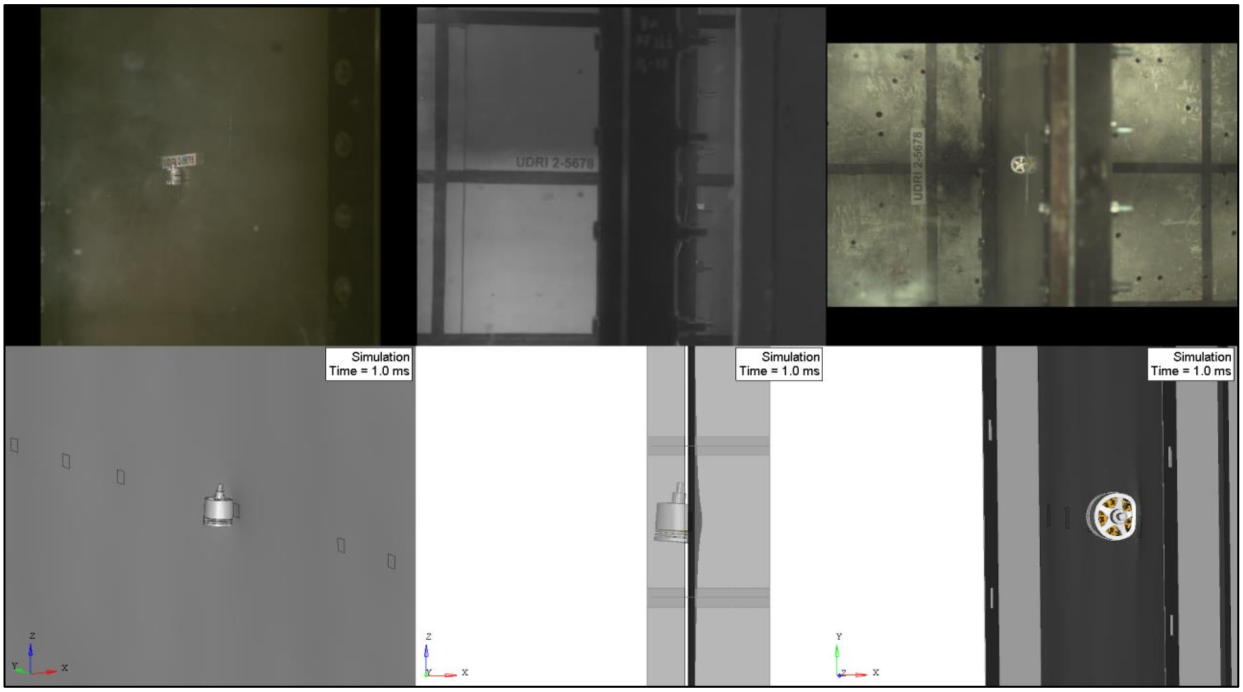

Figure 92. Comparison of motor impact 5678 on 6.35 mm (0.25″) thick aluminum panel at 136.2 m/s (264.8 kt) at t = 0.1 ms

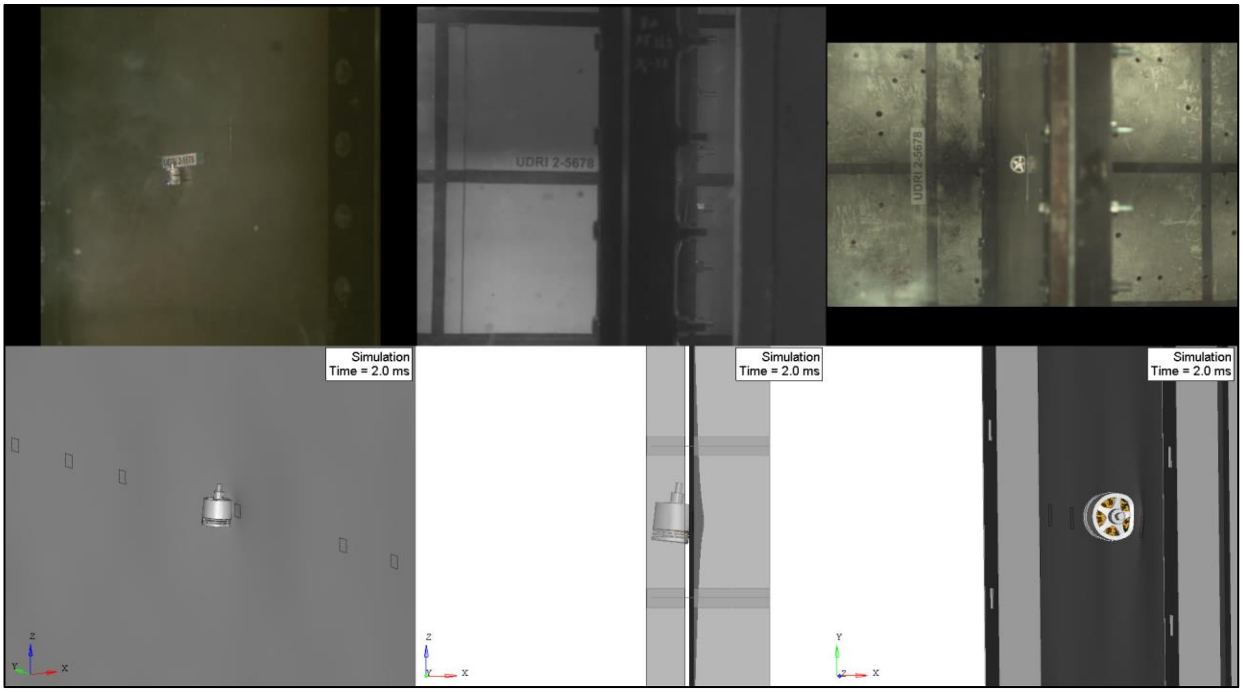

Figure 93. Comparison of motor impact 5678 on 6.35 mm (0.25″) thick aluminum panel at 136.2 m/s (264.8 kt) at t = 0.3 ms

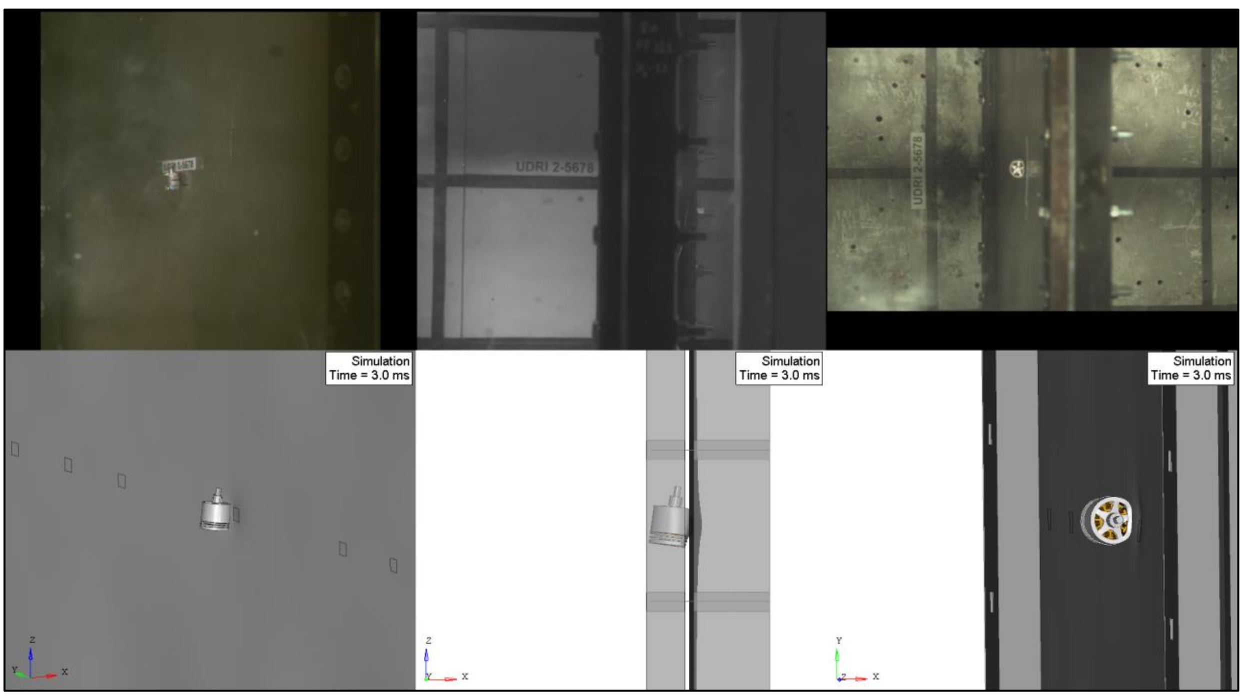

Figure 94. Comparison of motor impact 5678 on 6.35 mm (0.25″) thick aluminum panel at 136.2 m/s (264.8 kt) at t = 0.4 ms (end of contact)

Figure 95 shows the comparison between the test and simulation for the permanent deformation on the motor and the panel after the impact. The bottom right image shows the predicted permanent deformation in the panel by the FE simulation, which can be compared with the image above it.

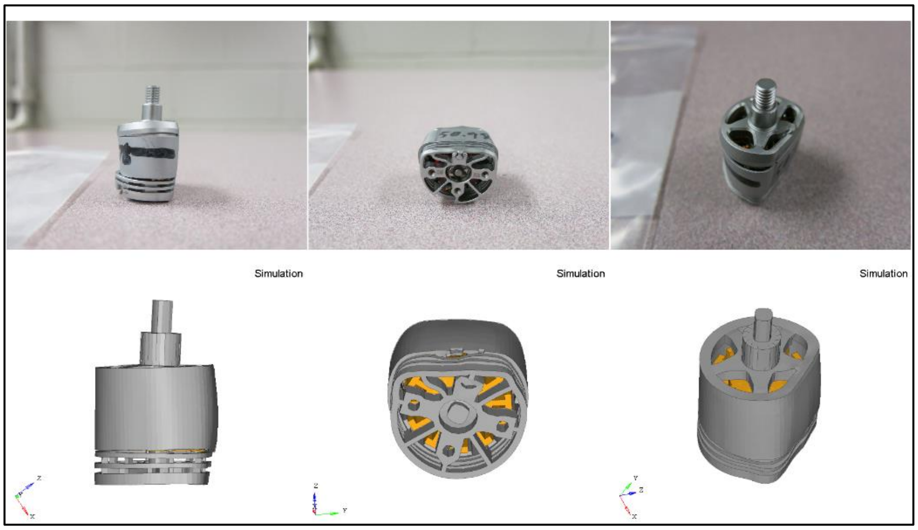

Figure 95. Component level test results for motor impact 5678 on 6.35 mm (0.25″) thick aluminum panel at 136.2 m/s (264.8 kt)

Figure 96 shows the comparison of the X (horizontal) and Y (vertical) strains as well as out-of-plane displacements (mm) of the component level test obtained from the DIC data and the equivalent contour plot results of the simulation.

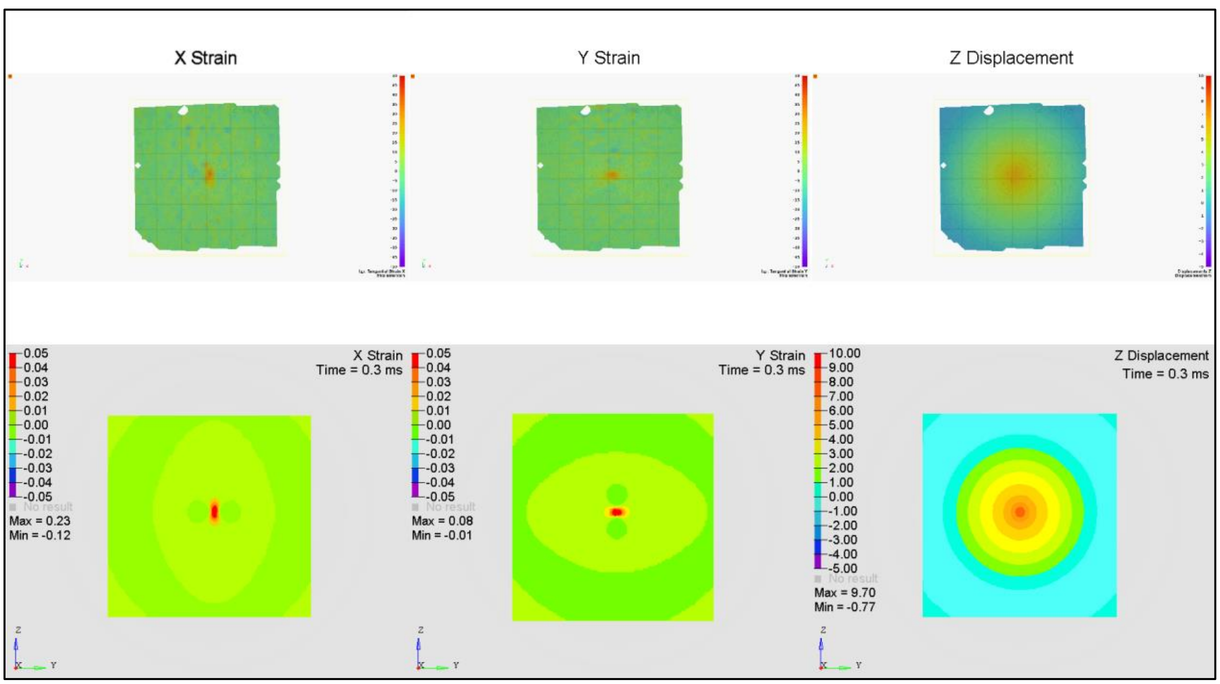

Figure 96. DIC data for motor impact 5678 on 6.35 mm (0.25″) thick aluminum panel at 136.2 m/s (264.8 kt) at the time of maximum panel deformation (t = 0.4 ms)

Figure 97 and Figure 98 below show the forces and strains for each load cell and the nine channels of strain transducers closest to the impact location respectively in the two test repetitions with the corresponding values obtained from the simulation. All the curves were filtered with a low-pass 15,000 Hz filter. See Appendix F for more details on the data processing methods followed.

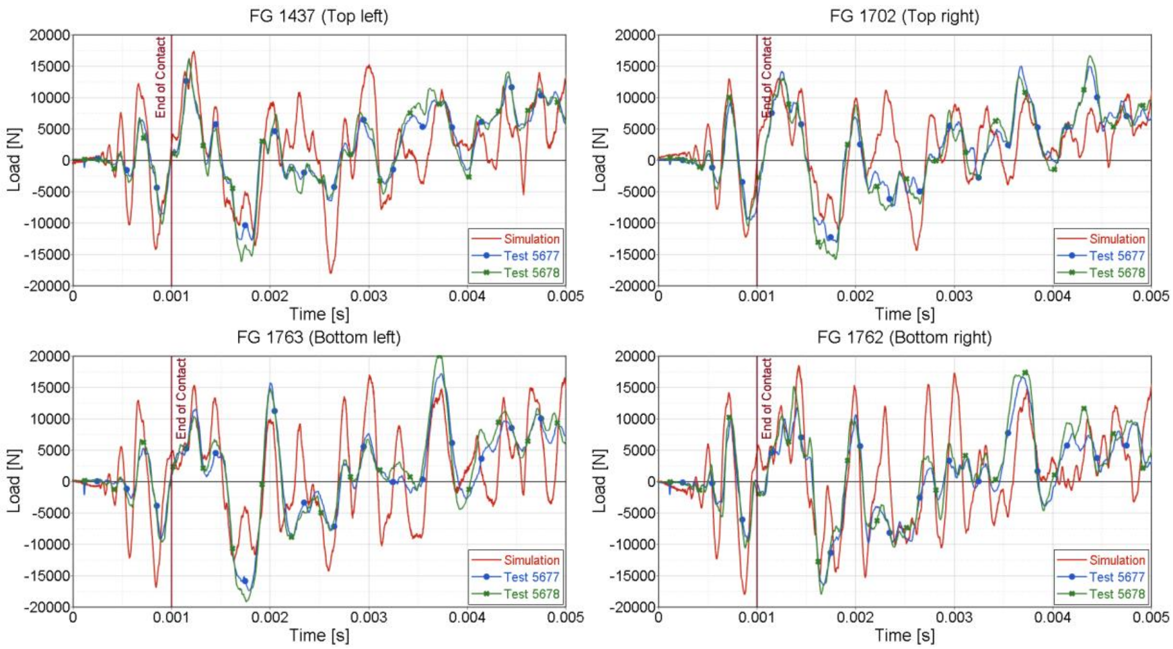

Figure 97. Reaction loads for motor impact on 6.35 mm (0.25″) panel at 128.6 m/s (250 kt)

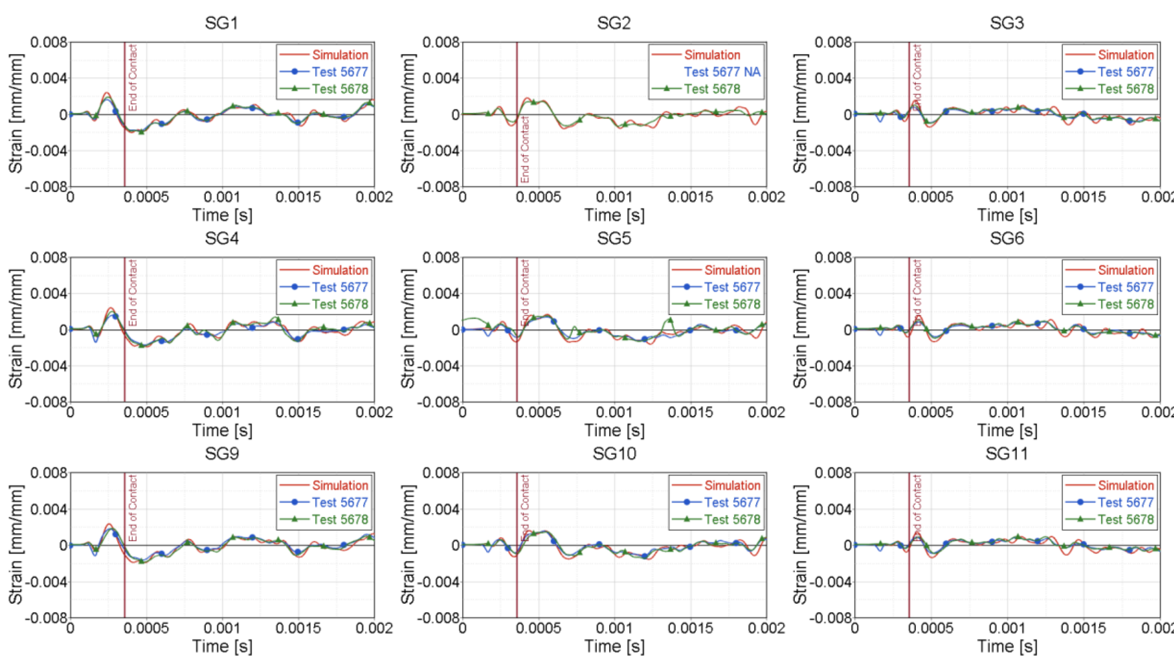

Figure 98. Strains for motor impact on 6.35 mm (0.25″) panel at 128.6 m/s (250 kt)

Figure 99 shows the displacement of the panel over the test period. All test repetitions showed great repeatability the simulation high correlation with the test results.

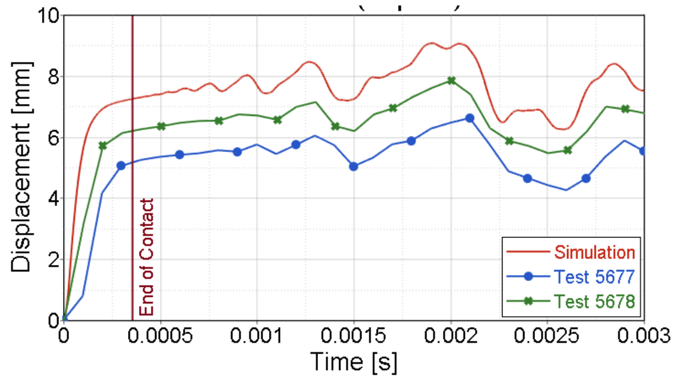

Figure 99. Panel displacement over test period obtained from DIC for motor impact on 6.35 mm (0.25″) panel at 128.6 (250 kt)

Figure 100 shows a summary of the most representative test results and impact conditions. An average column and error bar indicate the mean and standard deviation of the test results. A red bar indicates in each case the value from the simulation. The figure shows that the two repetitions of test 5 produced a considerable amount of variability.

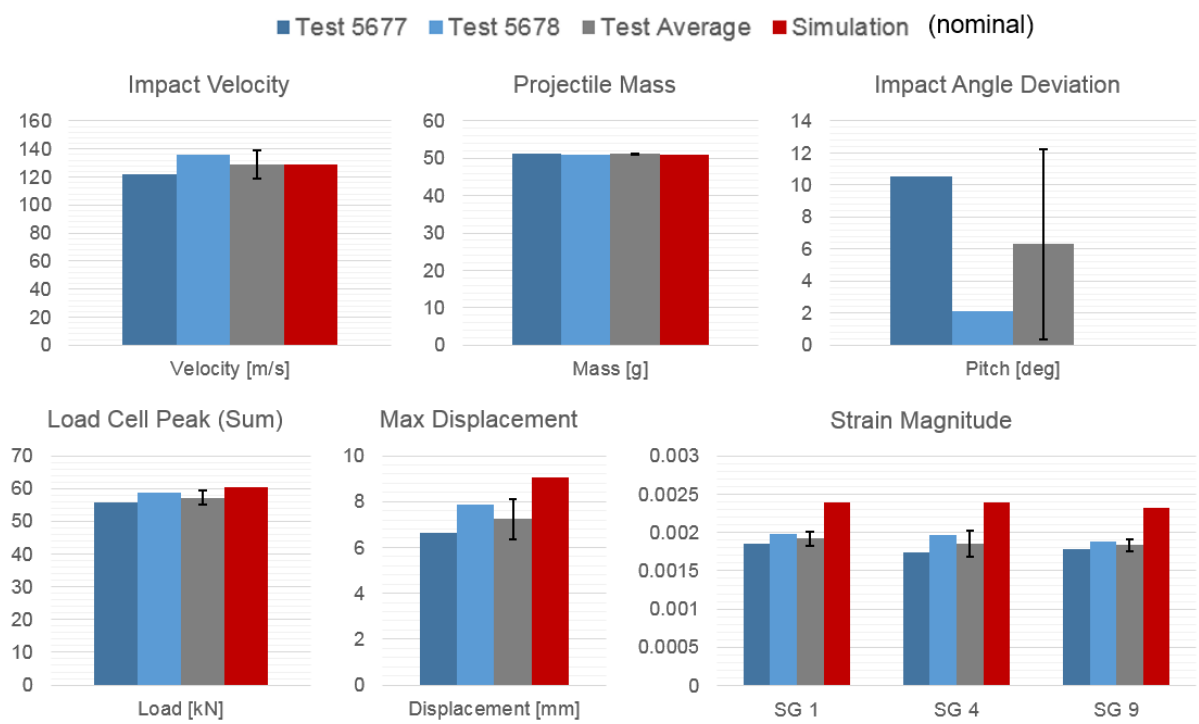

Figure 100. Summary of results for component level test 5, motor impact on 6.35 mm Al panel.

From Figure 100 it can be seen that the magnitude of load, displacement, and strain for the simulation is slightly over predicted for most of the cases. However, it can be seen in Figure 97 and Figure 98 however, that from a qualitative perspective, the shape, and overall performance of the simulation was good.

From the results presented in this section, it can be observed that the motor FE model produces simulations with high correlation with the respective physical testing. Consequently, it was considered verified for the conditions specified for this test (128.6 m/s and 6.35 mm thick panel).

2.4.4.11 Test 6 – Component Level Tests Results and Verification

For the test configuration (test 6) in which the camera impacts a 1.6 mm (0.063″) panel at 250 knots (128.6 m/s), two iterations with designations 5666 and 5667 were conducted. Out of these two iterations, 5667 had the least deviation from the nominal conditions.

The FE simulation was set up with an initial projectile velocity of 251.21 knots (129.2 m/s), pitch of 1.2 degrees and yaw of 8.6 degrees to match the test conditions from 5667. The non-structural mass of the camera was adjusted to match the 52.8 g measured in the test.

Figure 101, Figure 102, Figure 103 and Figure 104 below show the comparison of the kinematics between the test and simulation at four different instances of the event, starting at the beginning of the contact between the plate and the projectile and finishing at the end of it.

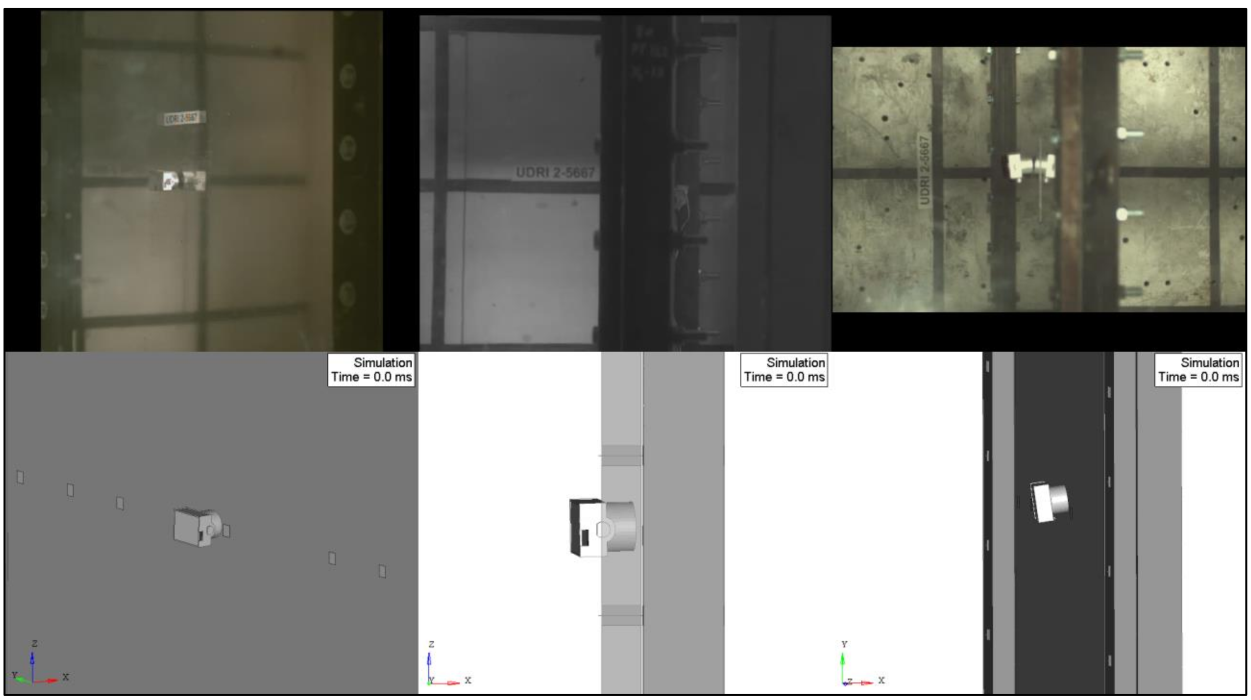

Figure 101. Comparison for camera impact 5667 on 1.6 mm (0.063″) thick aluminum panel at 129.2 m/s (251.2 kt) at t = 0 ms (beginning of contact)

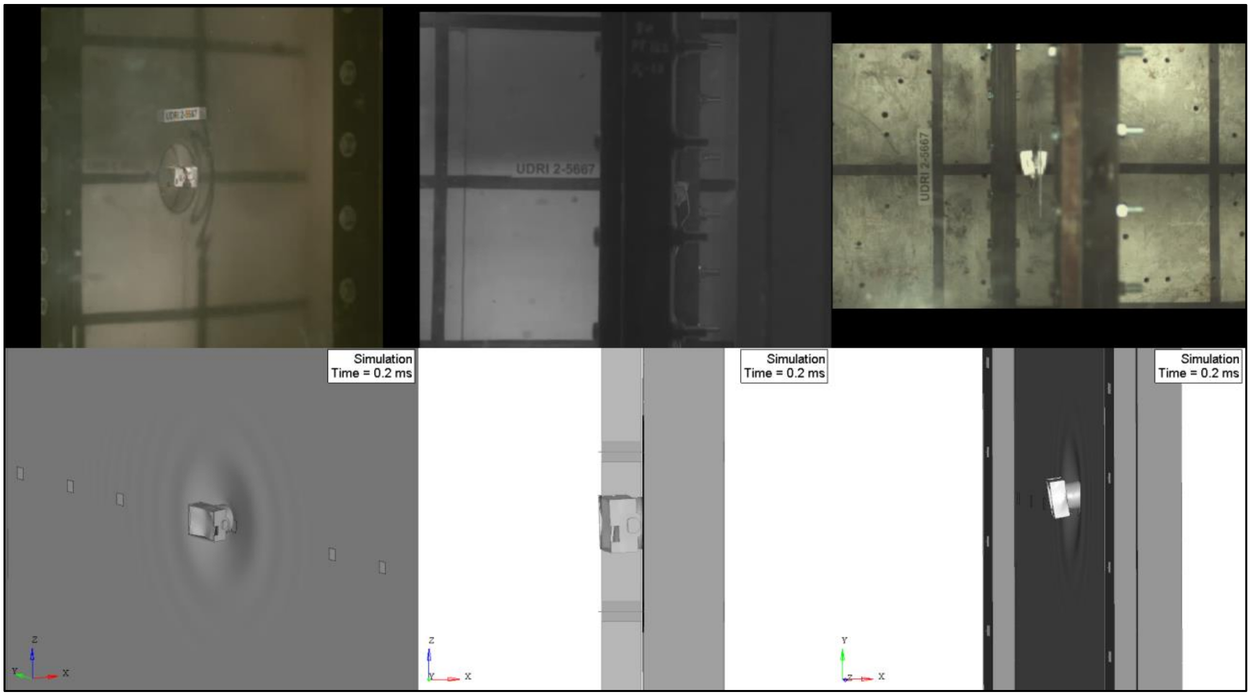

Figure 102. Comparison of camera impact 5667 on 1.6 mm (0.063″) thick aluminum panel at 129.2 m/s (251.2 kt) at t = 0.2 ms

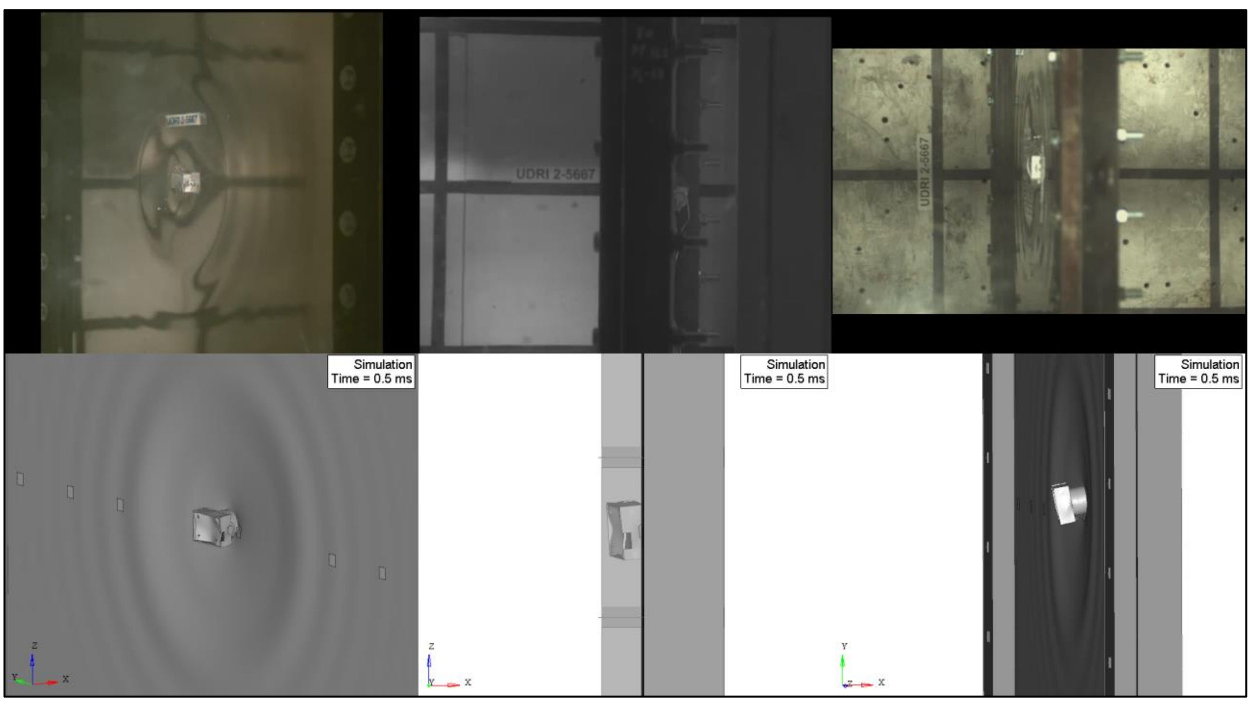

Figure 103. Comparison of camera impact 5667 on 1.6 mm (0.063″) thick aluminum panel at 129.2 m/s (251.2 kt) at t = 0.5 ms

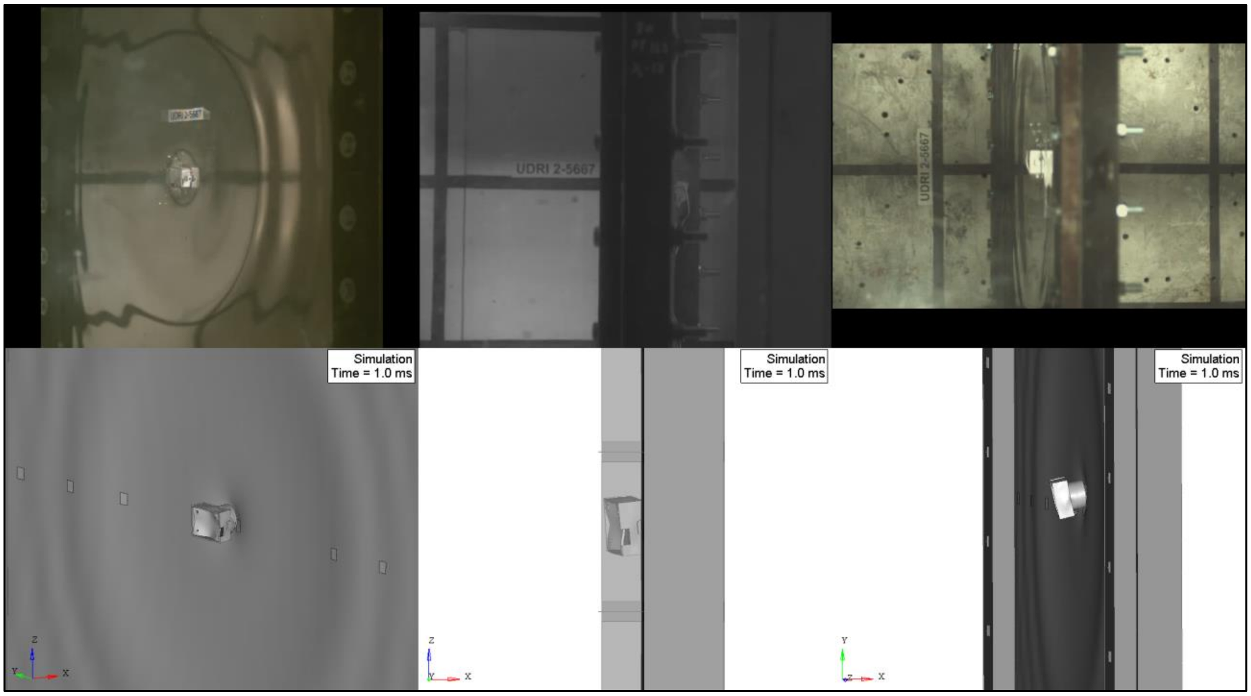

Figure 104. Comparison of camera impact 5667 on 1.6 mm (0.063”) thick aluminum panel at 129.2 m/s (251.2 kt) at t = 1 ms (end of contact)

Figure 105 shows the comparison between the test and simulation for the permanent deformation on the motor and the panel after the impact.

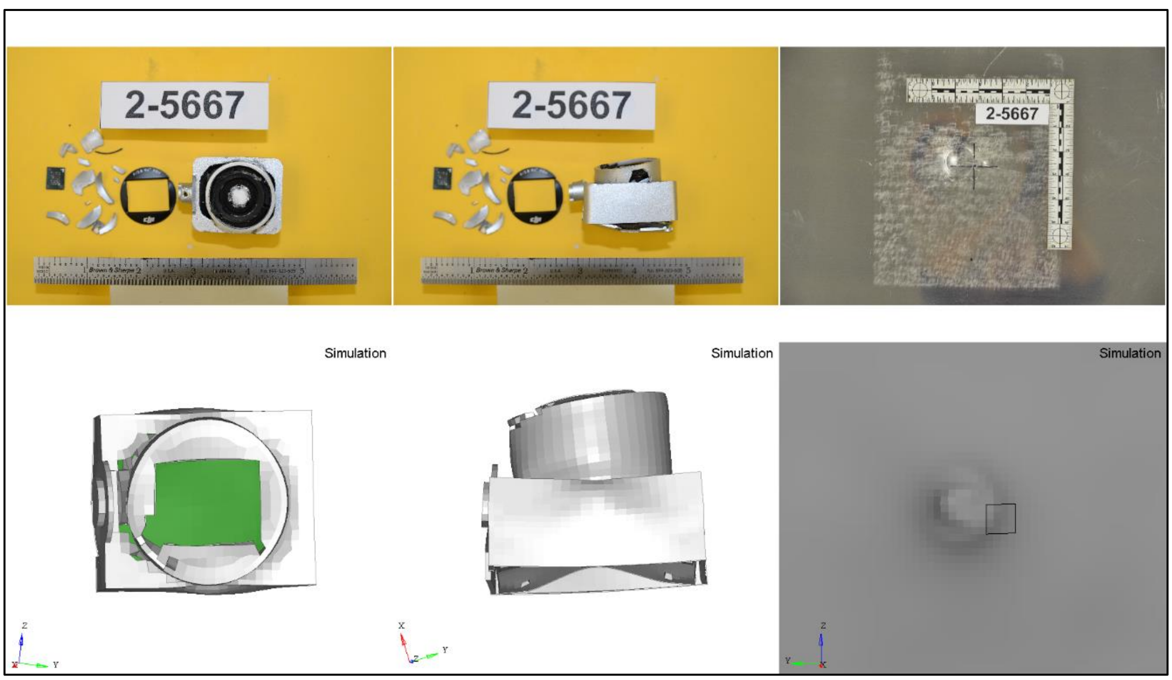

Figure 105. Component level test results for camera impact 5667 on 1.6 mm (0.063”) thick aluminum panel at 129.2 m/s (251.2 kt)

Figure 106 shows the comparison of the X (horizontal) and Y (vertical) strains as well as out-of-plane displacements (mm) of the component level test obtained from the DIC data and the equivalent contour plot results of the simulation.

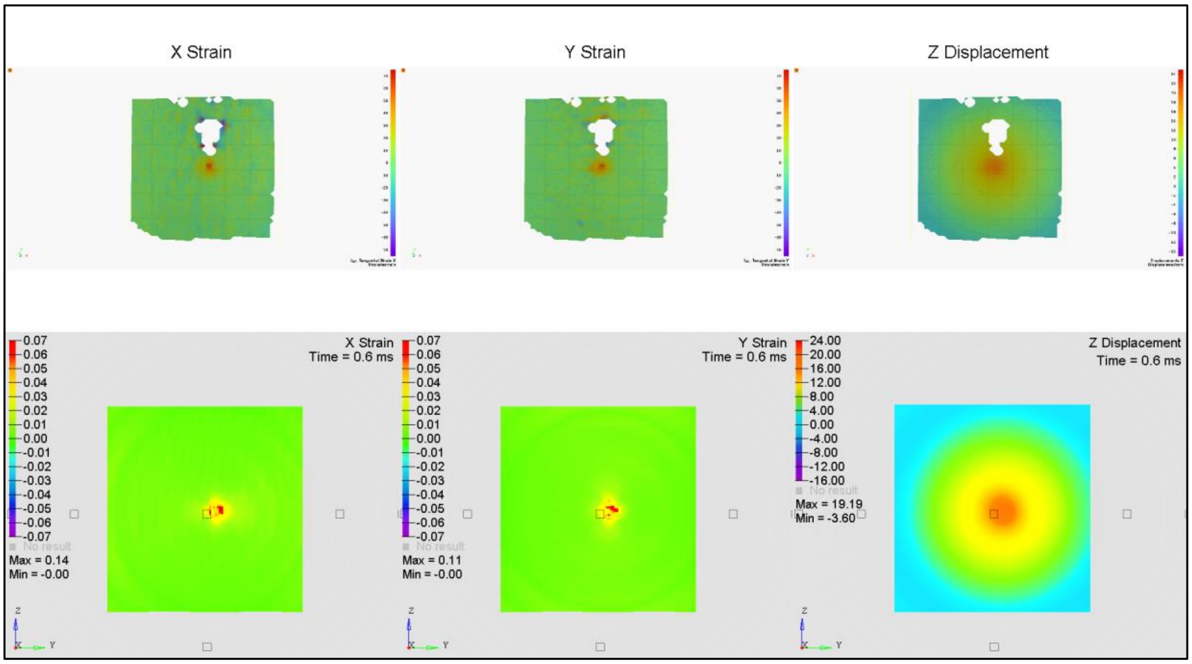

Figure 106. DIC data for camera impact 5667 on 1.6 mm (0.063") thick aluminum panel at 129.2 m/s (251.2 kt) at time of maximum panel deformation (t = 1 ms)

Figure 108 and Figure 109 below show the forces and strains for each load cell and the nine channels of strain transducers closest to the impact location respectively in the two test repetitions with the corresponding values obtained from the simulation. Figure 107 shows the displacement of the panel over the test period. All the curves were filtered with a low-pass 15,000 Hz filter. See Appendix F for more details on the data processing methods followed.

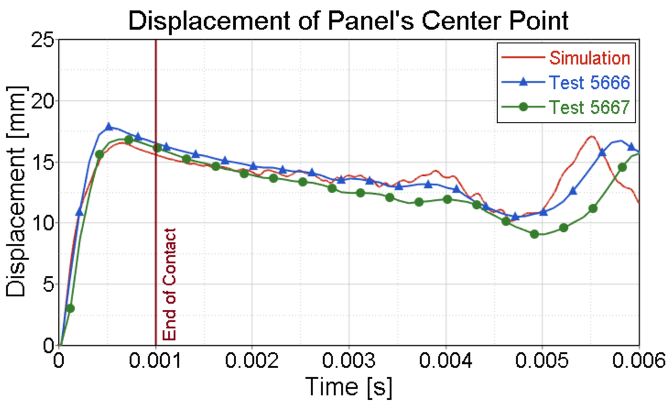

Figure 107. Panel displacement over test period obtained from DIC for camera impact on 1.6 mm (0.063") panel at 128.6 m/s (250 kt)

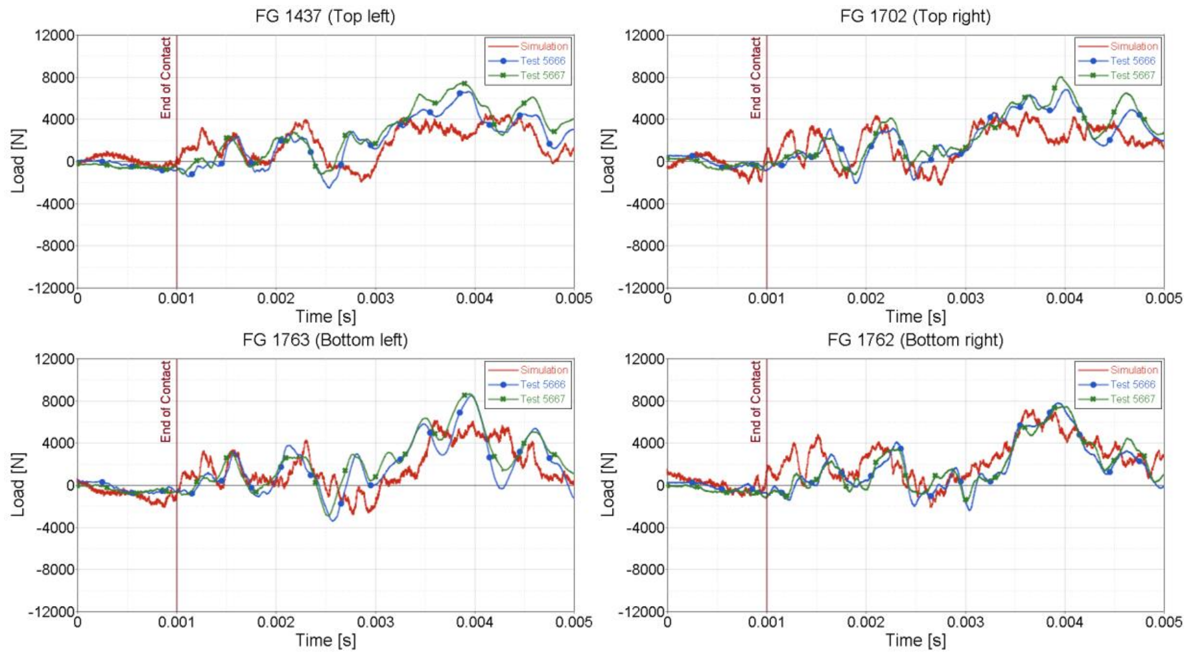

Figure 108. Reaction loads for camera impact on 1.6 mm (0.063″) panel at 128.6 m/s (250 kt)

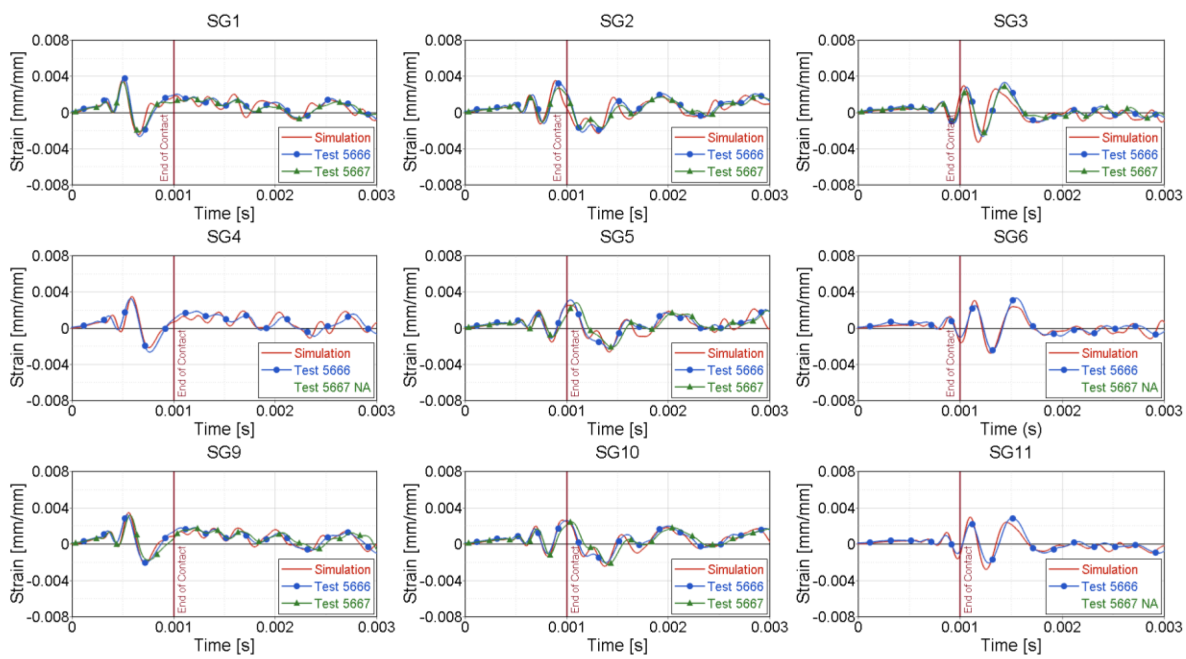

Figure 109. Strains for camera impact on 1.6 mm (0.063″) panel at 128.6 m/s (250 kt)

Figure 110 shows a summary of the most representative test results and impact conditions. An average column and error bar indicate the mean and standard deviation of the test results. A red bar indicates in each case the value from the simulation. The figure shows that the two repetitions of test 6 produced some amount of variability. It can be seen that the magnitude of displacement and strain for the simulation is close or within the variability of the tests for most of the cases, while for the load summation it is under predicted.

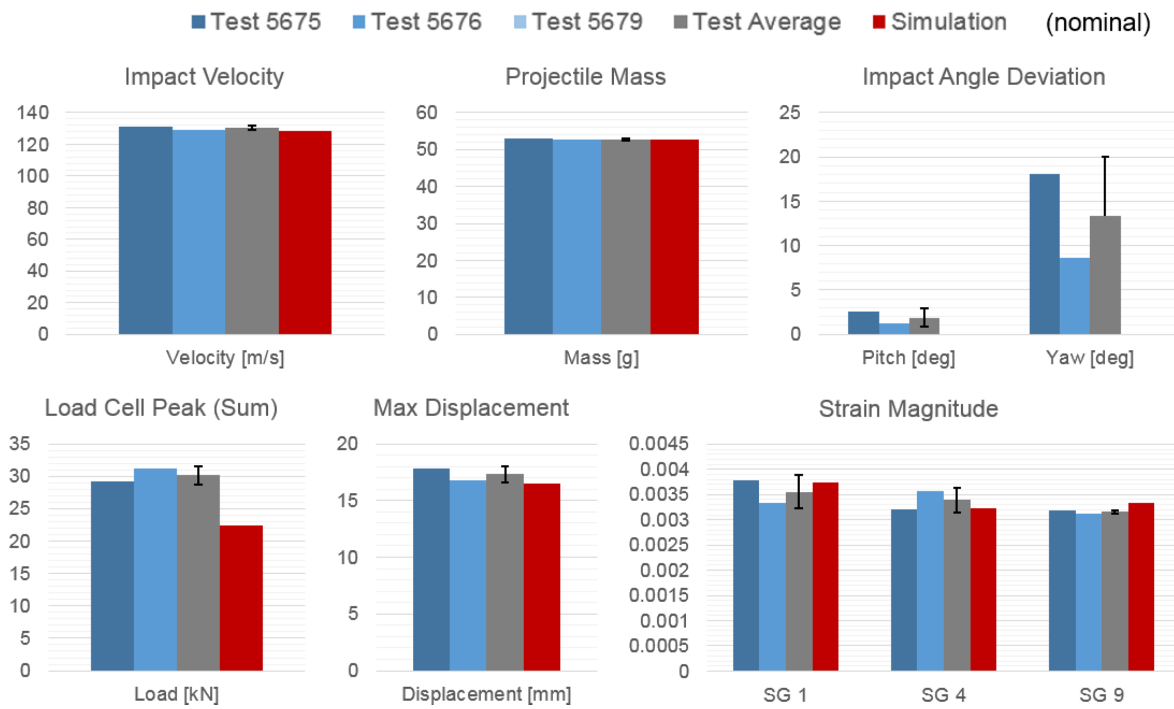

Figure 110. Summary of results for component level test 6, camera impact on 6.35 mm Al panel.

From the results presented in this section, it can be observed that the camera FE model produces simulations with high correlation with the respective physical testing, predicting well the damage of both the camera and the aluminum panel. It can be seen in Figure 108 and Figure 109 that, from a qualitative perspective, the shape, and overall performance of the simulation was good. Consequently, it was considered verified for the conditions specified for this test (128.6 m/s and 1.6 mm thick aluminum panel).

2.4.4.12 Battery Fire Risk Assessment

The potential risk of fire associated with Lithium batteries used in consumer UAS is assessed with respect to ballistic test results obtained in the energy range of this study. Battery impact tests were conducted as shown in 2.4.4.4 . The tests were designed to determine if batteries could ignite on impact but not to record thermal characteristics of the test articles. Accordingly, test witnesses recorded qualitative judgments regarding heat generated by the test articles after impact. Test iterations 5662, 5672, and 5679 used fully charged batteries while the remaining nine battery impact iterations were discharged prior to testing.

Test 5675, shown in Figure 111, yielded the following observation by NIAR Test Engineers: “Battery cells that were fractured but not destroyed continued to show electrical sparks discharging when they were manipulated by hand (they were bent and moved around during post-test inspection)”. It is important to note that the battery test article had been discharged prior to impact but showed signs of becoming a fire risk despite the minimal charge level.

Figure 111. Post impact view of battery debris from shot 5675

Test 5676 was recorded with similar observations: “Battery remained partially intact after impact [and] continued to release heat and audible discharges for more than four hours”. The battery cells, which generated heat and sparks, can be seen along with the damaged battery pack in Figure 112.

Figure 112. Post impact view of battery debris from shot 5676

Finally, test iteration 5679 used a fully charged battery pack, which was able to continue functioning after impact, as seen from the active LED battery charge meter in Figure 113 and Figure 114. Note that the electronics were partially functional despite the loss of some battery cells and significant deformation to those that remained connected.

Figure 113. Post impact view of battery debris from shot 5679

Figure 114. Post impact close-up view of battery debris from shot 5679

The damaged battery was collected in a specimen bag for further inspection as shown in Figure 115, note the internal layers of the individual battery cells being exposed but contained within foil wrappings; these cells are intact enough to actively produce heat and sparks. The larger piece of the battery produced significant heat and had enough integrity to operate its LED charge meter.

Figure 115. Post impact inspection of battery debris from shot 5679

Figure 116. Post impact view of battery debris from shot 5672

As a comparison to the preceding examples, which correspond to impact velocities of 100 knots, batteries that were impacted at higher energy levels did not produce excessive heat or sparks because the individual battery cells were broken apart. Test engineers remarked about these impact scenarios that the "battery was completely destroyed". This type of result is shown in Figure 116 with the carbon powder, battery cell foil and other layering materials unraveled and strewn throughout the test chamber.

In conclusion, it is determined from the test results that any battery cells, which remain mostly intact, can contribute to a risk of fire following an impact scenario.

2.4.5 Component Level Test Summary

In this section, the different component level tests conducted to verify the FE model of the UAS have been presented. The following paragraphs will summarize the testing conducted as well as identify further areas of work.

Firstly, the polycarbonate UAS body was subject to an impact of 110 J in a drop tower test. The event was filmed with high-speed cameras, and the reaction load and respective impulse was measured and recorded.

In addition, the UAS's battery, camera and motors were tested in a compressed air gun facility under impact velocities similar to those of the midair collision being studied in this project, between 56.6 and 128.6 m/s (110 and 250 knots). The kinematics was captured with high-speed cameras, and the reaction loads were measured and the strains in the impacted panel were measured with thirteen strain gages and a Digital Image Correlation system that measured the displacements of the impact area.

Finally, the full UAS assembly (excluding the battery) was dropped from a height of 5.18 m and impacted into a rigid flat plate, where the reaction loads were measured and recorded and the kinematics were captured with high-speed cameras.

All three tests were simulated with the FE model of the respective components of the UAS, replicating the conditions measured in the test. Every test showed high levels of correlation with both the kinematics and the time history data from the physical tests.

Therefore, it can be concluded that the FE model has been verified for the conditions set by the physical tests.

2.5 UAS FINITE ELEMENT MODEL RECOMMENDATIONS

Chapter 2 has presented the FE model of a quadcopter UAS that was designed for crashworthiness collision simulations in LS-DYNA software. It was verified with component level tests to ensure good correlation with physics within the envelope of conditions tested.

The model is intended to be used for assessing impact dynamics with aircraft structures to simulate mid-air collisions. It is recommended to limit the applications to impact velocities in range of 51.4-128.6 m/s (100-250 knots), for which component level tests verified the behavior of the main components of the UAS.

Further component level physical testing and verification would be required to increase accuracy in the following scenarios:

- Impact with rotorcraft moving blades.
- Engine ingestion.
- Ground collision.

3. TARGET DEFINITION - COMMERCIAL TRANSPORT & BUSINESS JETS

This chapter covers the modeling of targets subjected to UAS impact. The UAS airborne collision hazard severity evaluation was conducted through several WPs as defined in the project scope in section 1.2. The following WPs pertain to target modeling.

- *WP II. Target Definition:* Conduct a study to classify aircraft type and select a representative commercial transport jet, business jet and general aviation aircraft.
- *WP IV(a). Aircraft Target Commercial Jet:* Use the NIAR Aircraft Finite Element Analysis (FEA) library to define representative Part 25 Commercial Transport Jet components that can be subjected to UAS Impact.
- *WP IV(b). Aircraft Target Business Jet:* Use the NIAR Aircraft FEA library to define representative Part 23 Business Jet components that can be subjected to UAS Impact.

FE models were defined to study UAS airborne collision hazard severity. This was the only feasible option available to answer the questions in detail within the time frame and budget set for this research project. Fortunately, through several years of research, the NIAR has developed a library of full aircraft models for on-going crashworthiness research projects. These models have been created using a Physics Based Modeling approach for obtaining high fidelity models that can be used for a wide range of applications such as ditching, bird strike and crashworthiness research. Figure 117 and Figure 118 show the global aircraft models created by the NIAR for crashworthiness research. The availability of these aircraft models enabled us to select the areas and components of interest for this research program and refine them with the necessary details. The fact that these models were readily available resulted in great time and cost reductions allowing additional studies to be performed (different targets and projectiles) to provide better conclusions. If these models would have not been available, the majority of time and cost would have been spent developing a single target and only limited results would have been obtained.

In order to build these FE models, the NIAR followed a Physics Based Modeling approach, that takes advantage of advances in computational power, the latest computational tools, years of research in understanding the fundamental physics of the crashworthiness event, generated test-to-test variability data, and verified & validated (V&V) modeling methodologies. This approach uses the Building Block Approach as illustrated in Figure 119. The building block approach is the incremental development of analysis and supporting tests where typically there is an increase in size and complexity of the test article and a decrease in the number of supporting tests. In order to develop this method it is necessary to have a good understanding of the underlying physics and corresponding test variability from the coupon to the system level. The definition of the numerical model is not driven by system level test results; it is driven by a predefined, verified, and validated building block modeling methodology. Using this approach, simulations should be able to predict the system level test results within an acceptable scatter band. An objective verification criteria based on an understanding of the test-to-test variability is used to evaluate the numerical models.

At the coupon level, FE methodologies were defined for material characterization as part of an internal research project [33]. An example of material model verification is shown in section 3.3.5.2 At the connection level, different joint modeling techniques were evaluated through various research projects and applied to the development of the full aircraft models, as well as the targets under consideration [35]. Joint and connection details are documented in section 3.3.4 . A fuselage drop test performed by the FAA [36] was used to evaluate the FE model of the aircraft at the sub-assembly level by extracting the same section out of the NIAR model [37]. By validating multiple sub-assembly level models, the complete full aircraft model was developed, verified, and validated. The same approach and lessons learned were applied to create the NIAR business jet FE model.

Figure 117. NIAR narrow body aircraft model developed for crashworthiness research

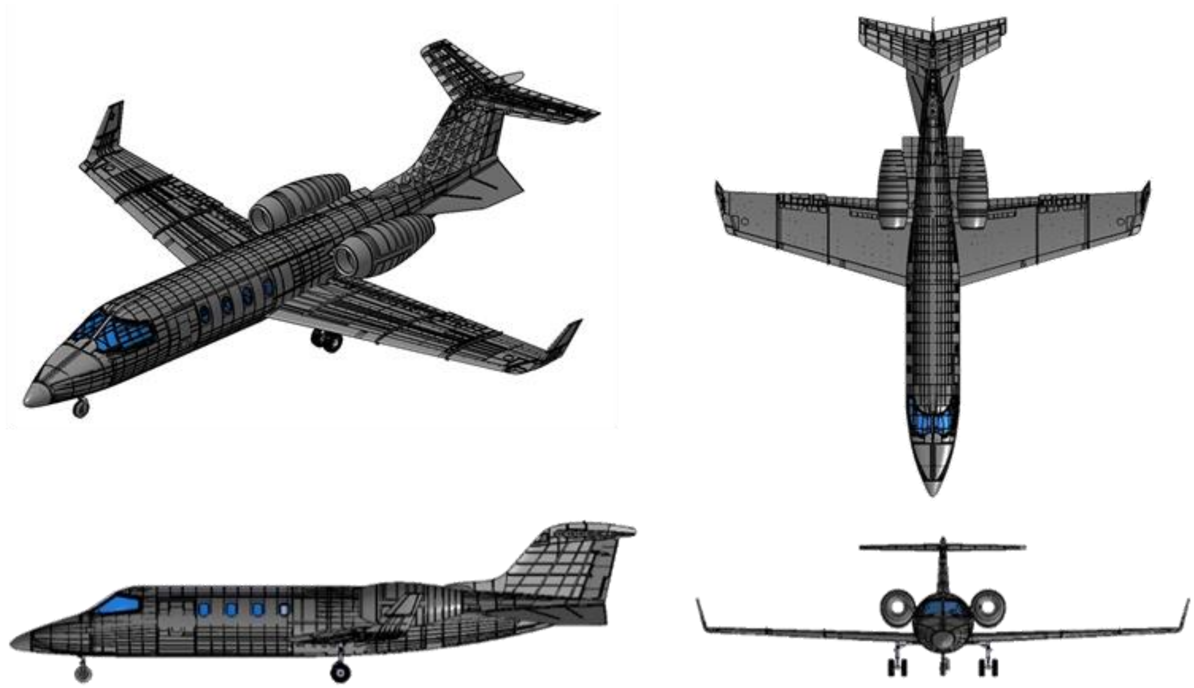

Figure 118. NIAR business jet aircraft model developed for crashworthiness research

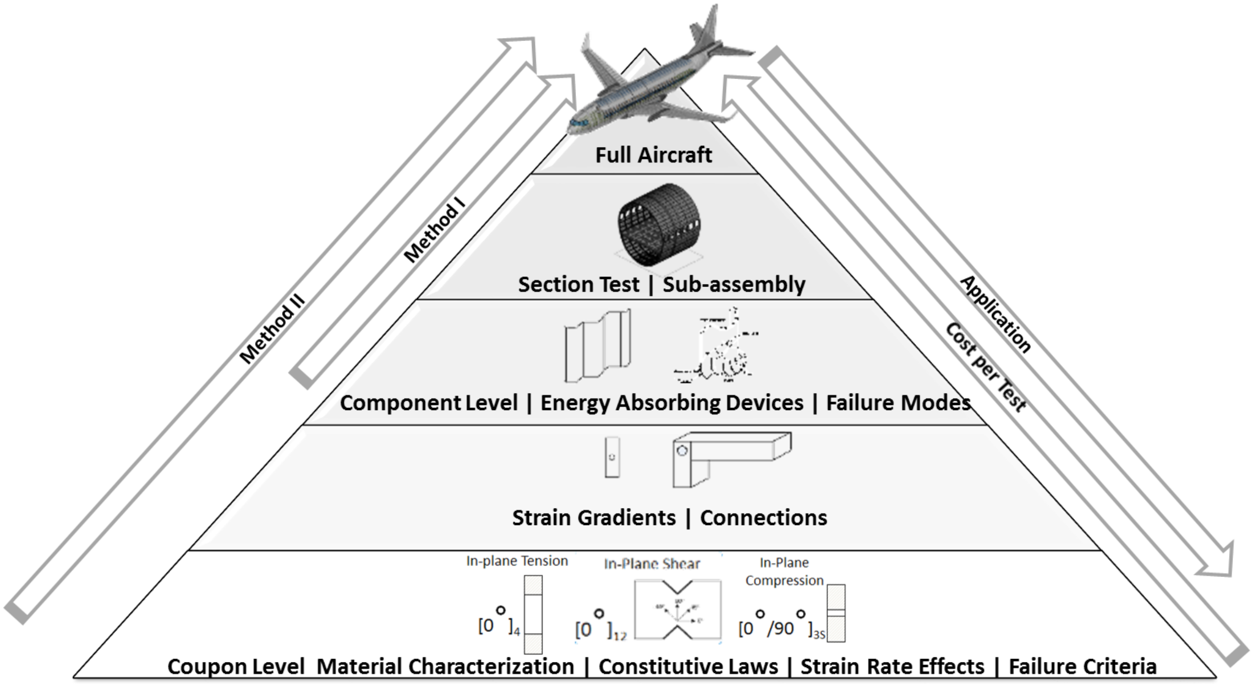

Figure 119. Building block approach for the NIAR narrow body aircraft model

3.1 RATIONALE FOR SELECTION OF TARGETS AND IMPACT AREAS

A review of the airspace usage was conducted to select a representative commercial transport jet and business jet. A summary of the justification for selection of representative aircraft models is provided in this section. Further information can also be found in the research conducted by Montana State University [20] as part of work for WP II.

3.1.1 Commercial Transport Jet

In the recent years, intercontinental travel in developing countries is increasing at a high rate and the future market demand for narrow-body aircraft is predicted to be the highest of all configurations. Figure 120 shows the prediction made by The Boeing Company [38] and Airbus Group [39] of the number of airplanes, which will enter service in a given twenty year period (2014 to 2034). Based on these predictions, single-aisle aircrafts are, and will continue to be, the most popular transport jet model in the market. Single-aisle or narrow body commercial transport jets typically have a seat configuration of 5-6 passengers per row. In addition, the number of passengers that these airliners can transport varies between 130 and 240. Therefore, potential mid-air collisions between a single-aisle aircraft and an UAS are important to study for ensuring occupant safety.

Moreover, as it can be seen in Table 11, both the Boeing 737 and Airbus A320 families are the best-selling aircraft, having by far the highest numbers of deliveries. The table summarizes the deliveries of single-aisle aircraft by Boeing [40] and Airbus [41].

Therefore, the narrow-body single-aisle aircraft, similar to Boeing 737 and Airbus A320, are the most popular transport jets in the world. Thus, a generic model of the narrow-body single-aisle aircraft configuration was reverse engineered and will be referred to as commercial transport jet in this report.

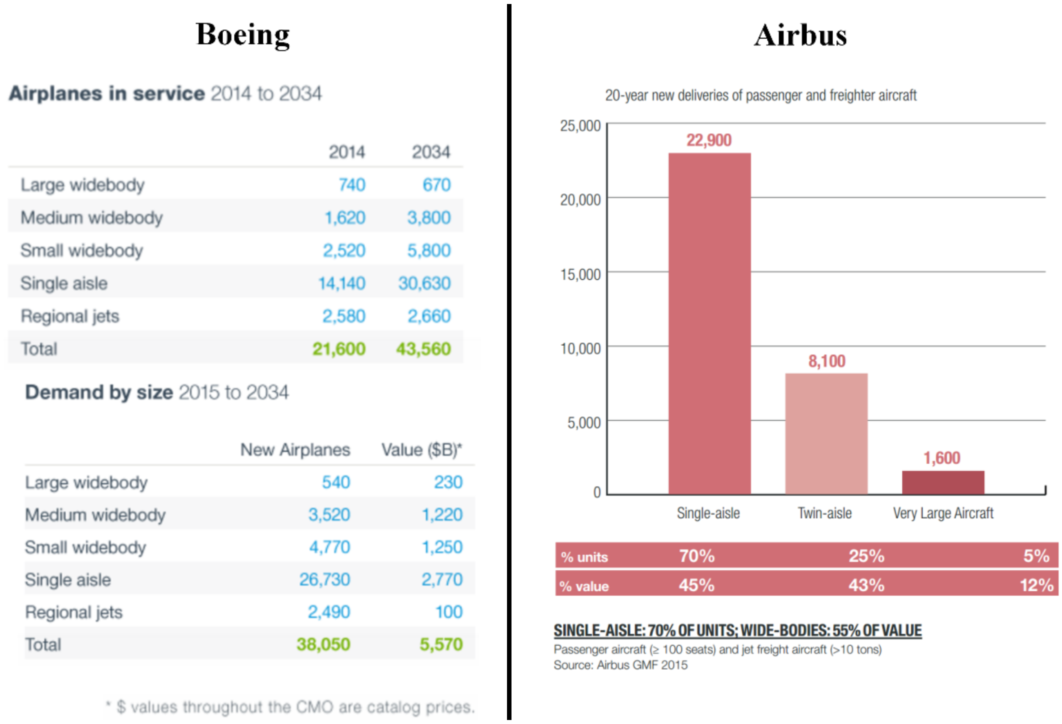
Boeing

Airplanes in service 2014 to 2034

	2014	2034
Large widebody	740	670
Medium widebody	1,620	3,800
Small widebody	2,520	5,800
Single aisle	14,140	30,630
Regional jets	2,580	2,660
Total	21,600	43,560

Demand by size 2015 to 2034

	New Airplanes	Value ($B)*
Large widebody	540	230
Medium widebody	3,520	1,220
Small widebody	4,770	1,250
Single aisle	26,730	2,770
Regional jets	2,490	100
Total	38,050	5,570

* $ values throughout the CMO are catalog prices.

Figure 120. Current market outlook published by Boeing and Airbus (2014 to 2034) [38] [39]

Table 11. Boeing and Airbus aircraft deliveries summary (up to May 2016) [40] [41]

	Boeing						Airbus			
Aircraft Type	737	747	757	767	777	787	A300/ A310	A320	A330/A340 /A350	A380
Total Deliveries	9048	1521	1049	1085	1041	417	816	7068	1680	190

3.1.1.1 Commercial Transport Jet Specifications

Table 12 shows specifications of the Boeing 737-800, Airbus A320, and commercial transport jet models developed by the NIAR. The specifications provide insight into the size and scale of the aircraft when compared to the UAS and the cruise and approach velocities. These velocities were the basis for selecting velocities for UAS impact studies.

Table 12. Boeing 737, A320, and NIAR commercial transport jet model specifications [42]

	B737-800		**A320**		**NIAR model**	
MTOW	79,015 kg	174,200 lb	77,000 kg	169,755 lb	79,000 kg	174,165 lb
Wing span	35.79 m	117 ft 5 in	34.09 m	111 ft 9 in	35.84 m	117 ft 7 in
Horizontal stabilizer span	14.35 m	47 ft 1 in	12.45 m	40 ft 10 in	14.27 m	46 ft 10 in
Vertical stabilizer span	7.06 m	23 ft 2 in	5.87 m	19.26 ft	7.21 m	23 ft 8 in
Fuselage length	38.02 m	124 ft 9 in	37.57 m	123 ft 3 in	37.97 m	124 ft 7 in
Cruise Altitude	10,955 m	35,940 ft	11,280 m	37,000 ft	11,000 m	36,089 ft
Max cruise speed [Mach]	0.82		0.82		0.82	
Cruising speed [Mach]	0.78		0.78		0.78	
Minimum landing speed	55.0 m/s	107 knot	N/A m/s	N/A knot	56.6 m/s	110 knot

3.1.2 Business Jet

Similarly, the Learjet 31A model was selected as a representative aircraft for the business jet category. Although this aircraft is not the most registered by the FAA, it has similar dimensions and specifications in comparison to many other business jets [43]. Thus, a generic model of similar size and design, as the Learjet 31A, was developed and will be referred to as business jet in this report.

3.1.2.1 Business Jet Specifications

The specifications for the Learjet 31A and the NIAR model are presented in Table 13. The velocities selected for UAS impact studies are explained in subsequent chapters.

Table 13. Learjet 31A and NIAR business jet model specifications [43][44]

	Learjet31A		**NIAR model**	
MTOW	7,711 kg	17,000 lb	7,711 kg	17,000 lb
Wing Span	13.35 m	43 ft 9 in	13.28 m	43 ft 7 in
Horizontal Stabilizer Span	4.48 m	14 ft 8 in	4.47 m	14 ft 8 in
Vertical Stabilizer Span	1.68 m	5 ft 6 in	2.67 m	8 ft 9 in
Length Overall	14.83 m	48 ft 8 in	14.71 m	48 ft 3 in
Cruise Altitude	13,105 m	43,000 ft	13,105 m	43,000 ft
Max Cruise Speed [Mach]	0.83		0.83	
Cruising Speed [Mach]	0.79		0.79	
Minimum Landing Speed	44 m/s	87 knot	44 m/s	87 knot

3.1.3 Aircraft Impact Areas

One of the main goals of this UAS impact research was to compare UAS impacts to bird strikes for which extensive regulations already exist for certification of aircraft. Thus, an important part of this research was to assess if UAS impacts on aircraft are analogous to those from bird strikes. The selection of components of the aircraft for UAS impact was therefore largely based on the Part 25 requirements for bird impacts. The regulations for bird strike impact were reviewed thoroughly and are summarized in Table 14. Based on the review, the empennage of Part 25 aircraft must withstand 8 lb bird impacts while the rest of the structure, including windshields, must withstand 4 lb bird impacts.

A survey of reported bird impacts on aircraft, between 1990 and 2014 in USA, was conducted by the FAA and a summary of the areas of aircraft impacted was documented [45]. Two pie charts indicating the location and the severity of bird strike cases and a summary table as presented in the report are shown in Figure 121 and Figure 122 respectively. The largest percentage of strikes occurred on the windshield, nose, wing/rotor, engine, and fuselage. Figure 121 and Figure 122 also indicate that the components most damaged due to bird impact were the wing/rotor and engines. If the probability of impact with an UAS into a certain area of the aircraft is assumed similar to a bird strike, two areas of interest can be noted: airframe and powerplants.

The structural evaluation of UAS impacts on aircraft structures is covered in this report. Therefore based on the Part 25 requirements and bird strike impact survey, the components selected for bird strike impact are the windshield, wing leading edge, horizontal stabilizer leading edge, and vertical stabilizer leading edge. A separate report to evaluate UAS ingestion and impact on engines components has been completed by Ohio State University (OSU) [3].

Another consideration of UAS impacts was how the UAS would be affected by the airflow characteristics over selected components of the aircraft. The argument is that turbulence and flow patterns may diminish the effects of an UAS impact or cause the UAS to completely avoid an impact. Therefore, the selection of localized areas for UAS impact was based on some preliminary Computational Fluid Dynamics (CFD) analyses using the aircraft Outer Mold Line (OML). Flow patterns, shown in Figure 123, were studied and the areas on the wing and stabilizers showing turbulent flow patterns were ignored. Thus, based on the information presented in this section, the selected components and impact areas were modeled with more detail necessary for obtaining accurate UAS impact FEA results. Details of the CAD and FE modeling of these components are presented in subsequent sections.

Table 14. Bird strike related regulations [46][47]

Category	**Chapter**	**Aircraft Component/ Bird Mass**	**Regulation**
Part 23	14 CFR 23.775 Windshield and Windows	Windshield 0.907 kg (2 lb)	Windshield panes directly in front of the pilots in the normal conduct of their duties, and the supporting structures for these panes, must withstand, without penetration, the impact of a two-pound bird when the velocity of the airplane (relative to the bird along the airplane's flight path) is equal to the airplane's maximum approach flap speed.
Part 25	14 CFR 25.631 Bird Strike Damage	Empennage 3.63 kg (8 lb)	The empennage structure must be designed to assure capability of continued safe flight and landing of the airplane after impact with an 8 lb bird when the velocity of the airplane is equal to V_C at sea level.
	14 CFR 25.775 Windshield and Windows	Windshield 1.81 kg (4 lb)	Windshield panes directly in front of the pilots in the normal conduct of their duties, and the supporting structures for these panes, must withstand, without penetration, the impact of a 4lb bird when the velocity of the airplane is equal to the value of V_C, at sea level.

Table 14 Continuation. Bird strike related regulations [46][47]

Part 25	14 CFR 25.571 Damage tolerance and fatigue evaluation of structure	Aircraft structure 1.81 kg (4 lb)	- Impact with a 4-pound bird when the velocity of the airplane is equal to V_C at sea level or 0.85 V_C at 8,000 feet, whichever is more critical. - The damaged structure must be able to withstand the static loads (considered as ultimate loads) which are reasonably expected to occur on the flight. Dynamic effects on these static loads need not be considered. Corrective action to be taken by the pilot following the incident must be considered. If significant changes in structural stiffness or geometry, or both, follow from a structural failure or partial failure, the effect on damage tolerance must be further investigated.
Part 29	14 CFR 29.631 Bird Strike	Rotorcraft Structure 1 kg (2.2 lb)	The rotorcraft must be designed to ensure capability of continued safe flight and landing (for Category A) or safe landing (for Category B) after impact with a 2.2-lb (1.0 kg) bird when the velocity of the rotorcraft (relative to the bird along the flight path of the rotorcraft) is equal to V_{NE} or V_H (whichever is the lesser) at altitudes up to 8,000 feet. Compliance must be shown by tests or by analysis based on tests carried out on sufficiently representative structures of similar design.

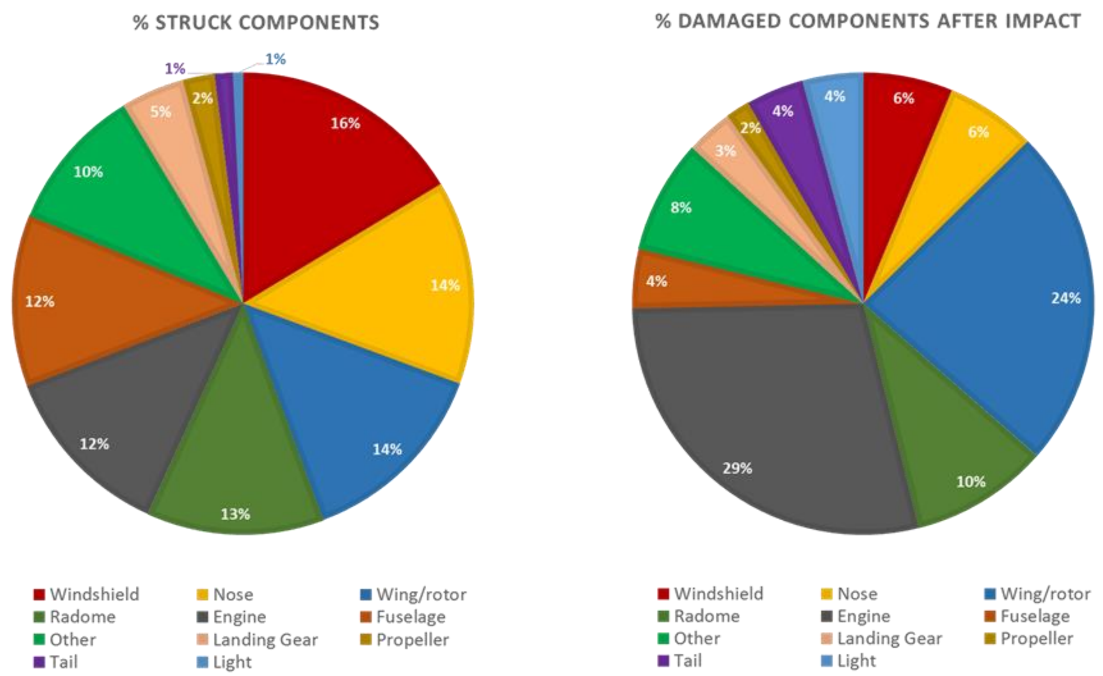

Figure 121. Numerical proportion of civil aircraft components reported as being impacted and damaged by birds, in the USA, 1990–2014 [45]

	Birds (25-year total)			
Aircraft component	Number struck	% of total	Number damaged	% of total
Windshield	21,937	16	971	6
Nose	19,133	14	984	6
Wing/rotor	18,332	14	3,683	24
Radome	16,638	12	1,497	10
Engine(s)[1]	16,636	12	4,417	29
Fuselage	16,107	12	643	4
Other	13,574	10	1,227	8
Landing gear	5,979	4	508	3
Propeller	2,953	2	265	2
Tail	1,740	1	621	4
Light	911	1	656	4
Total[2]	**133,940**	**100**	**15,472**	**100**

Figure 122. Civil aircraft components reported as being impacted and damaged by wildlife, in the USA, 1990–2014 [45]

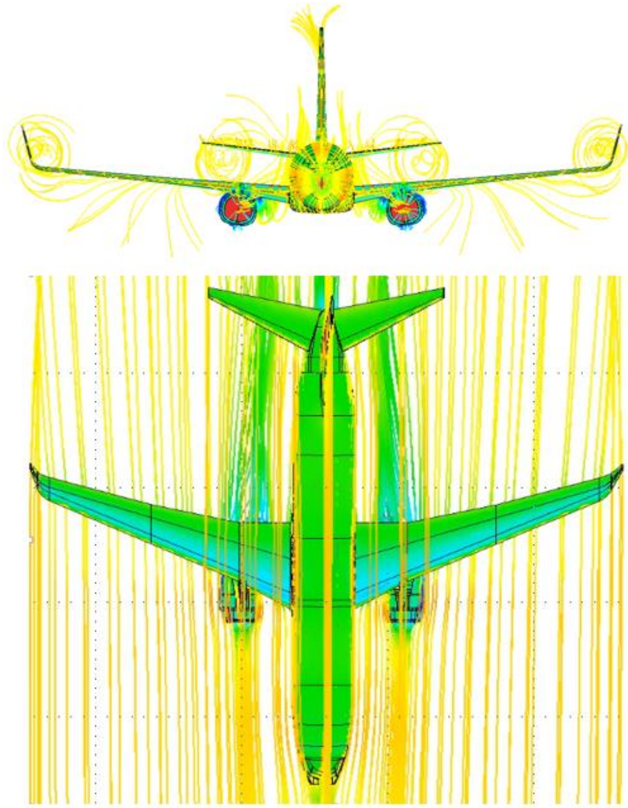

Figure 123. CFD flow analysis on the commercial jet model

3.2 CAD REVERSE ENGINEERING

CAD models for target areas were generated by the NIAR for UAS impact studies. Since the actual aircraft drawings were not available, the target areas were reverse engineered based on information available in technical manuals [48][49], books [50] and other online resources. Input from design engineers and Original Equipment Manufacturers (OEMs) helped in refining the models and verifying the fidelity of the structure.

Due to the unavailability of the proprietary aircraft drawings, some structural modeling assumptions were made in accordance with the information found in the literature. While for each aircraft category some specific simplifications were made, the following are a few common simplifications applicable to both the commercial transport jet model and the business jet model.

- Avionics and wires were not modeled.
- Fastener diameter and spacing were determined by means of repair specifications [48].
- Lightening holes and wire harnesses holes were modeled when data was available.

These simplifications would not significantly affect the predicted failure of the airframe primary structure and provide a reasonable stiffness when compared to the actual airframe, especially in the designated impact areas.

3.2.1 Commercial Transport Jet

The wing, windshield and horizontal and vertical stabilizers similar to a commercial transport jet were modeled for UAS impact. Details of these models are presented in this section. Figure 124 shows the overall dimensions of the commercial transport jet developed by the NIAR.

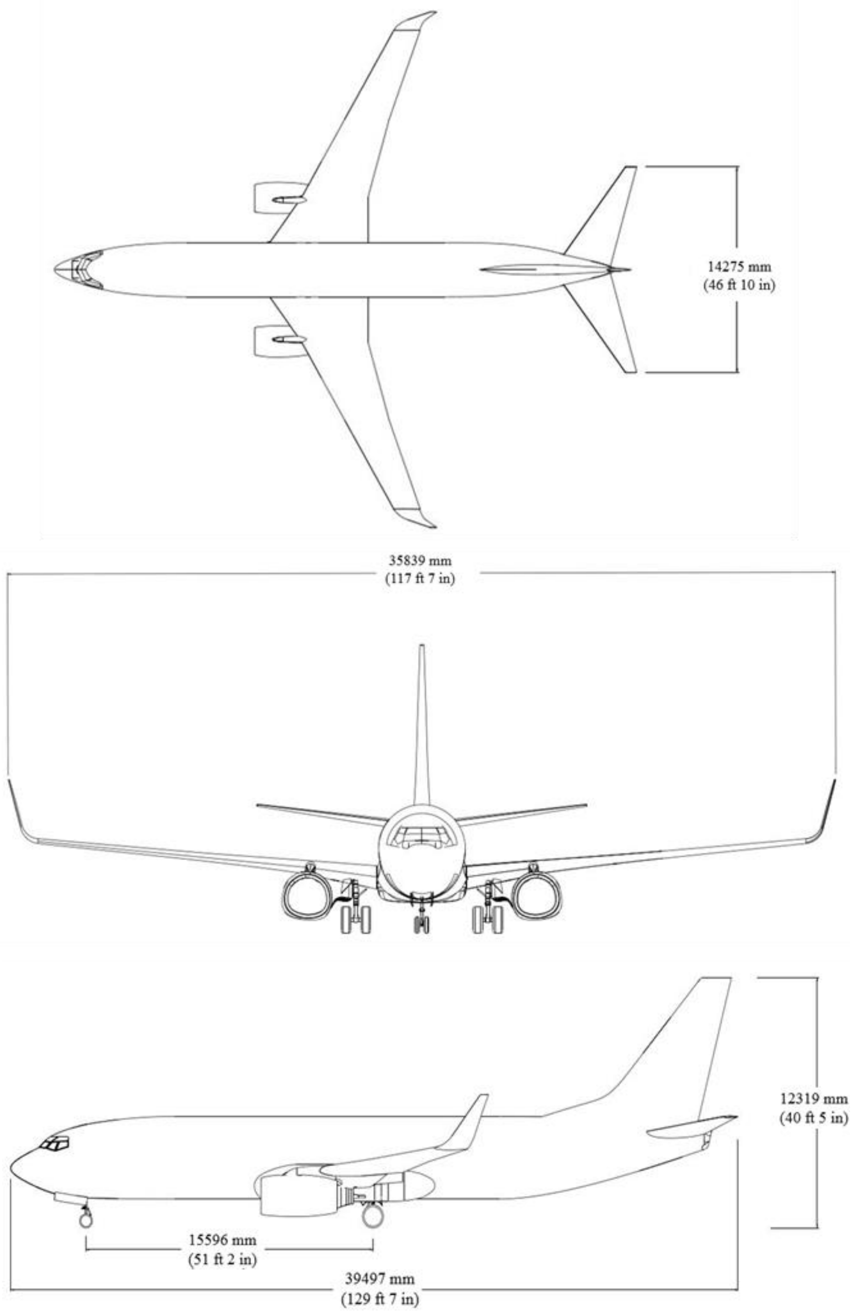

Figure 124. Commercial transport jet overall dimensions

3.2.1.1 Horizontal Stabilizer

Figure 125 shows the horizontal stabilizer CAD model. A plan view including the overall dimensions is included on the right of the figure. The internal structure of the horizontal stabilizer model is presented in Figure 126. The leading edge was refined in order to more accurately capture the stiffness characteristics of this target structure at the point of impact. The anti-icing systems, wires, access panels, and certain lightening holes were not accounted for in the geometry.

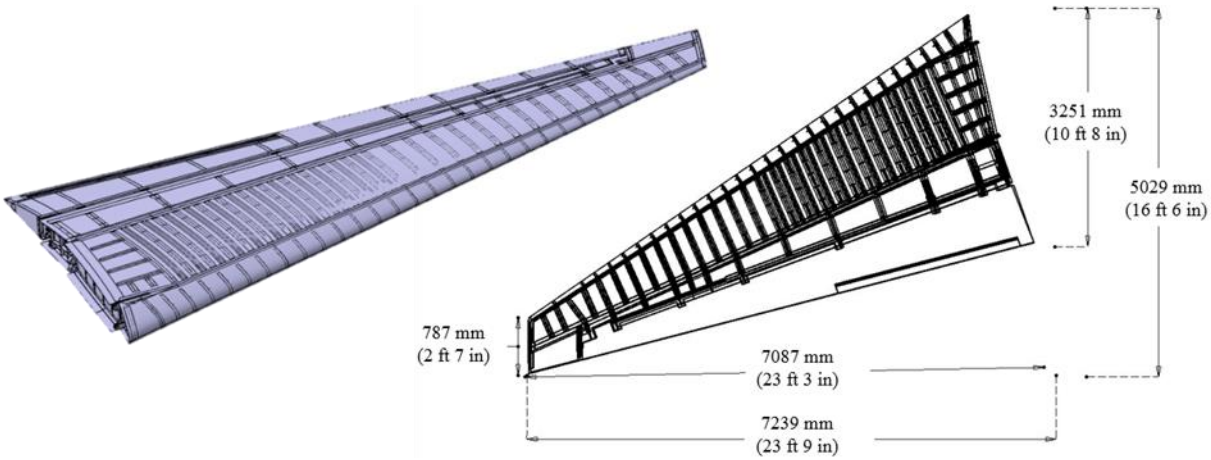

Figure 125. Commercial transport jet horizontal stabilizer

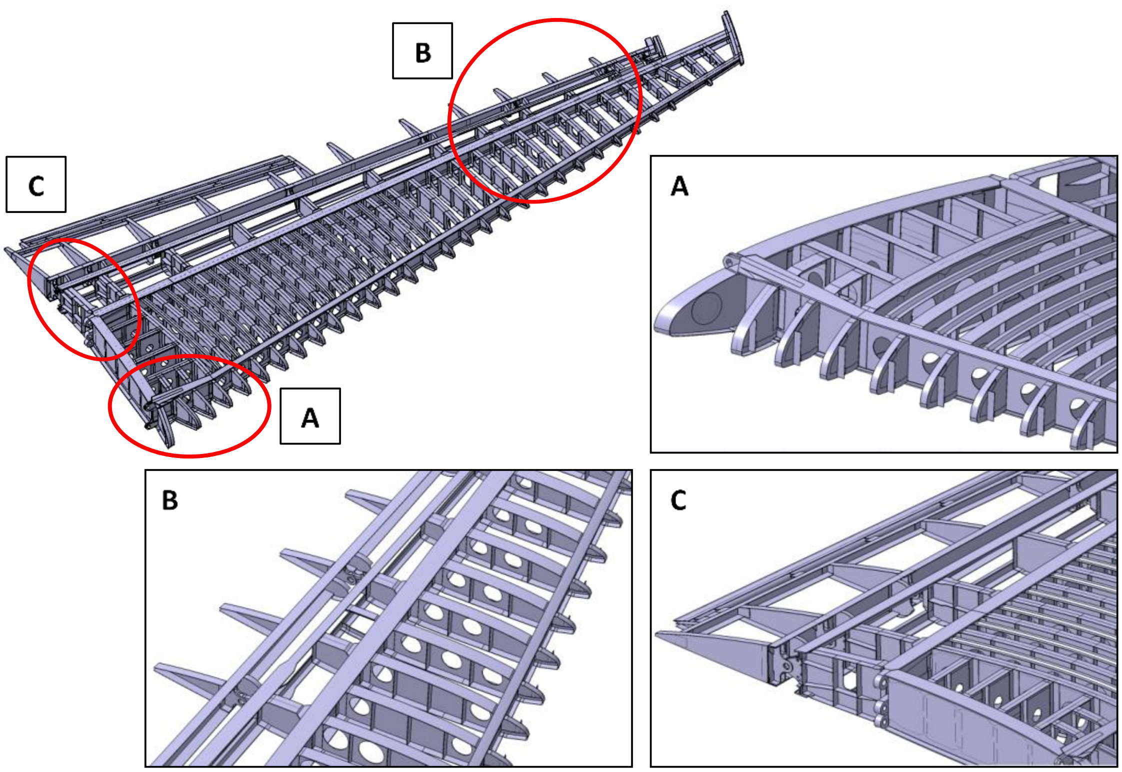

Figure 126. Commercial transport jet horizontal stabilizer CAD model

3.2.1.2 Vertical Stabilizer

The CAD model of the vertical stabilizer and a plan view including the overall dimensions are shown in Figure 127. Figure 128 shows detailed views of the construction of the vertical stabilizer. The leading edge was refined in order to more accurately capture the stiffness characteristics of the vertical stabilizer at the point of impact. The same assumptions made for the horizontal stabilizer were applied to the vertical stabilizer.

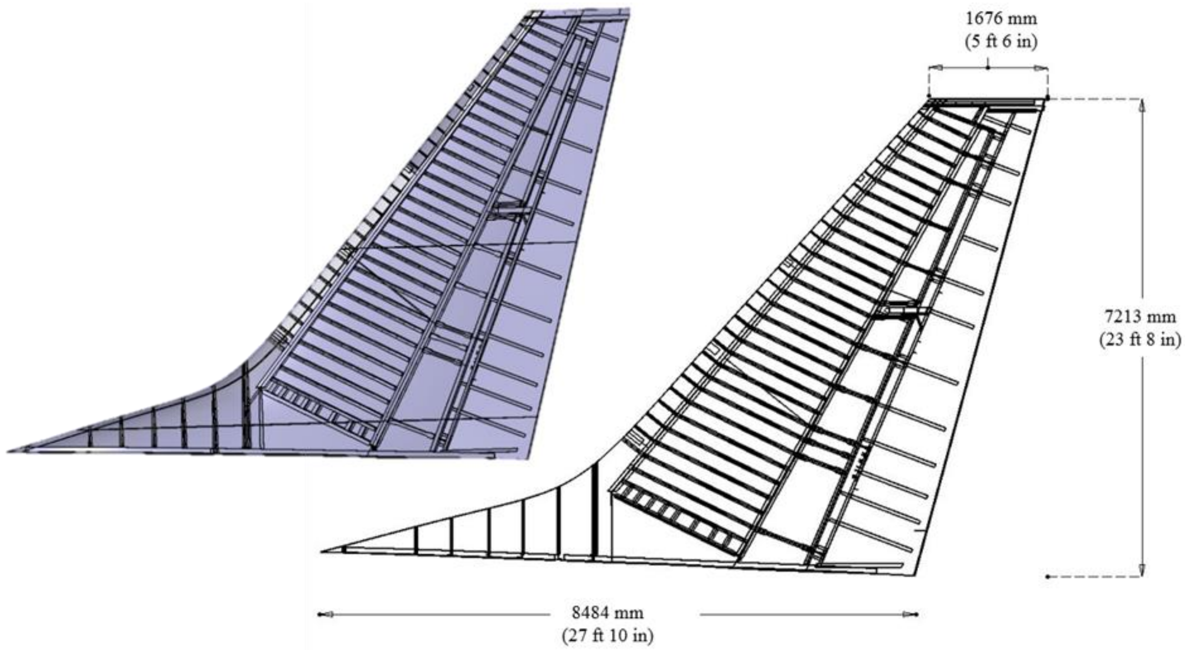

Figure 127. Commercial transport jet vertical stabilizer

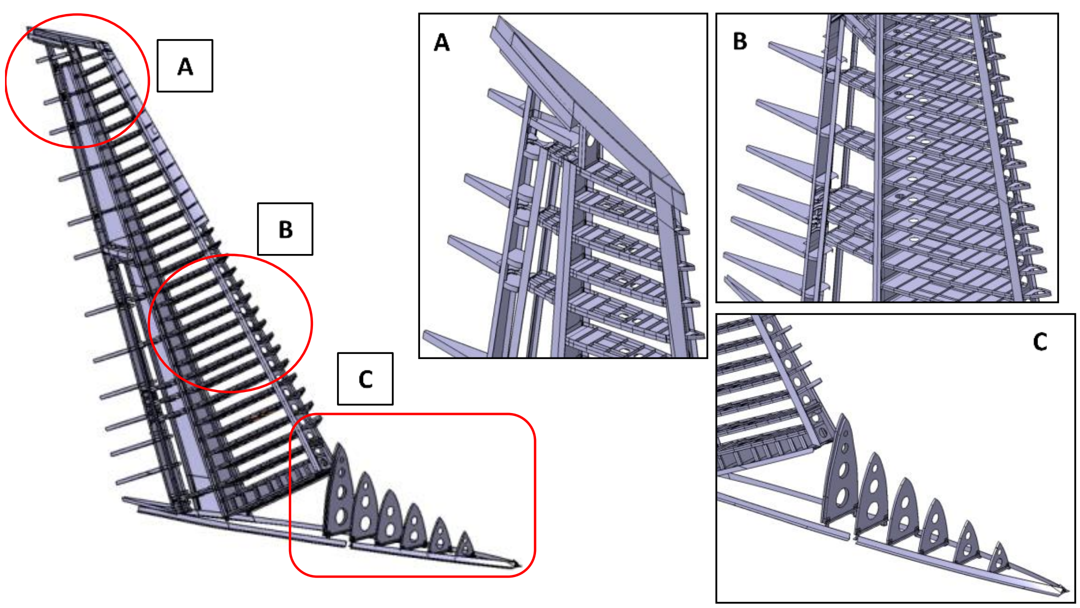

Figure 128. Commercial transport jet vertical stabilizer CAD construction

3.2.1.3 Windshield

Figure 129 shows the complete commercial transport jet forward fuselage CAD model. Figure 130 shows an isolated view of the windshield. Similar to the horizontal and vertical stabilizers, the windshield and surrounding structure were refined. Details of the windshield construction were obtained from a PPG technical data sheet [51]. Features of the windshield such as the silicon gasket, metal inserts, and edge fillers were not modeled. Figure 131 includes detailed images of the windshield cross-section.

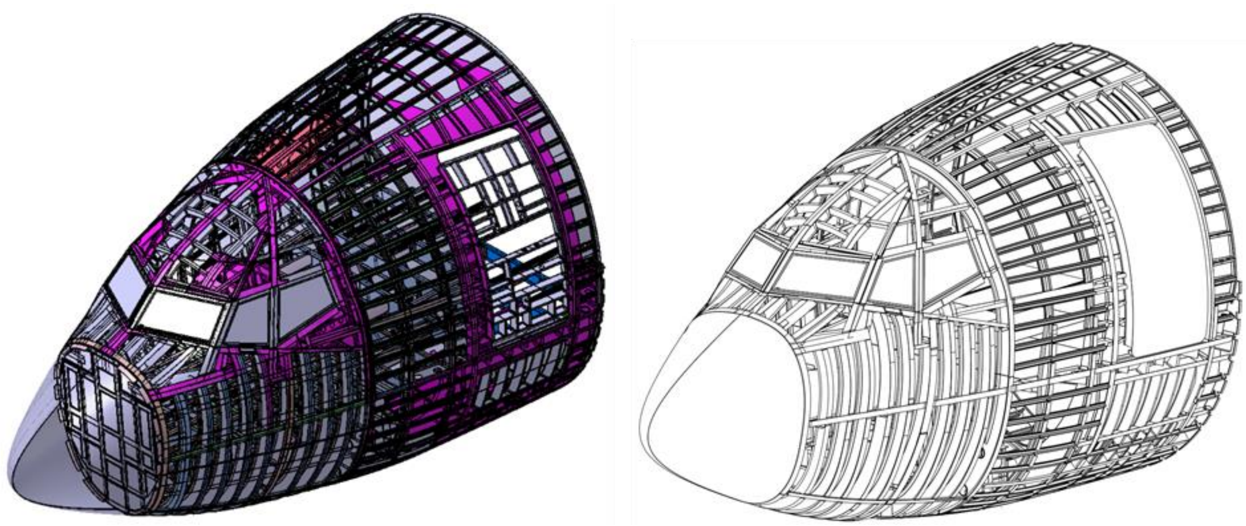

Figure 129. Commercial transport jet forward fuselage CAD construction

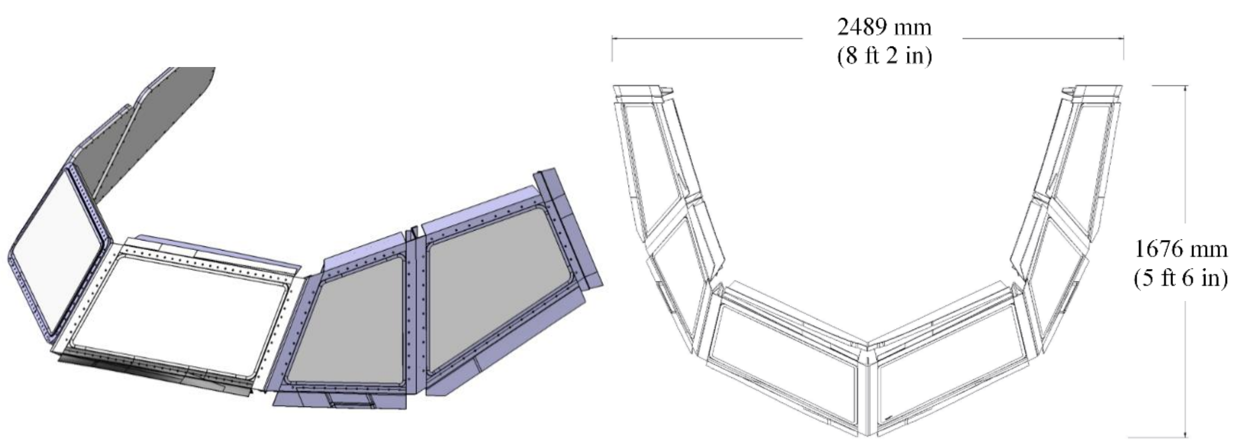

Figure 130. Commercial transport jet windshield

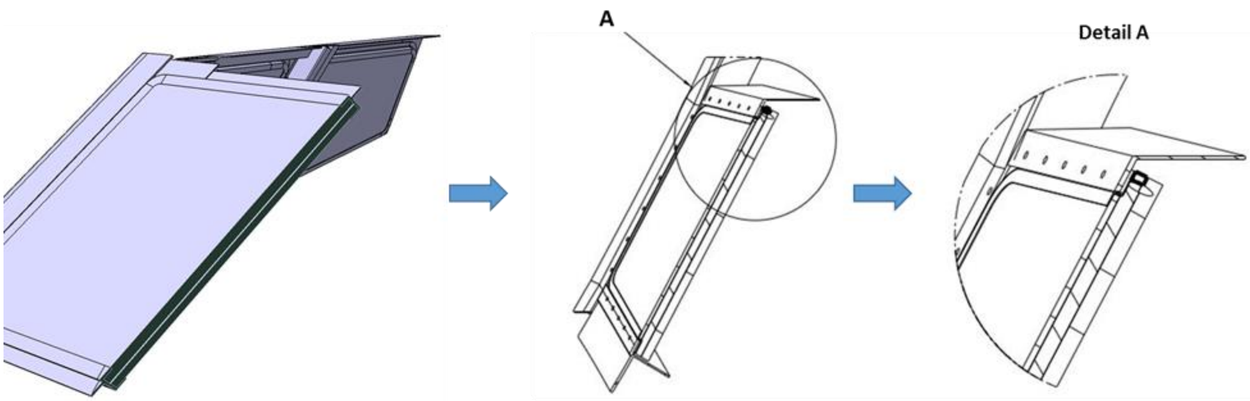

Figure 131. Commercial transport jet windshield cross-section

3.2.1.4 Wing

Figure 132 shows the commercial transport jet wing layout and the selected area for UAS impact studies. A leading edge of this size jet is typically made out of two main components: the fixed-wing and the slats. For this study, only the fixed leading edge of the wing was modeled. The effect of the UAS impacting on the actual slat will be considered in future studies.

The specific wing area selected for the UAS impact was the fixed-wing part spanning Slat 3 and part of Slat 2. The selection of Slat 3 was based on preliminary CFD analyses as discussed in section 3.1.3 . These analyses were used to identify areas with laminar flow around the wing leading edge in order to reduce the possibility of the UAS being redirected due to turbulent flow. In addition, because the fixed-wing structure under Slat 2 is different from that found on Slat 3, a section of the Slat 2 was included in the numerical model for evaluation purposes. At the same time, impacts to this Slat 2 section can be used to evaluate the possibility of wing spar rupture closer to the fuel tank.

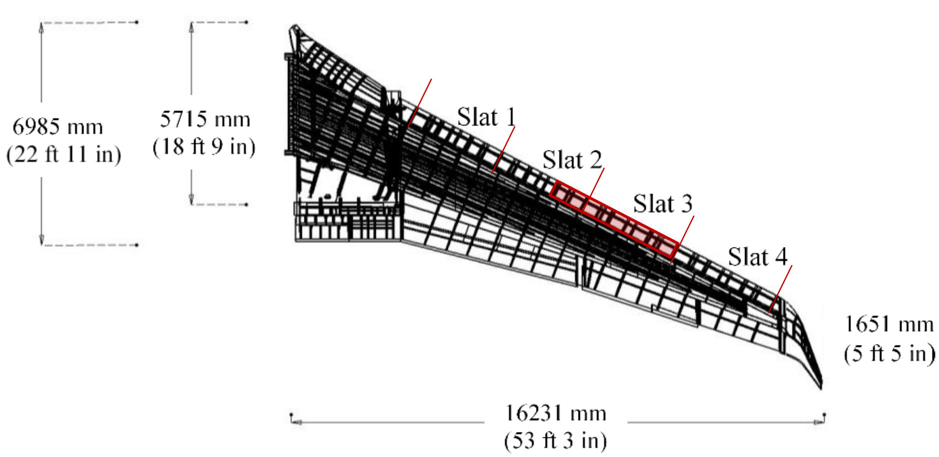

Figure 132. Commercial transport jet wing layout and selected area for UAS impacts

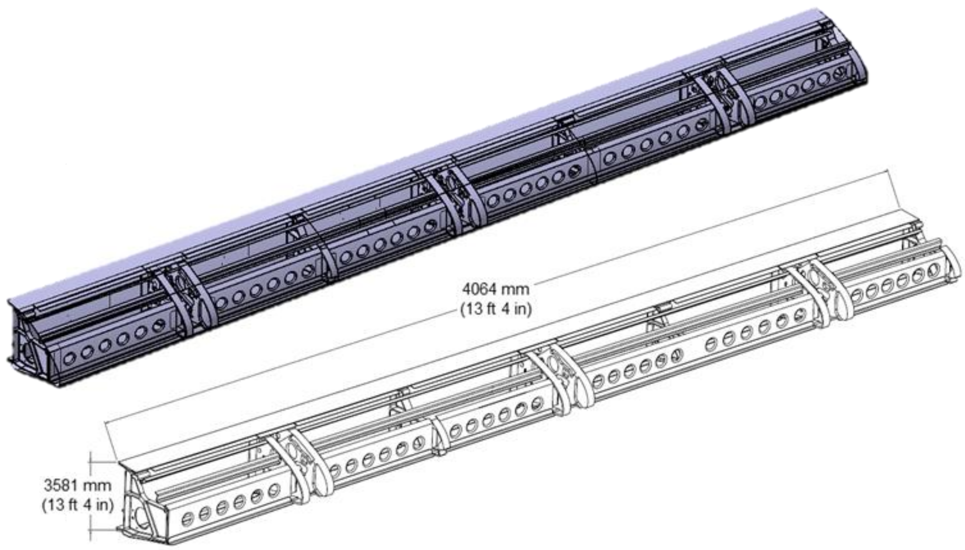

Figure 133. Commercial transport jet wing – leading edge CAD model

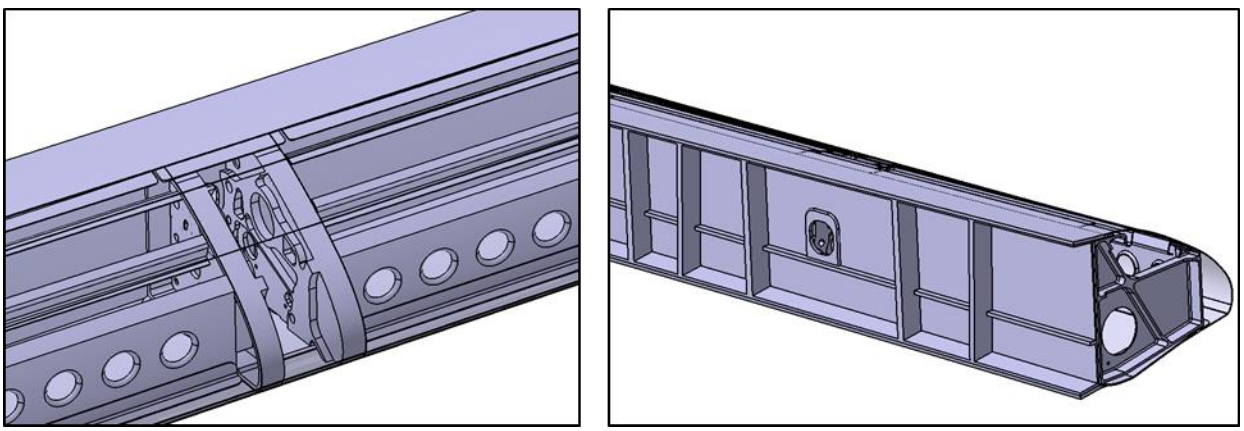

Figure 134. Commercial transport jet wing CAD model

3.2.2 Business Jet

The business jet model was developed following the same procedures as the commercial transport jet. Repair manuals and other technical sources provided most of the information needed to build the CAD model [49]. Figure 135 provides the overall dimensions of the business jet model. The following subsections present the construction details of the components of the business jet selected for collision studies.

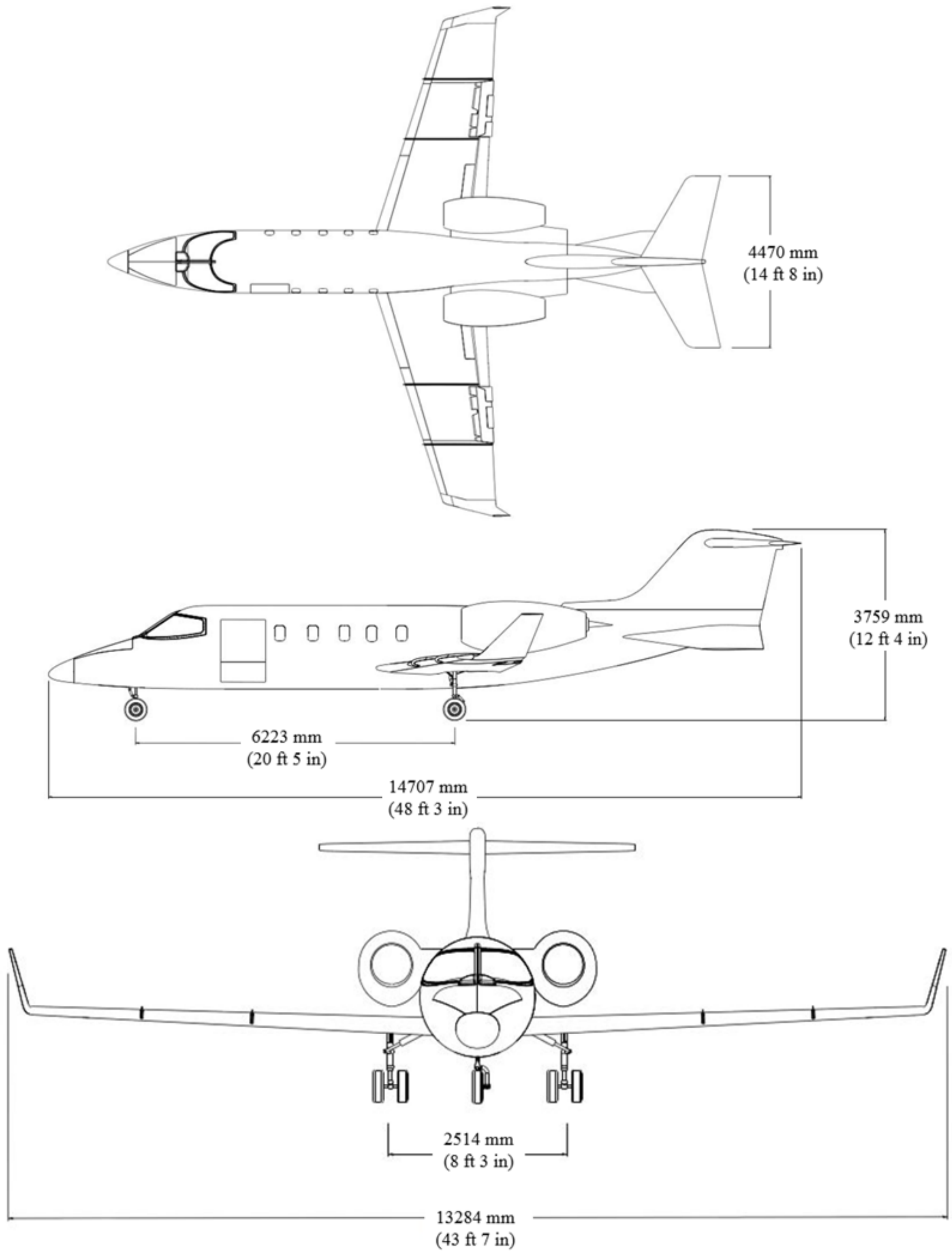

Figure 135. Business jet dimensions

3.2.2.1 Horizontal Stabilizer

Figure 136 shows the horizontal stabilizer CAD model. Figure 137 presents a top view of the internal structure and the overall dimensions of the business jet horizontal stabilizer. Leading edge ribs lightening holes were modeled to scale based on the available information. Anti-icing tubes and wiring were not modeled for the horizontal stabilizer.

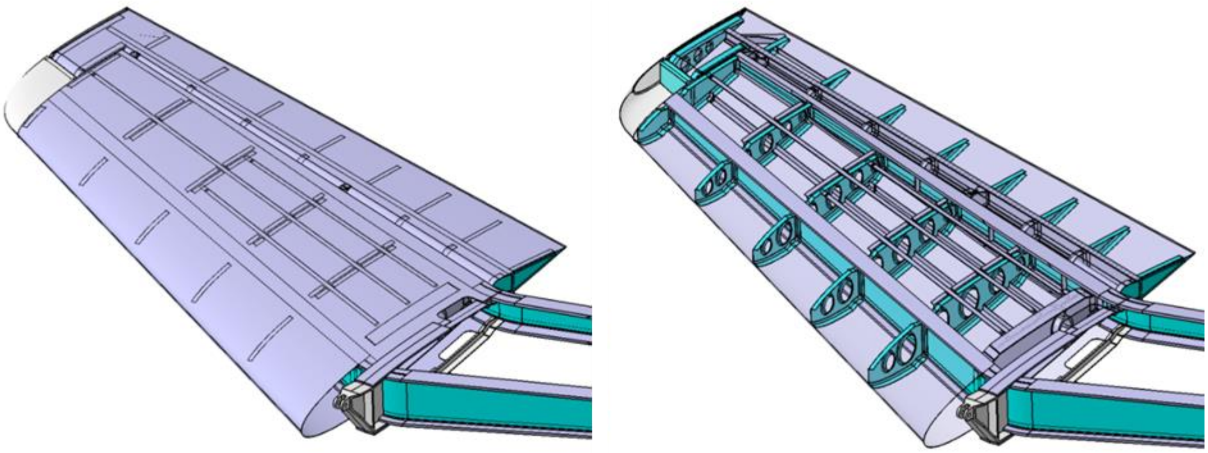

Figure 136.Business jet horizontal stabilizer

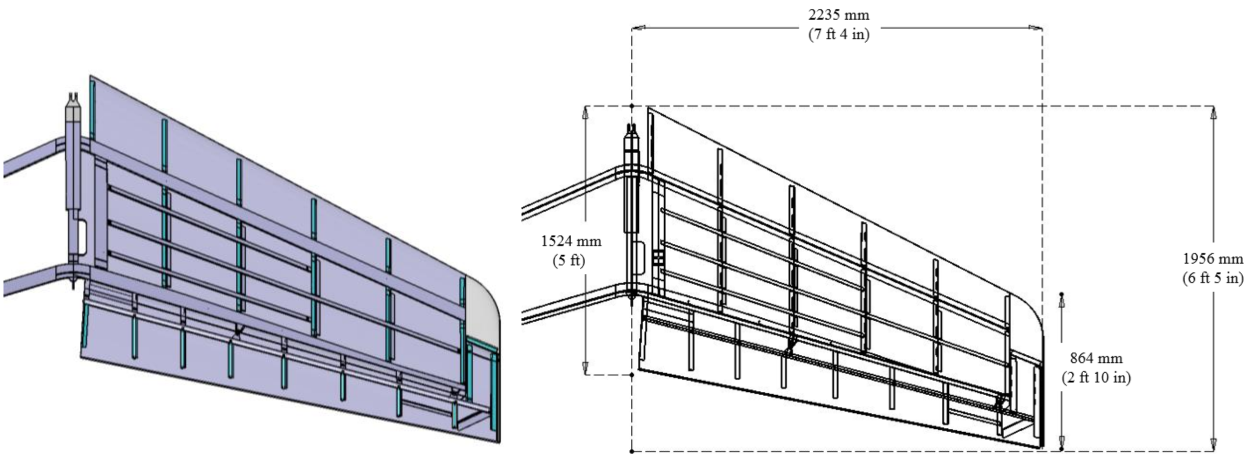

Figure 137. Business jet horizontal stabilizer CAD model and dimensions

3.2.2.2 Vertical Stabilizer

Figure 138 shows the internal structure of the business jet vertical stabilizer. Since the light (located on the tip) is not a critical structural component, it was highly simplified and was considered part of the aluminum skin. Figure 139 presents side view of the vertical stabilizer and a sketch with the main dimensions. The same assumptions for the horizontal stabilizer were made for the vertical stabilizer.

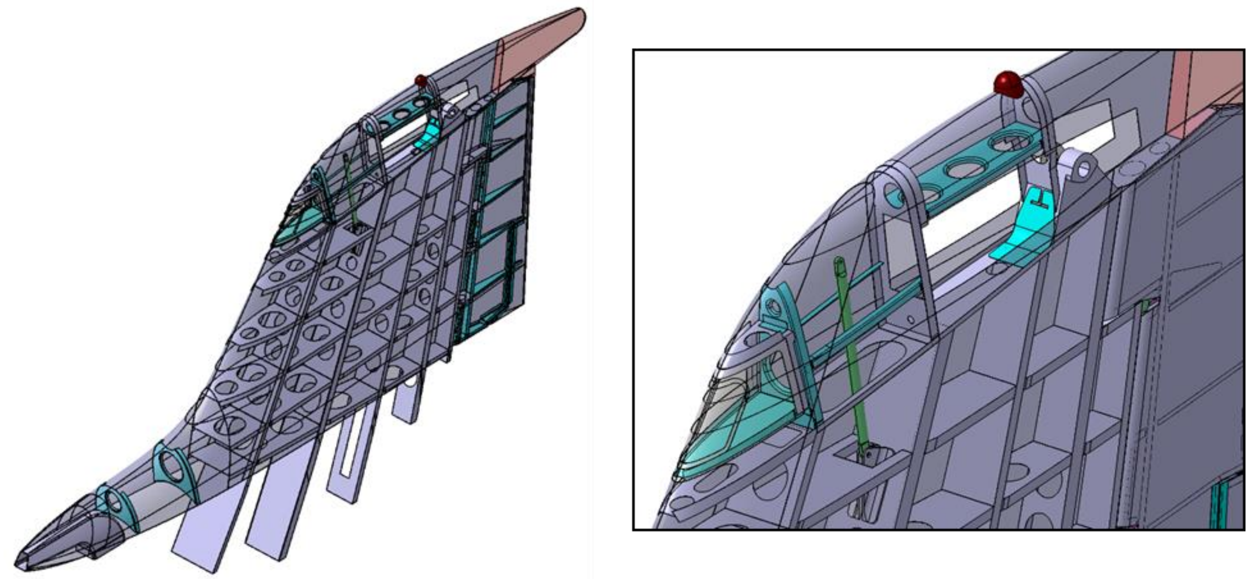

Figure 138. Business jet vertical stabilizer

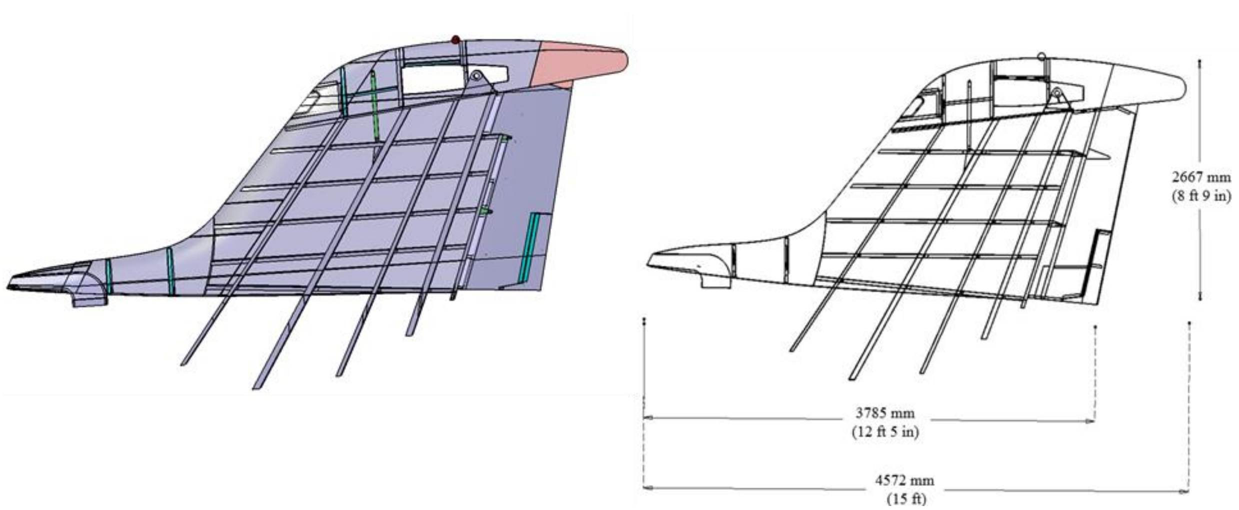

Figure 139. Business jet vertical stabilizer CAD construction and dimensions

3.2.2.3 Windshield

Figure 140 shows the detailed business jet forward fuselage CAD model. Figure 141 shows a detailed view of the business jet windshield and a sketch including the overall dimensions. Windshield details were obtained from a repair manual [49]. Parts such as silicone the gasket and inserts were not modeled. A detailed view of the windshield cross-section is shown in Figure 142.

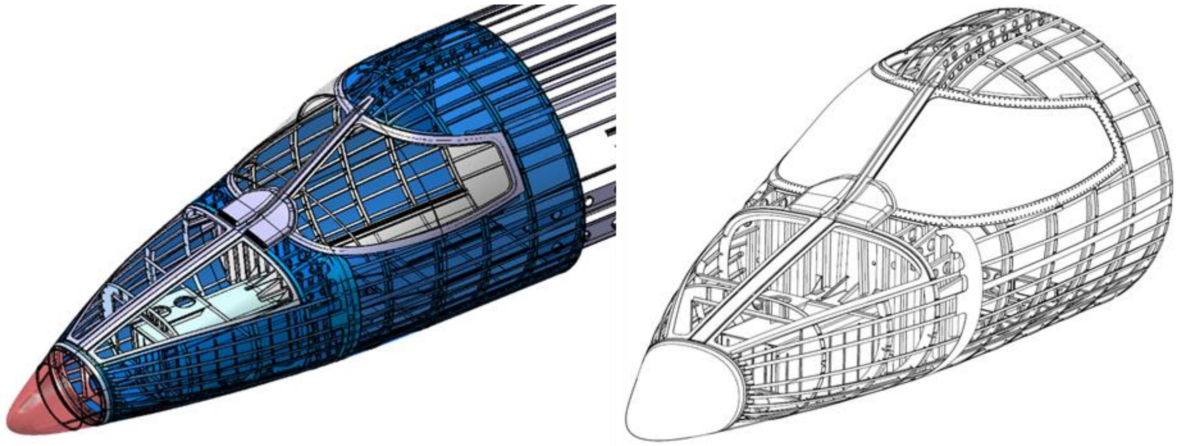

Figure 140. Business jet forward fuselage

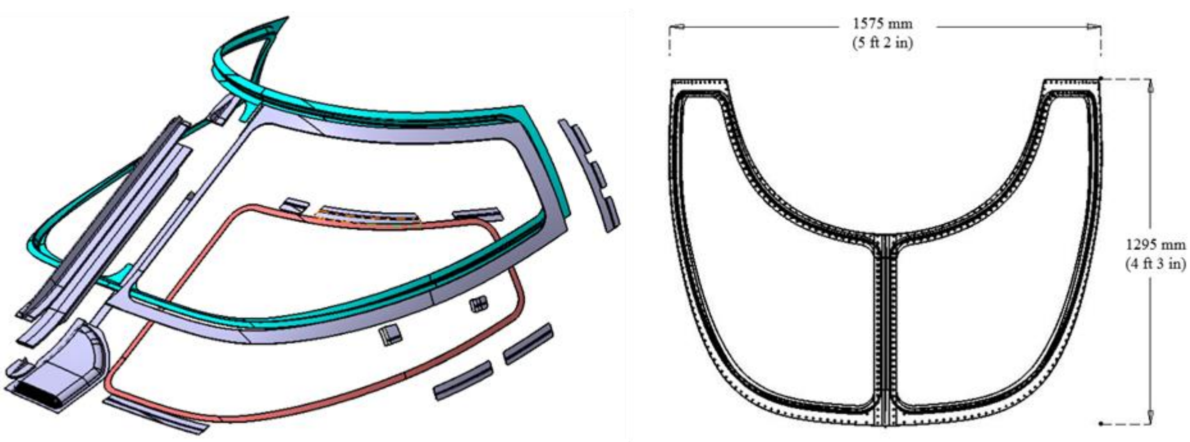

Figure 141. Business jet windshield CAD model

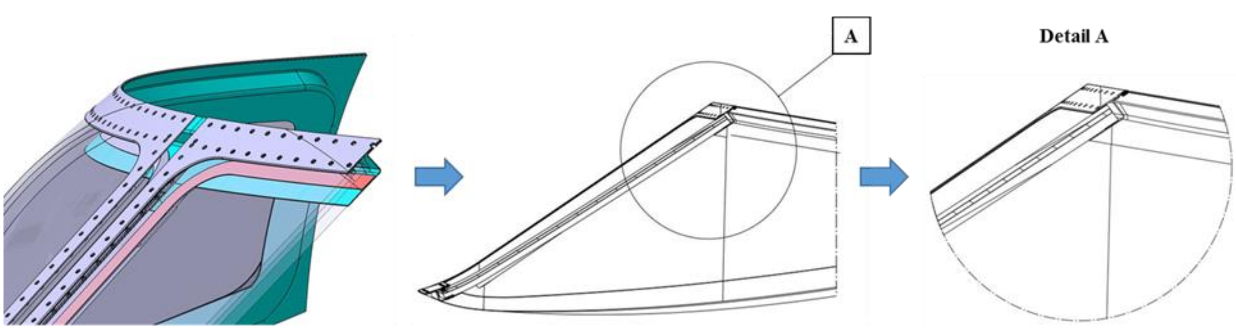

Figure 142. Business jet windshield cross-section

3.2.2.4 Wing

Figure 143 shows the business jet wing CAD model. Based on the available data, there were a smaller number of nose ribs along the leading edge than in the stabilizers. Relevant details such as the leading edge anti-icing pipe were modeled to keep an accurate leading edge stiffness. Figure 144 presents a top view of the business jet wing and a sketch with the principal dimensions of the wing. Internal wiring and access panels were not modeled. The control surfaces were fixed in place and the corresponding actuators were not modeled.

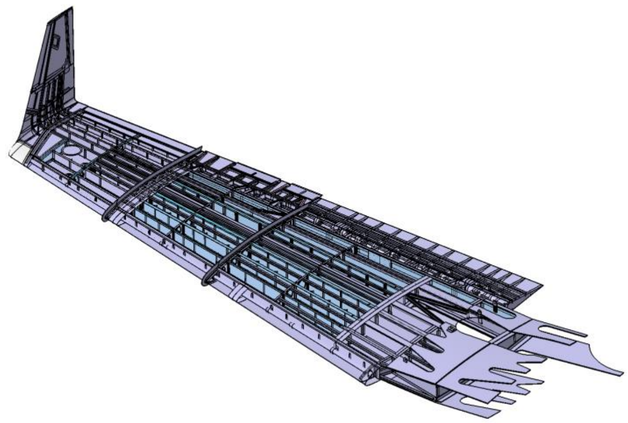

Figure 143 Business jet wing

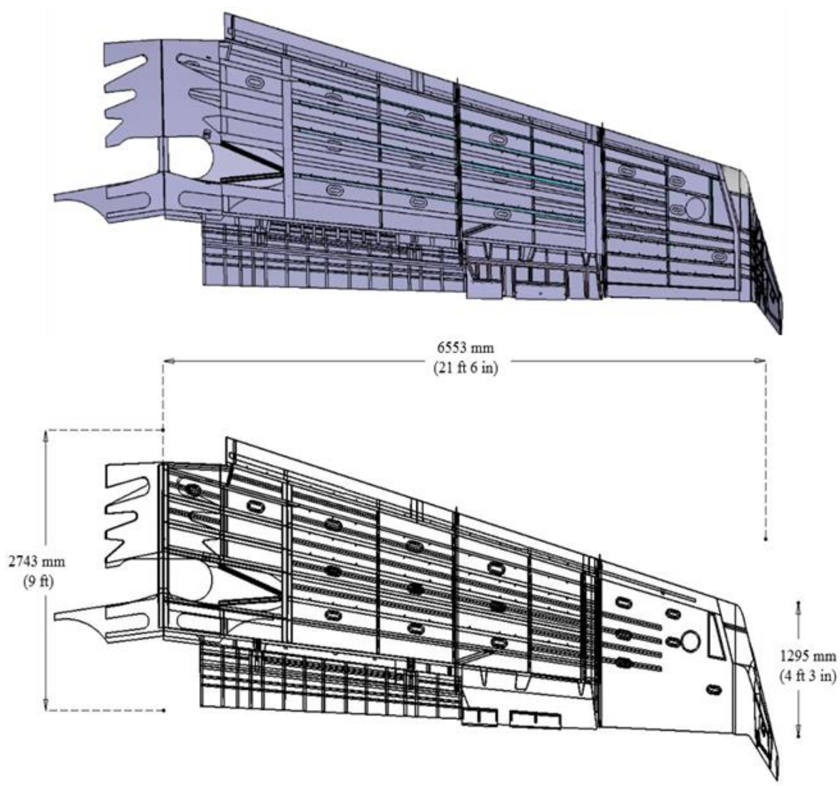

Figure 144. Business jet wing CAD model

3.3 TARGET FINITE ELEMENT MODELS

This section explains the process followed to develop the FE model of the commercial transport jet and the business jet components. The following procedure was carried out to create the FE model:

- Obtain CAD data (STP format) for each model.
- Clean up geometry prior to meshing (split surfaces where symmetric, defeature small details, etc.).
- Select element type for each part depending on geometry and element size constraints.
- Discretize (*i.e.* mesh) the geometry.
- Check quality criteria.
- Assign section properties: shell thicknesses and beam cross section.
- Assemble FE meshed parts.
- Check models for non-desired entities (free nodes, free edges, mesh overlap, duplicate elements, non-aligned element normal, etc.).
- Assign appropriate material properties.
- Add non-structural mass to nodes wherever necessary.
- Perform a mass check.
- Renumber model components to avoid clashes between the UAS and the target FE models.

A series of sensitivity studies were conducted in order to define the discretization (mesh) criteria, as well as the material models, that will be used for full-scale analyses. The accuracy of the FEA results largely depends on correct input and on a comprehensive understanding of parameters used in defining the numerical models. The results of these sensitivity studies and other FE model parameters selected for developing the target FE models are documented in subsequent sections.

3.3.1 Mesh Sensitivity Study

The computational cost of explicit dynamic analyses is driven by the minimum element length [21]. In addition, the deformations, loads, and failure modes are also influenced by element size. As a result, a mesh sensitivity study was performed to select an element size for FE discretization of targets so that a balance could be obtained between result accuracy and computational efficiency.

3.3.1.1 Mesh Sensitivity Study with Generic Motor Model and Flat Plate

To perform the study, a validated FE model of a 3.175 mm (0.125 in) flat plate was used [32]. A 3.2 mm element length was selected as a baseline for comparison to other element lengths. A FE model of a 34.2 g steel sphere, with similar dimensions as a motor of a sUAS, was created. The simulated spherical projectile was impacted to the flat plate FE model at a velocity of 250 knots (128.6 m/s). A schematic of the FE model is shown in Figure 144, and is similar to the setup used in previous simulations (chapter 2). Six different element lengths were studied as illustrated in Figure 146: 1.6 mm, 3.2 mm (baseline), 6.35 mm, 12.7 mm, 25.4 mm and 50.8 mm. Preliminary analyses indicated that a 6.35 mm element length correlated well with the 3.2 mm baseline. Therefore, a 5 mm element length was also evaluated to further understand the mesh sensitivity.

FE results for multiple element lengths were evaluated based on several different factors. The first factors studied were the damage and failure mode. Figure 147 illustrates the damage and effective plastic strain for different element lengths. Perforation was observed for all models up to a 6.35 mm element length. FE results for larger element lengths showed no damage. However, with a 6.35 mm element length, the failure modes were different from what was observed with the baseline model. Therefore, an intermediate 5 mm element size was considered.

Figure 149 shows the time history of reaction forces. Peak reaction forces are plotted in Figure 150. As the element size was decreased, the reaction force converged as would be expected. There was a clear improvement in the performance of the FE model with the 5 mm element length. Additionally, the computational running time for each FE model was compared as shown in Figure 148. The computational running time increases as the element size decreases, as would be expected. As previously mentioned, the computational cost of explicit dynamic analyses is driven by the minimum element length. While lower FE lengths give more accurate results, for this study, any element size lower than the baseline was considered undesirable. The runtime for the FE model with 5 mm element length was not significantly different from the baseline.

Thus, based on the mesh sensitivity analysis performed, a 5 mm element length was used for discretizing the impacted area of every target FE model described in Chapter 3. This element length provides a good balance between computational time and accuracy of results (stress gradients, failure prediction and reaction force). Verification of the mesh sensitivity study was achieved during the motor component level test (chapter 2.4.4.9), when the simulation predicted failure for the panel, and this prediction was verified by the test. This test showed a petaling failure mode on the panel.

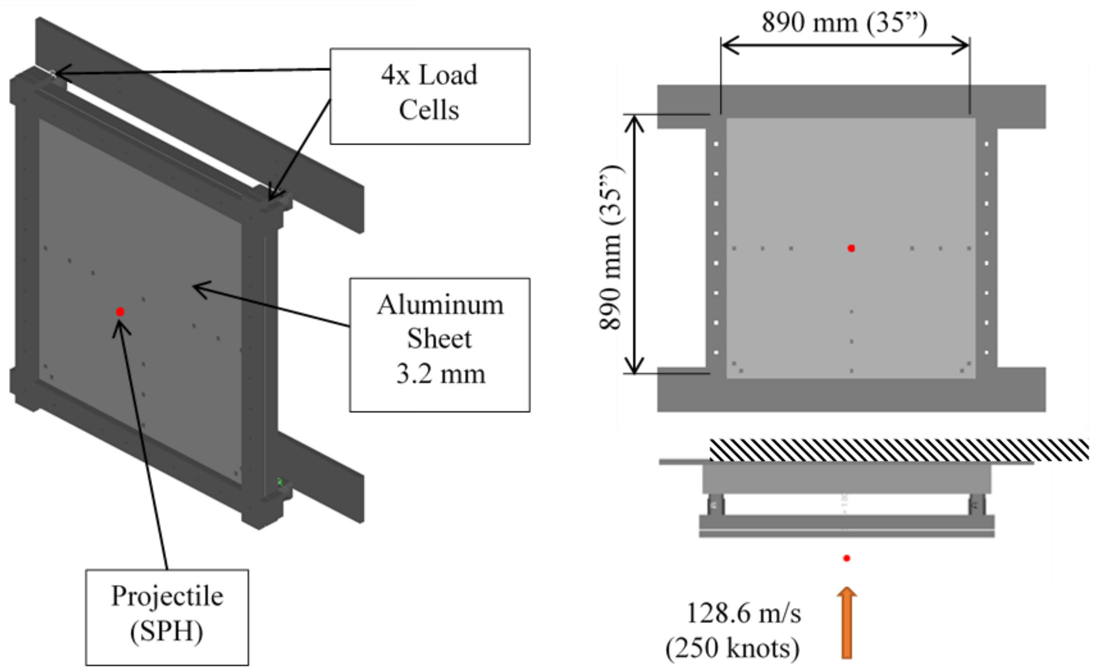

Figure 145. Mesh sensitivity study flat plate FE model

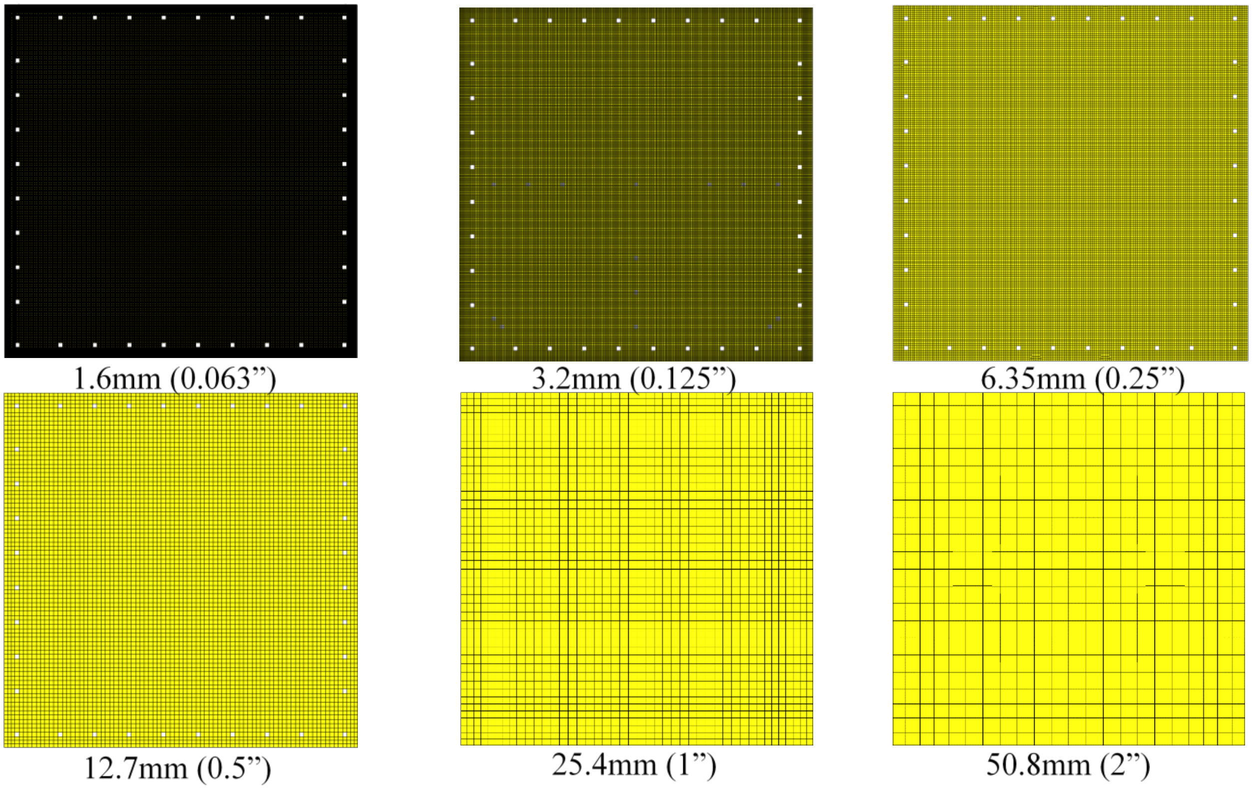

Figure 146. Illustration of mesh size compared for mesh sensitivity study

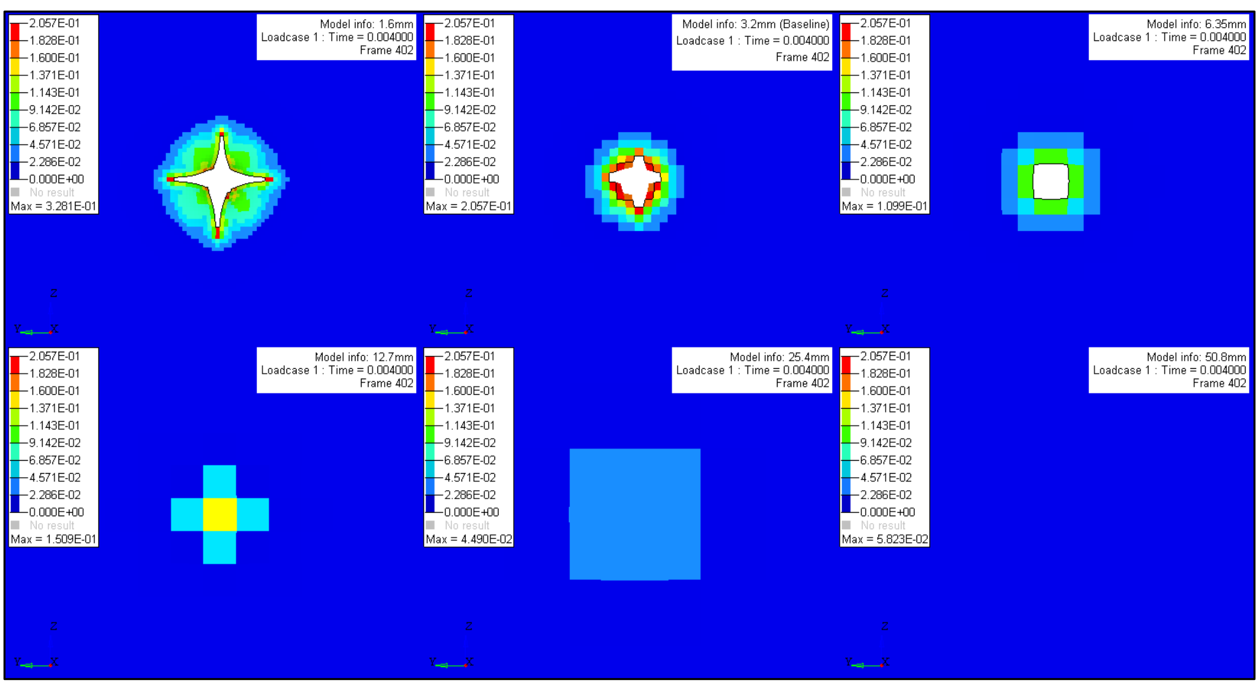

Figure 147. Damage and effective plastic strain comparison for mesh sensitivity study

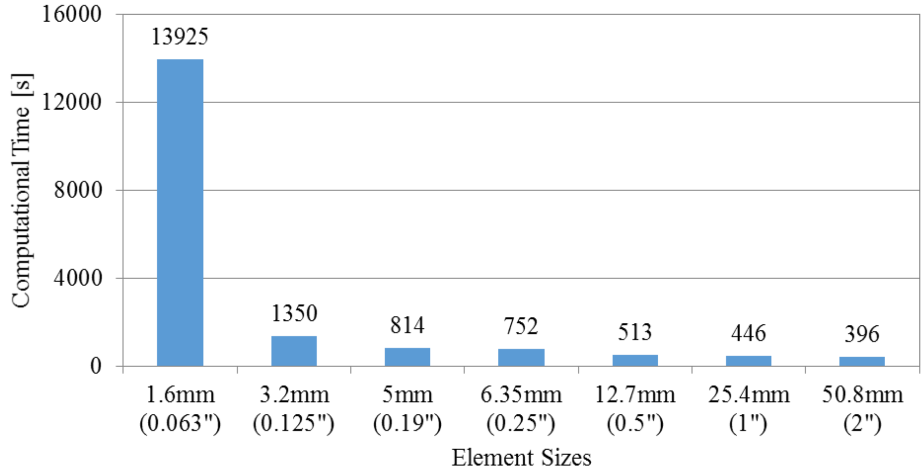

Figure 148. Computational time comparison for mesh sensitivity study

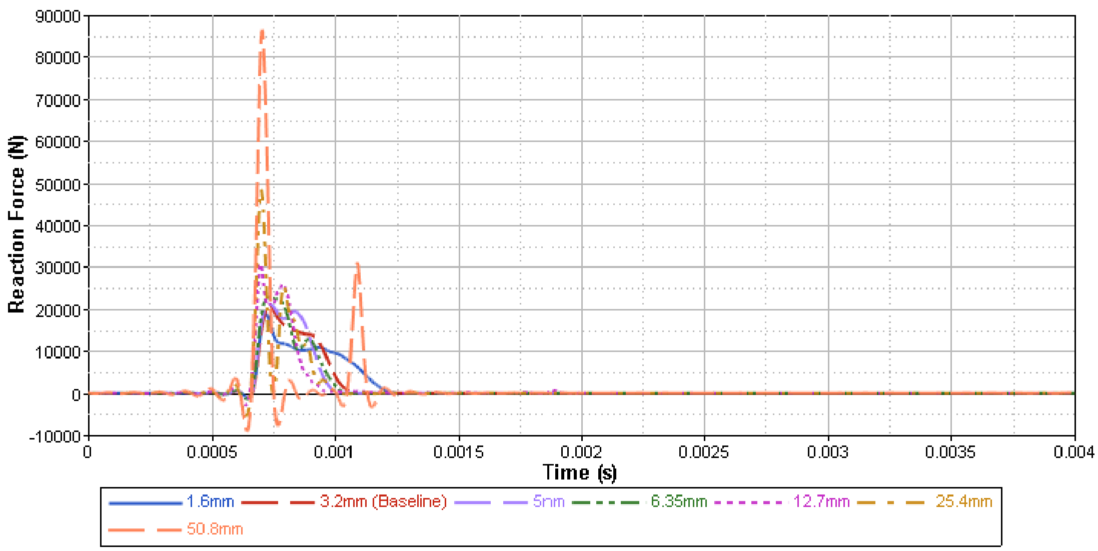

Figure 149. Reaction force time history for mesh sensitivity study

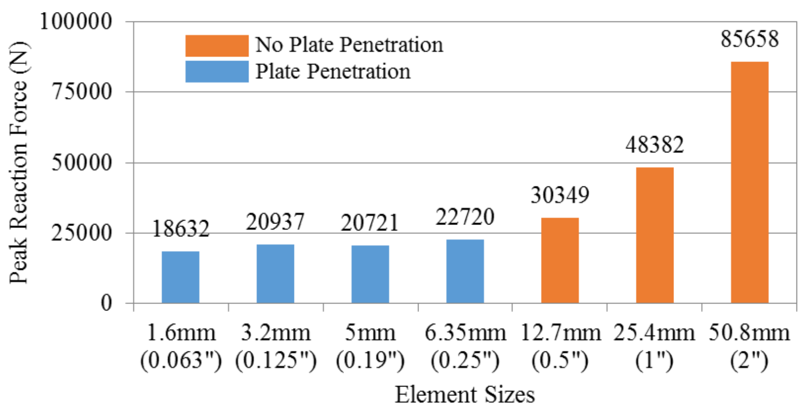

Figure 150. Peak reaction forces for different element lengths on flat plate impacted by a sphere.

3.3.1.2 Verification of Selected Mesh Size

As detailed in section 2.4.4 , ballistic tests were conducted on the same flat plate FE models described in section 3.3.1.1 using motor components of the quadcopter UAS to help verify the corresponding FE model. A 5 mm mesh size was used to discretize the flat plate for the motor verification study. Figure 151 shows the comparison of the test to the FEA. The results show good correlation in damage prediction.

Thus, the mesh sensitivity study follows the philosophy of the building block approach and the component level correlation to test helps define FE model parameters such as mesh size that would produce accurate results. This provides confidence in the possible damage prediction of the aircraft targets by using the mesh size documented on the previous section.

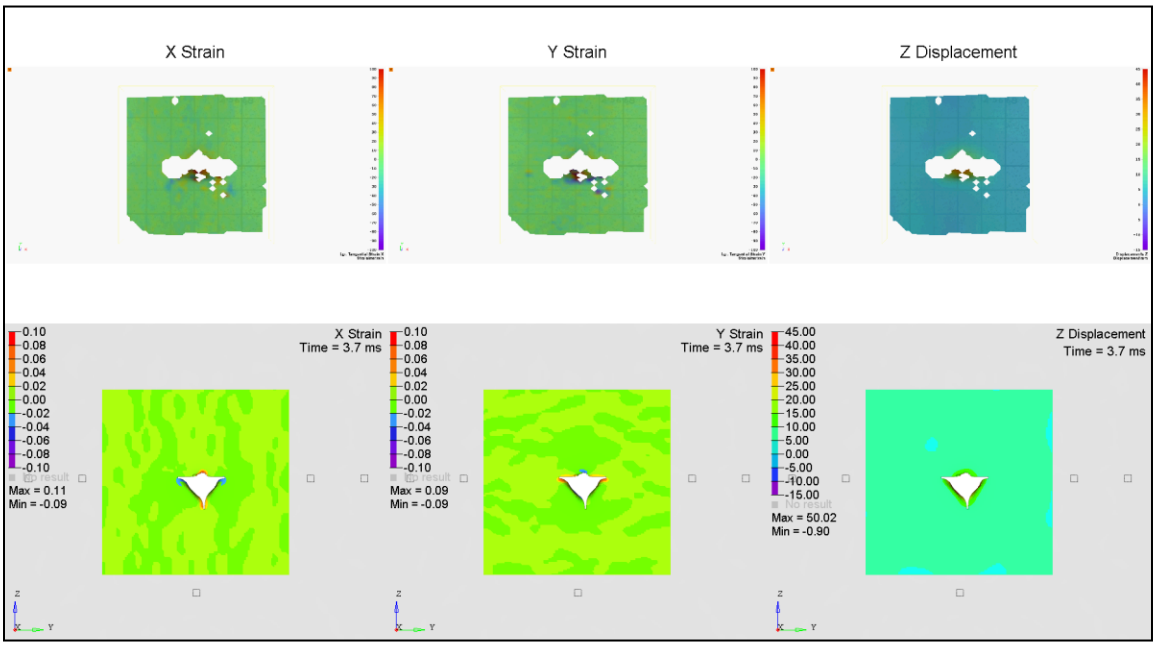

Figure 151. Mesh size verification on motor component level test.

3.3.2 Mesh Quality Criteria

Table 15 contains the criteria used to discretize the target areas of components of the commercial transport and business jet models. The quality criteria are based on recommended practices for crash analysis [52][53] and on the mesh sensitivity study detailed in section 3.3.1 .

The quality parameters are defined in section 2.3.1.1 . Larger element lengths were used for areas that were not directly impacted in order to reduce the element count and create more computationally efficient models.

Table 15. Mesh quality criteria. Target impact area.

Quality Parameter	Allowable Min.	Allowable Max.
Element Size	5 mm	8 mm
Aspect Ratio	-	5
Quad Angle	45°	140°
Tria Angle	30°	120°
Warp Angle	-	15°
Jacobian	0.7	-

Some decisions and assumptions were made while meshing in order to generate a good quality mesh for the crash analyses:

- Small fillets were defeatured and meshed with sharp edges.
- A minimum of two elements were kept on stiffeners to maintain the correct stiffness of the part.
- All sheet metal parts were meshed at the mid-surface using shell element technology.
- Whenever possible, at least three through-thickness elements were used when meshing with solid elements. If it was not feasible due to the element size constraint, a fully integrated formulation was used instead.
- The total number of trias in the model was limited to 5%, and any concentration of tria elements was avoided to maintain a homogeneous stress distribution.

3.3.3 Discretization

This section details the results of the discretization process applied to the geometry of the horizontal stabilizer, vertical stabilizer, wing, and forward fuselage of both aircraft models. The element types used for generating the FE model are detailed in section 2.3.1.2 . Table 16 summarizes the type and quantity of elements in each target model after the discretization process.

Table 16. Mesh elements quantity

		1D elements	2D elements	3D elements
NIAR Commercial Transport Jet	Front Section	32,473	798,264	349,779
	Horizontal Stab.	12,858	288,520	-
	Vertical Stab.	15,568	582,705	288
	Wing	1,371	302,070	-
NIAR Business Jet	Front Section	8,149	394,344	228,688
	Horizontal Stab.	2,548	124,518	-
	Vertical Stab.	2,901	158,433	122
	Wing	15,271	544,503	-

3.3.3.1 Commercial Transport Jet

The discretized target components of the commercial transport jet are shown from Figure 152 to Figure 161. The discretized FE model is compared against the CAD models.

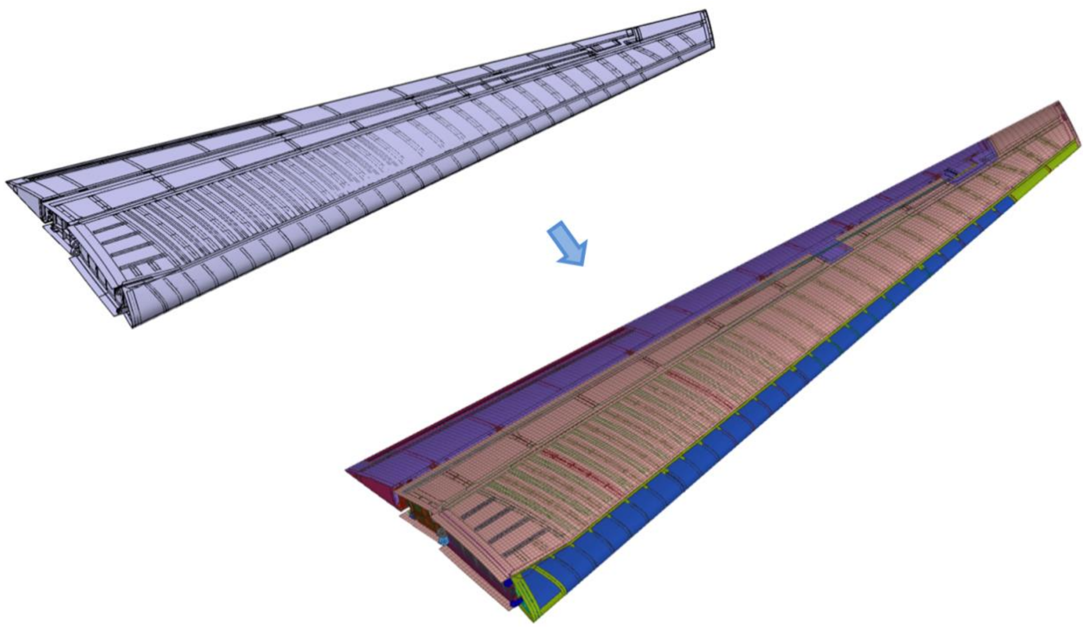

Figure 152. Commercial transport jet horizontal stabilizer - Geometry and mesh

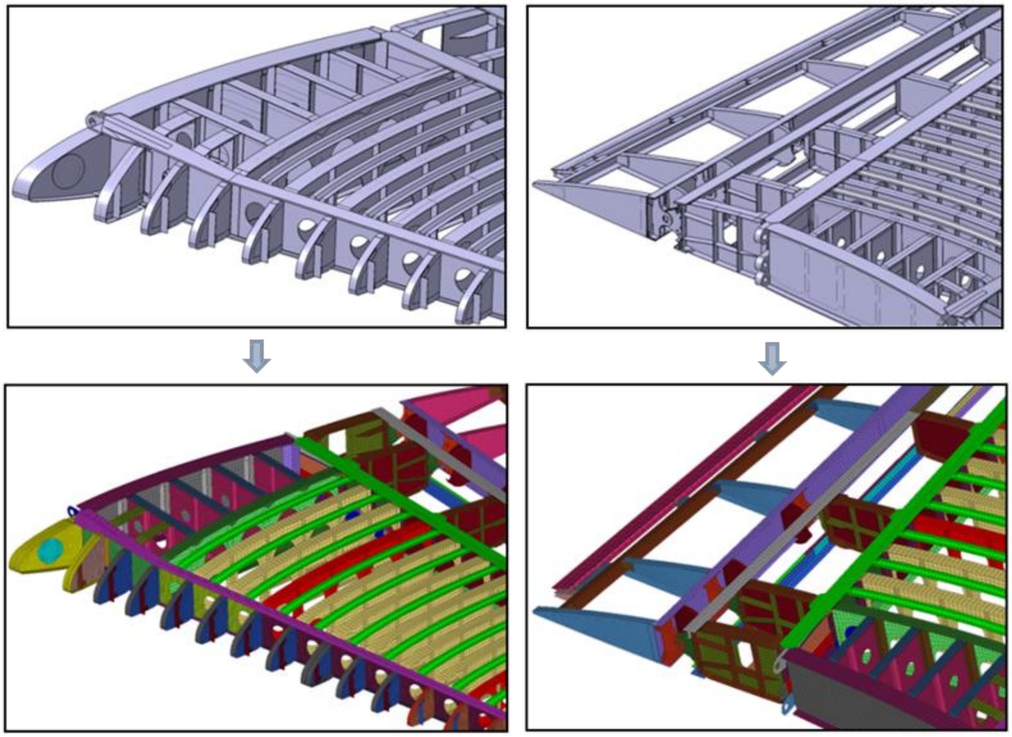

Figure 153. Commercial transport jet horizontal stabilizer - Internal structure geometry and mesh

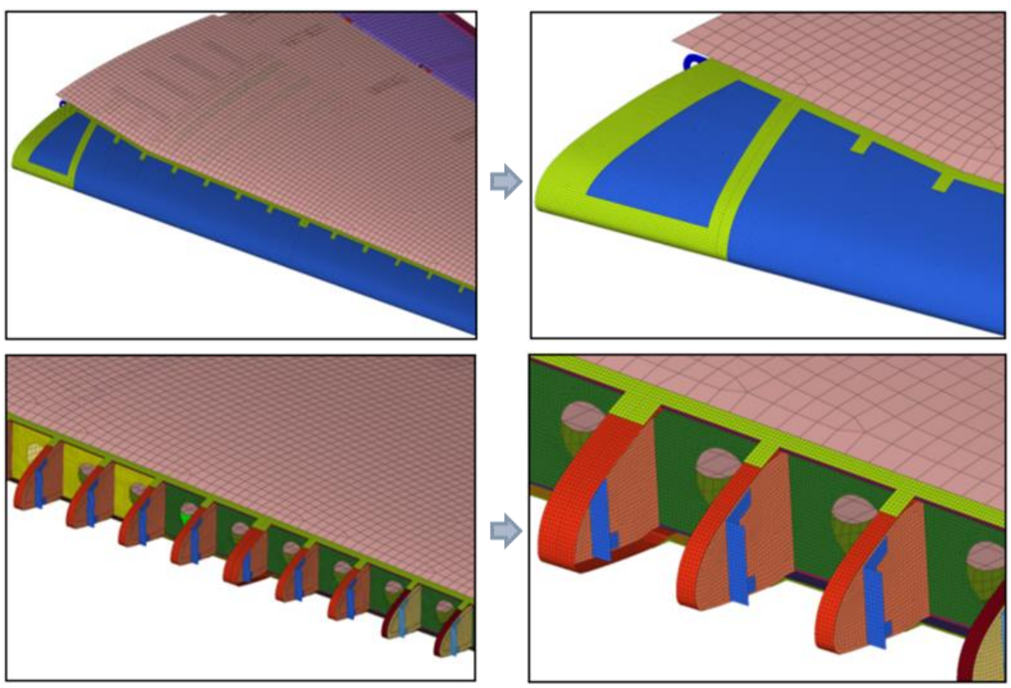

Figure 154. Commercial transport jet horizontal stabilizer - Mesh size

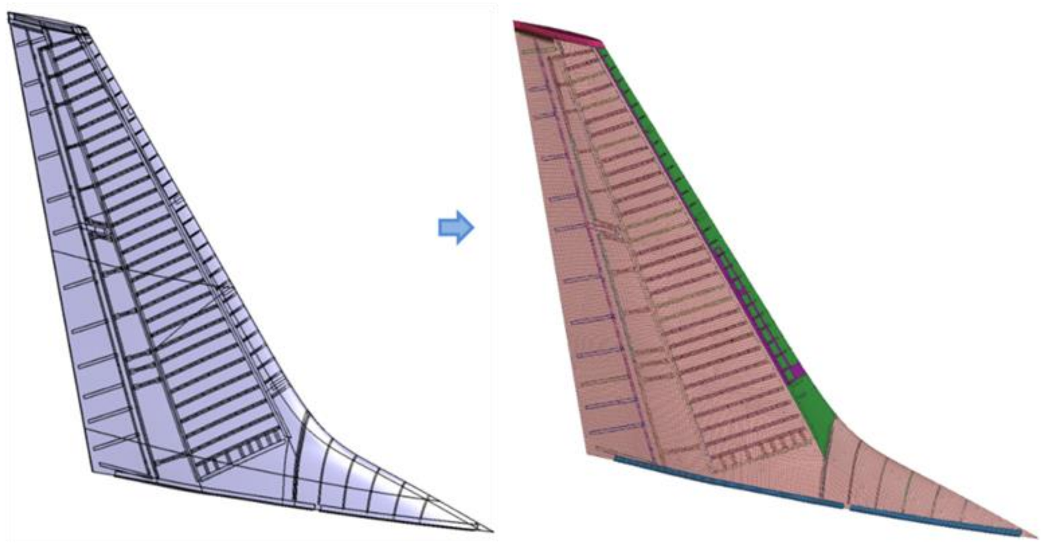

Figure 155. Commercial transport jet vertical stabilizer - Geometry and mesh

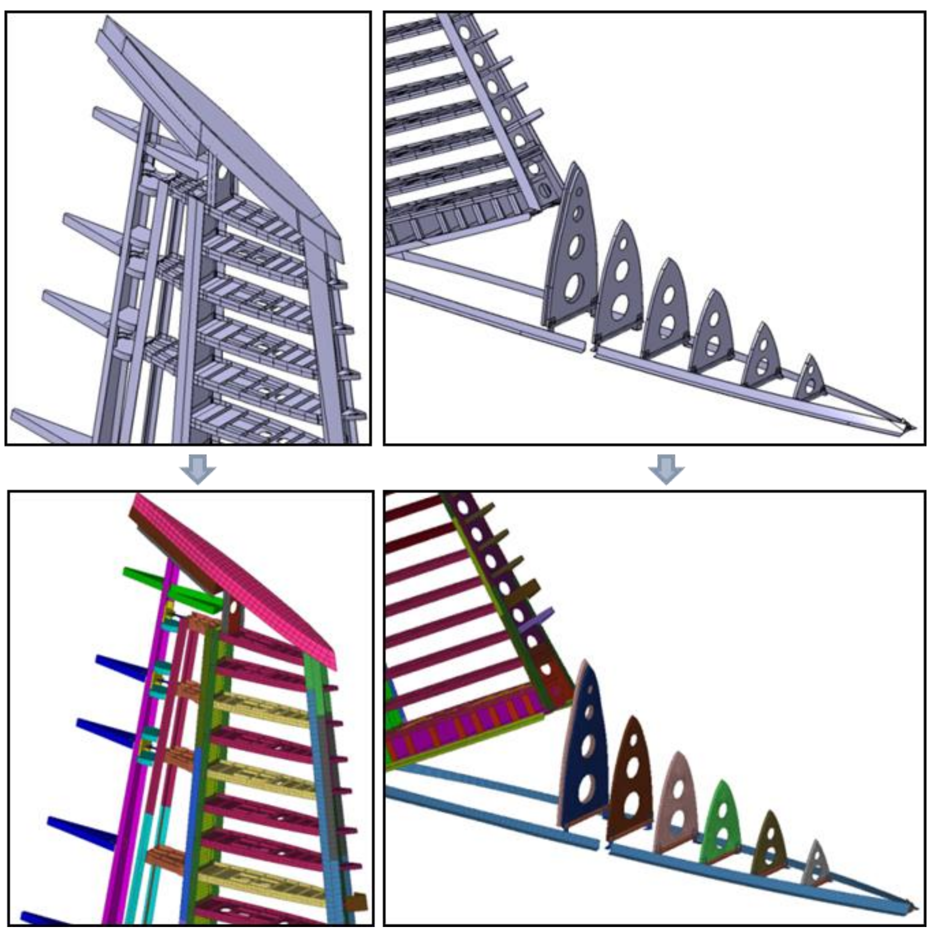

Figure 156. Commercial transport jet vertical stabilizer - Internal structure geometry and mesh

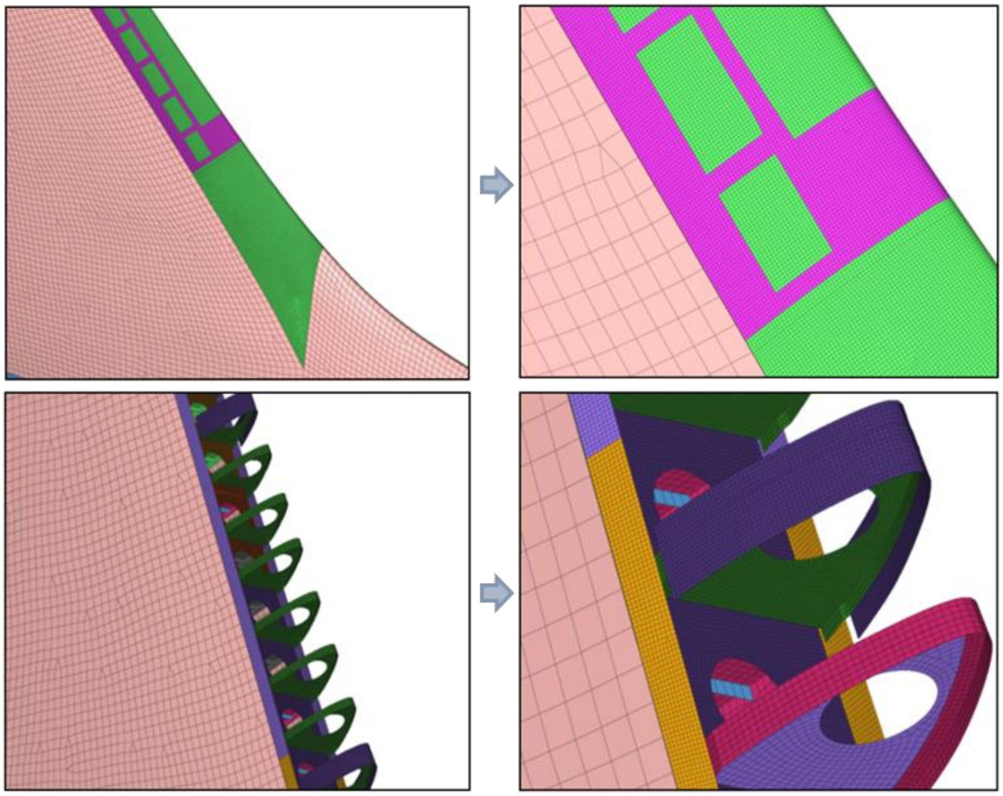

Figure 157. Commercial transport jet vertical stabilizer - Mesh size

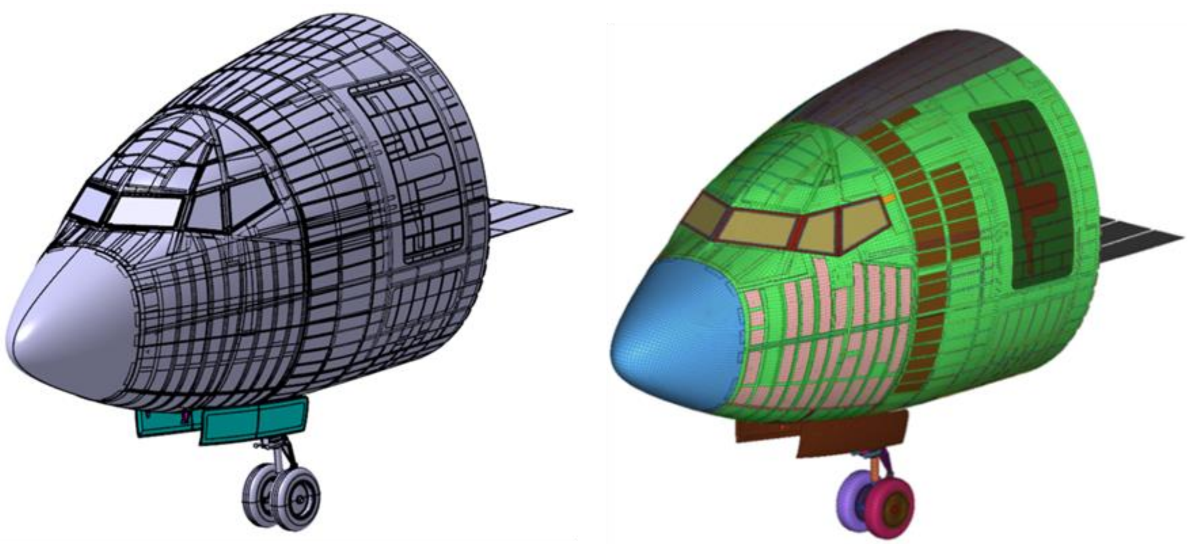

Figure 158. Commercial transport jet windshield - Geometry and mesh

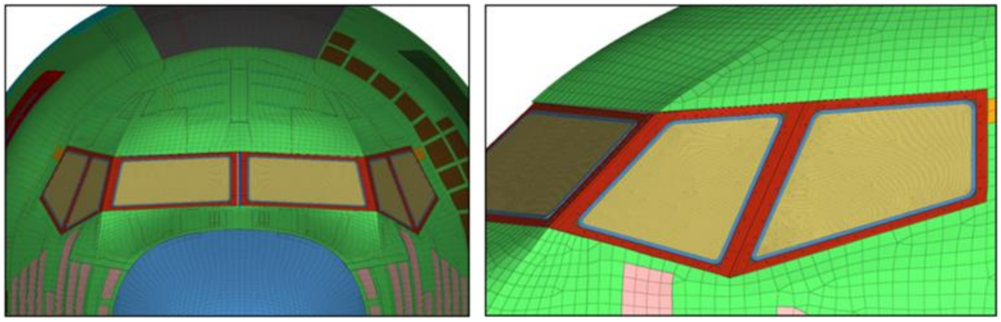

Figure 159. Commercial transport jet windshield - Mesh size

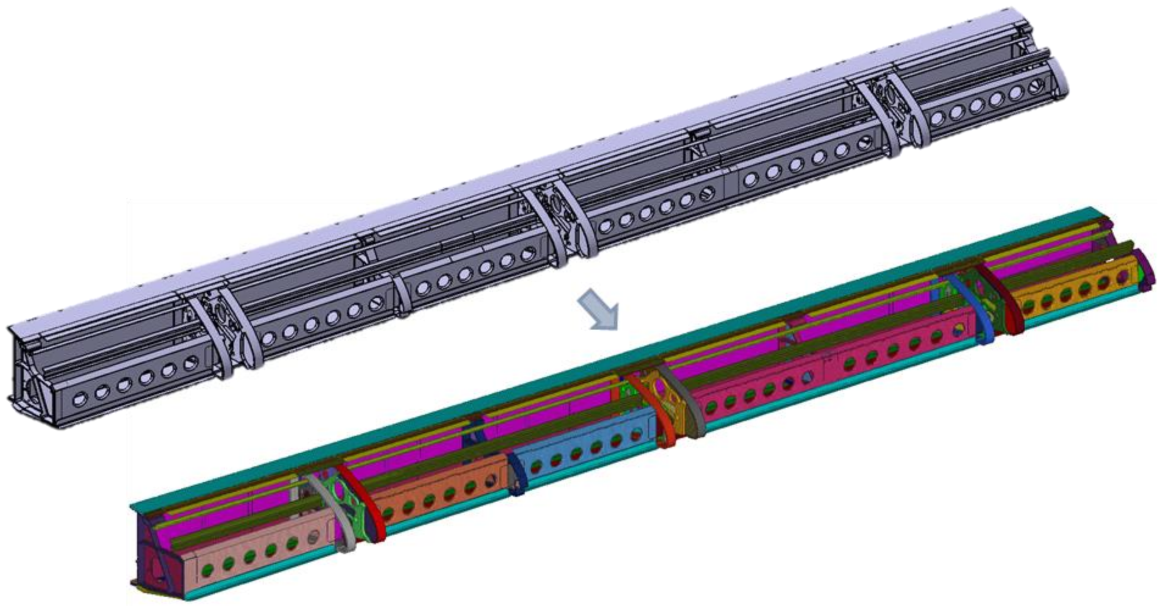

Figure 160. Commercial transport jet wing - Geometry and mesh

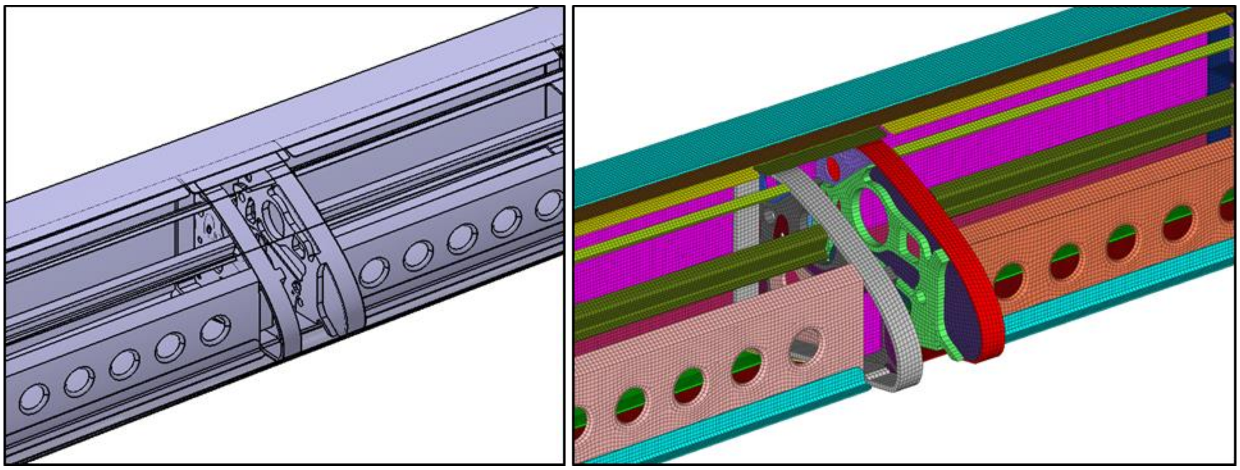

Figure 161. Commercial transport jet wing - Internal frames

3.3.3.2 Business Jet

The discretized target components of the business jet are shown from Figure 162 to Figure 169. The discretized FE model is compared against the CAD models.

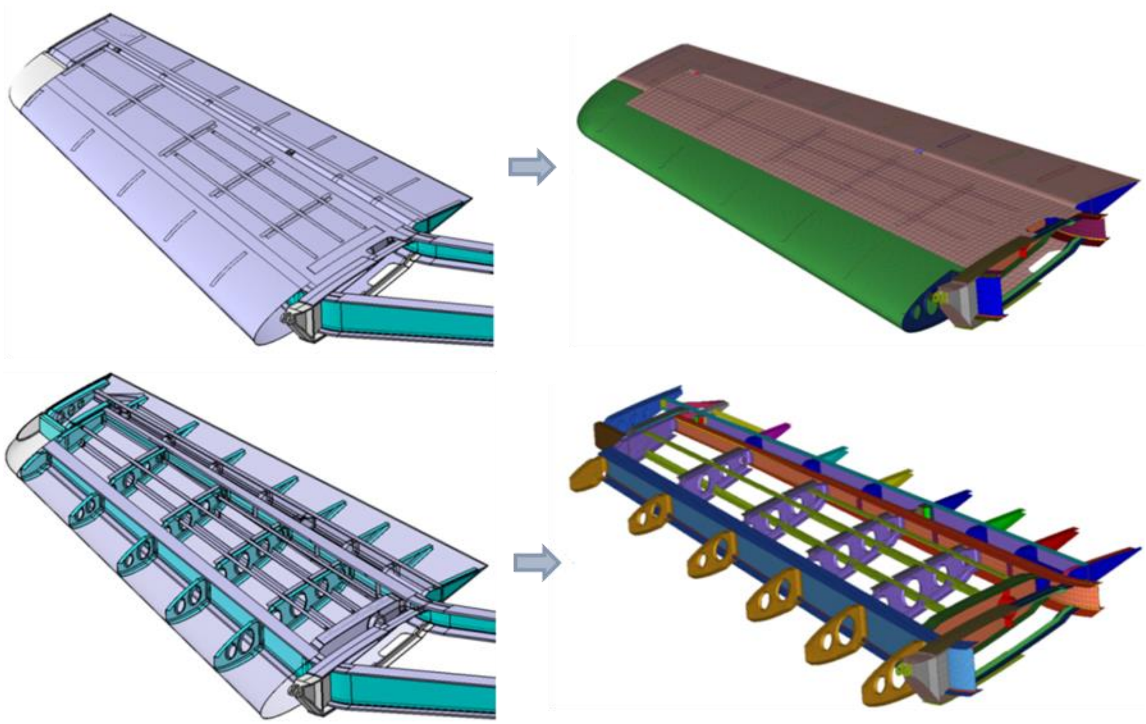

Figure 162. Business jet horizontal stabilizer - Geometry and mesh

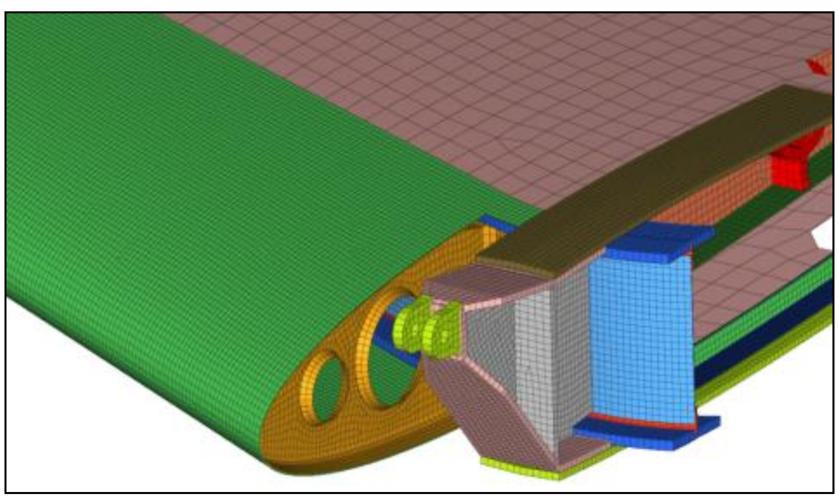

Figure 163. Business jet horizontal stabilizer - Mesh size

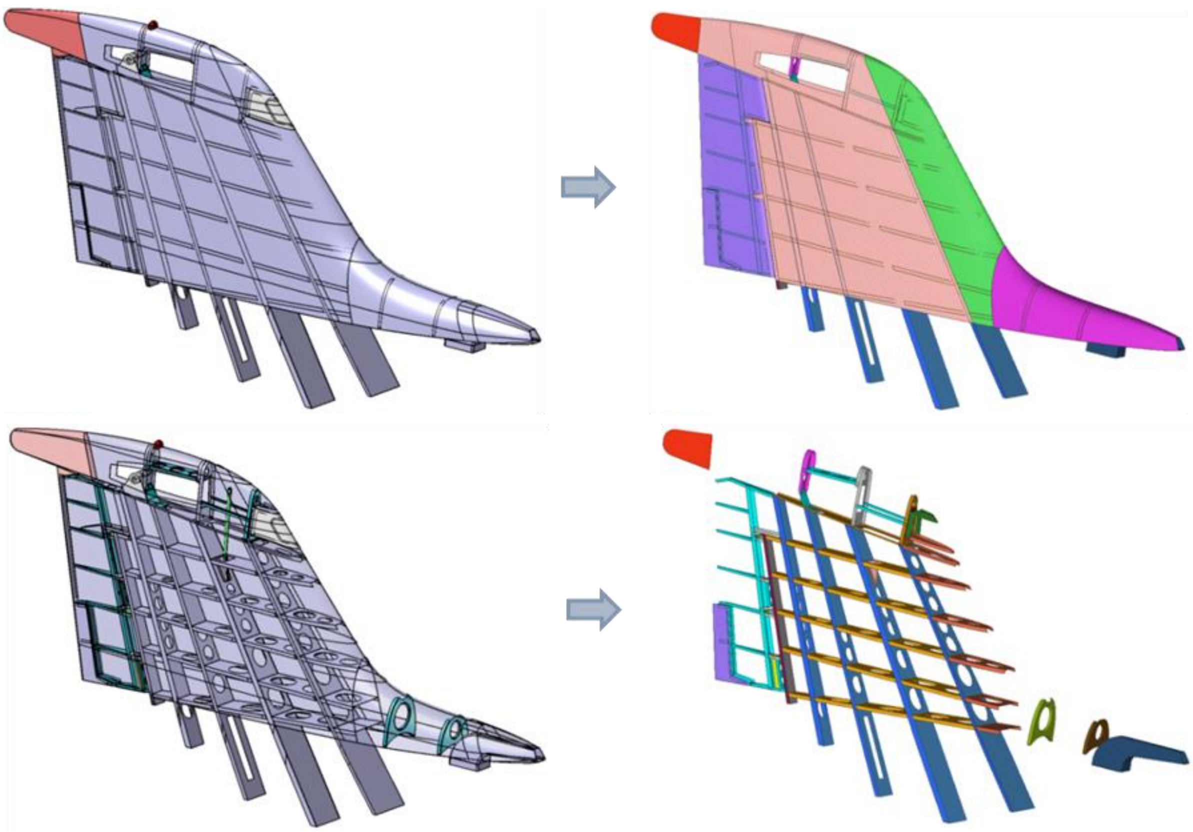

Figure 164. Business jet vertical stabilizer - Geometry and mesh

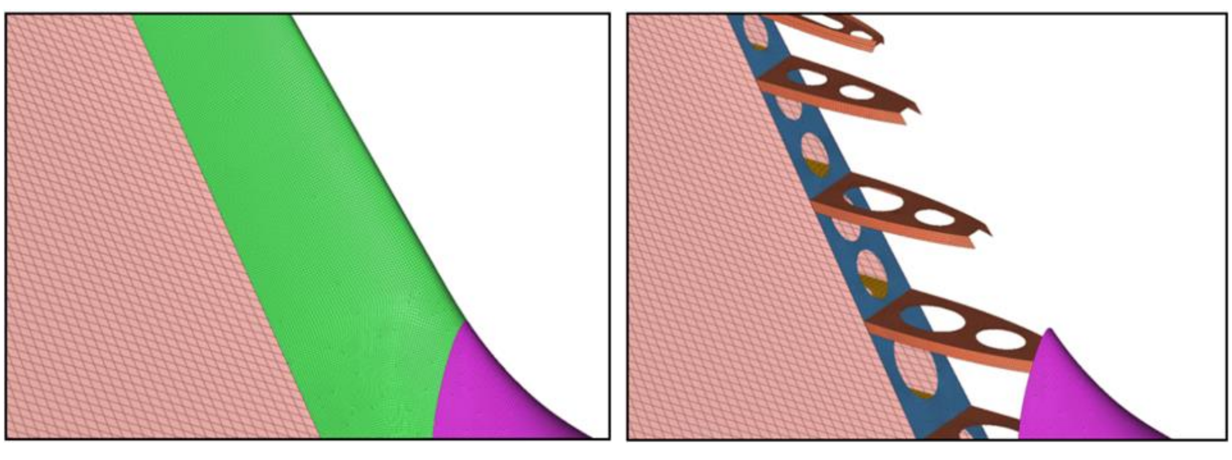

Figure 165. Business jet vertical stabilizer - Mesh size

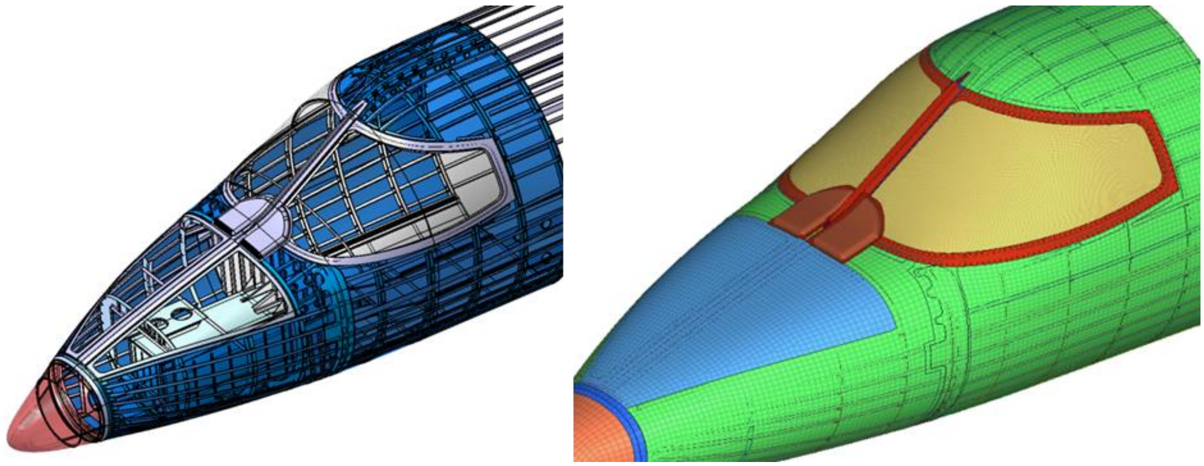

Figure 166. Business jet front section - Geometry and mesh

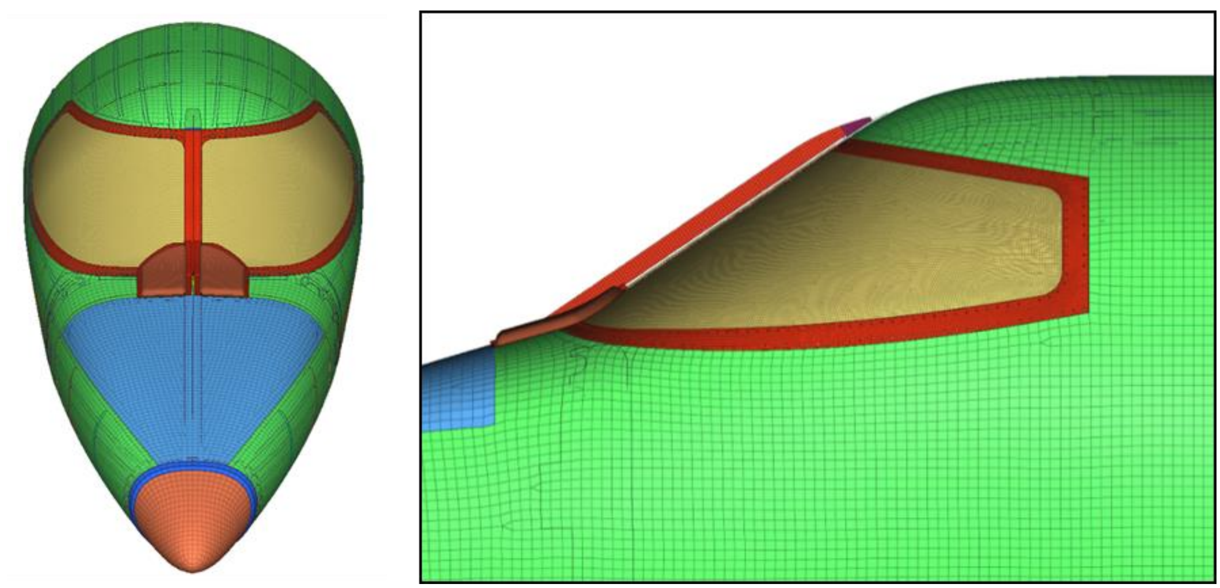

Figure 167. Business jet front section - Mesh size

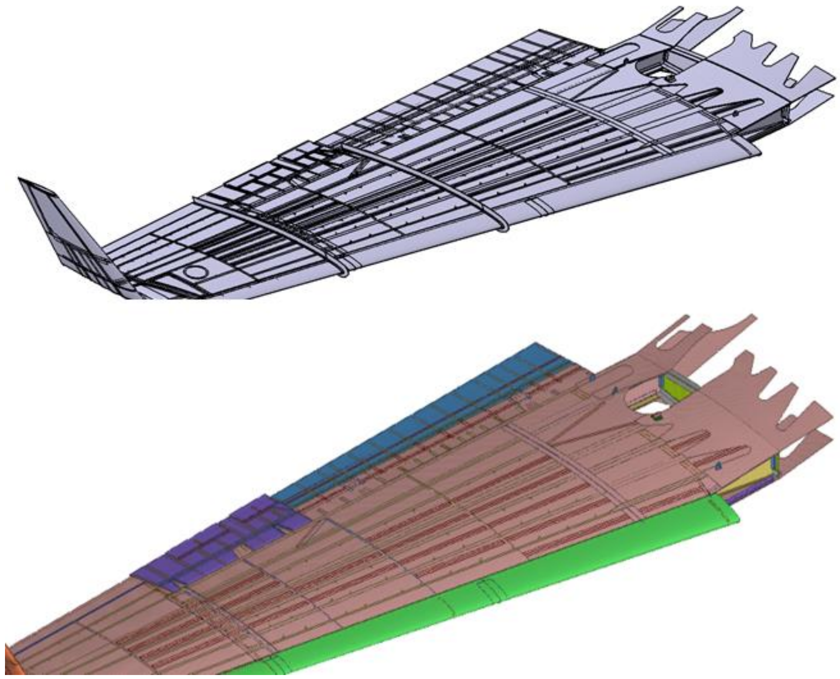

Figure 168. Business jet wing - Geometry and mesh

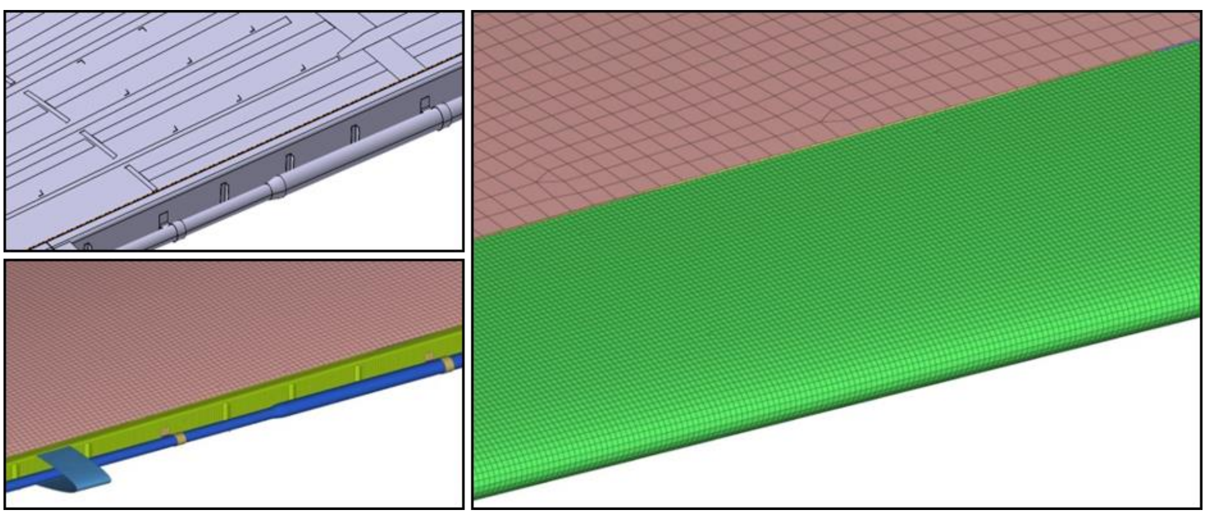

Figure 169. Business jet wing - Mesh size

3.3.4 Connections

The discretized models were connected using two connection types:

- Mesh independent spot-weld beam elements: this is one of the several options used to model fasteners in FE models. This connection is practical for large models because it is possible to automate the connection process. An example of a spot-weld beam connection between the front spar and the front web is shown in Figure 170.

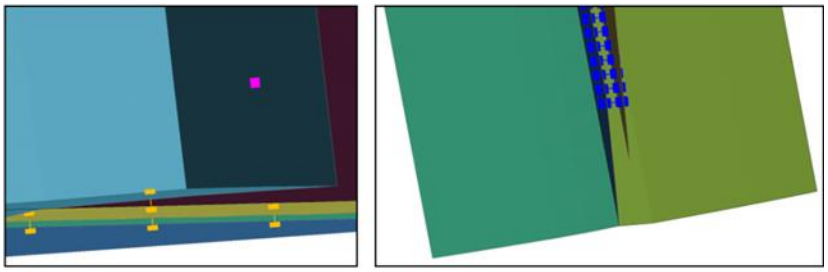

Figure 170. Spot-weld beam connection

- Nodal Rigid Body (NRB): the selected set of nodes is constrained to only allow rigid body motion. Figure 171 shows a NRB around a hole.

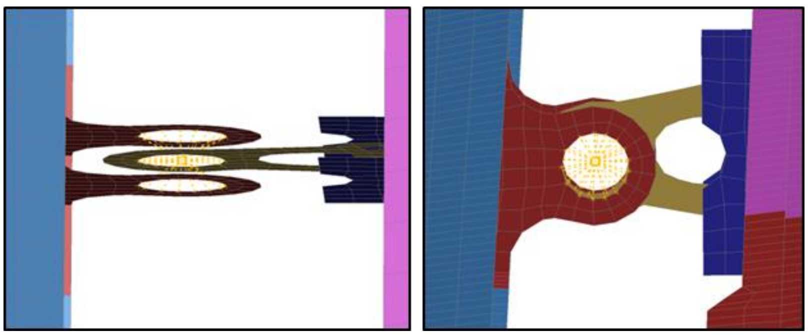

Figure 171. Nodal rigid body

Fastener locations on the target models were established using technical manuals [48][49] and using repair guidelines specified by the FAA Advisory Circular AC 43.13-1B [54]Two examples of the final FE model are shown in Figure 172. Connections are highlighted in different colors based on fastener diameter. The same procedure was followed for the rest of the target models. A summary of the total number of connections for the different target models is provided in Table 17.

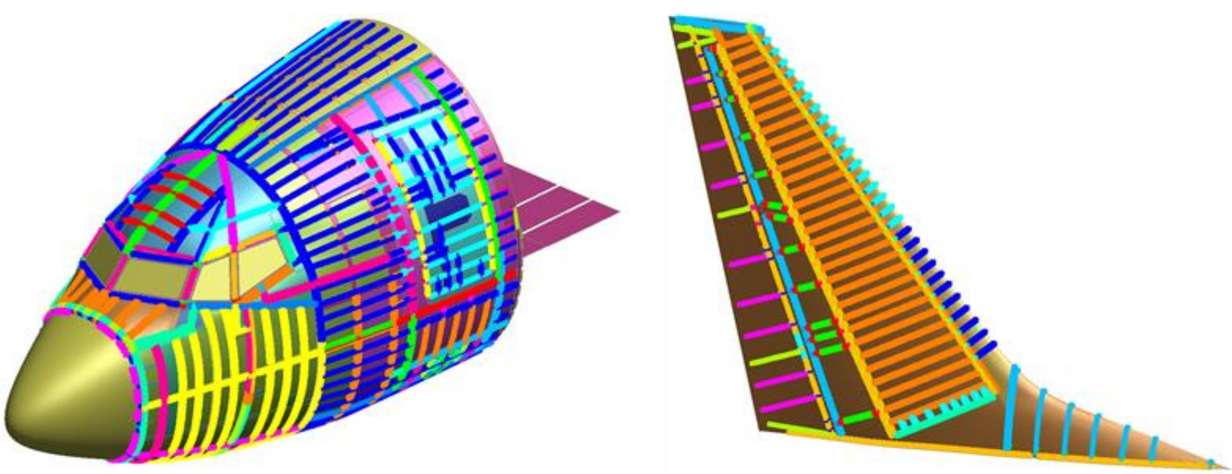

Figure 172. Commercial transport jet front section and vertical stabilizer connections.

Table 17. Target connections summary.

		Spot-weld beam	NRB
Commercial Transport Jet	Front Section	32473	402
	Horizontal Stab.	12858	34
	Vertical Stab.	15568	22
	Wing	1371	-
Business Jet	Front Section	8149	503
	Horizontal Stab.	2548	2
	Vertical Stab.	2901	2
	Wing	15271	36

3.3.5 Materials

LS-DYNA offers several ways to model the material response [24]. There are basic material cards, requiring minimal input as well as complex ones that capture the effects of strain rate, temperature, and triaxiality. Numerous plasticity models are also available. The correct material model definition is critical for accurate responses of the FE model.

Following the building block approach, verification studies were performed at the coupon level to gain confidence in material modeling for FEA.

3.3.5.1 Material Sensitivity Study

In the absence of test data, it is desirable for FE model crashworthiness predictions to be slightly conservative Therefore, a material sensitivity study was performed to understand the response and to select a FE material model for the targets.

It is also important to note that extensive coupon level testing is required to populate the parameters in the more advanced material models in LS-DYNA [24]. Due to the variety of target materials, parameters for advanced material models were not available for all target components. For this study, the major source for material data was the MMPDS [26]. MMPDS data generally provides enough information to populate the *MAT_024* or **MAT_PIECEWISE_LINEAR_PLASTICITY* material card. This material model captures plasticity and failure and was used for most of the components [24]. Based on research for developing target models, it was found that most skins, especially for the leading edge of the commercial transport jet are constructed using 2024-T3 clad aluminum. Fortunately, extensive research has been performed by the FAA [55][56] for populating and validating two different LS-DYNA material models. These are *MAT_015* or **MAT_JOHNSON_COOK* and *MAT_224* or **MAT_TABULATED_JOHNSON_COOK*. These three material models are defined in the LS-DYNA manuals [24].

For conducting the material sensitivity study, a preliminary quadcopter UAS model was impacted on a generic leading edge model at 200 knots (102.9 m/s). The skin of the leading edge model was modeled using 2024-T3 clad aluminum with a gage thickness of 0.063 in (1.6 mm). A schematic for the FE model setup for this study is shown in Figure 173. Three different LS-DYNA material models were used for the skin (first target component impacted), as shown in Table 18. The key independent variables governing the response of the selected materials are summarized in the table.

The damage and failure modes observed for the FE model results are presented in Figure 174. Based on the research performed by the FAA [55], the high fidelity *MAT_015* material model has been validated against several component level tests and articles from aircraft structures. Therefore, *MAT_015* was used as the baseline model for comparison of damage. The Fe model using MAT_224 showed similar damage characteristics as *MAT_015* results while the Fe model results based on *MAT_024* showed extensive damage on the leading edge. Due to the lack of material model parameters for the various target leading edge materials, the validated *MAT_015* model for 2024-T3 clad aluminum [55] was used to model the leading edge skins for all the targets. All the remaining components of the targets were modeled using *MAT_024* since that data was readily available from MMPDS [26].

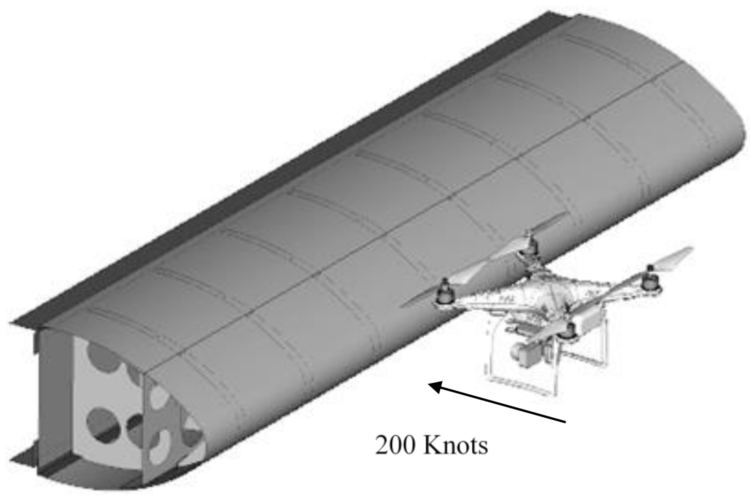

Figure 173. Material sensitivity study FE model set-up

Table 18.LS-DYNA material models compared

Model	LS-DYNA Material Model	Input Data Reference	Temperature Dependence	Strain-Rate Parameters	Triaxiality & Lode Surface	Plasticity
1	15	DOT/FAA/AR-03/57 [55]	YES	YES	NO	YES
2	224	DOT/FAA/TC-13/25 [56]	YES	YES	YES	YES
3	24	MMPDS-09 [26]	NO	NO	NO	YES*

* Plasticity is represented by tangent modulus not full range curve.

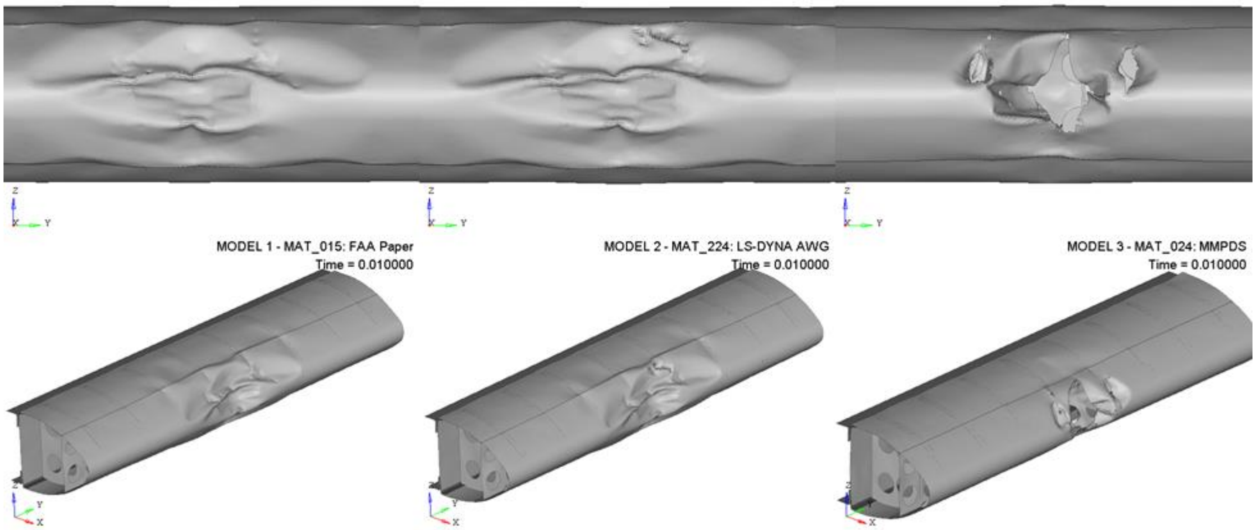

Figure 174. Damage and failure comparison of different LS-DYNA material models on a generic leading edge impacted by a quadcopter UAS model

The evaluation of material modeling at the component level is part of the building block approach. The verification at the component level provides assurance that the target models will produce accurate results.

3.3.5.2 Material Verification Methodology

Since test data for many materials were not available, material data from the MMPDS were used. The data from MMPDS provided sufficient information to populate the *MAT_024* material card [26]. *MAT_024* is an elastic-plastic material with an option to define an arbitrary stress versus strain curve and arbitrary strain rate dependency [24]. For most cases, the full range stress/strain curves were not available in MMPDS and therefore the materials were modeled as bi-linear elastic plastic where the stress strain behavior was approximated as straight lines using the Young's modulus and tangent modulus as shown in Figure 175.

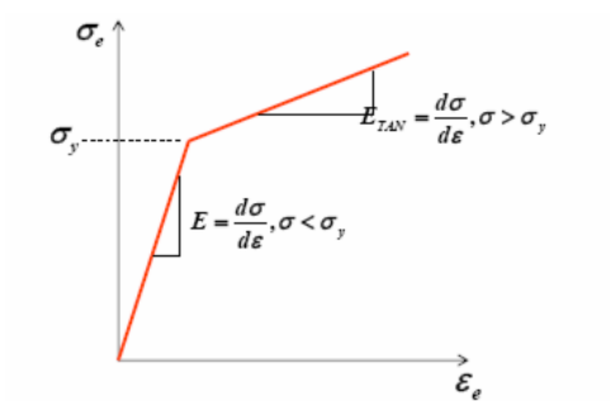

Figure 175. Stress strain curve for bi-linear elastic plastic [57]

The material verification study is performed using a FE model of a test coupon. As an example, consider the 6061-T6 aluminum data shown in Figure 176.

MMPDS-09
1 April 2014

Table 3.6.2.0(g). Design Mechanical and Physical Properties of 6061 Aluminum Alloy Extruded Rod, Bar, and Shapes

Specification	AMS 4161, AMS 4172, & AMS-QQ-A-200/8[a]	AMS-QQ-A-200/8[a]	AMS 4160 & AMS-QQ-A-200/8[a]	AMS 4150, AMS 4173 & AMS-QQ-A-200/8[a]				
Form	Extruded rod, bar, and shapes							
Temper	T4, T4510, and T4511	T42[b]	T62[b]	T6, T6510, and T6511				
Cross-sectional area, in.^{2}	...	...	...	...	≤ 32			
Thickness,[c] in.	≤ 3.000	All	All	≥ 0.250	≤ 1.000		1.001-6.500	
Basis	S	S	S	S	A	B	A	B
Mechanical Properties:								
F_{tu}, ksi:								
L	26	26	38	38	38	41	38	41
LT	...	...	...	...	37	40	33	35
F_{ty}, ksi:								
L	16	12	35	35	35	38	35	38
LT	...	...	...	...	33	36	28	31
F_{cy}, ksi:								
L	14	...	...	...	34	37	34	37
LT	...	...	...	...	35	38	30	33
F_{su}, ksi	16	...	...	...	26	28	19	21
F_{bru}[d], ksi:								
(e/D = 1.5)	42	...	...	...	64	69	52	57
(e/D = 2.0)	55	...	...	...	82	88	69	74
F_{bry}[d], ksi:								
(e/D = 1.5)	22	...	...	...	54	58	42	46
(e/D = 2.0)	26	...	...	...	60	65	50	55
e, percent (S-Basis):								
L	16	16	10[e]	10	10[e]	...	10	...
E, 10^3 ksi	9.9							
E_c, 10^3 ksi	10.1							
G, 10^3 ksi	3.8							
μi	0.33							
Physical Properties:								
ωi, lb/in.^{3}	0.098							
C, K, and αi	See Figure 3.6.2.0							

Last Revision: Apr 2012, MMPDS-07, Item 11-62.

a Mechanical properties were established under QQ-A-200/8.

b Design allowables were based upon data obtained from testing samples of material, supplied in the O to F temper, which were heat treated to demonstrate response to heat treatment by suppliers. Properties obtained by the user, however, may be lower than those listed if the material has been formed or otherwise cold- or hot-worked, particularly in the annealed temper, prior to solution heat treatment.

c The mechanical properties are to be based upon the thickness at the time of quench.

d Bearing values are "dry pin" values per Section 1.4.7.1.

e For thicknesses ≤ 0.249 inch, e = 8%.

Figure 176. MMPDS data for Aluminum 6061-T6 [26]

The set-up of the FE model of the coupon is shown in Figure 177. The stress/strain results of the FE analysis of the coupon are compared against the MMPDS data to verify the performance of the material as shown in Figure 178.

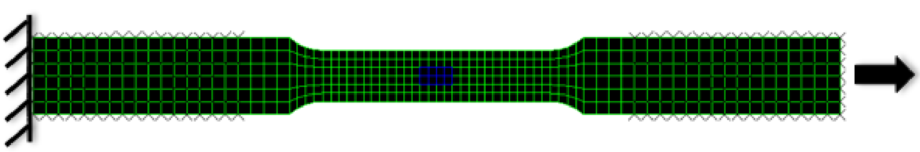

Figure 177. FEM of coupon for material verification

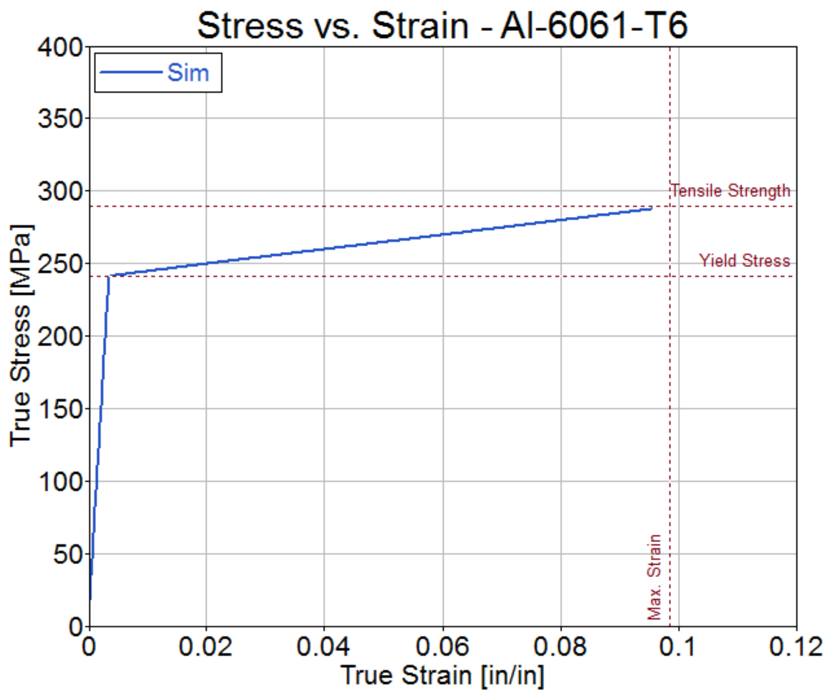

Figure 178. MMPDS Aluminum 6061-T6 material verification

3.3.5.3 Material Definition

This section presents the materials used for the target models. Figure 179 points out the impact areas of interest for a typical leading edge and windshield model. Table 19 summarizes the materials used for different target components, the LS-DYNA material card used for defining those materials and the source for material input data.

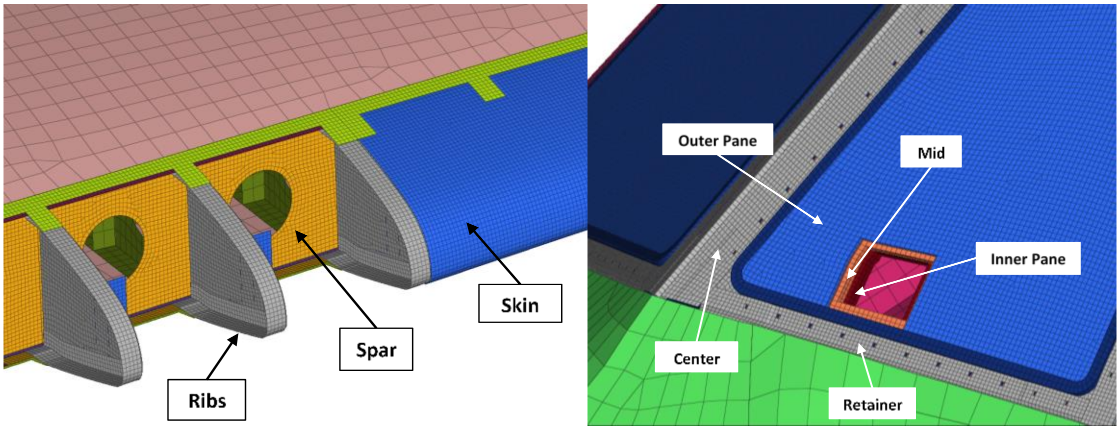

Figure 179. Leading edge (left) and windshield (right) impact area

Table 19. Commercial transport jet airframe materials at impact areas

		Part	Material	LS-DYNA MAT card	Reference
Commercial Transport Jet	Horizontal Stabilizer	Skin	2024-T3 Al	*MAT_015*	DOT/FAA/AR-03/57 [55]
		Ribs	2024-T42 Clad Al	*MAT_024*	MMPDS-09 [26]
		Front spar	7075-T6 Al	*MAT_024*	MMPDS-09 [26]
	Vertical Stabilizer	Skin	2024-T3 Al	*MAT_015*	DOT/FAA/AR-03/57 [55]
		Ribs	2024-T42 Clad Al	*MAT_024*	MMPDS-09 [26]
		Front spar	7075-T6 Al	*MAT_024*	MMPDS-09 [26]
	Wing	Skin	2024-T3 Al	*MAT_015*	DOT/FAA/AR-03/57 [55]
		Ribs	7050-T7451 Al	*MAT_024*	MMPDS-09 [26]
		Front spar	7050-T7451 Al	*MAT_024*	MMPDS-09 [26]
	Front Section	Outer pane	PMMA	*MAT_024*	Hidallana-Gamage [59]
		Mid layer	PVB	*MAT_024*	Wang. [58]
		Inner pane	MIL-PRF-25690	*MAT_124*	MIL-HDBK-17A [60]
		Center post	7050-T7452 Al	*MAT_024*	MMPDS-09 [26]
		Retainer	7075-T6 Al	*MAT_024*	MMPDS-09 [26]

Table 20. Business jet airframe materials at impact areas

		Part	Material	LS-DYNA MAT card	Reference
Business Jet	Horizontal Stabilizer	Skin	2024-T3 Al	*MAT_015*	DOT/FAA/AR-03/57 [55]
		Ribs	2024-T42 Clad Al	*MAT_024*	MMPDS-09 [26]
		Front spar	2024-T3 Clad Al	*MAT_024*	MMPDS-09 [26]
	Vertical Stabilizer	Skin	2024-T3 Al	*MAT_015*	DOT/FAA/AR-03/57 [55]
		Ribs	2024-T3 Al	*MAT_024*	MMPDS-09 [26]
		Front spar	2024-T3 Al	*MAT_024*	MMPDS-09 [26]
	Wing	Skin	2024-T3 Al	*MAT_015*	DOT/FAA/AR-03/57 [55]
		Nose Ribs	2024-T3 Al	*MAT_015*	DOT/FAA/AR-03/57 [55]
		Front spar	2024-T3 Al	*MAT_015*	DOT/FAA/AR-03/57 [55]
	Front Section	Outer pane	MIL-PRF-25690	*MAT_124*	MIL-HDBK-17A [60]
		Mid layer	MIL-PRF-5425	*MAT_124*	MIL-HDBK-17A [60]
		Inner pane	MIL-PRF-25690	*MAT_124*	MIL-HDBK-17A [60]
		Center post	2024-T3511 Al	*MAT_024*	MMPDS-09 [26]
		Retainer	2024-T3 Al	*MAT_024*	MMPDS-09 [26]

Figure 180 and Figure 181 respectively illustrate the materials that conform the different components of the commercial transport and business jets respectively.

Code	Material	Source
	Al 2024-T3	DOT/FAA/AR -03/57
	Al 2024-T3	MMPDS-09
	Al 2024-T3-CLAD	MMPDS-09
	Al 2024-T42-Clad	MMPDS-09
	Al 2024-T62	MMPDS-09
	Al 6061-T6	MMPDS-09
	Al 7075-T6	MMPDS-09
	Al 7075-T6-CLAD	MMPDS-09
	Al 7050-T7451	MMPDS-09
	PMMA	Ref 1
	PVB	Ref 2
	MIL-PRF-25690	MIL-HDBK-17A Part II

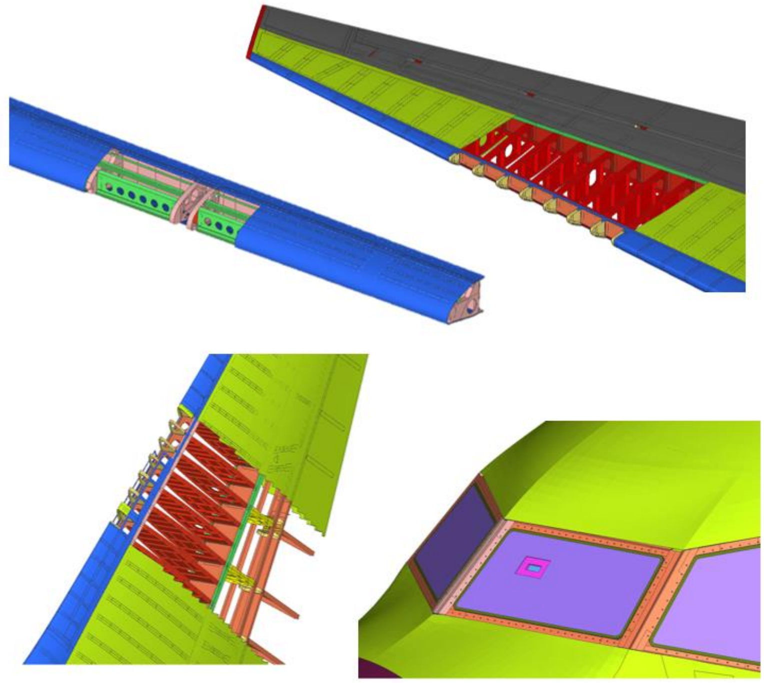

Figure 180. Commercial transport jet airframe materials of the subassemblies subject to study.

Code	Material	Source
	Al 2024-T3	DOT/FAA/AR -03/57
	Al 2024-T3	MMPDS-09
	Al 2024-T3-CLAD	MMPDS-09
	Al 2024-T42-Clad	MMPDS-09
	Al 2024-T62	MMPDS-09
	Al 6061-T6	MMPDS-09
	Al 7075-T73	MMPDS-09
	MIL-PRF-5425	MIL-HDBK-17A Part II
	MIL-PRF-25690	MIL-HDBK-17A Part II

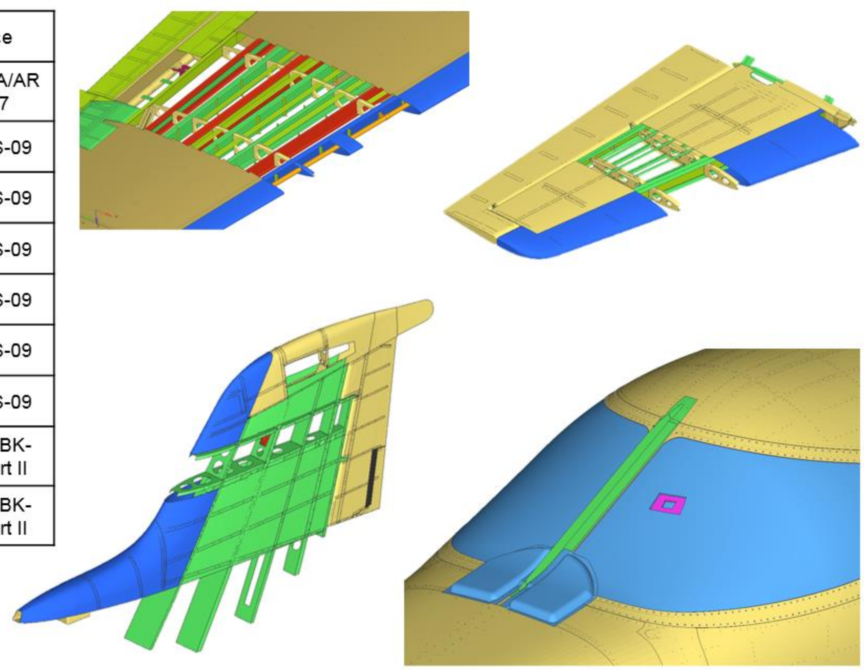

Figure 181. Business jet airframe materials of the subassemblies subject to study.

Similarly, Figure 182 and Figure 183 illustrate gage thicknesses of the metallic parts in the different subassemblies being studied for both commercial transport and business jets respectively.

Code	Thickness	
	0.5-1.0 mm	0.02-0.04 in
	1.0-1.5 mm	0.04-0.059 in
	1.5-2.0 mm	0.059-0.078 in
	2.0-3.0 mm	0.078-0.118 in
	3.0-5.0 mm	0.118-0.197 in
	5.0-7.0 mm	0.197-0.276 in
	> 7.0 mm	> 0.276 in

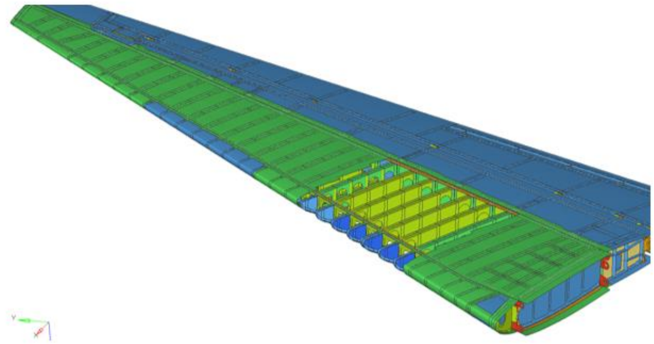

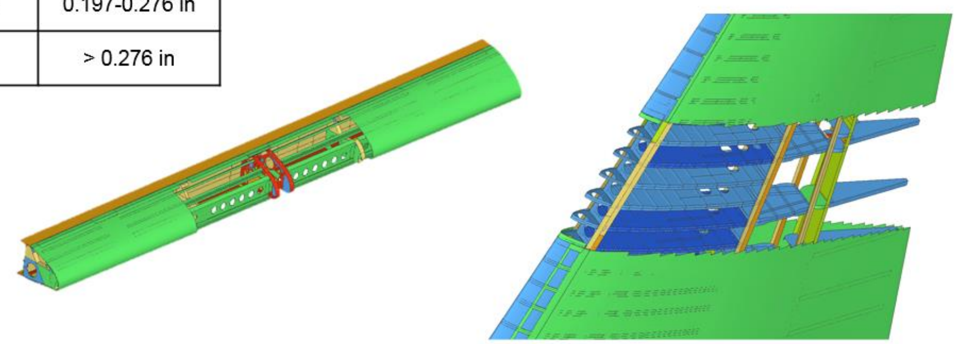

Figure 182. Commercial transport jet airframe gage thicknesses of metallic components.

Code	Thickness	
	0.5-1.0 mm	0.02-0.04 in
	1.0-1.5 mm	0.04-0.059 in
	1.5-2.0 mm	0.059-0.078 in
	2.0-3.0 mm	0.078-0.118 in
	3.0-5.0 mm	0.118-0.197 in
	5.0-7.0 mm	0.197-0.276 in
	> 7.0 mm	> 0.276 in

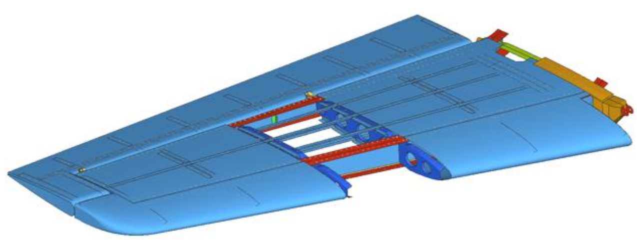

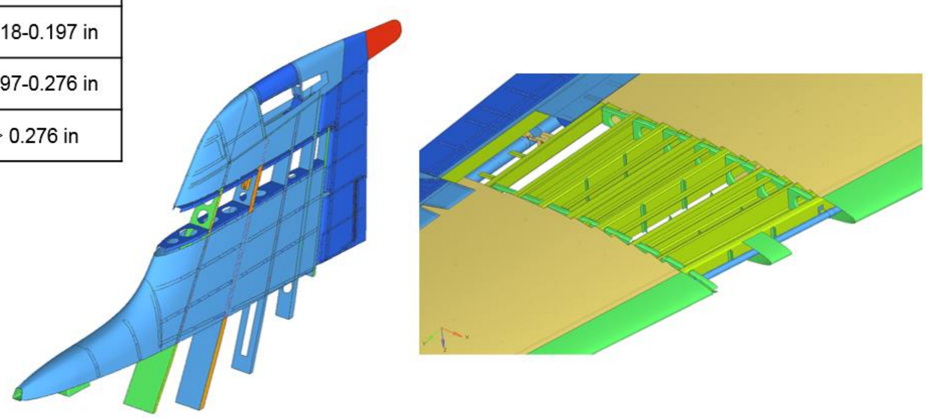

Figure 183. Business jet airframe gage thicknesses of metallic components subject to study.

3.3.5.4 Material Model Limitations

The selection of the material card for the different components was made based on the experimental data available and the sensitivity analysis conducted. In general, *MAT_024* provides conservative results due to its limitations. Some of these limitations are:

- Stress failure in the material card is defined for uniaxial tension conditions. Shear, compression or mixed stress states will also fail at the same uniaxial tension value leading to results that are more conservative.
- Input data coming from MMPDS-09 [26] contains material properties for quasi-static conditions. The results subjected to these values led to a conservative approach from a failure perspective.

The limitations presented above supported the decision of applying *MAT_015* where the impact area properties allowed it, reducing the conservatism of the target model, and providing results that are more realistic.

3.3.6 Contacts

For the general assembly of all target models, the **CONTACT_AUTOMATIC_SINGLE_SURFACE* contact card was used. **CONTACT_SPOTWELD* was also used to capture the contact between the spot-weld elements and the remaining 2D and 3D target elements.

4. UAS – COLLISION ANALYSIS

Once the FE models of both UASs and the commercial transport and business jets were completed, a series of impact scenarios were set up with the objective of characterizing the dynamic event of a midair collision.

This chapter provides, first, a justification of the impact boundary conditions (velocity, UAS orientation, etc.) selected for these baseline simulations. Second, a classification of the different levels of aircraft damage severity is presented. Subsequently, the baseline (worst-case) simulations for both commercial transport and business jets are described and summarized. All supplementary simulation results are available in APPENDIX B. Finally, conclusions are reached on whether a midair collision with a 1.2 kg (2.7 lb) quadcopter UAS is severe and the damage levels are presented.

The simulations presented in this chapter established a baseline to select the worst case scenarios to be used in further studies as reference for comparison of different parameters (mass, velocity) or situations (bird strike), presented in Chapters 5. and 6.

4.1 SELECTION OF IMPACT CONDITIONS

4.1.1 Impact Velocity

FAA General Operating and Flight Rules (14 CFR Part 91) [61] airworthiness requirements set the limits of operating speeds at different altitudes. The requirements are as follows:

- *91.817*: Mach 1 over land (with a few exceptions that are noted in Appendix B to 91.817)
- *91.117(a)*: 250 KIAS below 10,000 ft MSL
- *91.117(b)*: 200 KIAS below 2,500 ft within 4NM of the primary airport for Class C and D airspace (unless within Class B airspace)
- *91.117(c)*: 200 KIAS under the shelf of Class B airspace
- *91.117(c)*: 200 KIAS in a VFR corridor through Class B airspace

The Aeronautical Information Manual paragraph 5-7-2-j.2(b) indicates the following holding speeds:

- 200 KIAS below 6,000 ft.
- 230 KIAS from 6,001 to 14,000 ft.
- 265 KIAS above 14,000 ft.

It was assumed that the most probable high velocity impact scenario was either at landing/take-off or at holding flight phase. Consequently, the holding speed was selected as the baseline velocity for the aircraft; a maximum of 200 KIAS, as defined in *14 CFR Part 91.117(b)*, which at 2,500 ft is equivalent to approximately 208 knots (107.0 m/s) true airspeed (TAS). Figure 184 presents a schematic of the NAS classifications from the FAA [62].

The specifications of the UAS selected for this study, see section 2.1, provide the maximum velocity (16 m/s, 31.1 knots) and service ceiling (6,000 m, 19,685 ft). During the literature review phase of this project it was concluded that some newer UAS models of a similar type had enhanced specifications, with maximum speeds of up to 20 m/s (38.8 knots).

Therefore, to account for the relative velocities of a frontal impact, a velocity of 128.6 m/s (250 knots) was selected as the baseline for the study presented in this chapter. A broader range of velocities, from minimum landing to cruise speed, was investigated in a parametric study that is presented in Chapter 5.

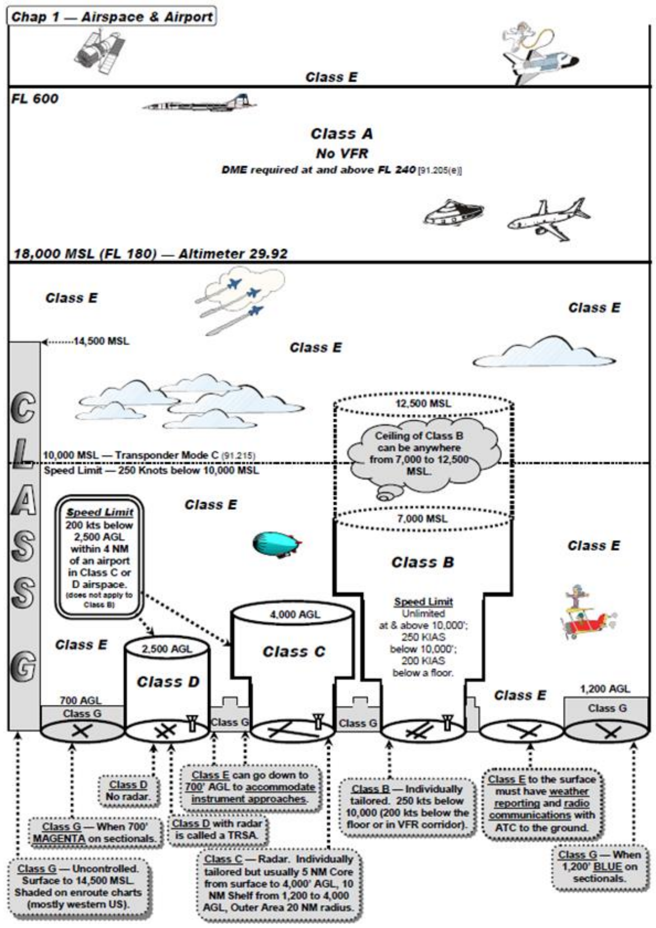

Figure 184. National Airspace System classifications [62]

4.1.2 Impact Conditions

In preliminary simulations, it was observed that small variations in the vertical or horizontal position of the UAS respect to the aircraft or in the angle of impact had important alterations in the levels of damage after impact. Consequently, it was understood that boundary and initial conditions were of extreme importance for simulating midair collision events. Fortunately, FE simulation possesses a great advantage over physical testing, allowing full control on the boundary and initial conditions of the simulation. In contrast, physical testing would require multiple and costly repetitions to arrive to the worst-case scenario.

Accordingly, a parametric study was completed with the objective of identifying the most critical local impact conditions to narrow down the number of simulations to be run for each of the impacted aircraft subassemblies. To achieve this, the UAS FE model was impacted into a wing leading edge FE model, developed and verified through simulation and testing by the NIAR in a previous project for bird strike [32]. The assembly was constructed from 2024-T3 aluminum alloy with a skin thickness of 1.22 mm. Several parameters were investigated, which are presented in the following sections. The criteria to select the worst case were based on the amount of damage introduced into the structure.

4.1.2.1 Impact Location

To determine the influence of the impact location along the leading edge, two set of impact locations were defined. Three centered impact locations were selected along the horizontal direction as it shown on the top of Figure 185. These locations were positioned in front of a nose rib (front rib), at a ¼ rib-to-rib distance from the center of the nose rib and in the middle location between two nose ribs. The second set had the aim of investigating the impact severity of three different vertical positions, which were vertically aligned with the mid-bay centered.

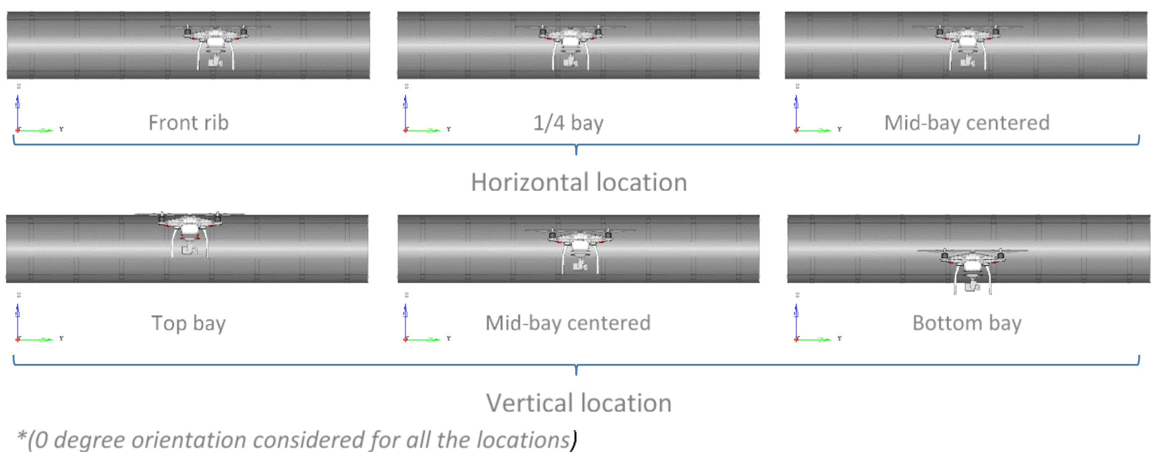

Figure 185 UAS impact location parametric study setup

Figure 186 presents the kinematics for the two sets of impact locations studied. The bottom center image shows the centered case, the left and right images show the upper and lower vertical impact respectively, and the top image shows a direct impact to the rib.

It was observed that when impacting close to the rib, most of the internal energy was absorbed by the UAS, and the target structure mostly received damage to the rib and little penetration into the airframe. In contrast, when the impact was centered between ribs, the skin of the airfoil absorbed most of the internal energy. In this case, the UAS perforated the skin and penetrated into the airframe severely damaging the spar.

Similarly, the vertical sensitivity study indicated that whenever the UAS impacted off-center with respect to the leading edge, a considerable part of the UAS mass was deflected, as it is illustrated in both bottom left and right images of Figure 186. It was concluded that the most damage occurred when the UAS CG was aligned with the leading edge of the airfoil and the UAS impacted at the center between two ribs.

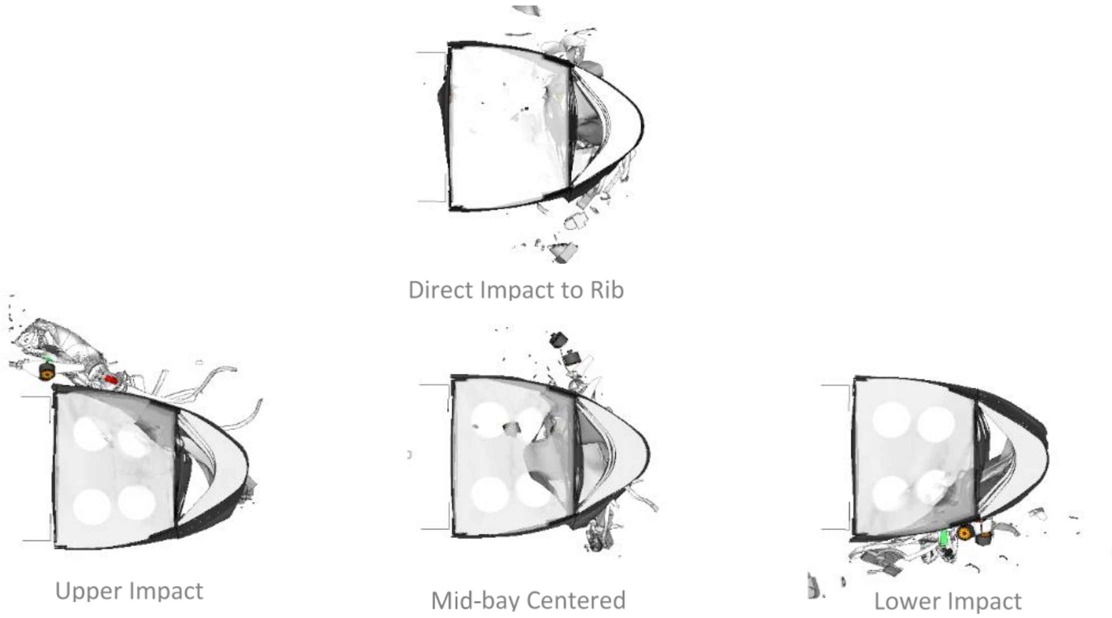

Figure 186. Kinematics of an UAS collision for impact location parametric study at 128.6 m/s

4.1.2.2 UAS Orientation

The influence of the UAS orientation against impact was also investigated. The purpose of this parametric study was to determine the UAS orientation (angle respect to vertical Z-axis) which causes the most severe damage to the leading edge structure.

Figure 187 presents the four orientations (0°, 45°, 90°, 180°) considered for this study. The impact location was based on the worst-case scenario found in the impact location parametric study (mid-bay centered). Figure 188 shows the kinematics for the orientation parametric study.

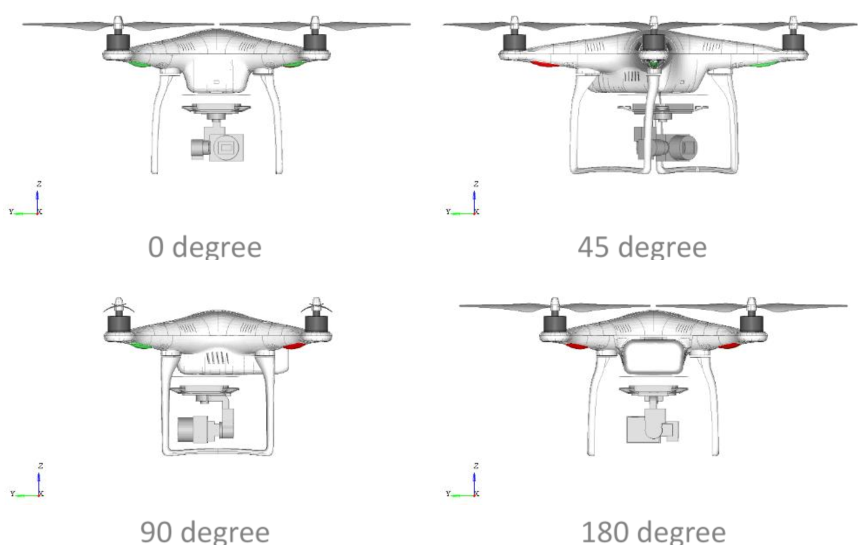

Figure 187. UAS parametric orientation study setup

It was observed that a 45-degree yaw angle of the UAS created considerably more damage than the other cases. It was apparent that in this scenario, having three masses aligned (two motors and the battery) concentrated more load at the center of the impact, increasing damage to internal components of the leading edge.

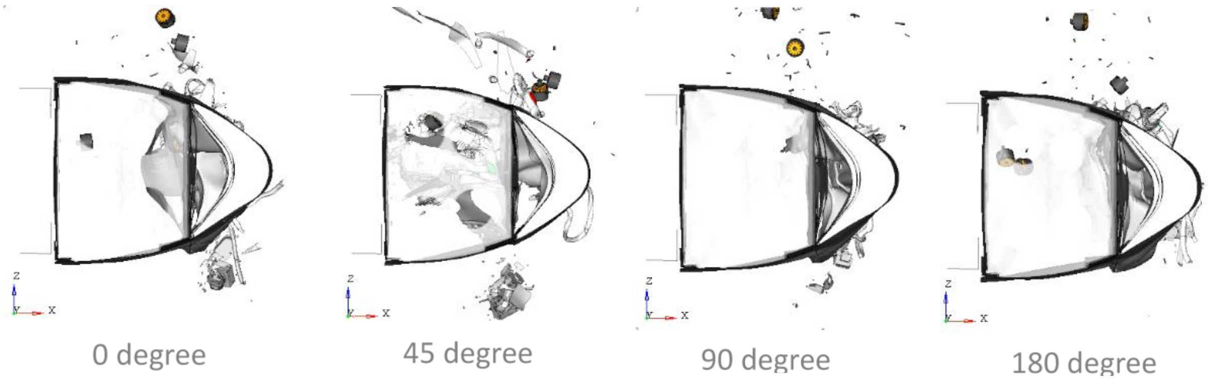

Figure 188. Kinematics of an UAS parametric orientation study at 128.6 m/s (250 knots)

4.1.2.3 Conclusions of Parametric Study

Table 21 presents the results of all the iterations for both parametric studies (location and orientation). Damage was assessed based on the integrity of the inner structure after the collision as well as considering if the UAS penetrated into the airframe.

Table 21 Impact conditions parametric study results

			Damage				
	Run	**Penetration**	**Skin**	**Front diaphragm**	**Front spar**	**Motors penetration**	**Battery penetration**
Orientation study	0°	x	x (cracked)	x (cracked)	x	x	x
	45°	x (severe)	x (cracked)	x (cracked)	x	x	x (front spar)
	90°	x	x (cracked)	x		x	
	180°	x	x (cracked)	x	x	x	
Position study	Mid-bay	x	x (cracked)	x (cracked)	x	x	x
	Front rib	x	x (cracked)	x	x	x	x
	1/4 bay	x	x (cracked)	x	x	x	x
	Top		x	x			x
	Bottom		x	x			

Based on the results obtained in the two parametric studies described above, an UAS orientated at 45 degree impacting with the CG aligned with the leading edge of the target between the two closest ribs was chosen as the most severe impact condition. It was consequently selected as baseline for the initial conditions of the collision study against the leading edges of the commercial and business jet targets. Figure 189 illustrates this case.

This study also highlighted the extremely importance of defining initial conditions that lead to the worst case levels of damage. Small deviations in the impact location might under predict the severity of the event.

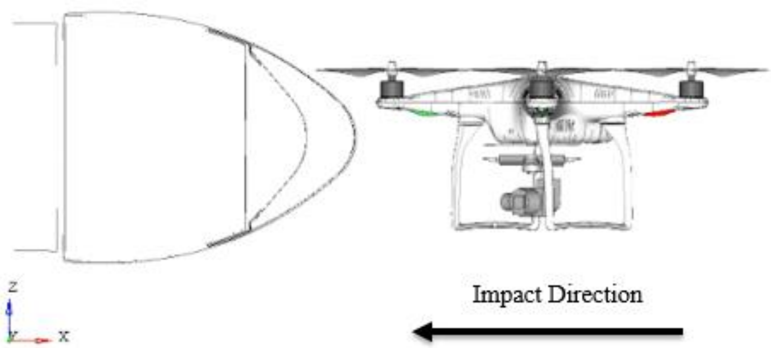

Figure 189. Critical UAS impact orientation

4.1.3 Load Case Name Convention

In order to provide a brief label that accurately describes each combination of UAS, aircraft type, target component, and local impact position the following convention is used to name each load case presented in this chapter:

Every impact condition will be coded using four characters (ABCD)

- A – Distinguishes between Commercial (C) and Business Jet Airplanes (B)
- B – Distinguishes between UAS Type:
    - 1.7 lb. Quadcopter (Q)
    - 4 lb. Fixed Wing (F)
- C – Distinguishes between impact area:
    - Vertical Stabilizer (V)
    - Horizontal Stabilizer (H)
    - Wing (W)
    - Cockpit Windshield (C)
- D – Distinguishes between impact location (1 through 5)

Example CQV4

- Commercial
- Quadcopter
- Vertical Stabilizer
- Impact Location #4

4.1.4 Simulation Matrix

Table 22 and Table 23 present the full simulation matrix performed for this chapter of the project.

Table 22. Simulation matrix of commercial transport jet airborne collision

Commercial Transport Jet															
Vertical Stabilizer				Horizontal Stabilizer					Wing				Windshield		
CQV1	CQV2	CQV3	CQV4	CQH1	CQH2	CQH3	CQH4	CQH5	CQW1	CQW2	CQW3	CQW4	CQC1	CQC2	CQC3

Table 23. Simulation matrix of business jet airborne collision

Business Jet										
Vertical Stabilizer			Horizontal Stabilizer			Wing			Windshield	
BQV1	BQV2	BQV3	BQH1	BQH2	BQH3	BQW1	BQW2	BQW3	BQC1	BQC2

4.2 DAMAGE CATEGORY DEFINITION

4.2.1 Damage Levels

Over 70 impact scenarios were analyzed as part of this study, not considering the other 70 involving the fixed-wing UAS. The simulations in this study concern many different types structure that behave in various manners during an impact event. In order to categorize the results of each scenario relative to one another, a set of criteria were established as shown in Table 24.

The lowest damage category, Level 1, generally corresponds to a minimal amount of localized damage. The next category, Level 2, represents significant visible damage to the external surface of the aircraft with some internal component damage but with no appreciable skin rupture. The third category, Level 3, describes impact events where the outer surface of the aircraft is compromised in a way that could allow ingress of foreign objects into the airframe, with some damage to substructure. Finally, Level 4 indicates damage that includes all of the preceding aspects as well as extensive damage to internal components and possibly compromising damage to primary structure.

Table 24. Damage level categories

Severity	Description	Example
Level 1	• Airframe undamaged. • Small deformations.	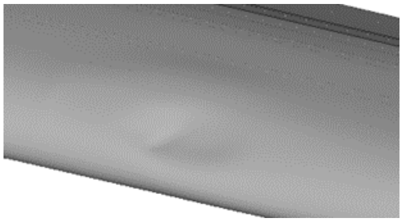
Level 2	• Extensive permanent deformation on external surfaces. • Some deformation in internal structure. • No failure of skin.	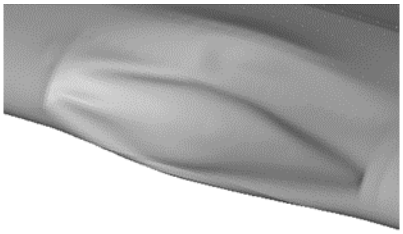
Level 3	• Skin fracture. • Penetration of at least one component into the airframe.	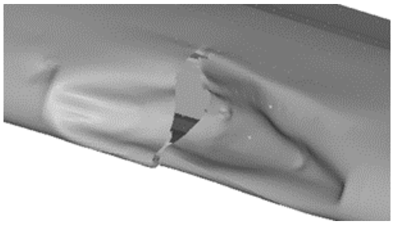
Level 4	• Penetration of UAS into airframe. • Failure of primary structure.	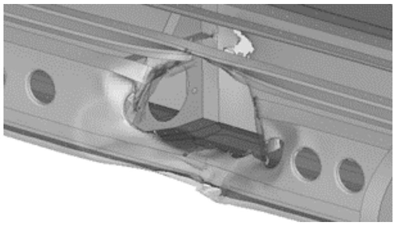

4.2.2 Fire Risk

The risk of fire associated with damaged Lithium-ion Polymer type batteries was addressed for each simulation based on the trends observed during component level ballistic testing, see Section 2.4.4.12 , and the particular kinematics of a given impact scenario. Table 25 presents the criteria used in this study.

Table 25. Risk of battery fire

Fire Risk	Description	Example
Yes	• UAS (including the battery) penetrates the airframe. • Battery deforms but stays undamaged. • Physical tests showed that partly damaged batteries created heat and sparks.	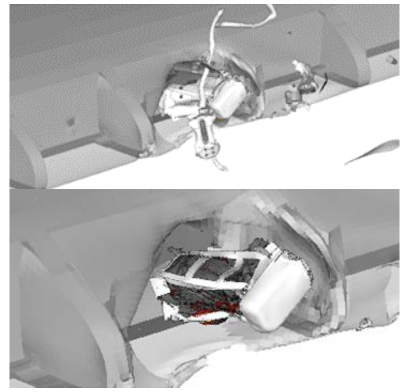
No	• The UAS does not penetrate the airframe.	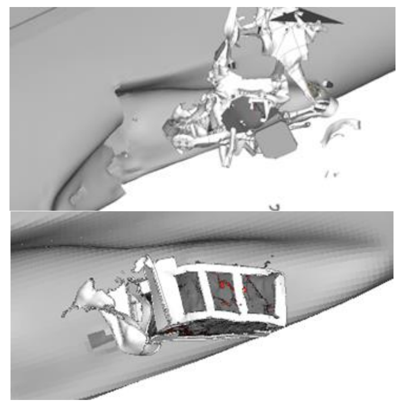
No	• UAS (including the battery) penetrates the airframe. • The battery sustains great damage, destroying its cells. • Physical tests showed that completely damaged batteries did not create heat and sparks.	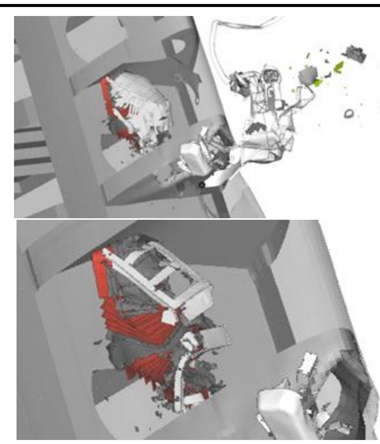

Note that the label of “Fire Risk” indicates a potential outcome rather than an impending event due to the qualitative nature of the assessment. Further studies and physical testing into this phenomenon would be required in order to determine any additional severity. During preliminary component level testing, the fire risk appeared inversely proportional to impact velocity. Higher velocities caused the battery to disintegrate, reducing the heat generated after impact, while lower velocities allowed the battery pack to remain consolidated, increasing the post-impact heat generation.

4.3 COMMERCIAL TRANSPORT JET AIRBORNE COLLISION STUDIES

As introduced in section 3.1.3 , the targets areas for impact on the NIAR commercial transport jet are vertical stabilizer (4.3.1), horizontal stabilizer (4.3.2), wing leading edge (4.3.3), and windshield (4.3.4). This section presents the results of explicit dynamic simulations of impacts of the 1.2 kg (2.7 lb) quadcopter UAS into the commercial transport jet. Table 26 and Figure 190 summarize the results of the collision studies on the commercial transport jet. This section will describe in detail the results in each of the four subassemblies.

Table 26. Commercial transport jet airborne collision simulation – Severity levels and fire risk

	Commercial Transport Jet															
	Vertical Stabilizer				Horizontal Stabilizer					Wing				Windshield		
Case	CQV1	CQV2	CQV3	CQV4	CQH1	CQH2	CQH3	CQH4	CQH5	CQW1	CQW2	CQW3	CQW4	CQC1	CQC2	CQC3
Severity	Level 3	Level 3	Level 3	Level 3	Level 3	Level 3	Level 4	Level 4	Level 4	Level 3	Level 3	Level 3	Level 2	Level 2	Level 2	Level 2
Fire Risk	No	No	No	No	Yes	Yes	Yes	No	No	No	No	No	No	No	No	No

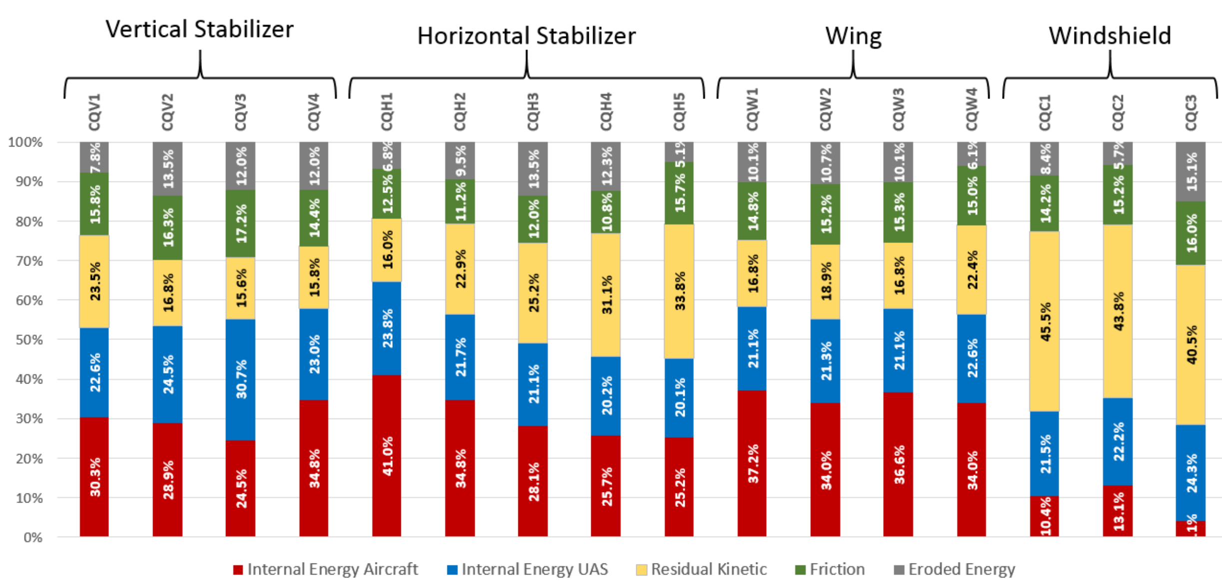

Figure 190. Commercial transport jet airborne collision simulation – Energy summary

As shown in Figure 190 for each one of the impact conditions we can quantify how the initial kinetic energy of the UAS prior to impact is transformed into aircraft and UAS internal energies through the structural deformations introduced during impact; a residual UAS kinetic energy that is a function of the UAS post impact debris mass moving at a post impact residual velocity; friction energy which is a function of the sliding contact energy between the UAS and the aircraft structure, and eroded energy from the mass of the UAS and aircraft eroded elements necessary to control the stability of the calculation.

4.3.1 Vertical Stabilizer

The vertical stabilizer of the commercial transport jet was subject to impact at four different locations that were selected based on the criteria described in Section 4.1.2 . The diagram in Figure 191 illustrates the positions being impacted and the naming assigned to each of the cases. The UAS was assigned an initial speed of 128.6 m/s (250 knots) in the local x-axis of the aircraft. Fixed boundary conditions of the vertical stabilizer were considered at the root of both front and rear spars.

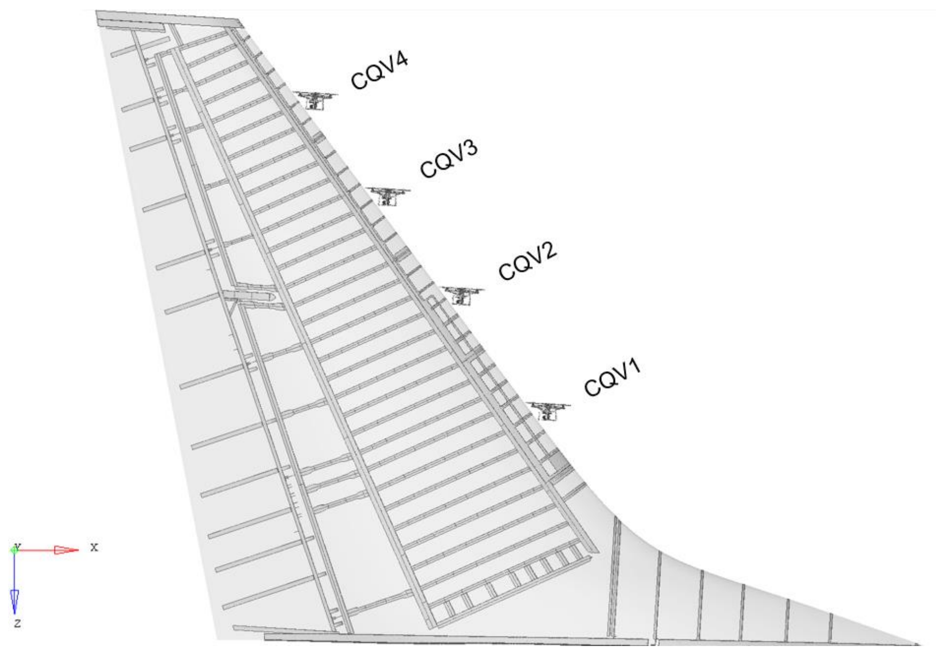

Figure 191. UAS impact locations – Commercial jet vertical stabilizer

4.3.1.1 Summary of Results – Commercial Transport Jet Vertical Stabilizer

A summary of the results for all four cases presented in Figure 191 is shown in the following figure. For each case, the left bar represents a summation of all the different energies involved in the impact event, measured at 10 ms after initial contact and normalized with the total energy at time zero. The percentage of total energy for each respective type of energy is shown. The right bar specifies the severity level (1-4), as described in section 4.2.1 , as well as an additional bar highlighting if the case generates a potential fire risk in the battery, following the criteria of section 0.

Figure 192 shows that, in general, there is a trend indicative of an increase in the internal energy absorbed by the aircraft structure when closer to the root of the vertical stabilizer. This phenomenon may be explained with the cross-sectional height of the airfoil at the impacted location. Closer to the root, the airfoil cross-section is thicker and has a greater nose radius. Consequently, the area of airframe that will have a more perpendicular contact with the impacting projectile is greater, allowing a greater transfer of energy and therefore an increase in internal energy.

The nose rib pitch of the commercial transport jet varies along the span, leaving the spar more exposed to a direct hit of the UAS if it penetrates the skin. For inner locations of the span, the rib pitch is small enough so that the web of the rib can interfere with the trajectory of the UAS and therefore protect the front spar. Moreover, the distance between the leading edge and the front spar is greater closer to the root. This allows a greater deformation of the skin, which is translated into a greater amount of internal energy being absorbed, decelerating the UAS more than at outboard locations prior to impact with the front spar. Additionally, it was observed that the severity of the impact caused the battery to be fully destroyed in every case, minimizing the potential for fire risk.

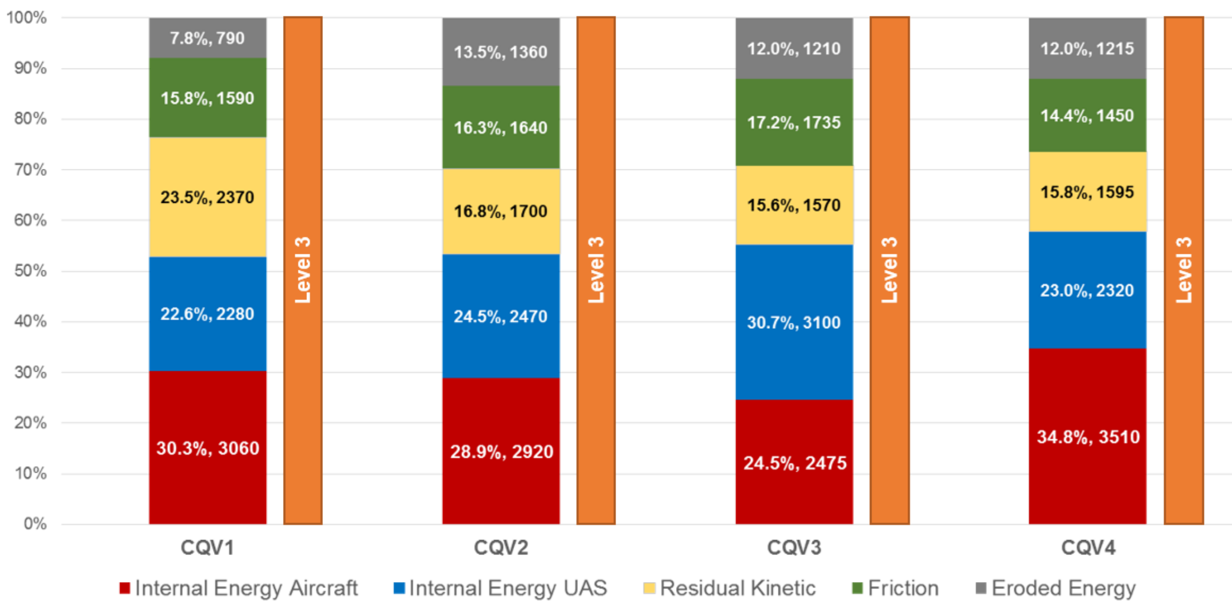

Figure 192. Summary bar chart of commercial transport jet vertical stabilizer cases

<u>4.3.1.2 Critical Case – CQV3</u>

As introduced in section 4.3.1.1 , CQV3 was considered the case that created more damage and therefore the most critical. The results of the remaining cases are found in APPENDIX B.

The UAS was impacted against the vertical stabilizer at 250 knots (128.6 m/s) in the local *x*-axis direction of the aircraft. The impact location selected was at approximately 70% of the vertical stabilizer span, with the CG of the UAS aligned with the leading edge, at the midpoint between ribs 19 and 20. Figure 193 depicts the kinematics of the event. Figure 194 shows the damage caused to structure of the vertical stabilizer.

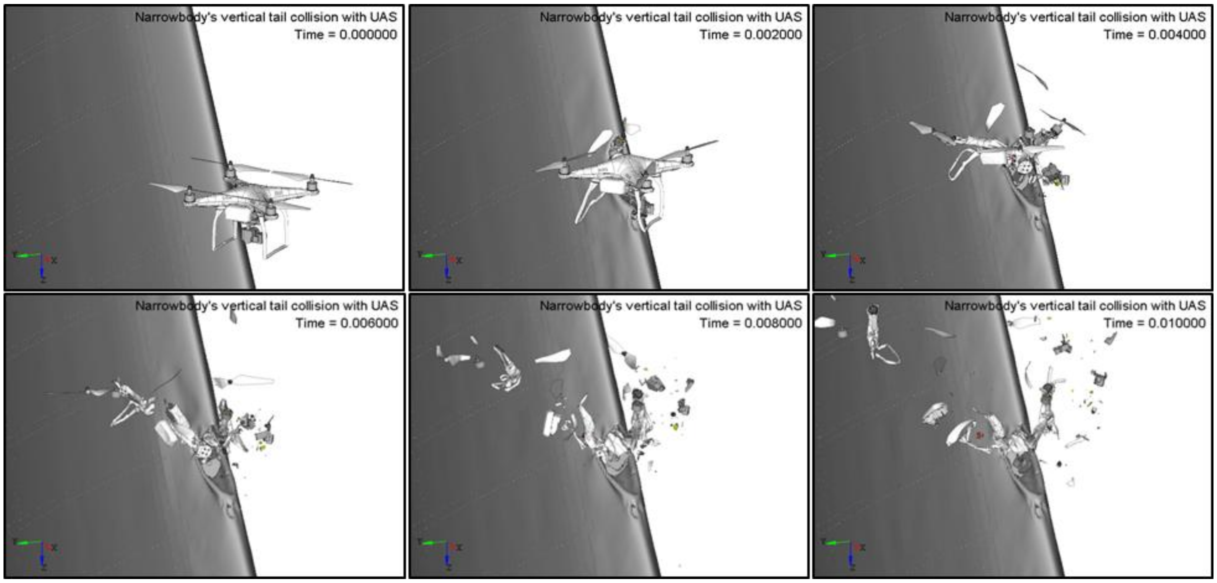

Figure 193. Kinematics of the impact between the commercial transport jet vertical stabilizer and a 1.2 kg (2.7 lb) UAS at location 4 at 128.6 m/s (250 knots)

The UAS damages the skin and the nose ribs, creating a 110x210 mm damage zone (*i.e.* puncture, large scale petaling, and plastic deformation) on the skin surface and allowing considerable portions of UAS mass (including the battery) to penetrate the airframe. The UAS entering the airframe has enough kinetic energy to impact and damage the front spar, but without perforation. The bottom left image at Figure 194 illustrates the damage and permanent deformation and damage caused to the ribs and the front spar. It did not involve failure of the primary structure, and consequently the severity was classified as Level 3.

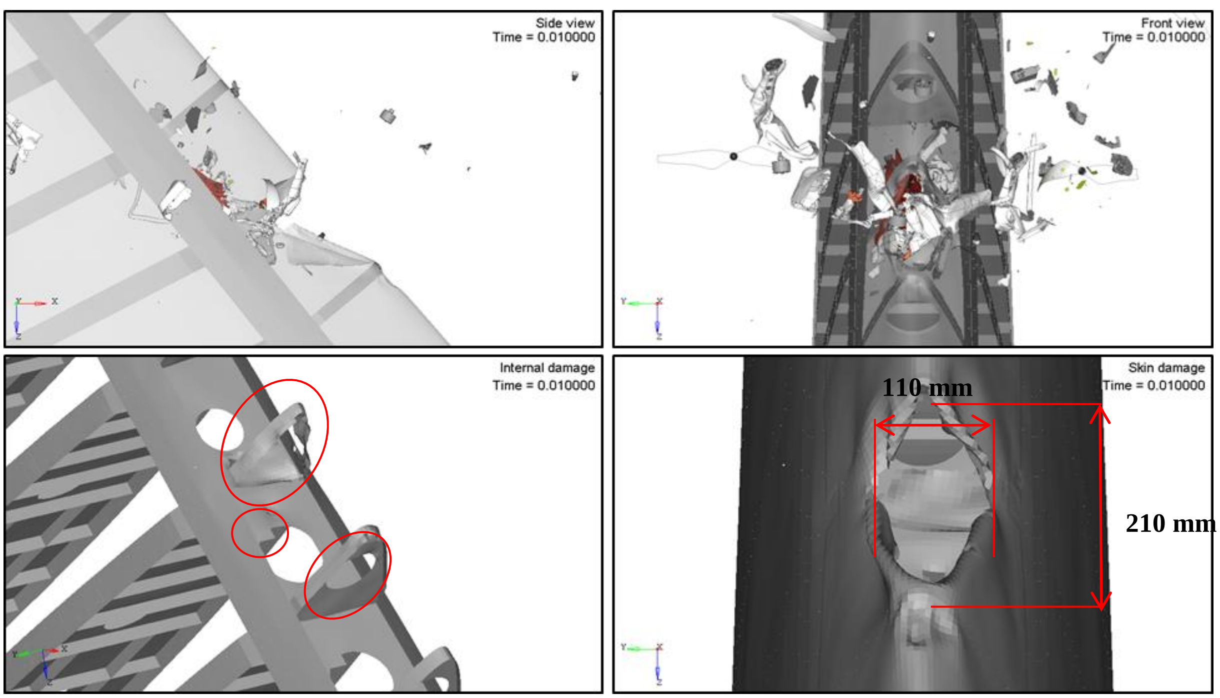

Figure 194. External/internal damage sustained by the commercial transport jet vertical stabilizer impacted at location 4 with a 1.2 kg (2.7 lb) UAS at 128.6 m/s (250 knots)

Figure 195 presents the impulse due to the contact force between UAS and vertical stabilizer, as well as the energy balance for both of them. Figure 196 shows the internal energies of UAS and vertical stabilizer parts directly involved in the impact.

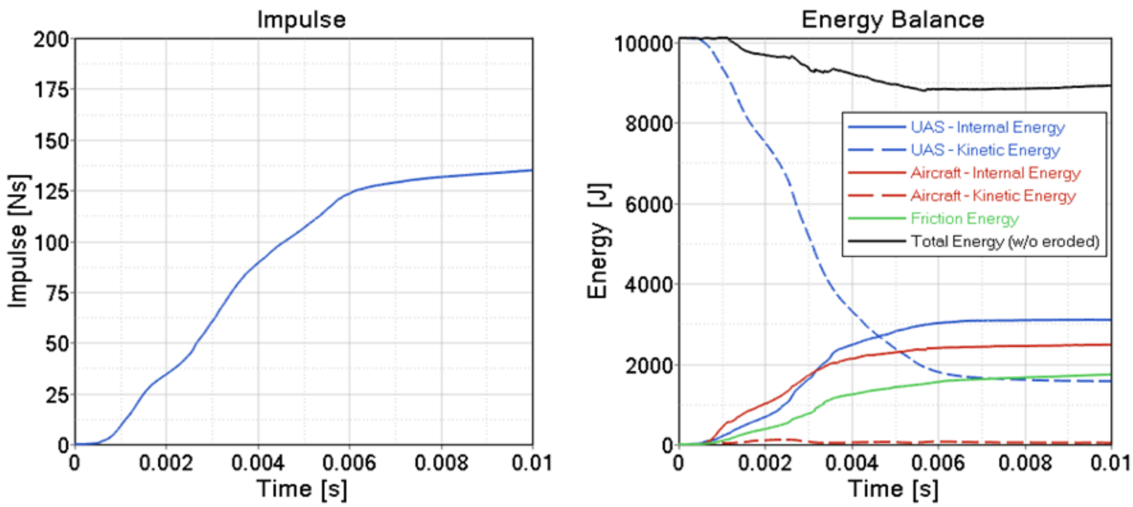

Figure 195. Impulse and energy balance of the impact between a commercial transport jet vertical stabilizer and a 1.2 kg (2.7 lb) UAS at 128.6 m/s (250 knots)

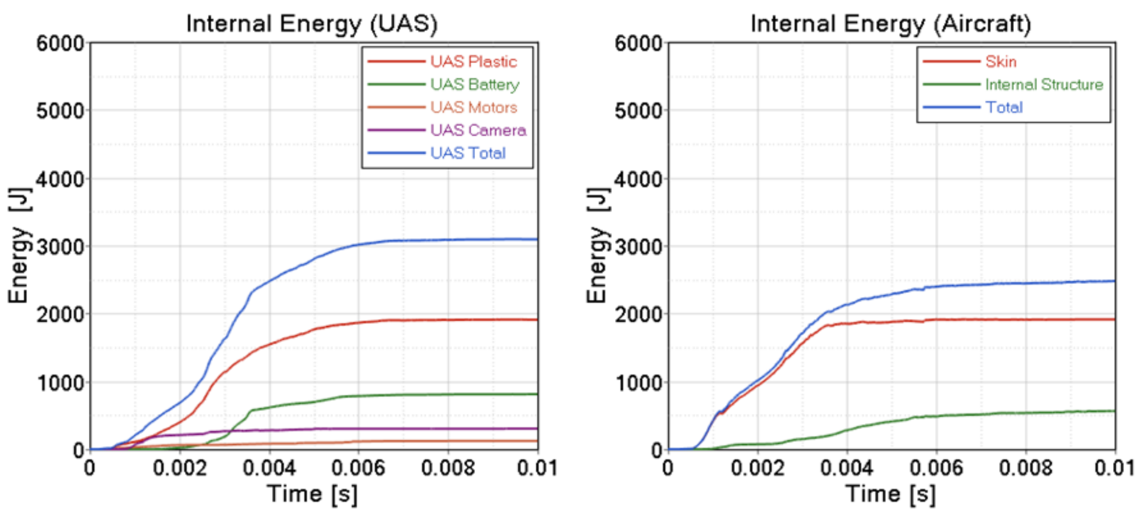

Figure 196. Internal energy per component of the impact between a commercial transport jet vertical stabilizer and a 1.2 kg (2.7 lb) UAS at 128.6 m/s (250 knots)

The energy balance plot includes the UAS and vertical stabilizer kinetic and internal energies as well as frictional energy and total energy (excluding eroded energy) for the event. The vertical stabilizer and the UAS absorb 24% and 34% of the impact energy respectively. The energy dissipated by friction reaches 17% of the total energy. In Figure 196, internal energies for the UAS parts and the vertical stabilizer show that the polycarbonate carcass of the UAS and the skin of the vertical stabilizer absorb the highest amount of internal energy.

4.3.2 Horizontal Stabilizer

The commercial transport jet horizontal stabilizer was subject to impact at five impact locations that were selected based on the criteria described in Section 4.1.2 . The diagram in Figure 197 illustrates the impact locations and the naming assigned to each of the cases. The initial velocity assigned to the UAS was 250 knots (128.6 m/s) along the local *x*-axis of the aircraft. Fixed boundary conditions were considered at the root of both front and rear spars of the horizontal stabilizer.

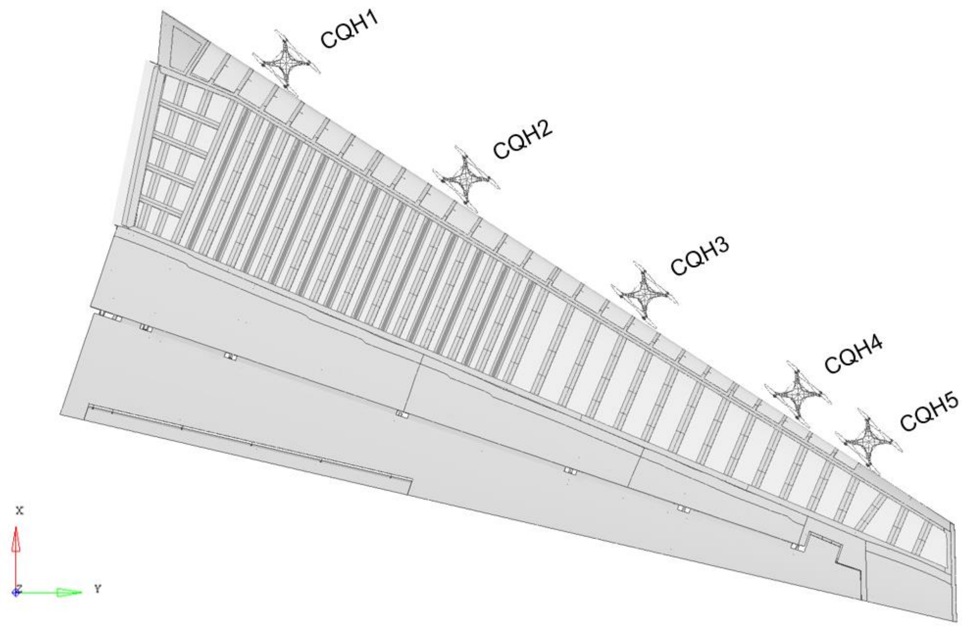

Figure 197. UAS impact locations – Commercial jet horizontal stabilizer

4.3.2.1 Summary of Results – Commercial Transport Jet Horizontal Stabilizer

A summary of the results of all five impact locations presented in Figure 197 is shown in Figure 198. Again, the left bar represents a summation of all the different energies involved in the impact event, measured at 10 ms after impact and normalized with the total energy at time zero. Each block indicates the percentage total energy for each respective type of energy. The right bar specifies the severity level (1-4), as well as an additional bar highlighting if the case generates a potential fire risk in the battery.

Similarly as with the vertical stabilizer, there is a trend indicative of an increase in the internal energy absorbed by the aircraft structure when closer to the root of the horizontal stabilizer. The inverse effect is observed for the residual kinetic energy. See 4.3.1.1 There is a change in severity from position 3 outwards. It was observed that in outer parts of the horizontal stabilizer (positions 3, 4 and 5), the front spar was damaged, and because it was considered as a primary structure the severity was increased to Level 4.

Consequently, position 3 was selected as the most critical for the horizontal stabilizer of the commercial transport jet because it was the only case identified as Level 4 and a risk of fire. In addition, damage induced to the front spar at positions closer to the root may be considered more critical due to the higher bending moment loads expected. Consequently, position 3 may be considered more critical than 4 and 5.

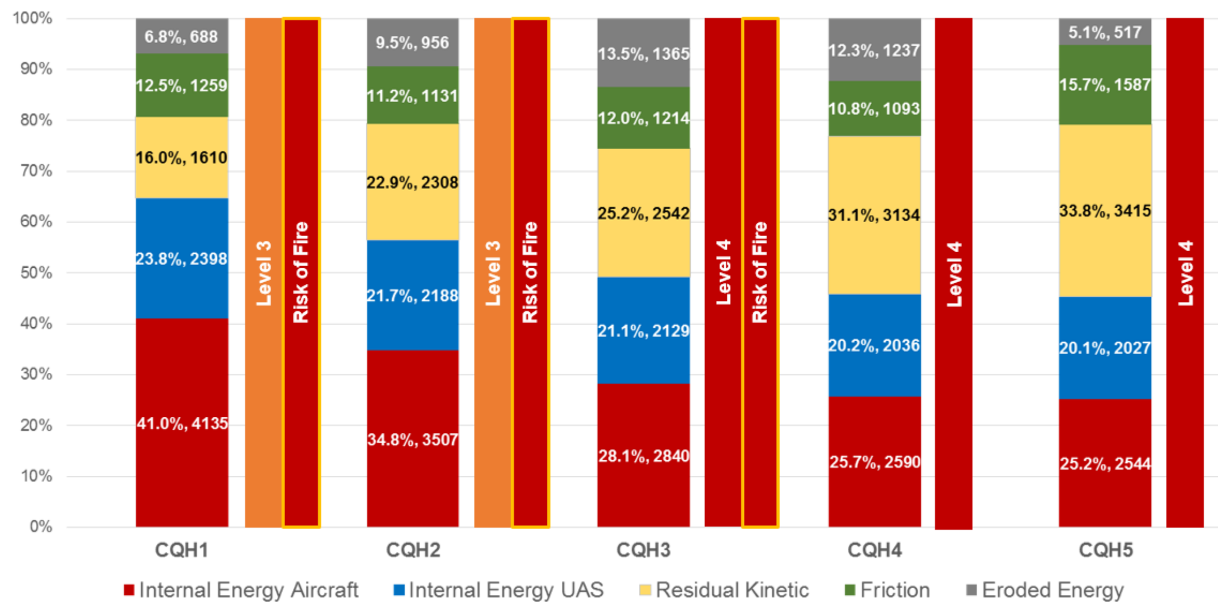

Figure 198. Summary bar chart of commercial transport jet horizontal stabilizer cases

4.3.2.2 Critical Case – CQH3

As introduced in section 4.3.2.1 , CQH3 was considered the most critical damaging case for the horizontal stabilizer. The following section presents the reader with the results of this specific simulation. The results of the remaining cases may be found in APPENDIX B.

In this case, the UAS was impacted against the horizontal stabilizer at 250 knots (128.6 m/s) along the local *x*-axis direction of the aircraft. The impact location selected was at approximately 60% of the horizontal stabilizer semi span, with the CG of the UAS aligned with the leading edge, at the midpoint between ribs 19 and 20. Figure 199 presents the kinematics of the event. Figure 200 shows the damage caused to the skin and internal structure (ribs and spar) of the horizontal stabilizer.

The UAS damages the skin and the nose ribs, creating a 239x117 mm and a 71x63 mm damage zone on the skin surface and allowing considerable portions of UAS mass (including the battery) to penetrate the airframe. The UAS entering the airframe has enough kinetic energy to impact and damage the front spar, causing a perforation of 73x53 mm. The bottom left image at Figure 200 illustrates the damage and permanent deformation caused to the ribs and the front spar. In this case, the front spar sustained critical damage.

Since the front spar is a critical load path of the horizontal stabilizer, it was considered a primary structure. Consequently, the damage introduced by the UAS in this case was classified as Level 4.

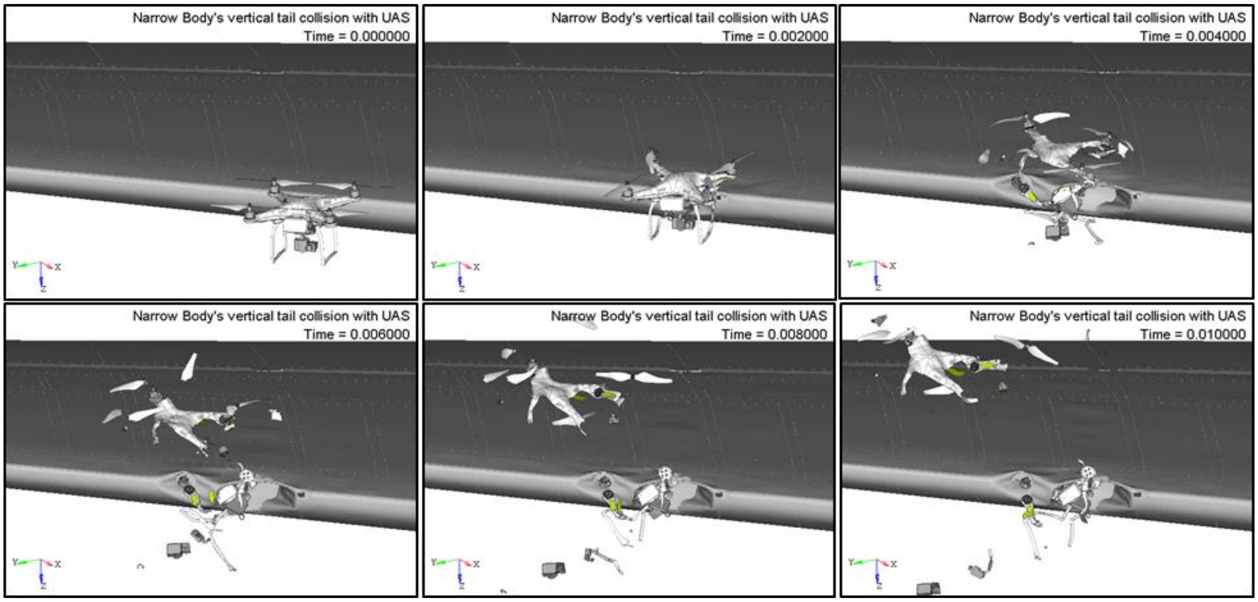

Figure 199. Kinematics of the impact between the commercial transport jet horizontal stabilizer and a 1.2 kg (2.7 lb) UAS at location 3 at 128.6 m/s (250 knots)

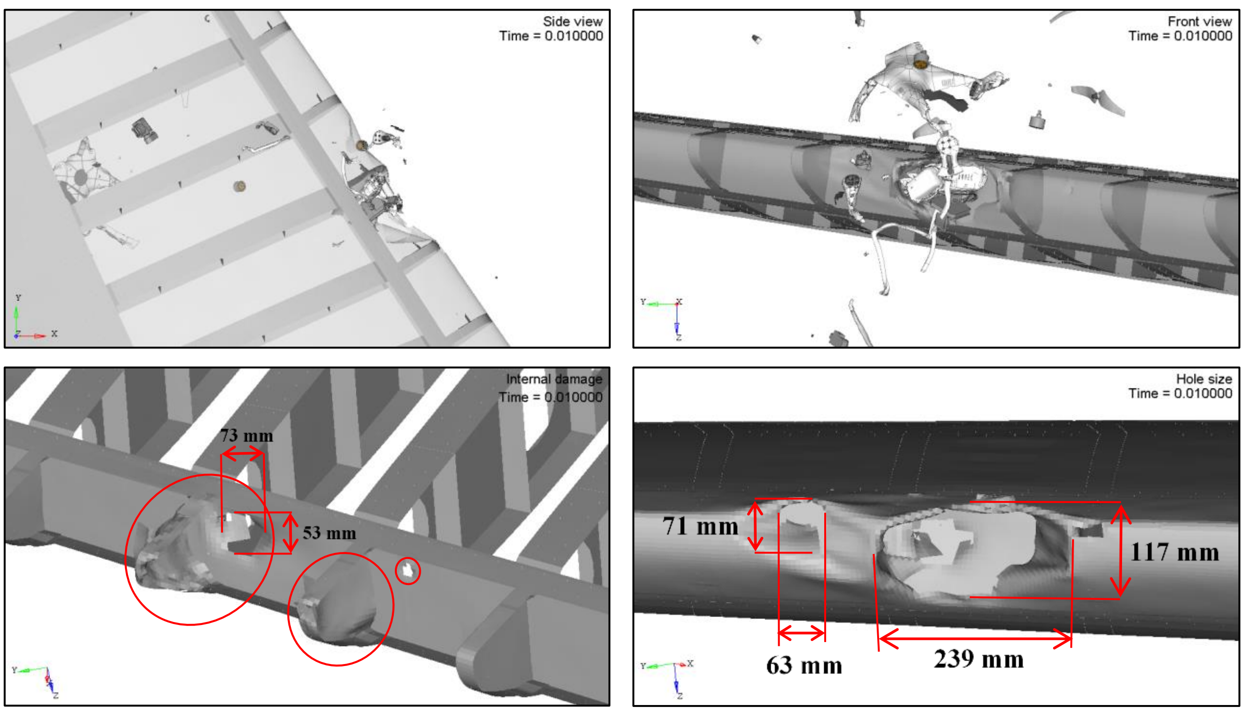

Figure 200. External/internal damage sustained by the commercial transport jet horizontal stabilizer impacted at location 3 with 1.2 kg (2.7 lb) UAS at 128.6 m/s (250 knots)

Figure 201 presents the impulse due to the contact force between the UAS and the horizontal stabilizer, as well as the energy balance for both of them. Figure 202 presents the internal energies of the UAS and horizontal stabilizer components directly involved in the impact.

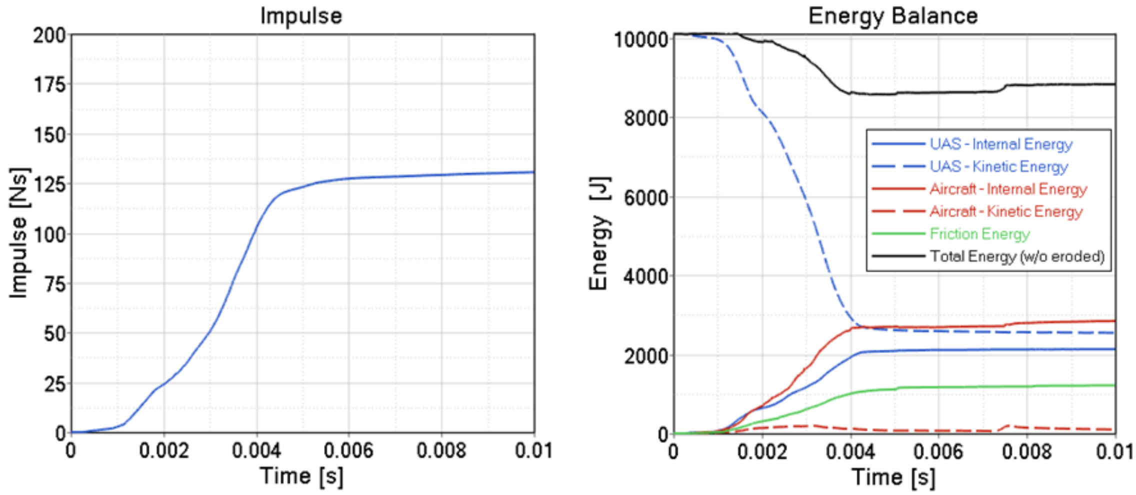

Figure 201. Impulse and energy balance of the impact between a commercial transport jet horizontal stabilizer and a 1.2 kg (2.7 lb) UAS at 128.6 m/s (250 knots)

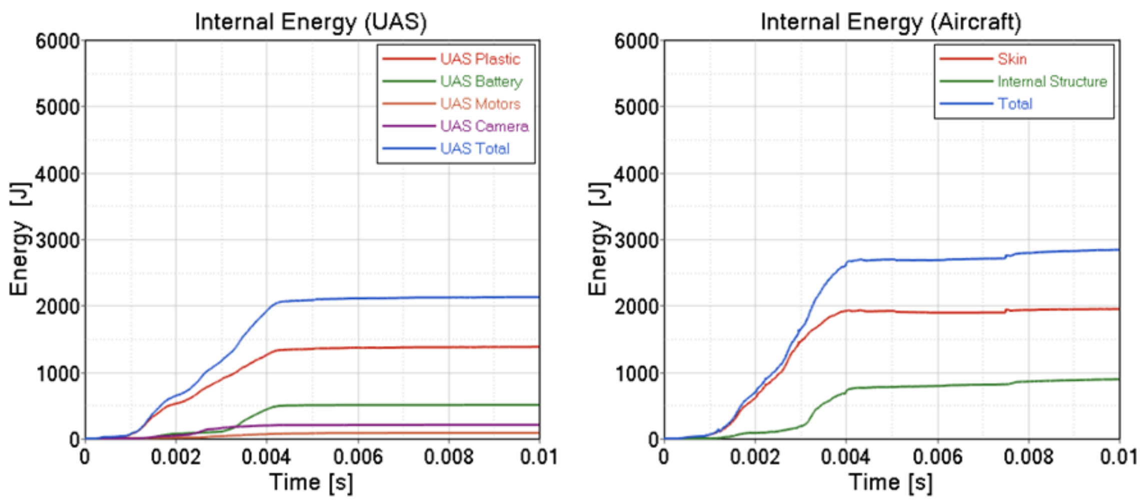

Figure 202. Internal energy per component of the impact between a commercial transport jet horizontal stabilizer at location 3 and a 1.2 kg (2.7 lb) UAS at 128.6 m/s (250 knots)

The energy balance plot includes the UAS and horizontal stabilizer kinetic and internal energies, as well as frictional energy and total energy (excluding the eroded energy) for the event. The aircraft and the UAS absorb a 28% and 21% of the impact energy, respectively. The energy dissipated by friction reaches 12% of the total energy. In Figure 202, the internal energies for the UAS parts and the stabilizer structure show that the skin of the horizontal stabilizer and the polycarbonate body of the UAS absorbed the most internal energy.

4.3.3 Wing Leading Edge

The commercial transport jet wing was subjected to impact at four impact locations that were selected based on the criteria described in section 4.1.2 . The diagram in Figure 203 illustrates the impact locations and the naming assigned to each of the cases. The initial velocity assigned to the

UAS was 250 knots (128.6 m/s) along the local x-axis of the aircraft. The boundary conditions of wing leading edge considered a full constraint at the inboard and outboard ends of the front spar and a symmetry constraint was applied at the free edge of the skin to represent the connection to the wing-box covers.

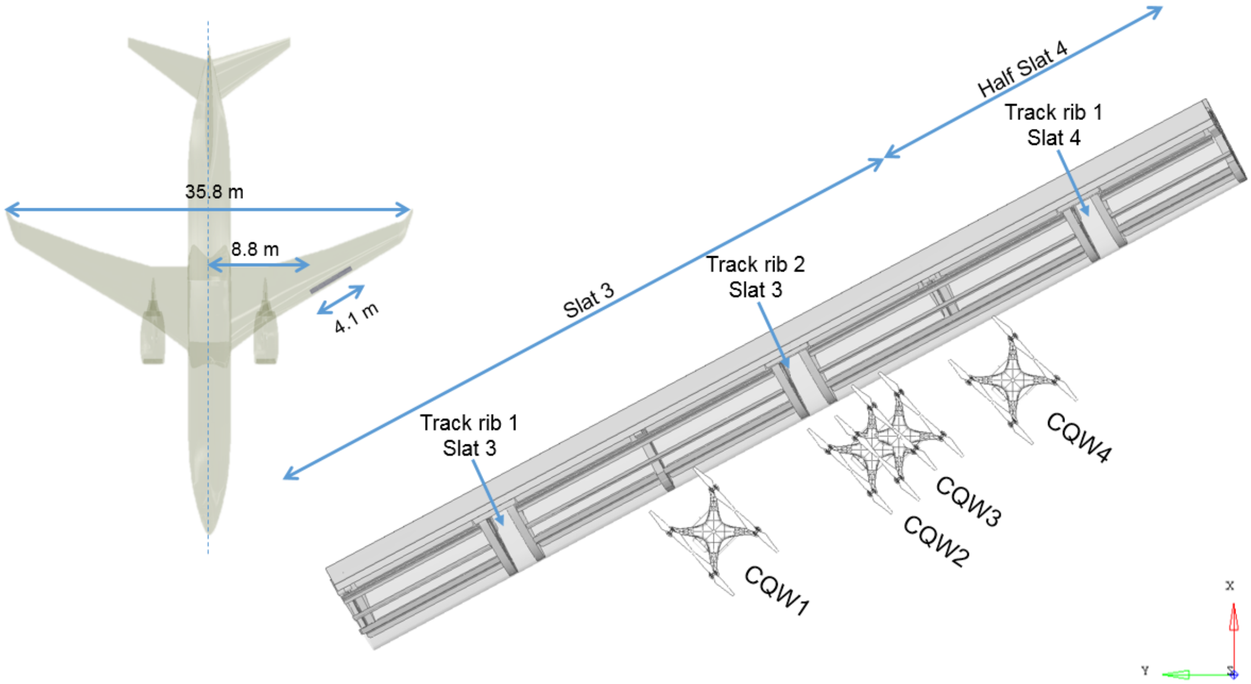

Figure 203. UAS impact locations – Commercial jet wing

4.3.3.1 Summary of Results – Commercial Transport Jet Wing

A summary of the results of all four cases presented in Figure 203 is shown in the following figure. For each case, the left bar represents a summation of all the different energies involved in the impact event, measured at 10 ms after impact and normalized with the total energy at time zero. Each block indicates the percentage of total energy for each respective type of energy. The right bar specifies the severity level (1-4), as well as an additional bar highlighting if the case generates a potential fire risk in the battery.

The impacted areas of the wing were concentrated only at one span-wise location, therefore span-wise effects may not be observed easily. However, a detailed model of the portion of the wing leading edge allowed a better look into local effects, such as how impacting closer to a slat track rib pair or impacting aiming the center of the rib bay may affect damage.

It was observed that an impact further from rigid areas (e.g. ribs) was more vulnerable, being the case of CQW1 and CQW3. In these two cases, the D-nose sub spar sustained greater damage. In addition, if these two cases are compared, it can be perceived in Figure 204 that in CQW1 the wing absorbs slightly more internal energy. For this reason, it was selected as the critical case.

It is worth noting that none of the cases showed situations where the battery penetrated the airframe, and therefore none of them can be considered with potential risk for fire.

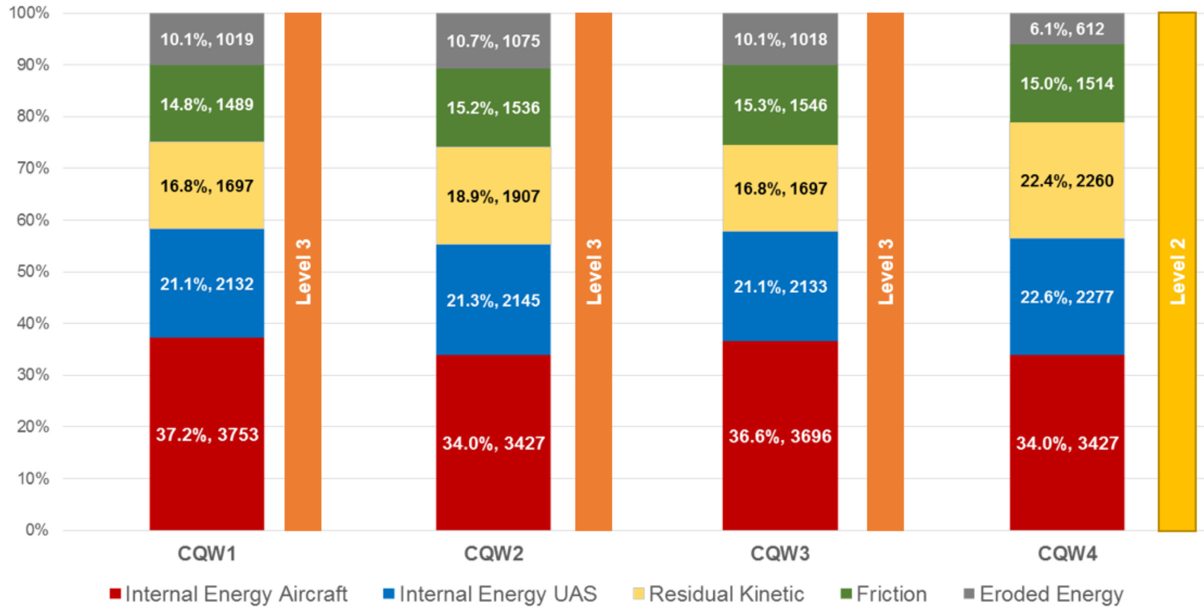

Figure 204. Summary bar chart of commercial transport jet wing cases

4.3.3.2 Critical Case – CQW1

As introduced in section 4.3.3.1 , CQW1 was considered the most critical damaging case for the wing leading edge. The following section contains the results of this specific simulation. The results of the remaining cases may be found in APPENDIX B

In this case, the UAS was impacted against the leading edge of the wing at 250 knots (128.6 m/s) in the local *x*-axis direction of the aircraft. The impact location selected was at the central area of slat 3, with the UAS CG aligned with the leading edge, aiming to impact the front spar at the midpoint between the intermediate rib and the slat track rib pair. Figure 205 depicts the kinematics of the event. Figure 206 shows the damage caused to the skin and internal structure (ribs and sub-spar) of the wing.

The UAS impacted the leading edge of the wing and created a vertical puncture on the D-nose skin surface and sub-spar, as shown in Figure 206 bottom left and bottom right images respectively. The UAS does not entirely penetrate the airframe after impact, but deforms an area of 566x129 mm the airframe.

Primary structural components, such as the front spar, remain undamaged. Small fragments of the UAS penetrate the airframe. Consequently, the damaged introduced by the UAS in this case was classified as Level 3.

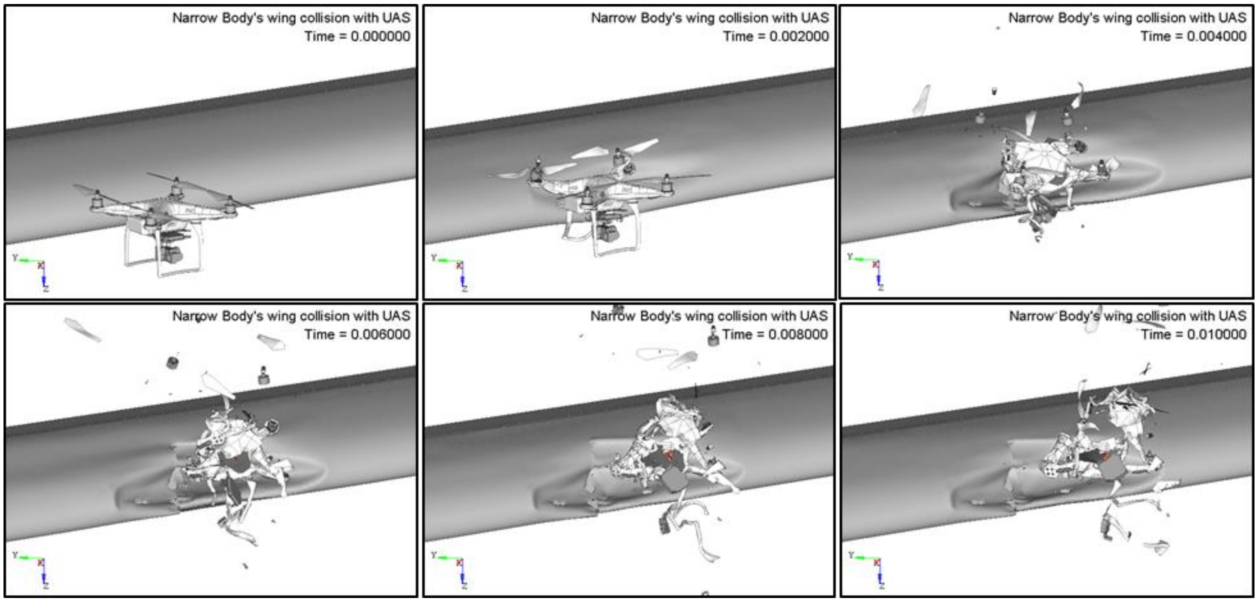

Figure 205. Kinematics of the impact between the commercial transport jet wing at location 1 and a 1.2 kg (2.7 lb) UAS at 128.6 m/s (250 knots)

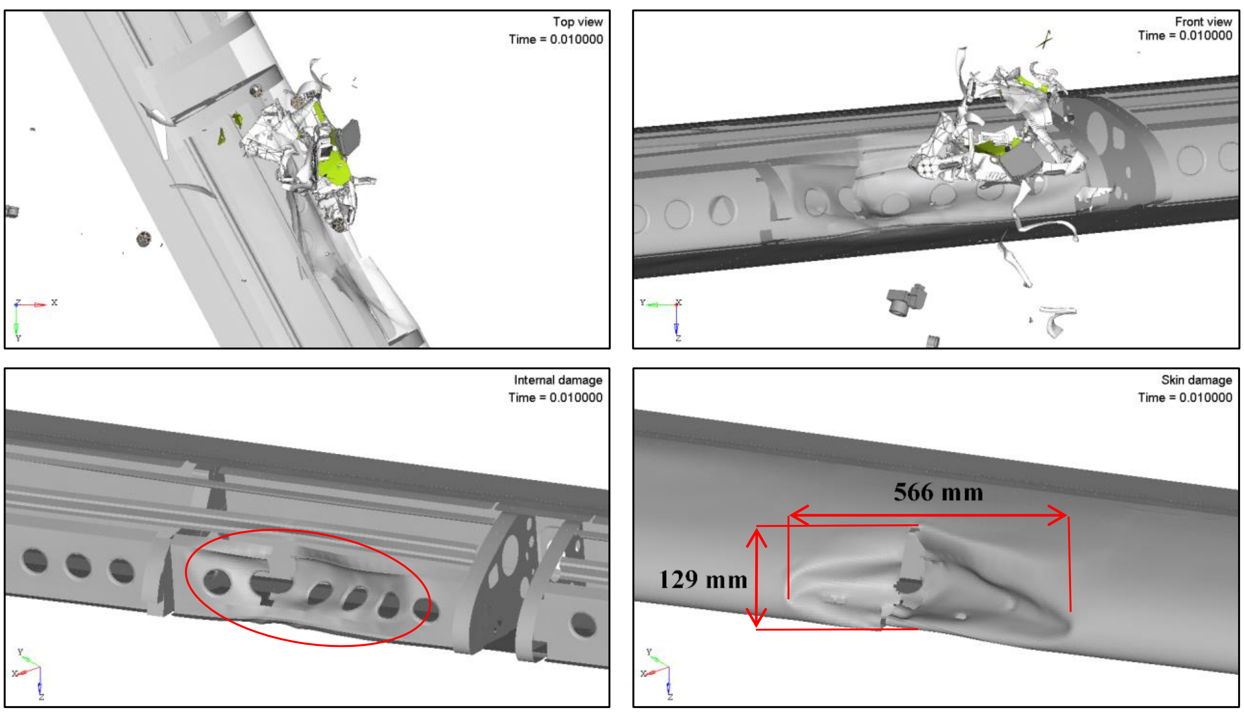

Figure 206. External/internal damage sustained by the commercial transport jet wing impacted at location 1 with a 1.2 kg (2.7 lb) UAS at 128.6 m/s (250 knots)

Figure 207 presents the impulse due to the contact force between UAS and wing, as well as the energy balance for both of them. Figure 208 shows the internal energies of UAS and wing parts directly involved in the impact.

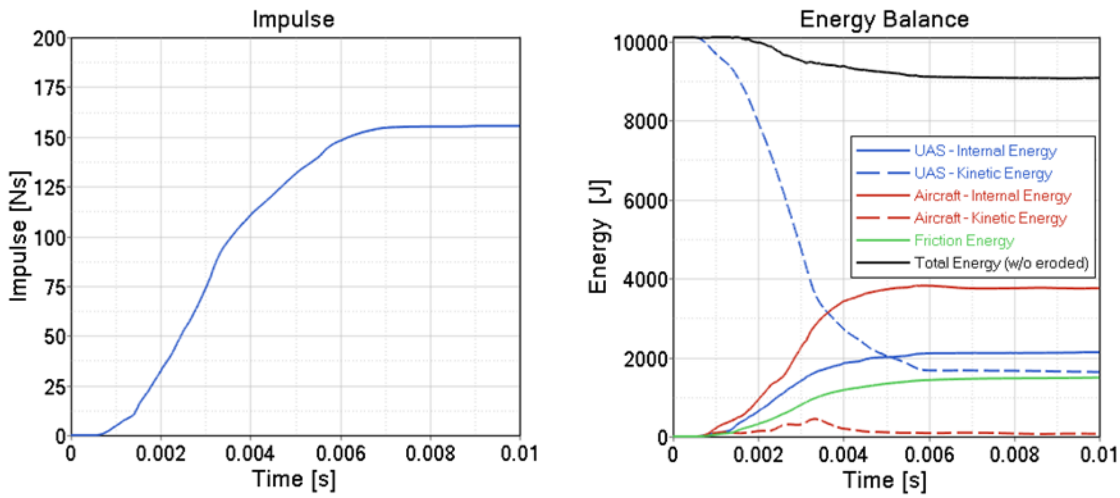

Figure 207. Impulse and energy balance of the impact between a commercial transport jet wing and a 1.2 kg (2.7 lb) UAS at 128.6 m/s (250 knots)

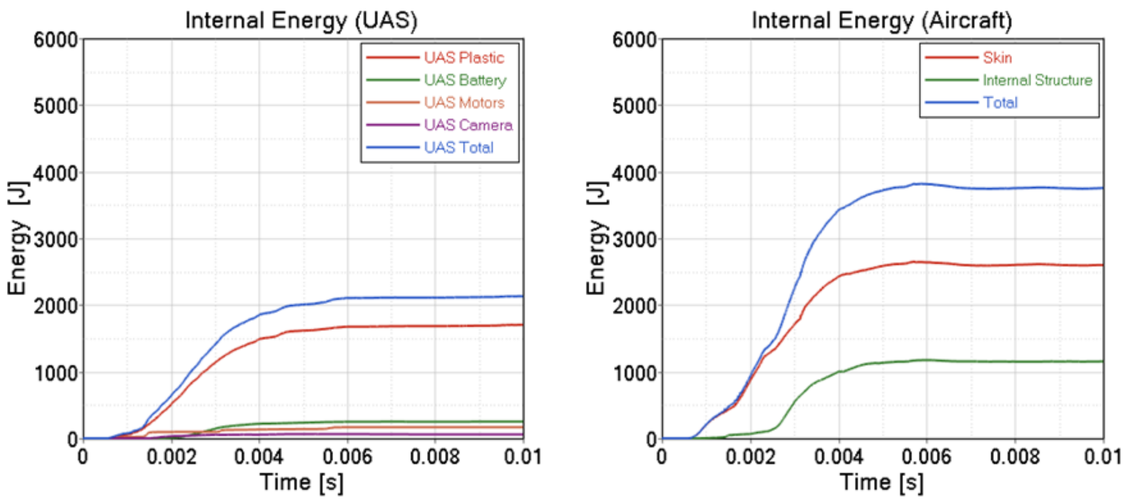

Figure 208. Internal energy per component of the impact between a commercial transport jet wing and a 1.2 kg (2.7 lb) UAS at 128.6 m/s (250 knots)

The energy balance plot includes the UAS and wing kinetic and internal energies as well as frictional energy and total energy (excluding eroded energy) for the event. The wing and the UAS absorb 37% and 21% of the impact energy, respectively. The energy dissipated by friction reaches 15% of the total energy. In Figure 208, internal energies for the UAS parts and the wing show that the polycarbonate carcass of the UAS and the skin of the wing absorb the highest amount of internal energy.

4.3.4 Windshield

The windshield of the commercial transport jet was subjected to impact at three different locations that were selected based on the criteria described in Section 4.1.2 . The diagram in Figure 209 illustrates the impact locations and the naming assigned to each of the cases. The UAS was assigned an initial speed of 250 knots (128.6 m/s) in the local x-axis of the aircraft. Symmetry boundary conditions were considered for forward fuselage at the skin edge to simulate the connection to the rest of the aircraft.

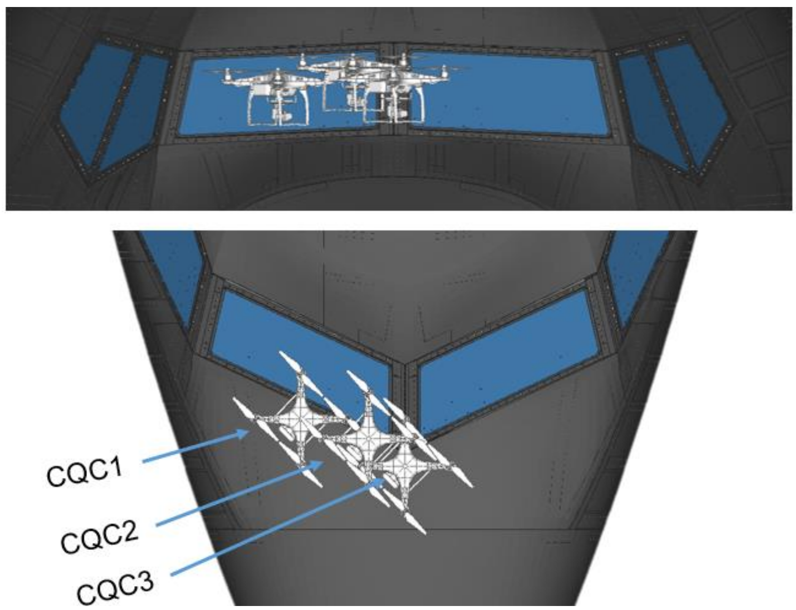

Figure 209. UAS impact locations – Commercial jet windshield

4.3.4.1 Summary of Results – Commercial Transport Jet Windshield

A summary of the results of all three cases presented in Figure 209 is shown in the following figure. For each case, the left bar represents a summation of all the different energies involved in the impact event, measured at 10 ms and normalized with the total energy at time zero. Each block indicates the percentage of total energy for each respective type of energy. The right bar specifies the severity level (1-4), as well as an additional bar highlighting if the case generates a potential fire risk in the battery.

If compared with other impacted areas of the Commercial Transport Jet, the UAS impacts on the windshield resulted in a much higher residual kinetic energy. Due to the low angle impact in the transparency (approximately 45°), the UAS was deflected without any considerable damage to the windshield, as shown in Figure 211 and Figure 212. The windshield has a thick multilayered construction with a very high bulk stiffness. Consequently, a great amount of the deformation due to the impact is absorbed by the UAS. This can be seen from the energy distribution, where the internal energy absorbed by the UAS is much greater than that of the aircraft.

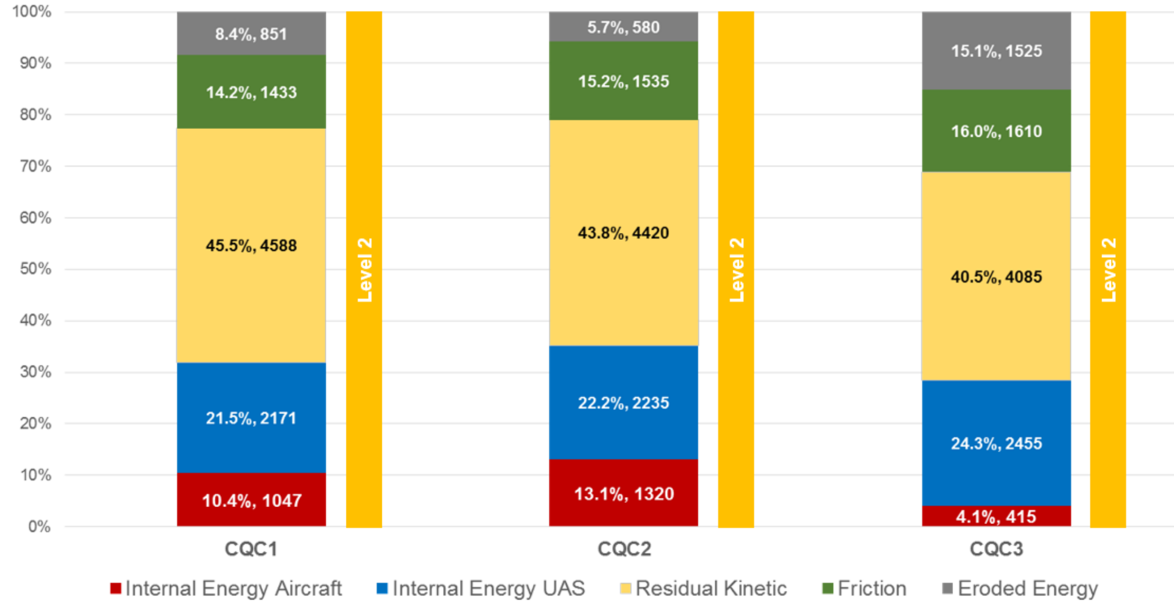

Figure 210. Summary bar chart of commercial transport jet windshield cases

<u>4.3.4.2 Critical Case – CQC1</u>

As introduced in section 4.3.4.1 , CQC1 was considered the most critical damaging case. The following section presents the reader with the results of this specific simulation. The results of the remaining cases may be found in APPENDIX B.

In this case, the UAS was impacted against the center of the windshield at 250 knots (128.6 m/s) in the local *x*-axis direction of the aircraft. Figure 211 depicts the kinematics of the event. Figure 212 shows the damage caused to the windshield and surrounding structure.

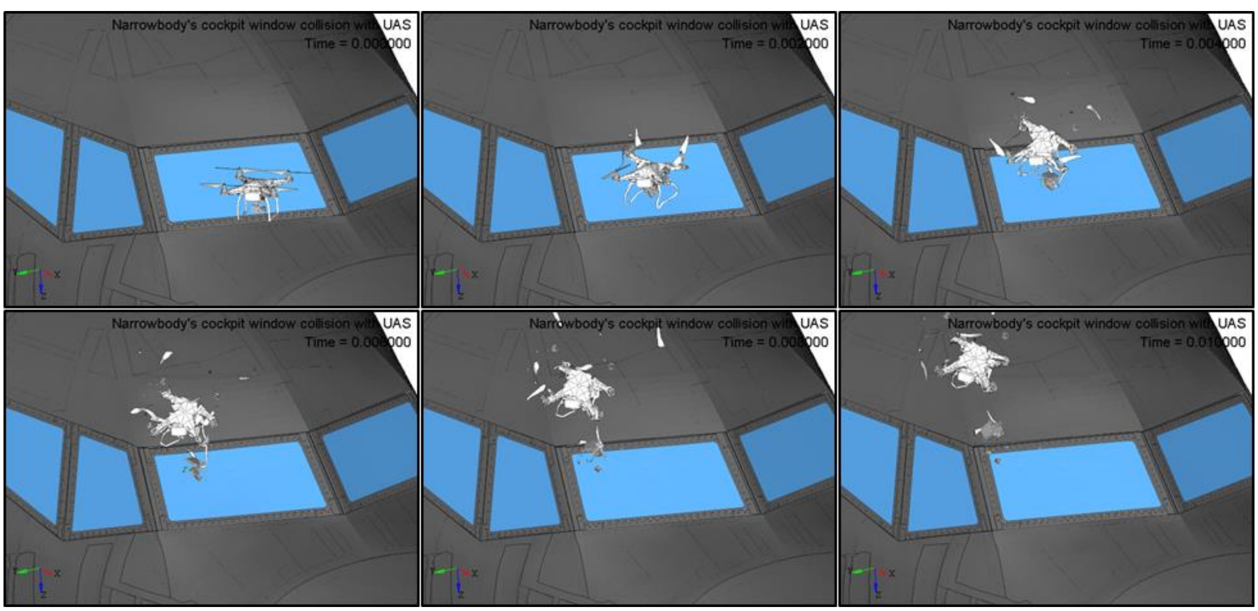

Figure 211. Kinematics of the impact between the commercial transport jet windshield at location 1 and a 1.2 kg (2.7 lb) UAS at 128.6 m/s (250 knots).

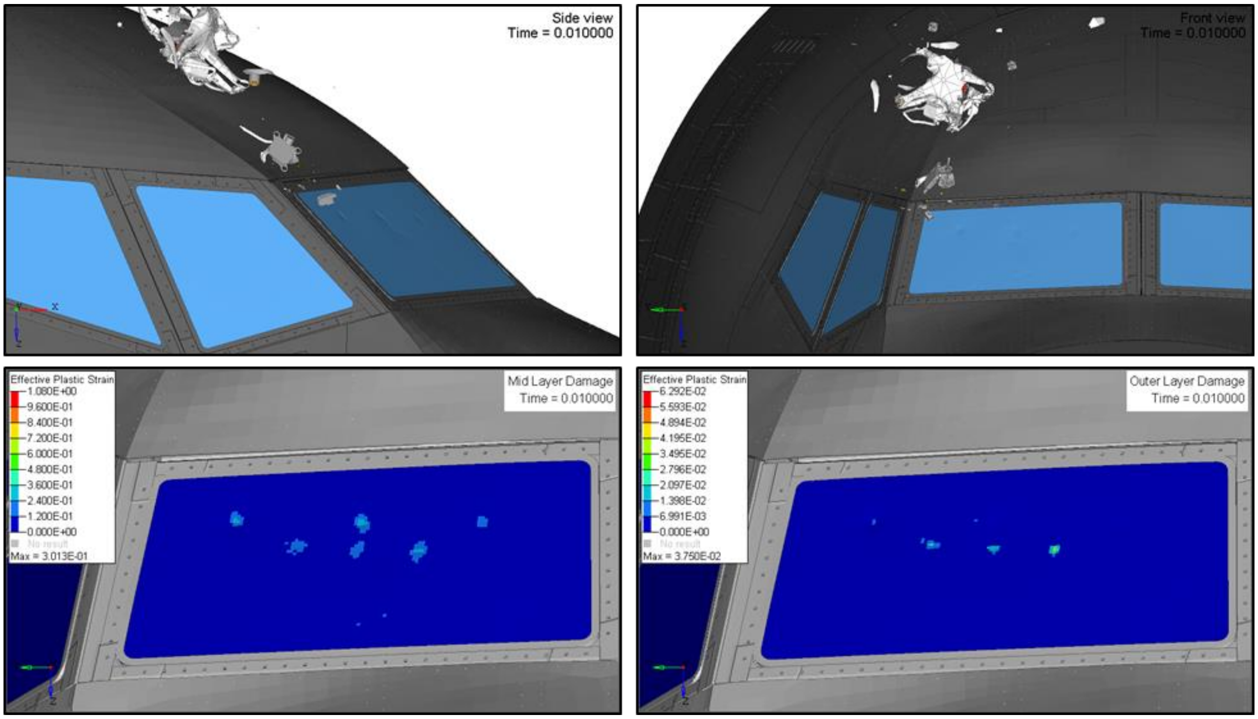

Figure 212 External/internal damage sustained by the commercial transport jet windshield impacted at location 1 with a 1.2 kg (2.7 lb) UAS at 128.6 m/s (250 knots)

The bottom two images present the contour plot of the effective plastic strain after impact on the outer (bottom-left image) and middle (bottom-right image) layers of the transparency, which were the components that experienced greater damage. The legend was adjusted so that maximum value corresponded to the failure strain of the material of each respective layer.

The UAS impacted the windshield and slid over it due to the small windshield angle. The windshield did not sustain any fractures or major damage. However, it did experience some permanent deformation in the outer layer of the transparency that can be observed in the bottom images in Figure 212. Due to the small deformations experienced in the transparency and the lack of major damage or penetration, the severity of the event was categorized as Level 2.

Figure 213 presents the impulse due to the contact force between UAS and forward fuselage, as well as the energy balance for both of them. Figure 214 shows the internal energies of UAS and the forward fuselage components directly involved in the impact.

The energy balance plot includes the UAS and forward fuselage kinetic and internal energies as well as frictional energy and total energy for the event. The forward fuselage and the UAS absorb 10% and 22% of the impact energy respectively. The energy dissipated by friction reaches 14% of the total energy. In Figure 214, internal energies for the UAS parts and the forward fuselage show that the polycarbonate body of the UAS and the windshield absorbed the highest amount of internal energy.

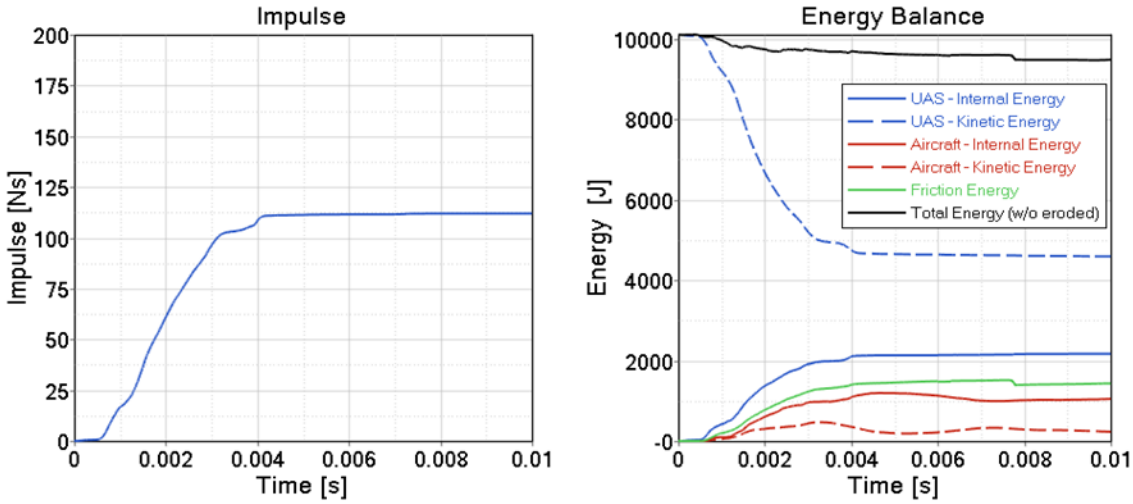

Figure 213. Impulse and energy balance of the impact between a commercial transport jet windshield and a 1.2 kg (2.7 lb) UAS at 128.6 m/s (250 knots)

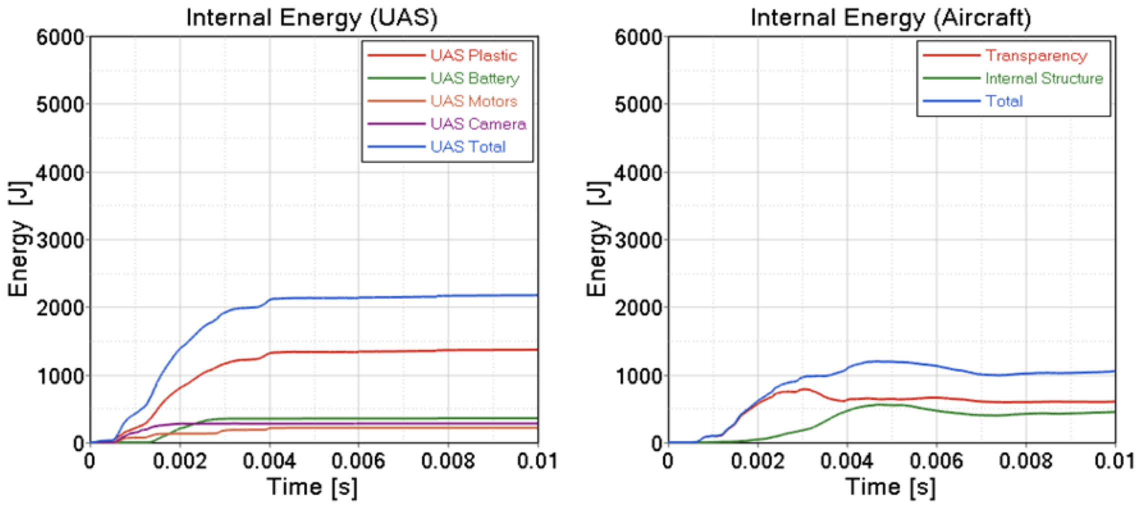

Figure 214. Internal energy per component of the impact between a commercial transport jet windshield and a 1.2 kg (2.7 lb) UAS at 128.6 m/s (250 knots)

4.4 BUSINESS JET AIRBORNE COLLISION STUDIES

As introduced in section 3.1.3 , the targets areas for impact on the NIAR commercial transport jet are vertical stabilizer (4.4.1), horizontal stabilizer (4.4.2), wing leading edge (4.4.3), and windshield (4.4.4). This section presents the results of explicit dynamic simulations of impacts of the 1.2 kg (2.7 lb) quadcopter UAS into the business jet.

Table 27 and Figure 215 summarize the results of the collision studies on the business jet. This section will describe in detail the results in each of the four subassemblies.

Table 27. Business jet airborne collision simulation – Severity levels and fire risk

	Business Jet										
	Vertical Stabilizer			Horizontal Stabilizer			Wing			Windshield	
Case	BQV1	BQV2	BQV3	BQH1	BQH2	BQH3	BQW1	BQW2	BQW3	BQC1	BQC2
Severity	Level 3	Level 3	Level 2	Level 3	Level 4	Level 4	Level 3	Level 2	Level 2	Level 2	Level 2
Fire Risk	Yes	No	No	Yes	No	Yes	Yes	No	No	No	No

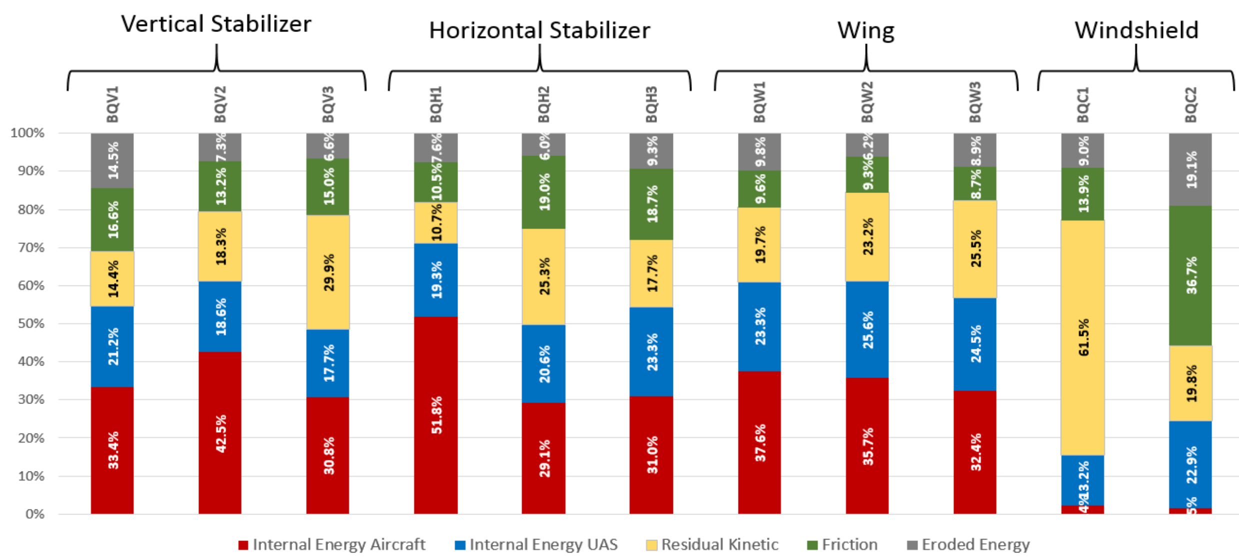

Figure 215. Business jet airborne collision simulation – Energy summary

As shown in Figure 215 for each one of the impact conditions we can quantify how the initial kinetic energy of the UAS prior to impact is transformed into aircraft and UAS internal energies through the structural deformations introduced during impact; a residual UAS kinetic energy that is a function of the UAS post impact debris mass moving at a post impact residual velocity; friction energy which is a function of the sliding contact energy between the UAS and the aircraft structure, and eroded energy from the mass of the UAS and aircraft eroded elements used to increase the stability of the calculation.

4.4.1 Vertical Stabilizer

The vertical stabilizer of the business jet was subjected to impact at three different locations that were selected based on the criteria described in section 4.1.2 . The diagram in Figure 216 illustrates the positions being impacted and the naming assigned to each of the cases. The UAS was assigned an initial speed of 128.6 m/s (250 knots) in the local *x*-axis of the aircraft. The vertical stabilizer was constrained for displacement and rotation at the lower edge of the five spar members and the forward duct interface. The following subsections present the analysis results of the three different impact scenarios.

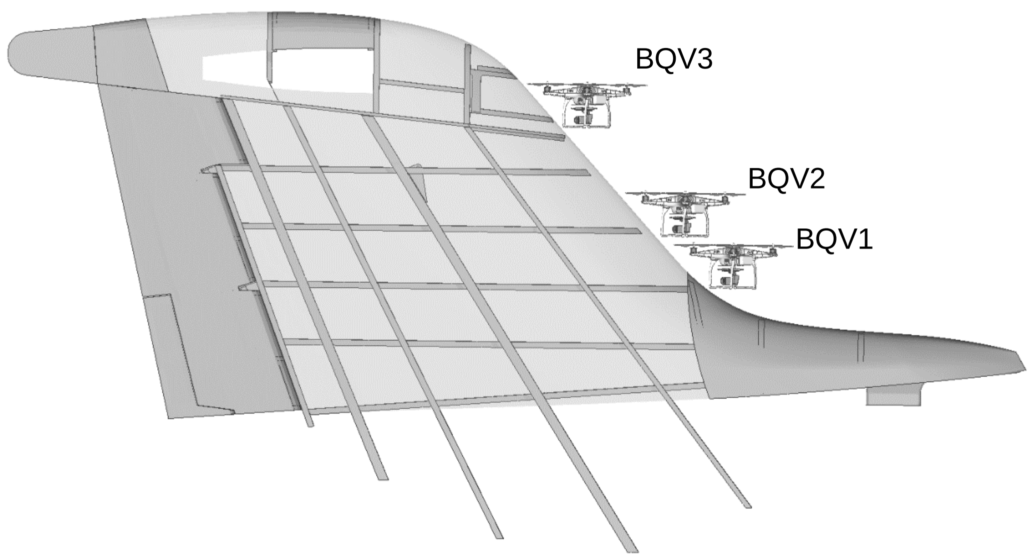

Figure 216. UAS impact locations – Business jet vertical stabilizer

4.4.1.1 Summary of Results – Business Jet Vertical Stabilizer

A summary of the results of all three cases presented in Figure 216 is shown in the following figure. For each case, the left bar represents a summation of all the different energies involved in the impact event, measured at 12 ms and normalized with the total energy at time zero. Each block indicates the percentage of total energy for each type of energy. The right bar specifies the severity level (1-4), as described in Section 4.2.1 , as well as an additional bar highlighting if the case generates a potential fire risk in the battery, following the criteria of Section 0.

Damage severity was determined based on a combination of the visual assessment of damage shown in the simulation and the impact energy distribution among the components involved. The majority of the UAS kinetic energy for these impact simulations was transferred to the internal energy of the horizontal stabilizer. BQV2 was selected as the critical case because it sustained the most damage of the three.

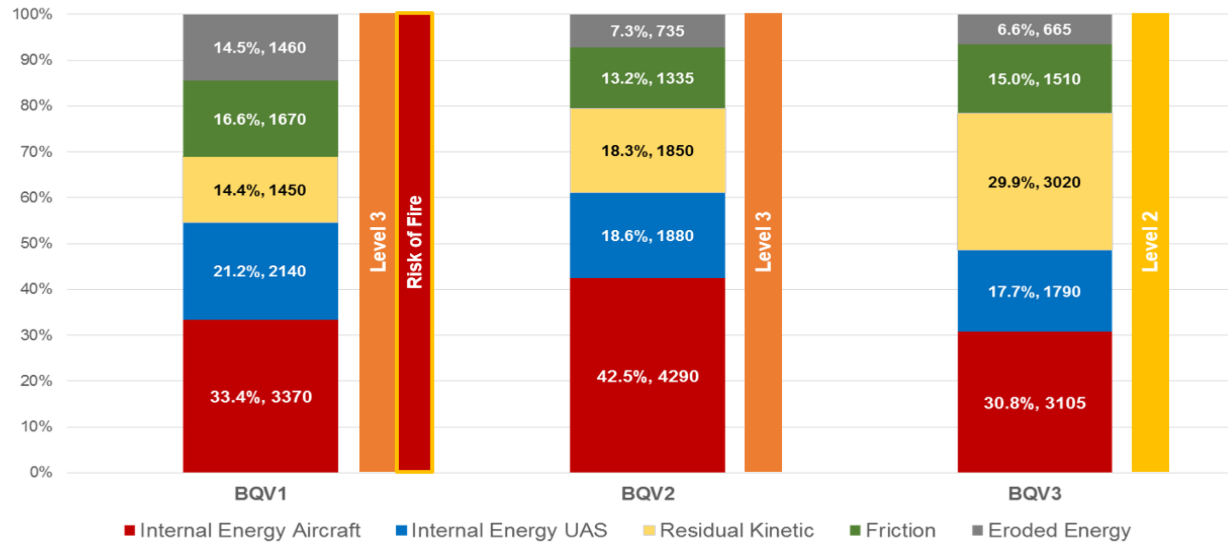

Figure 217. Summary bar chart of business jet vertical stabilizer cases

4.4.1.2 Critical Case - BQV2

Of the three impact locations, BQV2 was considered most critical damaging case. The results of the remaining cases are found in APPENDIX B.

The middle portion of the vertical stabilizer between ribs 2 and 3 was chosen for impact in this case. The UAS was impacted against the vertical stabilizer at 128.6 m/s (250 knots) in the local *x*-axis direction of the aircraft. Figure 218 depicts the kinematics of the event. Figure 219 shows the damage caused to the skin and inner frames of the vertical stabilizer.

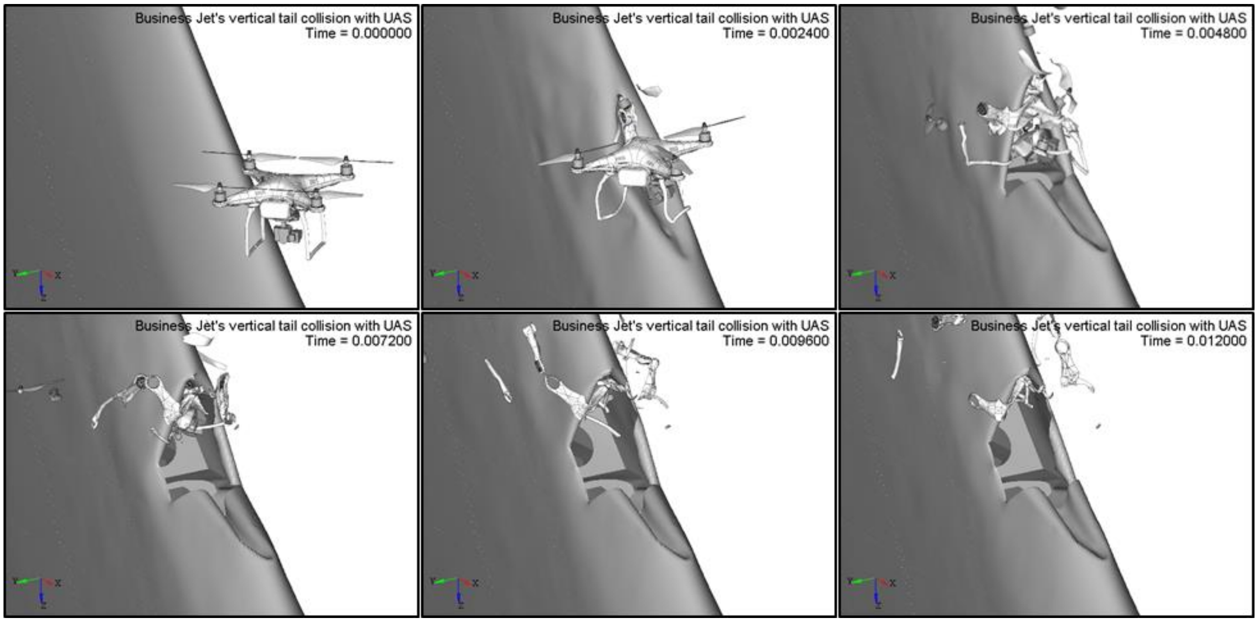

Figure 218. Kinematics of the impact between the business jet vertical stabilizer at location 2 and a 1.2 kg (2.7 lb) UAS at 128.6 m/s (250 knots)

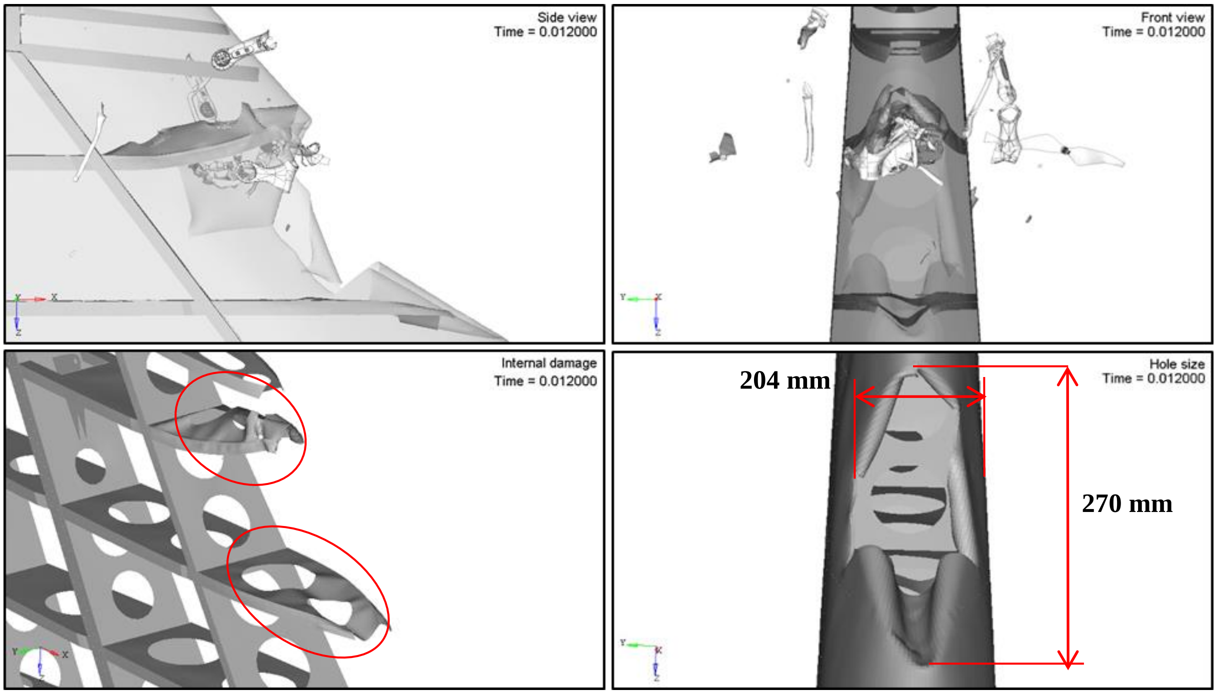

Figure 219. External/internal damage sustained by the business jet vertical stabilizer impacted at location 2 with a 1.2 kg (2.7 lb) UAS at 128.6 m/s (250 knots)

The UAS damaged the skin and the upper and lower ribs, creating a damaged zone of 204x270 mm on the skin surface. The permanent deformation of the ribs can be seen in the bottom left image in Figure 219. This impact considerably reduced the velocity of the UAS components such that the spar sustained no damage. The damage introduced by the UAS involved perforation of the skin but no damage to the primary structure, and consequently the severity was classified as Level 3.

Figure 220 shows the impulse due to the contact force between UAS and vertical stabilizer, as well as the energy balance. Figure 221 shows the internal energies of UAS and vertical stabilizer parts directly involved in the impact.

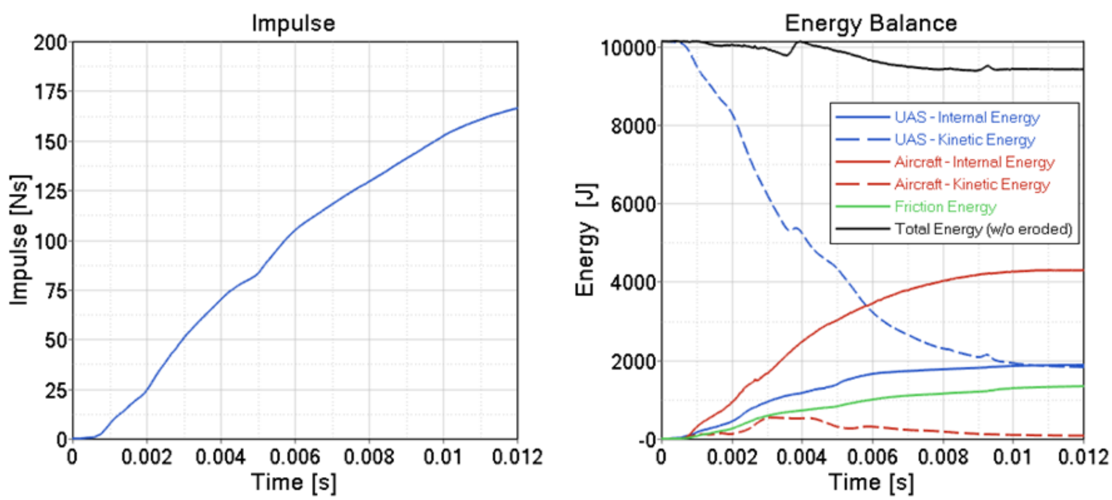

Figure 220. Impulse and energy balance of the impact between a business jet vertical stabilizer at location 2 and a 1.2 kg (2.7 lb) UAS at 128.6 m/s (250 knots)

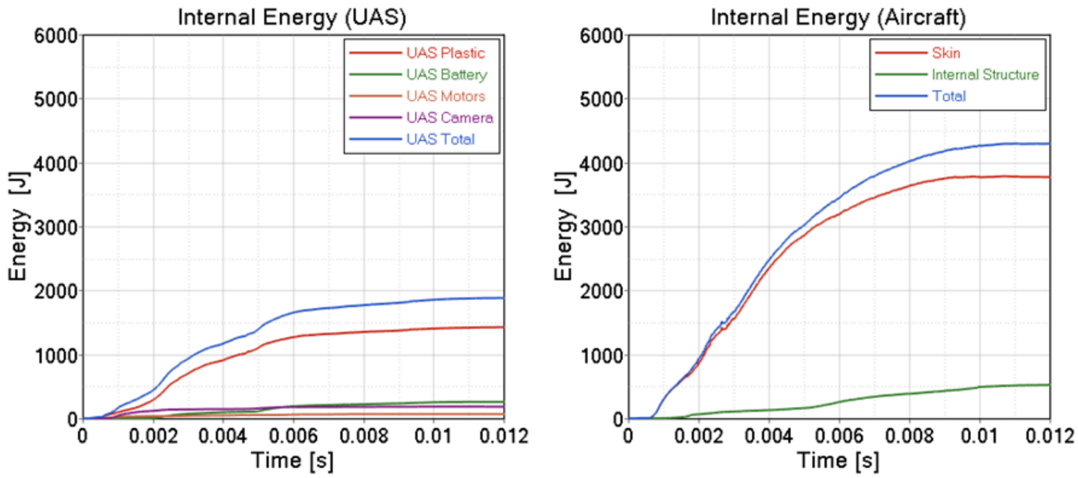

Figure 221. Internal energy per component of the impact between a business jet vertical stabilizer at location 2 and a 1.2 kg (2.7 lb) UAS at 128.6 m/s (250 knots)

The energy balance plot includes the UAS and vertical stabilizer kinetic and internal energies as well as frictional energy and total energy for the event. The vertical stabilizer and UAS absorbed 42% and 19% of the impact energy, respectively, while the friction energy reaches 13% of the total energy. In Figure 221, internal energies for the UAS parts and the vertical stabilizer show that the polycarbonate and skin absorbed the highest amount of internal energies respectively.

4.4.2 Horizontal Stabilizer

The business jet horizontal stabilizer was subject to impact at three impact locations. Locations were selected for maximum penetration of the UAS into the structure of the aircraft. The initial velocity assigned to the UAS was 128.6 m/s (250 knots) along the local x-axis of the aircraft. In addition, the stabilizer was constrained for displacements and rotations at the forward and aft spars as well as the forward actuator attachment and aft pivot lug. The following subsections present the analysis results of the five different case scenarios.

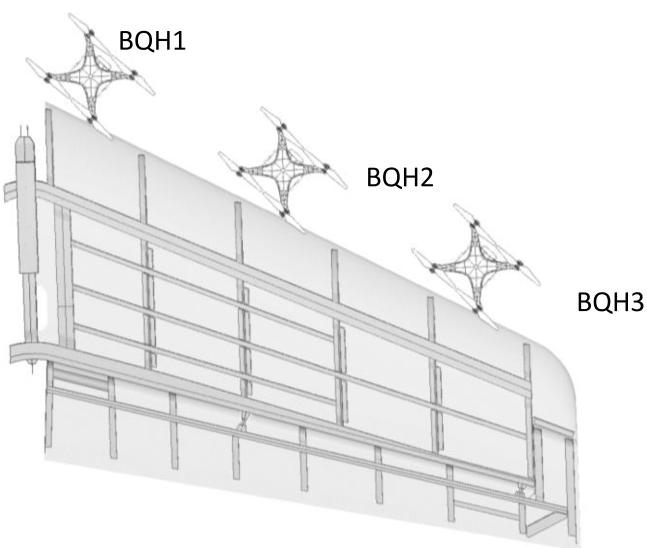

Figure 222. UAS impact locations – Business jet horizontal stabilizer

4.4.2.1 Summary of Results – Business Jet Horizontal Stabilizer

A summary of the results of the three cases presented in Figure 222 is shown in Figure 223. For each case, the left bar represents a summation of all the different energies involved in the impact event, measured at 15 ms after impact and normalized with the total energy at time zero. Each block indicates the percentage of total energy for each type of energy. The right bar specifies the severity level (1-4), as well as an additional bar highlighting if the case generates a potential fire risk in the battery.

As shown in Figure 223, the largest energy transfer was to the internal energy of the aircraft. The location of impact BQH1 near the root rib of the horizontal stabilizer allowed more energy to be absorbed by the aircraft structure than BQH2 and BQH3 because the rib deflected away from the vertical stabilizer. However, outboard areas 2 and 3 received severe damage in the primary structure, raising the severity level to 4. BQH2 was especially severe, as most of the UAS (including the battery) penetrated into the airframe beyond the front spar. Consequently, this case was selected as the most critical.

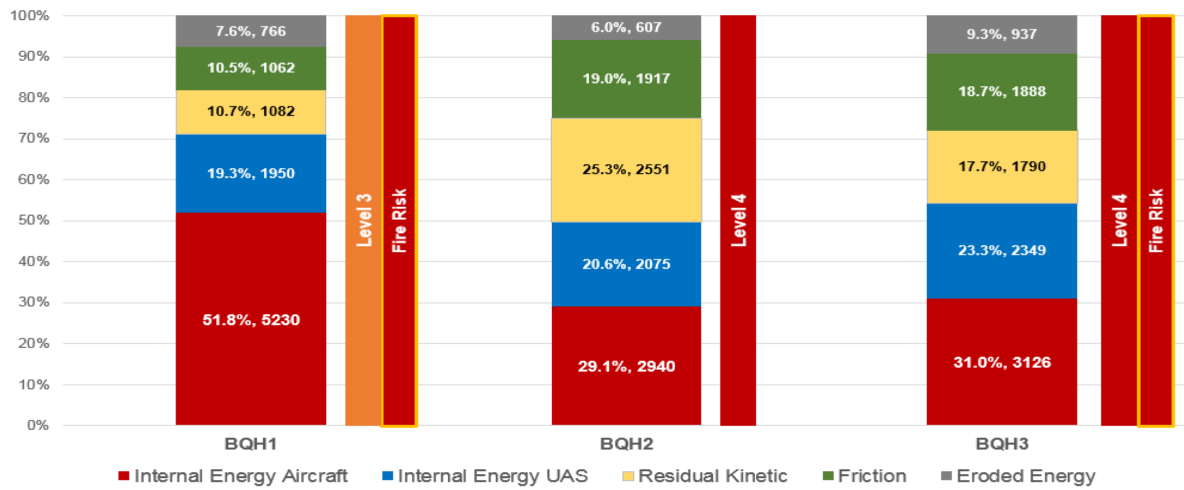

Figure 223. Summary bar chart of business jet horizontal stabilizer cases

4.4.2.2 Critical Case – BQH2

Of the three impact locations, BQH2 was considered the most critical damaging. The results of the remaining cases may be found in APPENDIX B.

Impact location 2 is located on the center of the horizontal stabilizer leading edge, between the two center nose ribs. The UAS was impacted against the stabilizer at 128.6 m/s (250 knots) along the local *x*-axis direction of the aircraft. Figure 224 presents the kinematics of the event. Figure 225 shows the damage caused to the inner frames and the skin.

The UAS damaged the skin and the nose ribs, creating a 573x135 mm damaged zone on the skin surface and allowing a significant fraction of the UAS mass to penetrate until it hits the front spar. On the bottom left image at Figure 225, perforation caused to the front spar, as well the deformation affecting the nose ribs was observed. Since the front spar is a critical load path for the horizontal stabilizer, it was considered a primary structure. Consequently, the damage introduced by the UAS in this case was classified as Level 4.

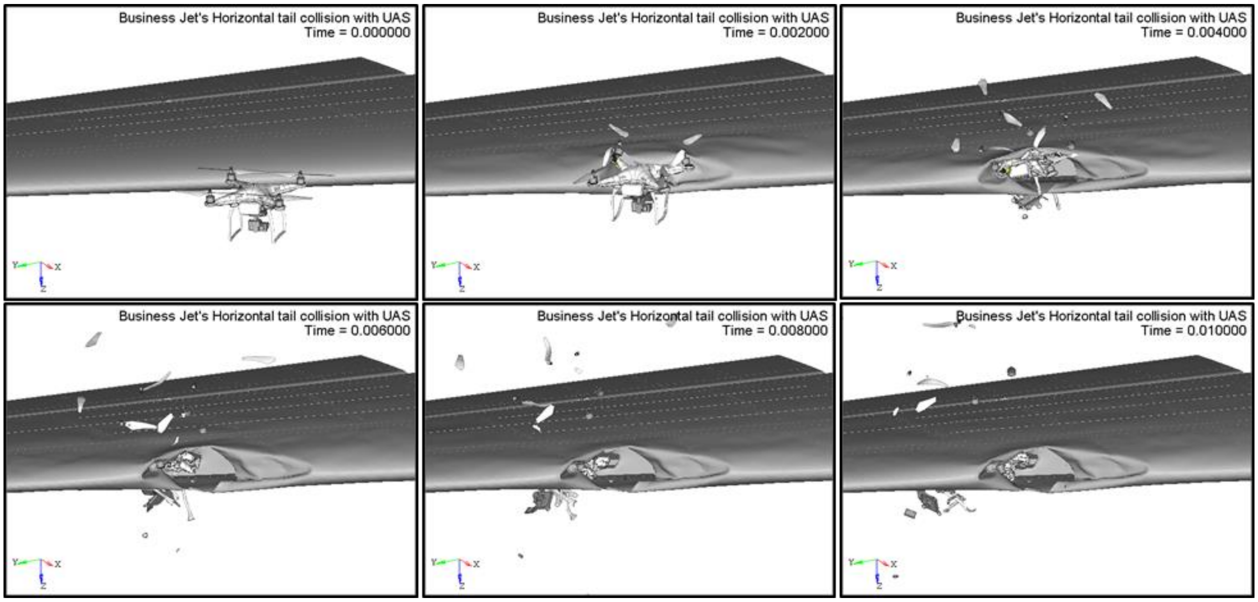

Figure 224. Kinematics of the impact between the business jet horizontal stabilizer at location 2 and a 1.2 kg (2.7 lb) UAS at 128.6 m/s (250 knots)

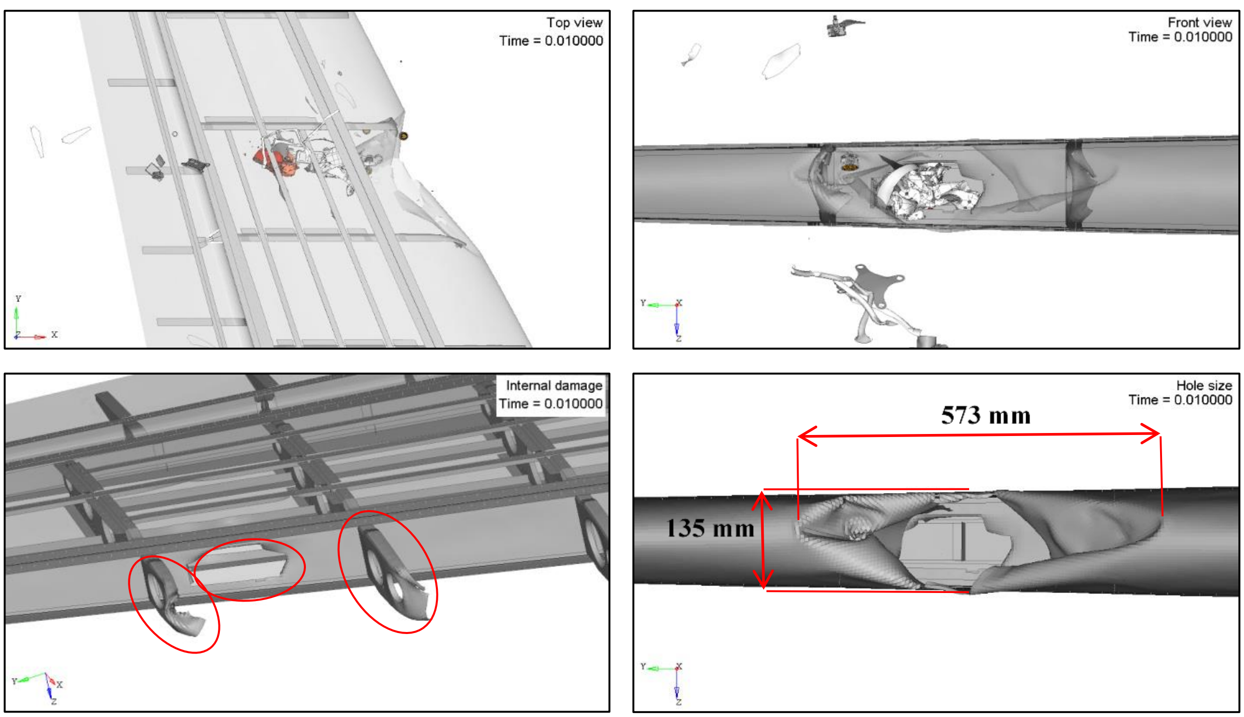

Figure 225. External/internal damage sustained by the business jet horizontal stabilizer impacted at location 2 with a 1.2 kg (2.7 lb) UAS at 128.6 m/s (250 knots)

Figure 226 shows the impulse due to the contact force between the UAS and the horizontal stabilizer, as well as the energy balance for both of them. Figure 227 presents the internal energies of the UAS and horizontal stabilizer parts directly involved on the impact.

The energy balance plot includes the UAS and horizontal stabilizer kinetic and internal energies, frictional energy and total energy for the event. The stabilizer and UAS absorbed 29% and 21% of the impact energy, respectively, while the energy dissipated by friction reached 19% of the total energy. In Figure 227, internal energies for the UAS parts and the stabilizer structure show that the skin and the polycarbonate absorbed the highest internal energies of the event.

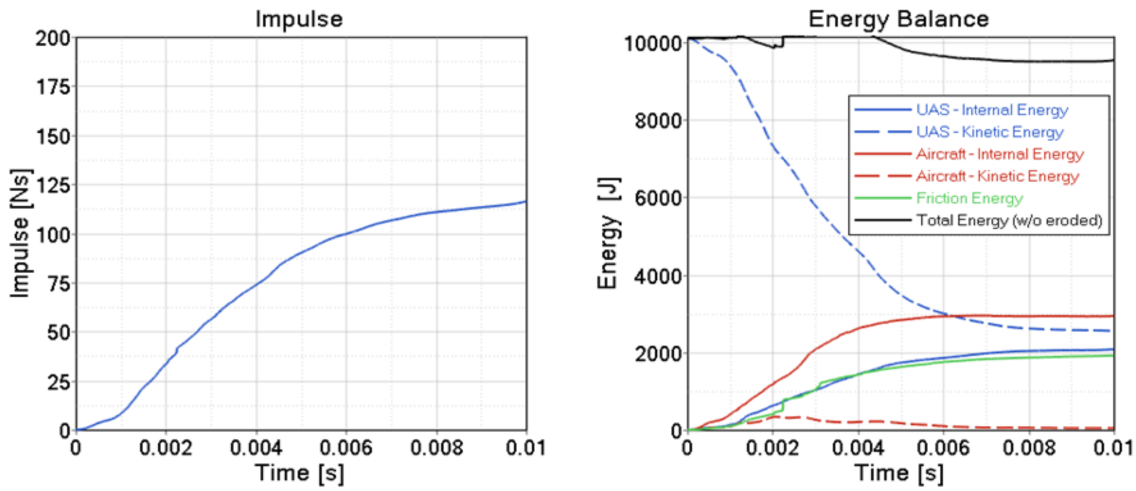

Figure 226. Impulse and energy balance of the impact between a business jet horizontal stabilizer and a 1.2 kg (2.7 lb) UAS at 128.6 m/s (250 knots)

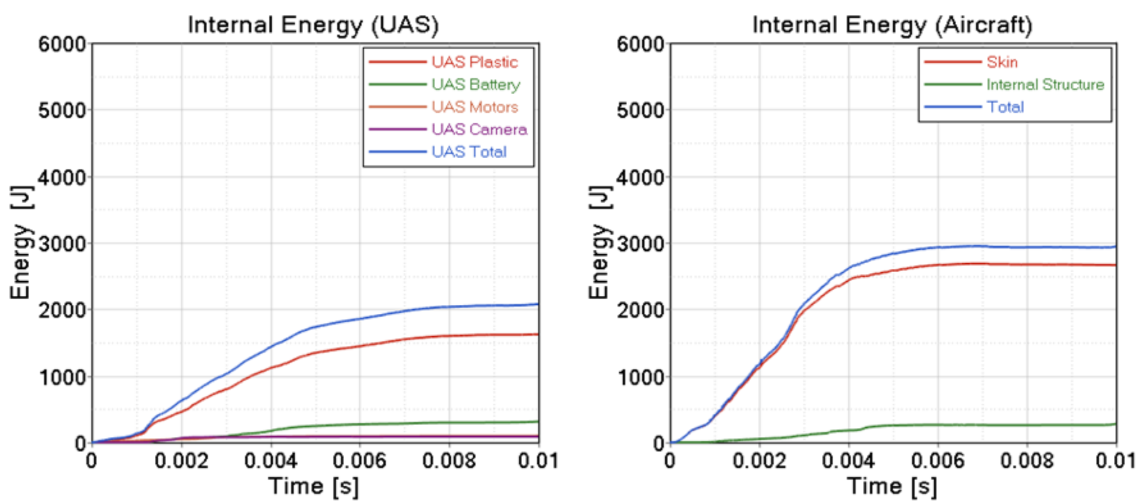

Figure 227. Internal energy per component of the impact between a business jet horizontal stabilizer and a 1.2 kg (2.7 lb) UAS at 128.6 m/s (250 knots)

4.4.3 Wing Leading Edge

The wing of the business jet was subject to impact at three different locations. The locations were selected for maximum penetration of the UAS upon impact. The UAS was assigned an initial speed of 128.6 m/s (250 knots) in the local *x*-axis of the aircraft. Nodal displacements and rotations were constrained at the centerline of the fuselage and at the wing-to-fuselage attachment fittings. The following subsections present the analysis results of the three different scenarios.

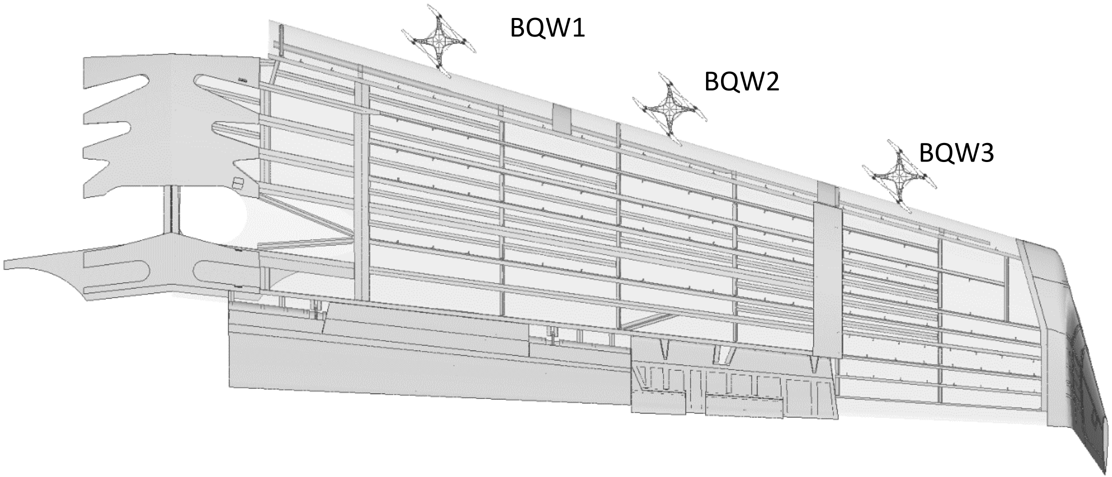

Figure 228. UAS impact locations – Business jet wing leading edge

4.4.3.1 Summary of Results – Business Jet Wing

A summary of the results of the three cases presented in Figure 228 is shown in the following figure. For each case, the left bar represents a summation of all the different energies involved in the impact event, measured at 10 ms and normalized with the total energy at time zero. Each block indicates the percentage of total energy for each type of energy. The right bar specifies the severity level (1-4), as well as an additional bar highlighting if the case generates potential fire risk in the battery.

As shown in Figure 229, the internal energy absorbed by the aircraft structure increased when the UAS impacted closer to the root. In contrast, the residual kinetic energy decreased the closer the UAS impacted to the root.

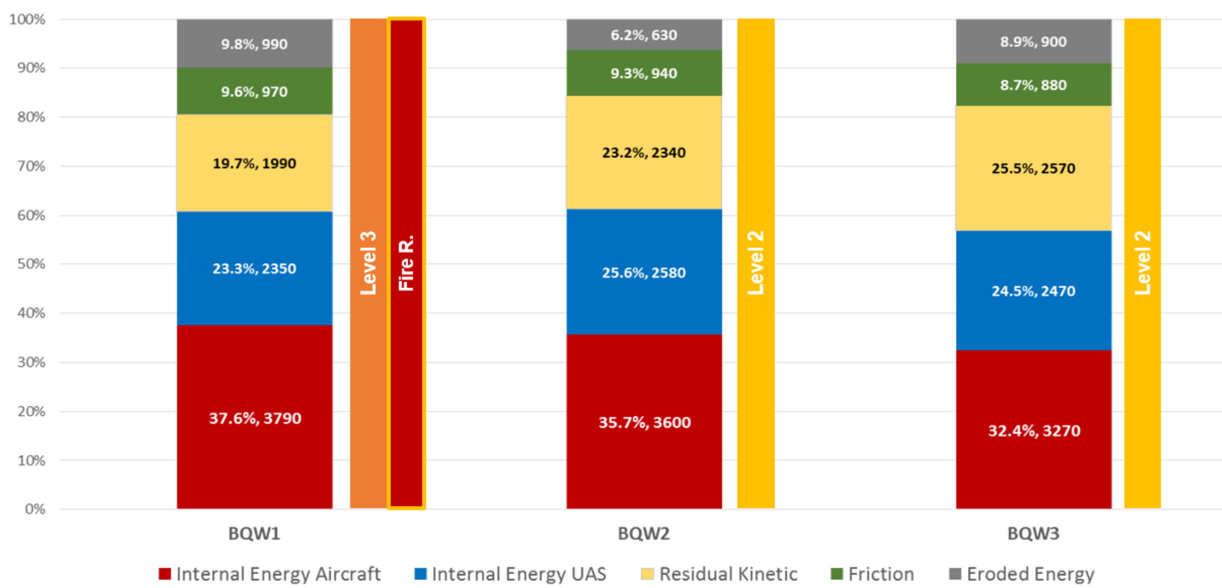

Figure 229. Summary bar chart of business jet wing cases

Both phenomena may be explained with the cross-sectional height of the airfoil at the impacted location. The cross-section of the wing closer to the root was thicker than at the tip and had a greater nose radius. Consequently, the area of airframe that had a more perpendicular contact with the impacting projectile was greater, allowing a greater transfer of energy and therefore an increase in internal energy. Locations that offered less projected frontal area and had decreased nose radii tended to deflect the impact. This trend also explains the greater residual kinetic energy for outboard regions of the horizontal stabilizer. For these, a greater portion of the UAS was deflected upwards and/or downwards.

4.4.3.2 Critical Case - BQW1

The portion of the wing near the fuselage, between ribs 1 and 2, was chosen as the critical impact case for the wing leading edge. The UAS was impacted against the wing at 128.6 m/s (250 knots) in the local *x*-axis direction of the aircraft. Figure 230 depicts the kinematics of the event. Figure 231 shows the damage caused to the skin and inner frames of the wing.

The UAS damaged the skin and the anti-ice tube, creating a 66x137 mm damaged zone on the skin surface. Permanent deformation of the tube can be seen in the bottom left image in Figure 231. This impact considerably reduced the velocity of the UAS components, so the spar was not impacted and sustained no damage. The damage introduced by the UAS involved perforation of the skin but no damage to the primary structure, and consequently the severity was classified as Level 3.

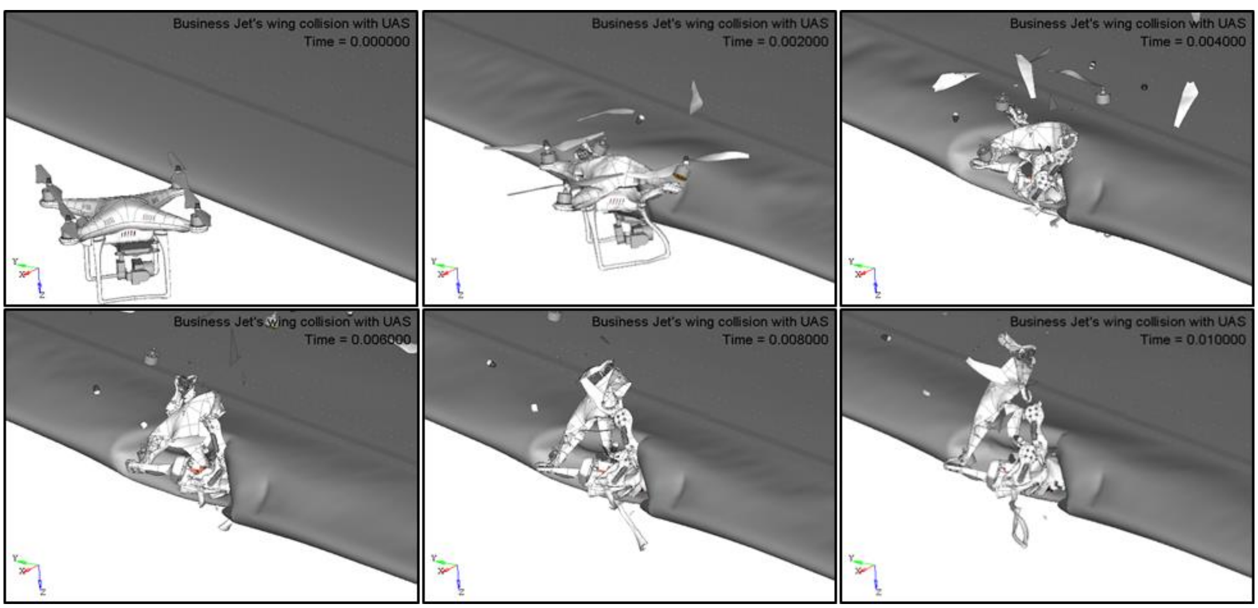

Figure 230. Kinematics of the impact between the business jet wing at location 1 and a 1.2 kg (2.7 lb) UAS at 128.6 m/s (250 knots)

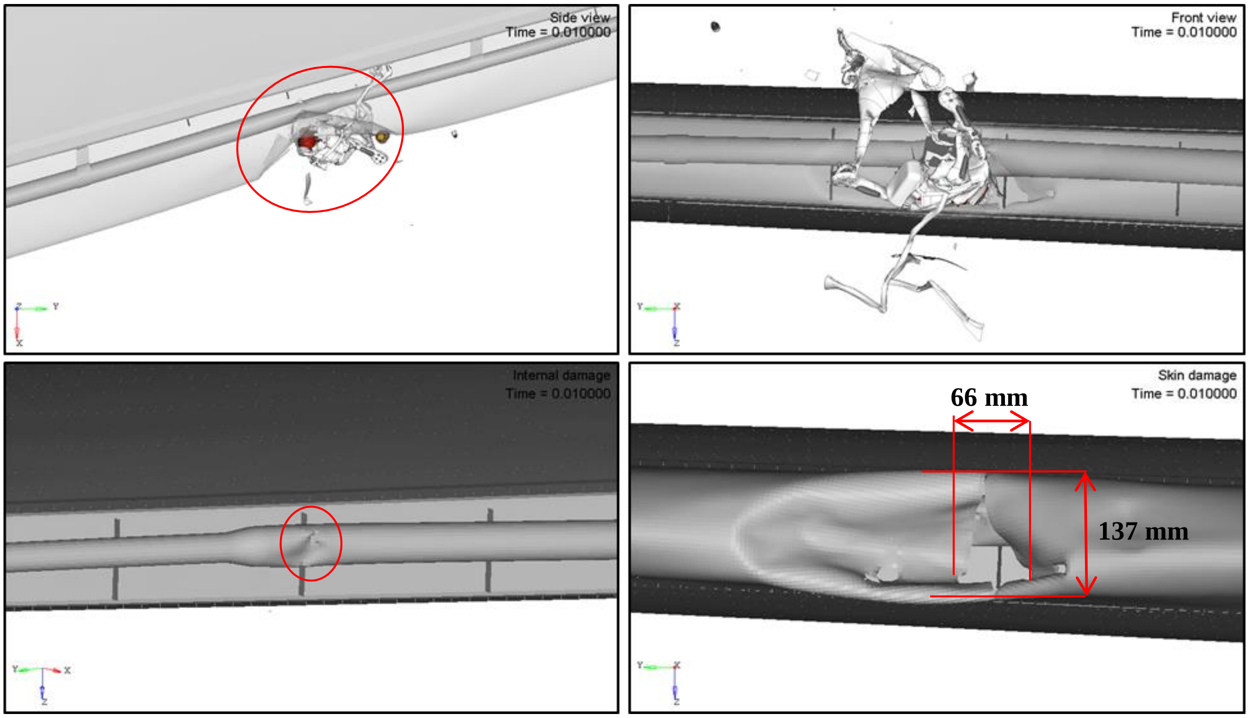

Figure 231. External/internal damage sustained by the business jet wing impacted at location 1 with a 1.2 kg (2.7 lb) UAS at 128.6 m/s (250 knots)

Figure 232 shows the impulse due to the contact force between UAS and wing, as well as the energy balance for both of them. Figure 233 shows the internal energies of UAS and wing parts directly involved in the impact.

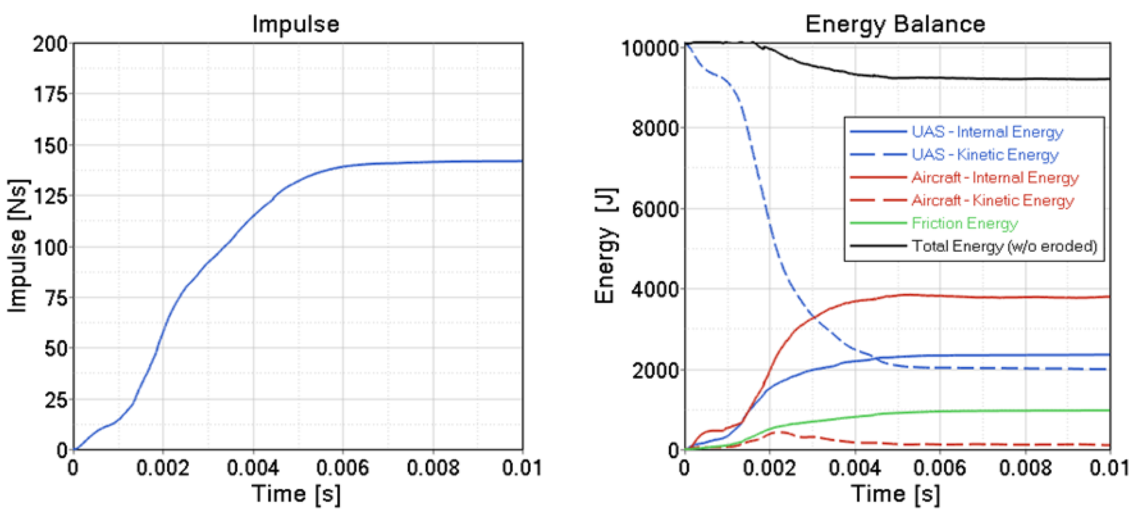

Figure 232. Impulse and energy balance of the impact between a business jet wing and a 1.2 kg (2.7 lb) UAS at 128.6 m/s (250 knots)

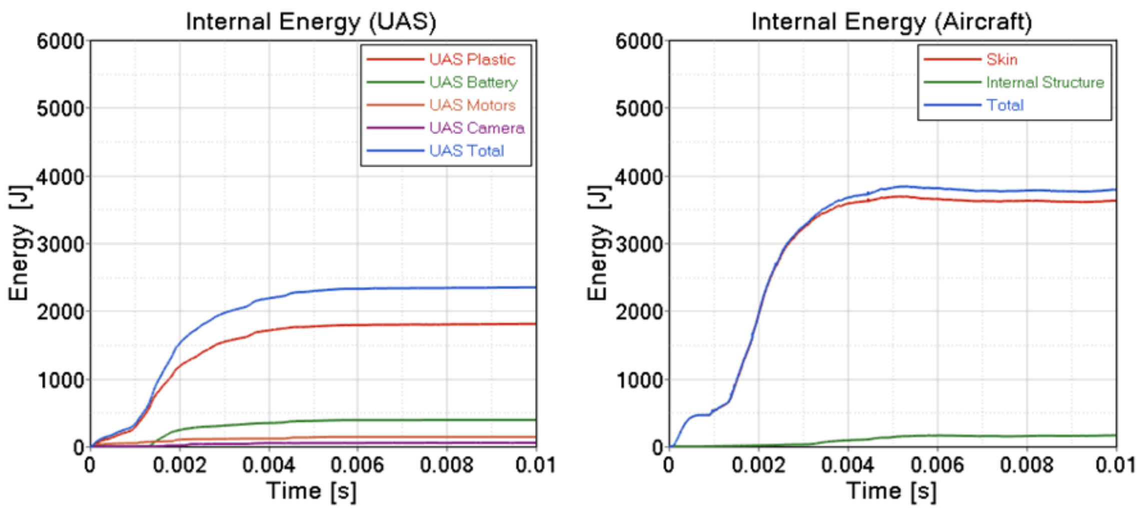

Figure 233. Internal energy per component of the impact between a business jet wing and a 1.2 kg (2.7 lb) UAS at 128.6 m/s (250 knots)

The energy balance plot includes the UAS and wing kinetic and internal energies as well as frictional energy and total energy for the event. The wing and UAS absorbed 38% of the impact energy, respectively, while the energy dissipated by friction reached 10% of the total energy. In Figure 233, the UAS polycarbonate body and the wing skin absorbed the highest amount of internal energies.

4.4.4 Windshield

The windshield of the business jet was subjected to impact at two different locations. The locations were selected for maximum penetration of the UAS.

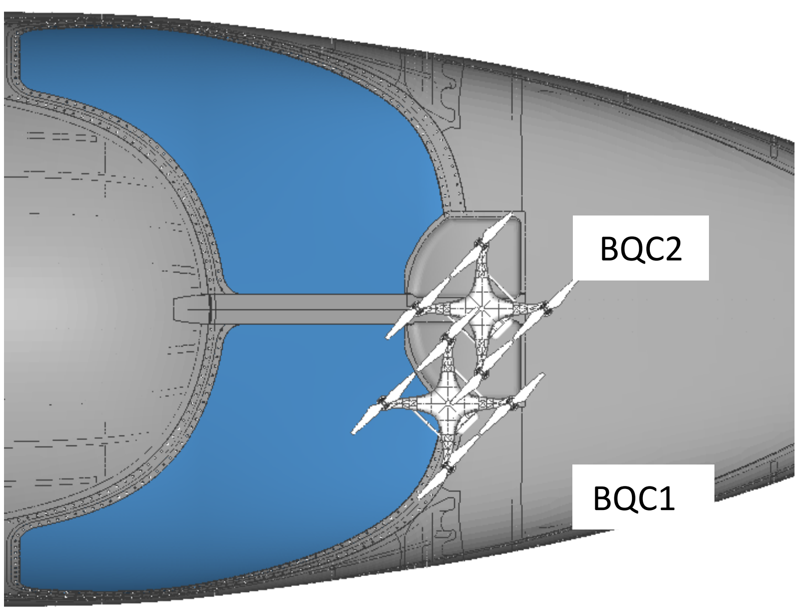

Figure 234. UAS impact locations – Business jet cockpit windshield

An initial velocity of 128.6 m/s (250 knots) along the local *x*-axis of the aircraft was applied to the UAS. Axial displacements were constrained at all nodes around the perimeter of the fuselage at the aft-most boundary of the cockpit. The following subsections present the analysis results for the two different scenarios.

4.4.4.1 Summary of Results – Business Jet Cockpit Windshield

A summary of the results of the three cases presented in Figure 234 is shown in Figure 235. For each case, the left bar represents a summation of all the different energies involved in the impact event, measured at 10 ms and normalized with the total energy at time zero. Each block indicates the percentage of total energy for each type of energy. The right bar specifies the severity level (1-4), as well as an additional bar highlighting if the case generates a potential fire risk in the battery.

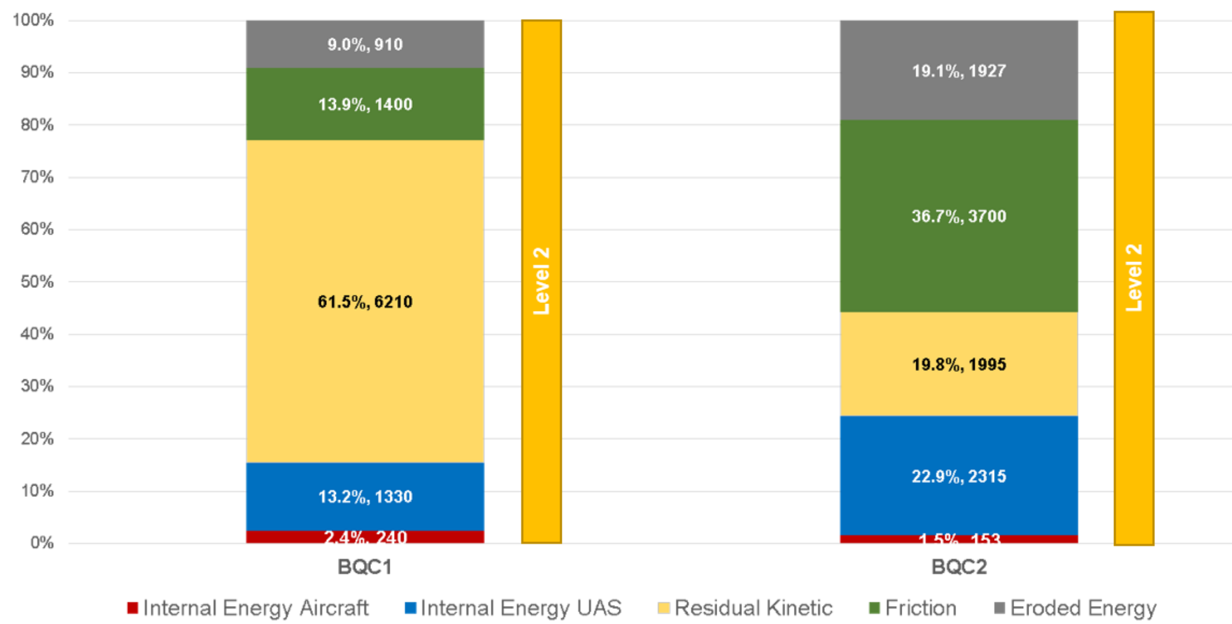

Figure 235. Summary bar chart of business jet horizontal stabilizer cases

The two plots show a notable difference in the distribution of energy during the impact event.

Impact scenario BQC1 involved less friction than BQC2. This trend is considered reasonable because BQC1 was a direct impact to the windshield transparency while BQC2 was an impact to a metallic piece of structure where the ductility of the material could impose greater surface traction. In case BQC1, the residual kinetic energy of the UAS was greater than for BQC2 due to the minimal amount of friction in the impact as well as the inclined angle of the windshield at the off-center contact location. The internal energy of the UAS was greater for BQC2 due to the greater friction energy transferred between the components.

4.4.4.2 Critical Case - BQC1

Impact location 1 was chosen based on two conditions: *(i)* the collision was as perpendicular as possible to the surface, and *(ii)* to limit the influence of the center post stiffness. Hence, the UAS was located at 1/3 of the distance outboard from the center post. The UAS was impacted against the windshield at 128.6 m/s (250 knots) along the local *x*-axis direction of the aircraft. Figure 236 presents the kinematics of the event. Figure 237 shows the damage caused to the windshield and the internal structure.

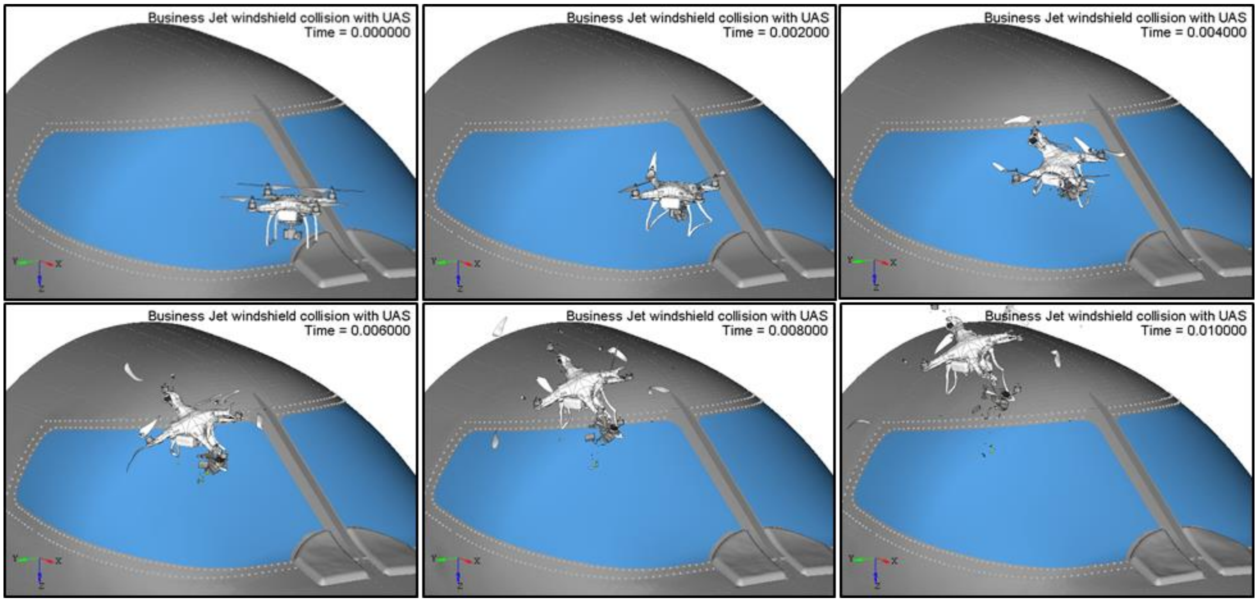

Figure 236. Kinematics of the impact between the business jet windshield and a 1.2 kg (2.7 lb) UAS at 128.6 m/s (250 knots)

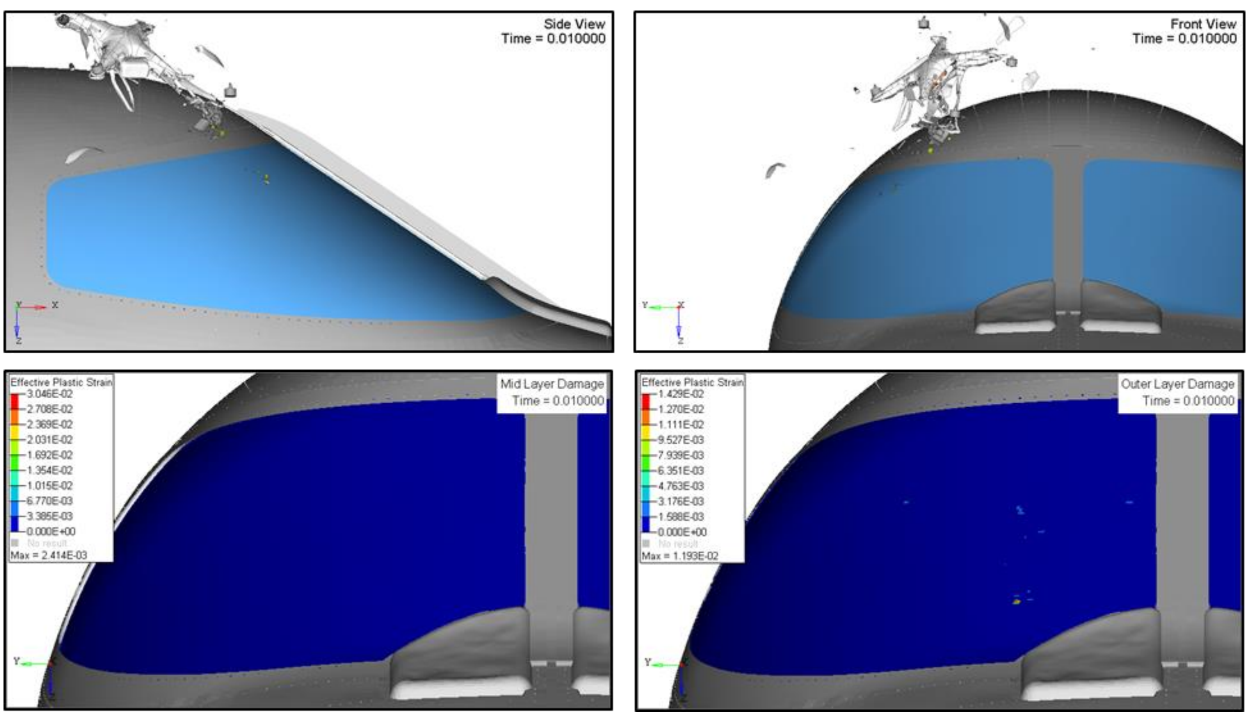

Figure 237. External/internal damage sustained by the business jet windshield impacted at location 1 with a 1.2 kg (2.7 lb) UAS at 128.6 m/s (250 knots)

The UAS impacted the windshield and slides over due to the windshield inclination angle. The windshield did not sustain any visible damage. The permanent deformation on the windshield is presented on the bottom right image in Figure 237. The bottom two images present the contour plot of the effective plastic strain after impact on the outer (bottom-left image) and mid (bottom-right image) layers of the transparency, which were the components that experienced greater damage. The legend was adjusted to the failure strain of the material of the respective layer.

As it can be observed, there is no critical damage on the windshield surface and the surrounding structure. Due to the small deformations experienced in the transparency and the lack of major damage or penetration, the severity of the event was categorized as Level 2.

Figure 238 shows the impulse due to the contact force between the UAS and the forward fuselage, as well as the energy balance for both of them. Figure 239 shows the internal energies of the UAS and the forward fuselage parts directly involved in the impact.

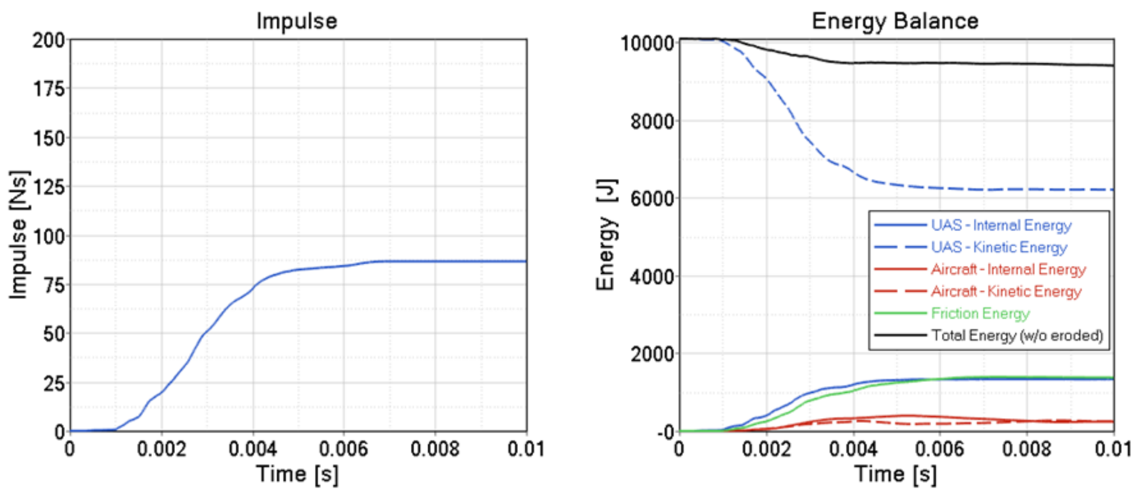

Figure 238. Impulse and energy balance of the impact between a business jet windshield and a 1.2 kg (2.7 lb) UAS at 128.6 m/s (250 knots)

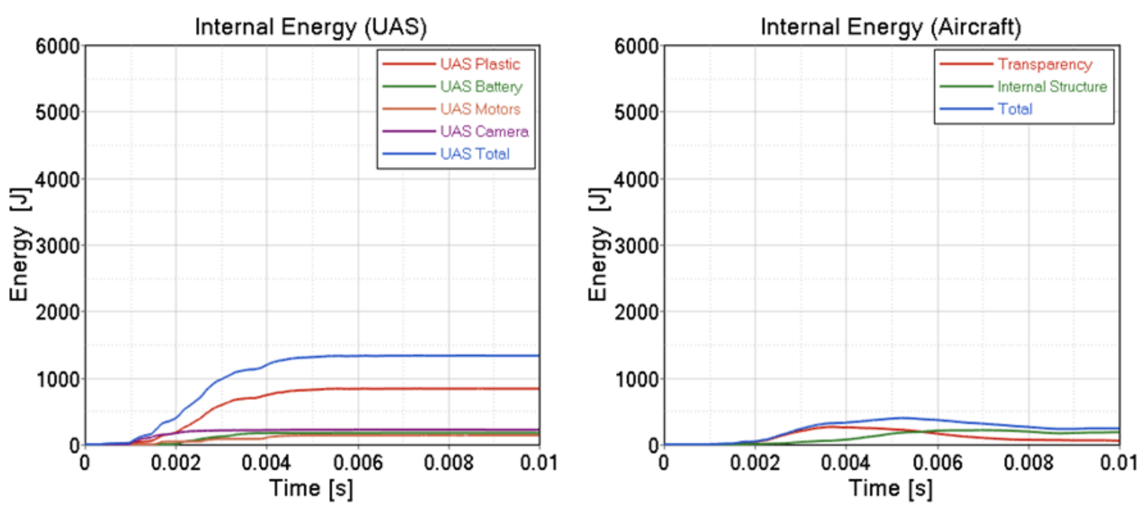

Figure 239. Internal energy per component of the impact between a business jet windshield and a 1.2 kg (2.7 lb) UAS at 128.6 m/s (250 knots)

The energy balance plot includes the UAS and forward fuselage kinetic and internal energies, frictional energy and total energy for the event. The forward fuselage absorbed 2% of the impact energy, while the UAS absorbed 13% of it. The energy dissipated by friction reached 14% of the total energy. Due to the oblique angle of the windshield, a substantial fraction of the total energy after impact was residual kinetic energy. Figure 239 shows that the UAS polycarbonate and the windshield internal structure absorb the highest amount of internal energies.

4.5 CONCLUSIONS

Chapter 4 presented the results of a total of 27 baseline simulations of collisions between a 1.2 kg (2.7 lb) quadcopter UAS and critical areas of the NIAR's commercial transport and business jets at 128.6 m/s (250 knots). Worst case scenarios were selected for further studies, presented in chapters 5. and 6. The diagrams in Figure 240 and Figure 241 present levels of severity at each location for both aircraft respectively. Levels are based on the damage severity description in section 4.2.1

From the images, the tail was generally more vulnerable for both aircraft if impacted by the quadcopter UAS. For the same type of impact, the commercial transport jet was more susceptible to receive critical damage than the business jet. Features such as a greater spacing between ribs or a smaller distance between the leading edge skin and the front spar may increase the chances of a severe collision. The specific design features of the business jet modeled for this project possibly resulted in less damage when compared to the commercial transport jet. Moreover, the windshields of both aircraft sustained relatively less damage after impact of the components investigated.

Based on the results of the simulations presented in this chapter, the impact severity of a midair collision between a 1.2 kg (2.7 lb) quadcopter UAS with a commercial transport jet or a business jet aircraft is high. This statement is limited to a collision having the characteristics presented in this chapter. A different UAS configuration or mass, other impact velocities or orientations and other factors may result in different severity levels, as investigated in chapter 5. Furthermore, the level of damage severity for a given impact appears to be due to the UAS components that represent concentrated masses, parts that utilize dense or stiff materials, and alignment of the masses within the UAS as a whole. A comparison between quadcopter UAS impacts and bird strikes with similar kinetic energies is presented in chapter 6. . A comparison with also the fixed-wing UAS configuration is given in chapter 5.

Figure 240. Summary of collision severity levels on commercial transport jet

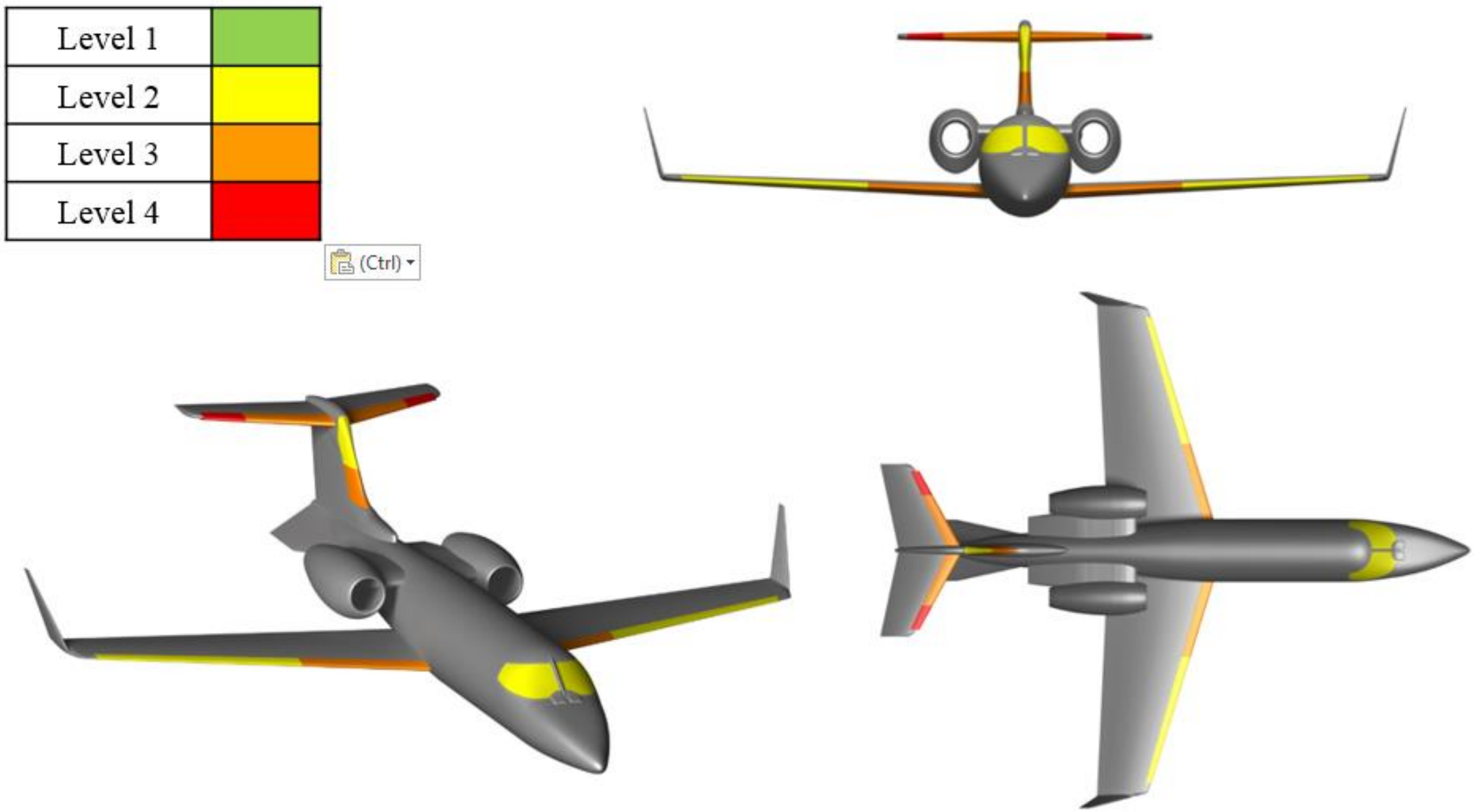

Figure 241. Summary of collision severity levels on business jet

5. KINETIC ENERGY PARAMETRIC STUDIES

5.1 INTRODUCTION

Following the baseline impact simulations discussed in chapter 4. , a parametric study was performed to determine the sensitivity of the FE models to variations in the parameters that define the impact energy: UAS mass and relative impact velocity. The mass of the UAS was scaled from 1.2 kg (2.7 lb) to 1.8 kg (4.0 lb), as described in section 5.2.1 . The velocities chosen for this study, detailed in section 5.3.1 , are representative of cruise and landing speeds for each aircraft type; 187.8 m/s (365 knots) and 56.7 m/s (110 knots) for the commercial transport jet, 167.2 m/s (325 knots) and 44.8 m/s (87 knots) for the business jet. The results from these two velocities were compared to the baseline 128.6 m/s (250 knots) simulations discussed in chapter 4.

5.1.1 Load Case Name Convention

In order to provide a brief label that accurately describes each combination of UAS, aircraft type, target component, and impact location the following convention is used to name each load case:

The baseline impact conditions were coded using four characters (ABCD)

- A – Distinguishes between Commercial Transport (C) and Business (B) Jets
- B – Distinguishes between UAS type:
  - 1.2 kg (2.7 lb) Quadcopter (Q) or 1.8 kg (4.0 lb) Quadcopter (Qs)
  - 1.8 kg (4 lb) Fixed-Wing (F) or 3.6 kg (8.0 lb) Fixed-Wing (Fs)
  - 1.2 kg (2.7 lb) Bird (B2) or 1.8 kg (4.0 lb) Bird (B4)
- C – Distinguishes between impact area:
  - Vertical Stabilizer (V)
  - Horizontal Stabilizer (H)
  - Wing (W)
  - Cockpit Windshield (C)
- D – Distinguishes between impact location (1 through 5)

Example CQV4:

- Commercial
- Quadcopter
- Vertical Stabilizer
- Impact Location 4

The velocity studies utilized an additional character in the labeling code in order to differentiate between the baseline runs and the variations on the baselines, as follows:

- For baseline runs, use the original code
  - Example CQV4
    - Indicates holding velocity – 128.6 m/s (250 knots)
- For landing velocity cases, add letter “L” after the impact area designation
  - Example CQVL4
    - Commercial transport jet landing velocity – 56.7 m/s (110 knots)
- For cruise velocity cases, add letter “C” after the impact area designation
  - Example CQVC4
    - Commercial transport jet cruise velocity – 187.8 m/s (365 knots)

5.2 MASS SENSITIVITY STUDY

In this study, the influence of UAS mass on the severity of a mid-air collision was investigated. This study was limited to the baseline 1.2 kg (2.7 lb) UAS and one scaled-up 1.8 kg (4 lb) version of the UAS. This mass later allowed a comparison with a bird strike of standard mass, as defined in the Airworthiness Requirements and presented in chapter 6. In future work, a more extensive selection of masses (see Section 6.3.2) can be used to better understand the influence of UAS kinetic energy, which will allow establishing thresholds of severity.

Table 28 presents the simulation matrix with all the mass comparisons studied in this chapter. Eight different simulations of the scaled-up 1.8 kg (4.0 lb) UAS FE model was performed with identical boundary and initial conditions as the critical load cases presented in chapter 4. These results for scaled-up UAS were compared to the baseline UAS results discussed in chapter 4.

Table 28 Load case definition

	Commercial Transport Jet				Business Jet			
	Vertical Stabilizer	Horizontal Stabilizer	Wing Leading Edge	Windshield	Vertical Stabilizer	Horizontal Stabilizer	Wing Leading Edge	Windshield
Baseline 1.2 kg (2.7 lb)	CQV3	CQH3	CQW1	CQC1	BQV2	BQH1	BQW1	BQC1
Scaled 1.8 kg (4.0 lb)	CQsV3	CQsH3	CQsW1	CQsC1	BQsV2	BQsH1	BQsW1	BQsC1

The following section presents the methodology followed to scale the UAS, the summary with all the results of the simulations completed and some examples of observed differences in damage.

5.2.1 UAS Scaling Methodology

In order to perform simulations with a greater mass, a scaled version of the 1.2 kg (2.7 lb) UAS model may be produced. The procedure followed assumed that all the components of a scaled UAS would increase its mass linearly in an equal ratio, independently of its construction, design etc. Consequently, if materials are not varied, the density remains constant and therefore a quadratic relationship between linear dimensions can be stablished (so volume is proportional to mass). The scaling factor can be calculated using the equation presented below.

$$ScaleFactor = \sqrt[3]{{Mass\ Scaled\ UAS}/{Mass\ Baseline\ UAS}}$$

Any 2-dimentional element (**ELEMENT_SHELL*) would have to account for the scaling of its thickness in the respective section property. Similarly, 1-dimensional elements (**ELEMENT_BEAM*) require a quadratic scaling of the cross sectional area in its section property. Finally, non-structural mass (**ELEMENT_MASS*) demand a linear scaling [22].

Therefore, in order to obtain an UAS of 1.8 kg (4 lb), the mesh of the FE model was scaled linearly (in all directions) with a factor of 1.143. Additionally, the thickness of components meshed with shell elements (2-dimensional) was increased with the same factor. Finally, any non-structural mass was incremented proportionally to the mass ratio of the scaling, in this case 1.493. The following figure compares a 1.2 and 1.8 kg UAS in the same scale.

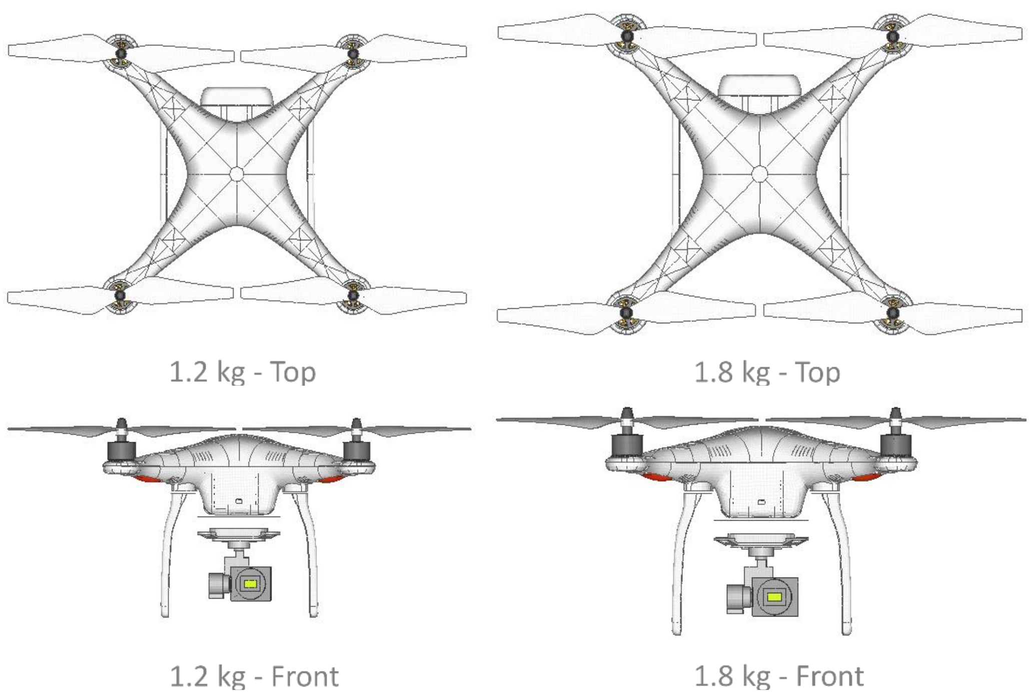

Figure 242. Comparison of geometry of the 1.2 and 1.8 kg UAS FE models

Scaling should be limited so the quality of the FE model is not affected. Scaling up or down the FE model will intrinsically imply a change in element size. This will consequently increase computational time when downscaling or may affect the performance of contact algorithms when upscaling.

5.2.2 Simulation Results

Table 29 presents the levels of severity of the impacts with the scaled-up UAS and the respective baseline simulations. Additional comparisons of the kinematics, reaction force, impulse, and energies are presented in APPENDIX C.

Table 29 Mass scaled impact simulation results

	Commercial Transport Jet				Business Jet			
	Vertical Stabilizer	Horizontal Stabilizer	Wing	Windshield	Vertical Stabilizer	Horizontal Stabilizer	Wing	Windshield
Baseline 1.2 kg (2.7 lb)	Level 3	Level 4	Level 3	Level 2	Level 3	Level 4	Level 3	Level 2
Scaled-up 1.8 kg (4.0 lb)	Level 3	Level 4	Level 3	Level 3	Level 4	Level 4	Level 3	Level 2

At a first glance, it can be observed that for all the cases the upscaled UAS creates equal or more damage than the baseline. Only the for the cases involving the windshield of the commercial transport jet and the vertical and horizontal stabilizer undergo an increment in the level of severity.

5.2.2.1 Commercial Jet

Figure 243 illustrates the damage sustained by the horizontal stabilizer after impact of a 1.2 kg (2.7 lb) and a 1.8 kg (4.0 lb) UAS.

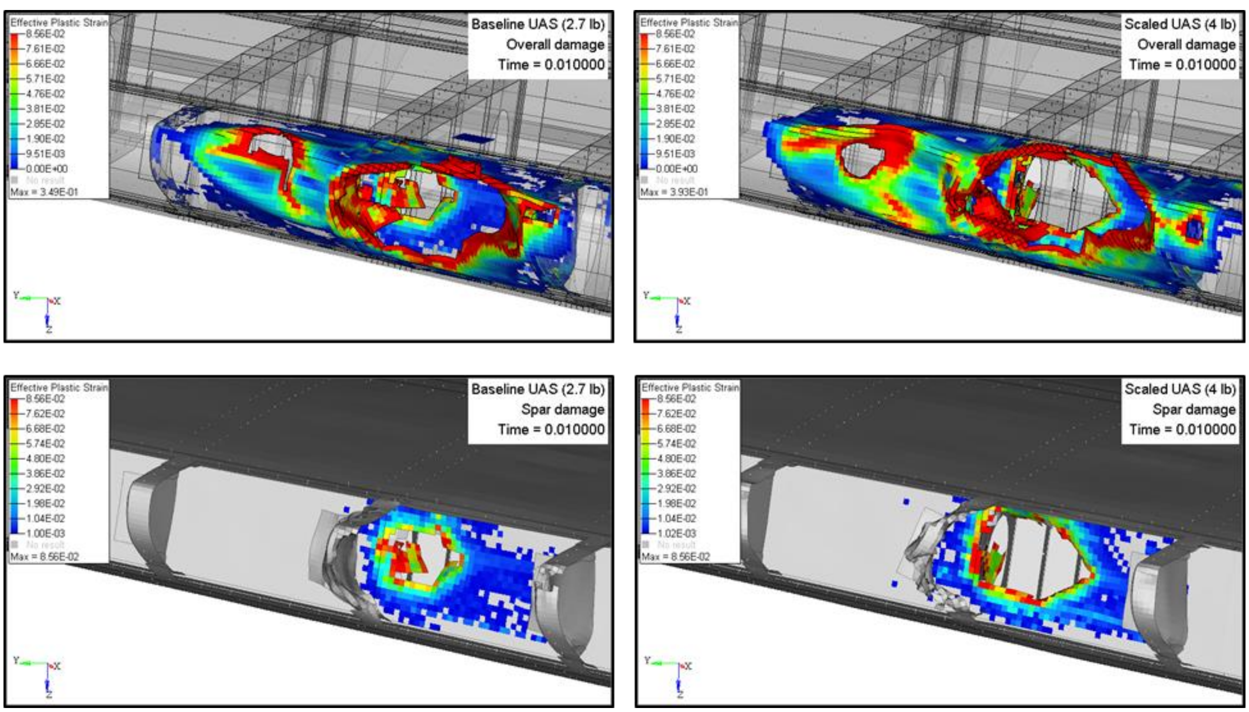

Figure 243. Comparison of skin and internal damage produced by a 2.7/4.0 lb. (1.2/1.8 kg) UAS after impact with a commercial transport jet horizontal stabilizer

This case was selected to illustrate a situation in which the level of severity resulted to be the same for the baseline and scaled-up simulations. The top images show the contour plot of the effective plastic strain of all the components of the aircraft 10 ms after impact. Only effective plastic strains greater than 0.001 are shown on the plots; consequently, any translucent area would be deformed in the elastic region of the material with no permanent deformation. The lower set of images in Figure 243 was limited to the front spar. The skin sustained a similar amount of damage in both cases. However, the perforation size on the web of the front spar is greater for the case with the higher mass UAS. Even though both cases presented level 4 damage, the extent of the permanent deformation and actual failure of the material was greater in the collision with the scaled-up UAS.

Similarly, Figure 244 presents the comparison of the damage sustained by the windshield. Both images display the contour plot of the effective plastic strain of the inner layer of the transparency after impact. The inner layer was selected for the plot because it sustained more deformation and the only one that fractured.

From a comparison of both images in Figure 244, the impact of a 1.8 kg (4.0 lb) UAS created a damage greater area on the windshield compared with a 1.2 kg (2.7 lb) UAS. The damage was enough to create a fracture of the inner layer of the transparency of approximately the same length as the UAS diameter. This fact inherently raised the damage severity level from 2 to 3.

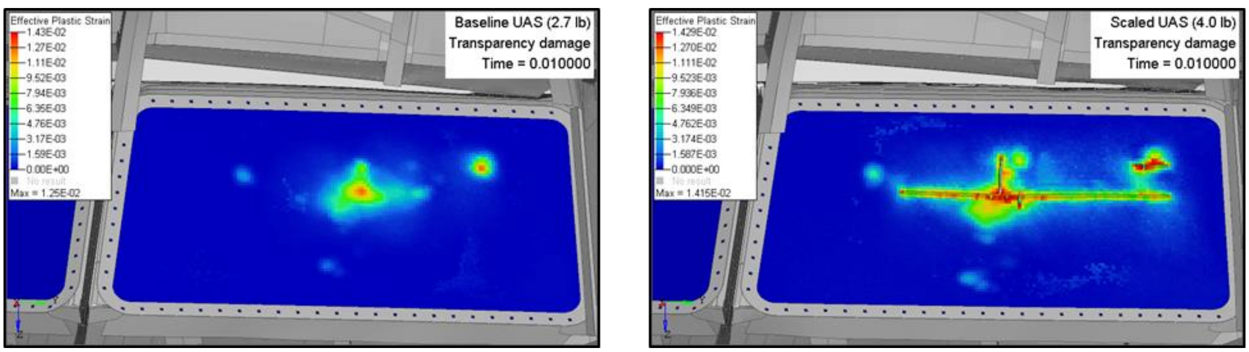

Figure 244. Comparison of the effective plastic deformation sustained by the inner layer of the commercial transport jet transparency after impact with a 1.2/1.8 kg (2.7/4 lb) UAS

5.2.2.2 Business Jet

Similarly, Figure 245 presents the resultant damage in the vertical stabilizer of the business jet aircraft due to impact of a 1.2 kg (2.7 lb) and a 1.8 kg (4.0 lb) UAS. The top images show the contour plot of the effective plastic strain 15 ms after impact. Only plastic strains greater than 0.001 are shown on the plots; consequently, any translucent area would be deformed in the elastic region of the material with no permanent deformation. The lower image portrays a similar plot but limited to the front spar, so a comparison of the damage to the primary structure can be stablished.

It can be seen that the front spar sustains critical damage and severe permanent deformation after impact of the 1.8 kg (4.0 lb) UAS, while it remains undamaged for the baseline simulation. Consequently, the level of severity was raised to level 4 for the case with the scaled-up UAS.

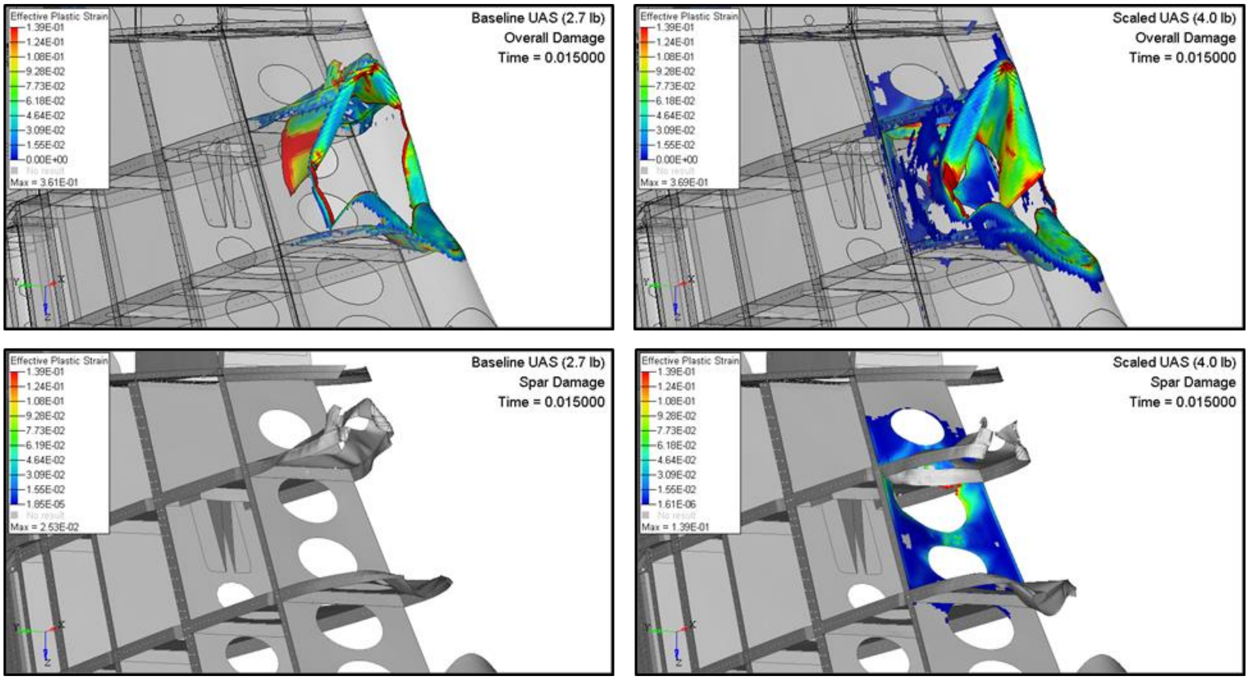

Figure 245. Comparison of damage in business jet vertical stabilizer result of an impact with 1.2 and 1.8 kg UAS

5.3 VELOCITY PARAMETRIC STUDY

The impact velocity used for the baseline simulations is representative of the airspeed of an aircraft while in a holding pattern prior to landing. In order to characterize the potential damage severity of a collision occurring at alternate velocities, two additional velocities were selected from the literature [42][43][44] to represent a lower energy impact as well as a higher energy scenario. The selections represent a practical minimum energy level collision that might occur during landing and an effective maximum energy level indicative of an impact near cruise conditions. Note that the maximum viable velocity is limited by the increasingly small timestep required to obtain a converged solution. In order to investigate higher energy interactions, the contact algorithms, failure criteria, and energy control definitions may need to be re-evaluated. Moreover, additional higher velocity verification tests may become necessary. In all cases, the kinematics and energy distribution of the simulations were reviewed to determine if the results were feasible and the solution was stable. If so, the damage severity levels were compared to their baseline counterparts.

5.3.1 Velocity Determination

The velocities used in this study were selected from a spectrum of landing and cruise conditions that were available for a commercial transport jet and a business jet similar to the models being used. The simulated impact conditions and load case labels for the commercial transport and business jets are shown in Table 30.

Table 30 Commercial transport and business jet velocity variation load cases

	Commercial Transport Jet				Business Jet			
	Vertical Stabilizer	Horizontal Stabilizer	Wing Leading	Cockpit Windshield	Vertical Stabilizer	Horizontal Stabilizer	Wing Leading	Cockpit Windshield
Holding – 128.6 m/s (250 knots)	CQV3	CQH3	CQW1	CQC1	BQV2	BQH1	BQW1	BQC1
Landing – 56.7 m/s (110 knots)	CQVL3	CQHL3	CQWL1	CQCL1	BQVL2	BQHL1	BQWL1	BQCL1
Cruise – 187.8 m/s (365 knots)	CQVC3	CQHC3	CQWC1	CQCC1	BQVC2	BQHC1	BQWC1	BQCC1

5.3.2 Simulation Results

The four aircraft regions studied in chapter 4. were used to perform sixteen additional simulations with varied impact velocities. Results are compared to the critical cases outlined in chapter 4. and presented in APPENDIX D. Table 31 presents the levels of severity of the impacts with the UAS with the corresponding levels for the respective baseline simulations.

Table 31 Velocity impact simulation results

	Commercial Transport Jet				Business Jet			
	Vertical Stabilizer	Horizontal Stabilizer	Wing	Cockpit Windshield	Vertical Stabilizer	Horizontal Stabilizer	Wing	Cockpit Windshield
Landing Velocity	Level 2	Level 2	Level 2	Level 1	Level 2	Level 2	Level 2	Level 1
Holding Velocity	Level 3	Level 4	Level 3	Level 2	Level 3	Level 4	Level 3	Level 2
Cruise Velocity	Level 4	Level 4	Level 4	Level 4	Level 4	Level 4	Level 3	Level 3

5.3.2.1 Commercial Transport Jet

Typical results for a 1.2 kg (2.7 lb) UAS simulated to impact to the commercial transport jet are presented in this section. The remaining results and comparisons can be found in Appendix D.1 . In general, the increased velocity cases imparted more visible damage to more components while the reduced velocity impacts created noticeably less damage than the baseline.

As shown in Figure 246, the effective plastic strain of the windshield transparency increased in relation to the increase in impact velocity. The effective plastic strain is plotted as a spectrum from blue to red indicating yield strains up to the material failure strains. The contour plots show that the low velocity case (left) and baseline case (middle) had localized regions of the windshield with plastic strain but that the increased velocity case (right) had a noticeably higher effective plastic strain as well as material failure. Note that the upper boundary of the windshield surround structure separated from the adjoining crown structure indicating failure in the fasteners or metallic components.

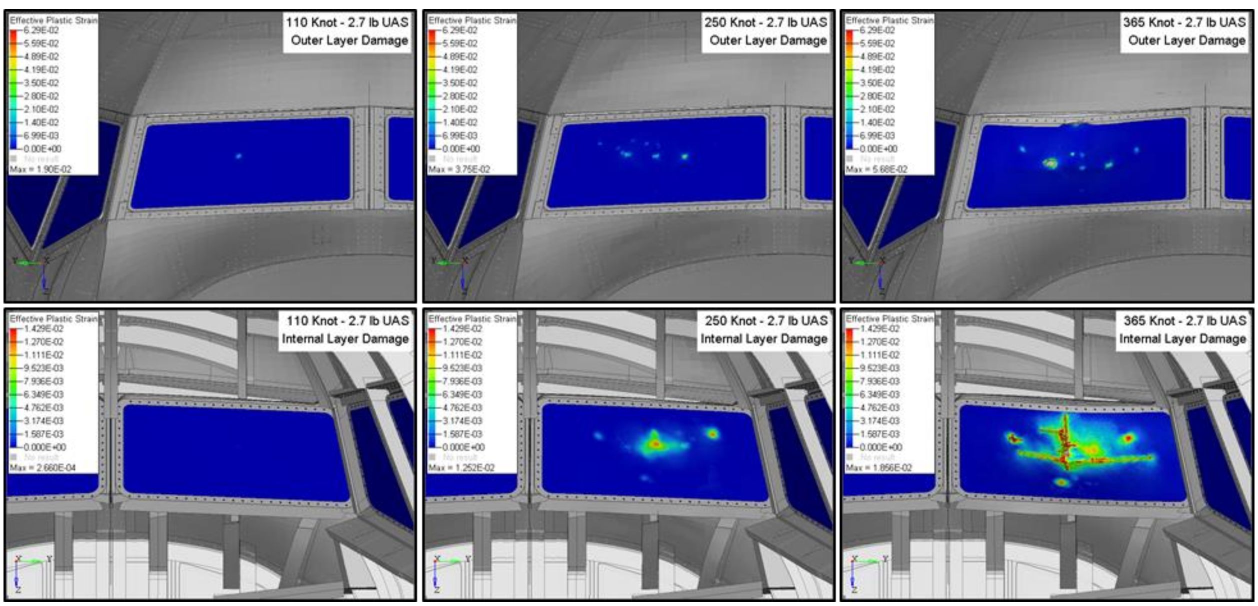

Figure 246. Comparison of windshield damage for CQCL1, CQC1, and CQCC1 – 56.7/128.6/187.8 m/s (110/250/365 knots)

The damage to the wing leading edge is shown in Figure 247 for 1.2 kg (2.7 lb) quadcopter UAS impacts at three velocities. The three images in the upper half of Figure 247 show effective plastic strains (strains above the material yield limit) for all components while the three lower images show effective plastic strains for only the forward spar. The leading edge of the commercial transport jet’s wing showed an increase in damage severity due to the increased impact energy for the cruise velocity case, as seen in the right hand side of Figure 247. The UAS penetrated through the skin and immediate substructure, allowing it to impact the forward spar. The spar web deformed and ruptured as shown in the bottom right-hand plot. This damage is considered level 4 severity. The landing velocity case (left) showed minimal damage beyond the deformation of the leading edge skin.

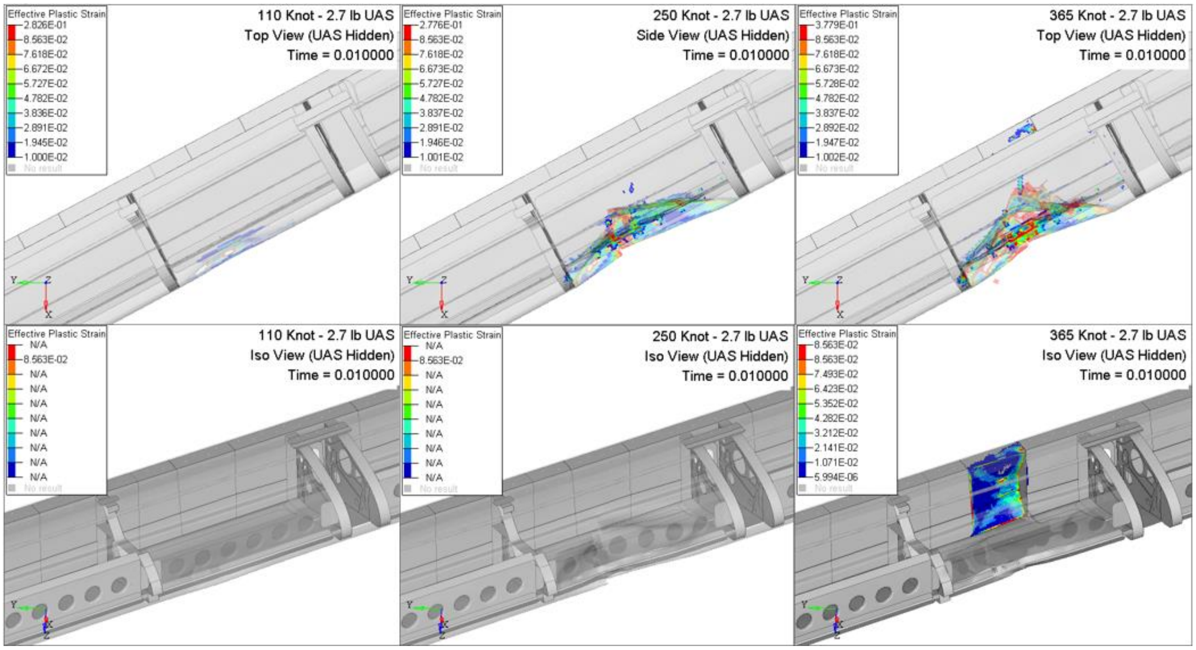

Figure 247. Comparison of wing leading edge damage for CQWL1, CQW1, and CQWC1 – 56.7/128.6/187.8 m/s (110/250/365 knots)

5.3.2.2 Business Jet

Typical results for a 1.2 kg (2.7 lb) UAS simulated impact to the business jet are presented in this section. The remaining results and comparisons can be found in Appendix D.2 . In general, the increased velocity cases imparted more visible damage to more components while the reduced velocity impact created noticeably less damage than the baseline.

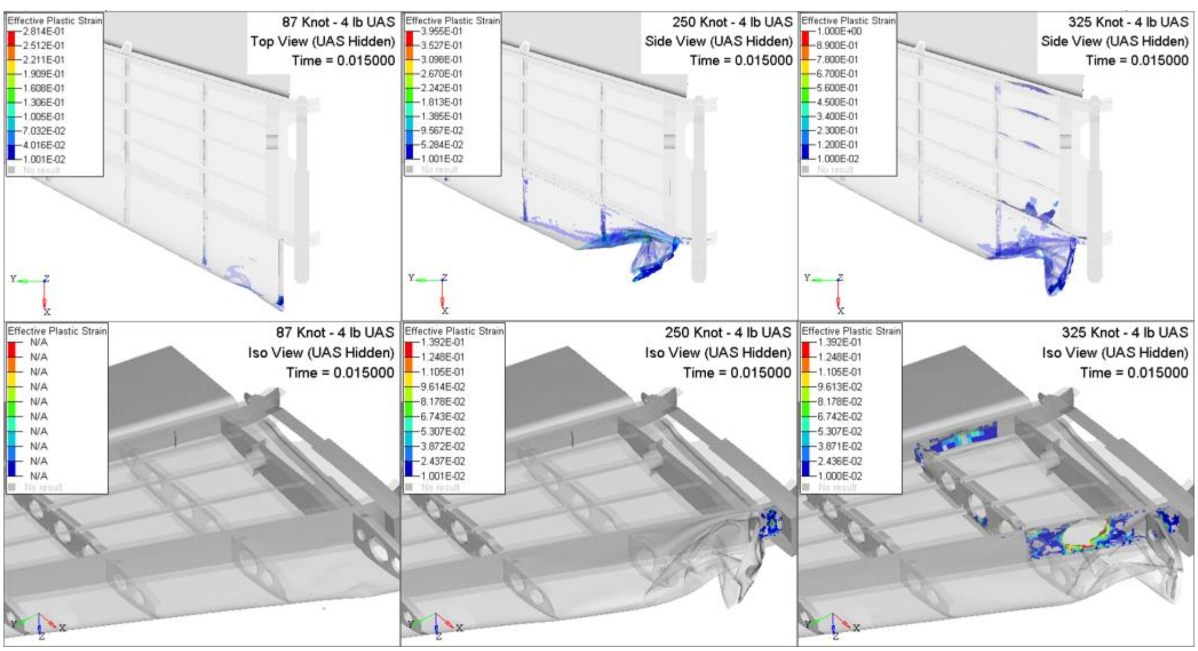

Figure 248. Comparison of horizontal stabilizer damage for BQHL1, BQH1, and BQHC1 – 44.8/128.6/167.2 m/s (87/250/325 knots)

The effective plastic strain after impact to the horizontal stabilizer is plotted in Figure 248 for three different velocities. Gray coloration corresponds to the elements that are below the yield strain limit for the material and a spectrum from blue to red indicates yield strains up to the material failure strains. The effective plastic strain plots in the upper half of Figure 248 show the plastic strain that was predicted for all of the components whereas the lower half shows only the plastic strains in the forward spar, aft spar, and rib members. The high energy cruise velocity case (right) was distinguished from the lower energy simulations (left and center) by the extensive internal damage caused by the UAS penetrating through the leading edge and forward spar. The aft spar of the horizontal stabilizer was also damaged but had no penetrations. As shown in the figure, the effective plastic strain due to an impact to the horizontal stabilizer increased with increasing velocity.

5.4 CONCLUSIONS

In this study, the quadcopter UAS mass and relative impact velocity were varied in order to explore differences in the impact energy of a collision. The kinetic energy of a midair collision between an UAS and two common manned aircraft, a commercial transport jet and a business jet, has been studied in terms of the mass of the UAS and its relative impact velocity. The simulation results were compared to their baseline impact counterparts and damage severity trends were presented.

5.4.1 Mass

The UAS was scaled-up from 1.2 kg (2.7 lb) to 1.8 kg (4.0 lb) in order to assess the potential increase in damage severity imparted by a larger UAS than was characterized in the baseline simulations of chapter 4. The mass of the UAS in this parametric study contributed to a linear increase in the kinetic energy of the collision. The increased kinetic energy resulted in increased damage severity levels in three of the eight simulations and more extensive damage for those cases where the damage level classification remained the same.

5.4.2 Velocity

The velocity of the eight critical baseline simulations (four for each aircraft) was varied to determine impact reactions at typical aircraft landing speeds, as well as in the range of cruise velocities, in order to assess the minimum and maximum damage that can be expected for similar midair collisions. The landing velocity considered for the commercial and business jets was 56.7 m/s (110 knots) and 44.8 m/s (87 knots), respectively, and the cruise velocity was 187.8 m/s (365 knots) and 167.2 m/s (325 knots), respectively. An impact velocity increase (or decrease) in this study contributed to a quadratic increase (or decrease) in the total impact energy. The damage severity levels increased for five of the eight cruise velocity cases and the damage caused was more extensive in those cases where the level remained the same. Similarly, the landing velocity cases showed decreased severity levels in seven of the eight cases studied (all equal or below level 2).

Not surprisingly, the velocity component of the impact energy contributes to a greater amount of damage than does the mass of the UAS but that incremental increases in either parameter correlate to incrementally greater amounts of aircraft damage in terms of both severity and extent.

5.4.3 Future Work

These results indicate that a minimum damage threshold could be near the landing speed of a typical aircraft for an impact with a 1.2 kg (2.7 lb) quadcopter UAS. The spectrum of damage has proven to be highly variable for greater velocities and masses. In order to determine acceptable thresholds or categories for each parameter, it is recommended to perform additional studies that account for a finer gradation of masses and velocities that may be possible for the UAS and aircraft discussed in this investigation.

Furthermore, to reliably extend these results to all UAS and aircraft types it is recommended to investigate other potential combinations of UAS mass and impact velocity. This topic is further discussed in chapter 7.

6. UAS IMPACT COMPARISON TO EQUIVALENT BIRD STRIKES

A parametric study was performed to determine if a mid-air collision with a quadcopter UAS is comparable to a bird strike with an equivalent impact energy. The four critical baseline simulations for each aircraft (chapter 4) were used as a basis for comparing and contrasting the impact kinematics, energy transfers, and damage severity associated with soft-bodied projectiles such as birds.

6.1 BIRD STRIKE REQUIREMENTS

The current regulations regarding bird strike are summarized as follows [46][47]:

- FAA's 14 CFR Part 25.517 or EASA's CS-25.631
    - The airplane must be capable of successfully completing a flight during which likely structural damage occurs as a result of an impact with a 4-pound bird when the velocity of the airplane relative to the bird along the airplane's flight path is equal to Vc at sea level or 0.85Vc at 8,000 feet, whichever is more critical.
    - The damaged structure must be able to withstand the static loads (considered as ultimate loads) which are reasonably expected to occur on the flight. Dynamic effects on these static loads need not be considered.
- FAA's 14 CFR Part 25.631
    - The empennage structure must be designed to assure capability of continued safe flight and landing of the airplane after impact with an 8-pound bird when the velocity of the airplane (relative to the bird along the airplane's flight path) is equal to VC at sea level, selected under §25.335(a).
- FAA's 14 CFR Part 25.775 and EASA's CS-25.775
    - Windshield and supporting structure must withstand with no penetration the bird impact conditions specified in 25.631.
- FAA's 14 CFR Part 23.775 and EASA's CS-23.775
    - GA Aircraft are required to demonstrate single bird impact resistance of up to 0.91 kg at maximum approach flap speed and at least one pane with sufficient forward vision remaining to allow continued safe flight.

6.2 COMPARISON STUDY

In order to determine any possible discrepancies between bird strikes and quadcopter UAS-aircraft midair collisions, a study was performed for each of the critical cases identified in chapter 4. The quadcopter UAS was replaced with a simulated gelatin bird of equivalent mass. The NIAR has previously conducted numerous simulations of bird strike events and compared the results with physical testing, also utilizing the gelatin bird substitutes [32]. Smooth Particle Hydrodynamics (SPH) [21] nodes were used to represent the gelatin bird models. The bird substitute was modeled as a cylinder with a semispherical cap. The kinematics of the substitute bird correlates well with the impact behavior observed in both bird strike testing and simulation. In each bird strike simulation, the boundary and initial conditions used in the UAS critical baseline cases were applied to the bird and aircraft target region to represent a direct replacement of the UAS projectile with the bird substitute.

Table 32 presents the simulation matrix with all the bird strike comparisons studied in this chapter. 2.7 lb (1.2 kg) and 4 lb (1.8 kg) bird FE models were used in eight different simulations, with identical initial and boundary conditions as the critical load cases presented in chapter 4. These simulations were compared with the simulations presented in chapters 4. and 5. The following section summarizes all the simulation results and some representative examples of observed differences in damage.

Table 32 Load case definition of UAS impact comparison to bird strike

	Commercial Transport Jet				Business Jet			
	Vertical Stabilizer	Horizontal Stabilizer	Wing Leading Edge	Windshield	Vertical Stabilizer	Horizontal Stabilizer	Wing Leading Edge	Windshield
Baseline UAS 2.7 lb (1.2 kg)	CQV3	CQH3	CQW1	CQC1	BQV2	BQH1	BQW1	BQC1
2.7 lb (1.2 kg) Bird	CB2V3	CB2H3	CB2W1	CB2C1	BB2V2	BB2H1	BB2W1	BB2C1
Scaled UAS 4.0 lb (1.8 kg)	CQsV3	CQsH3	CQsW1	CQsC1	BQsV2	BQsH1	BQsW1	BQsC1
4 lb (1.8 kg) Bird	CB4V3	CB4H3	CB4W1	CB4C1	BB4V2	BB4H1	BB4W1	BB4C1

6.2.1 1.2 kg (2.7 lb) Bird – Simulation Results

The four aircraft regions for each aircraft studied in chapter 4. were selected to perform a total eight simulations with a 1.2 kg (2.7 lb) bird FE model. Results were compared to those for the critical cases outlined in chapter 4. and are presented in APPENDIX E. Table 33 presents the impact severity levels for the scaled bird model to the respective baseline simulation.

For all cases, the quadcopter UAS created equal or more damage than the corresponding bird. The cases involving the horizontal stabilizer and wing of the commercial transport jet and the vertical stabilizer and wing of the business jet demonstrated a reduction in the level of severity when impacted by the simulated bird as opposed to the UAS model.

Table 33 UAS and bird impact simulation results

	Commercial Transport Jet				Business Jet			
	Vertical Stabilizer	Horizontal Stabilizer	Wing	Windshield	Vertical Stabilizer	Horizontal Stabilizer	Wing	Windshield
Baseline 1.2 kg (2.7 lb) UAS	Level 3	Level 4	Level 3	Level 2	Level 3	Level 4	Level 3	Level 2
1.2 kg (2.7 lb) Bird	Level 3	Level 2	Level 2	Level 2	Level 2	Level 2	Level 2	Level 1

6.2.1.1 Commercial Jet

Typical results for the simulated 1.2 kg (2.7 lb) UAS and bird strike impacts to the commercial transport jet are presented in this section. The remaining impact simulation results can be found in Appendix E.1 . The following sections detail the impact characteristics of each projectile with images showing the resultant damage and discussion of the associated damage mechanisms.

Figure 249 depicts the kinematics of the simulated airborne collisions involving the horizontal stabilizer of a commercial transport jet, a 2.7 lb (1.2 kg) UAS in the upper half of the figure and a 2.7 lb (1.2 kg) bird in the lower half.

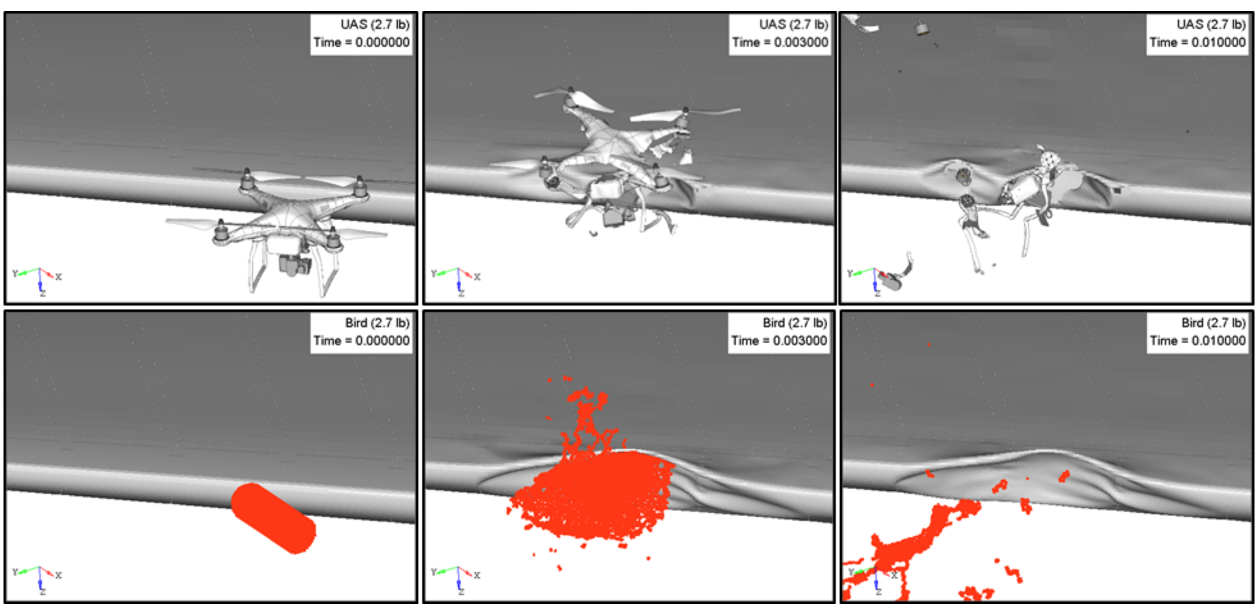

Figure 249. Kinematics of a commercial transport jet horizontal stabilizer impacted by an UAS (left) and a bird (right), of 2.7 lb (1.2 kg) – CQH3 vs. CB2W1

The idealized bird impacted the leading edge of the horizontal stabilizer; the mass of the bird was distributed throughout the impact region in a fluid-like fashion, allowing to follow the path of least resistance and to deflect away from the solid boundary of the aircraft. In contrast, the UAS impacts resulted in highly localized deformation/failure in the impact region and generally did not conform to the contour of the leading edge. The kinematics for the remaining cases is similar to that of Figure 249 and can be found in Appendix E.1 .

Figure 250 illustrates the damage sustained by the horizontal stabilizer of a commercial transport jet after impact with a 2.7 lb (1.2 kg) UAS, on the left-hand side of the figure, and a 2.7 lb (1.2 kg) bird on the right.

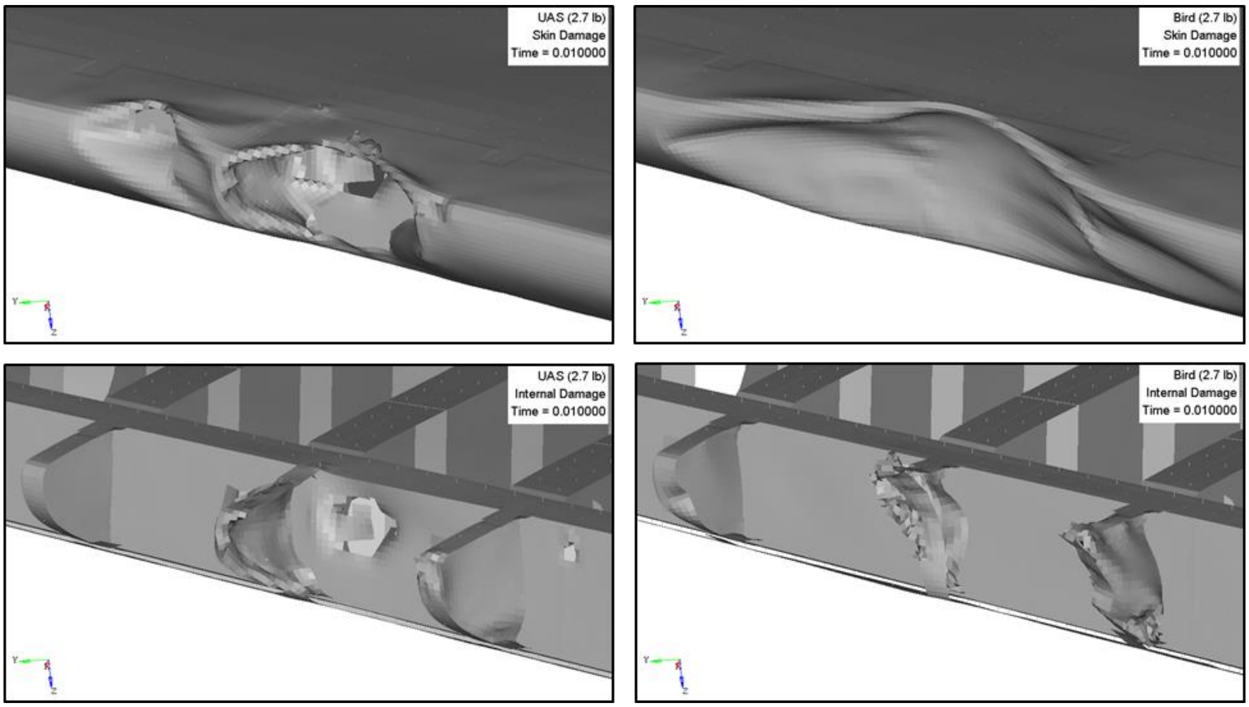

Figure 250. Comparison of damage on a commercial transport jet horizontal stabilizer, produced by a 2.7 lb (1.2 kg) UAS (left) and bird (right) impact at 128.6 m/s (250 knots)

The simulated bird strike in Figure 250 created more distributed skin deformation of the leading edge of the horizontal stabilizer indicative of a soft-bodied impact. The UAS, on the other hand, created a more compact region of intense damage with skin penetration and more extensive damage to internal components. Such damage is an indication that the impact involved concentrated masses composed of rigid or dense materials. The simulated bird damaged the leading edge ribs to a greater degree than the UAS, but this damage is considered less critical than the skin and forward spar perforations caused by the UAS.

Similarly, Figure 251 presents the damage sustained by the commercial transport jet wing leading edge. As with the horizontal stabilizer, the wing leading edge was dented by the bird strike impact, with some substructural deformation. This damage is considered less critical than that of the UAS impact, which resulted in a fracture in the leading edge skin and substructure. This penetration increases the potential for a significant fraction of the UAS to become lodged in the airframe.

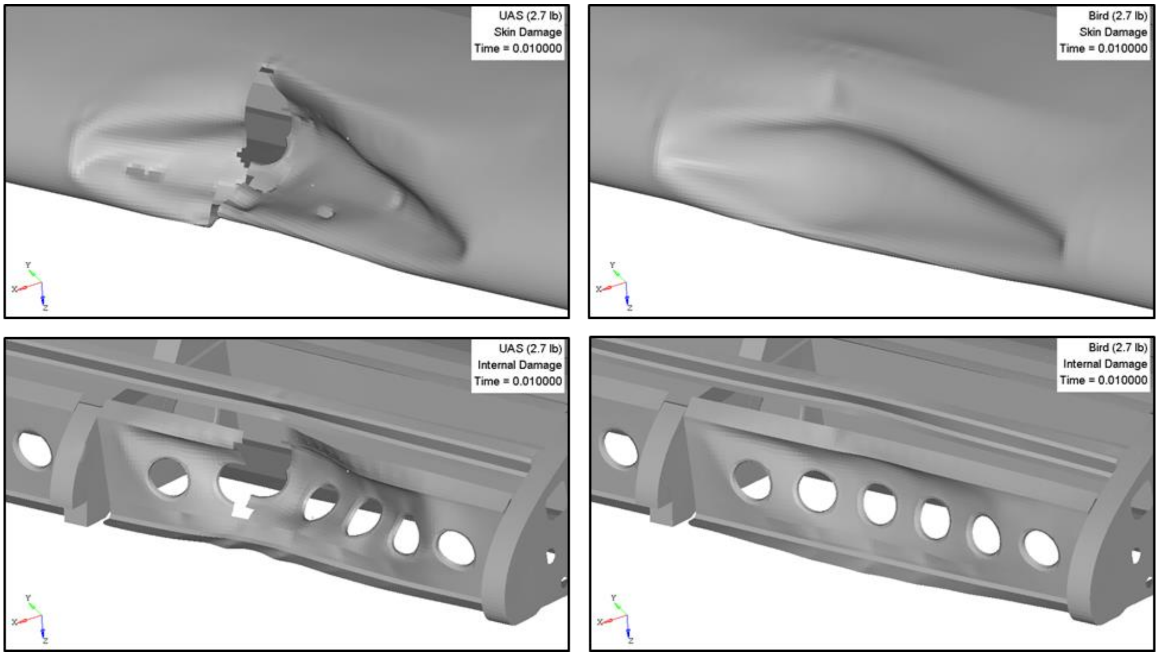

Figure 251. Comparison of skin and internal damage produced by a 2.7 lb (1.2 kg) UAS and Bird after impact with a commercial transport jet wing leading edge

6.2.1.2 Business Jet

As with the commercial transport jet, typical results for simulated 1.2 kg (2.7 lb) UAS and bird impacts to the business jet are presented in this section. The remaining impact simulations can be found in Appendix E.2 . Figure 252 and Figure 253 present the resultant damage in the vertical stabilizer and wing of the business jet due to impact with 2.7 lb (1.2 kg) UAS and bird projectiles.

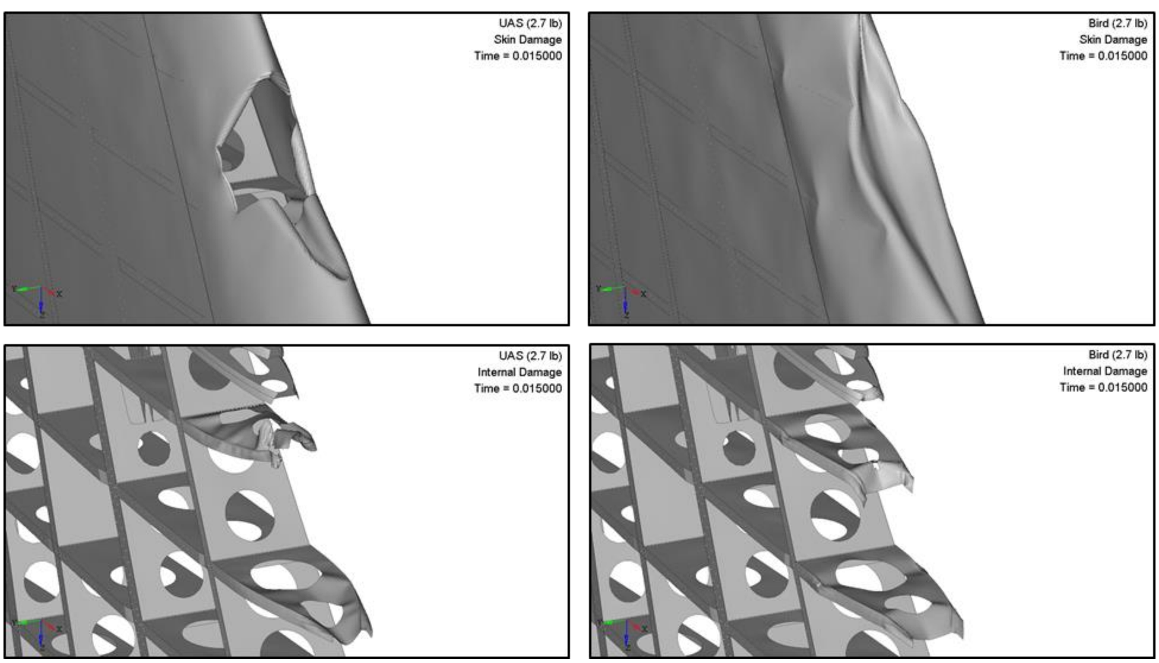

Figure 252. Comparison of skin and internal damage produced by a 2.7 lb (1.2 kg) UAS and Bird - business jet vertical stabilizer

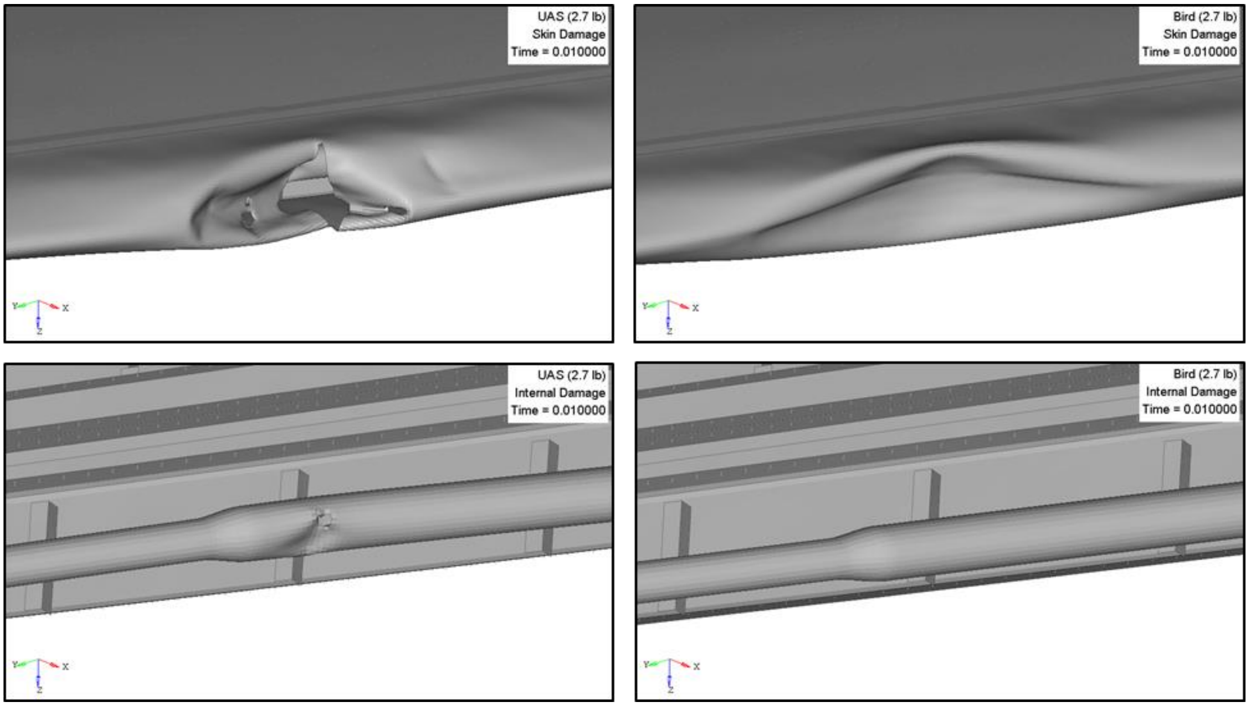

Figure 253. Comparison of skin and internal damage produced by a 2.7 lb (1.2 kg) UAS and Bird after impact with a business jet wing leading edge

The damage sustained by both the wing leading edge and the vertical stabilizer present similarities to the commercial transport jet scenarios. Both structures sustained an extensive permanent deformation of the skin by the bird strike impact, showing also some deformed substructure. In contrast, the UAS impact resulted in a perforation of the leading edge skin with partial penetration of the UAS. Additionally, in the case of the vertical stabilizer, the UAS impact produced damage to components of the substructure.

Consequently, the damage produced by the bird strike was considered less critical than that of the UAS impact in both cases.

6.2.2 4 lb Bird – Simulation Results

The four impact locations for each aircraft studied in chapter 4. were selected to perform eight additional FE simulations with a 4.0 lb (1.8 kg) bird model. Results were compared to those for the critical cases outlined in chapter 5. and are presented in APPENDIX E. Table 34 presents the impact severity levels of the scaled UAS with respect to the corresponding baseline simulation.

For each case, the UAS created equal or more damage than the bird. This corresponded to a reduction in the level of severity when impacted by the bird as opposed to the UAS model. In these cases, the bird strike was not comparable to an UAS impact.

Table 34 Scaled-up UAS and bird impact simulation results

	Commercial Transport Jet				Business Jet			
	Vertical Stabilizer	Horizontal Stabilizer	Wing	Windshield	Vertical Stabilizer	Horizontal Stabilizer	Wing	Windshield
Upscaled 4 lb (1.8 kg) UAS	Level 3	Level 4	Level 3	Level 3	Level 4	Level 4	Level 3	Level 2
4 lb (1.8 kg) Bird	Level 3	Level 2	Level 2	Level 2	Level 2	Level 2	Level 2	Level 1

6.2.2.1 Commercial Jet

Typical results for simulated 1.8 kg (4.0 lb) UAS and bird impacts to the commercial transport jet are presented in this section. The remaining impact simulations can be found in Appendix E.3 . The following sections detail the impact characteristics of each projectile with images showing the resultant damage and discussion of the associated damage mechanisms.

Figure 254 and Figure 255 show the typical damage associated with quadcopter UAS impacts (left-hand side of the figures) compared to the damage that typical for bird strikes (right-hand side).

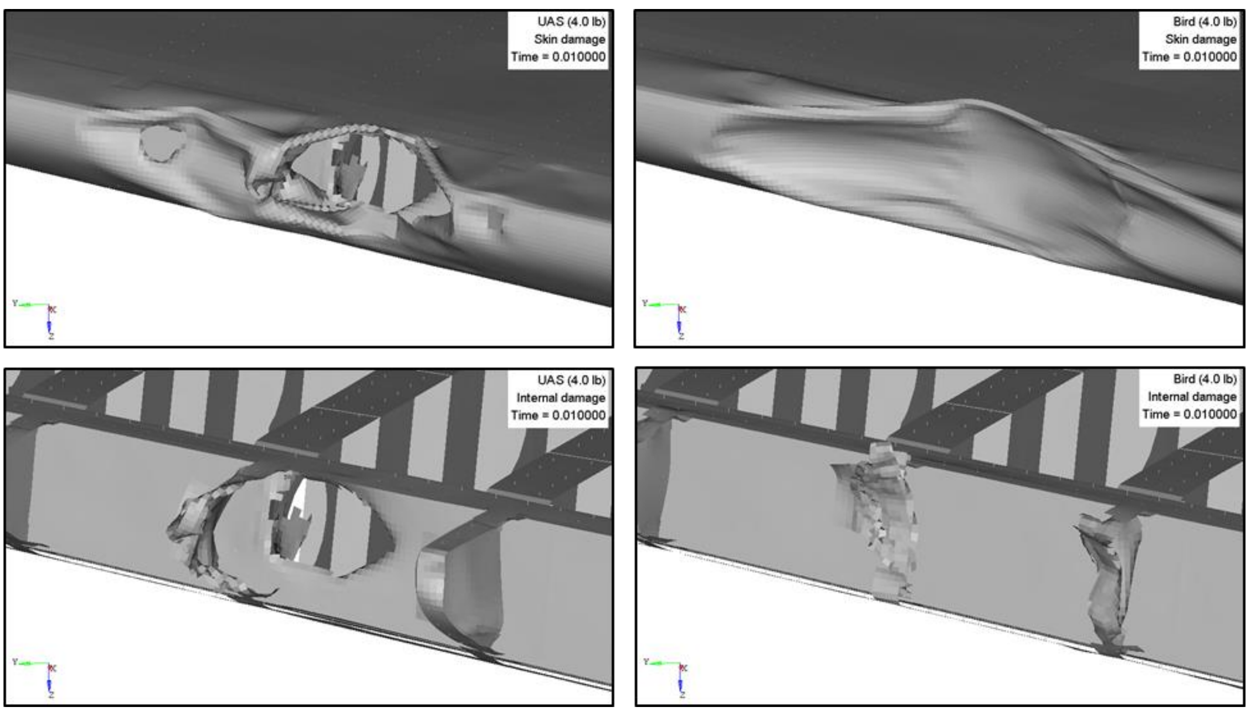

Figure 254 Comparison of skin and internal damage produced by a 4.0 lb (1.8 kg) UAS and Bird after impact with a commercial transport jet horizontal stabilizer

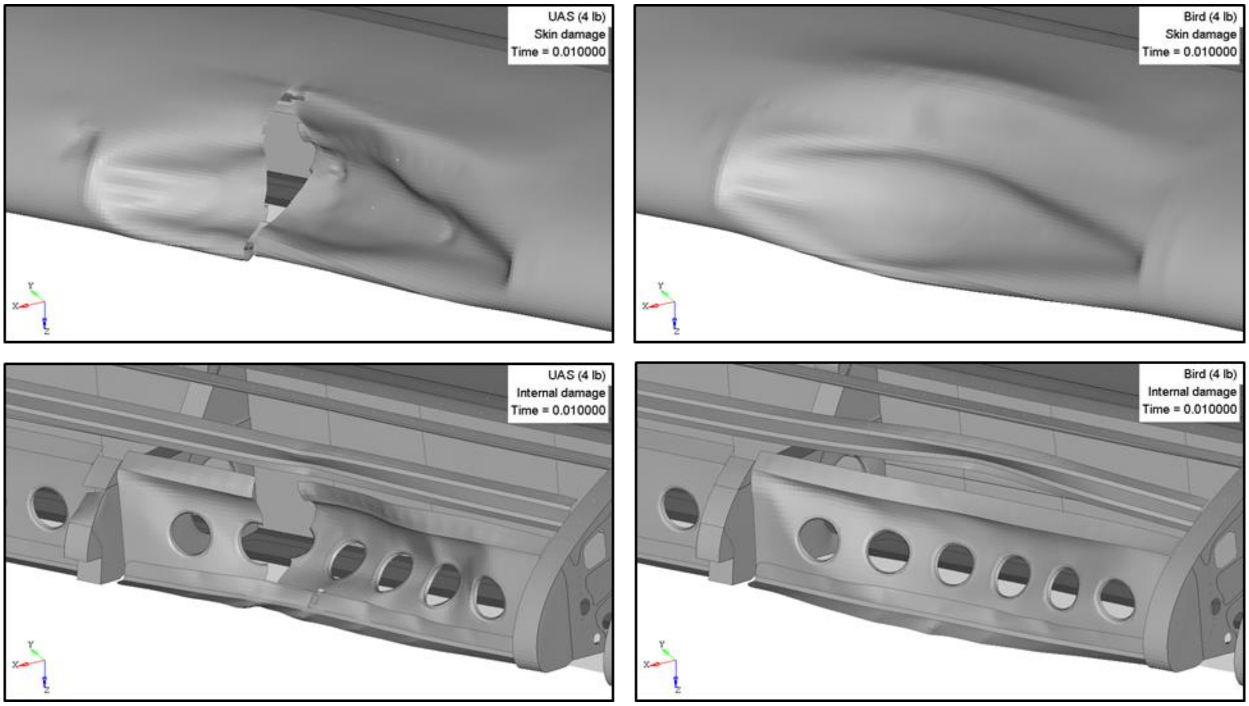

Figure 255 Comparison of skin and internal damage produced by a 4.0 lb (1.8 kg) UAS and Bird after impact with a commercial transport jet wing leading edge

In the case of the horizontal stabilizer, the skin, forward spar and adjoining rib structure were all penetrated by the UAS, indicating that the relatively high mass components (motor, battery, and camera) remained intact and energetic enough to cause successive instances of severe damage. This is in contrast to the bird impact where the kinetic energy of the projectile was deflected by the deformed leading edge skin.

The same trends were seen in the wing leading edge cases; the bird caused skin deformations but was ultimately deflected due to its relatively soft composition while the UAS creates discreet dents and penetrations that propagate into large-scale openings, allowing additional structural members to be impacted.

6.2.2.2 Business Jet

As with the commercial transport jet, typical results for simulated 1.8 kg (4.0 lb) UAS and bird impacts to the business jet are presented in this section. The remaining impact simulations can be found in Appendix E.4 .

Figure 256 and Figure 257 present the resultant damage in the vertical stabilizer and the wing of the business jet due to impact with 4.0 lb (1.8 kg) UAS and bird projectiles. Common features are recognizable upon inspection, torn leading edge skin and discreet impact damage with the UAS collisions and distributed skin deformations and damage to connected members associated with the bird strikes. In the case of the vertical stabilizer, the UAS was able to intrude into the airframe and damage the forward spar. For the wing, the UAS was lodged in the opening that it created in the leading edge.

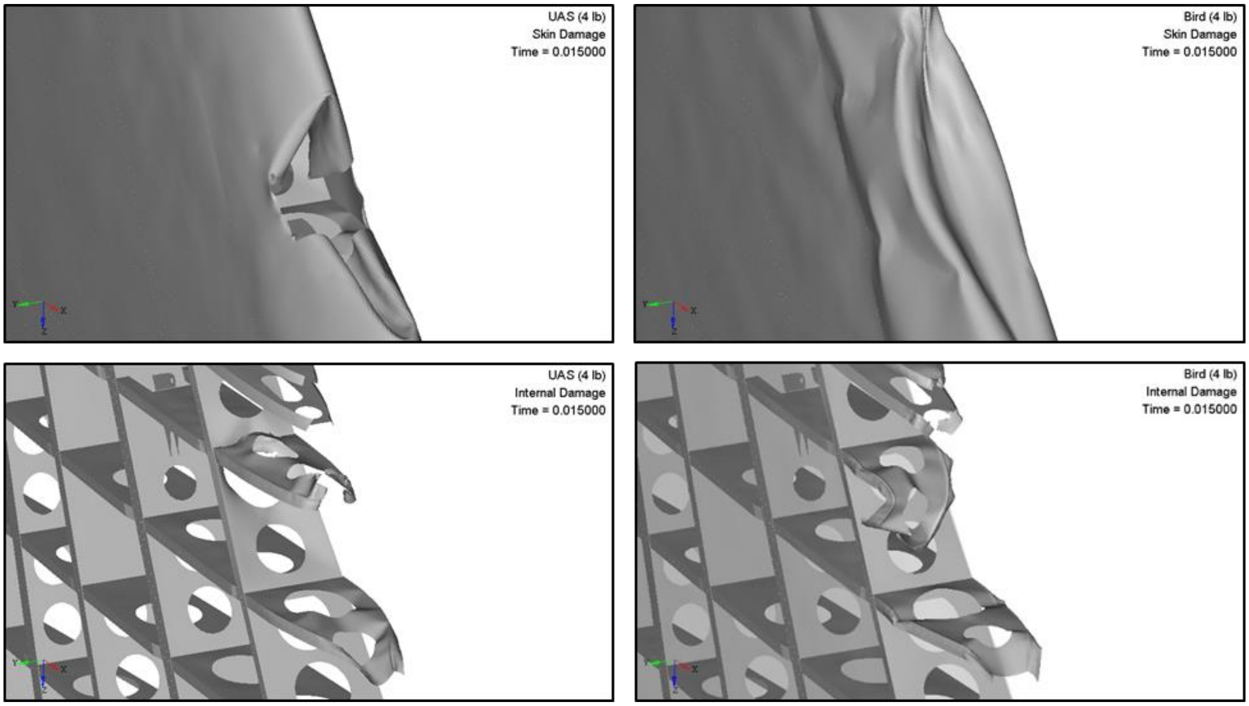

Figure 256. Comparison of skin and internal damage produced by a 4.0 lb (1.8 kg) UAS and Bird after impact with a business jet vertical stabilizer

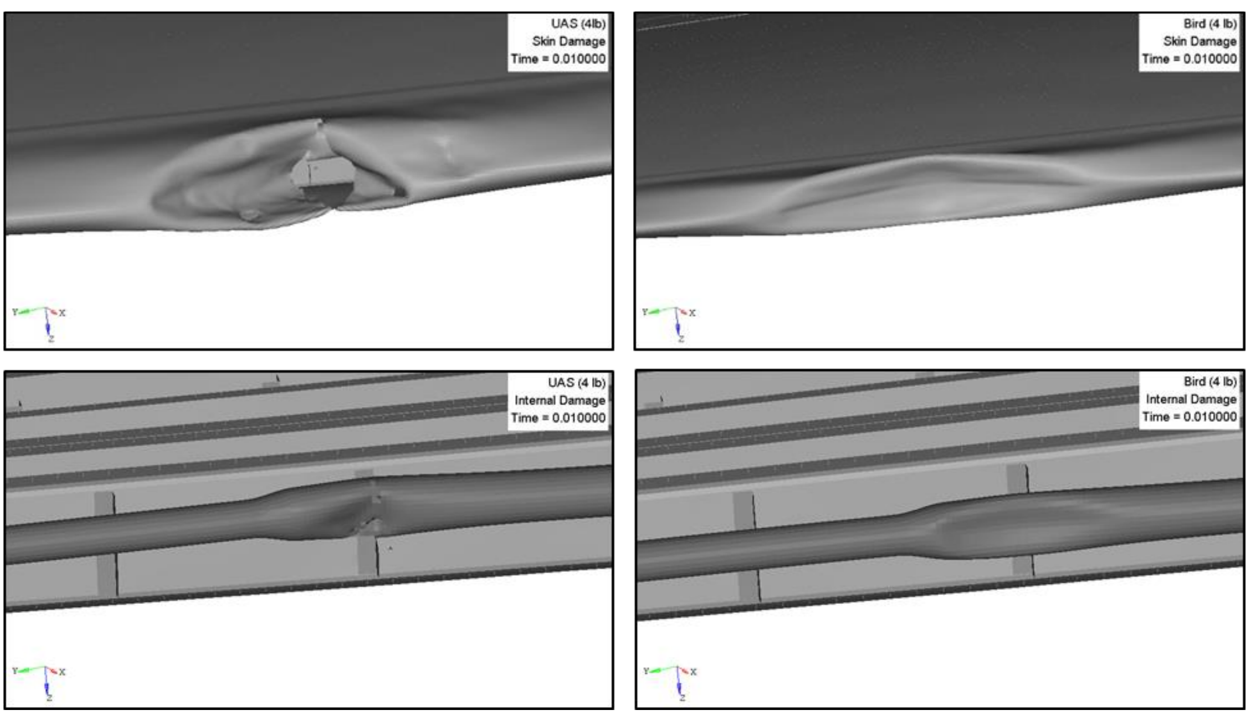

Figure 257. Comparison of skin and internal damage produced by a 4.0 lb (1.8 kg) UAS and Bird after impact with a business jet wing leading edge

6.3 CONCLUSIONS

This study assessed whether a quadcopter UAS impact can be considered equivalent to a bird strike. The simulations utilized identical boundary conditions and impact energies in order to demonstrate the behavior of the two impact types.

Airborne collisions involving hard-bodied projectiles have characteristic features that distinguish them from bird strikes. Primarily, the damage zones for the UAS showed notable dents and penetrations due to the discrete masses and rigid, dense materials. In most cases, the initial dents and perforations caused by the impact of the motor allowed significant fractions of the UAS to penetrate the skin of the aircraft and damage internal components (including primary structure) in a majority of the simulations. This is considered level 4 damage while the bird impact was classified as level 3. This trend was typical of the two impact types.

6.3.1 Summary

Quadcopter UAS impacts are likely to cause more damage than bird strikes of equivalent energy. The UAS impacts were generally associated with greater damage levels due to the hard-bodied mechanical construction of the UAS, its components made of dense, rigid, materials and its discrete distribution of masses. The initial impact penetrations (caused by contact with a dense, rigid, motor) were exacerbated as subsequent UAS components, such as the battery pack, impacted the aircraft structure causing progressively more and more damage including UAS ingress into the airframe.

6.3.2 Future Work

The results of this study indicate that the two projectile types have different characteristics and that the impact energy is only one of the factors that predict damage severity. Simulations using other UAS configurations may provide additional insights into the impact dynamics of midair collision.

7. COMPARISON BETWEEN BIRD, QUADCOPTER AND FIXED-WING UAS IMPACTS

An additional study was performed to determine if a mid-air collision between a fixed-wing UAS and a given aircraft is comparable to similar collisions involving quadcopter UASs and birds with an equivalent impact energy. One critical baseline simulation was used as a basis for comparing the impact kinematics, energy transfers, and damage severity associated with each projectile.

7.1 UAS CONFIGURATION COMPARISON

The range of UAS configurations currently available for consumer applications is extensive, encompassing many configurations of multicopter layouts as well as fixed-wing type puller/pusher UAS designs. This study utilized the quadcopter UAS FE model used in preceding chapters as well as the fixed-wing UAS FE model presented in [2]. Figure 258 presents a three-view CAD representation of the fixed wing UAS.

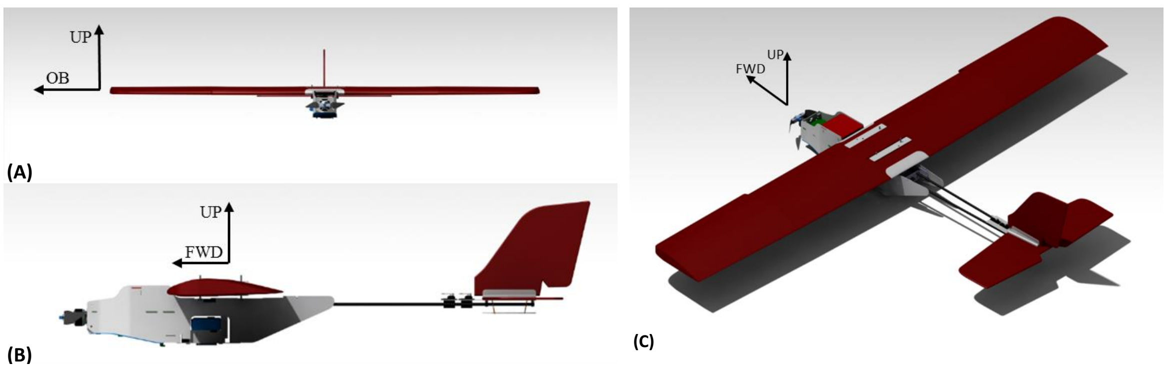

Figure 258 Fixed-wing UAS CAD model views – forward, side, and isometric

One primary feature of the fixed-wing design, as opposed to the quadcopter, is that the critical masses (motor, battery, and camera) are generally aligned with the flight direction. For this reason, the most damaging impact orientation is assumed a head-on collision.

7.2 COMPARISON STUDY

Table 35 presents the simulation matrix for the comparisons studied in this chapter. 4.0 lb (1.8 kg) UAS and bird FE models were used in three different simulations. Identical initial and boundary conditions were applied consistent with the critical business jet load case presented in chapter 4.

Table 35 Load case definition

	4.0 lb (1.8 kg) Bird	4.0 lb (1.8 kg) (Scaled-up) Quadcopter UAS	4.0 lb (1.8 kg) Fixed-wing UAS
Business Jet Vertical Stabilizer	BB4V2	BB4V2	BFV2

The simulation setup is depicted in Figure 259 for the scaled-up quadcopter UAS. The remaining fixed-wing and bird impacts utilize the same target location as the quadcopter.

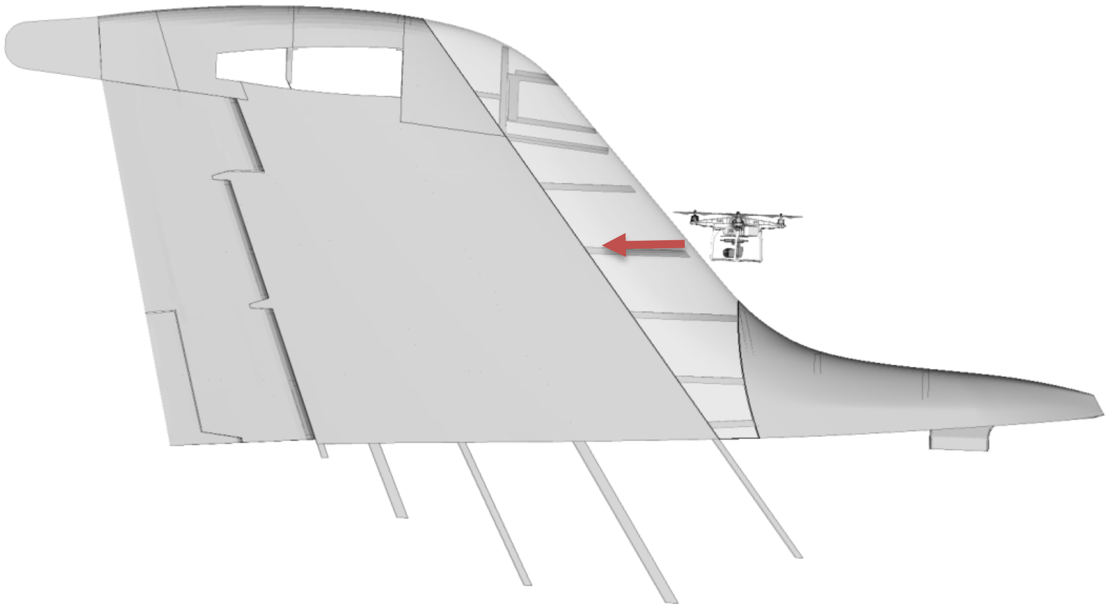

Figure 259. UAS impact location – business jet vertical stabilizer

7.2.1 Simulation Results – Bird, Quadcopter and Fixed-Wing UASs

The vertical stabilizer of the business jet studied in chapter 4. was selected to perform a total of three simulations with 1.8 kg (4.0 lb) projectile FE models. Table 36 presents the impact severity levels for the bird, scaled-up quadcopter UAS, and baseline fixed-wing UAS simulations.

Table 36 Bird and UAS impact simulation results

	4.0 lb (1.8 kg) Bird	4.0 lb (1.8 kg) (Scaled-up) Quadcopter UAS	4.0 lb (1.8 kg) Fixed-wing UAS
Business Jet Vertical Stabilizer	Level 2	Level 4	Level 4

The impact kinematics of the three simulations is illustrated in Figure 260. The distributed damage associated with a bird impact (top) is characteristic of the bird strike results discussed in chapter 6. As shown in Figure 261, the idealized bird projectile (left column) created a dent in the leading edge skin, which extended over a longer region of the vertical stabilizer than the two UAS impacts but did not penetrate the skin. The scaled-up quadcopter impact (middle column) resulted in critical damage and permanent deformation to the front spar along with intrusion of the UAS into the airframe. Similarly, the fixed-wing UAS collision resulted in penetration of the leading edge skin, significant permanent deformation of the adjoining structure, but with less damage to the front spar (right column) than the scaled-up quadcopter.

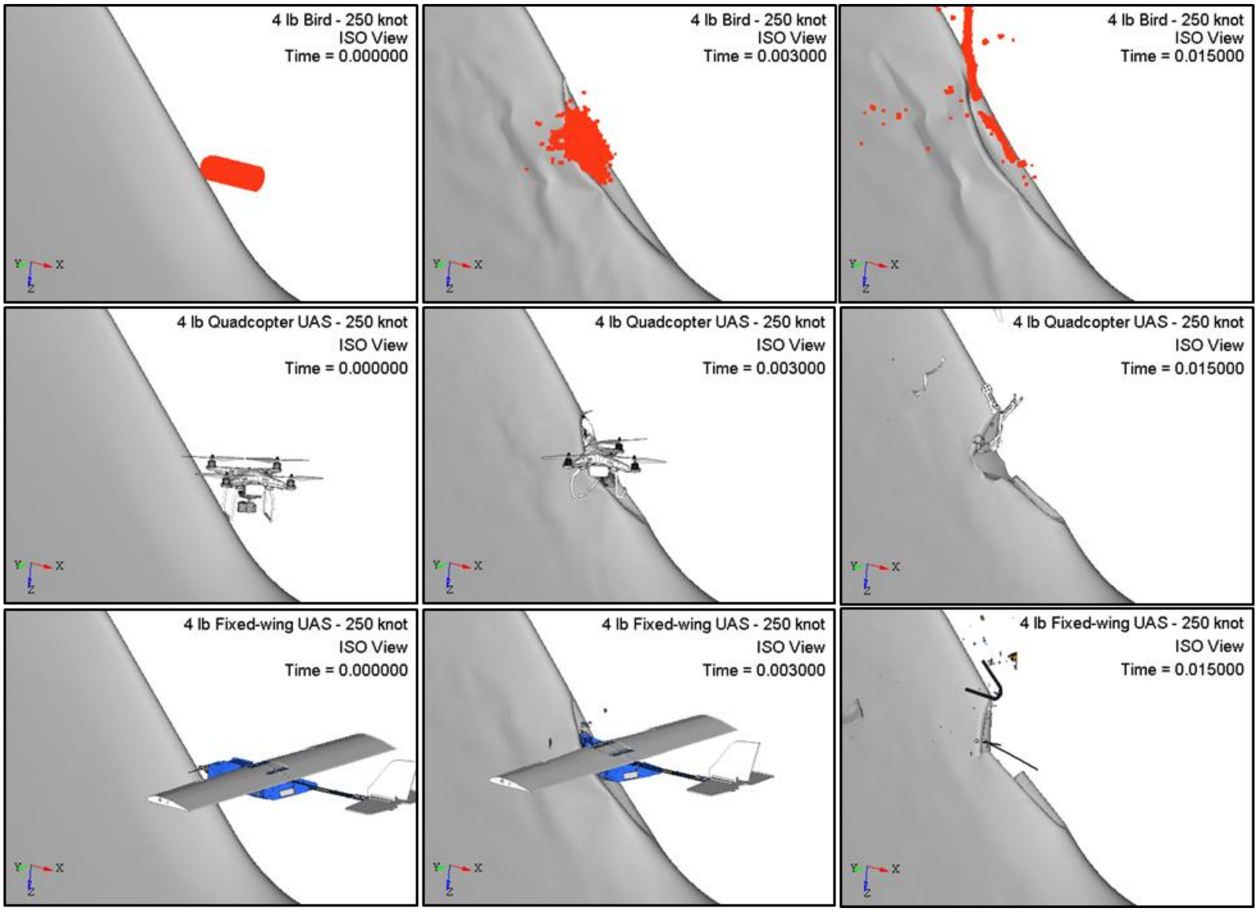

Figure 260 Comparison of impact kinematics for 4.0 lb (1.8 kg) projectiles: bird (top), quadcopter (middle), and fixed-wing UAS (bottom)

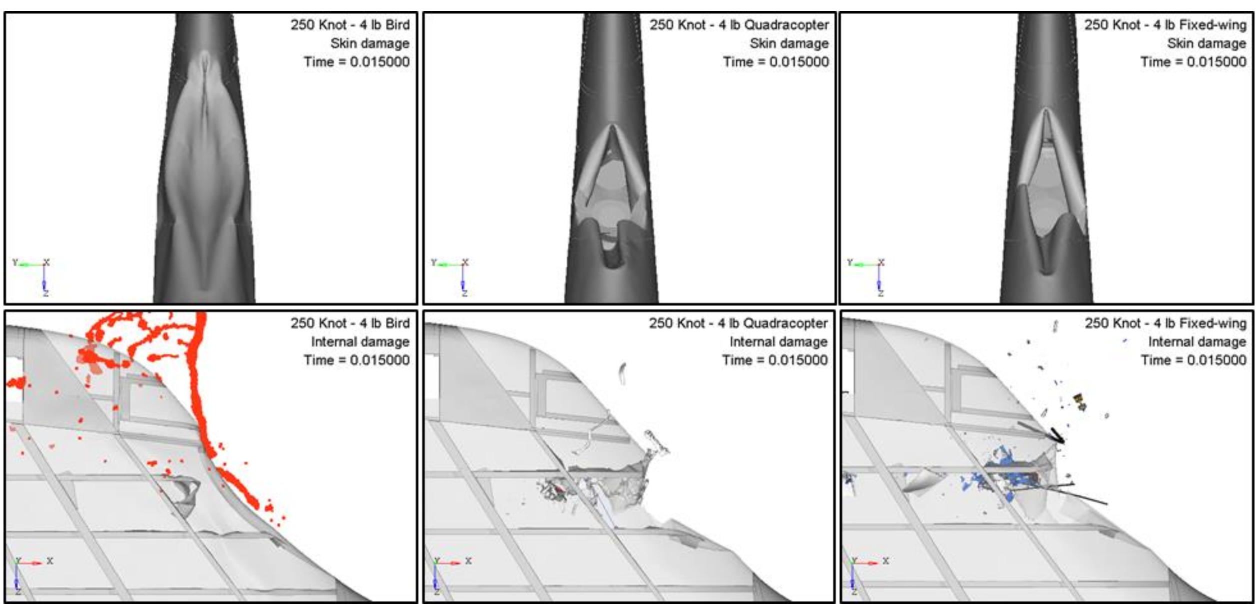

Figure 261 Comparison of skin and internal damage produced by 4.0 lb (1.8 kg) projectiles: bird (left), quadcopter (middle), and fixed-wing UAS (right)

Figure 262 shows close-up views of the impacted region for each projectile (top) and effective plastic strain plots for the front spar (bottom). The contact force and impulse of each impact are shown in Figure 263. Note that the bird strike simulation creates the largest contact force magnitude but that this is not associated with corresponding damage levels. The energy balance plots shown in Figure 264 indicate that each of the three projectiles have differing ratios for each energy, attributed to their differing configurations and constructions.

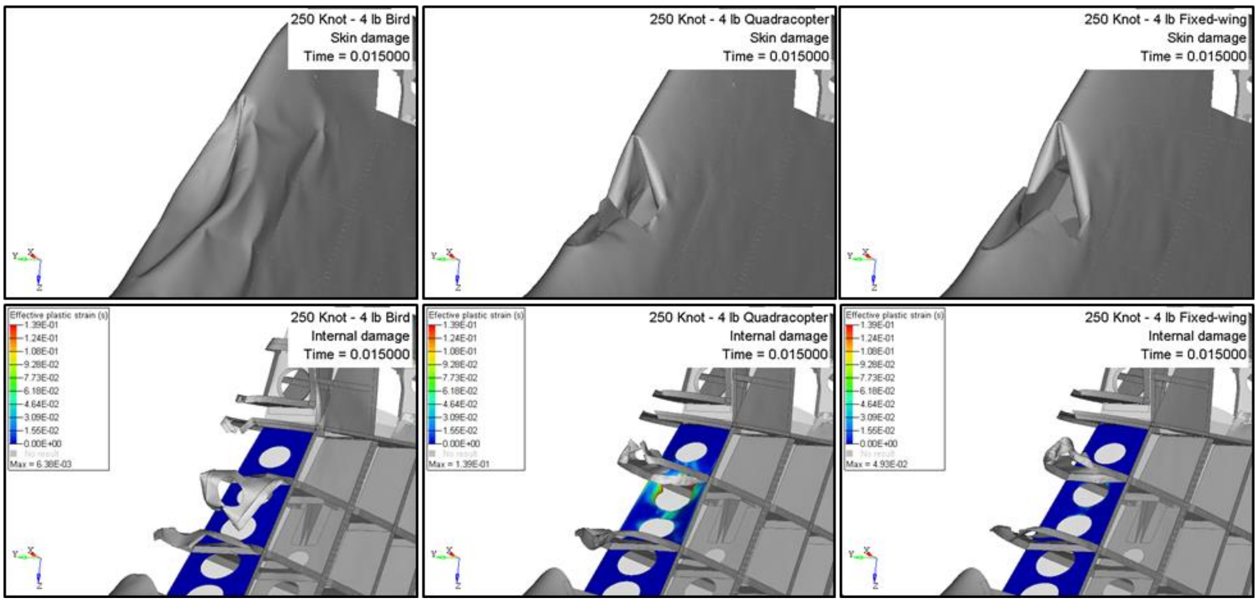

Figure 262 Comparison of skin and internal damage produced by 4.0 lb (1.8 kg) projectiles: bird (left), quadcopter (middle), and fixed-wing UAS (right)

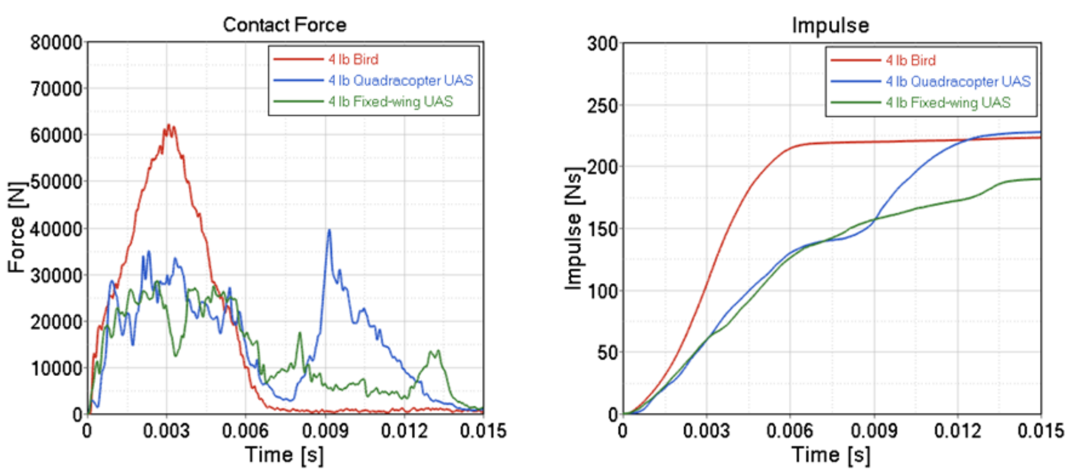

Figure 263 Contact force and impulse plots produced by 4.0 lb (1.8 kg) projectiles: bird, quadcopter and fixed-wing UAS

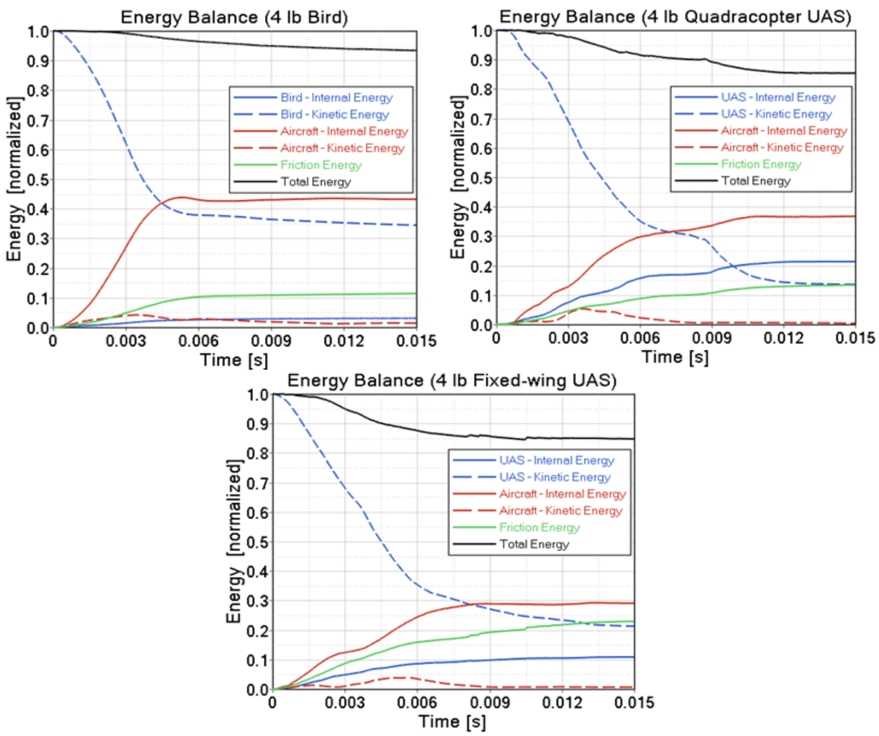

Figure 264 Normalized energy balance plots produced by 4.0 lb (1.8 kg) projectiles: bird, quadcopter, and fixed-wing UAS

7.2.2 Comparison of UAS Architectures – Quadcopter and Fixed Wing

The fixed-wing UAS was utilized in impact simulations at the same impact locations and velocity (128.6 m/s (250 knots)) as the baseline quadcopter simulations presented in chapter 4. The spatial distribution of damage at a given impact location on the aircraft was distinct for the two UAS architectures. Moreover, the locations on the aircraft with critical damage were also different in many instances for quadcopter and fixed-wing UAS impact. However, damage initiation and propagation due to aligned localized rigid masses tended to be similar for both UAS configurations. The damage levels sustained at identical impact locations for the fixed-wing and scaled-up quadcopter UASs are shown in Table 37.

Table 37 Quadcopter and fixed-wing simulation results

	Commercial Transport Jet				Business Jet			
	Vertical Stabilizer	Horizontal Stabilizer	Wing	Windshield	Vertical Stabilizer	Horizontal Stabilizer	Wing	Windshield
Scaled-up Quadcopter 1.8 kg (4.0 lb)	Level 3	Level 4	Level 3	Level 3	Level 4	Level 4	Level 3	Level 2
Baseline Fixed-wing 1.8 kg (4.0 lb)	Level 3	Level 4	Level 3	Level 2	Level 4	Level 4	Level 3	Level 3

7.3 CONCLUSIONS

This study assessed whether airborne collisions involving 1.8 kg (4.0 lb) bird, quadcopter UAS, and fixed-wing UAS can be considered equivalent to one-another. The simulations utilized identical initial and boundary conditions at an impact velocity of 128.6 m/s (250 knots).

Airborne collisions involving hard-bodied projectiles have characteristic features that distinguish them from bird strikes. The dense, rigid, components of both UAS models perforated the aircraft skin, which allowed a significant fraction of the remaining mass of the UAS to enter the airframe and damage the internal aircraft structural components. The data shown in Table 37 indicates that the two distinct UAS architectures impart similar levels of damage, which generally exceeded that for energetically similar bird strikes.

7.3.1 Future Work

In order to determine the similarities and differences between other UAS types, it is recommended to perform additional simulations that account for more UAS configurations and masses.

8. CONCLUSIONS

According to the latest industry forecast studies, the UAS market volume is expected to reach 4.7 million units by 2020 [1]. Nonetheless, safety, regulatory, social, and technical challenges need to be addressed before the sight of an unmanned aircraft in the sky becomes as common and accepted by the public as its manned counterparts. The effect of an airborne collision between an UAS and a manned aircraft is a concern to the public and government officials at all levels. The primary goal of regulating UAS operations into the NAS system is to ensure an appropriate level of safety. Research is needed to define airborne hazard severity thresholds for collisions between unmanned and manned aircraft.

The results presented in this report focus the initial effort on analyzing a small quadcopter UAS configuration impacting on a typical commercial transport jet and a typical business jet certified under *14CFR Part 25 or Part 23* requirements [47] [46].

This research will help determine airworthiness requirements for unmanned aircraft based on their potential hazard severity to other airspace users in the NAS. The resulting severity thresholds will be based on UAS characteristics (kinetic energy, structure, shape, materials, etc.) under credible encounter scenarios and will provide for test criteria used to evaluate applicable operational and airworthiness standards. UAS that meet test criteria based on thresholds for these characteristics may be certified as airworthy under different criteria than other UAS [19].

The main research questions being answered through this research are [19]:

- What are the hazard severity criteria for an UAS collision (weight, kinetic energy, etc.)?
- What is the severity of an UAS collision with an aircraft in the air?
- Can an UAS impact be classified similar to a bird strike?
- Will an UAS impacting an engine be similar to a bird engine ingestion?
- What are the characteristics of an UAS where it will not be a risk to an aircraft collision in the air?
- Can the severity of an UAS mid-air collision with an aircraft be characterized into categories based on the UAS and what would those categories look like?

It is important to emphasize that the intent of this research was not to do an assessment of already certified products (*e.g. 14 CFR Part 23/25/27/29/33*) but to analyze the characteristics of small UAS that contribute to the damage of the airframe of manned aircraft as a result of an airborne collision.

8.1 TECHNICAL APPROACH

Due to the complexity of the problem, full-scale test article availability, time and budget constraints, it was decided to conduct the R&D effort by using the NIAR physics based FE modeling techniques based on the Building Block Approach methodology. Conducting these type of impact studies by analysis provides critical insight into the crashworthiness response of the target and the projectile. With physical testing, it is not possible to quantify internal energy distributions during the transient dynamic impact. It is also very difficult to conduct large-scale tests involving target air vehicles and UAS projectiles and to control the exact impact locations and attitude of the UAS projectile.

8.1.1 Building Block Approach FEA Model Development and Verification

In order to build the UAS and target aircraft FE models, the NIAR followed a physics based modeling approach. This methodology takes advantage of advances in computational power, the latest computational tools, years of research in understanding the fundamental physics of the crashworthiness event, generated test-to-test variability data, and Verified & Validated (V&V) building block modeling methods.

The building block approach is the incremental development of analysis and supporting tests where typically there is an increase in size and complexity of the test article and a decrease in number of supporting tests. In order to develop this method it is necessary to have a good understanding of the physics and testing variability from the coupon to the system level. Full-scale level test results do not drive the definition of the numerical model; it is driven by a predefined, verification and validation building block modeling methodology.

Using this approach, simulations should be able to predict the system level test results within the scatter of the physical system test results. An objective verification criterion is used to evaluate the numerical models, where the correlation level between simulation and testing is defined by an understanding of the test-to-test variability of the physical system under evaluation.

8.1.2 Verification of the FEA Model: Coupon to Sub-Assembly Level Testing

A FE model of a typical quadcopter UAS was developed for the airborne collision studies. Different component level tests were conducted to verification the UAS FE model. The following paragraphs will summarize the testing conducted as well as identify further areas of work.

Coupon Level Testing:

- Basic coupon level testing verification was performed for the various material systems of the UAS
- Coupon level verification studies from technical literature were conducted.

Component Level Testing:

- The polycarbonate UAS body was subject to an impact of 110 J in a drop tower test. The event was filmed with high-speed cameras, and the reaction load and respective impulse were measured and recorded.
- The UAS's battery, camera and motors were tested in a compressed air gun facility under impact velocities similar to those of the midair collision being studied in this project, between 110 and 250 knots (56.6 and 128.6 m/s). The kinematics were captured with high-speed cameras, the reaction loads and the strains in the impacted panel were measured with four load cells and thirteen strain gages respectively and a DIC system that captured the displacements of the impact area.

Sub-Assembly Level Testing:

- The full UAS assembly (excluding the battery) was released from a height of 17 feet (5.18 m) and impacted into a rigid flat plate, where the reaction loads were measured and recorded. The kinematics was captured with high-speed cameras.

All tests were virtually replicated with the FE simulations. The simulation models correlated within the scatter of the data of the aforementioned test conditions. Therefore, it can be concluded that the FE model was verified for the conditions set by the physical tests.

The model is intended to be used for assessing impact dynamics with aircraft structures and to simulate mid-air collisions. There FE models should be limited to relative impact velocities between 110 and 250 knots (56.6 and 128.6 m/s), for which component level tests verified the behavior of the main components of the UAS. Further coupon to component level tests should be conducted in the future in order to use this UAS FEA model for ground collisions impact scenarios or lower velocity airborne collisions with GA aircraft and rotorcraft.

8.1.3 Selection Impact Conditions

As presented in Chapter 4, following the airworthiness requirements listed in the FAA General Operating and Flight Rules (14 CFR Part 91) [61], it was assumed that the most probable high velocity impact scenario was either at landing/take-off or at holding flight phases. For this cases, and considering the categories of aircraft being studied in this report, the maximum flight speed is limited to 200 KIAS (*14 CFR Part 91.117(b)*), which at 2,500 ft is approximately 280 knots (107 m/s). Considering a frontal impact between the UAS and the aircraft to be a worst-case scenario, an impact velocity can be stablished by adding the relative speeds of both bodies. Therefore, an impact velocity of 250 knots (128.6 m/s) was defined for all the airborne collision studies.

Moreover, a parametric study was completed with the objective of identifying the most critical local impact conditions and narrowing down the number of simulations to be run in each of the impacted aircraft subassemblies. To achieve this, the FE UAS model was impacted into a wing leading edge FE model, developed and validated through simulation and testing by NIAR in a previous project for bird strike [32]. The influence of the yaw angle of the UAS and the local position of its CG respect to the impacted aircraft was studied.

Based on the results obtained in these parametric studies, an UAS orientated at 45° impacting with the CG aligned with the leading edge of the target between the two closest ribs was identified as the most severe impact condition. This impact condition was consequently selected as baseline for the initial conditions of the collision study involving commercial and business jet targets.

This study also highlighted the importance of having ideal initial conditions to produce the worst-case levels of damage. Small deviations in the impact location might under predict the severity of the event.

8.1.4 Proposed Evaluation Criteria for Airborne Collisions

The results from over 140 impact scenarios (including both quadcopter and fixed-wing UAS configurations) were analyzed and categorized relative to one another, and a set of impact severity criteria was defined as shown in Table 38.

The lowest damage category, Level 1, generally corresponds to a minimal amount of localized damage. The next category, Level 2, represents significant visible damage to the external surface of the aircraft with some internal component damage but with no appreciable skin rupture. The third category, Level 3, describes impact events where the outer surface of the aircraft is compromised in a way that could allow ingress of foreign objects into the airframe, with some damage to substructure. Finally, Level 4 indicates damage that includes all of the preceding aspects as well as extensive damage to internal components and possibly compromising damage to primary structure.

Table 38. Damage level categories

Severity	Description	Example
Level 1	• Airframe undamaged. • Small deformations.	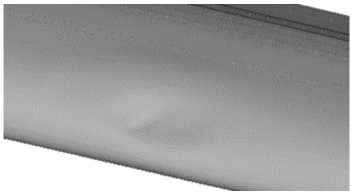
Level 2	• Extensive permanent deformation on external surfaces. • Some deformation in internal structure. • No failure of skin.	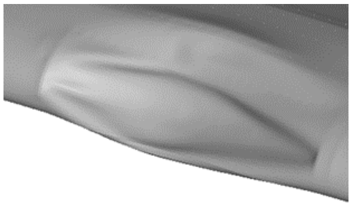
Level 3	• Skin fracture. • Penetration of at least one component into the airframe.	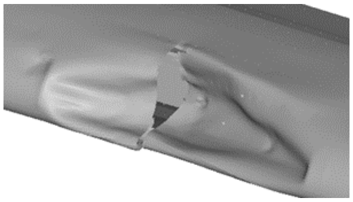
Level 4	• Penetration of UAS into airframe. • Failure of parts of the primary structure.	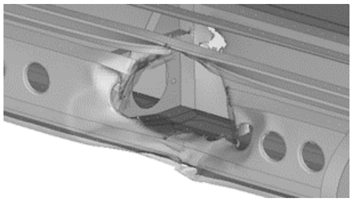

The risk of fire associated with damaged LiPo type batteries was addressed for each simulation based on the trends observed during component level ballistic testing, see Section 2.4.4.12 and the particular kinematics of a given impact scenario.

Table 39 presents the battery risk fire criteria used in this study. Note that the label of "Fire Risk" indicates a potential outcome rather than an impending event due to the qualitative nature of the assessment. Further studies and physical testing into this phenomenon would be required in order to determine any additional severity. During component level testing, the fire risk corresponded inversely to the velocity of impact; higher velocities caused the battery to disintegrate reducing the heat generated after impact, while lower velocities allowed the battery pack to remain consolidated, increasing the post-impact heat generation.

Table 39. Risk of battery fire

Fire Risk	Description	Example
Yes	• UAS (including the battery) penetrates the airframe. • Battery deforms but stays undamaged. • Physical tests showed that partly damaged batteries created heat and sparks.	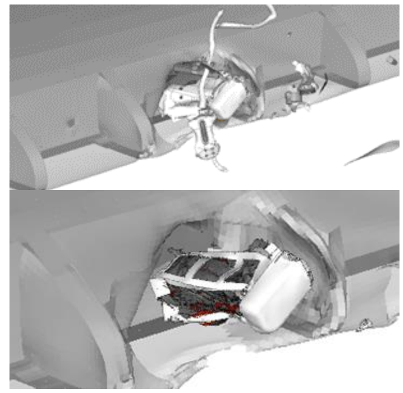
No	• The UAS does not penetrate the airframe.	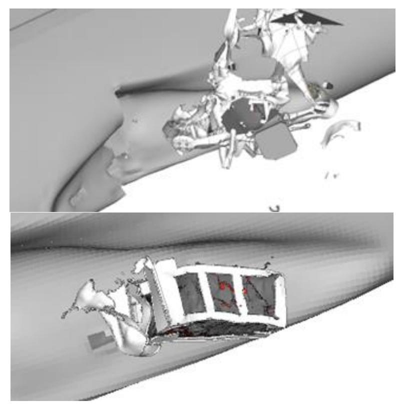
No	• UAS (including the battery) penetrates the airframe. • The battery sustains great damage, destroying its cells. • Physical tests showed that completely damaged batteries did not create heat and sparks.	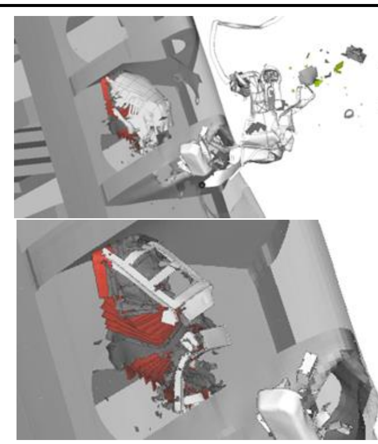

8.2 AIRBORNE COLLISION SEVERITY EVALUATION

8.2.1 Unmanned Aircraft Systems Impact Severity Classification

Conventional 14 CFR system safety analyses include hazards to flight crew and occupants that may not be applicable to unmanned aircraft. However, UAS operations may pose unique hazards to other aircraft and people on the ground. It is necessary to determine hazard severity thresholds for UAS using safety characteristic factors that affect the potential severity of UAS in collisions with other aircraft in possible airborne encounters. The factors that determine the outcome of an airborne collision are numerous and complex and are highly dependent on the structural design and materials used for the construction of the UAS. The criteria summarized in Table 38 and Table 39 were used to evaluate the UAS Impact Severity Classification.

8.2.2 Commercial Transport Jet Airborne Collision

As introduced in chapter 3, the targets areas selected for impact on the NIAR commercial transport jet were the vertical stabilizer (4.3.1), horizontal stabilizer (4.3.2), wing leading edge (4.3.3), and windshield (4.3.4). Sixteen explicit dynamic simulations of impacts of the 1.2 kg (2.7 lb) quadcopter UAS into the commercial transport jet were conducted. As defined in section 4.1.1 , an impact velocity of 250 knots (128.6 m/s) was defined for these airborne collision studies. Figure 265 illustrates the locations selected for impact on the commercial transport jet. Table 40 summarizes the results of the collision studies, in terms of severity level and risk of fire

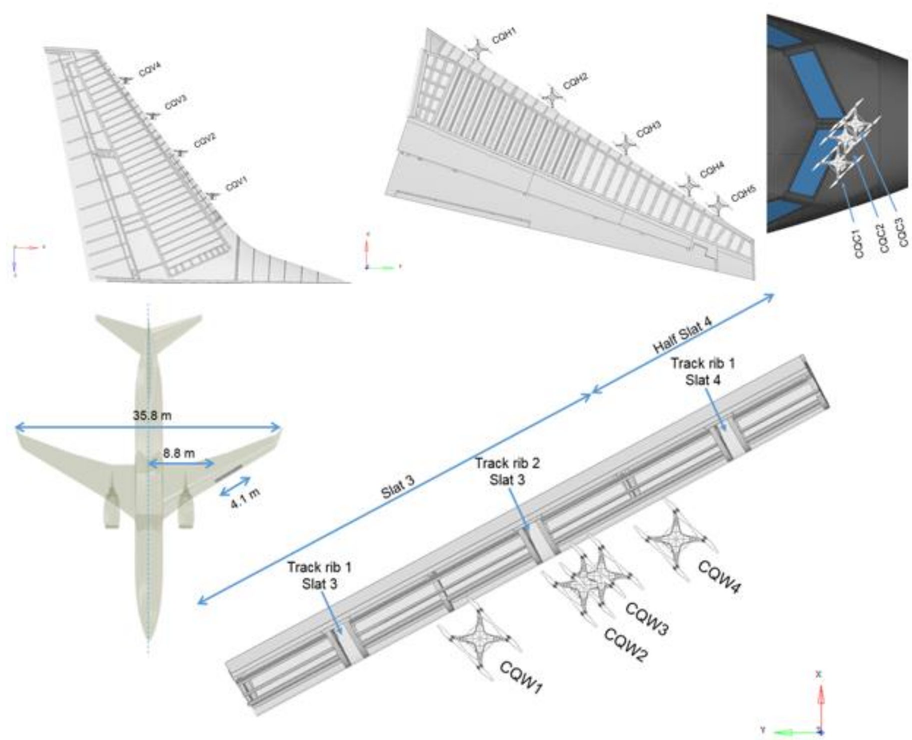

Figure 265. Commercial transport jet airborne collision impact locations

Table 40. Commercial transport jet airborne collision simulation results – Severity levels

	Commercial Transport Jet															
	Vertical Stabilizer				Horizontal Stabilizer					Wing				Windshield		
Case	CQV1	CQV2	CQV3	CQV4	CQH1	CQH2	CQH3	CQH4	CQH5	CQW1	CQW2	CQW3	CQW4	CQC1	CQC2	CQC3
Severity	Level 3	Level 3	Level 3	Level 3	Level 3	Level 3	Level 4	Level 4	Level 4	Level 3	Level 3	Level 3	Level 2	Level 2	Level 2	Level 2
Fire Risk	No	No	No	No	Yes	Yes	Yes	No	No	No	No	No	No	No	No	No

Table 40 shows consistent levels of damage at all locations for each impact target component, indicating that the impact behavior of the UAS for a given target structure is generally not affected by local features in the structure. The impact energy level was such that localized structural variations do not significantly increase or decrease the overall damage level. The nomenclature convention was defined in section 4.1.3.

Table 40 shows a change in severity from position 3 outboard in the horizontal stabilizer (from case CQH3 to CQH5). It was observed that in outer parts of the horizontal stabilizer, the front spar was damaged and even perforated. Consequently, and because it was considered to be primary structure, the severity was increased to Level 4. These were the most severe cases found in the collision with the commercial transport jet.

Additionally, it was observed that the nature of the impact caused the battery to penetrate the airframe and remain partially damaged in three cases involving the horizontal stabilizer, creating potential for post impact fire risk.

A summary of the results, in terms of energy balance, of all cases is shown in Figure 266. For each case, the bar represents a summation of all the different energies involved in the impact event, measured at 10 ms after impact, and normalized with the total energy at time zero. Each block indicates the ratio (in percentage) of energy versus total energy. For each case, we can quantify how the initial kinetic energy of the UAS prior to impact is transformed into aircraft and UAS internal energies through the structural deformations introduced during impact; a residual UAS kinetic energy that is a function of the UAS post-impact debris mass moving at a post impact residual velocity; friction energy which is a function of the sliding contact energy between the UAS and the aircraft structure, and eroded energy from the mass of the UAS and aircraft eroded elements to increase the stability of the calculation.

In general, the internal energy absorbed by the aircraft structure increased when the UAS impacted closer to the root for any lifting surface. Note that the cases were numbered from root to tip, so smaller numbers would be inboard. This phenomenon may be explained with the cross-sectional height of the airfoil at the impacted location. Closer to the root, the airfoil cross-section is thicker and has a greater leading edge radius. Consequently, the area of airframe that will have a more perpendicular contact with the impacting projectile is greater, allowing a greater transfer of energy and therefore an increase in internal energy.

The impacted areas of the wing were concentrated at one span-wise location. Therefore, span-wise effects cannot be assessed. However, a detailed model of the portion of the wing leading edge allowed a better look into local effects, such as how impacting closer to a slat track rib pair or impacting aiming the center of the rib bay may affect damage. It was observed that an impact further from rigid areas (*e.g.* ribs) were more vulnerable (*i.e.* cases CQW1 and CQW3). In these two cases, the D-nose sub-spar sustained greater damage. None of the cases involved battery penetration of the airframe. Hence, the risk of fire was negligible.

If compared with other areas of the commercial transport jet, the UAS impacts on the windshield resulted in much higher residual kinetic energies. Due to the low angle impact in the transparency (~45°), the UAS impacts were deflected without inducing considerable damage to the windshield. The windshield is constructed with a thick multilayered transparency with very high stiffness. Consequently, a great amount of the deformation due to the impact was absorbed by the UAS, since the internal energy of the UAS resulted to be much greater than the one of the aircraft.

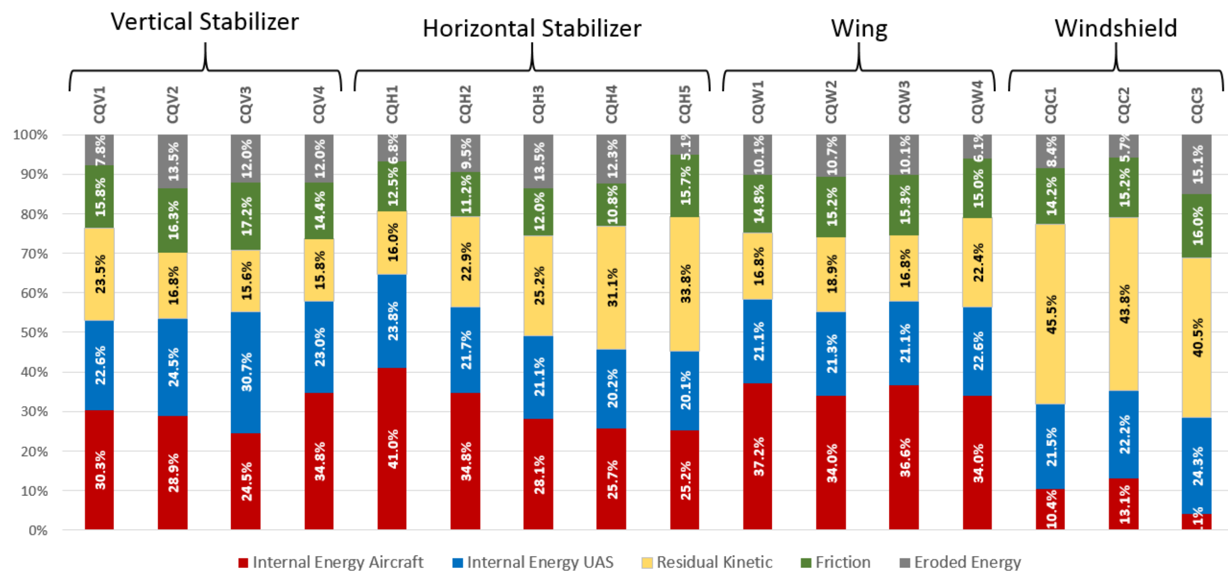

Figure 266. Commercial transport jet airborne collision simulation results – Energy summary

8.2.3 Business Jet Airborne Collision

As introduced in chapter 3, the targets areas selected for impact on the NIAR business jet were the vertical stabilizer (4.4.1), horizontal stabilizer (4.4.2), wing leading edge (4.4.3), and windshield (4.4.4). Sixteen explicit dynamic simulations of impacts of the 1.2 kg (2.7 lb) quadcopter UAS into the business jet were conducted. As defined in section 4.1.1 an impact velocity of 128.6 m/s (250 knot) was defined for these air-borne collision studies. Table 41 summarizes the results of the collision studies, in terms of severity level and risk of fire, on the business jet. Figure 267 illustrates the locations selected for impact on the business jet.

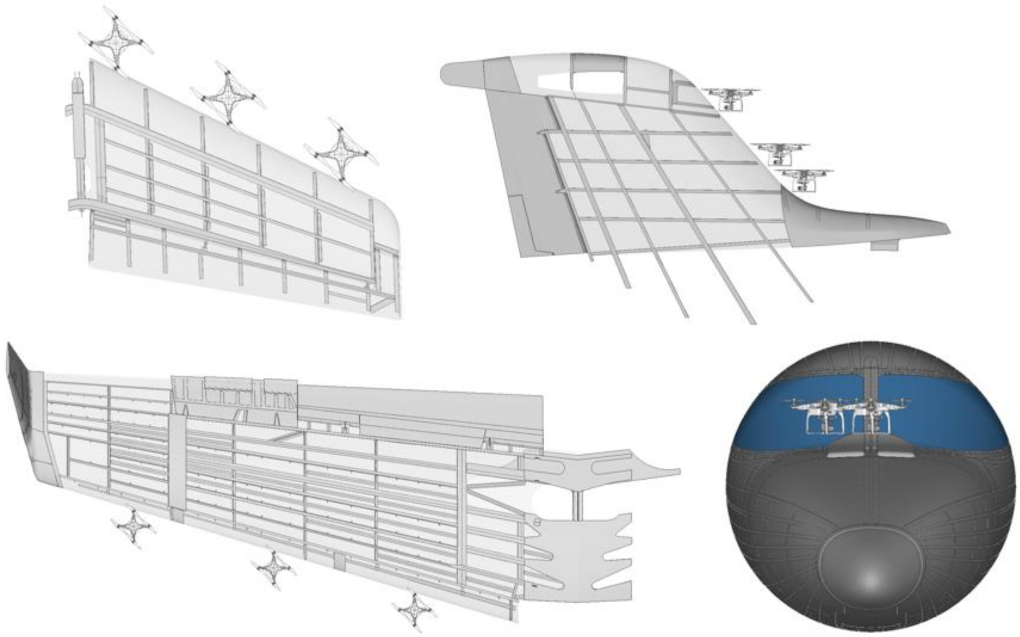

Figure 267 Business jet airborne collision impact locations

Table 41. Business jet airborne collision simulation results – Severity levels

	Business Jet										
	Vertical Stabilizer			Horizontal Stabilizer			Wing			Windshield	
Case	BQV1	BQV2	BQV3	BQH1	BQH2	BQH3	BQW1	BQW2	BQW3	BQC1	BQC2
Severity	Level 3	Level 3	Level 2	Level 3	Level 4	Level 4	Level 3	Level 2	Level 2	Level 2	Level 2
Fire Risk	Yes	No	No	Yes	No	Yes	Yes	No	No	No	No

Table 41 shows a change in severity from position 2 outboard in the horizontal stabilizer (from case BQH2 and BQH3). It was observed that in outer parts of the horizontal stabilizer, the front spar (primary structure) was damaged and even perforated. Consequently, the severity was increased to Level 4. These were the most severe cases found in the collision with the business jet.

Furthermore, every case involving the inboard area of a lifting surface, the battery penetrated into the airframe and remained partially damaged, creating potential for post impact fire risk.

A summary of the results of all cases is shown in Figure 268. For each case, the bar represents a summation of all the different energies involved in the impact event, measured at 10 ms, and normalized with the total energy at time zero. Each block indicates the ratio (in percentage) of energy versus total energy. Similarly to the commercial transport jet, Figure 268 shows that in general the internal energy absorbed by the aircraft structure increased when impacts occurred closer to the root of any lifting surface. Cases involving the wing presented lower levels of damage in the airframe. A skin that was slightly thicker than the stabilizer and the pipe of the anti-icing system absorbed most of the damage, protecting the front spar from a direct impact of the UAS. In addition, the UAS impacts on the windshield present a much higher residual kinetic energy. The UAS was also deflected without any significant damage.

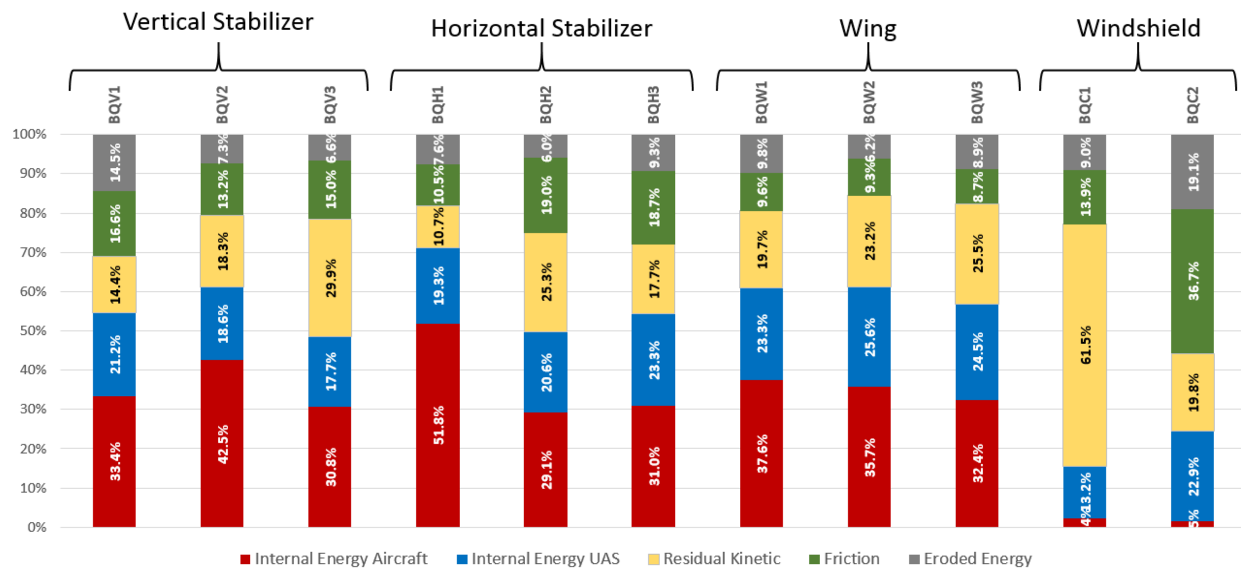

Figure 268 Business jet airborne collision simulation results – Energy summary

8.2.4 Airborne Collision Impact Severity Study Conclusions

According to the simulations presented in Chapter 4, an airborne collision between a commercial transport jet and a 1.2 kg (2.7 lb) quadcopter UAS at 250 knots may result in a damage severity level of medium-high (3-4) in the horizontal and vertical stabilizer, medium (2-3) in the leading edge of the wing and medium-low (2) in the windshield. Figure 269 illustrates the severity levels in each area of the aircraft analyzed. Equally, an airborne collision between a business jet and a 1.2 kg (2.7 lb) quadcopter UAS may result in a damage severity level of medium-high (3-4) in the horizontal and vertical stabilizer, medium (2-3) in the leading edge of the wing and medium-low (2) in the windshield. Figure 268 shows the discussed levels on the business jet airframe. Most of the damage to both aircraft was produced by the stiffer structural components (motors, camera, etc.) of the UAS. This is consistent with observations from component level physical testing and simulations (chapter 2).

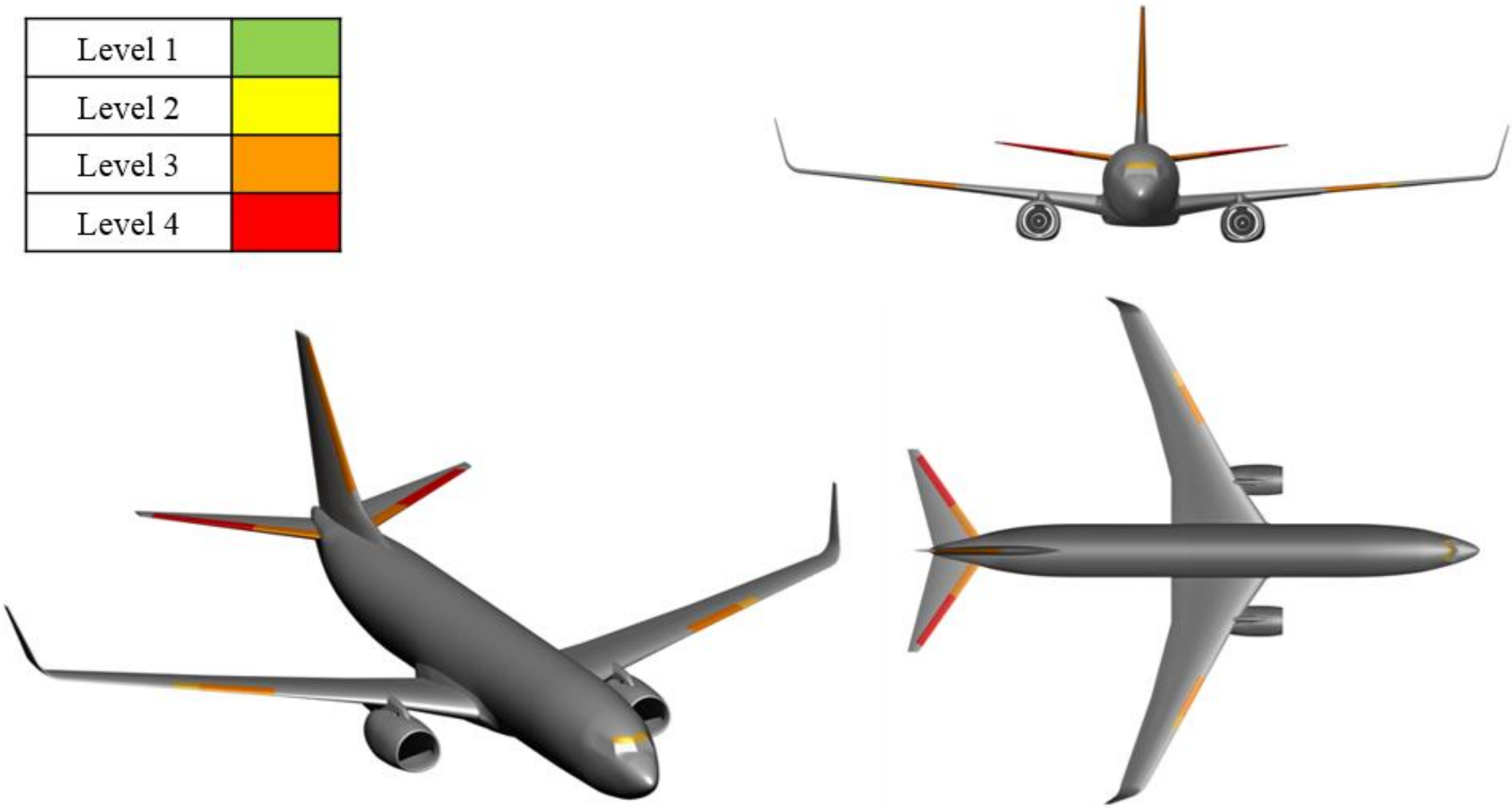

Figure 269. Summary of collision severity levels on commercial transport jet

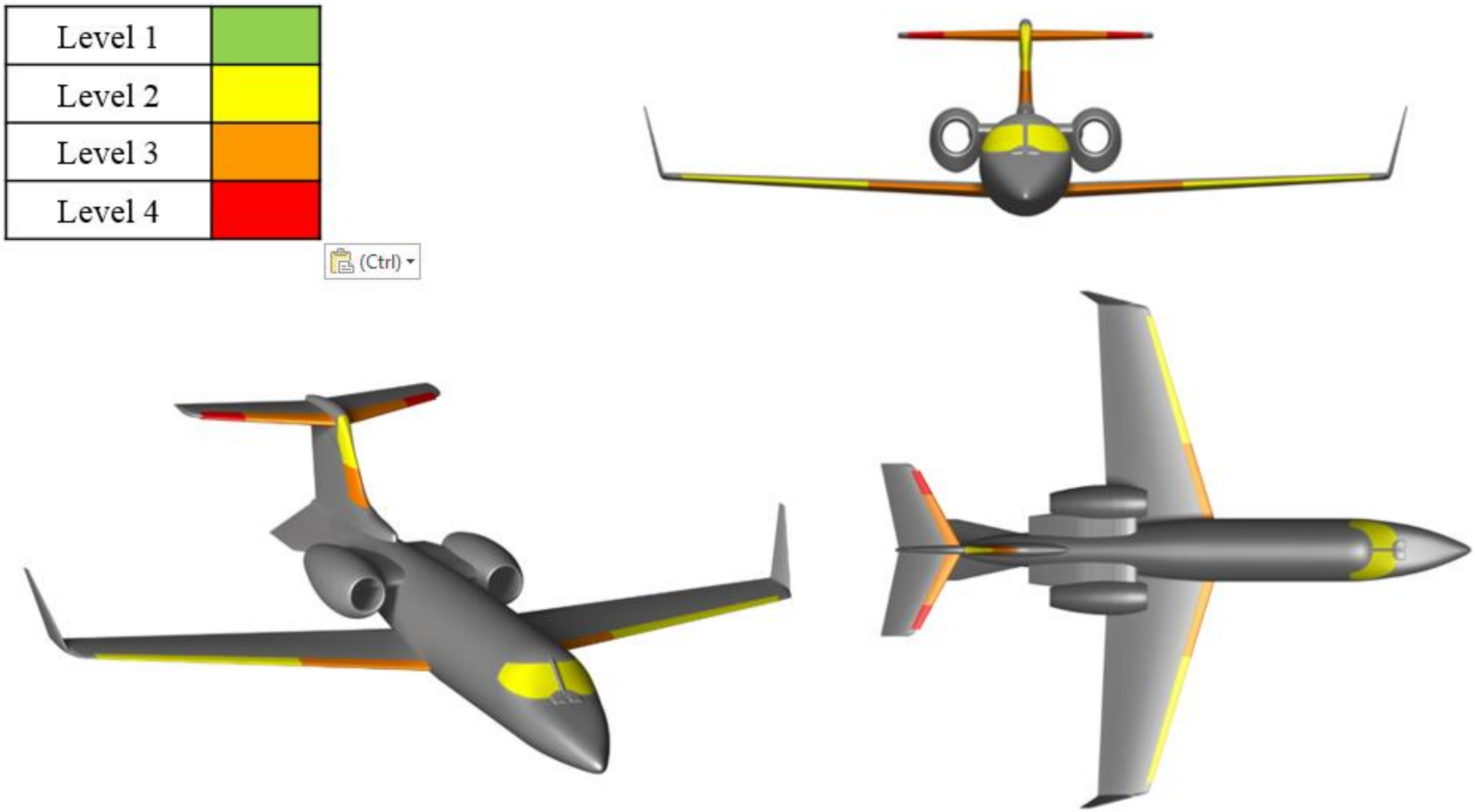

Figure 270. Summary of collision severity levels on business jet

8.3 IMPACT KINETIC ENERGY AND UAS ARCHITECTURE PARAMETRIC ANALYSIS

The kinetic energy of a mid-air collision between an UAS and the two manned aircraft being studied in this project was characterized in terms of the UAS mass and relative impact velocity. The parametric study results and calculated damage severity levels were compared to those of the corresponding baseline simulations. The results of this study are summarized in the following two subsections. The worst-case impact conditions for each location identified in the airborne collision studies were used as a baseline for the parametric analyses. The effect of the UAS configuration on the damage experience by the target aircraft during airborne collisions was assessed.

8.3.1 Mass

The quadcopter UAS was scaled-up from the 1.2 kg (2.7 lb) baseline mass to 1.8 kg (4.0 lb) in order to assess the potential increase in damage severity imparted by a heavier UAS. An impact velocity of 250 knots (128.6 m/s) was defined for these airborne collision studies.

Table 42 presents the levels of severity of the impacts with the scaled-up UAS compared to their respective baseline simulation. The mass of the UAS in this parametric study contributed to a linear increase in the kinetic energy of the collision. The increased kinetic energy resulted in increased damage severity levels in three of the eight simulations and more extensive damage for those cases where the damage level classification remained the same.

Table 42 Mass scaled quadcopter UAS impact simulation results

	Commercial Transport Jet				Business Jet			
	Vertical Stabilizer	Horizontal Stabilizer	Wing	Windshield	Vertical Stabilizer	Horizontal Stabilizer	Wing	Windshield
Baseline quadcopter UAS 1.2 kg (2.7 lb)	Level 3	Level 4	Level 3	Level 2	Level 3	Level 4	Level 3	Level 2
Scaled-up quadcopter UAS 1.8 kg (4.0 lb)	Level 3	Level 4	Level 3	Level 3	Level 4	Level 4	Level 3	Level 2

8.3.2 Impact Velocity

The impact velocity was varied to determine impact reactions at typical aircraft landing, holding, and cruise velocities for the business and commercial transport jets in order to assess the minimum and maximum damage that can be expected for similar midair collisions. The landing velocity considered for the commercial transport and business jets was 56.7 m/s (110 knots) and 44.8 m/s (87 knots), respectively, and the cruise velocity was 187.8 m/s (365 knots) and 167.2 m/s (325 knots), respectively. The holding velocity was 128.6 m/s (250 knots) for both aircraft. In all cases, the UAS mass remained as 1.2 kg (2.7 lb). An increase (or decrease) in the impact velocity resulted in a quadratic increase (or decrease) in the total impact energy.

As shown in Table 43, the quadcopter UAS impacts resulted in increased damage severity levels for five of the eight cruise velocity cases. The landing velocity cases showed decreased severity levels in all eight cases over the baseline, all of them equal or below level 2. The damage was more extensive at higher velocities even for cases where the severity level remained the same.

Table 43 Velocity impact simulation results

	Commercial Transport Jet				Business Jet			
	Vertical Stabilizer	Horizontal Stabilizer	Wing	Cockpit Windshield	Vertical Stabilizer	Horizontal Stabilizer	Wing	Cockpit Windshield
Landing Velocity (110/87 knots)	Level 2	Level 2	Level 2	Level 1	Level 2	Level 2	Level 2	Level 1
Holding Velocity (250/250 knots)	Level 3	Level 4	Level 3	Level 2	Level 3	Level 4	Level 3	Level 2
Cruise Velocity (365/325 knots)	Level 4	Level 4	Level 4	Level 4	Level 4	Level 4	Level 3	Level 3

8.3.3 Conclusions Velocity and Mass Influence on Impact Damage

Mass (*m*) and velocity (*V*) have a linear or quadratic (respectively) relationship with the severity of the collision, as expected from the equation of kinetic energy (E).

$$E = \frac{1}{2}mV^2$$

The impact velocity contributed to a greater amount of damage than the mass of the UAS. However, incremental increases in either parameter correlate to increased severity and extent of airframe damage.

Consequently, both velocity and mass have been identified as key factors on the severity of an airborne collision between an UAS and an aircraft. Aircraft velocities above minimum landing speeds are considered critical for quadcopter UAS masses equal to or above 1.2 kg (2.7 lb).

Note that the minimum landing velocity was selected to stablish an absolute lower limit for impact velocity in the collision studies. However, a higher velocity is typical at normal operation of aircraft at take-off and landing, and therefore greater damage levels are expected. A more detailed velocity parametric analysis would be required to obtain conclusions of the actual risk posed by an aiborne collision happening at those flight phases.

Finally, in this study the UAS masses investigated were between 1.2 kg and 3.6 kg (2.7 and 8.0 lb). Lower mass UASs will need to be studied in the future in order to determine a threshold in mass that will introduce level 1 or no damage into the airframe.

8.4 UAS IMPACT COMPARISONS TO EQUIVALENT BIRD IMPACTS

This study was conducted with the goal of determining whether an UAS impact can be considered equivalent to a bird strike with identical mass and initial kinetic energy. Idealized birds of two different masses, 1.2 kg (2.7 lb) and 1.8 kg (4.0 lb), were selected for the comparison with the quadcopter UASs of same mass (Chapter 5).

The NIAR has conducted numerous studies of bird strike events and compared the results with physical testing [32]. SPH modeling techniques [21] were used to define the gelatin substitute bird models. These SPH bird models have been validated with experimental data [20, 31].

Table 44 presents structural damage severity levels for each impact simulation. For all the cases, the UAS created equal or more damage than the analogous bird. Hence, the bird strike cannot be considered equivalent to an UAS collision with the same mass and impact energy.

Table 44 UAS and bird impact simulation results

	Commercial Transport Jet				Business Jet			
	Vertical Stabilizer	Horizontal Stabilizer	Wing	Windshield	Vertical Stabilizer	Horizontal Stabilizer	Wing	Windshield
Baseline 1.2 kg (2.7 lb) UAS	Level 3	Level 4	Level 3	Level 2	Level 3	Level 4	Level 3	Level 2
1.2 kg (2.7 lb) Bird	Level 3	Level 2	Level 2	Level 2	Level 2	Level 2	Level 2	Level 1
Upscaled 4 lb (1.8 kg) UAS	Level 3	Level 4	Level 3	Level 3	Level 4	Level 4	Level 3	Level 2
4 lb (1.8 kg) Bird	Level 3	Level 2	Level 2	Level 2	Level 2	Level 2	Level 2	Level 1

The simulations presented in Chapter 6 identified that airborne collisions involving hard-bodied projectiles have characteristic features that distinguish them from bird strikes. Primarily, the damage zones for the UAS showed notable dents and penetrations due to the discrete masses and rigid, dense materials. The initial dents and penetrations produced after impact of the motor, allowed a significant fraction of the UAS assembly to break through the skin of the aircraft and damage internal components (including the front spar in some cases) in a majority of the simulations.

Figure 271 presents an example of the comparison UAS/Bird Strike, in this case against the horizontal stabilizer of the business jet. The UAS created a smaller impact damage region but the perforation of the skin caused further penetration into the airframe and damage to internal components of the aircraft, including the forward spar. On the contrary, the bird deformed considerably the external surface of the stabilizer, but with no penetration into the airframe. Consequently, the UAS impact is considered Level 4 damage while the bird impact was classified as Level 2.

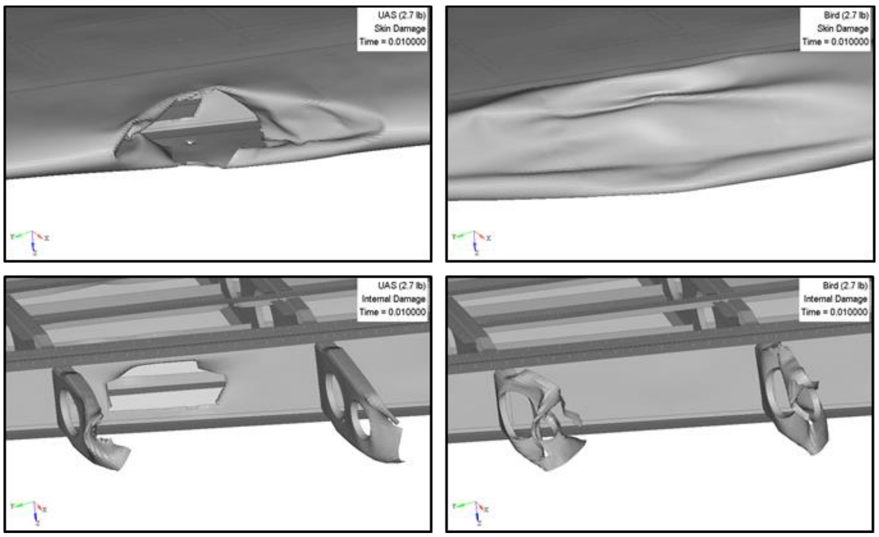

Figure 271 Comparison of damage after impact of a 1.2 kg (2.7 lb) UAS/Bird into a business jet horizontal stabilizer

8.4.1 Bird Strike – UAS Strike Comparison Conclusions

Quadcopter UAS impacts are likely to cause more damage than bird strikes with an equivalent initial kinetic energy (mass and velocity). Since birds behave like a fluid during high velocity impacts, density is the main parameters that drive the magnitude of the damage in the target structure. In contrast, UASs do not exhibit this behavior. Structural rigidity (a combination of structural geometry and material properties) drives the magnitude of the damage in the target structure.

The UAS impacts shown in this study were associated with greater damage levels than equivalent bird strikes due to the dense and rigid construction of the UAS. Initial motor impact and consequent perforations exacerbated subsequent impact damage as other high-density UAS components (*i.e.* battery) impacted the underlying aircraft structure causing progressively more structural damage, as well as in some cases the UAS ingress into the airframe. Therefore a 2.7lb/4lb bird and a 2.7lb/4lb UAS will introduce profoundly different levels of damage to the aircraft structure.

Even though *14 CFR Part 25* aircraft were designed to withstand bird impact under the conditions described in *14 CFR 25.631: Bird Strike, 14 CFR FAR 25.775: Windshields and windows*, aircraft may not experience the same level as with bird strikes when impacted by an UAS equivalent in weight.

8.5 UAS SYSTEM ARCHITECTURE

This study was conducted with the goal of determining whether airborne collisions involving 1.8 kg (4.0 lb) quadcopter or fixed-wing UAS architectures can be considered equivalent to one-another. The simulations utilized identical initial and boundary conditions and impact energies.

As shown in the impact comparison presented in chapters 6 and 7, airborne collisions involving hard-bodied projectiles have characteristic features that distinguish them from bird strikes. The primary similarity between the UAS simulations shown in chapter 7 is that the dense, rigid, components (motors and batteries) of both UAS models created penetrations in the aircraft skin which allowed the remaining mass of the UAS to enter the airframe and damage the internal components.

The differences perceived in the damage severity levels between quadcopter and fixed-wing UASs of the same mass indicate that the layout of the main UAS components is critical to the energy transfer during an airborne collision (see Table 46). The predicted critical damage occurred when the majority of the masses were aligned with the impact direction. The quadcopter UAS was oriented at the most critical yaw angle configuration, 45°. At this orientation, the quadcopter UAS motor and battery align with the impact axis similar to the fixed-wing configuration as shown in Figure 272. Therefore, the damage levels to the aircraft airframe are similar for both UAS architectures.

Table 45 Quadcopter and fixed-wing UAS impact simulation results - Comparison at identical impact locations

	Commercial Transport Jet				Business Jet			
	Vertical Stabilizer	Horizontal Stabilizer	Wing	Windshield	Vertical Stabilizer	Horizontal Stabilizer	Wing	Windshield
Scaled Quadcopter 1.8 kg (4.0 lb)	Level 3	Level 4	Level 3	Level 3	Level 4	Level 4	Level 3	Level 2
Baseline Fixed-wing 1.8 kg (4.0 lb)	Level 3	Level 4	Level 3	Level 2	Level 4	Level 4	Level 3	Level 3

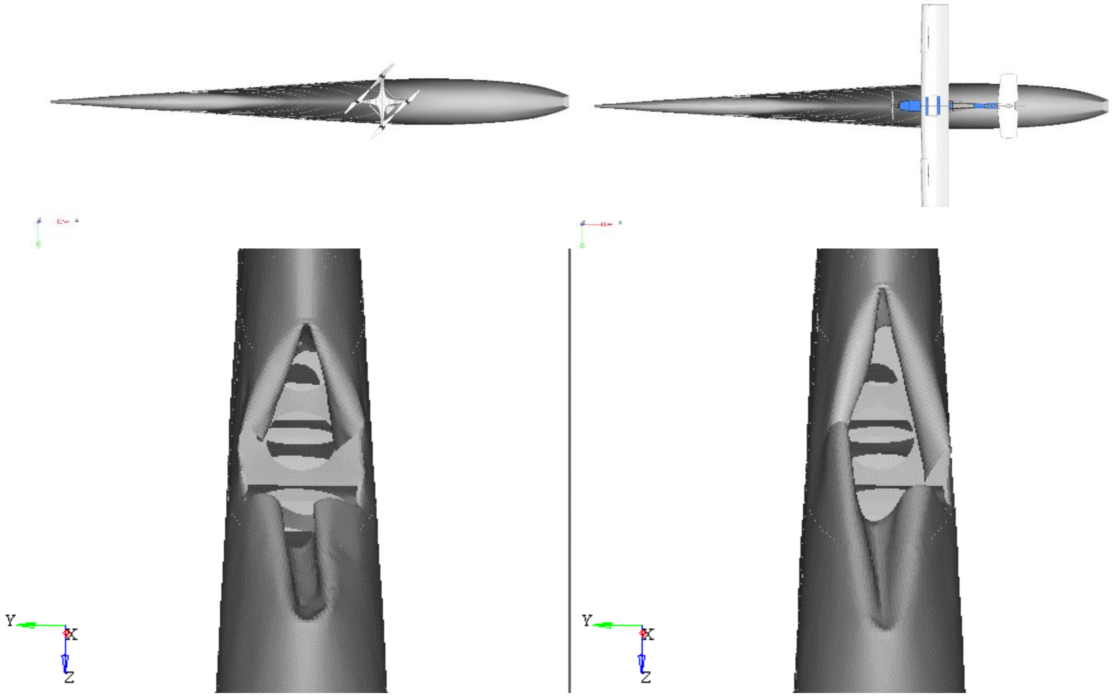

Figure 272 Comparison of damage after impact of a 1.8 kg (4.0 lb) quadcopter (left) and a fixed-wing (right) UAS into a business jet vertical stabilizer

8.6 FUTURE WORK

The research presented in this report shows that there is a risk of primary aircraft structure failures for several of the impact scenarios analyzed (commercial transport and business jets) with the quadcopter UAS configuration. Further research is needed to support the UAS airborne collision work:

8.6.1 UAS Airborne Collision R&D Roadmap

Define a Research and Development Roadmap to coordinate and prioritize airborne collision research activities required to support the FAA rulemaking objectives and timelines.

8.6.2 Airborne Collision Studies Phase II: General Aviation and Rotorcraft

Conduct a similar study as the one presented in this report to analyze mid-air-collisions with GA aircraft and rotorcraft. The data generated in Phase I and Phase II can be used to aid in the development of an UAS Mid-Air-Collision Equivalent Level of Safety in order to regulate UAS operations in the NAS. This research should include additional component level testing at lower impact velocities from 50 to 100 knots to cover the GA impact collision scenarios and higher velocities as required by the tip speeds of rotorcraft blades and GA propellers.

8.6.3 Airborne Collision Standard: Development of an UAS Mid-Air-Collision Equivalent Level of Safety

The primary goal of regulating UAS operations in the NAS is to assure an appropriate level of safety. This goal is quantified by national aviation agencies as an "Equivalent Level of Safety" with that of manned aviation. There are major key differences between manned and unmanned aviation that span the requisite level of automation as well as the distinct variety of architectures and materials used for the construction of UASs. These differences could introduce new failure modes and consequently increased perceived risk, which will need to be evaluated [7].

In order to have an Equivalent Level of Safety, the Range Commanders Council UAS operation guidelines stated that any UAS operation or test must show a level of risk to human life no greater than that for an operation or test of a piloted aircraft [9]. The aforementioned metrics can be used to provide statistical probabilities of UAS mid-air collisions according to specific parameters defined for the evaluation.

The risk assessment to develop an Airborne Collision UAS Impact Severity Classification can be divided into three elements:

- **Estimation of the probability of mid-air collision** between UASs and manned aircraft. This will be a function of the operating airspace, aircraft operated within the airspace, and the UAS configurations operating within the shared airspace. Methods to estimate the probability of impact are presented in references [10] [11].
- **Evaluation of damage potential for typical UASs.** Assess damage severity for mid-air collisions scenarios between unmanned aircraft (classes based on weight, architecture, operational characteristics (altitude, velocity)) and manned aircraft (commercial transport and business jets, GA, rotorcraft, etc.). Several groups advocate use of simplified ballistic penetration models [15], and similar principles as those used for existing bird strike requirement or kinetic energy thresholds [16][17]. The objective of this project will be to evaluate the severity of a typical quad and fixed wing UAS airborne collision. These results will be compared with current proposed penetration mechanics and energy based criteria.
- Once the probability of an airborne collision is determined, **the damage models can be combined with the probabilistic collision models to define appropriate Equivalent Level of Safety criteria.**

Using the data presented in this report and the data that will be developed in Phase II for GA aviation and rotorcraft, a project should be carried out in the near future to define the acceptable Equivalent Level of Safety to regulate UAS operations in the NAS.

8.6.4 UAS Certification by Analysis Protocol Development

In order to address the airborne collision severity levels for future UAS designs it is necessary to develop a methodology that will enable industry to study the Equivalent Level of Safety of new UAS designs.

It would be very difficult for UAS manufacturers to conduct future full scale physical testing to evaluate the structural impact behavior of UASs into various airframe locations. The limitations with physical testing are the following:

- Cost of representative airframe structures for testing is prohibitive.
- There would be no standard representative airframe structure available to conduct testing for all the possible UAS and collision scenarios.
- It is very difficult to conduct high velocity impact testing for complete UAS assemblies since their structures are not designed to withstand the aerodynamic loads generated by the required relative impact velocities (200+ knots)
- The UAS airframes likely will not withstand the acceleration levels required to achieve impact velocities (200+ knots) in the range of typical impact scenarios.
- It is difficult to quantify the damage, energy distributions, and overall crashworthiness behavior with full-scale experimental data only.

Based on the results of Phase I for the airborne collision studies we recommend to develop a Certification by Analysis protocol supported by the Building Block Approach to be able to conduct future UAS impact evaluations and crashworthiness certification of UAS configurations (similar research efforts are ongoing for certification of aircraft interiors and airframe crashworthiness per *AC20-146*).

8.6.5 Mass, Impact Velocity and Architecture Risk Classification

Develop a reference damage level matrix based on mass, velocity, and UAS configurations to cover the range of UAS configurations under the 55 lb limit defined by the Small Unmanned Aircraft Rule (*Part 107*).

9. REFERENCES

[1] "Raise of the Drones. Managing the Unique Risks Associated with Unmanned Aircraft Systems", Alliance Global Corporate & Specialty, 2016.

[2] Olivares G., Lacy, T., Kota, K., Ricks, T., Jayakody, N., Gomez, L., Espinosa de los Monteros, J., and Baldridge, R., "Volume III – UAS Airborne Collision Severity Evaluation – Fixed Wing", Federal Aviation Administration, Report DOT/FAA/AR-XX/XX, (to be published).

[3] D'Souza, K., Gregory, J.W., "Volume IV – UAS Airborne Collision Severity Evaluation – Engine Ingestion", Federal Aviation Administration, Draft Report DOT/FAA/AR-XX/XX (to be published).

[4] Public Law 112-95, Section 331(8).

[5] FAA Advisory Circular AC 107-2, "Small Unmanned Aircraft System (sUAS)", Washington, DC, 2016.

[6] Micro Unmanned Aircraft Systems Aviation Rulemaking Committee, "ARC Recommendations Final Report", 2016.

[7] Dalamagkidis, K., Valavanis, K., and Piegl, L. A., *On Integrating Unmanned Aircraft Systems into the National Airspace System*, 2nd ed., Springer Netherlands, 2012.

[8] Unmanned Aircraft Systems: accessed at https://www.faa.gov/data_research/aviation/aerospace_forecasts/media/Unmanned_Aircraft_Systems.pdf

[9] Range Safety Group, Range Commanders Council, "Range Safety Criteria for Unmanned Air Vehicles", Document 323-99, 2001.

[10] Lum, C. W., and Waggoner, B., "A Risk Based Paradigm and Model for Unmanned Aerial Systems in the National Airspace", *Infotech@Aerospace Conferences*, 2011-1424, AIAA, St. Louis, MO, 2011.

[11] Weibel, R., Hansman, R. J., "Safety Considerations for Operation of Different UAVs in the NAS", *AIAA 3rd Unmanned Unlimited Technical Conference, Workshop and Exhibit*, Paper No. 2004-6421, AIAA, Chicago, IL, 2004.

[12] McQuarrie, D. A., and Simon, J. D., *Physical Chemistry: A Molecular Approach*, University Science Books, 1997.

[13] McGeer, T., Newcome, L., and Vagners, J., "Quantitative Risk Management as a Regulatory Approach to Civil UAVs", *International Workshop on UAV Certification*, 1999.

[14] McGeer, T., "Aerosonde Hazard Estimation", The Insitu Group, 1994.

[15] Civil Aviation Safety Authority, "Potential Damage Assessment of a Mid-Air Collision with a Small UAV", Technical Report, 2013.

[16] Fraser, C. S. R., and Donnithorne-Tait, D., "An Approach to the Classification of Unmanned Aircraft", *26th International Conference on Unmanned Air Vehicle Systems 2011*, Bristol, UK, 2011, pp. 157-211.

[17] Marshall, M. M., Anderson, E. E., and Tighe, D. E., "A Literature Review in Support of TCRG 14-05: UAS Systems Safety Criteria", Draft Report, FAA Award 14-G-007, 2015.

[18] Jimenez, H., Mavris, D., Hoffman, D., Mines, J., and O'Sullivan, S., "A Survey of Evaluation Methods for Unmanned Aircraft Risk and Safety to Third Parties", Report, Federal Aviation Administration, 2015.

[19] FAA COE Task: A11LUAS.COE.7 .2 UAS Airborne Collision Severity Evaluation.

[20] Cairns, D. S., Johnson, G., Edens, M., and Arnold, F., "Volume I – UAS Airborne Collision Severity Evaluation – Projectile and Target Definition", Federal Aviation Administration, Report DOT/FAA/AR-XX/XX, (to be published).

[21] "LS-DYNA Theory Manual", *LS-DYNA R8.0 User Manual,* Livermore Software Technology Corporation, 2015.

[22] "LS-DYNA Keywords User's Manual", *LS-DYNA R8.0 User Manual Vol. I,* Livermore Software Technology Corporation, 2015.

[23] "Modeling Guidelines Document", Ver. 15-1, LS-DYNA Aerospace Working Group, 2015.

[24] "LS-DYNA Keywords User's Manual – Material Models", *LS-DYNA R8.0 User's Manual Vol. II,* Livermore Software Technology Corporation, 2015.

[25] Dwivedi, A., Bradley, A., and Casem, D., "Mechanical Response of Polycarbonate with Strength Model Fits", Technical Report ARL-TR-5899, U.S. Army Research Lab., 2012.

[26] MMPDS-09, *Metallic Material Properties Development and Standardization (MMPDS)*, Chapter 9, Ed. 7, Battelle Memorial Institute, 2014.

[27] Ravi-Chandar, K., and Satapathy, S., "Mechanical Properties of G-10 Glass-Epoxy Composite", Technical Report IAT.R0466, Institute for Advanced Technology, The University of Texas Austin, 2007.

[28] Sahraei, E., Hill, R., and Wierzbicki, T., "Calibration and Finite Element Simulation of Pouch Lithium-Ion Batteries for Mechanical Integrity", *Journal of Power Sources*, Vol. 201, 2012, pp. 307-321.

[29] Sahraei, E., Meier, J., and Wierzbicki, T., "Characterizing and Modeling Mechanical Properties and Onset of Short Circuit for Three Types of Lithium-Ion Pouch Cells", *Journal of Power Sources*, Vol. 247, 2014, pp. 503-516.

[30] Stander, N., Roux, W., Basudhar, A., Eggleston, T., Goel, T., and Craig, K., *LS-OPT User's Manual, Ver. 5.1*, Livermore Software Technology Corporation, 2014.

[31] "Properties and Selection: Nonferrous Alloys and Special Purpose Materials", *ASM Handbook*, Vol. 2, ASM International, 1990.

[32] Olivares, G., "Simulation and Modeling of Bird Strike Testing", NIAR Report No. 09-039, National Institute for Aviation Research, 2009.

[33] Olivares G., Raju, S. K., and Acosta, J. F., "Certification by Analysis – Composite Materials Modeling", Draft Report DOT/FAA/AR-XX/XX, (not published).

[34] Olivares, G., Zinzuwadia, C., and Dhole N., "Crashworthiness Analysis of a Generic Narrow Body Aircraft", Draft Report DOT/FAA/AR-XX/XX, (not published).

[35] Olivares, G., and Zinzuwadia, C., "Joint modeling for large scale crashworthiness FE models – Single-point bolted joint", Draft Report DOT/FAA/AR-XX/XX, (not published).

[36] Jackson, K.E., and Fasanella, E.L., "Crash Simulation of Vertical Drop Tests of Two Boeing 737 Fuselage Sections", Report DOT/FAA/AR-02/62, Federal Aviation Administration, 2002.

[37] Olivares, G., Zinzuwadia, C., and Gomez, L., "Crashworthiness Certification by Analysis – Accident Reconstruction", Draft Report, DOT/FAA/AR-XX/XX, (not published).

[38] "Current Market Outlook 2014-2034", The Boeing Company, URL: http://www.boeing.com/commercial/market/long-term-market/

[39] "Delivering the Future – Global Market Forecast 2014-2034", Airbus SAS, URL: http://www.airbus.com/company/market/forecast/

[40] "Orders and Deliveries", The Boeing Company, URL: http://www.boeing.com/commercial/#/orders-deliveries/

[41] "Orders and Deliveries", Airbus SAS, URL: http://www.airbus.com/company/market/orders-deliveries/

[42] Jackson, P., *Jane's All the World's Aircraft 2007-2008*, Jane's Information Group, 2007.

[43] Jackson, P., *Jane's All the World's Aircraft 1999-2000*, Jane's Information Group, 1999.

[44] *Learjet 31A Airplane Flight Manual*, Bombardier Learjet Inc., 1991.

[45] Dolbeer, R.A., Wright, S.E., Weller, J.R., Anderson, A.L., and Begier, M.J., "Wildlife strikes to civil aircrafts in the United States 1990-2014", National Wildlife Strike Database, Serial Report No. 21, Federal Aviation Administration, 2015.

[46] U.S. Code of Federal Regulations, Title 14, Part 25, "Airworthiness standards: transport category airplanes", Washington, DC, U.S. Government Publishing Office, 2016.

[47] U.S. Code of Federal Regulations, Title 14, Part 23, "Airworthiness standards: normal, utility, acrobatic, and commuter category airplanes", Washington, DC, U.S. Government Publishing Office, 2016.

[48] *737-800 Structural Repair Manual*, The Boeing Company, 2013.

[49] *Learjet 20/30 Structural Repair Manual*, Bombardier Learjet, 2015.

[50] Niu, M.C., *Airframe Structural Design*, Conmilit Press Ltd., 1993.

[51] "PPG Aerospace Transparencies, Technical Data, Cockpit Windows, Next-Generation 737, Classic 737, 727, 707 Airplanes", PPG Industries, Huntsville, Alabama.

[52] Du Bois, P. A., "Crashworthiness engineering with LS-DYNA", Daimler-Chrysler AG, 2000.

[53] Day, J., and Bala, S., "General Guidelines for Crash Analysis in LS-DYNA", Livermore Software Technology Corporation, 2012.

[54] FAA Advisory Circulatory AC 43.13-1B, "Acceptable Methods, Techniques, and Practices - Aircraft Inspection and Repair", Federal Aviation Administration, 1998.

[55] Kay, G., “Failure Modeling of Titanium 6Al-4V and Aluminum 2024-T3 With the Johnson-Cook Material Model”, Report DOT/FAA/AR-03/57, Federal Aviation Administration, 2003.

[56] Buyuk, M., “Development of a New Metal Material Model in LS-DYNA. Part 2: Development of A Tabulated Thermo-Viscoplastic Material Model With Regularized Failure for Dynamic Ductile Failure Prediction of Structures Under Impact Loading”, Technical Report DOT/FAA/TC-13/25, P2, Federal Aviation Administration, 2014.

[57] Bala, S., “Material modeling in LS-DYNA”, LSTC Training Notes, Livermore Software Technology Corporation, 2005.

[58] Wang, J., Xu, Y., and Zhang, W., “Finite Element Simulation of PMMA Aircraft Windshield against Bird Strike by Using a Rate and Temperature Dependent Nonlinear Viscoelastic Constitutive Model”, *Composite Structures*, Vol. 108, 2014, pp. 21-30.

[59] Hidallana-Gamage, H.D., “Response of Laminated Glass Panels to Near Field Blast Events”, PhD Thesis, Queensland University of Technology, Australia, 2015.

[60] Hassard, R.S., “Plastic for Aerospace Vehicles. Part II Transparent Glazing Materials”, MIL-HDBK-17A Part II, Air Force Materials Lab., 1973.

[61] U.S. Code of Federal Regulations, Title 14, Part 91, “General Operation and Flight Rules”, Washington, DC, U.S. Government Publishing Office, 2016.

[62] “Airspace Made Easy”, Federal Aviation Administration, URL: https://www.faasafety.gov/files/events/ea/ea03/2012/ea0345029/airspace_made_easy.pdf

[63] Sprague, M. A., and Geers, T. L., “A Spectral-Element Method for Modelling Cavitation in Transient Fluid-Structure Interaction,” *International Journal of Numerical Methods in Engineering*, Vol, 60, pp. 2467–2499, 2004.

[64] “HyperGraph 2D User’s Guide”, *HyperWorks 14.0,* Altair Engineering Inc., 2015.

APPENDIX A – IDENTIFICATION OF UAS CRITICAL COMPONENTS

A.1 MATERIAL STUDY

The objective of this study was to understand the behavior of materials typical of an UAS construction under impact conditions similar to a bird strike. To achieve this, several simulations compared the material behavior and load transfer to the target of 1.81 kg (4 lb) projectiles of different materials (steel, ABS plastic, an equivalent battery material) with a 1.81 kg (4 lb) bird projectile under a 330 knots (169.8 m/s) impact.

A.1.1 Setup

Figure 273 shows the setup for the study in which a 1.81 kg (4 lb) projectile was impacted against a 3.175 mm thick aluminum panel at 330 knots (169.8 m/s).

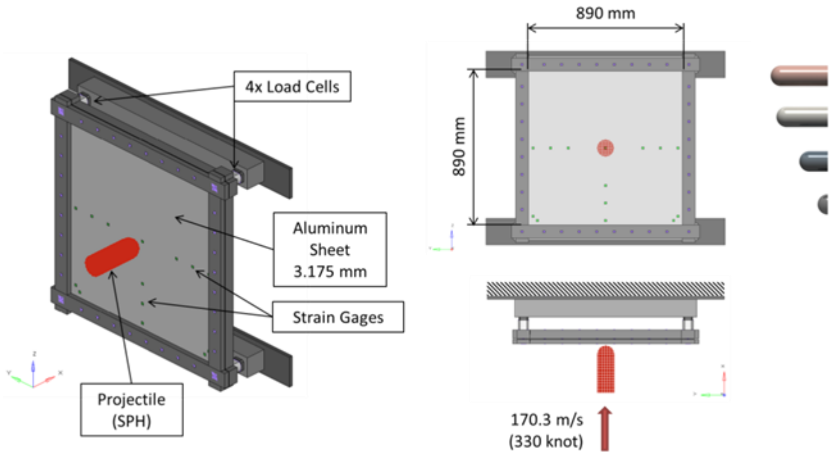

Figure 273 Material study setup

The panel was based on the design for a previous project of NIAR that involved bid strike testing, and from which a validated FE model was available to use in this project. A similar configuration was used for the ballistic component level tests in Section 2.4.4

All the projectiles had the same mass and diameter but variable lengths to account for the material density variations. The material properties used were the same as described in Section 2.3.2 . Each projectile was modelled using the Smoothed-Particle Hydrodynamics (SPH) method, available in LS-Dyna software.

A.1.2 Results and Conclusions

Figure 269 and 270 illustrate the effective plastic strain and the energy transfer due to the impact of four different projectiles.

From the results, it can be inferred that the materials with higher strength and stiffness induced greater damage and higher loads into the aluminum panel. UAS components such as the motors or the camera are constructed with these materials, so they will be identified as potential sources of damage into the aircraft structure.

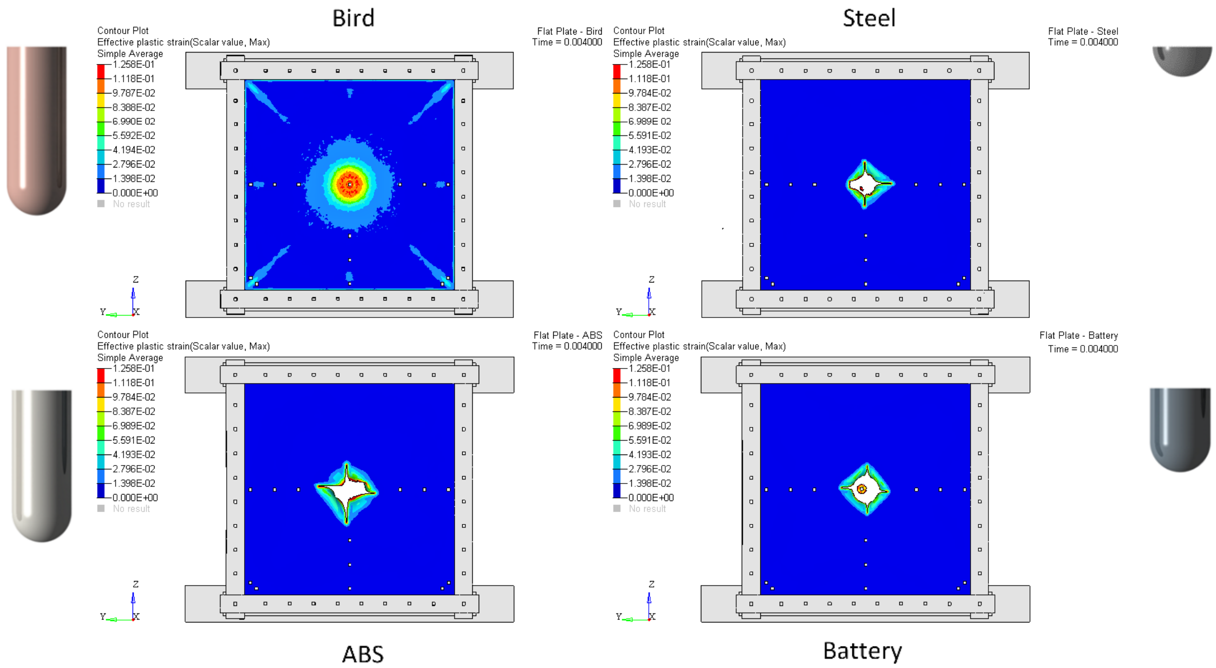

Figure 274. Material study results – effective plastic strain

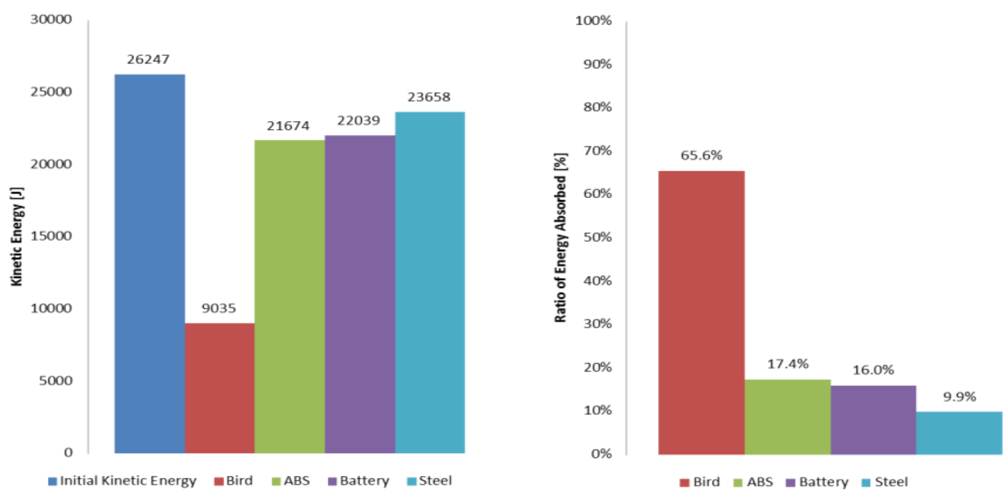

Figure 275 Material study results – energy transfer

A.2 Mass distribution study

The objective of this study was to understand the influence of concentrating or spreading the mass of the projectile. The steel projectile of the study presented in A.1 was used as a baseline. The 1.81 kg (4 lb) spherical steel projectile was spread into several (2, 4, 6 and 8) spherical masses.

A.2.1 Setup

Figure 276 shows the setup for the study in which the 1.81 kg (4 lb) steel projectile was impacted against a 3.175 mm thick aluminum panel at 330 knots (169.8 m/s).

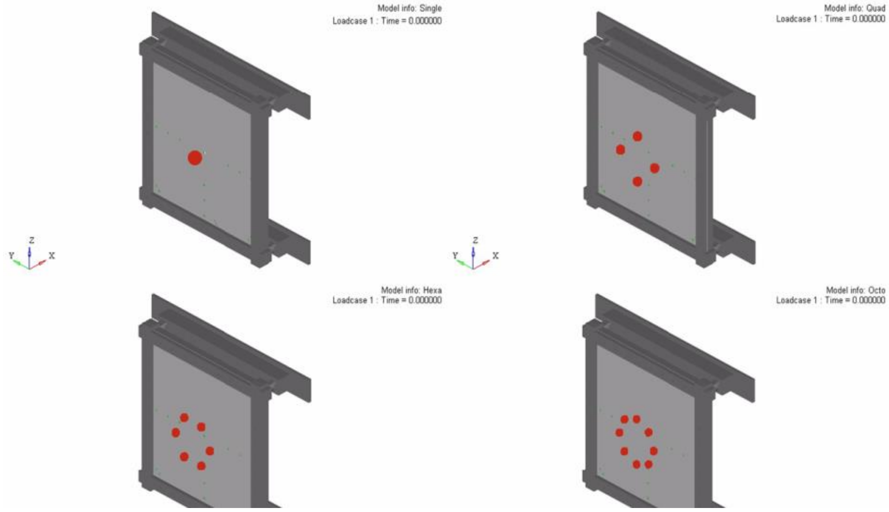

Figure 276. Mass distribution study setup

The masses were independent bodies and had no physical connection between them. The radius of mass distribution was set to 330 mm. The mass spreading represents motor distribution on the UAS. The same panel model and impact conditions were setup for this study as in A.1 .

A.2.2 Results and Conclusions

Figure 277 and Figure 278 show the effective plastic strain and the energy transfer due to the impact of projectile spread into different spherical masses.

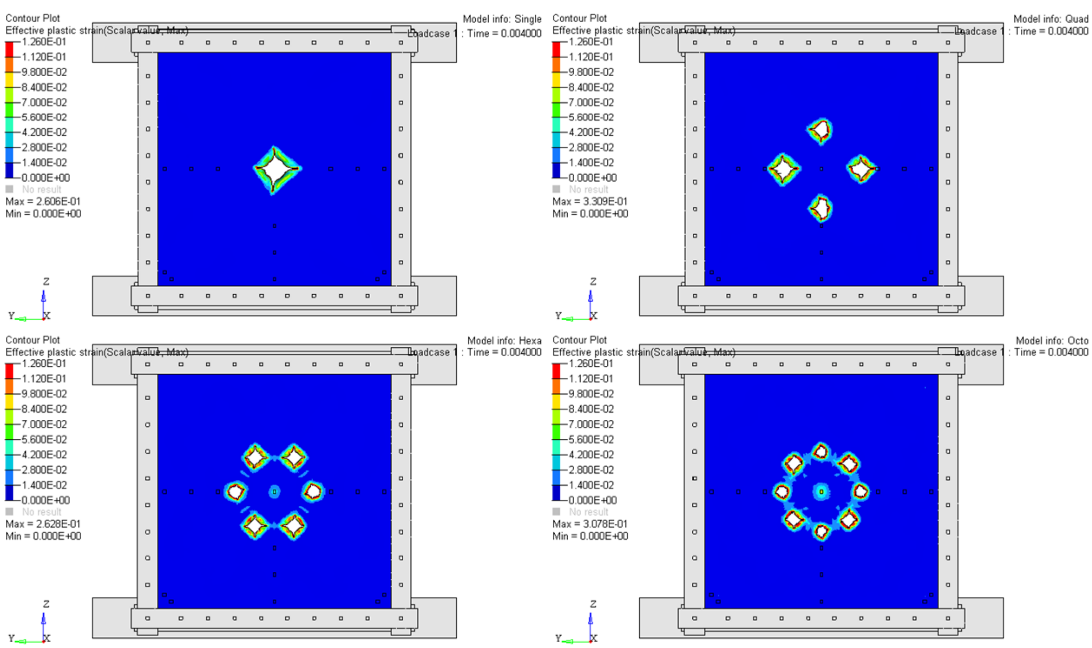

Figure 277. Mass distribution study results – effective plastic strain

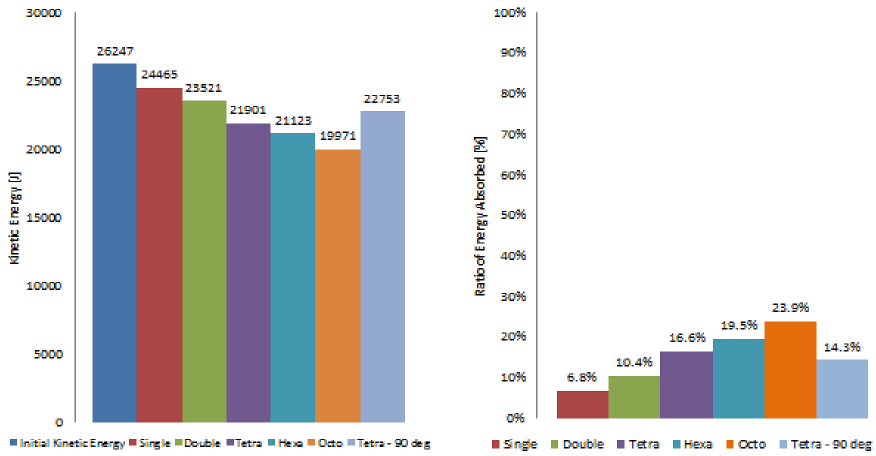

Figure 278. Mass distribution study results – energy transfer

A.3 Comparison with hail impact

The objective of this study was to investigate how materials of an UAS will behave under impact loads if compared with a well-known event in aircraft, hail impact. Impact of 34 g (0.07 lb) projectiles of different materials of UAS were compared with a hail impact of same mass and observed the material behavior and load transfer into the structure.

A.3.1 Setup

Figure 279 shows the setup for the study in which the 34 g projectiles were impacted against aluminum panel for velocities ranging from 110 to 350 knots (56.6 to 180 m/s). The projectiles had a spherical shape with varying diameters to account for the variation in material density.

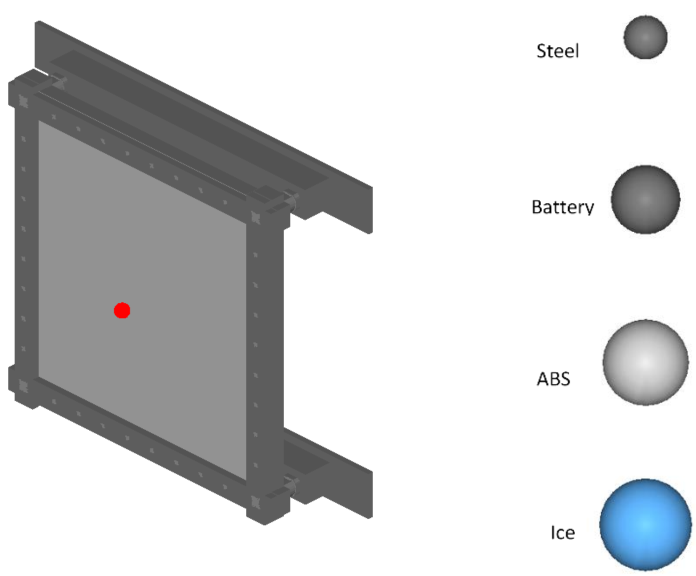

Figure 279. Comparison with hail impact setup

A.3.2 Results and Conclusions

Figure 280 depicts the effective plastic strain and Figure 281 shows the contact loads and permanent deformation in the aluminum panel due to the impact of projectiles at 350 knots (180 m/s).

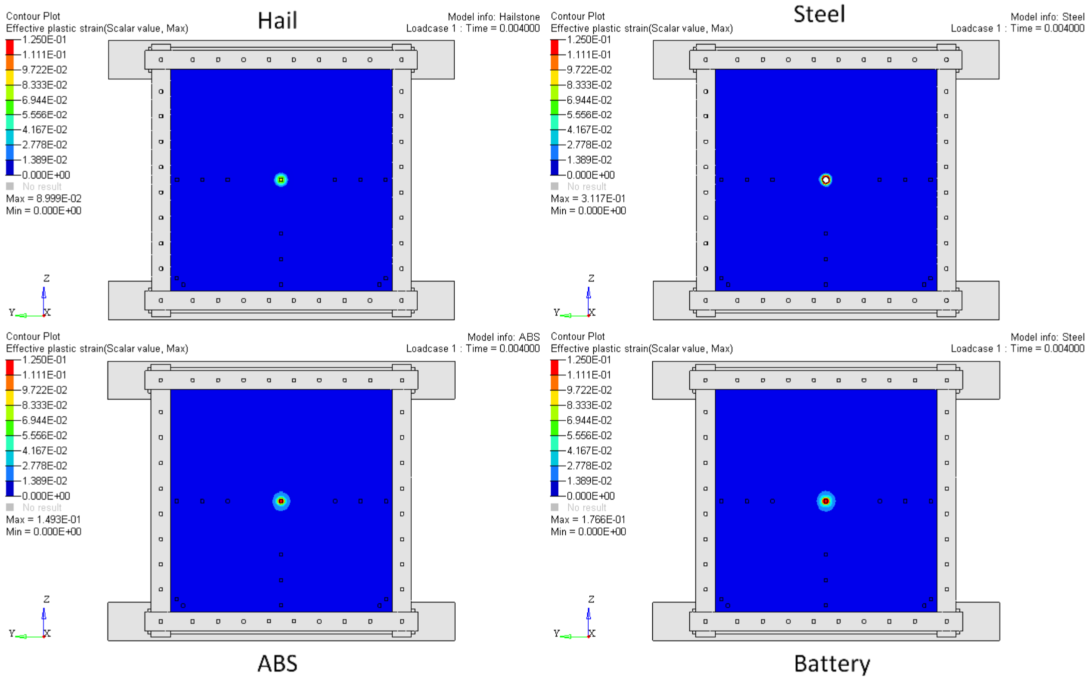

Figure 280. Comparison with hail impact results – effective plastic strain at 350 knots (180 m/s)

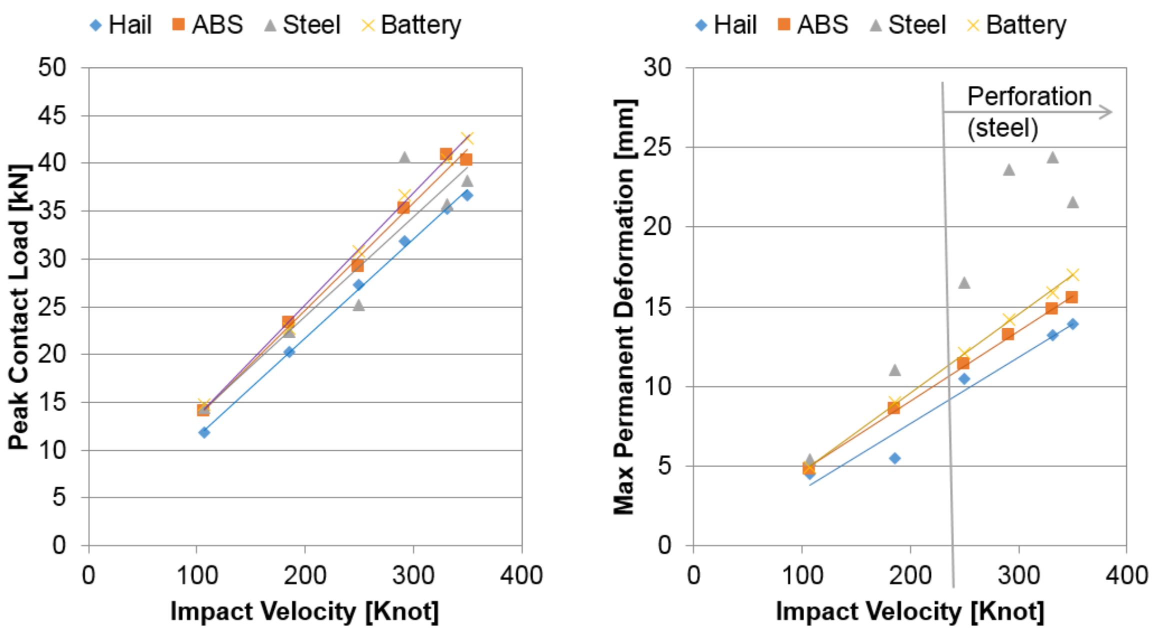

Figure 281. Comparison with hail impact results – contact loads and permanent deformation at 350 knots (180 m/s)

It was observed that the steel projectile was the only producing perforation of the plate. Hail behaved as a fluid, spreading the load on the surface of the panel, while ABS and Battery material behaved in a stiffer manner, but not enough to produce failure in the panel.

It can be concluded that the stronger material, steel produced maximum deformation on the panel at speeds over 200 knots compared to other materials. This indicates the criticality of the motor, which has the mass comparable to a hailstone and that may introduce much more damage into the airframe.

APPENDIX B – AIRBORNE COLLISION ANALYSIS REPORT

B.1 COMMERCIAL TRANSPORT JET

B.1.1 Vertical Stabilizer

B.1.1.1 CQV1

The UAS was impacted against the vertical stabilizer at 128.6 m/s (250 knots) in the local x-axis direction of the aircraft. The impact location selected was at approximately 40% of the vertical stabilizer span, with the center of gravity of the UAS aligned with the midpoint between ribs 6 and 7. Figure 282 depicts the kinematics of the event. Figure 111 shows the damage caused to the skin and inner frames of the vertical stabilizer.

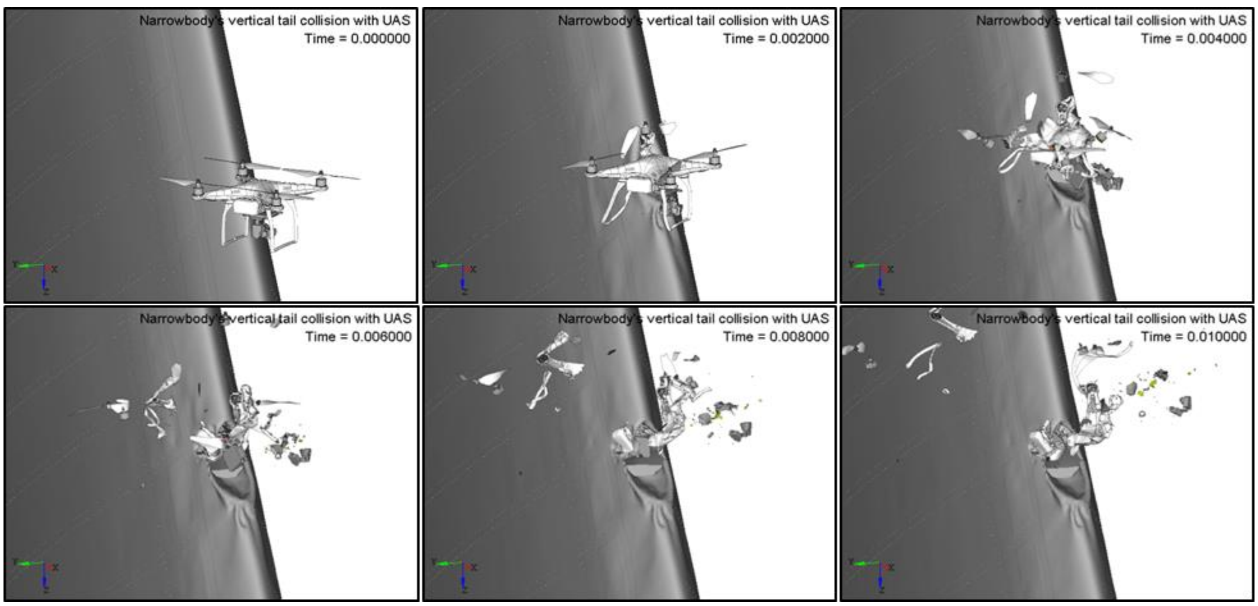

Figure 282. Kinematics of the impact between a commercial transport jet vertical stabilizer at location 1 and a 1.2 kg (2.7 lb) UAS at 128.6 m/s (250 knots)

The UAS damages the skin and the upper and lower ribs, creating a damaged zone of 116x244 mm on the skin surface. The permanent deformation in the ribs can be seen in the bottom left image in Figure 111. These impacts considerably reduce the velocity of the UAS components and the front spar is able to hold off the UAS components without sustaining any damage.

The damage introduced by the UAS involved perforation of the skin but no damage to the primary structure, and consequently the severity was classified as Level 3.

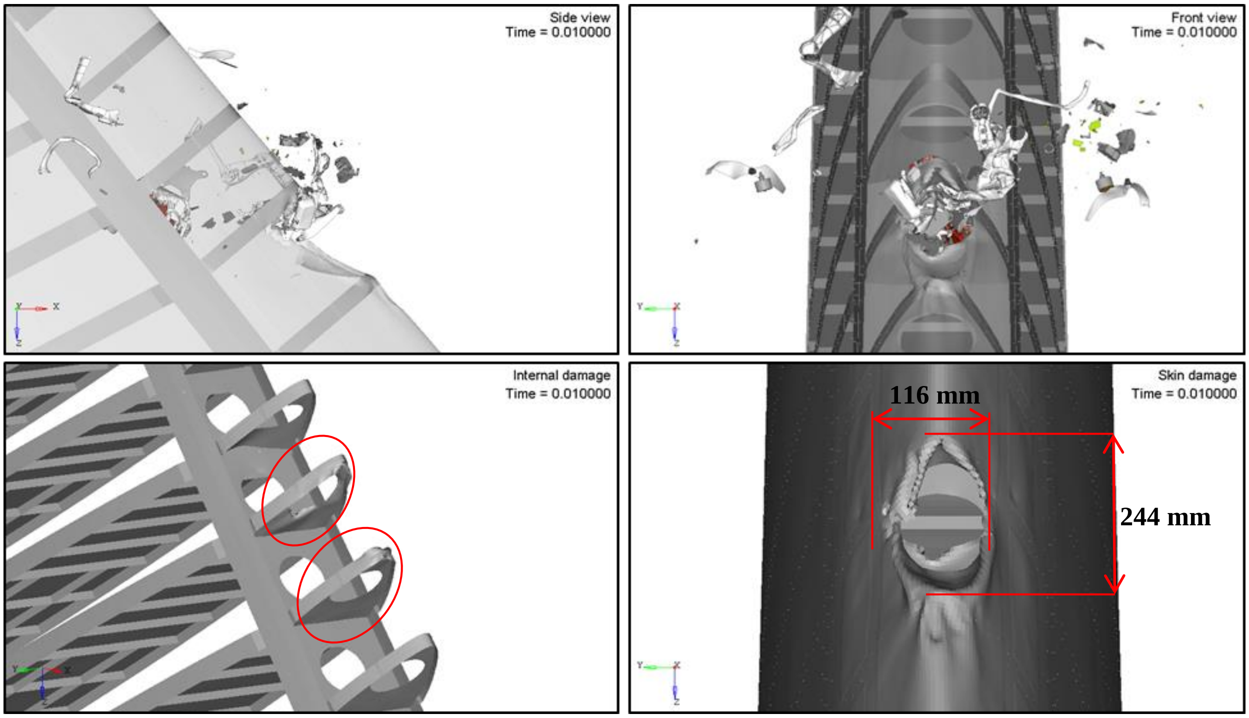

Figure 283. External/internal damage sustained by a commercial transport jet vertical stabilizer impacted at location 1 with a 1.2 kg (2.7 lb) UAS at 128.6 m/s (250 knots)

Figure 284 shows the impulse due to the contact force between UAS and vertical stabilizer, as well as the energy balance for both of them. Figure 285 shows the internal energies of UAS and vertical stabilizer parts directly involved in the impact.

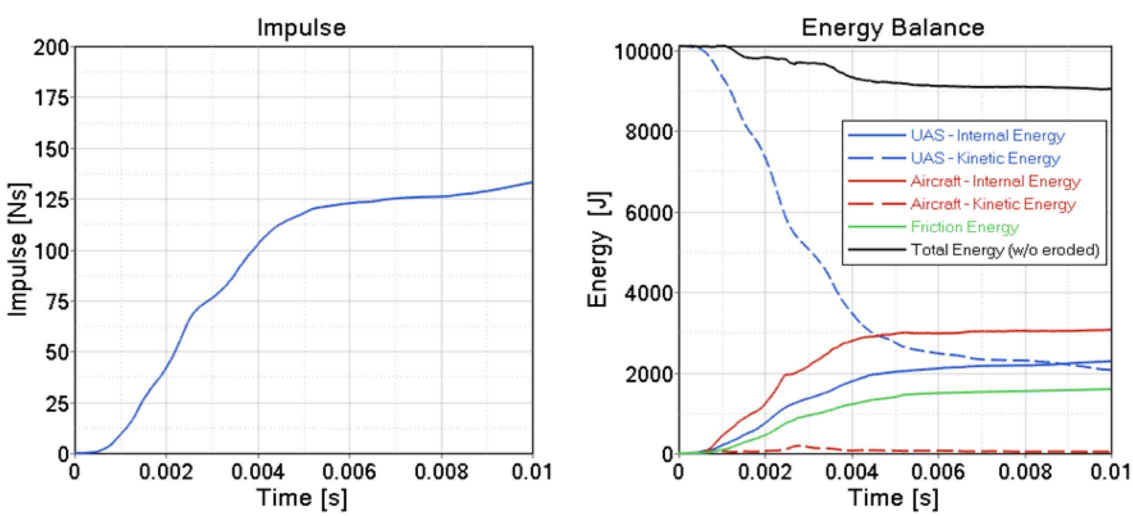

Figure 284. Impulse and energy balance of the impact between a commercial transport jet vertical stabilizer at location 1 and a 1.2 kg (2.7 lb) UAS at 128.6 m/s (250 knots)

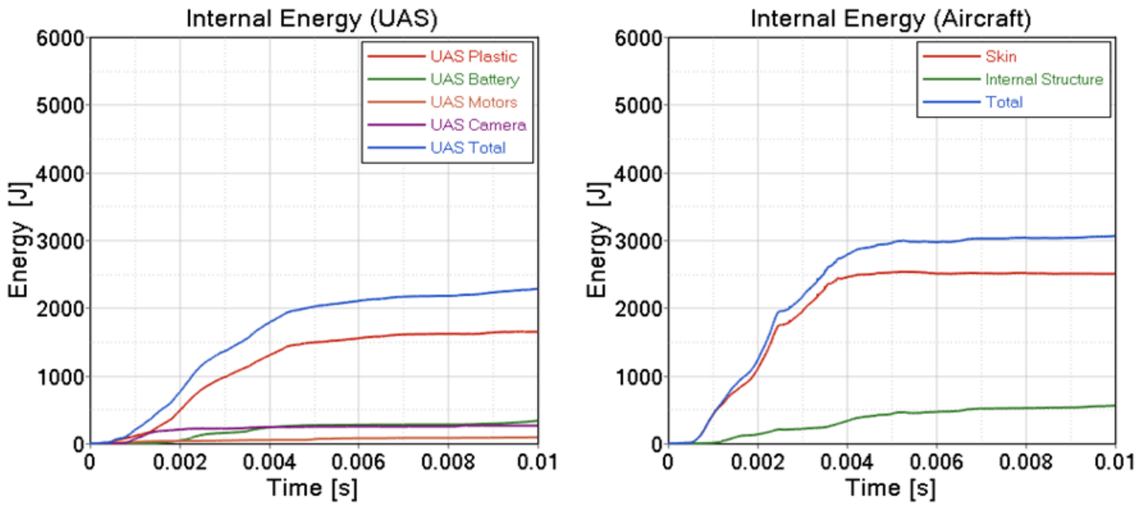

Figure 285. Internal energy per component of the impact between a commercial transport jet vertical stabilizer at location 1 and a 1.2 kg (2.7 lb) UAS at 128.6 m/s (250 knots)

The energy balance plot includes the UAS and vertical stabilizer kinetic and internal energies as well as frictional energy and total energy for the event. The vertical stabilizer absorbs 30% of the impact energy, while the UAS absorbs 23% of it and the energy dissipated by friction reaches 16% of the total energy. In Figure 285, internal energies for the UAS parts and the vertical stabilizer show that the polycarbonate and skin absorb the highest amount of internal energies respectively.

B.1.1.2 CQV2

The UAS was impacted against the vertical stabilizer at 128.6 m/s (250 knots) in the local x-axis direction of the aircraft. The impact location selected was at approximately 55% of the vertical stabilizer span, with the center of gravity of the UAS aligned with the midpoint between ribs 13 and 14. Figure 286 depicts the kinematics of the event. Figure 287 shows the damage caused to the skin and inner frames of the vertical stabilizer.

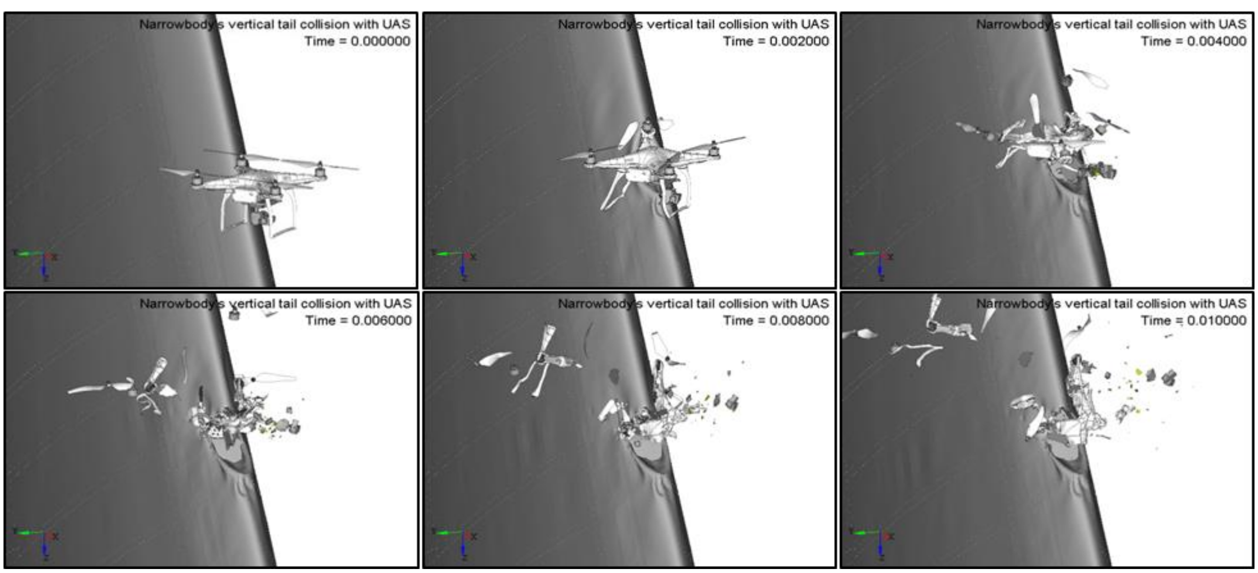

Figure 286. Kinematics of the impact between a commercial transport jet vertical stabilizer at location 2 and a 1.2 kg (2.7 lb) UAS at 128.6 m/s (250 knots)

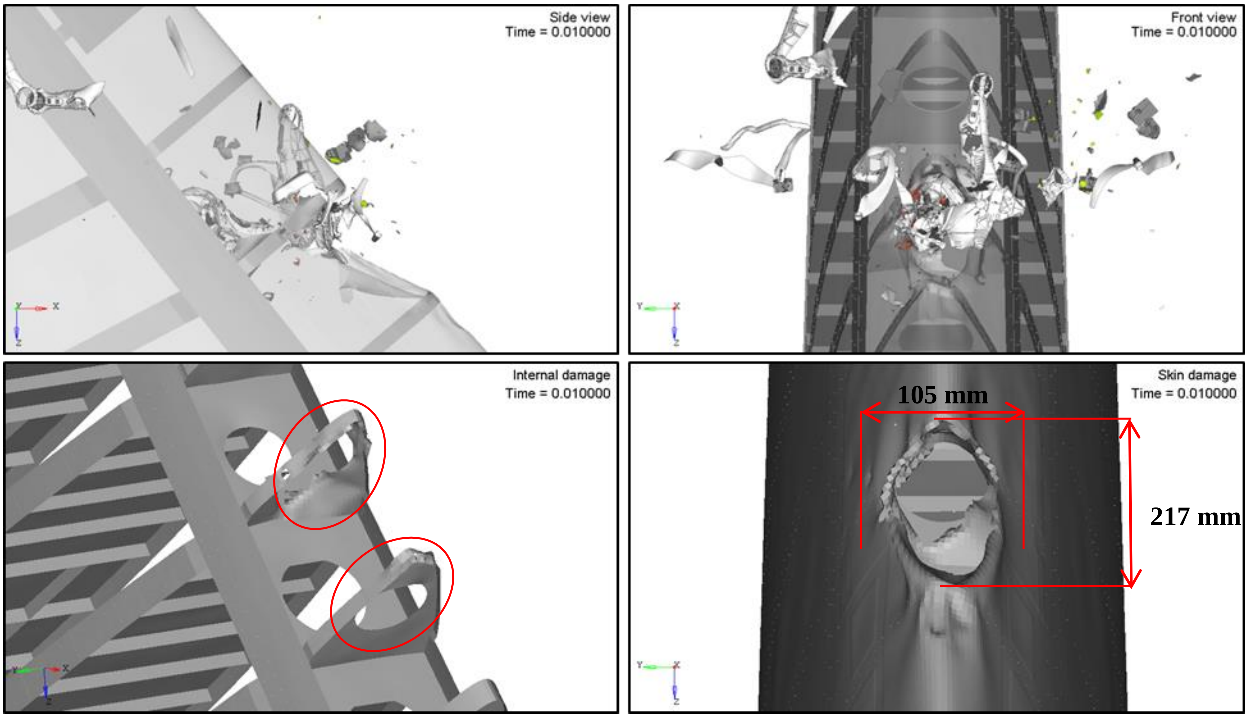

Figure 287. External/internal damage sustained by a commercial transport jet vertical stabilizer impacted at location 2 and a 1.2 kg (2.7 lb) UAS at 128.6 m/s (250 knots)

The UAS damages the skin and the upper and lower ribs, creating a damaged zone of 105x217 mm on the skin surface. The permanent deformation in the ribs can be seen in the bottom left image in Figure 287. These impacts considerably reduce the velocity of the UAS components and the front spar is able to hold off the UAS components without sustaining any damage.

The damage introduced by the UAS involved perforation of the skin but no damage to the primary structure, and consequently the severity was classified as Level 3.

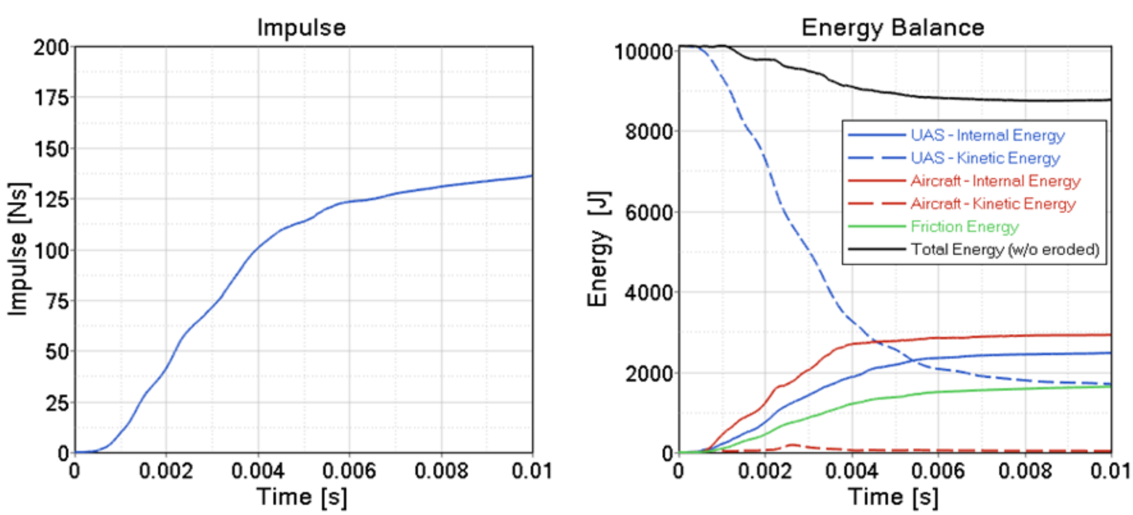

Figure 288. Impulse and energy balance of the impact between a commercial transport jet vertical stabilizer at location 2 and a 1.2 kg (2.7 lb) UAS at 128.6 m/s (250 knots)

Figure 288 shows the impulse due to the contact force between UAS and vertical stabilizer, as well as the energy balance for both of them. Figure 289 shows the internal energies of UAS and vertical stabilizer parts directly involved in the impact.

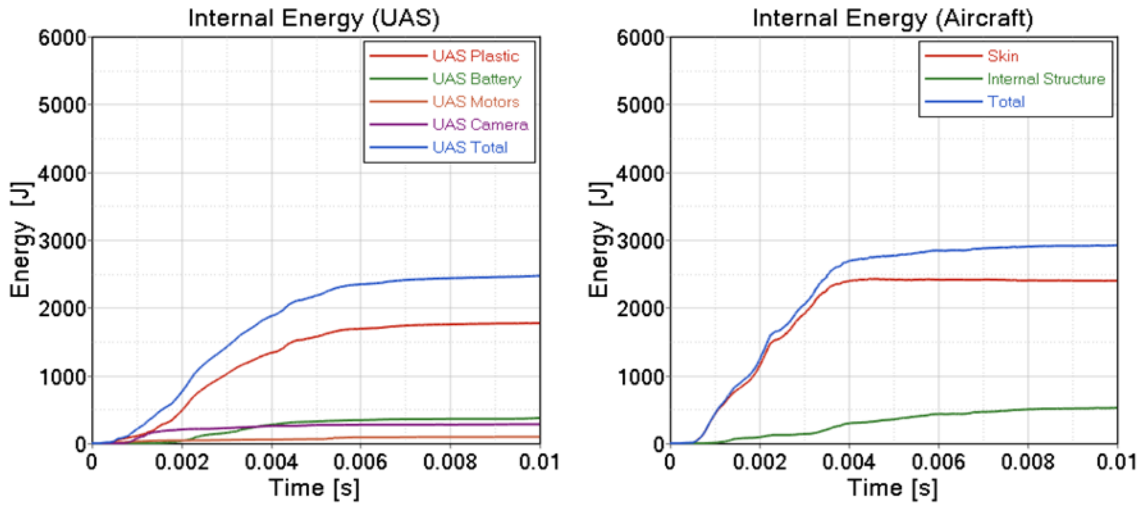

Figure 289. Internal energy per component of the impact between a commercial transport jet vertical stabilizer at location 2 and a 1.2 kg (2.7 lb) UAS at 128.6 m/s (250 knots)

The energy balance plot includes the UAS and vertical stabilizer kinetic and internal energies as well as frictional energy and total energy for the event. The vertical stabilizer absorbs 29% of the impact energy, while the UAS absorbs 25% of it and the energy dissipated by friction reaches 16% of the total energy. In Figure 289, internal energies for the UAS parts and the vertical stabilizer show that the polycarbonate and skin absorb the highest amount of internal energies respectively.

B.1.1.3 CQV3

This impact location was identified as the critical baseline simulation for the commercial transport jet vertical stabilizer and is discussed in section 4.3.1.1 of the main report body.

B.1.1.4 CQV4

The UAS was impacted against the vertical stabilizer at 128.6 m/s (250 knots) in the local x-axis direction of the aircraft. The impact location selected was at approximately 85% of the vertical stabilizer span, with the center of gravity of the UAS aligned with the midpoint between ribs 25 and 26. Figure 290 depicts the kinematics of the event. Figure 291 shows the damage caused to the skin and inner frames of the vertical stabilizer.

The UAS damages the skin, the upper and lower ribs, and the front spar, creating a damaged zone of 108x208 mm on the skin surface. The permanent deformation in the ribs can be seen in the bottom left image in Figure 291. These impacts considerably reduce the velocity of the UAS components and the front spar is able to hold off the UAS components without sustaining any major damage.

The damage introduced by the UAS involved perforation of the skin but no damage to the primary structure, and consequently the severity was classified as Level 3.

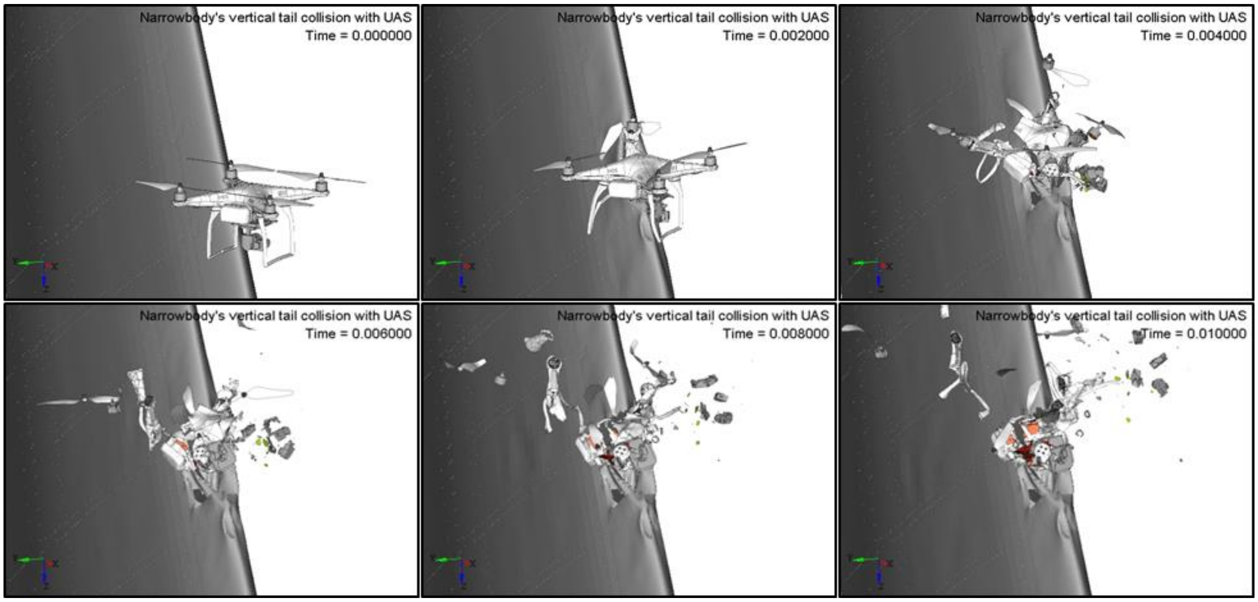

Figure 290. Kinematics of the impact between a commercial transport jet vertical stabilizer at location 4 and a 1.2 kg (2.7 lb) UAS at 128.6 m/s (250 knots)

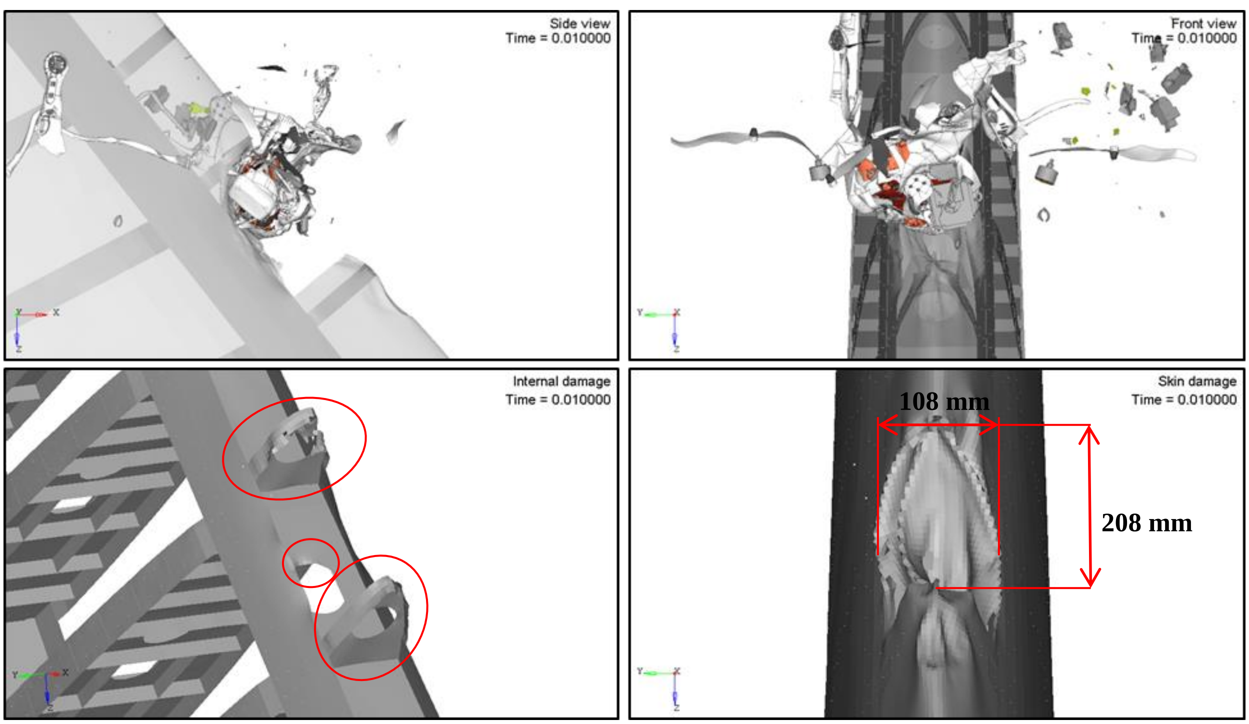

Figure 291. External/internal damage sustained by a commercial transport jet vertical stabilizer impacted at location 4 and a 1.2 kg (2.7 lb) UAS at 128.6 m/s (250 knots)

Figure 292 shows the impulse due to the contact force between UAS and vertical stabilizer, as well as the energy balance for both of them. Figure 293 shows the internal energies of UAS and vertical stabilizer parts directly involved in the impact.

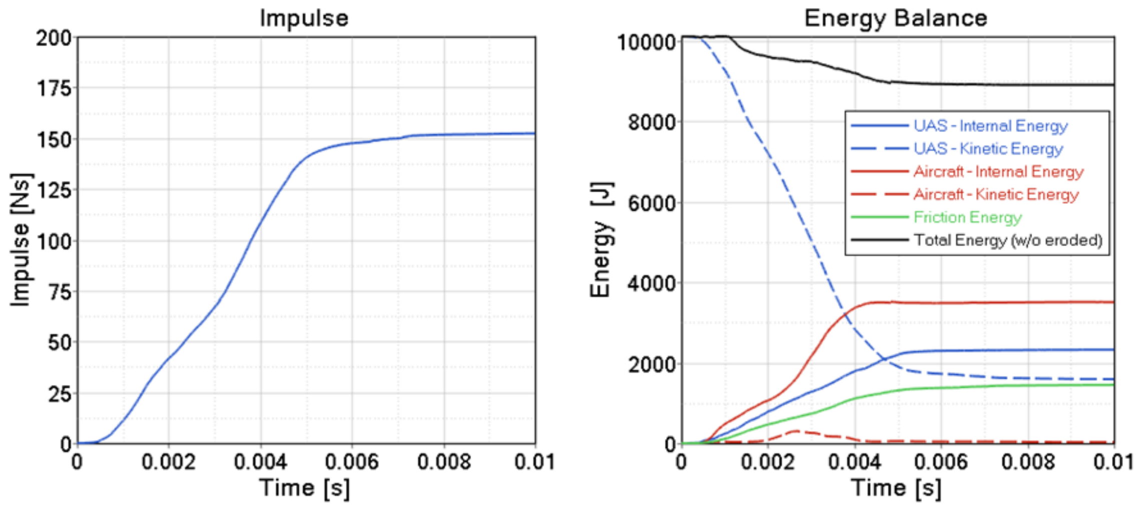

Figure 292. Impulse and energy balance of the impact between a commercial transport jet vertical stabilizer at location 4 and a 1.2 kg (2.7 lb) UAS at 128.6 m/s (250 knots)

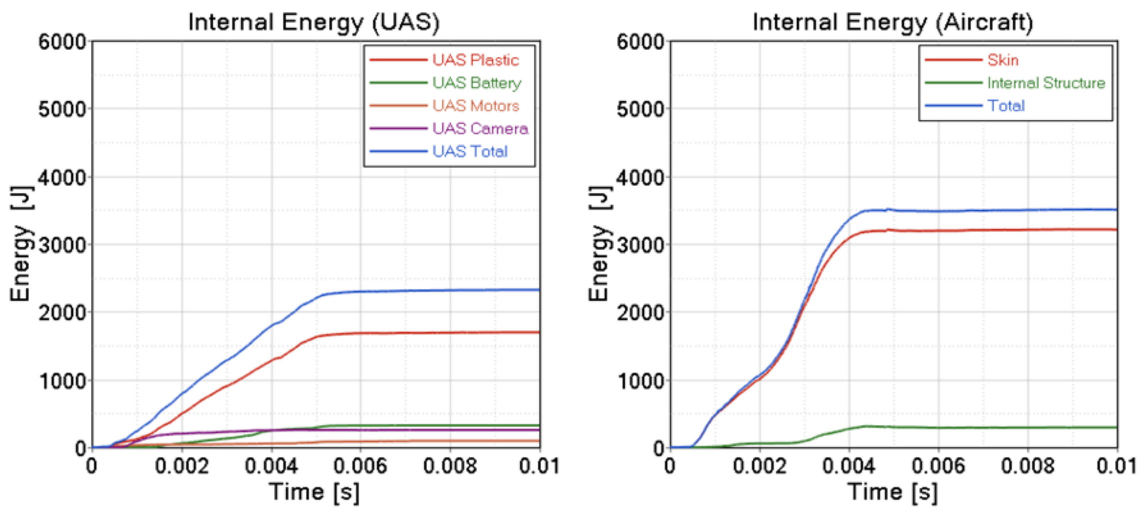

Figure 293. Internal energy per component of the impact between a commercial transport jet vertical stabilizer at location 4 and a 1.2 kg (2.7 lb) UAS at 128.6 m/s (250 knots)

The energy balance plot includes the UAS and vertical stabilizer kinetic and internal energies as well as frictional energy and total energy for the event. The vertical stabilizer absorbs 35% of the impact energy, while the UAS absorbs 23% of it and the energy dissipated by friction reaches 16% of the total energy. In Figure 293, internal energies for the UAS parts and the vertical stabilizer show that the polycarbonate and skin absorb the highest amount of internal energies respectively.

B.1.2 Horizontal Stabilizer

B.1.2.1 CQH1

The UAS was impacted against the horizontal stabilizer at 128.6 m/s (250 knots) along the local x-axis direction of the aircraft. The impact location selected was at approximately 15% of the horizontal stabilizer semispan, with the center of gravity of the UAS aligned with the midpoint between ribs 5 and 6. Figure 294 presents the kinematics of the event. Figure 295 shows the damage caused to the inner frames and the skin.

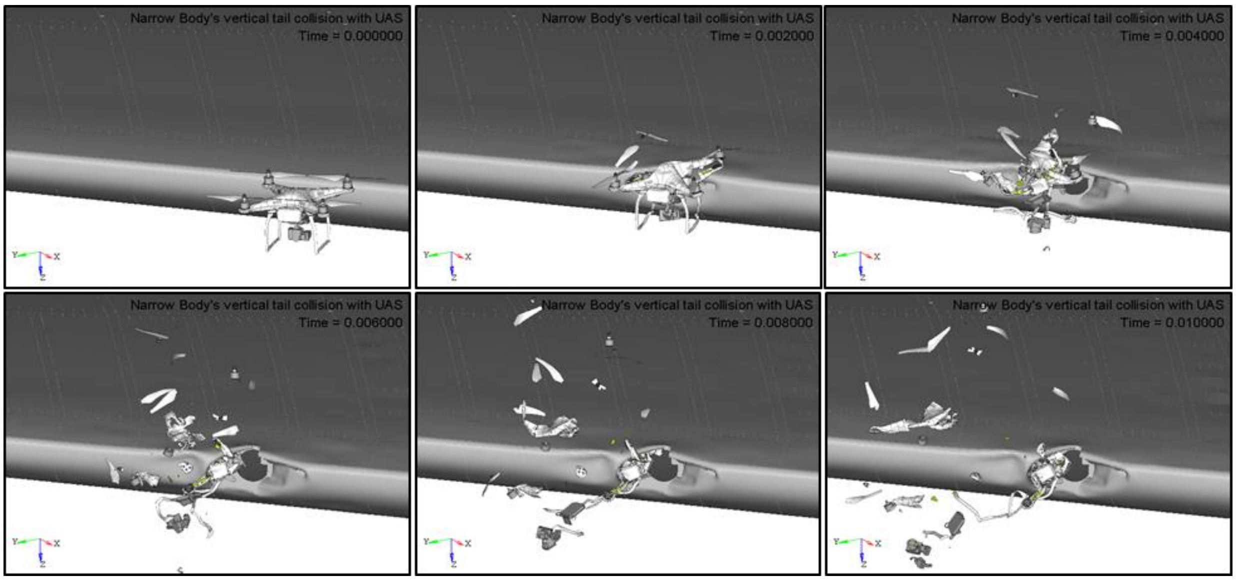

Figure 294. Kinematics of the impact between a commercial transport jet horizontal stabilizer at location 1 and a 1.2 kg (2.7 lb) UAS at 128.6 m/s (250 knots)

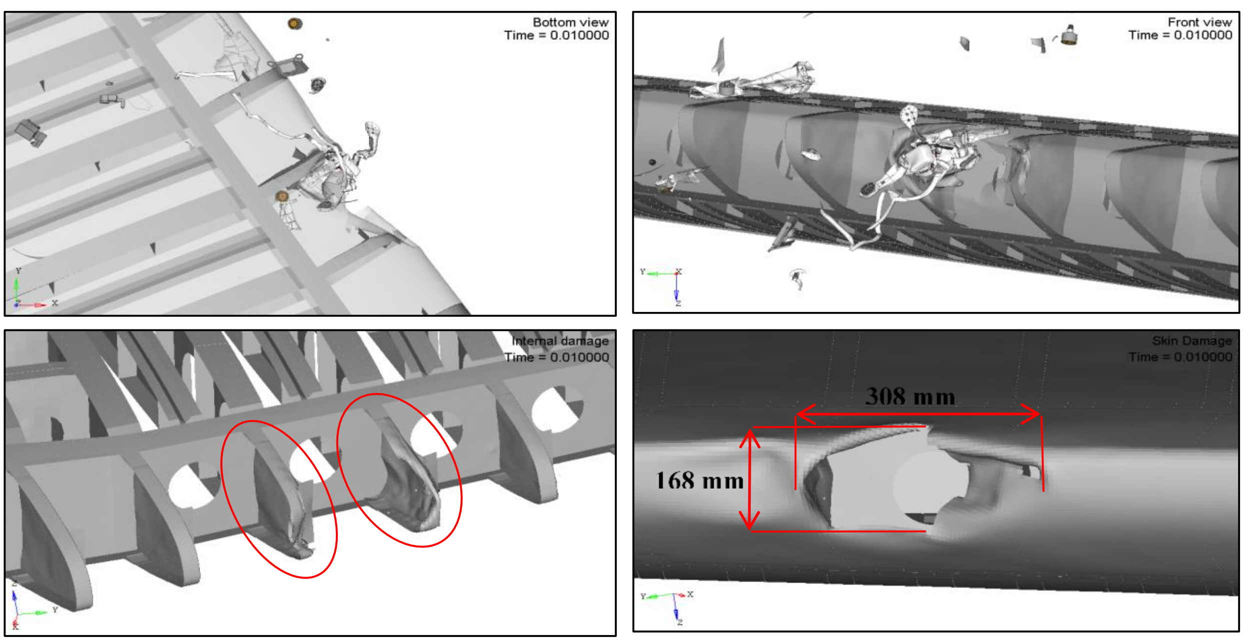

Figure 295. External/internal damage sustained by a commercial transport jet horizontal stabilizer impacted at location 1 and a 1.2 kg (2.7 lb) UAS at 128.6 m/s (250 knots)

The UAS damages the skin and the nose ribs, creating a damaged zone of 308x168 mm on the skin surface and allowing the rest of the UAS mass to penetrate until it loses its velocity before reaching the front spar. On the bottom left image at Figure 295, it can be appreciated the permanent deformation caused to the ribs. The front spar did not sustain any critical damage.

The damage introduced by the UAS involved perforation of the skin but no damage to the primary structure, and consequently the severity was classified as Level 3.

Figure 296 shows the impulse due to the contact force between the UAS and the horizontal stabilizer, as well as the energy balance for both of them. Figure 297 presents the internal energies of the UAS and horizontal stabilizer parts directly involved on the impact.

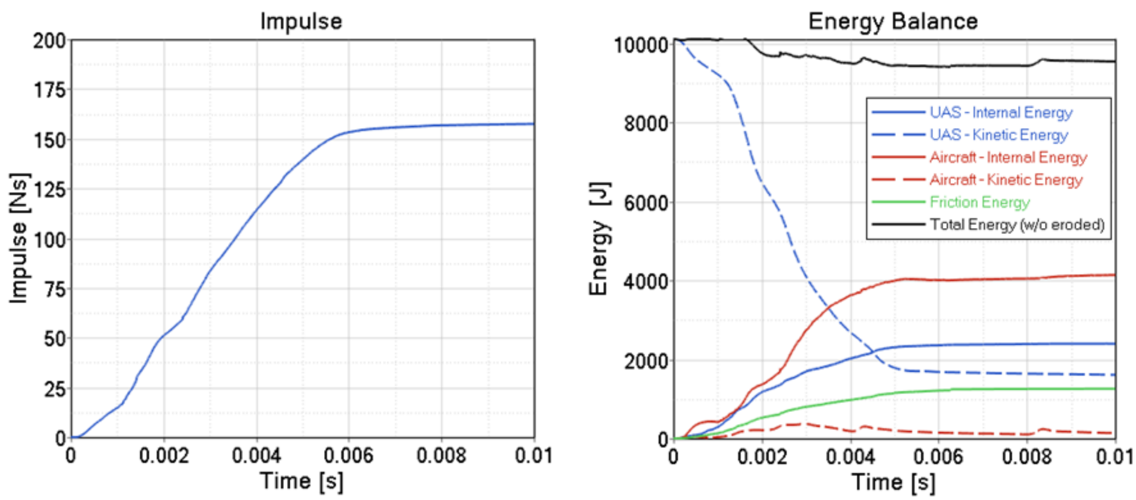

Figure 296. Impulse and energy balance of the impact between a commercial transport jet horizontal stabilizer at location 1 and a 1.2 kg (2.7 lb) UAS at 128.6 m/s (250 knots)

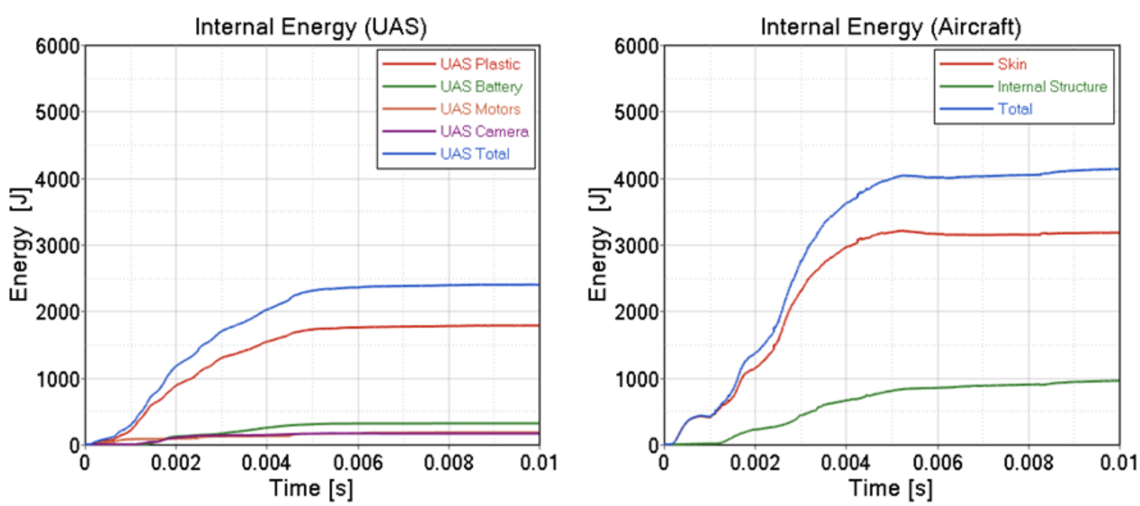

Figure 297. Internal energy per component of the impact between a commercial transport jet horizontal stabilizer at location 1 and a 1.2 kg (2.7 lb) UAS at 128.6 m/s (250 knots)

The energy balance plot includes the UAS and horizontal stabilizer kinetic and internal energies, as well as frictional energy and total energy for the event. The stabilizer absorbs 41% of the impact energy, while the UAS takes 24% of it and the energy dissipated by friction reaches 16% of the total energy. In Figure 297, internal energies for the UAS parts and the stabilizer structure show that the skin and the polycarbonate absorb the highest internal energies of the event.

B.1.2.2 CQH2

The UAS was impacted against the horizontal stabilizer at 128.6 m/s (250 knots) along the local x-axis direction of the aircraft. The impact location selected was at approximately 40% of the horizontal stabilizer semispan, with the center of gravity of the UAS aligned with the midpoint between ribs 12 and 13. Figure 298 presents the kinematics of the event. Figure 299 shows the damage caused to the inner frames and the skin.

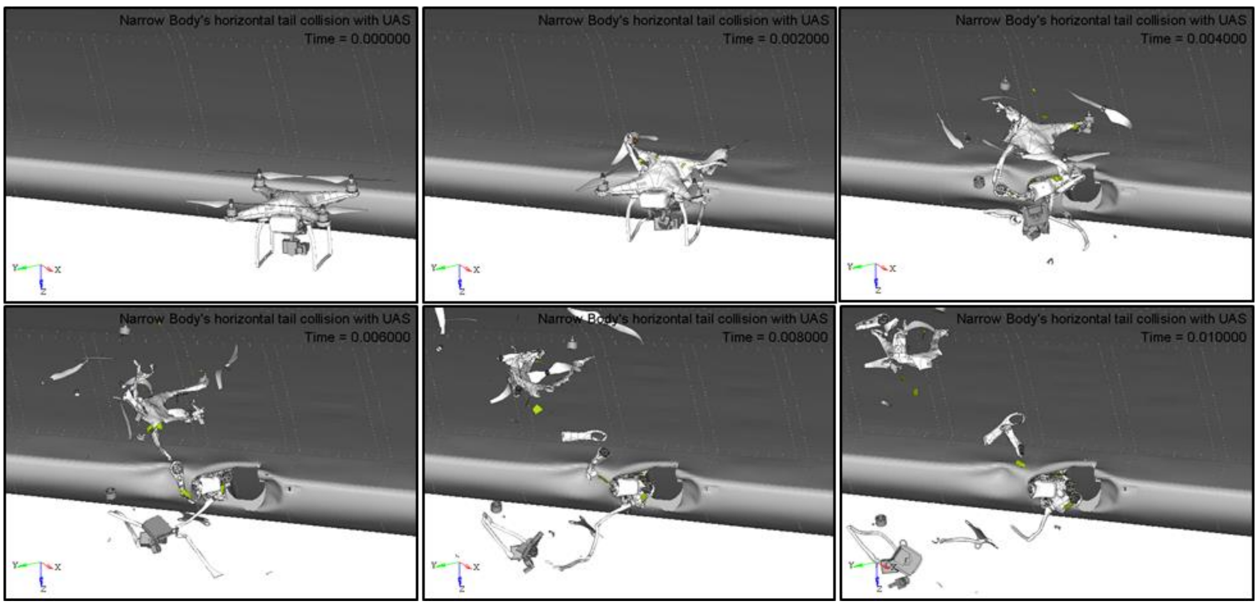

Figure 298. Kinematics of the impact between a commercial transport jet horizontal stabilizer at location 2 and a 1.2 kg (2.7 lb) UAS at 128.6 m/s (250 knots)

The UAS damages the skin and the nose ribs, creating a damaged zone of 238x129 mm on the skin surface and allowing the rest of the UAS mass to penetrate until it loses its velocity before reaching the front spar. On the bottom left image at Figure 299, it can be appreciated the permanent deformation caused to the ribs. The front spar did not sustain to any critical damage.

The damage introduced by the UAS involved perforation of the skin but no damage to the primary structure, and consequently the severity was classified as Level 3.

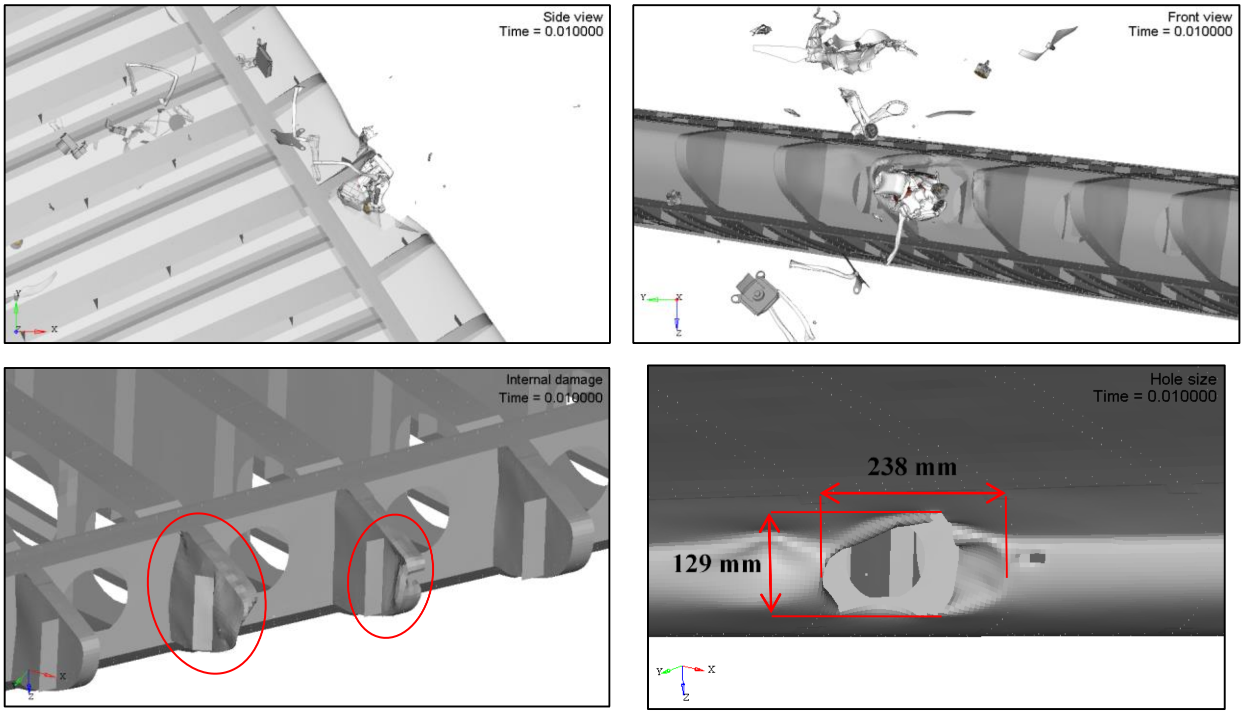

Figure 299. External/internal damage sustained by a commercial transport jet horizontal stabilizer at location 2 and a 1.2 kg (2.7 lb) UAS at 128.6 m/s (250 knots)

Figure 300 shows the impulse due to the contact force between the UAS and the horizontal stabilizer, as well as the energy balance for both of them. Figure 301 presents the internal energies of the UAS and horizontal stabilizer parts directly involved on the impact.

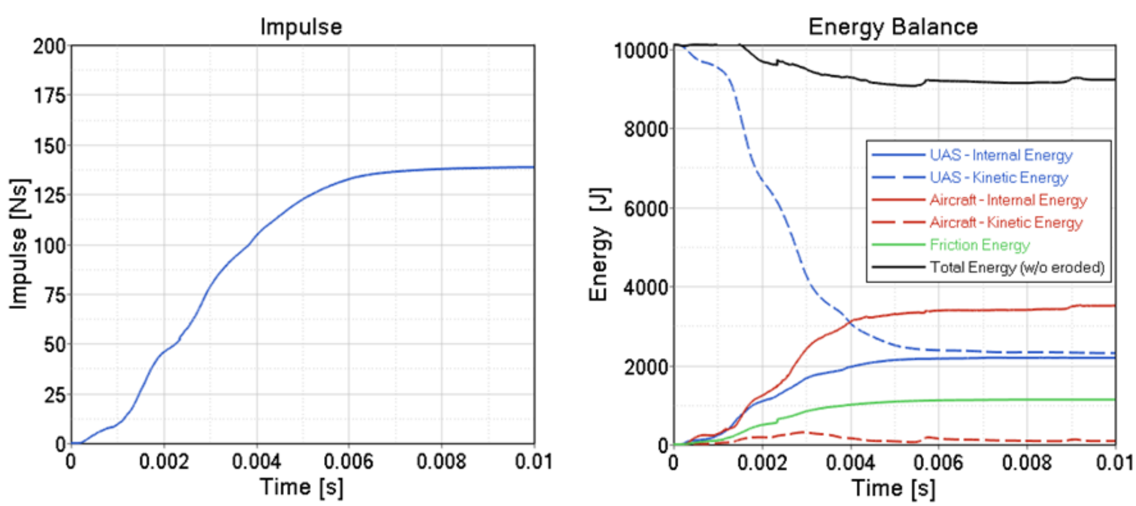

Figure 300. Impulse and energy balance of the impact between a commercial transport jet horizontal stabilizer at location 2 and a 1.2 kg (2.7 lb) UAS at 128.6 m/s (250 knots)

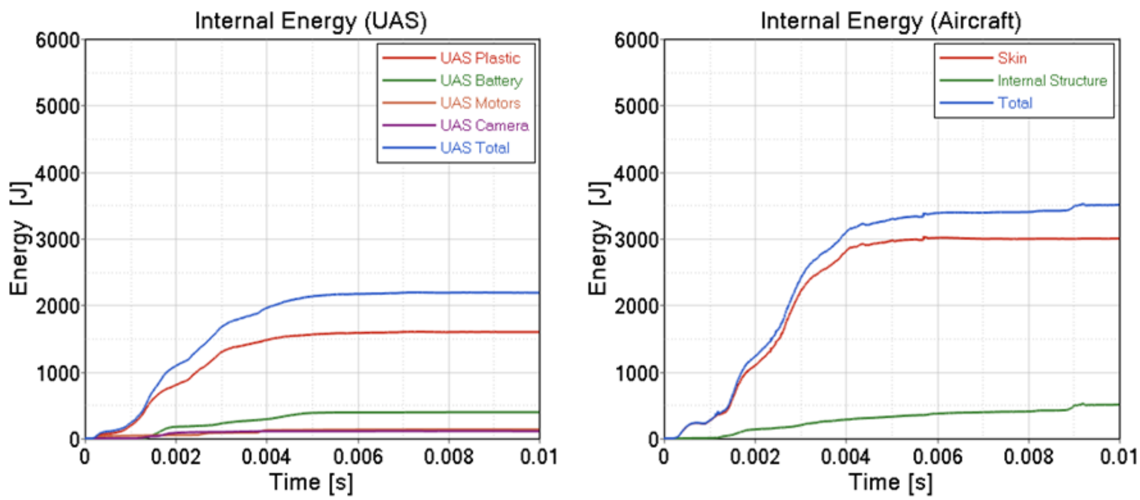

Figure 301. Internal energy per component of the impact between a commercial transport jet horizontal stabilizer at location 2 and a 1.2 kg (2.7 lb) UAS at 128.6 m/s (250 knots)

The energy balance plot includes the UAS and horizontal stabilizer kinetic and internal energies, as well as frictional energy and total energy for the event. The stabilizer absorbs 35% of the impact energy, while the UAS takes 22% of it and the energy dissipated by friction reaches 11% of the total energy. In Figure 301, internal energies for the UAS parts and the stabilizer structure show that the skin and the polycarbonate absorb the highest internal energies of the event.

B.1.2.3 CQH3

This impact location was identified as the critical baseline simulation for the commercial transport jet horizontal stabilizer and is discussed in section 4.3.2.1 of the main report body.

B.1.2.4 CQH4

The UAS was impacted against the horizontal stabilizer at 128.6 m/s (250 knots) along the local x-axis direction of the aircraft. The impact location selected was at approximately 80% of the horizontal stabilizer semispan, with the center of gravity of the UAS aligned with the midpoint between ribs 25 and 26. Figure 302 presents the kinematics of the event. Figure 303 shows the damage caused to the inner frames and the skin.

The UAS damages the skin and the nose ribs, creating a damaged zone of 237x85 mm on the skin surface and allowing the rest of the UAS mass to penetrate until it perforates the front spar, causing a fracture of 78x51 mm. On the bottom left image at Figure 303, it can be appreciated the damage and permanent deformation caused to the ribs and the front spar. In this case, the front spar sustained critical damage.

The damage introduced by the UAS involved perforation of the skin and damage to the primary structure, and consequently the severity was classified as Level 4.

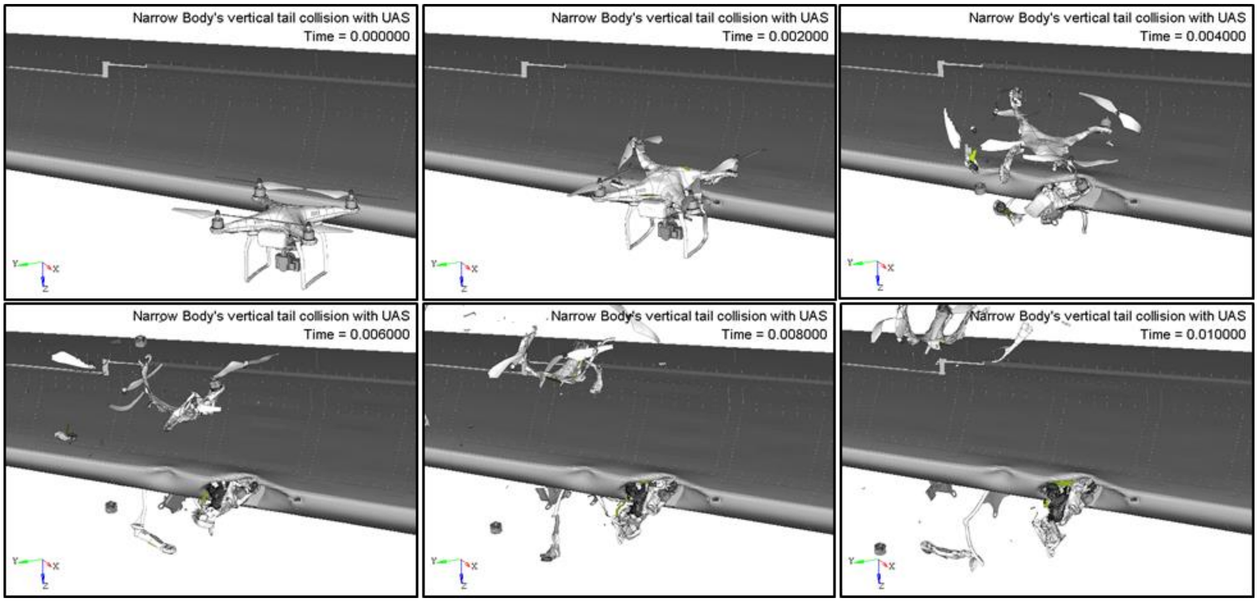

Figure 302. Kinematics of the impact between a commercial transport jet horizontal stabilizer at location 4 and a 1.2 kg (2.7 lb) UAS at 128.6 m/s (250 knots)

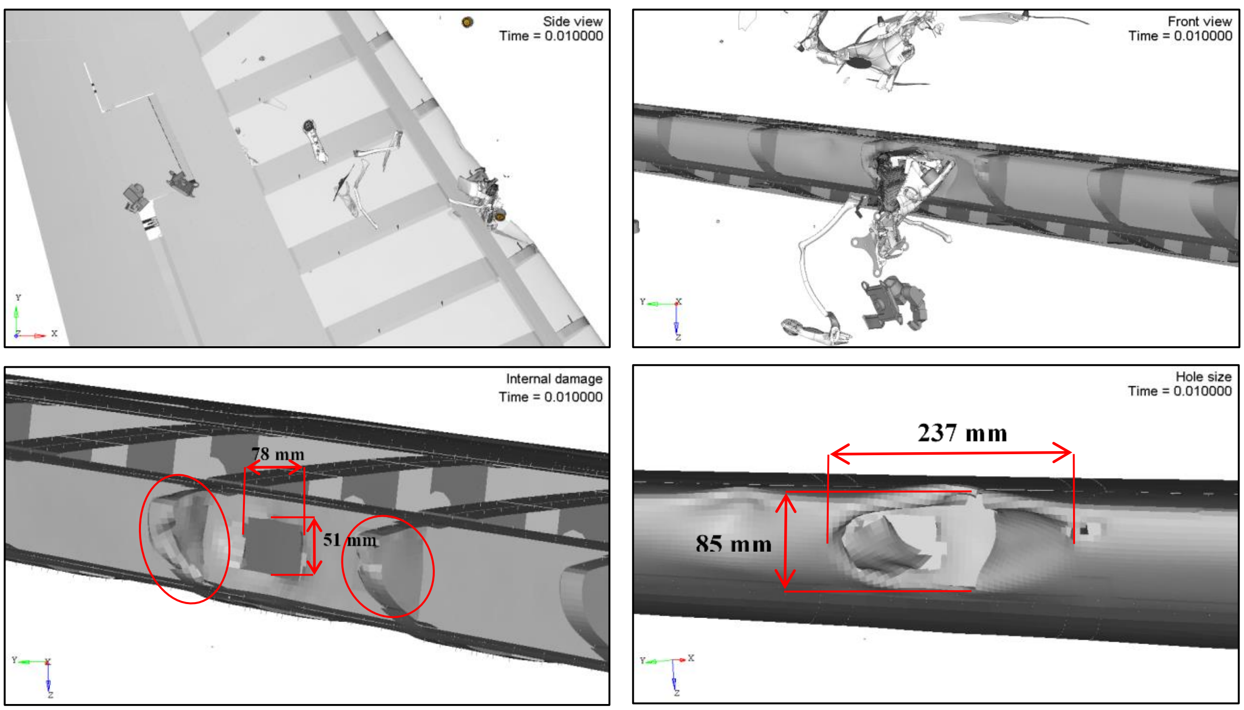

Figure 303. External/internal damage sustained by a commercial transport jet horizontal stabilizer impacted at location 4 and a 1.2 kg (2.7 lb) UAS at 128.6 m/s (250 knots)

Figure 304 shows the impulse due to the contact force between the UAS and the horizontal stabilizer, as well as the energy balance for both of them. Figure 305 presents the internal energies of the UAS and horizontal stabilizer parts directly involved on the impact.

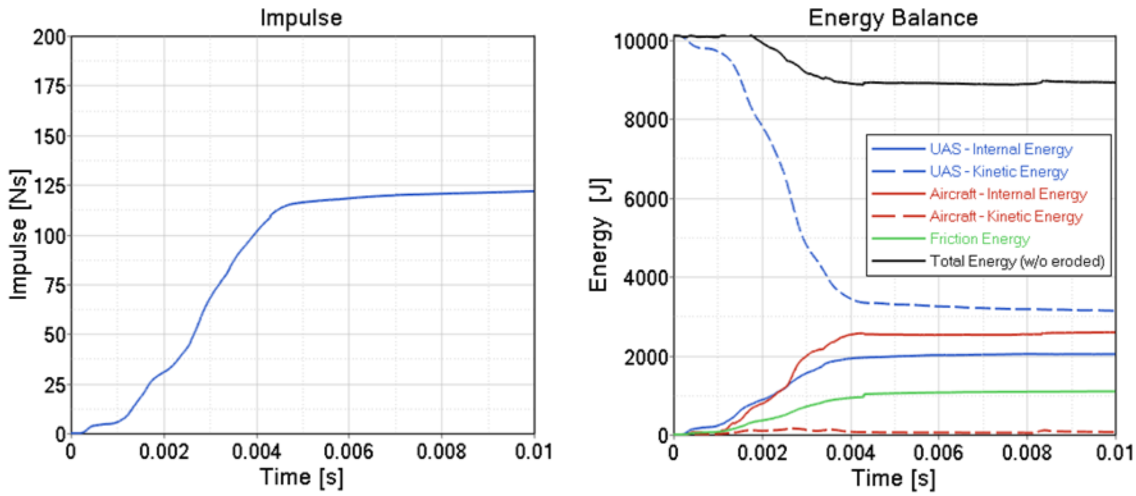

Figure 304. Impulse and energy balance of the impact between a commercial transport jet horizontal stabilizer at location 4 and a 1.2 kg (2.7 lb) UAS at 128.6 m/s (250 knots)

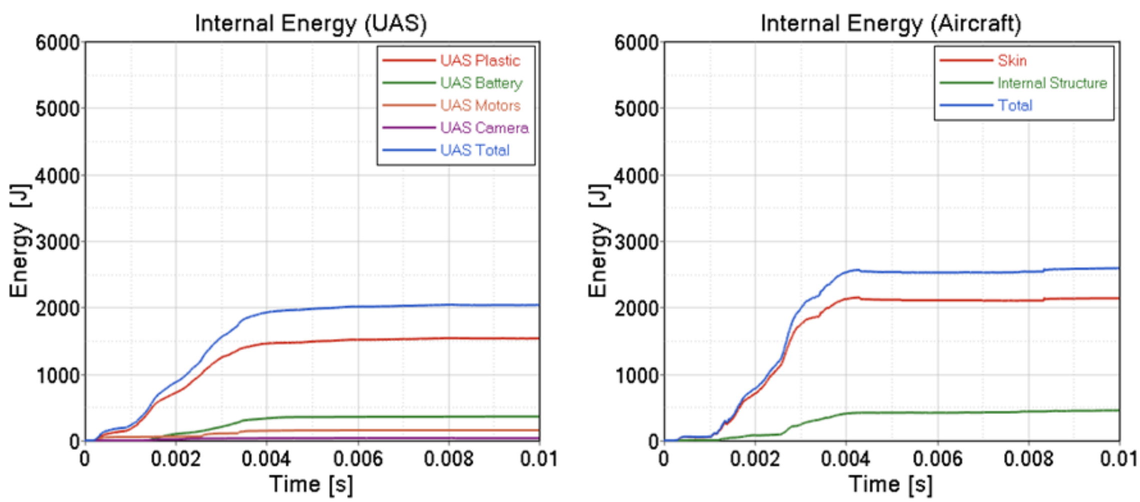

Figure 305. Internal energy per component of the impact between a commercial transport jet horizontal stabilizer at location 4 and a 1.2 kg (2.7 lb) UAS at 128.6 m/s (250 knots)

The energy balance plot includes the UAS and horizontal stabilizer kinetic and internal energies, as well as frictional energy and total energy for the event. The stabilizer absorbs 26% of the impact energy, while the UAS takes 20% of it and the energy dissipated by friction reaches 11% of the total energy. In Figure 305, internal energies for the UAS parts and the stabilizer structure show that the skin and the polycarbonate absorb the highest internal energies of the event.

B.1.2.5 CQH5

The UAS was impacted against the horizontal stabilizer at 128.6 m/s (250 knots) along the local x-axis direction of the aircraft. The impact location selected was at approximately 90% of the horizontal stabilizer semispan, with the center of gravity of the UAS aligned with the midpoint between ribs 28 and 29. Figure 306 presents the kinematics of the event. Figure 307 shows the damage caused to the inner frames and the skin.

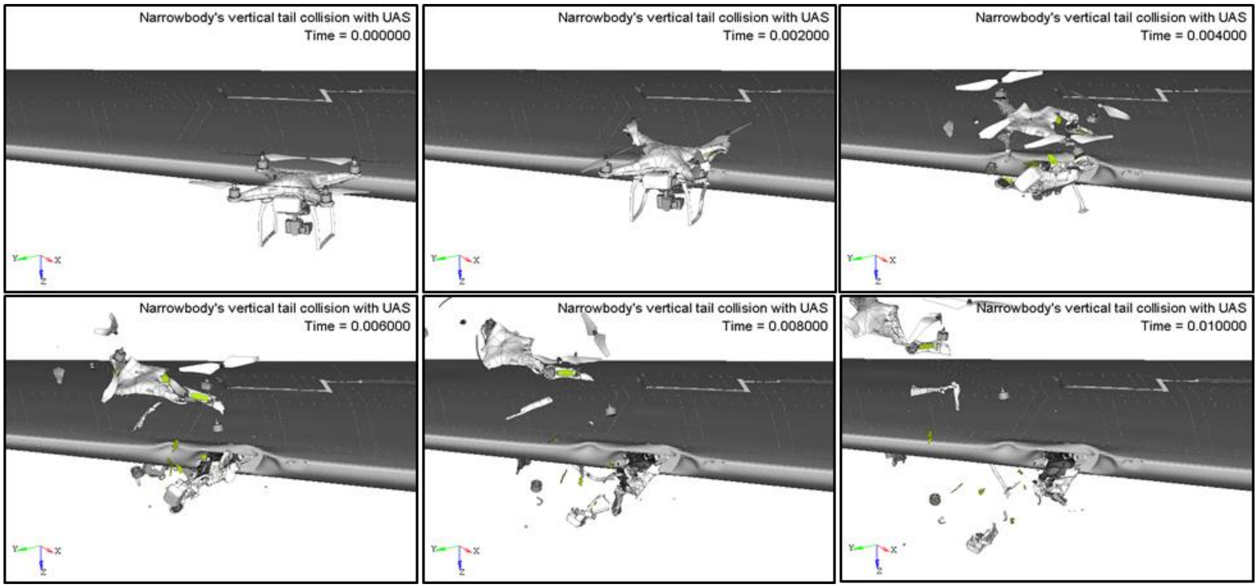

Figure 306. Kinematics of the impact between a commercial transport jet horizontal stabilizer at location 5 and a 1.2 kg (2.7 lb) UAS at 128.6 m/s (250 knots)

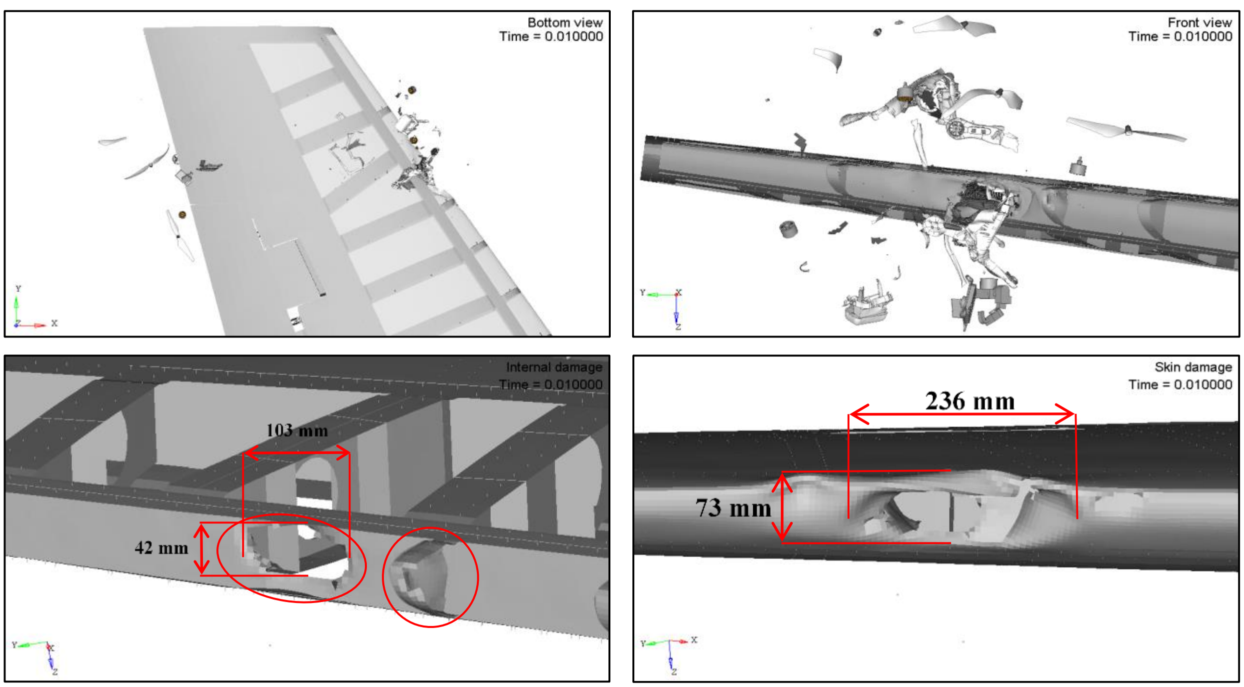

Figure 307. External/internal damage sustained by a commercial transport jet horizontal stabilizer impacted at location 5 and a 1.2 kg (2.7 lb) UAS at 128.6 m/s (250 knots)

The UAS damages the skin and the nose ribs, creating a damaged zone of 236x73 mm on the skin surface and allowing the rest of the UAS mass to penetrate until it perforates the front spar, causing a fracture of 103x42 mm. On the bottom left image at Figure 307, it can be appreciated the damage caused to the ribs and the front spar. In this case, the front spar sustained critical damage.

The damage introduced by the UAS involved perforation of the skin and damage to the primary structure, and consequently the severity was classified as Level 4.

Figure 308 shows the impulse due to the contact force between the UAS and the horizontal stabilizer, as well as the energy balance for both of them. Figure 309 presents the internal energies of the UAS and horizontal stabilizer parts directly involved on the impact.

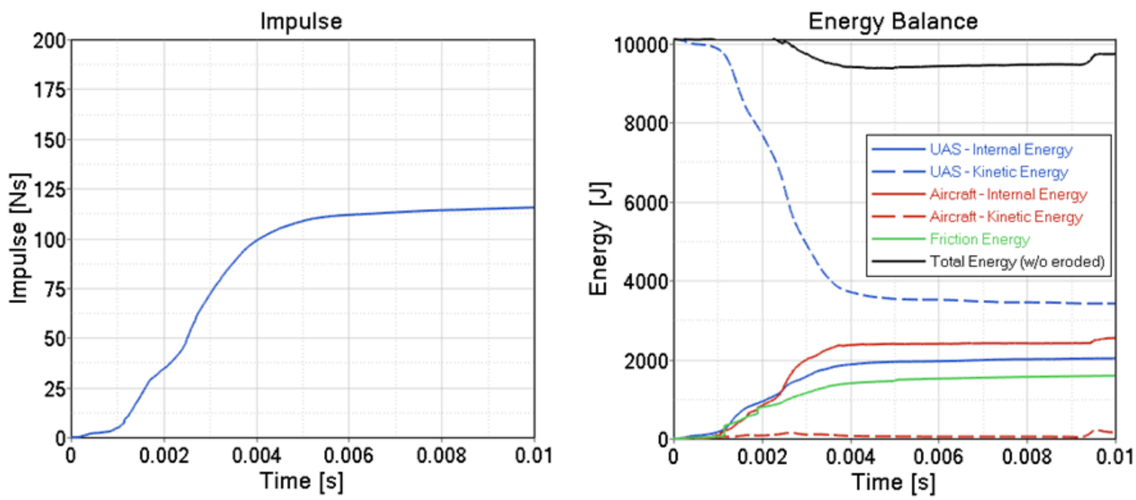

Figure 308. Impulse and energy balance of the impact between a commercial transport jet horizontal stabilizer at location 5 and a 1.2 kg (2.7 lb) UAS at 128.6 m/s (250 knots)

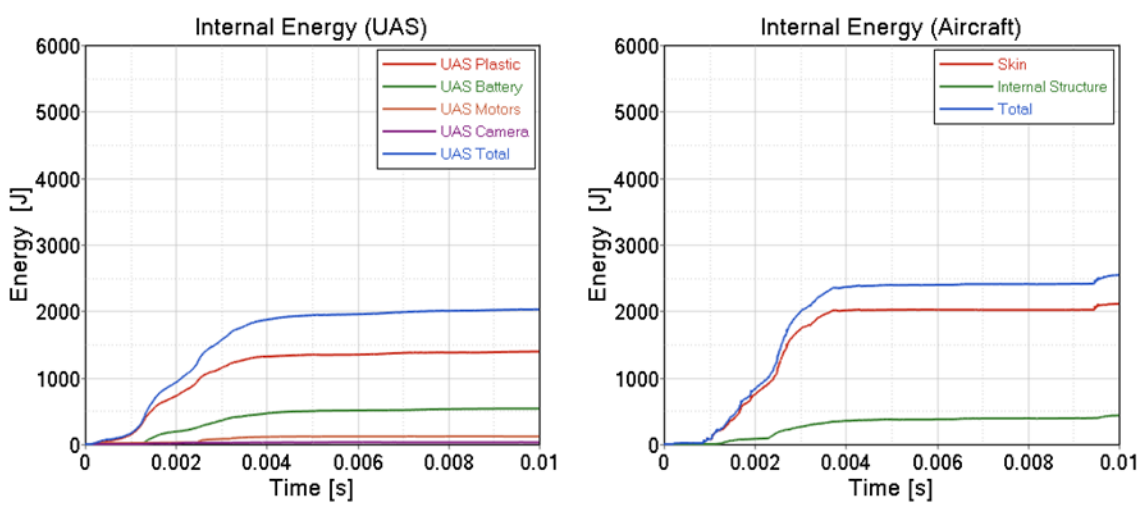

Figure 309. Internal energy per component of the impact between a commercial transport jet horizontal stabilizer at location 5 and a 1.2 kg (2.7 lb) UAS at 128.6 m/s (250 knots)

The energy balance plot includes the UAS and horizontal stabilizer kinetic and internal energies, as well as frictional energy and total energy for the event. The stabilizer absorbs 25% of the impact energy, while the UAS takes 20% of it and the energy dissipated by friction reaches 16% of the total energy. In Figure 309, internal energies for the UAS parts and the stabilizer structure show that the skin and the polycarbonate absorb the highest internal energies of the event.

B.1.3 Wing

B.1.3.1 CQW1

This impact location was identified as the critical baseline simulation for the commercial transport jet wing and is discussed in section 4.3.3.1 of the main report body.

B.1.3.2 CQW2

In this case, the UAS was impacted against the leading edge of the wing at 128.6 m/s (250 knots) in the local x-axis direction of the aircraft. The impact location selected was at the outer portion of slat 3, with the center of gravity of the UAS aligned with the leading edge, aiming to impact the leading edge close to the slat track rib pair. Figure 310 depicts the kinematics of the event. Figure 311 shows the damage caused to the skin and internal structure of the wing.

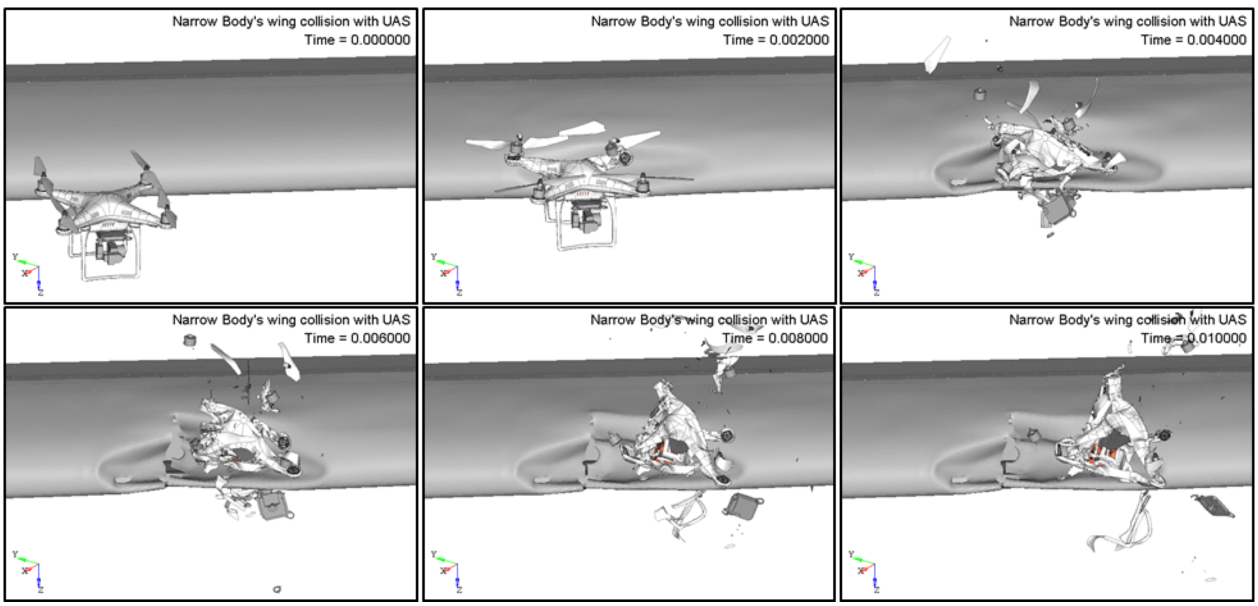

Figure 310. Kinematics of the impact between a commercial transport jet wing at location 2 and a 1.2 kg (2.7 lb) UAS at 128.6 m/s (250 knots)

The UAS impacts the leading edge of the wing, creating a vertical fracture on the D-nose skin surface and sub spar, which can be perceived in Figure 311 bottom left and bottom right images respectively. The UAS does not entirely penetrate the airframe after impact, but deforms the leading edge skin area between ribs.

Primary structural components, such as the front spar, remain undamaged. Consequently, the damaged introduced by the UAS in this case was classified as Level 3.

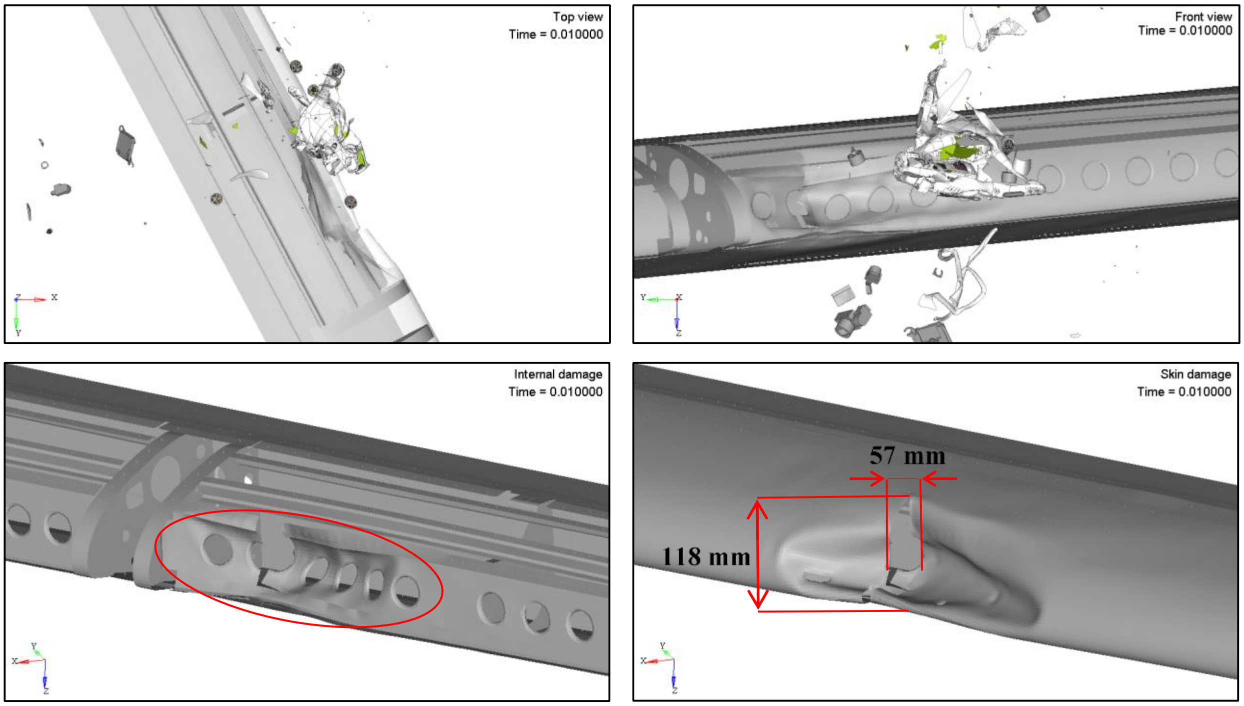

Figure 311. External/internal damage sustained by a commercial transport jet wing impacted at location 2 and a 1.2 kg (2.7 lb) UAS at 128.6 m/s (250 knots)

Figure 312 presents the impulse due to the contact force between UAS and wing, as well as the energy balance for both of them. Figure 313 shows the internal energies of UAS and wing parts directly involved in the impact.

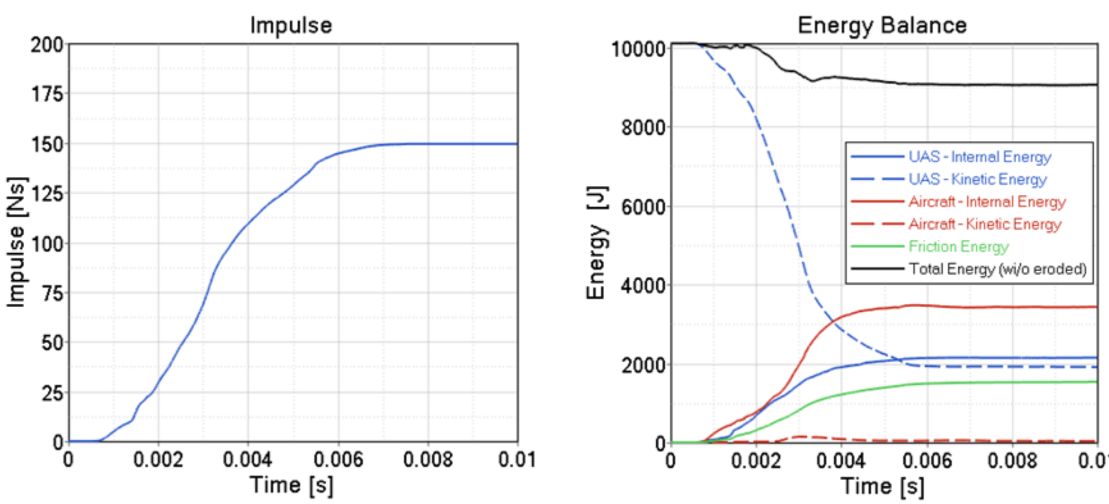

Figure 312. Impulse and energy balance of the impact between a commercial transport jet wing at location 2 and a 1.2 kg (2.7 lb) UAS at 128.6 m/s (250 knots)

The energy balance plot includes the UAS and wing kinetic and internal energies as well as frictional energy and total energy (excluding eroded energy) for the event. The wing and the UAS absorb 34% and 21% of the impact energy respectively. The energy dissipated by friction reaches

15% of the total energy. In Figure 313, internal energies for the UAS parts and the wing show that the polycarbonate carcass of the UAS and the skin of the wing absorb the highest amount of internal energy.

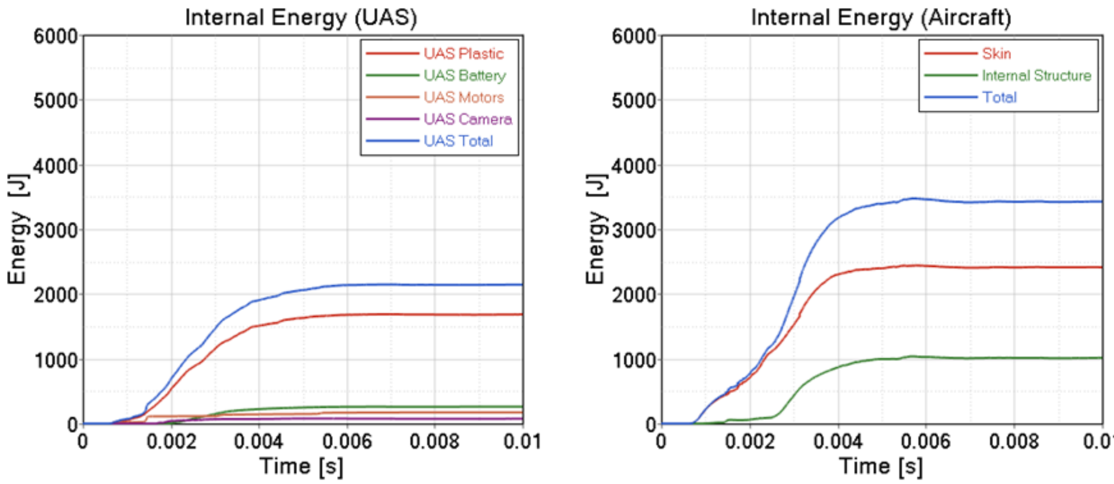

Figure 313. Internal energy per component of the impact between a commercial transport jet wing at location 2 and a 1.2 kg (2.7 lb) UAS at 128.6 m/s (250 knots)

B.1.3.3 CQW3

In this case, the UAS was impacted against the leading edge of the wing at 128.6 m/s (250 knots) in the local x-axis direction of the aircraft. The impact location selected was at the outer portion of slat 3, with the center of gravity of the UAS aligned with the leading edge, aiming to impact the front spar at the midpoint between the intermediate rib and the slat track rib pair.

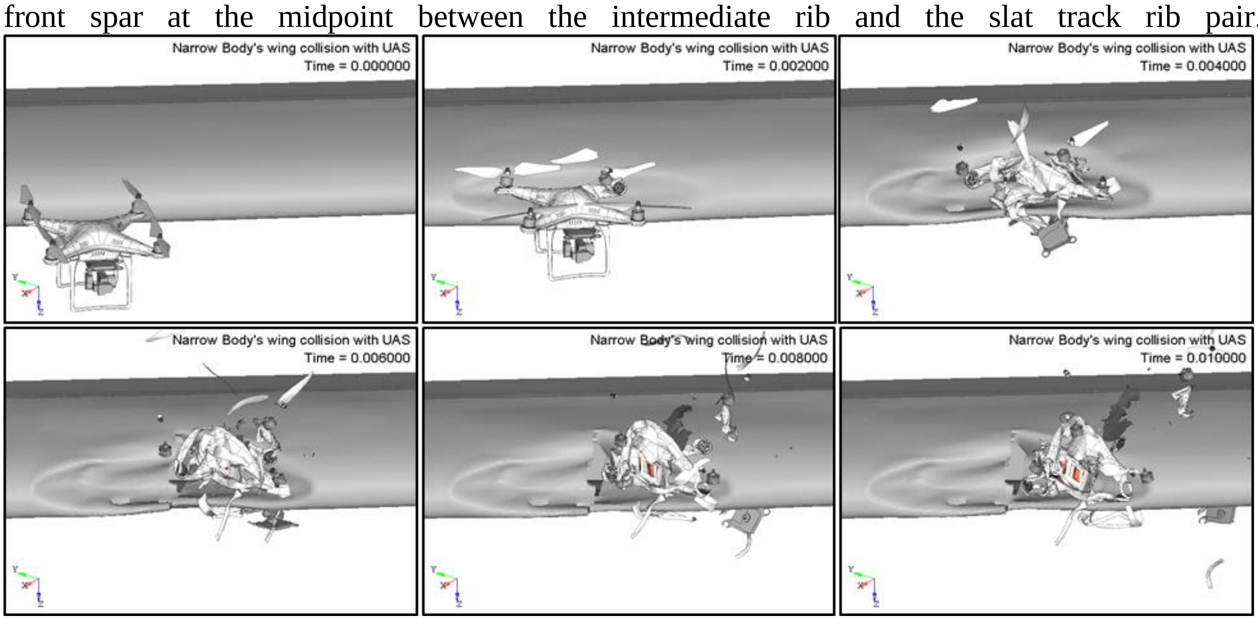

Figure 314 depicts the kinematics of the event. Figure 315 shows the damage caused to the skin and internal structure (ribs and spar) of the wing.

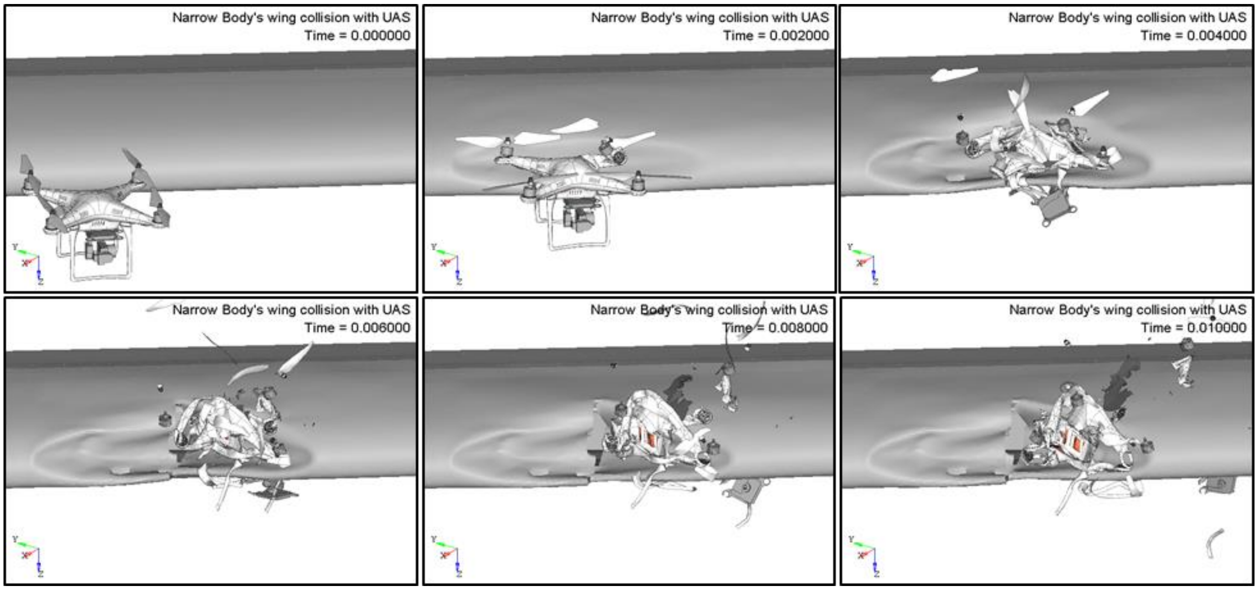

Figure 314. Kinematics of the impact between a commercial transport jet wing at location 3 and a 1.2 kg (2.7 lb) UAS at 128.6 m/s (250 knots)

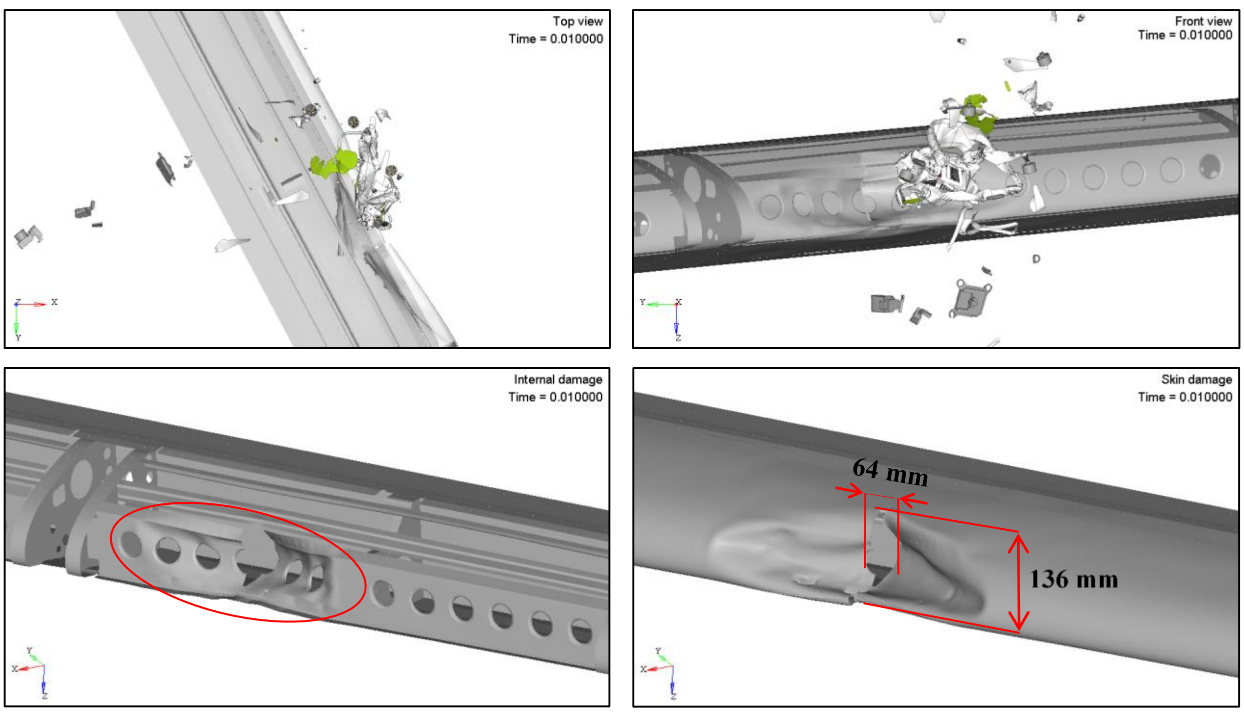

Figure 315. External/internal damage sustained by a commercial transport jet wing impacted at location 3 and a 1.2 kg (2.7 lb) UAS at 128.6 m/s (250 knots)

The UAS impacts the leading edge of the wing, creating a vertical fracture on the D-nose skin surface and sub spar, which can be perceived in Figure 315 bottom left and bottom right images respectively. The UAS does not entirely penetrate the airframe after impact, but deforms the leading edge skin area between ribs. Primary structural components, such as the front spar, remain undamaged. Consequently, the damaged introduced by the UAS in this case was classified as Level 3.

Figure 316 presents the impulse due to the contact force between UAS and wing, as well as the energy balance for both of them. Figure 317 shows the internal energies of UAS and wing parts directly involved in the impact. The energy balance plot includes the UAS and wing kinetic and internal energies as well as frictional energy and total energy (excluding eroded energy) for the event. The wing and the UAS absorb 37% and 21% of the impact energy respectively. The energy dissipated by friction reaches 15% of the total energy. In Figure 317, internal energies for the UAS parts and the wing show that the polycarbonate carcass of the UAS and the skin of the wing absorb the highest amount of internal energy.

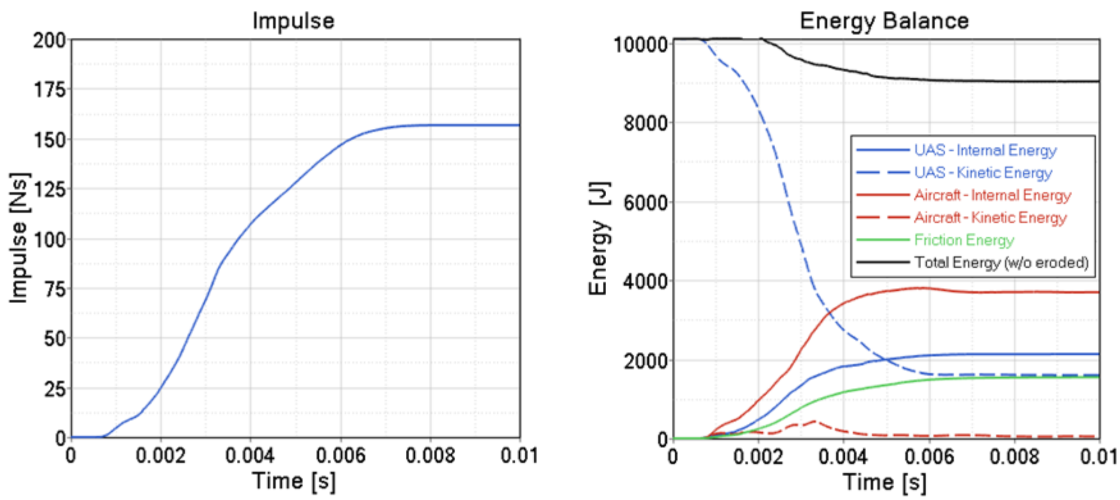

Figure 316. Impulse and energy balance of the impact between a commercial transport jet wing at location 3 and a 1.2 kg (2.7 lb) UAS at 128.6 m/s (250 knots)

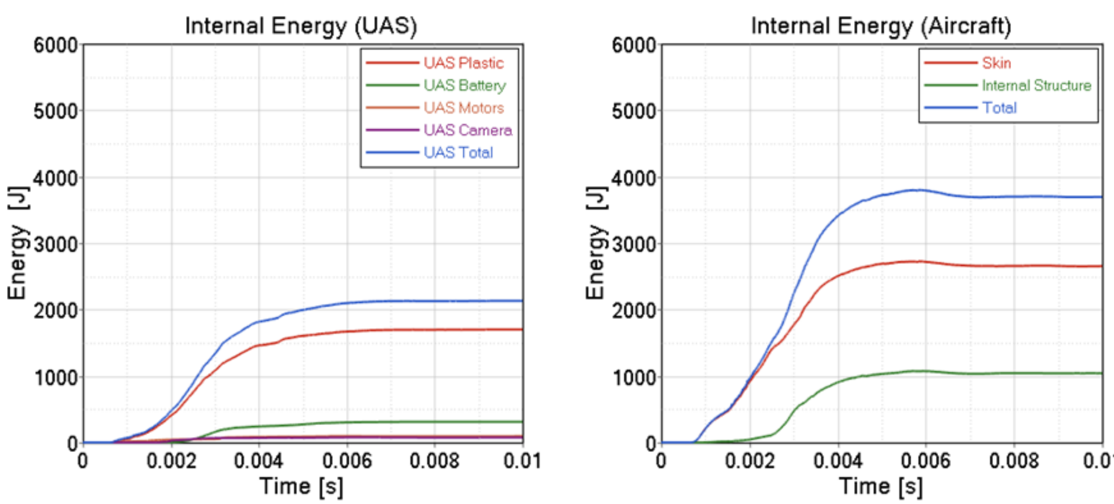

Figure 317. Internal energy per component of the impact between a commercial transport jet wing at location 3 and a 1.2 kg (2.7 lb) UAS at 128.6 m/s (250 knots)

B.1.3.4 <u>CQW4</u>

In this case, the UAS was impacted against the leading edge of the wing at 128.6 m/s (250 knots) in the local x-axis direction of the aircraft. The impact location selected was at the inboard portion of slat 4, with the center of gravity of the UAS aligned with the leading edge, aiming to impact the front spar at the midpoint between the intermediate rib and the slat track rib pair. Figure 318 depicts the kinematics of the event. Figure 319 shows the damage caused to the skin and internal structure (ribs and spar) of the wing.

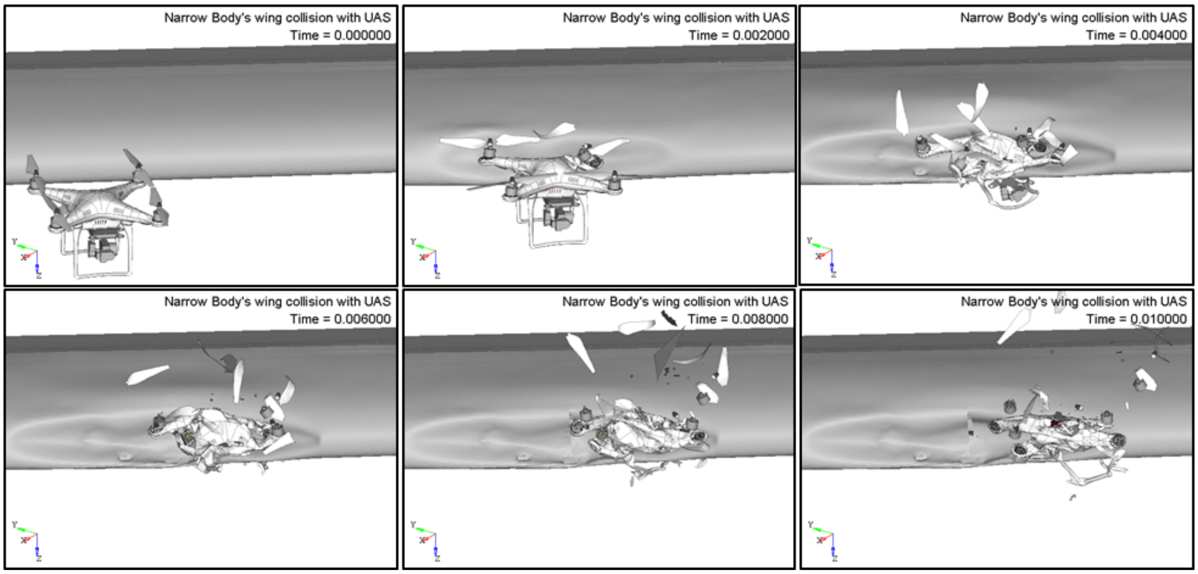

Figure 318. Kinematics of the impact between a commercial transport jet wing at location 4 and a 1.2 kg (2.7 lb) UAS at 128.6 m/s (250 knots)

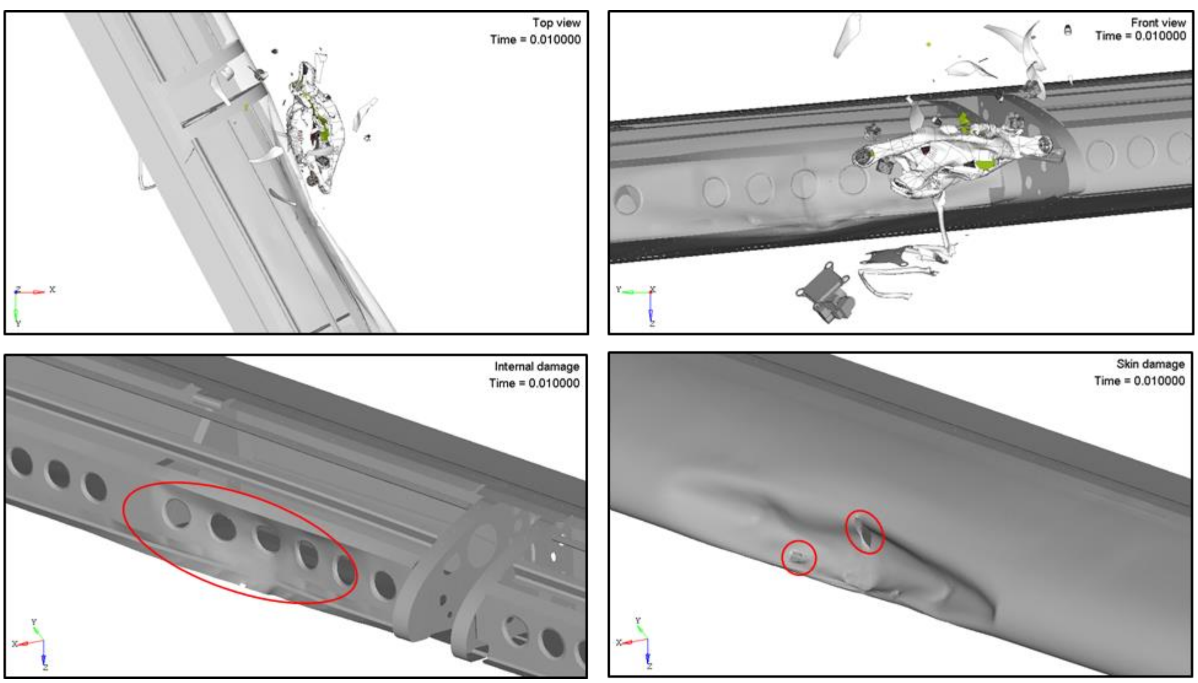

Figure 319. External/internal damage sustained by a commercial transport jet wing impacted at location 4 and a 1.2 kg (2.7 lb) UAS at 128.6 m/s (250 knots)

The UAS impacts the leading edge of the wing, creating a small fracture on the D-nose skin surface, which can be perceived in Figure 319 bottom right image. The UAS does not entirely penetrate the airframe after impact, but deforms the leading edge skin area as well as part of the nose sub spar between ribs. Primary structural components, such as the front spar, remain undamaged. Consequently, the damaged introduced by the UAS in this case was classified as Level 2.

Figure 320 presents the impulse due to the contact force between UAS and wing, as well as the energy balance for both of them. Figure 321 shows the internal energies of UAS and wing parts directly involved in the impact.

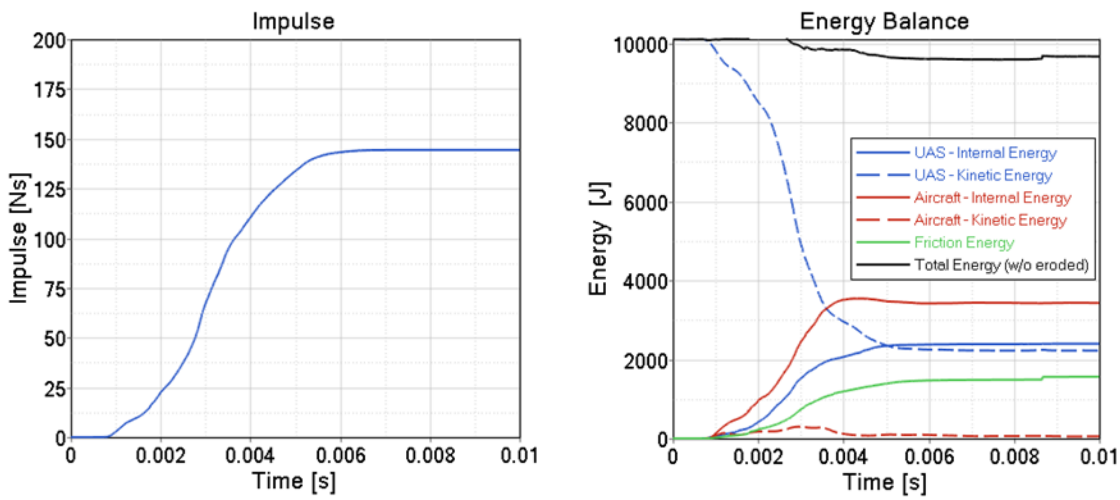

Figure 320. Impulse and energy balance of the impact between a commercial transport jet wing at location 4 and a 1.2 kg (2.7 lb) UAS at 128.6 m/s (250 knots)

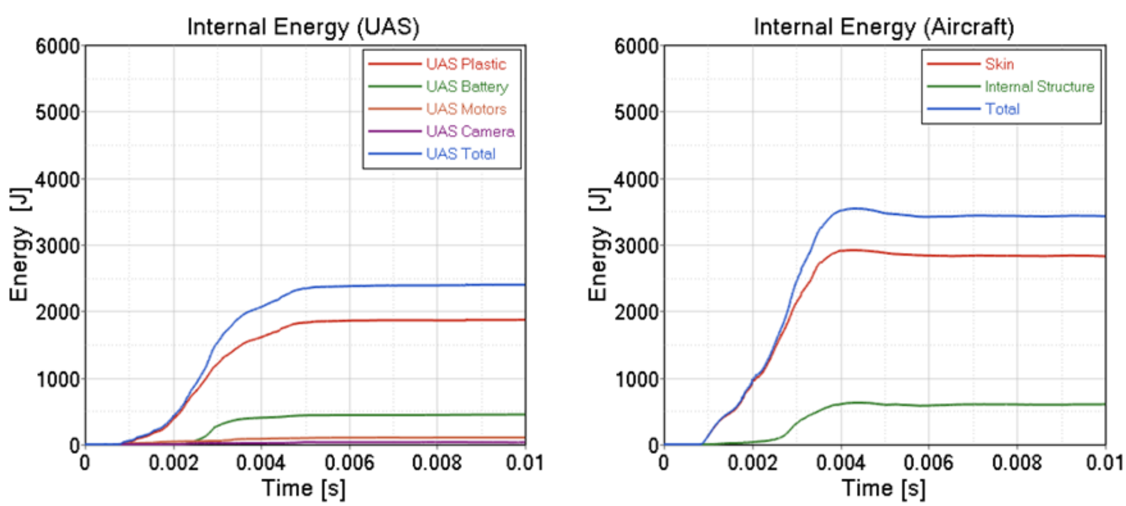

Figure 321. Internal energy per component of the impact between a commercial transport jet wing at location 4 and a 1.2 kg (2.7 lb) UAS at 128.6 m/s (250 knots)

The energy balance plot includes the UAS and wing kinetic and internal energies as well as frictional energy and total energy (excluding eroded energy) for the event. The wing and the UAS absorb 34% and 23% of the impact energy respectively. The energy dissipated by friction reaches

15% of the total energy. In Figure 321, internal energies for the UAS parts and the wing show that the polycarbonate carcass of the UAS and the skin of the wing absorb the highest amount of internal energy.

B.1.4 Windshield

B.1.4.1 CQC1

This impact location was identified as the critical baseline simulation for the commercial transport jet windshield and is discussed in section 4.3.4.1 of the main report body.

B.1.4.2 CQC2

The corner of the windshield near the center frame was chosen for impact in this case. The UAS was impacted against the windshield at 128.6 m/s (250 knots) in the local x-axis direction of the aircraft. Figure 322 depicts the kinematics of the event. Figure 323 shows the damage caused to the windshield and surrounding structure of the windshield.

The UAS damages the windshield and slides over it due to the steep windshield angle. The windshield did not sustain any fractures or major damage. The permanent deformation in the windshield can be seen in the bottom right image in Figure 323.

Primary structural components, such as the windshield frame, remain undamaged. Moreover, the transparency sustained permanent deformation but no penetration of external parts into the cockpit. Consequently, the damaged introduced by the UAS in this case was classified as Level 2.

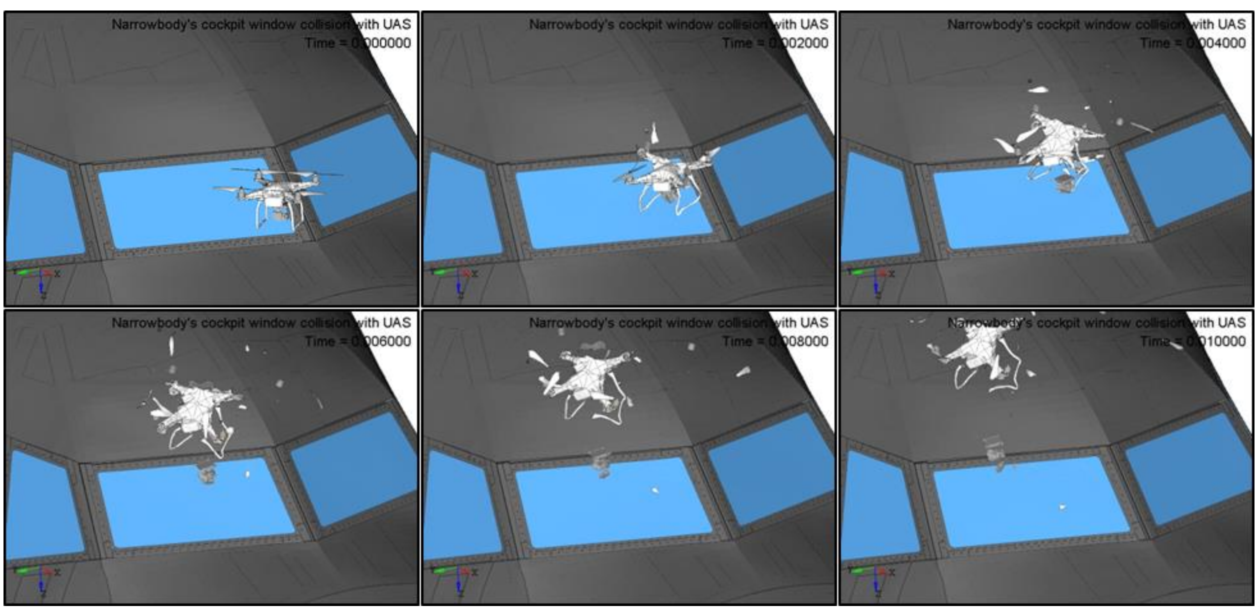

Figure 322. Kinematics of the impact between a commercial transport jet windshield at location 2 and a 1.2 kg (2.7 lb) UAS at 128.6 m/s (250 knots)

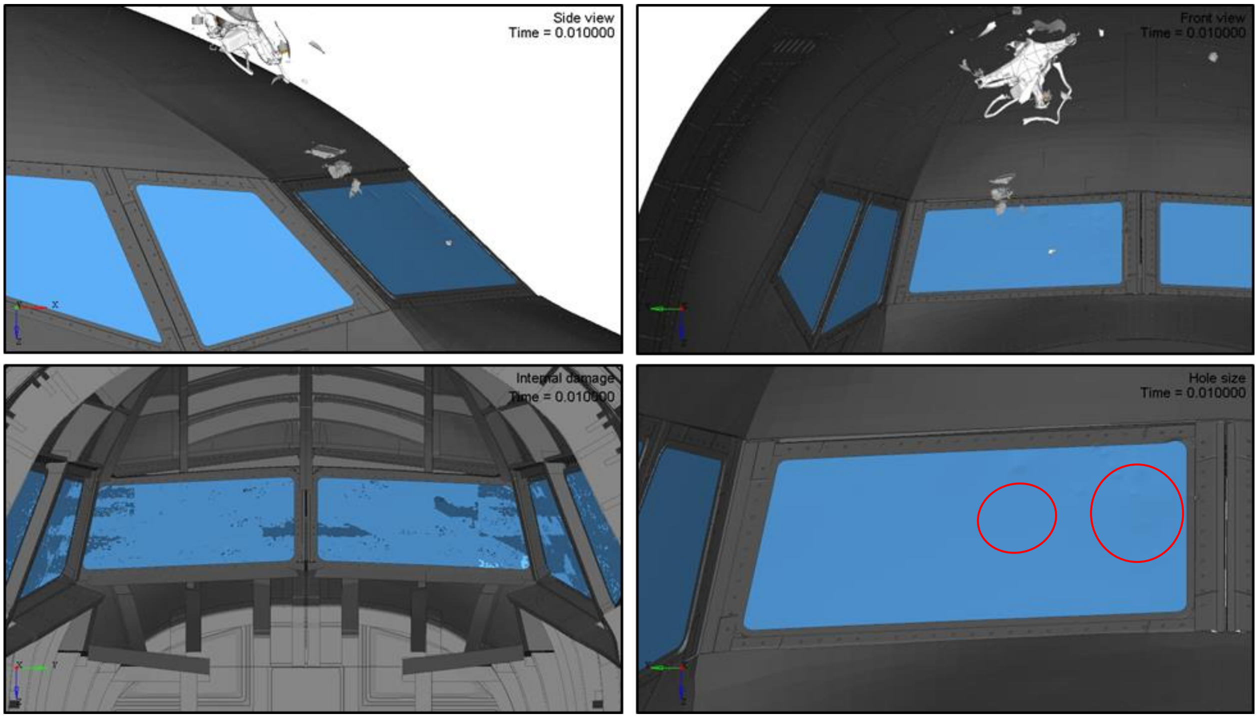

Figure 323. External/internal damage sustained by a commercial transport jet windshield impacted at location 2 and a 1.2 kg (2.7 lb) UAS at 128.6 m/s (250 knots)

Figure 324 shows the impulse due to the contact force between UAS and forward fuselage, as well as the energy balance for both of them. Figure 325 shows the internal energies of UAS and the forward fuselage parts directly involved in the impact.

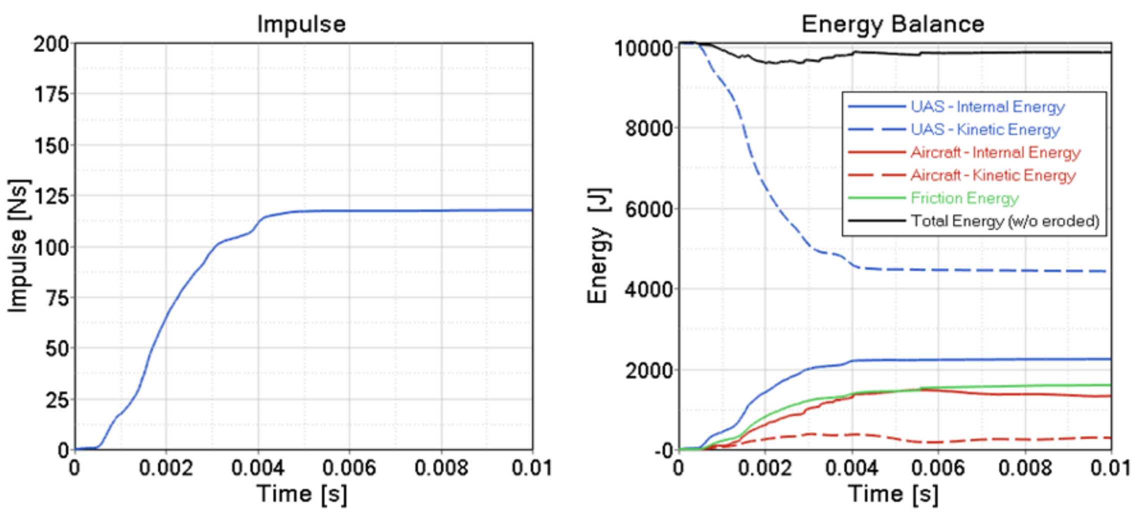

Figure 324. Impulse and energy balance of the impact between a commercial transport jet windshield at location 2 and a 1.2 kg (2.7 lb) UAS at 128.6 m/s (250 knots)

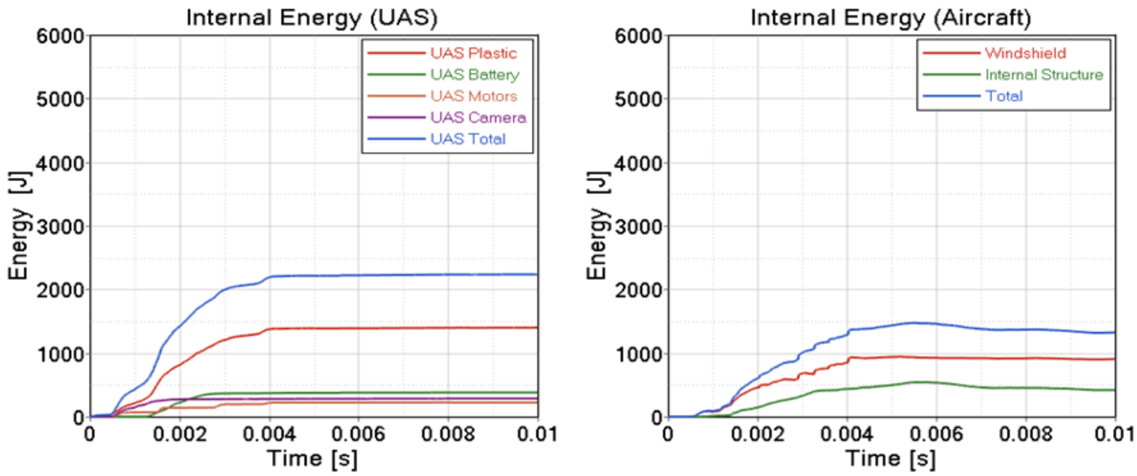

Figure 325. Internal energy per component of the impact between a commercial transport jet windshield at location 2 and a 1.2 kg (2.7 lb) UAS at 128.6 m/s (250 knots)

The energy balance plot includes the UAS and forward fuselage kinetic and internal energies as well as frictional energy and total energy for the event. The forward fuselage absorbs 13% of the impact energy, while the UAS absorbs 22% of it and the energy dissipated by friction reaches 15% of the total energy. In Figure 325, internal energies for the UAS parts and the forward fuselage show that the polycarbonate and windshield absorb the highest amount of internal energies respectively.

B.1.4.3 CQC3

The center frame of the windshield was chosen for impact in this case. The UAS was impacted against the frame at 128.6 m/s (250 knots) in the local x-axis direction of the aircraft. Figure 326 depicts the kinematics of the event.

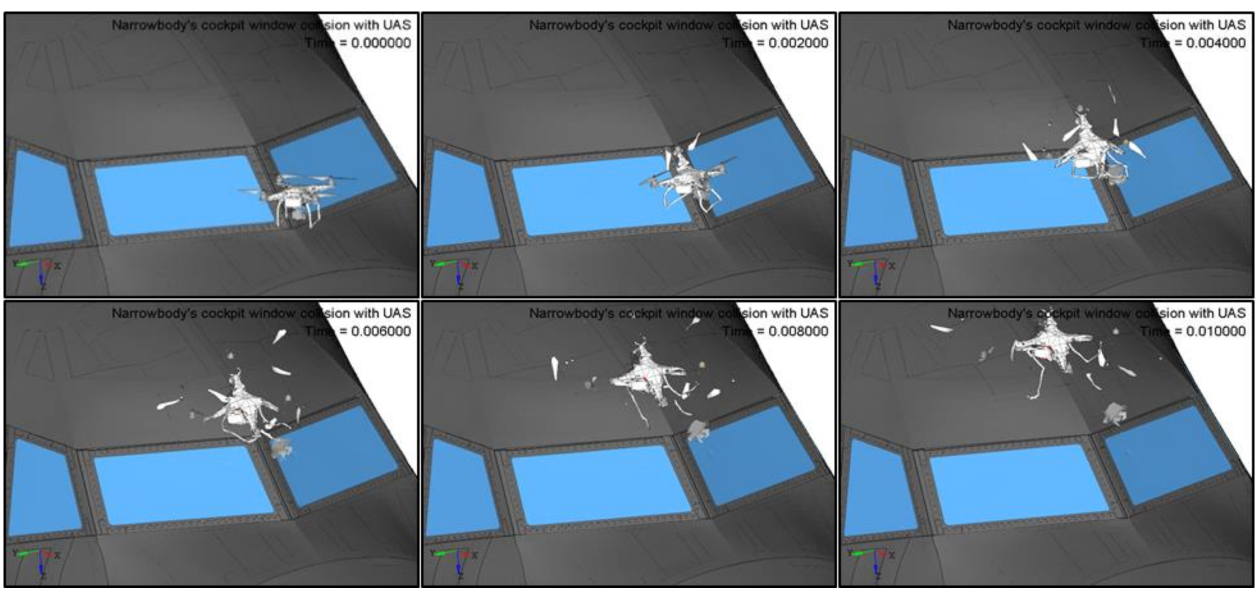

Figure 326. Kinematics of the impact between a commercial transport jet windshield at location 3 and a 1.2 kg (2.7 lb) UAS at 128.6 m/s (250 knots)

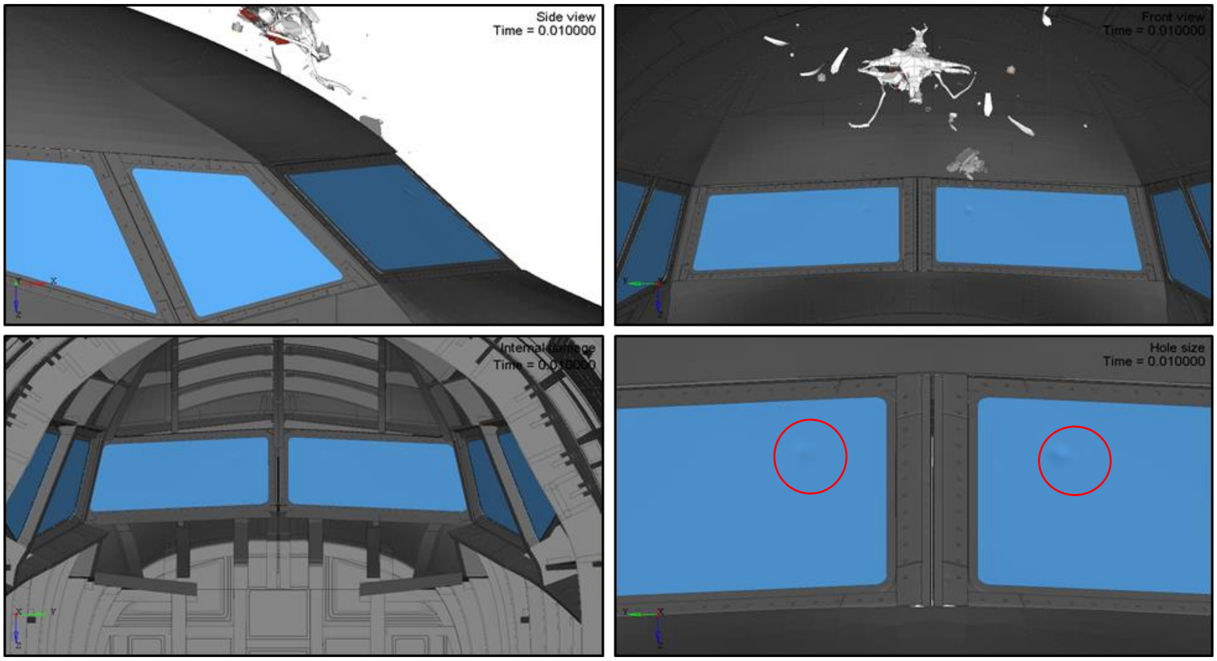

Figure 327. External/internal damage sustained by a commercial transport jet windshield impacted at location 3 and a 1.2 kg (2.7 lb) UAS at 128.6 m/s (250 knots)

The UAS damages the windshield and slides over it due to the steep windshield angle. The windshield and the center frame did not sustain any fractures or major damage. The permanent deformation in the windshield can be seen in the bottom right image in Figure 322. Primary structural components, such as the windshield frame, remain undamaged. Moreover, the transparency sustained permanent deformation but no penetration of external parts into the cockpit. Consequently, the damaged introduced by the UAS in this case was classified as Level 2.

Figure 328 shows the impulse due to the contact force between UAS and forward fuselage, as well as the energy balance for both of them. Figure 329 shows the internal energies of UAS and the forward fuselage parts directly involved in the impact.

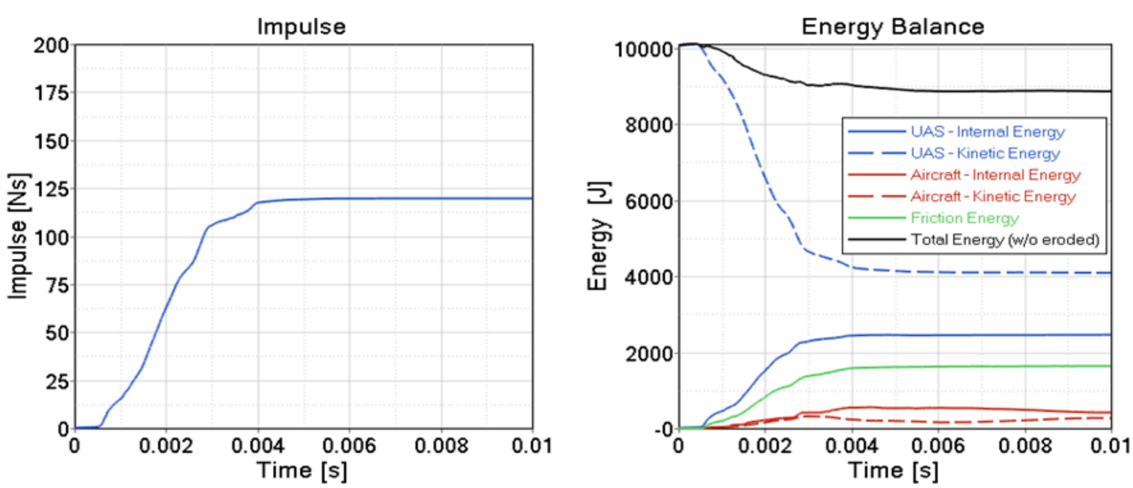

Figure 328. Impulse and energy balance of the impact between a commercial transport jet windshield at location 3 and a 1.2 kg (2.7 lb) UAS at 128.6 m/s (250 knots)

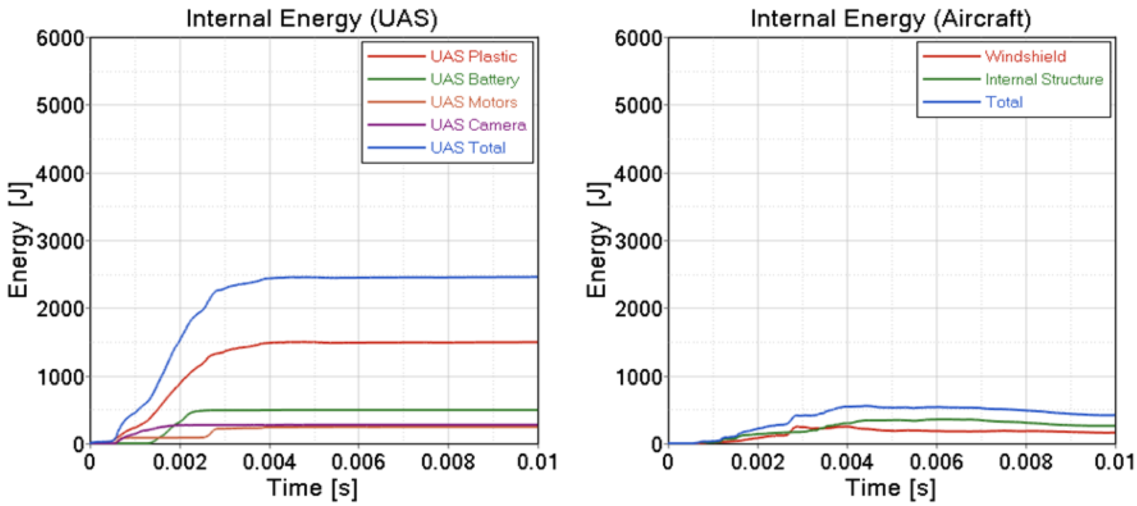

Figure 329. Internal energy per component of the impact between a commercial transport jet windshield at location 3 and a 1.2 kg (2.7 lb) UAS at 128.6 m/s (250 knots)

The energy balance plot includes the UAS and forward fuselage kinetic and internal energies as well as frictional energy and total energy for the event. The forward fuselage absorbs 4% of the impact energy, while the UAS absorbs 24% of it and the energy dissipated by friction reaches 18% of the total energy. In Figure 329, internal energies for the UAS parts and the forward fuselage show that the polycarbonate and internal structure absorb the highest amount of internal energies respectively.

B.1.5 Summary of Results of Collision with Commercial Transport Jet

Assembly	Case	Severity	Fire Risk	Internal Energy Aircraft [J]	Internal Energy UAS [J]	Residual Kinetic Energy [J]	Friction Energy [J]	Eroded Energy [J]
Vertical Stabilizer	CQV1	Level 3	No	3060	2280	2370	1590	1070
	CQV2	Level 3	No	2920	2470	1700	1640	1350
	CQV3	Level 3	No	2475	3100	1570	1735	1190
	CQV4	Level 3	No	3510	2320	1595	1450	1200
Horizontal Stabilizer	CQH1	Level 3	Yes	4135	2398	1610	1259	566
	CQH2	Level 3	Yes	3507	2188	2308	1131	884
	CQH3	Level 4	Yes	2840	2129	2542	1214	1276
	CQH4	Level 4	No	2590	2036	3134	1093	1190
	CQH5	Level 4	No	2544	2027	3415	1587	373
Wing	CQW1	Level 3	No	3753	2132	1697	1489	1020
	CQW2	Level 3	No	3427	2145	1907	1536	1039
	CQW3	Level 3	No	3696	2133	1649	1546	1018
	CQW4	Level 2	No	3427	2398	2277	1561	427
Windshield	CQC1	Level 2	No	1047	2171	4588	1433	851
	CQC2	Level 2	No	1320	2235	4420	1535	290
	CQC3	Level 2	No	415	2455	1610	4085	1250

B.2 BUSINESS JET

B.2.1 Vertical Stabilizer

B.2.1.1 BQV1

The lower portion of the vertical stabilizer between ribs 1 and 2 was chosen for impact in this case. The UAS was impacted against the vertical stabilizer at 128.6 m/s (250 knots) in the local x-axis direction of the aircraft. Figure 325 depicts the kinematics of the event. Figure 326 shows the damage caused to the skin and inner frames of the vertical stabilizer.

The UAS damages the skin and the upper and lower ribs, creating a damaged zone of 238x245 mm on the skin surface. The permanent deformation in the ribs can be seen in the bottom left image in Figure 326.

These impacts considerably reduce the velocity of the UAS components and the spar is able to hold off the UAS components without sustaining any damage. The damage introduced by the UAS involved perforation of the skin but no damage to the primary structure, and consequently the severity was classified as Level 3.

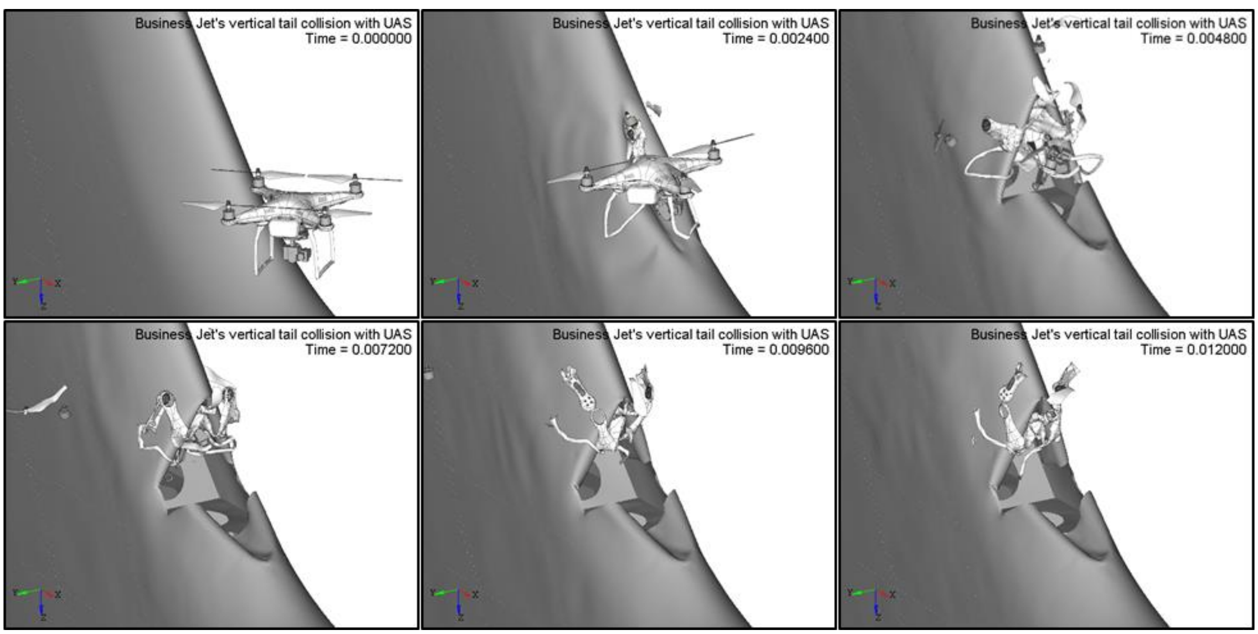

Figure 330. Kinematics of the impact between a business jet vertical stabilizer at location 1 and a 1.2 kg (2.7 lb) UAS at 128.6 m/s (250 knots)

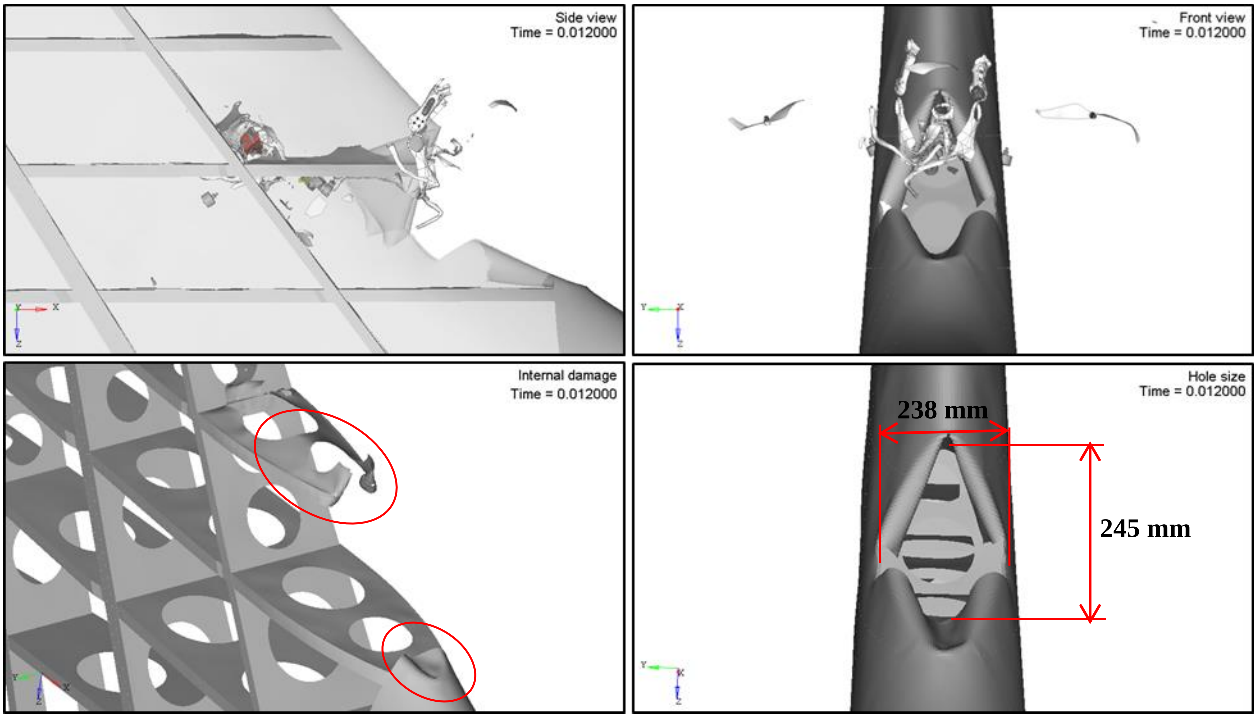

Figure 331.External/internal damage sustained by a business jet vertical stabilizer at location 1 and a 1.2 kg (2.7 lb) UAS at 128.6 m/s (250 knots)

Figure 332 shows the impulse due to the contact force between UAS and vertical stabilizer, as well as the energy balance for both of them. Figure 333 shows the internal energies of UAS and vertical stabilizer parts directly involved in the impact.

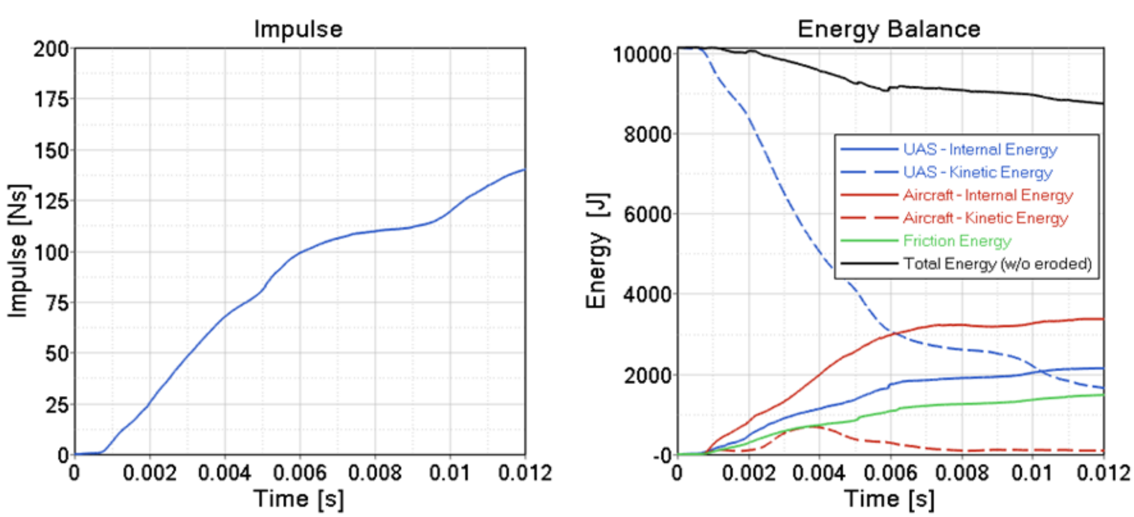

Figure 332. Impulse and energy balance of the impact between a business jet vertical stabilizer at location 1 and a 1.2 kg (2.7 lb) UAS at 128.6 m/s (250 knots)

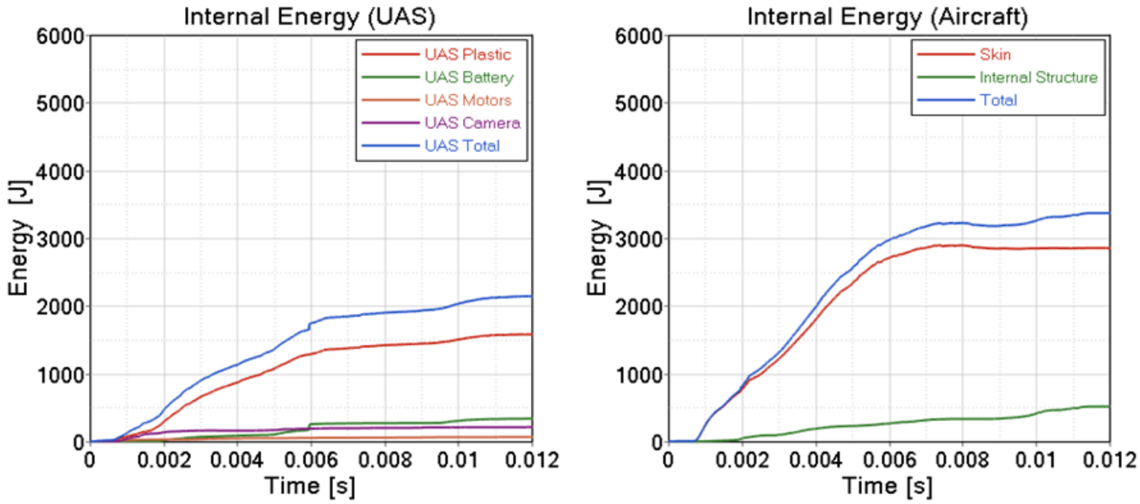

Figure 333. Internal energy per component of the impact between a business jet vertical stabilizer at location 1 and a 1.2 kg (2.7 lb) UAS at 128.6 m/s (250 knots)

The energy balance plot includes the UAS and vertical stabilizer kinetic and internal energies as well as frictional energy and total energy for the event. The vertical stabilizer absorbs 33% of the impact energy, while the UAS absorbs 22% of it and the energy dissipated by friction reaches 16% of the total energy. In Figure 333, internal energies for the UAS parts and the vertical stabilizer show that the polycarbonate and skin absorb the highest amount of internal energies respectively.

B.2.1.2 BQV2

This impact location was identified as the critical baseline simulation for the business jet vertical stabilizer and is discussed in section 4.4.1.1 of the main report body.

B.2.1.3 BQV3

The upper most portion of the vertical stabilizer between fin tip ribs 1 and 2 was selected to impact the UAS in this case. This portion of the vertical stabilizer holds the horizontal stabilizer, which is not too far from the impact location. If the UAS does penetrate by a considerable amount, it might damage the connections or the mechanisms for operating the horizontal stabilizer. The UAS was impacted against the vertical stabilizer at 128.6 m/s (250 knots) in the local x-axis direction of the aircraft. Figure 334 depicts the kinematics of the event. Figure 335 shows the damage caused to the skin and inner frames of the vertical stabilizer.

The UAS impacts the skin with a low angle, deforming the skin and nose ribs, but without creating perforation of the skin. Due to the small impact angle, the UAS slides on the surface of the vertical tail deflecting a great part of it's kinetic energy. Figure 335 shows that most of the damage in the aircraft is sustained by the skin, leaving the front spar with no damage.

The damage introduced by the UAS involved deformation of the skin but no perforation neither damage to the primary structure, and consequently the severity was classified as Level 2.

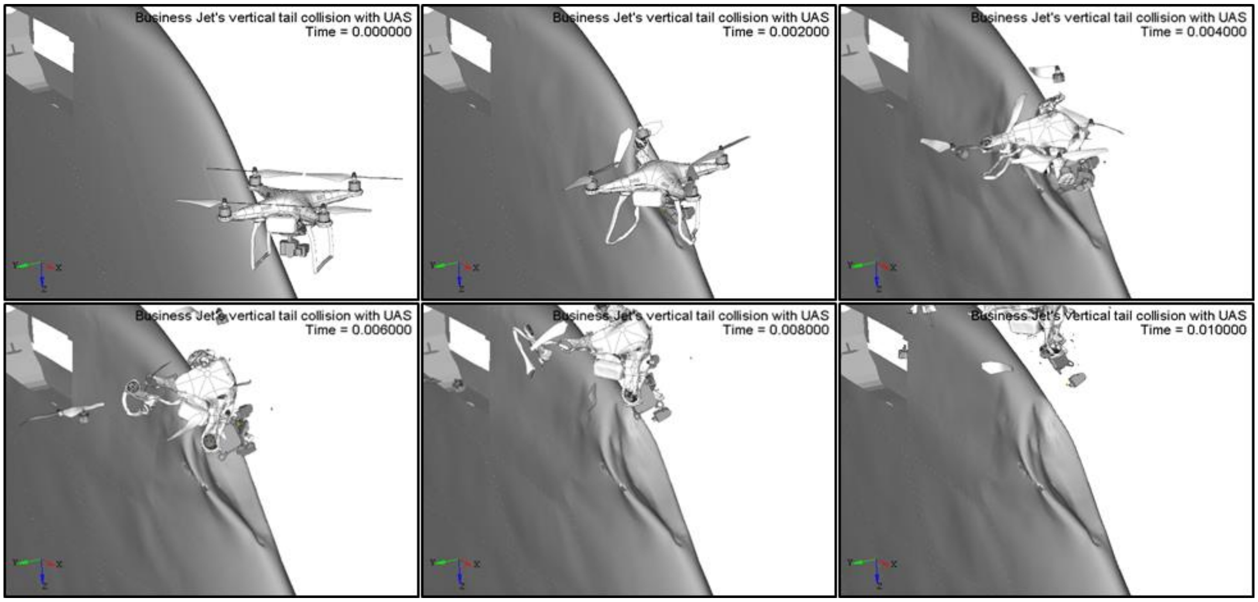

Figure 334. Kinematics of the impact between a business jet vertical stabilizer at location 3 and a 1.2 kg (2.7 lb) UAS at 128.6 m/s (250 knots)

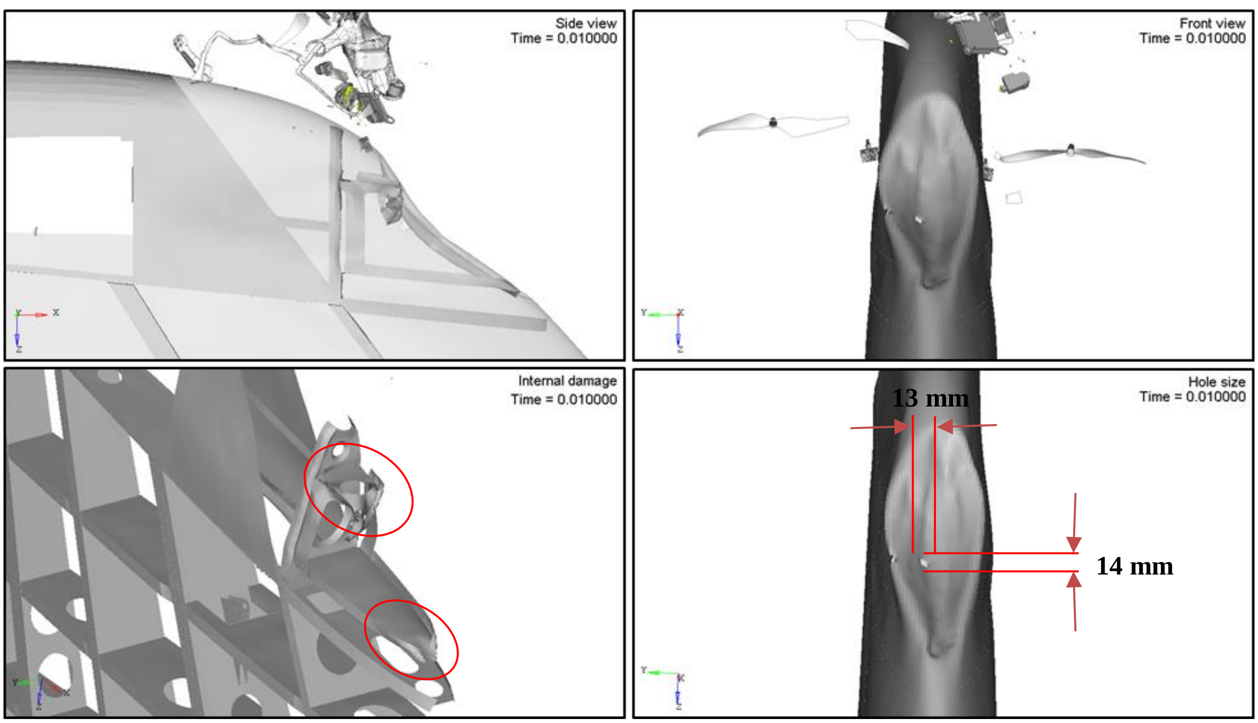

Figure 335. External/internal damage sustained by a business jet vertical stabilizer impacted at location 3 and a 1.2 kg (2.7 lb) UAS at 128.6 m/s (250 knots)

Figure 336 shows the impulse due to the contact force between UAS and vertical stabilizer, as well as the energy balance for both of them. Figure 337 shows the internal energies of UAS and vertical stabilizer parts directly involved in the impact.

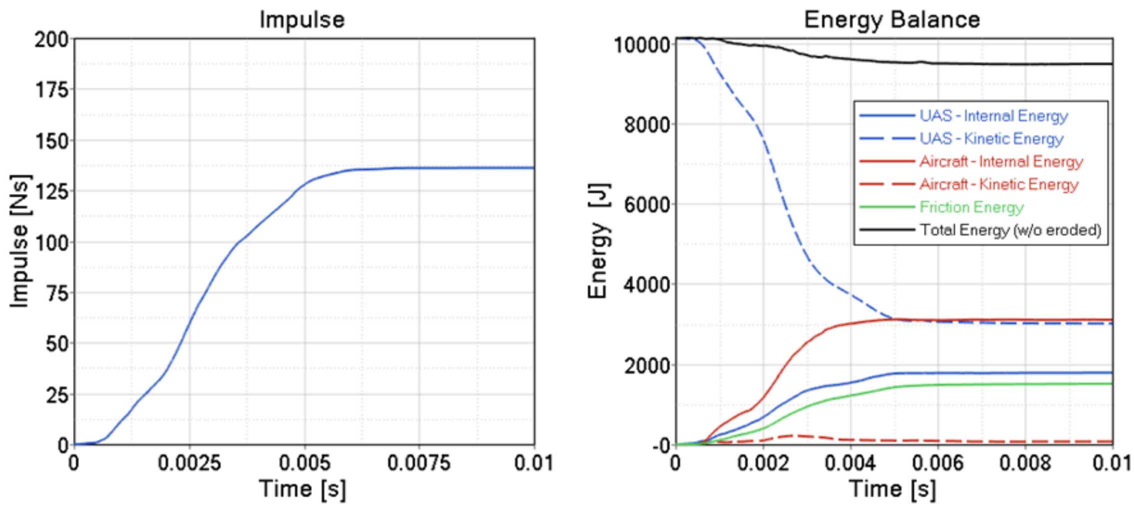

Figure 336. Impulse and energy balance of the impact between a business jet vertical stabilizer at location 3 and a 1.2 kg (2.7 lb) UAS at 128.6 m/s (250 knots)

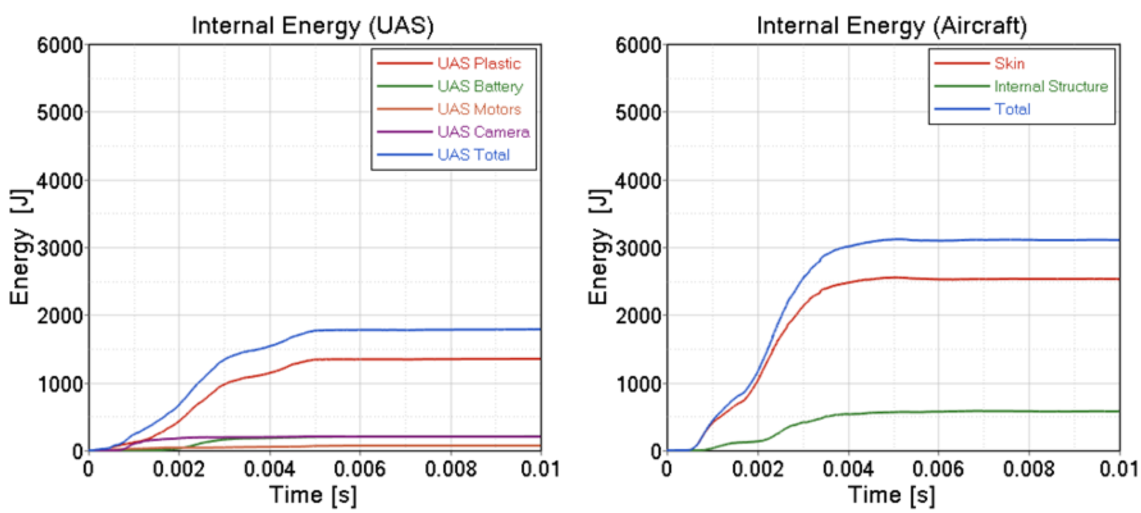

Figure 337. Internal energy per component of the impact between a business jet vertical stabilizer at location 3 and a 1.2 kg (2.7 lb) UAS at 128.6 m/s (250 knots)

The energy balance plot includes the UAS and vertical stabilizer kinetic and internal energies as well as frictional energy and total energy for the event. The vertical stabilizer absorbs 30% of the impact energy, while the UAS absorbs 19% of it and the energy dissipated by friction reaches 17% of the total energy. In Figure 337, internal energies for the UAS parts and the vertical stabilizer show that the polycarbonate and skin absorb the highest amount of internal energies respectively.

B.2.2 Horizontal Stabilizer

B.2.2.1 BQH1

Impact location 1 was located next to the horizontal stabilizer's root rib. The UAS was impacted against the stabilizer at 128.6 m/s (250 knots) along the local x-axis direction of the aircraft. Figure 338 presents the kinematics of the event. Figure 339 shows the damage caused to the inner frames and the skin.

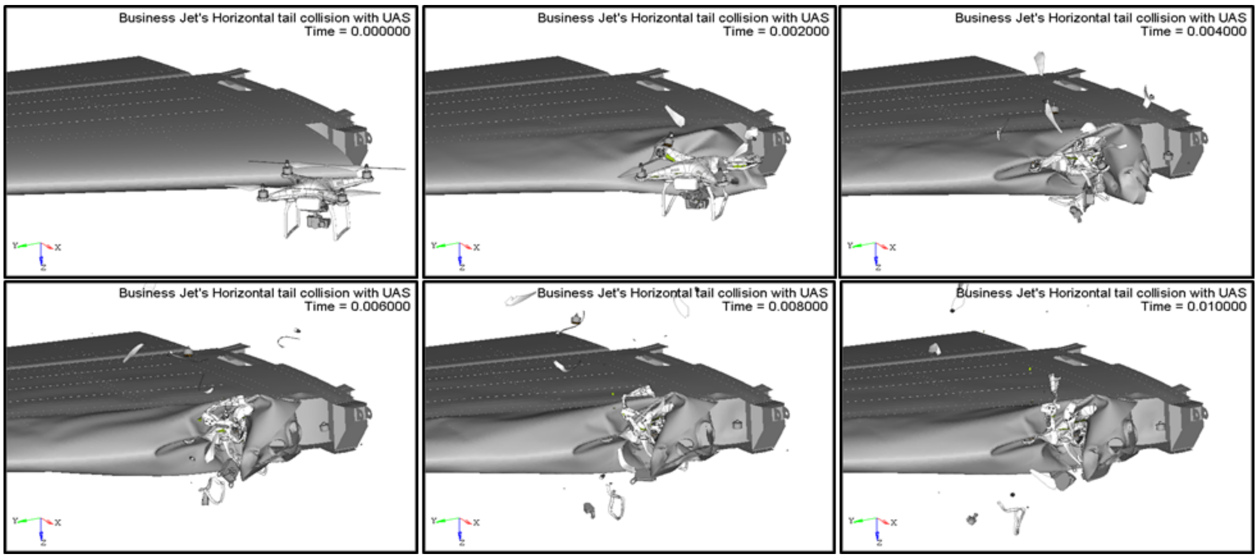

Figure 338. Kinematics of the impact between a business jet horizontal stabilizer at location 1 and a 1.2 kg (2.7 lb) UAS at 128.6 m/s (250 knots)

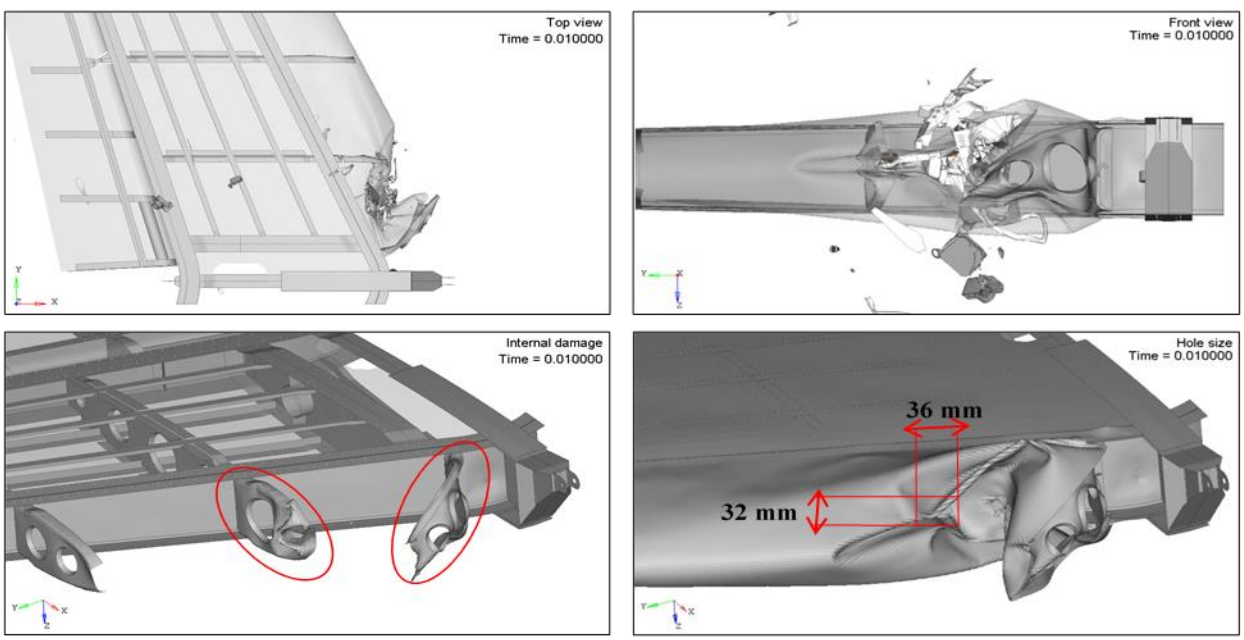

Figure 339. External/internal damage sustained by a business jet horizontal stabilizer impacted at location 1 with a 2.7lb UAS at 250 knots.

The UAS damages the skin and the nose ribs, creating a damaged zone of 36x32 mm on the skin surface and allowing the rest of the UAS mass to penetrate until it hits the front spar. In the bottom left image at Figure 339, the permanent deformation caused to the nose ribs can be seen. The front spar did not sustain critical damage.

The damage introduced by the UAS involved perforation of the skin but no damage to the primary structure, and consequently the severity was classified as Level 3.

Figure 340 shows the impulse due to the contact force between the UAS and the horizontal stabilizer, as well as the energy balance for both of them. Figure 341 presents the internal energies of the UAS and horizontal stabilizer parts directly involved on the impact.

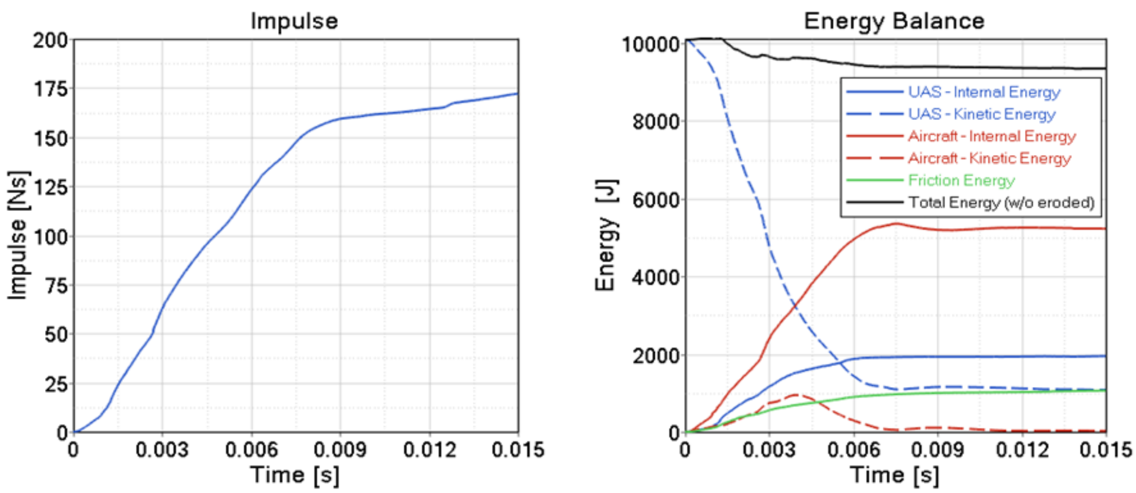

Figure 340. Impulse and energy balance of the impact between a business jet horizontal stabilizer at location 1 and a 1.2 kg (2.7 lb) UAS at 128.6 m/s (250 knots)

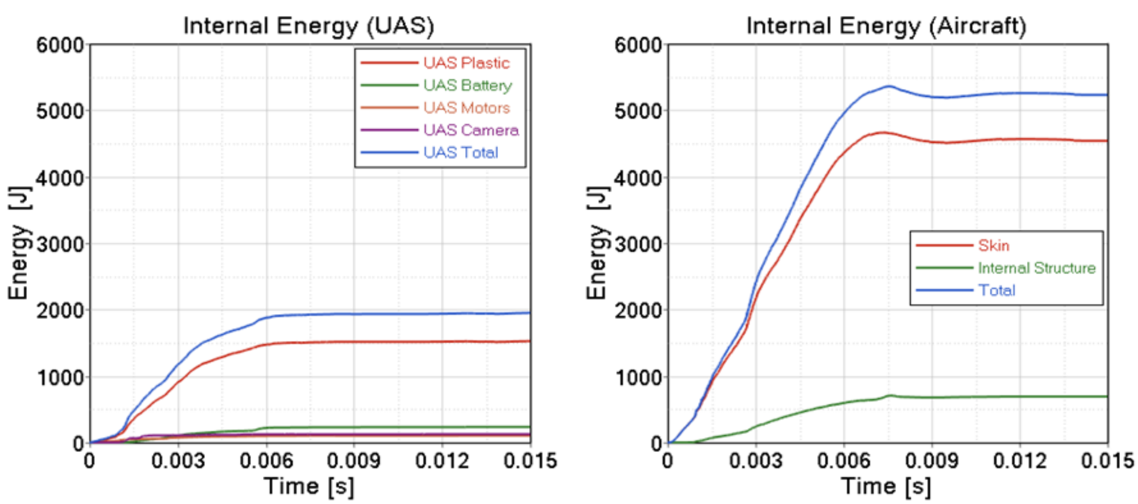

Figure 341. Internal energy per component of the impact between a business jet horizontal stabilizer at location 1 and a 1.2 kg (2.7 lb) UAS at 128.6 m/s (250 knots)

The energy balance plot includes the UAS and horizontal stabilizer kinetic and internal energies, as well as frictional energy and total energy for the event. The stabilizer absorbs 52% of the impact energy, while the UAS takes 19% of it and the energy dissipated by friction reaches 11% of the total energy. In Figure 341, internal energies for the UAS parts and the stabilizer structure show that the skin and the polycarbonate absorb the highest internal energies of the event.

B.2.2.2 BQH2

This impact location was identified as the critical baseline simulation for the business jet horizontal stabilizer and is discussed in section 4.4.2.1 of the main report body.

B.2.2.3 BQH3

Impact location 1 was located near to the horizontal stabilizer tip. The UAS was impacted against the stabilizer at 128.6 m/s (250 knots) along the local x-axis direction of the aircraft. Figure 342 presents the kinematics of the event. Figure 342 shows the damage caused to the inner frames and the skin.

The UAS damages the skin and the nose ribs, creating a damaged zone of 534x115 mm on the skin surface and allowing the rest of the UAS mass to penetrate until it hits the front spar. On the bottom left image at Figure 343 it can be appreciated the permanent deformation caused to the front spar and the nose ribs. The front spar sustained critical damage.

The damage introduced by the UAS involved perforation of the skin and damage to the primary structure, and consequently the severity was classified as Level 4.

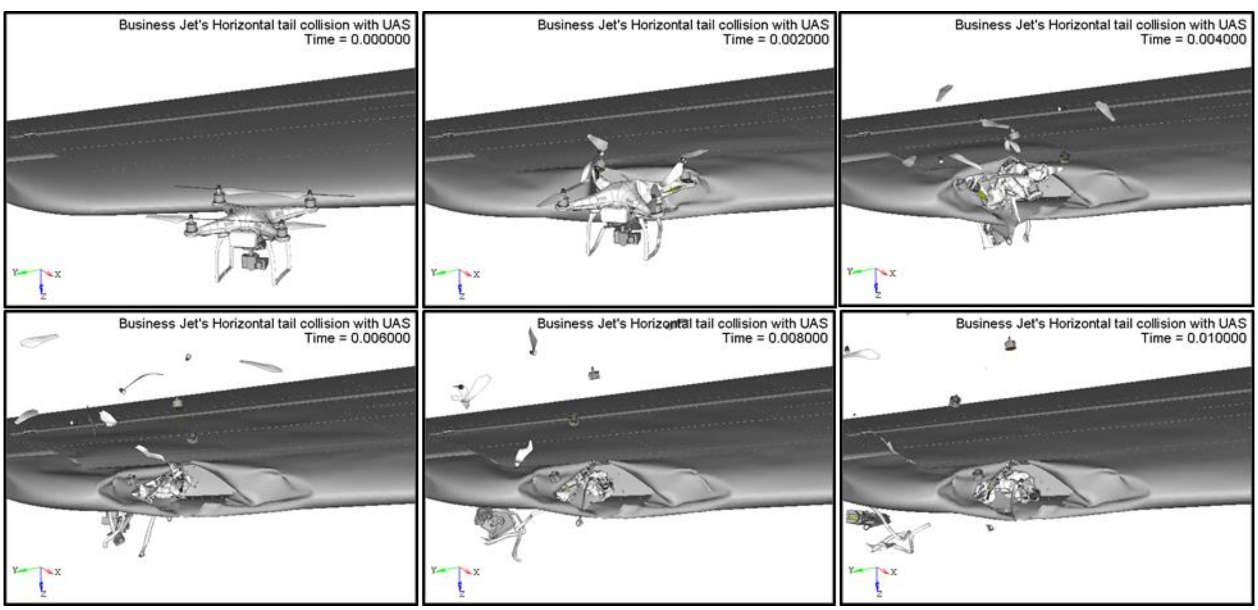

Figure 342. Kinematics of the impact between a business jet horizontal stabilizer at location 3 and a 1.2 kg (2.7 lb) UAS at 128.6 m/s (250 knots)

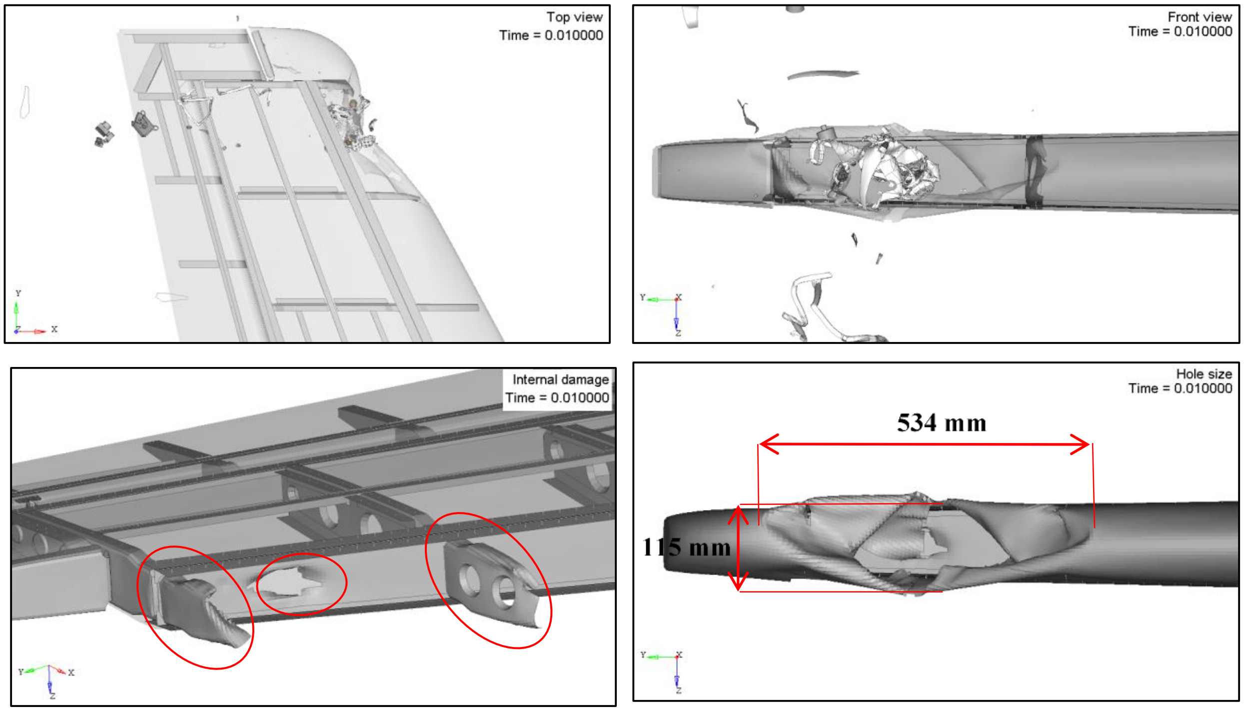

Figure 343. External/internal damage sustained by a business jet horizontal stabilizer impacted at location 3 and a 1.2 kg (2.7 lb) UAS at 128.6 m/s (250 knots)

Figure 344 shows the impulse due to the contact force between the UAS and the horizontal stabilizer, as well as the energy balance for both of them. Figure 345 presents the internal energies of the UAS and horizontal stabilizer parts directly involved on the impact.

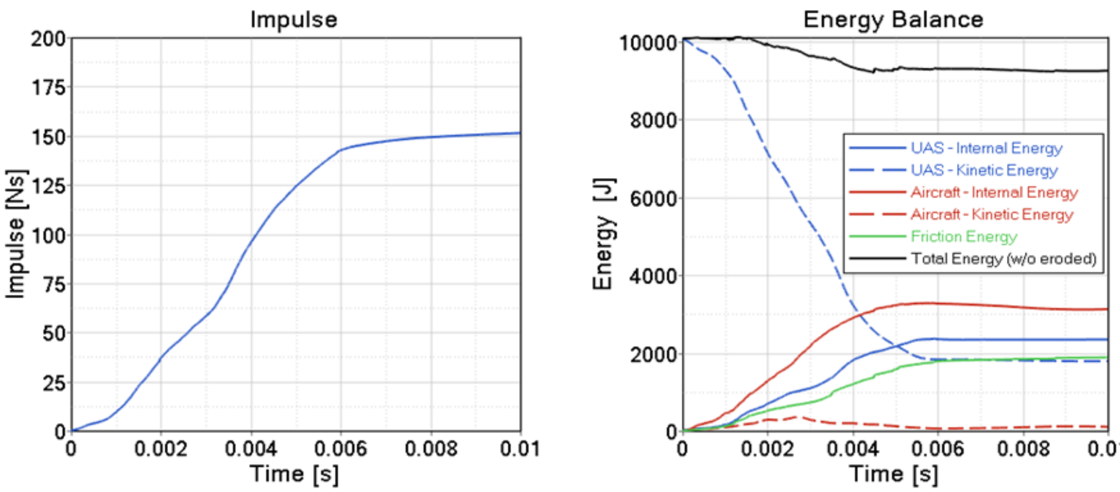

Figure 344. Impulse and energy balance of the impact between a business jet horizontal stabilizer at location 3 and a 1.2 kg (2.7 lb) UAS at 128.6 m/s (250 knots)

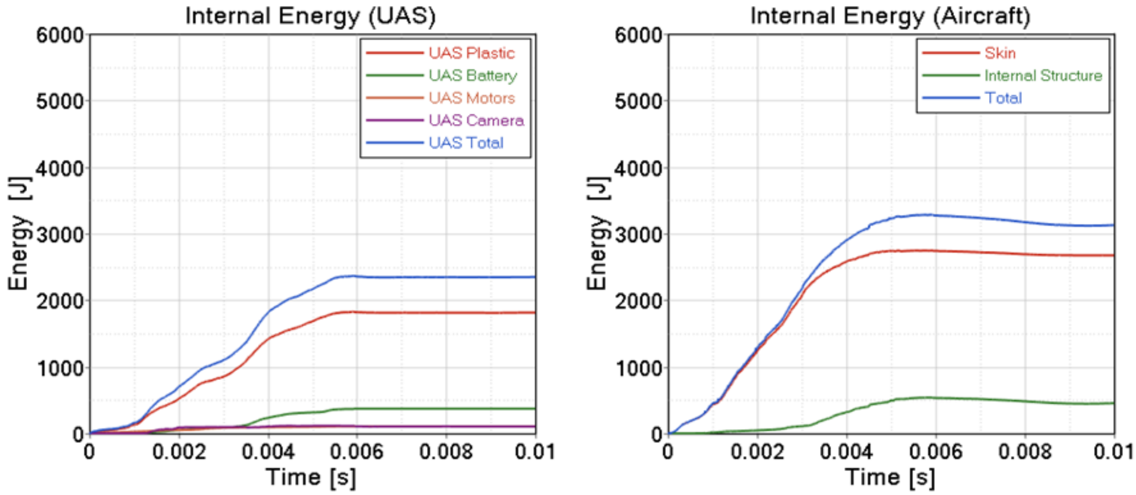

Figure 345. Internal energy per component of the impact between a business jet horizontal stabilizer at location 3 and a 1.2 kg (2.7 lb) UAS at 128.6 m/s (250 knots)

The energy balance plot includes the UAS and horizontal stabilizer kinetic and internal energies, as well as frictional energy and total energy for the event. The stabilizer absorbs 31% of the impact energy, while the UAS takes 23% of it and the energy dissipated by friction reaches 19% of the total energy. In Figure 345, internal energies for the UAS parts and the stabilizer structure show that the skin and the polycarbonate absorb the highest internal energies of the event.

B.2.3 Wing

B.2.3.1 BQW1

This impact location was identified as the critical baseline simulation for the business jet wing and is discussed in section 4.4.3.1 of the main report body.

B.2.3.2 BQW2

The middle portion of the wing between ribs 2 and 3 was chosen for impact in this case. The UAS was impacted against the wing at 128.6 m/s (250 knots) in the local x-axis direction of the aircraft. Figure 346 depicts the kinematics of the event. Figure 347 shows the damage caused to the skin and inner frames of the wing.

The UAS damages the skin, creating a damaged zone of 40x16 mm on the skin surface. This impact considerably reduces the velocity of the UAS components and the spar does not sustain any damage, as there was no impact against it.

The damage introduced by the UAS involved deformation of the skin but no perforation neither damage to the primary structure, and consequently the severity was classified as Level 2.

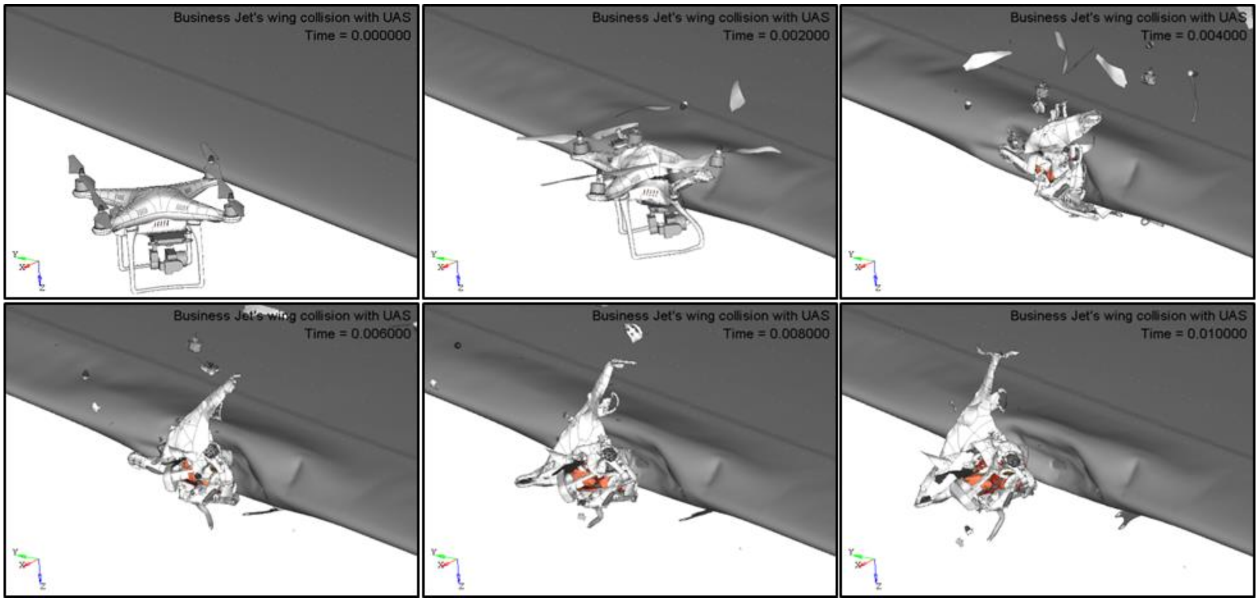

Figure 346. Kinematics of the impact between a business jet wing at location 2 and a 1.2 kg (2.7 lb) UAS at 128.6 m/s (250 knots)

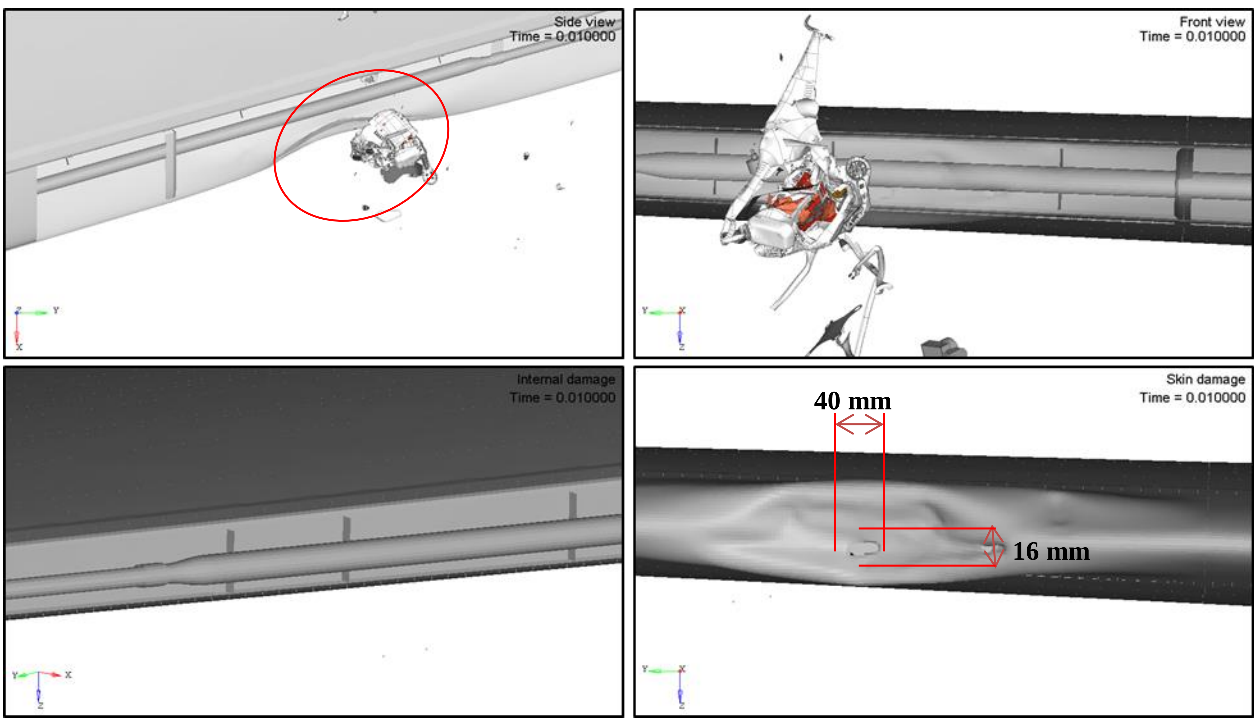

Figure 347. External/internal damage sustained by a business jet wing impacted at location 2 and a 1.2 kg (2.7 lb) UAS at 128.6 m/s (250 knots)

Figure 348 shows the impulse due to the contact force between UAS and wing, as well as the energy balance for both of them. Figure 349 shows the internal energies of UAS and wing parts directly involved in the impact.

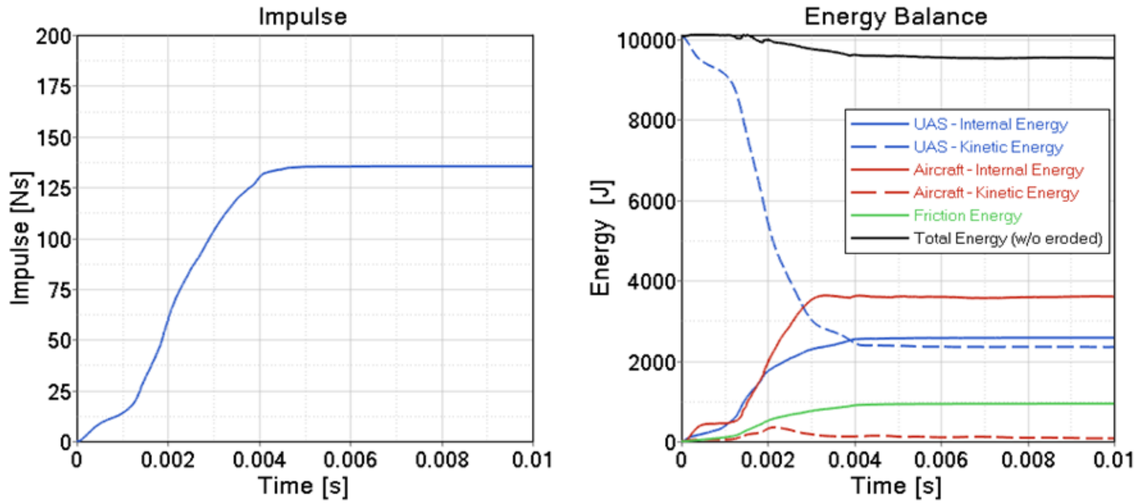

Figure 348. Impulse and energy balance of the impact between a business jet wing at location 2 and a 1.2 kg (2.7 lb) UAS at 128.6 m/s (250 knots)

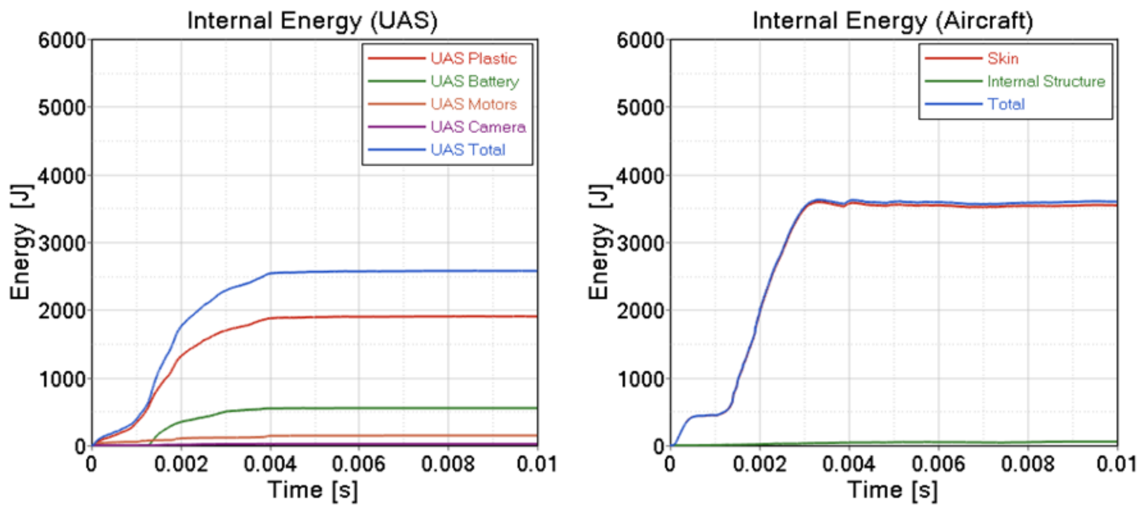

Figure 349. Internal energy per component of the impact between a business jet wing at location 2 and a 1.2 kg (2.7 lb) UAS at 128.6 m/s (250 knots)

The energy balance plot includes the UAS and wing kinetic and internal energies as well as frictional energy and total energy for the event. The wing absorbs 38% of the impact energy, while the UAS absorbs 26% of it and the energy dissipated by friction reaches 10% of the total energy. In Figure 349, internal energies for the UAS parts and the wing show that the polycarbonate and skin absorb the highest amount of internal energies respectively.

B.2.3.3 BQW3

The portion of the wing near the edge between ribs 3 and 4 was chosen for impact in this case. The UAS was impacted against the wing at 128.6 m/s (250 knots) in the local x-axis direction of the aircraft. Figure 350 depicts the kinematics of the event. Figure 351 shows the damage caused to the skin and inner frames of the wing.

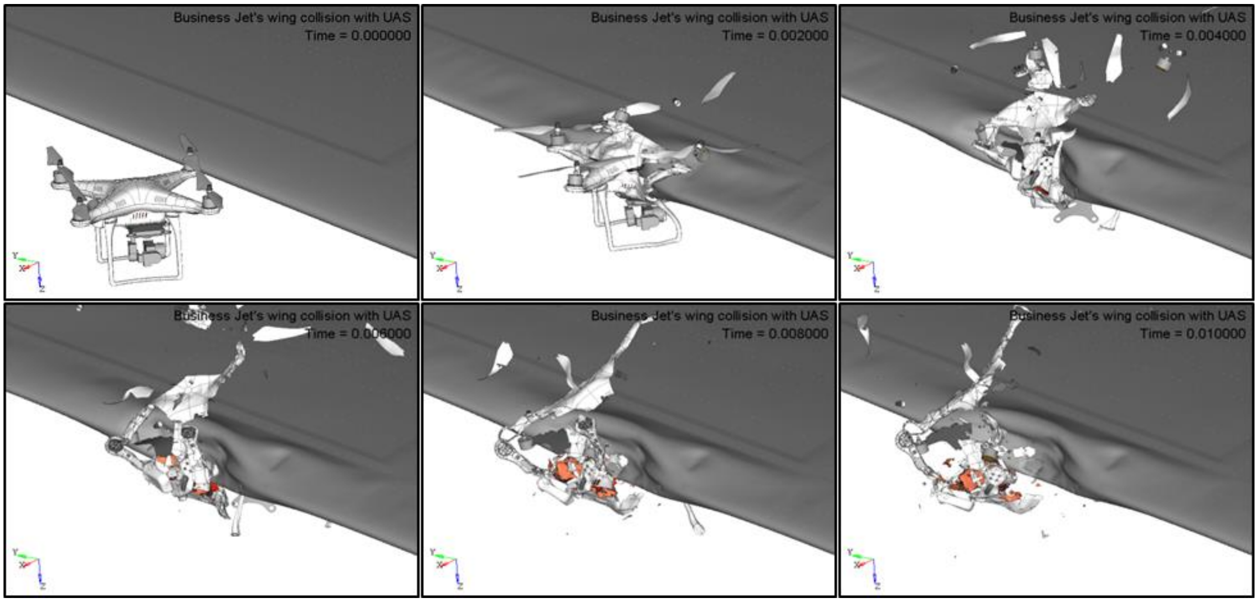

Figure 350. Kinematics of the impact between a business jet wing at location 3 and a 1.2 kg (2.7 lb) UAS at 128.6 m/s (250 knots)

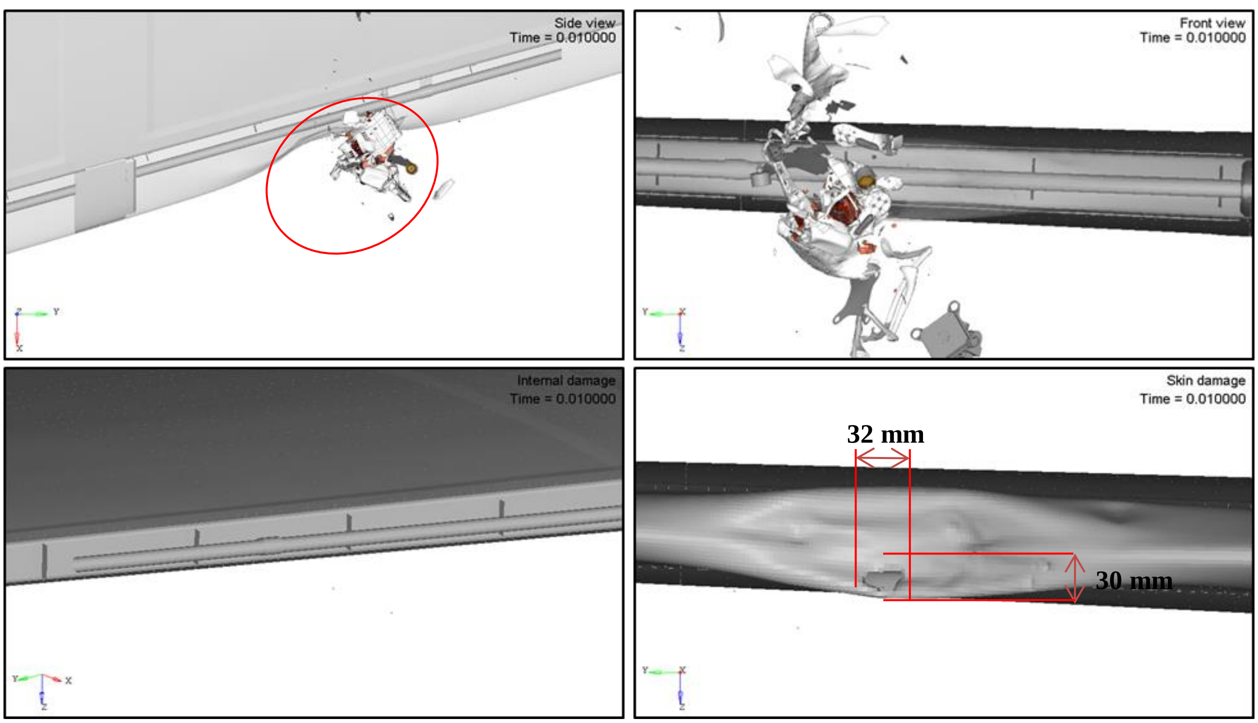

Figure 351. External/internal damage sustained by a business jet wing impacted at location 3 and a 1.2 kg (2.7 lb) UAS at 128.6 m/s (250 knots)

The UAS damages the skin, creating a damaged zone of 32x30 mm on the skin surface. This impact considerably reduces the velocity of the UAS components and the spar does not sustain any damage, as there is no impact against it.

The damage introduced by the UAS involved deformation of the skin but no perforation neither damage to the primary structure, and consequently the severity was classified as Level 2.

Figure 352 shows the impulse due to the contact force between UAS and wing, as well as the energy balance for both of them. Figure 353 shows the internal energies of UAS and wing parts directly involved in the impact.

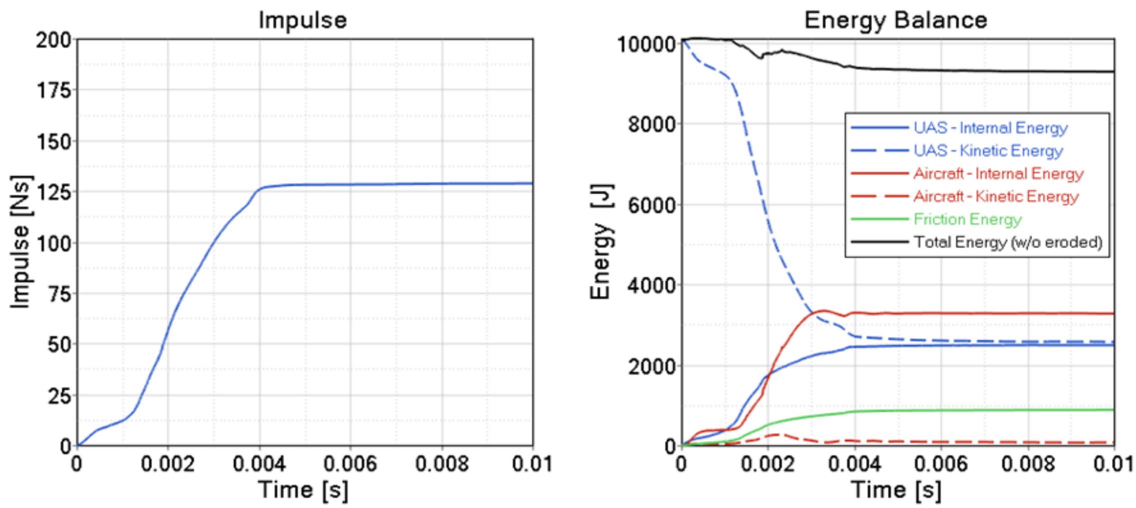

Figure 352. Impulse and energy balance of the impact between a business jet wing at location 3 and a 1.2 kg (2.7 lb) UAS at 128.6 m/s (250 knots)

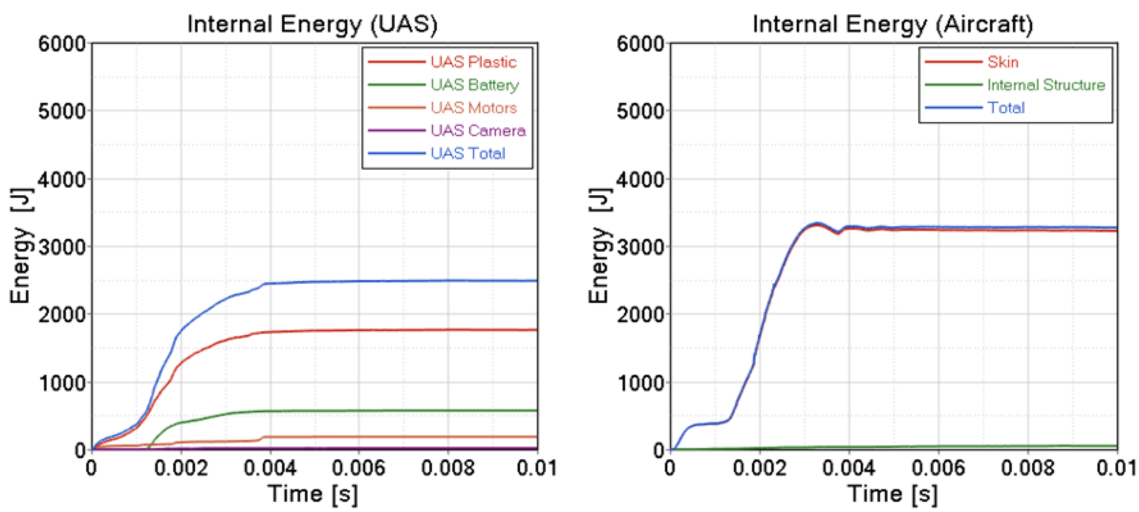

Figure 353. Internal energy per component of the impact between a business jet wing at location 3 and a 1.2 kg (2.7 lb) UAS at 128.6 m/s (250 knots)

The energy balance plot includes the UAS and wing kinetic and internal energies as well as frictional energy and total energy for the event. The wing absorbs 32% of the impact energy, while the UAS absorbs 25% of it and the energy dissipated by friction reaches 10% of the total energy. In Figure 353, internal energies for the UAS parts and the wing show that the polycarbonate and skin absorb the highest amount of internal energies respectively.

B.2.4 Windshield

B.2.4.1 BQC1

This impact location was identified as the critical baseline simulation for the business jet windshield and is discussed in section 4.4.3.1 of the main report body.

B.2.4.2 RBQC2

Impact location 2 was chosen on the middle of the center post. The UAS was impacted against the windshield at 128.6 m/s (250 knots) along the local x-axis direction of the aircraft. Figure 354 presents the kinematics of the event. Figure 355 shows the damage caused to the windshield and the internal structure.

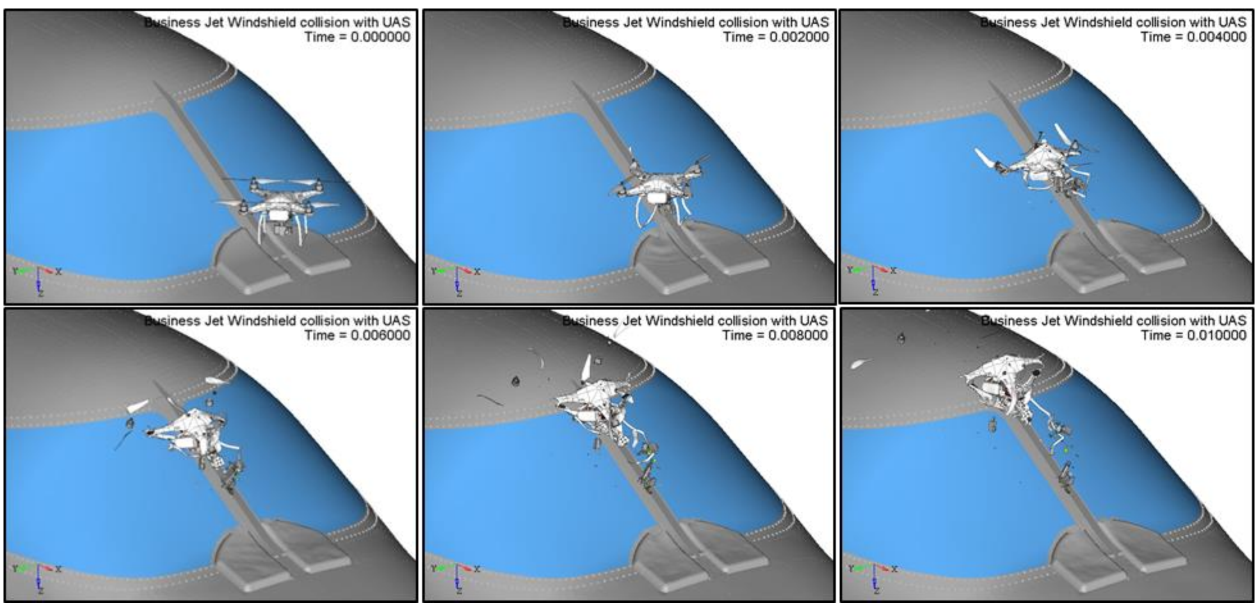

Figure 354. Kinematics of the impact between a business jet windshield at location 2 and a 1.2 kg (2.7 lb) UAS at 128.6 m/s (250 knots)

The UAS impacts the center post and slides over as a result of the deflected structure. The windshield did not sustain any fracture or major damage. The permanent deformation on the center post and the structure near to it is presented on the bottom right image in Figure 355. As it can be observed, there is no critical damage on the center post surface and the surrounding structure.

The damage introduced by the UAS involved deformation of the frame but no damage to the primary structure, and consequently the severity was classified as Level 2.

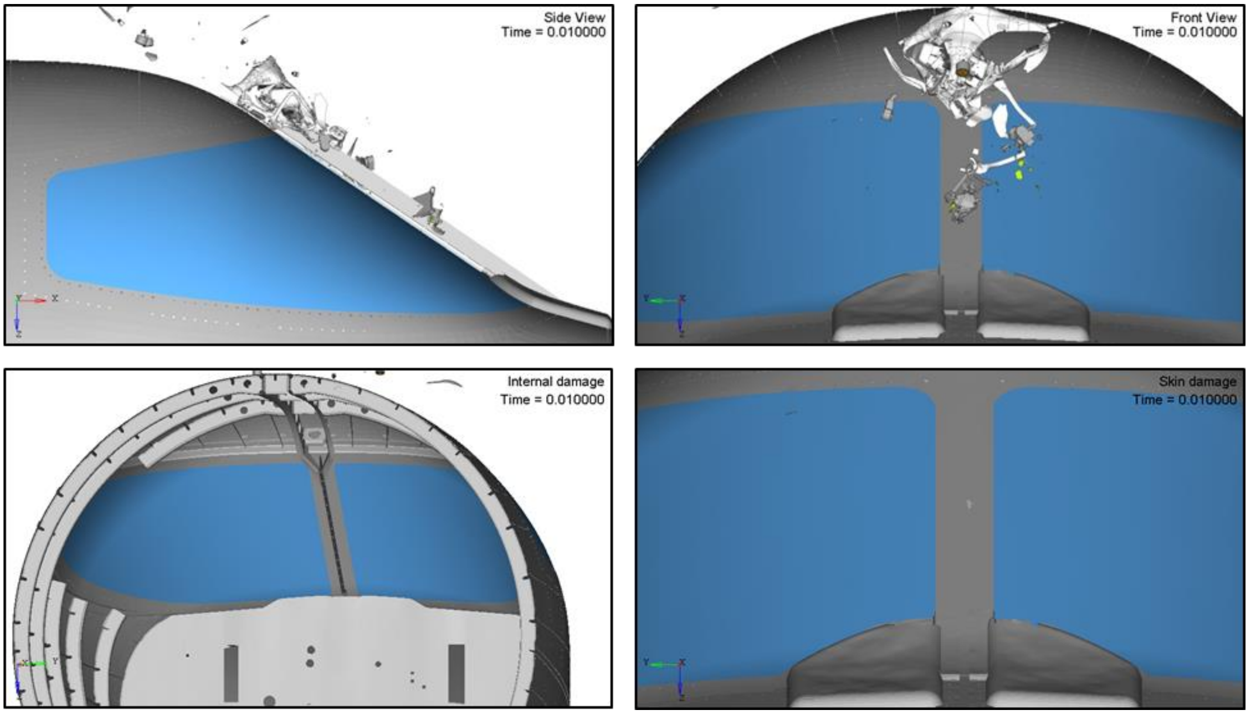

Figure 355. External/internal damage sustained by a business jet windshield impacted at location 2 and a 1.2 kg (2.7 lb) UAS at 128.6 m/s (250 knots)

Figure 356 shows the impulse due to the contact force between the UAS and the forward fuselage, as well as the energy balance for both of them. Figure 357 shows the internal energies of the UAS and the forward fuselage parts directly involved in the impact.

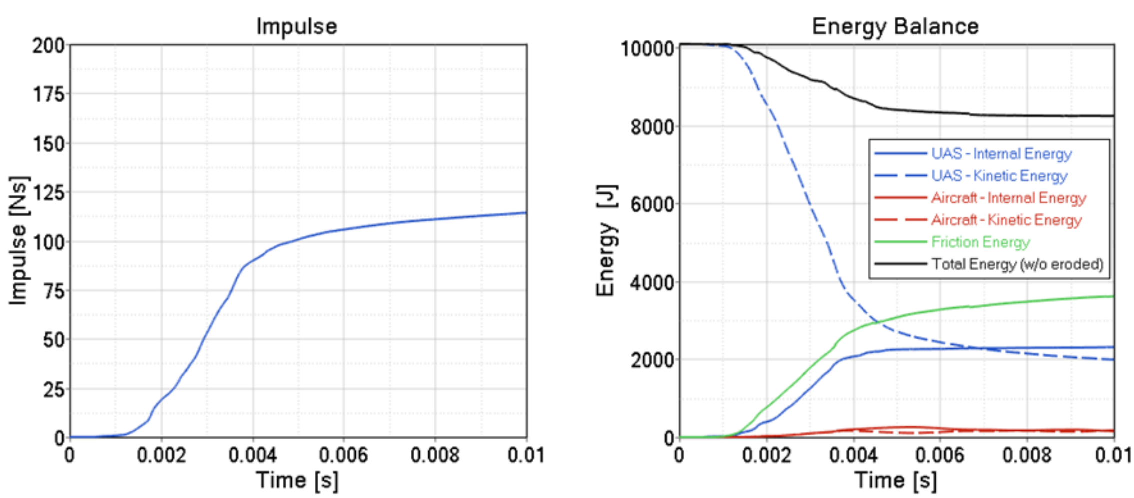

Figure 356. Impulse and energy balance of the impact between a business jet windshield at location 2 and a 1.2 kg (2.7 lb) UAS at 128.6 m/s (250 knots)

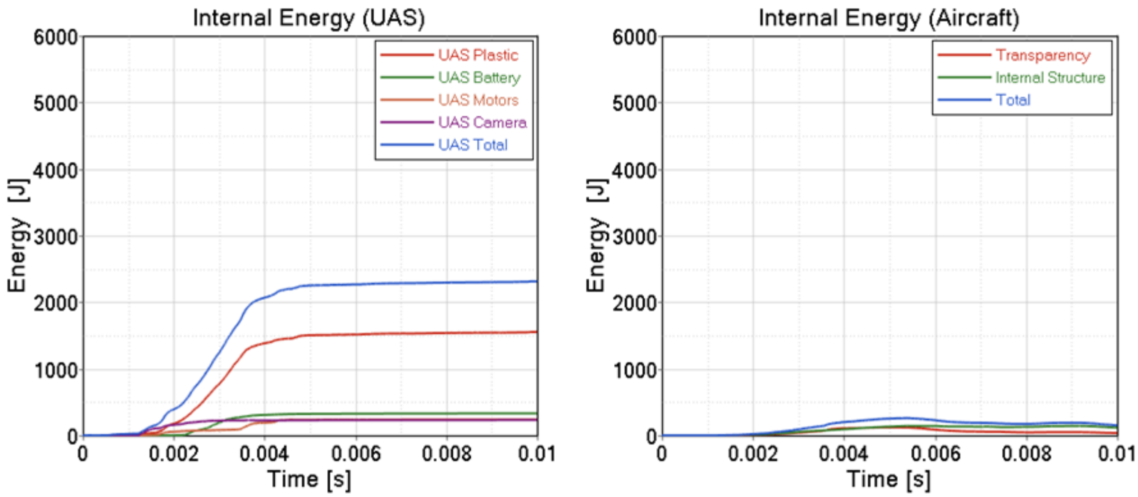

Figure 357. Internal energy per component of the impact between a business jet windshield at location 2 and a 1.2 kg (2.7 lb) UAS at 128.6 m/s (250 knots)

The energy balance plot includes the UAS and forward fuselage kinetic and internal energies as well as frictional energy and total energy for the event. The forward fuselage absorbs 2% of the impact energy, while the UAS absorbs 28% of it and the energy dissipated by friction reaches 43% of the total energy. In Figure 357, internal energies for the UAS parts and forward fuselage show that the polycarbonate and internal structure absorb the highest amount of internal energies respectively.

B.2.5 Summary of Results of Collision with Business Jet

Assembly	**Case**	**Severity**	**Fire Risk**	**Internal Energy Aircraft [J]**	**Internal Energy UAS [J]**	**Residual Kinetic Energy [J]**	**Friction Energy [J]**	**Eroded Energy [J]**
Vertical Stabilizer	BQV1	Level 3	Yes	3370	2140	1450	1670	1357
	BQV2	Level 3	No	4290	1880	1850	1335	685
	BQV3	Level 2	No	3105	1790	3020	1510	620
Horizontal Stabilizer	BQH1	Level 3	Yes	3100	2400	1755	1620	1100
	BQH2	Level 4	No	3280	2356	1730	1725	945
	BQH3	Level 4	Yes	4790	1875	1255	1230	915
Wing	BQW1	Level 3	Yes	3790	2350	1990	970	910
	BQW2	Level 2	No	3600	2580	2340	940	575
	BQW3	Level 2	No	3270	2470	2570	880	830
Windshi eld	BQC1	Level 2	No	240	1330	6210	1400	600
	BQC2	Level 2	No	153	2315	1995	3700	1800

APPENDIX C – MASS SENSITIVITY STUDY

C.1 TRANSPORT JET – BASELINE UAS (1.2 KG) VS SCALED UAS (1.8 KG)

C.1.1 Vertical Stabilizer

Impact simulations of a 1.2 kg (2.7 lb) UAS (case CQV3) and 1.8 kg (4 lb) UAS (case CQsV3) against a vertical stabilizer are compared in terms of damage severity and kinematics. The initial conditions for both cases were based on CQV3, which was identified as the most critical case in the baseline simulations (see Section 4.3.1.1). Figure 358 depicts the comparison of the kinematics of the event. Figure 359 shows the comparison of the damage caused to the skin and the inner structure of the vertical stabilizer.

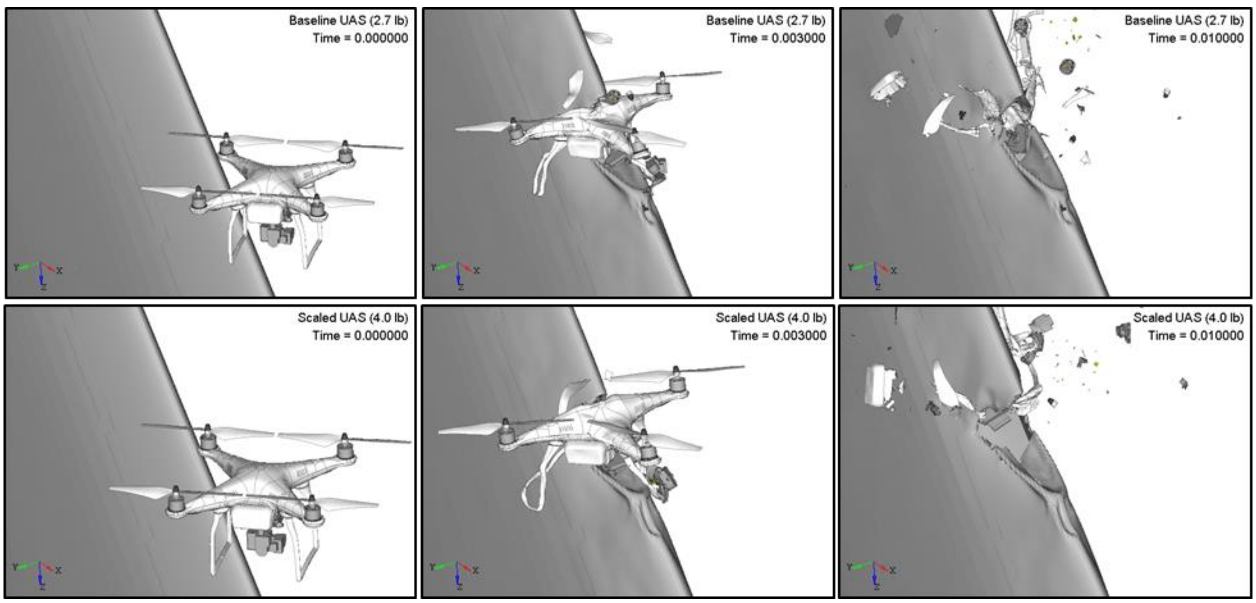

Figure 358. Comparison of the kinematics of impact between a commercial transport jet vertical stabilizer and a 1.2/1.8 kg (2.7/4.0 lb) UAS at 128.6 m/s (250 knots)

The 1.8 kg (4.0 lb) UAS damaged the skin, upper and lower ribs, and the lightening hole above the impact location in the front spar while the 1.2 kg (2.7 lb) UAS damaged the skin, just the upper rib, and the front spar to a lesser degree. It can also be perceived in Figure 359 that the damage introduced into the skin, the ribs, and the front spar was considerably more spread out for the case of 1.8 kg 4.0 lb) UAS than of the 1.2 kg (2.7 lb) UAS.

The damage introduced by both the UAS is classified as Level 3. Even with the same level, in terms of damage, the 1.8 kg (4.0 lb) UAS can be considered as slightly more severe than the 1.2 kg (2.7 lb) UAS.

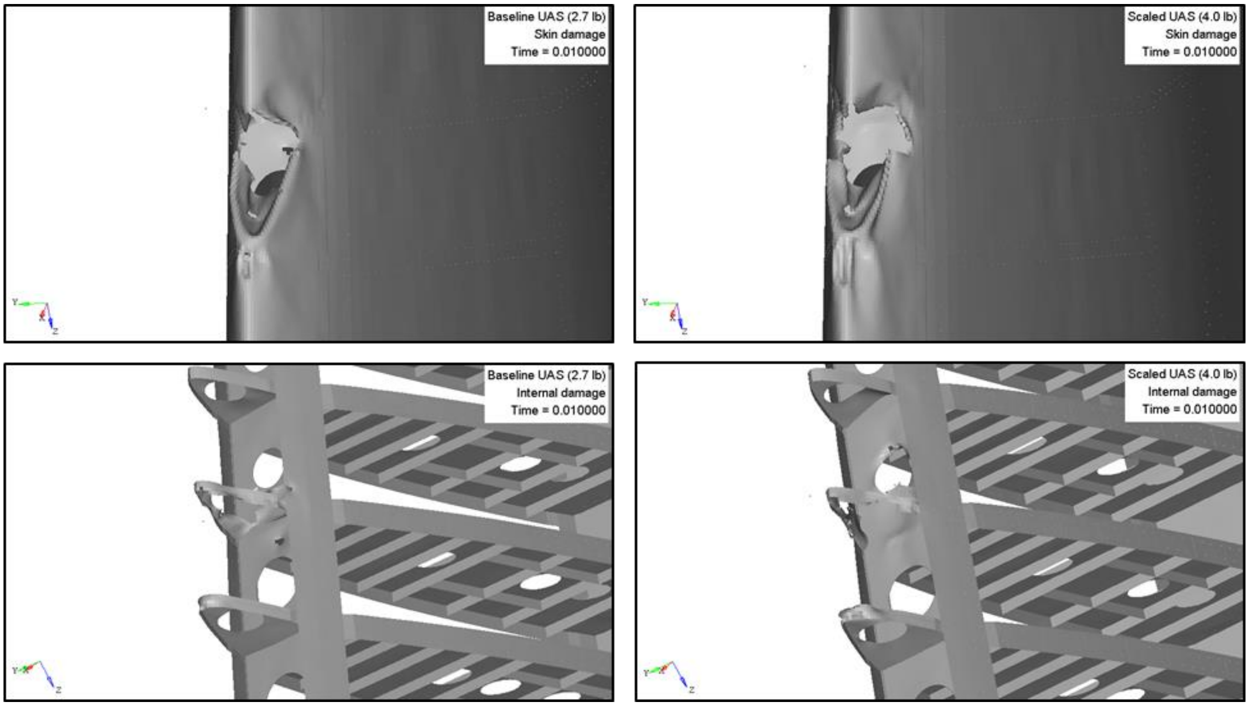

Figure 359. Comparison of external/internal damage sustained by a commercial transport jet vertical stabilizer impacted with a 1.2/1.8 kg (2.7/4.0 lb) UAS at 128.6 m/s (250 knots)

Figure 360 shows the comparison for the contact force and impulse between the 1.2/1.8 kg (2.7/4.0 lb) UAS and vertical stabilizer. Figure 361 shows the energy balance, normalized with the initial kinetic energy, for the impact comparison.

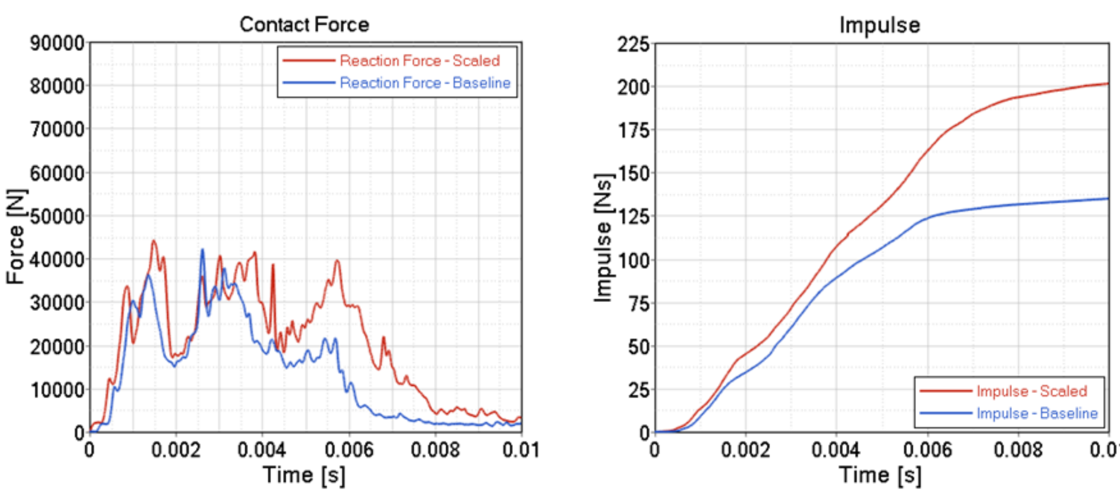

Figure 360. Comparison of the contact force and impulse of the impact between a commercial transport jet vertical stabilizer and a 1.2/1.8 kg (2.7/4.0 lb) UAS at 128.6 m/s (250 knots)

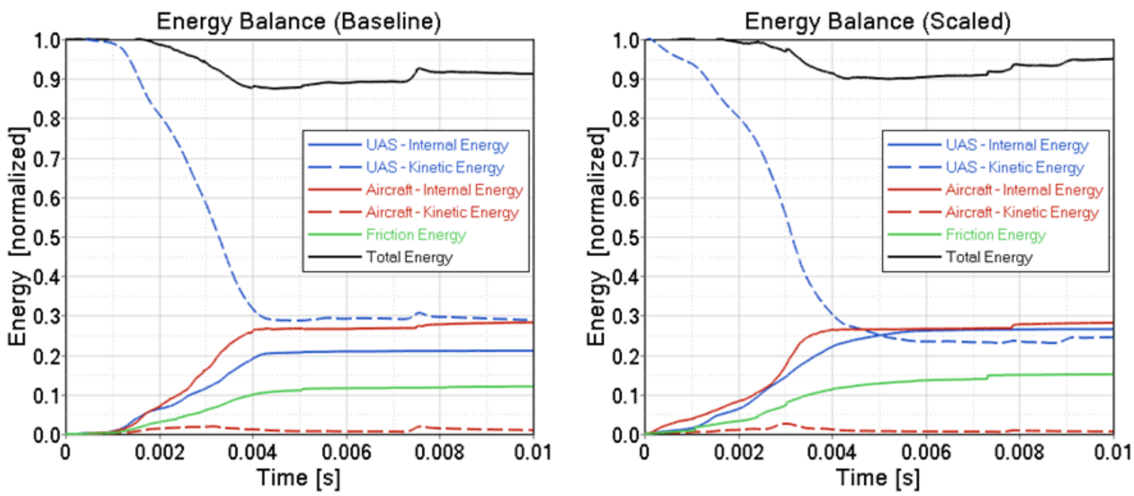

Figure 361. Comparison of the energy balance of the impact between a commercial transport jet vertical stabilizer and a 1.2/1.8 kg (2.7/4.0 lb) UAS at 128.6 m/s (250 knots)

The impulse for the 1.8 kg (4.0 lb) UAS was greater than for the 1.2 kg (2.7 lb) UAS. From the energy balance comparison, it can be observed that the 1.8 kg (4.0 lb) UAS absorbed a similar ratio of internal energy than the 1.2 kg (2.7 lb) UAS. In addition, it is apparent that the residual kinetic energy of the 1.8 kg (4.0 lb) UAS after impact was smaller relatively than the 1.2 kg (2.7 lb) UAS. However, it can be seen that the higher mass UAS absorbed about an 8% more energy than the lower mass UAS, relatively to the impact energy.

C.1.2 Horizontal Stabilizer

Impact simulations of a 1.2 kg (2.7 lb) UAS (case CQH3) and 1.8 kg (4 lb) UAS (case CQsH3) against a horizontal stabilizer are compared in terms of damage severity and kinematics. The initial conditions for both cases were based on CQH3, which was identified as the most critical case in the baseline simulations (see Section 4.3.2.1). Figure 362 depicts the comparison of the kinematics of the event. Figure 363 shows the comparison of the damage caused to the skin and the inner structure of the horizontal stabilizer.

The 1.8 kg (4.0 lb) UAS damaged the skin, the nose ribs, and the front spar while the 1.2 kg (2.7 lb) UAS damaged the skin, the nose ribs, and the front spar to a lesser degree. It can also be perceived in Figure 363 that the damage introduced into the skin, the ribs, and the front spar was considerably greater for the case of 1.8 kg (4.0 lb) UAS than of the 1.2 kg (2.7 lb) UAS.

The damage introduced by both the UAS is classified as Level 4 with risk of fire due to the battery. Even with the same level, in terms of damage, the 1.8 kg (4.0 lb) UAS can be considered as more severe than the 1.2 kg (2.7 lb) UAS.

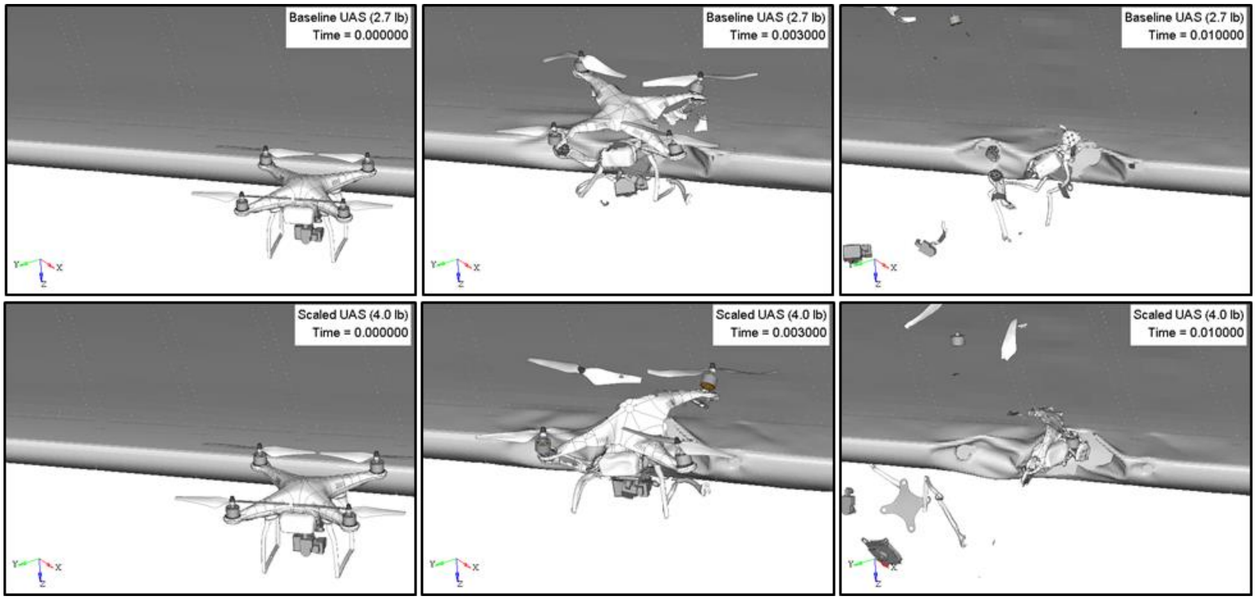

Figure 362. Comparison of the kinematics of impact between a commercial transport jet horizontal stabilizer and a 1.2/1.8 kg (2.7/4.0 lb) UAS at 128.6 m/s (250 knots)

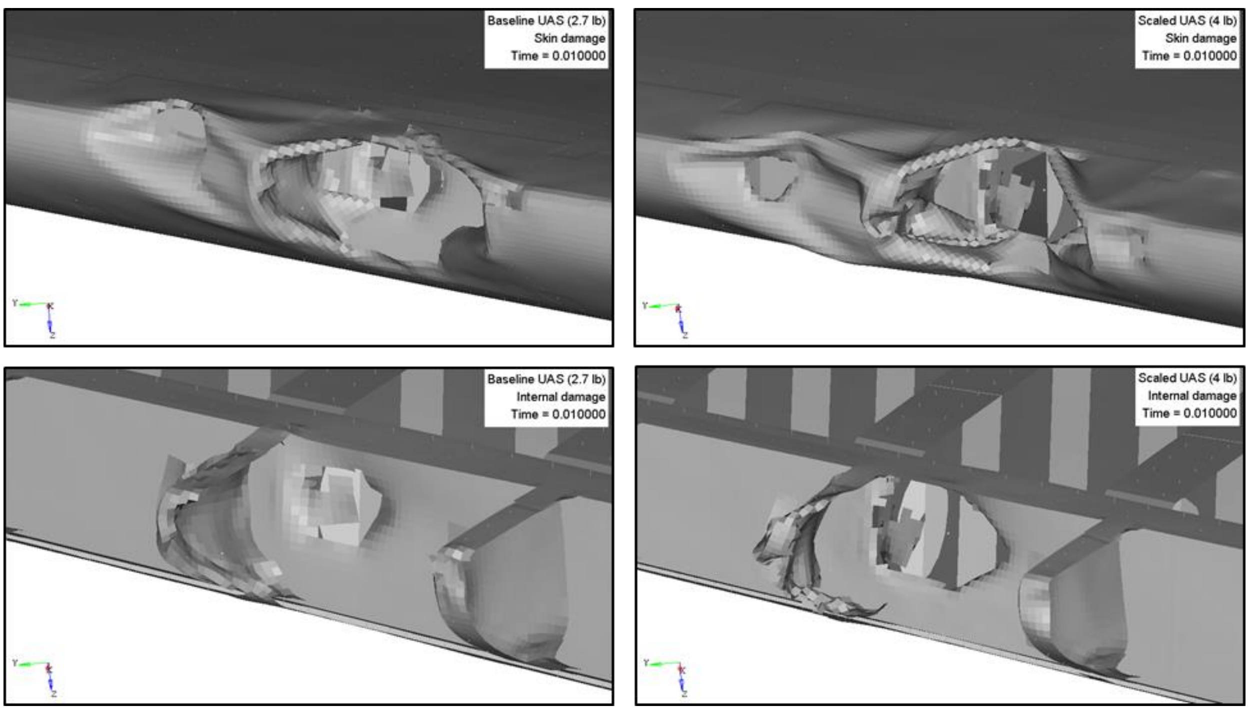

Figure 363. Comparison of external/internal damage sustained by a commercial transport jet horizontal stabilizer impacted with a 1.2/1.8 kg (2.7/4.0 lb) UAS at 128.6 m/s (250 knots)

Figure 364 shows the comparison for the contact force and impulse between the 1.2/1.8 kg (2.7/4.0 lb) UAS and horizontal stabilizer. Figure 365 shows the energy balance, normalized with the initial kinetic energy, for the impact comparison.

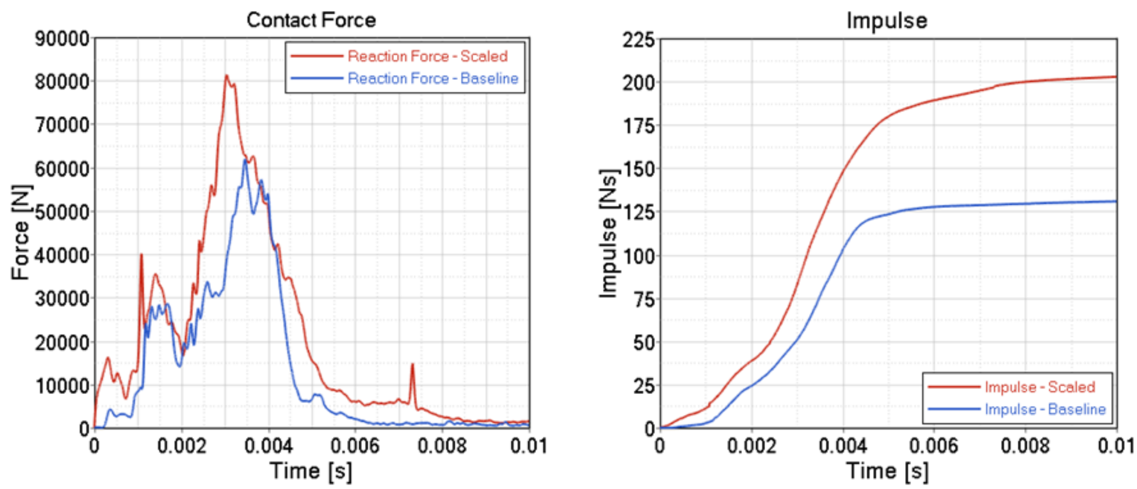

Figure 364. Comparison of the contact force and impulse of the impact between a commercial transport jet horizontal stabilizer and a 1.2/1.8 kg (2.7/4.0 lb) UAS at 128.6 m/s (250 knots)

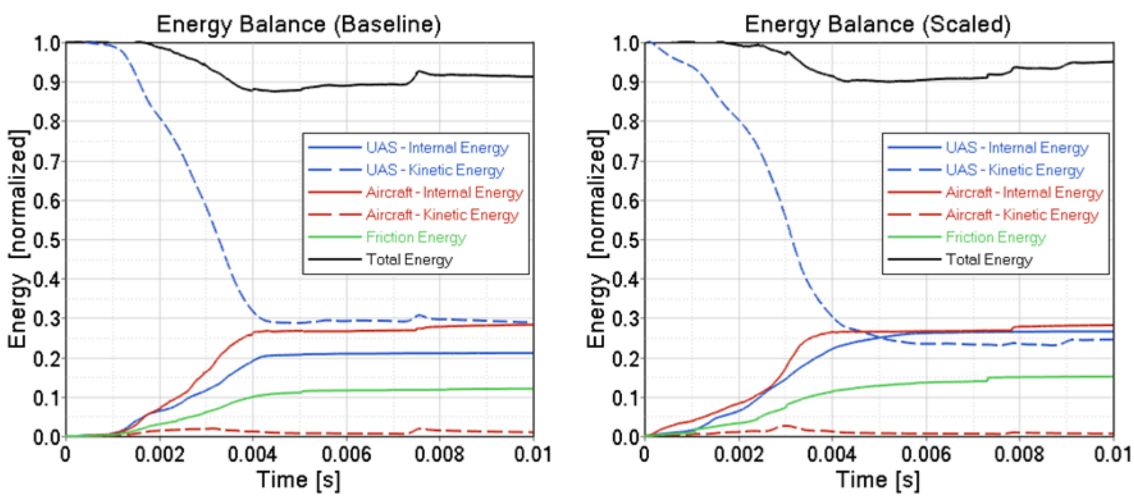

Figure 365. Comparison of the energy balance of the impact between a commercial transport jet horizontal stabilizer and a 1.2/1.8 kg (2.7/4.0 lb) UAS at 128.6 m/s (250 knots)

The impulse for the 1.8 kg (4.0 lb) UAS was greater than for the 1.2 kg (2.7 lb) UAS. From the energy balance comparison, it can be observed that the 1.8 kg (4.0 lb) UAS absorbed a similar ratio of internal energy than the 1.2 kg (2.7 lb) UAS. In addition, it is apparent that the residual kinetic energy of the 1.8 kg (4.0 lb) UAS after impact was smaller relatively than the 1.2 kg (2.7 lb) UAS. However, it can be seen that the higher mass UAS absorbed about a 4% more energy than the lower mass UAS, relatively to the impact energy.

C.1.3 Wing Leading Edge

Impact simulations of a 1.2 kg (2.7 lb) UAS (case CQW1) and 1.8 kg (4 lb) UAS (case CQsW1) against a wing leading edge are compared in terms of damage severity and kinematics. The initial conditions for both cases were based on CQW1, which was identified as the most critical case in the baseline simulations (see Section 4.3.3.1). Figure 366 depicts the comparison of the kinematics of the event. Figure 367 shows the comparison of the damage caused to the skin and the inner structure of the wing.

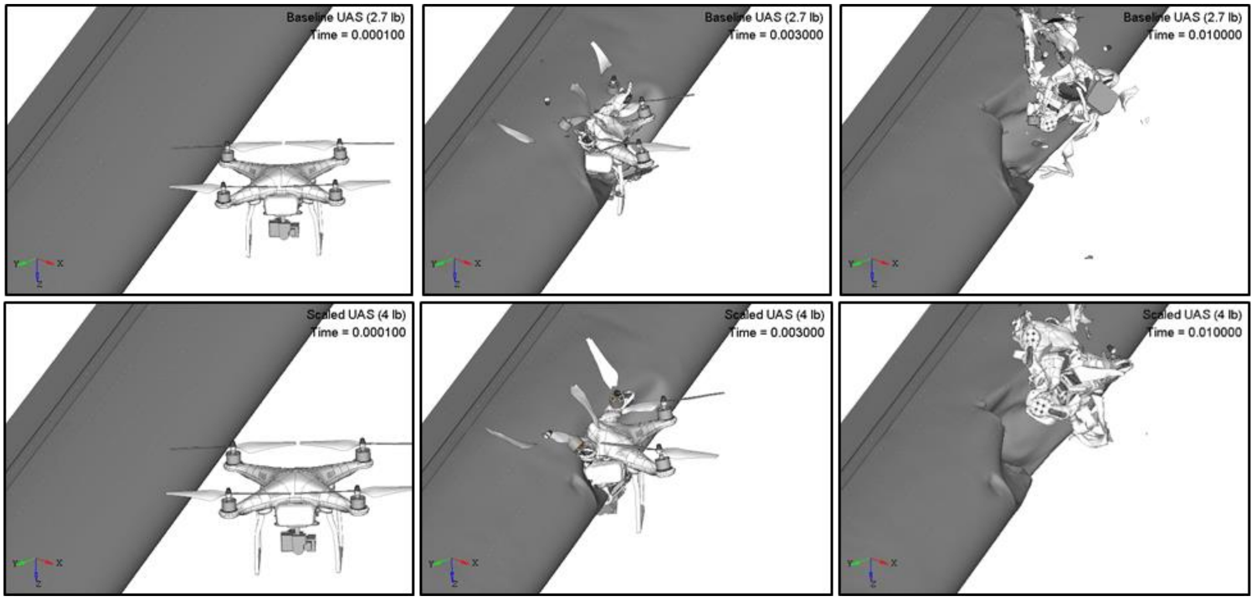

Figure 366. Comparison of the kinematics of impact between a commercial transport jet wing and a 1.2/1.8 kg (2.7/4.0 lb) UAS at 128.6 m/s (250 knots)

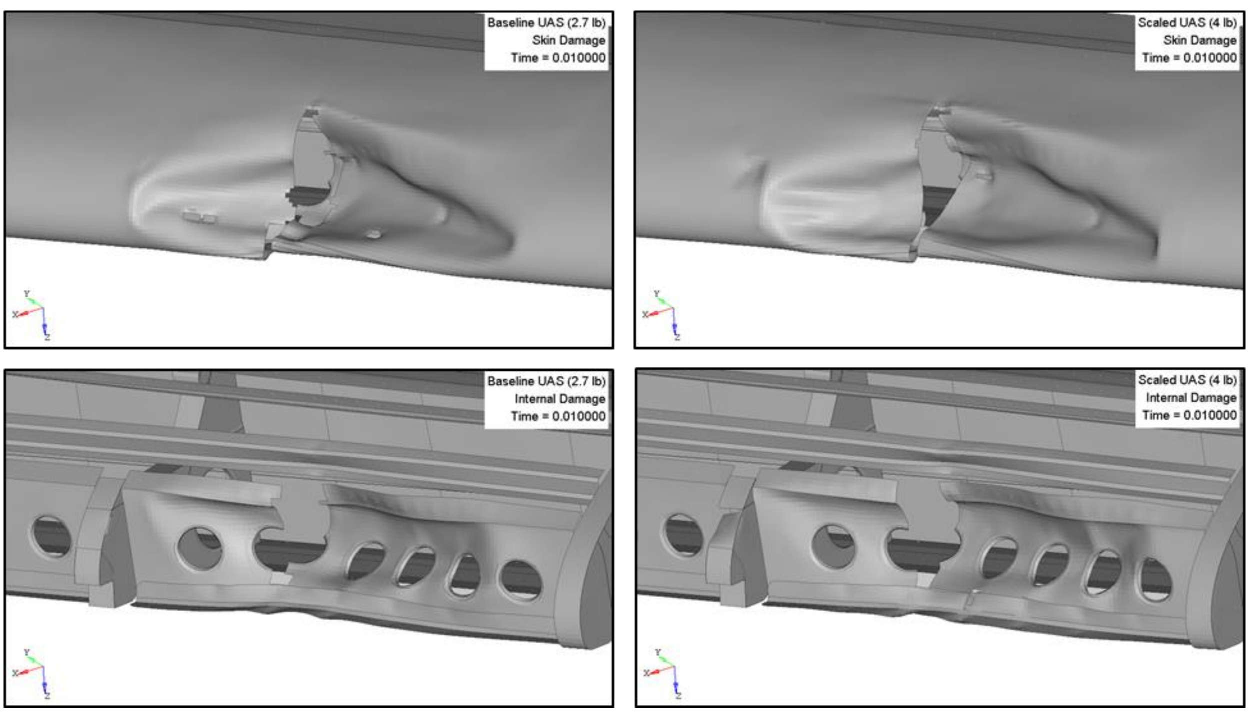

Figure 367. Comparison of external/internal damage sustained by a commercial transport jet wing impacted with a 1.2/1.8 kg (2.7/4.0 lb) UAS at 128.6 m/s (250 knots)

The 1.8 kg (4.0 lb) UAS damaged the D-nose skin surface, the hold down rib, and the sub spar while the 1.2 kg (2.7 lb) UAS damaged the skin and the sub spar to a lesser degree. It can also be perceived in Figure 367 that the damage introduced into the skin and the sub spar was greater for the case of 1.8 kg (4.0 lb) UAS than of the 1.2 kg (2.7 lb) UAS.

The damage introduced by both the UAS is classified as Level 3. In addition, the risk of fire due to the battery is present only for the impact of the 1.8 kg (4.0 lb) UAS. Even with the same level, in terms of damage, the 1.8 kg (4.0 lb) UAS can be considered as slightly more severe than the 1.2 kg (2.7 lb) UAS.

Figure 368 shows the comparison for the contact force and impulse between the 1.2/1.8 kg (2.7/4.0 lb) UAS and wing. Figure 369 shows the energy balance, normalized with the initial kinetic energy, for the impact comparison.

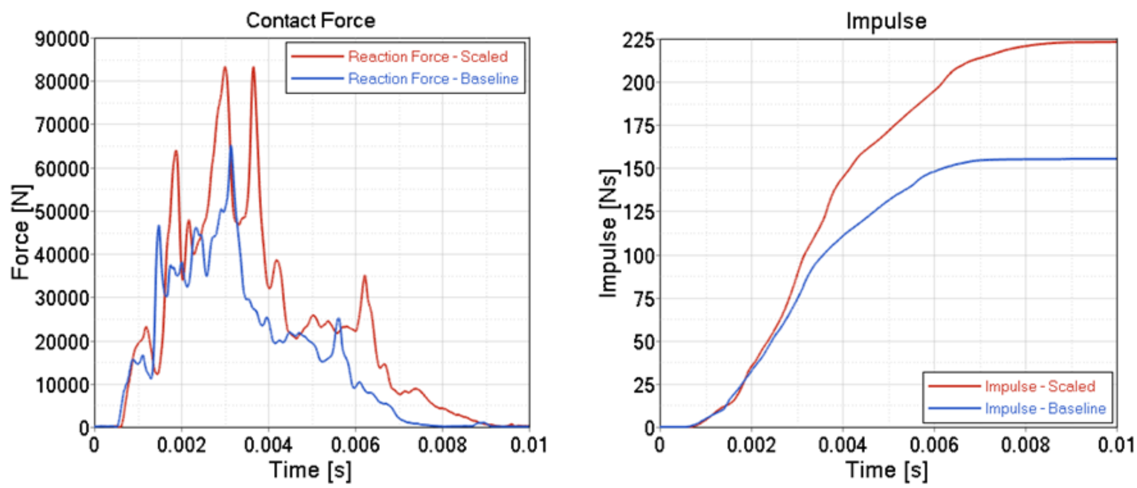

Figure 368. Comparison of the contact force and impulse of the impact between a commercial transport jet wing and a 1.2/1.8 kg (2.7/4.0 lb) UAS at 128.6 m/s (250 knots)

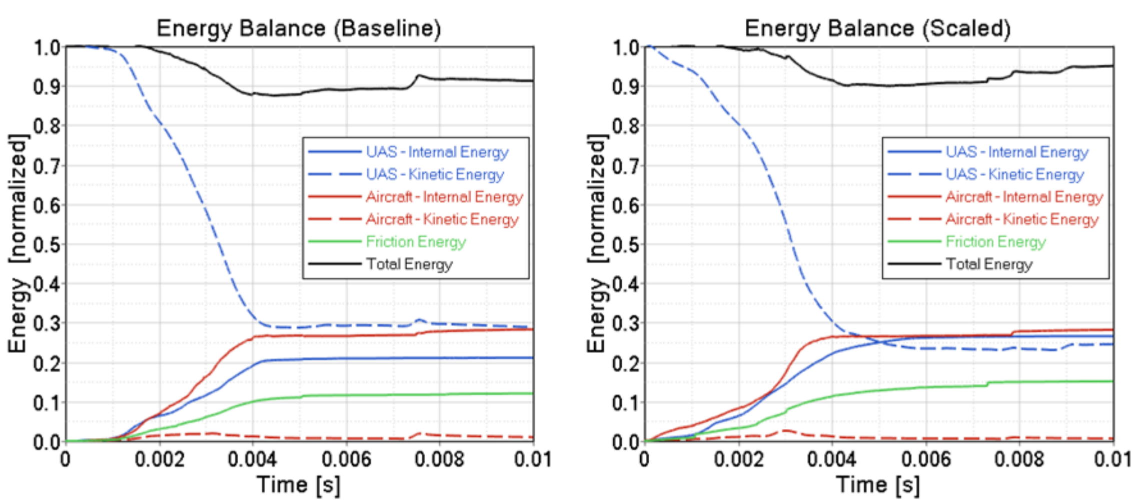

Figure 369. Comparison of the energy balance of the impact between a commercial transport jet wing and a 1.2/1.8 kg (2.7/4.0 lb) UAS at 128.6 m/s (250 knots)

The impulse for the 1.8 kg (4.0 lb) UAS was greater than for the 1.2 kg (2.7 lb) UAS. From the energy balance comparison, it can be observed that the 1.8 kg (4.0 lb) UAS absorbed a similar ratio of internal energy than the 1.2 kg (2.7 lb) UAS. In addition, it is apparent that the residual kinetic energy of the 1.8 kg (4.0 lb) UAS after impact was smaller relatively than the 1.2 kg (2.7 lb) UAS. However, it can be seen that the higher mass UAS absorbed about a 5% more energy than the lower mass UAS, relatively to the impact energy.

C.1.4 Windshield

Impact simulations of a 1.2 kg (2.7 lb) UAS (case CQC1) and 1.8 kg (4 lb) UAS (case CQsC1) against a windshield are compared in terms of damage severity and kinematics. The initial conditions for both cases were based on CQC1, which was identified as the most critical case in the baseline simulations (see Section 4.3.4.1). Figure 370 depicts the comparison of the kinematics of the event. Figure 371 shows the comparison of the damage caused to the windshield and surrounding structure.

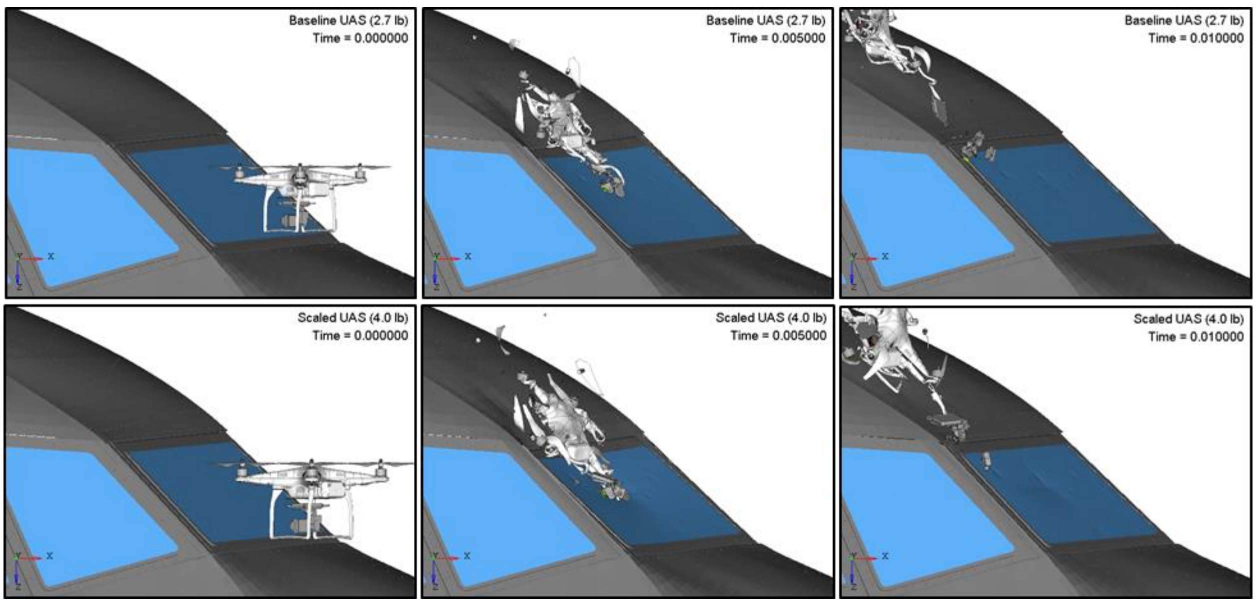

Figure 370. Comparison of the kinematics of impact between a commercial transport jet windshield and a 1.2/1.8 kg (2.7/4.0 lb) UAS at 128.6 m/s (250 knots)

Both the UAS impacted the windshield and slid over it due to the small windshield angle, leaving some permanent deformation. The internal structure did not sustain any visible damage. It can also be perceived in Figure 371 that the damage introduced into windshield was greater for the case of 1.8 kg (4.0 lb) UAS than of the 1.2 kg (2.7 lb) UAS.

In terms of damage, the 1.8 kg (4.0 lb) UAS can be classified as Level 3 while the 1.2 kg (2.7 lb) UAS can be classified as Level 2.

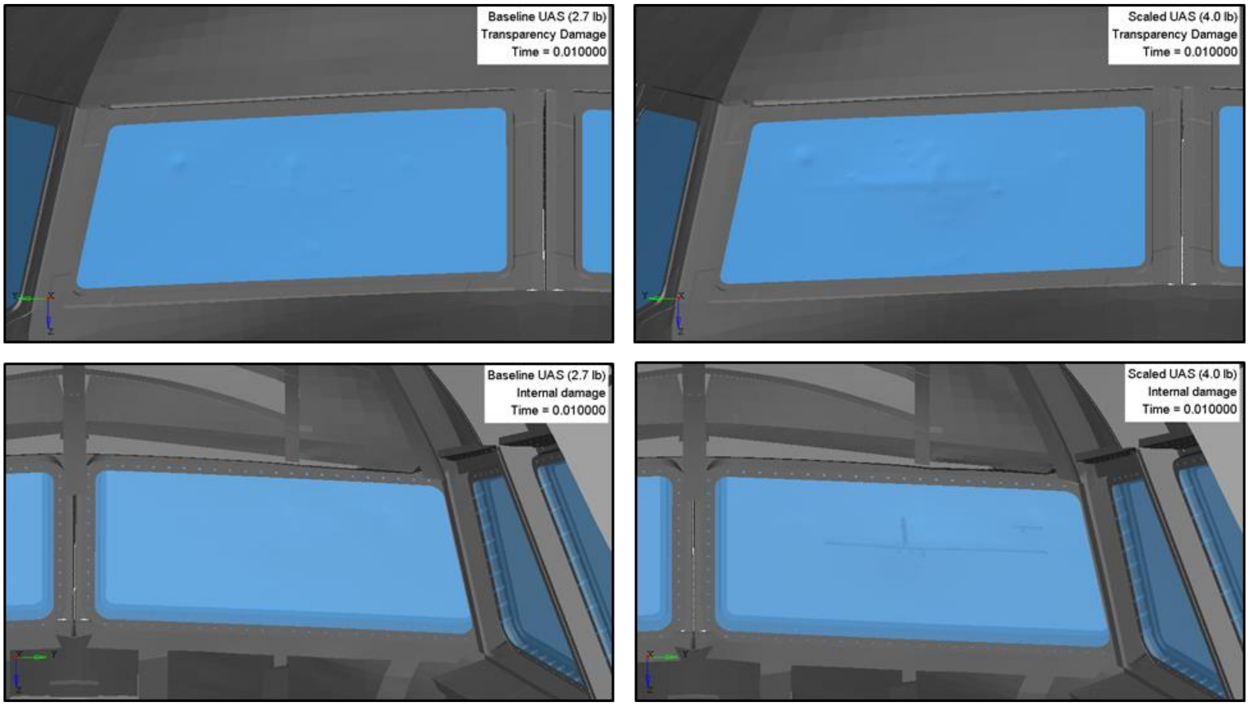

Figure 371. Comparison of external/internal damage sustained by a commercial transport jet windshield impacted with a 1.2/1.8 kg (2.7/4.0 lb) UAS at 128.6 m/s (250 knots)

Figure 372 shows the comparison for the contact force and impulse between the 1.2/1.8 kg (2.7/4.0 lb) UAS and windshield. Figure 373 shows the energy balance, normalized with the initial kinetic energy, for the impact comparison.

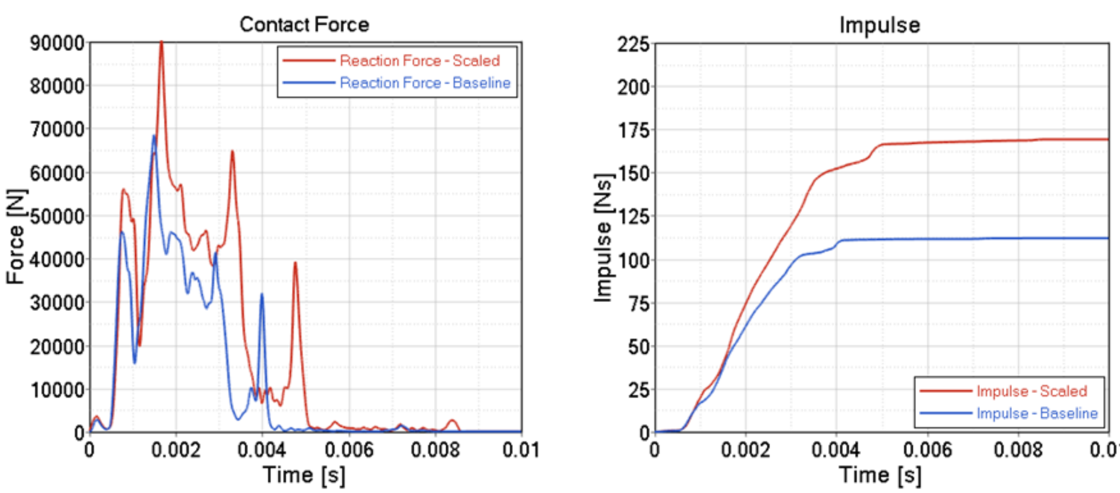

Figure 372. Comparison of the contact force and impulse of the impact between a commercial transport jet windshield and a 1.2/1.8 kg (2.7/4.0 lb) UAS at 128.6 m/s (250 knots)

The impulse for the 1.8 kg (4.0 lb) UAS was greater than for the 1.2 kg (2.7 lb) UAS. From the energy balance comparison, it can be observed that the 1.8 kg (4.0 lb) UAS absorbed a similar ratio of internal energy than the 1.2 kg (2.7 lb) UAS. In addition, it is apparent that the residual kinetic energy of the 1.8 kg (4.0 lb) UAS after impact was smaller relatively than the 1.2 kg (2.7 lb) UAS. However, it can be seen that the higher mass UAS absorbed about and 5% more energy than the lower mass UAS, relatively to the impact energy.

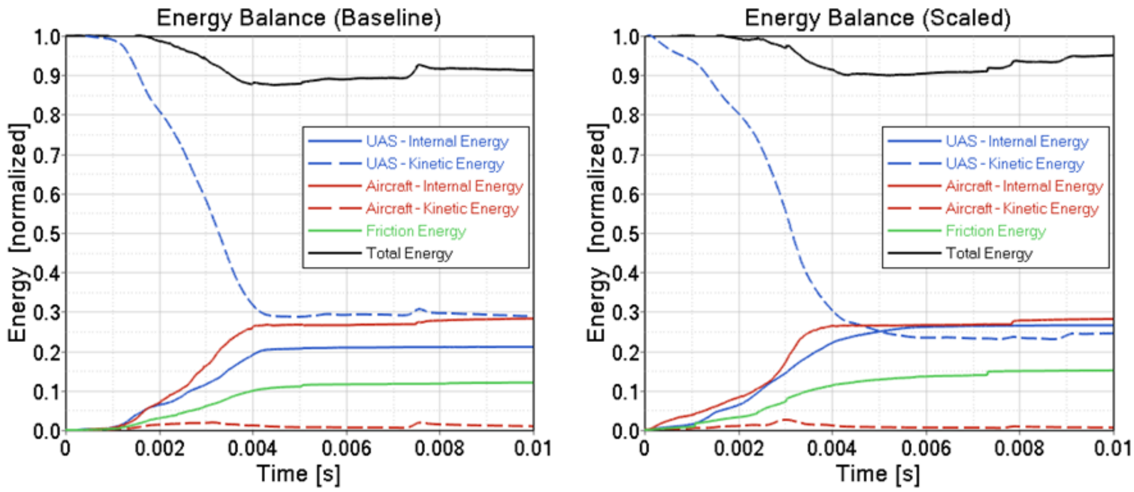

Figure 373. Comparison of the energy balance of the impact between a commercial transport jet windshield and a 1.2/1.8 kg (2.7/4.0 lb) UAS at 128.6 m/s (250 knots)

C.2 BUSINESS JET – BASELINE UAS (1.2 KG) VS SCALED UAS (1.8 KG)

C.2.1 Vertical Stabilizer

Impact simulations of a 1.2 kg (2.7 lb) UAS (case BQV2) and 1.8 kg (4 lb) UAS (case BQsV2) against a vertical stabilizer are compared in terms of damage severity and kinematics. The initial conditions for both cases were based on BQV2, which was identified as the most critical case in the baseline simulations (see Section 4.4.1.1). Figure 374 depicts the comparison of the kinematics of the event. Figure 375 shows the comparison of the damage caused to the skin and the inner structure of the vertical stabilizer.

The 1.8 kg (4.0 lb) UAS damaged the skin, upper and lower ribs, and the front spar while the 1.2 kg (2.7 lb) UAS only damaged the skin, upper and lower ribs to a lesser degree. It can also be perceived in Figure 375 that the damage introduced into the skin and the ribs was greater for the case of 1.8 kg (4.0 lb) UAS than of the 1.2 kg (2.7 lb) UAS.

The damage introduced by the 1.2 kg (2.7 lb) UAS is classified as Level 3 whereas the damage introduced by the 1.8 kg (4.0 lb) UAS is classified as Level 4. In terms of damage, the 1.8 kg (4.0 lb) UAS can be considered as more severe than the 1.2 kg (2.7 lb) UAS.

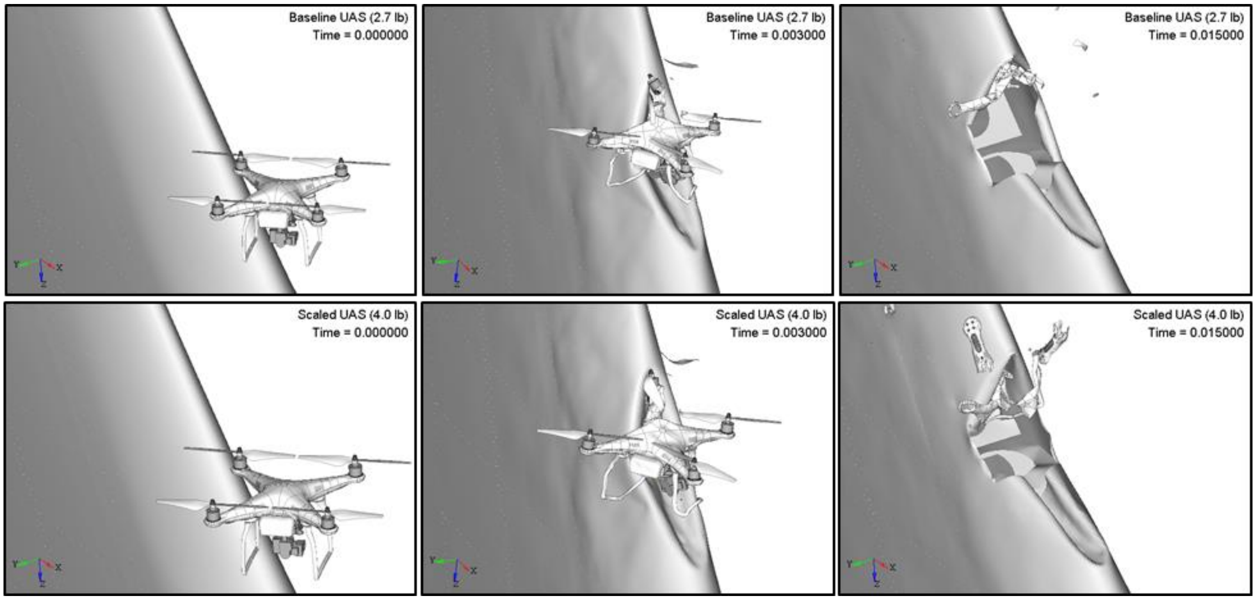

Figure 374. Comparison of the kinematics of impact between a business jet vertical stabilizer and a 1.2/1.8 kg (2.7/4.0 lb) UAS at 128.6 m/s (250 knots)

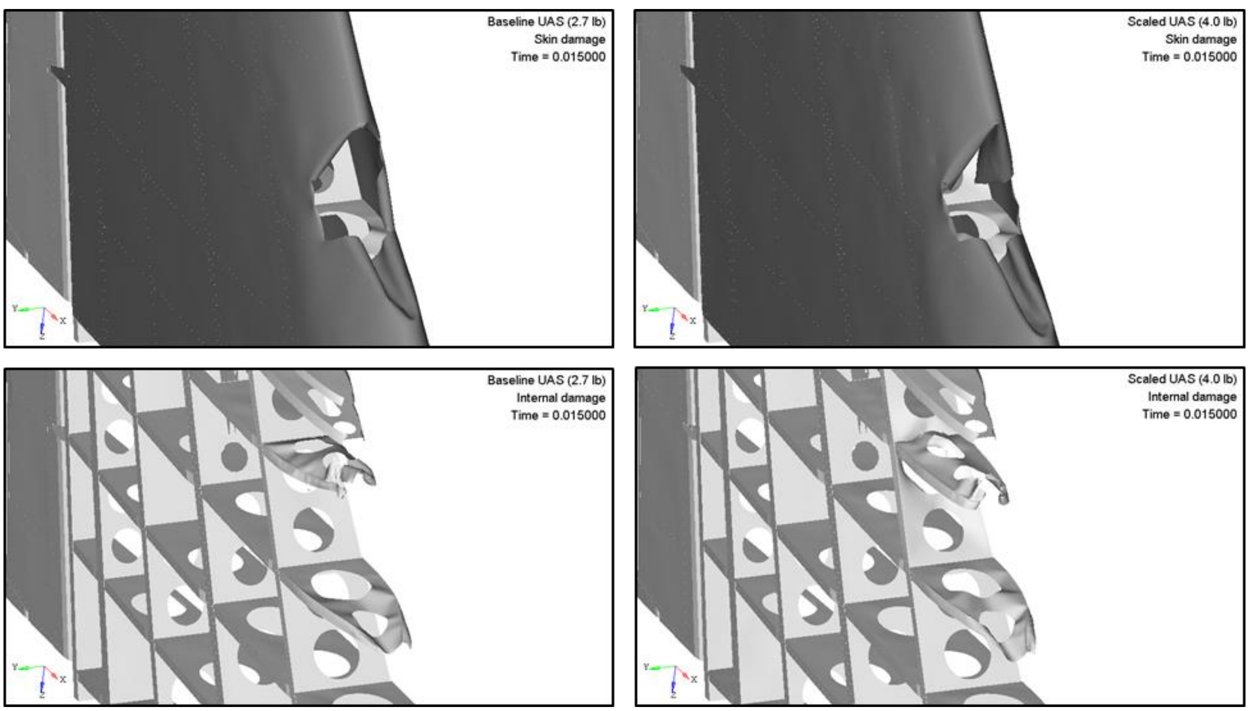

Figure 375. Comparison of external/internal damage sustained by a business jet vertical stabilizer impacted with a 1.2/1.8 kg (2.7/4.0 lb) UAS at 128.6 m/s (250 knots)

Figure 376 shows the comparison for the contact force and impulse between the 1.2/1.8 kg (2.7/4.0 lb) UAS and vertical stabilizer. Figure 377 shows the energy balance, normalized with the initial kinetic energy, for the impact comparison.

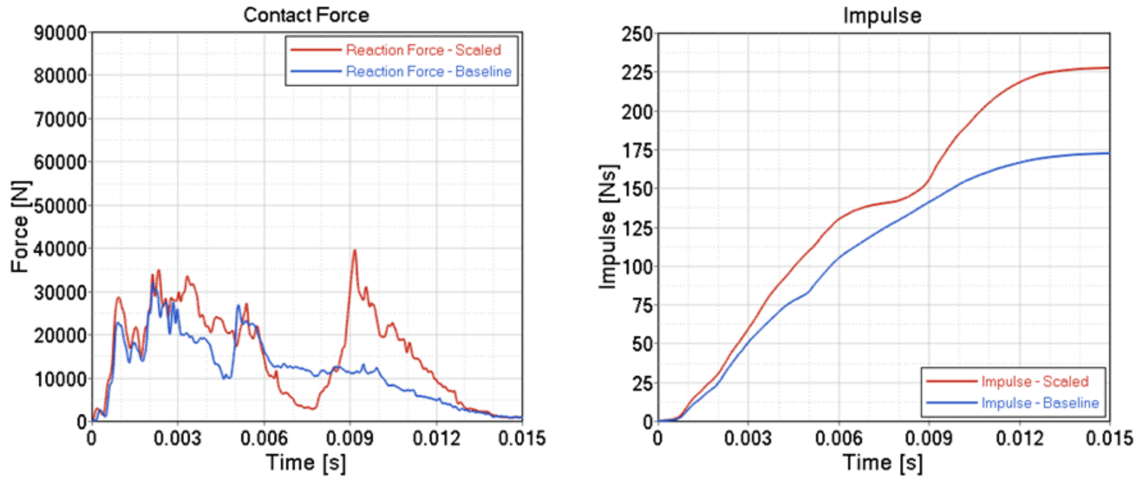

Figure 376. Comparison of the contact force and impulse of the impact between a business jet vertical stabilizer and a 1.2/1.8 kg (2.7/4.0 lb) UAS at 128.6 m/s (250 knots)

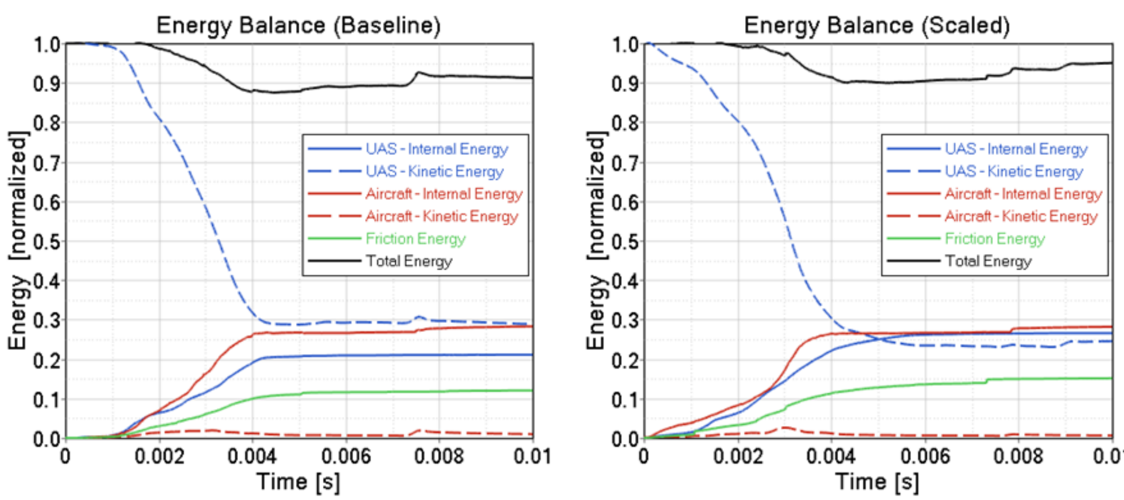

Figure 377. Comparison of the energy balance of the impact between a business jet vertical stabilizer and a 1.2/1.8 kg (2.7/4.0 lb) UAS at 128.6 m/s (250 knots)

The impulse for the 1.8 kg (4.0 lb) UAS was greater than for the 1.2 kg (2.7 lb) UAS. From the energy balance comparison, it can be observed that the 1.8 kg (4.0 lb) UAS absorbed a similar ratio of internal energy than the 1.2 kg (2.7 lb) UAS. In addition, it is apparent that the residual kinetic energy of the 1.8 kg (4.0 lb) UAS after impact was smaller relatively than the 1.2 kg (2.7 lb) UAS. However, it can be seen that the higher mass UAS absorbed about a 5% more energy than the lower mass UAS, relatively to the impact energy.

C.2.2 Horizontal Stabilizer

Impact simulations of a 1.2 kg (2.7 lb) UAS (case BQH2) and 1.8 kg (4 lb) UAS (case BQsH2) against a horizontal stabilizer are compared in terms of damage severity and kinematics. The initial conditions for both cases were based on BQH2, which was identified as the most critical case in the baseline simulations (see Section 4.4.2.1). Figure 378 depicts the comparison of the kinematics of the event. Figure 379 shows the comparison of the damage caused to the skin and the inner structure of the horizontal stabilizer.

Figure 378. Comparison of the kinematics of impact between a business jet horizontal stabilizer and a 1.2/1.8 kg (2.7/4.0 lb) UAS at 128.6 m/s (250 knots)

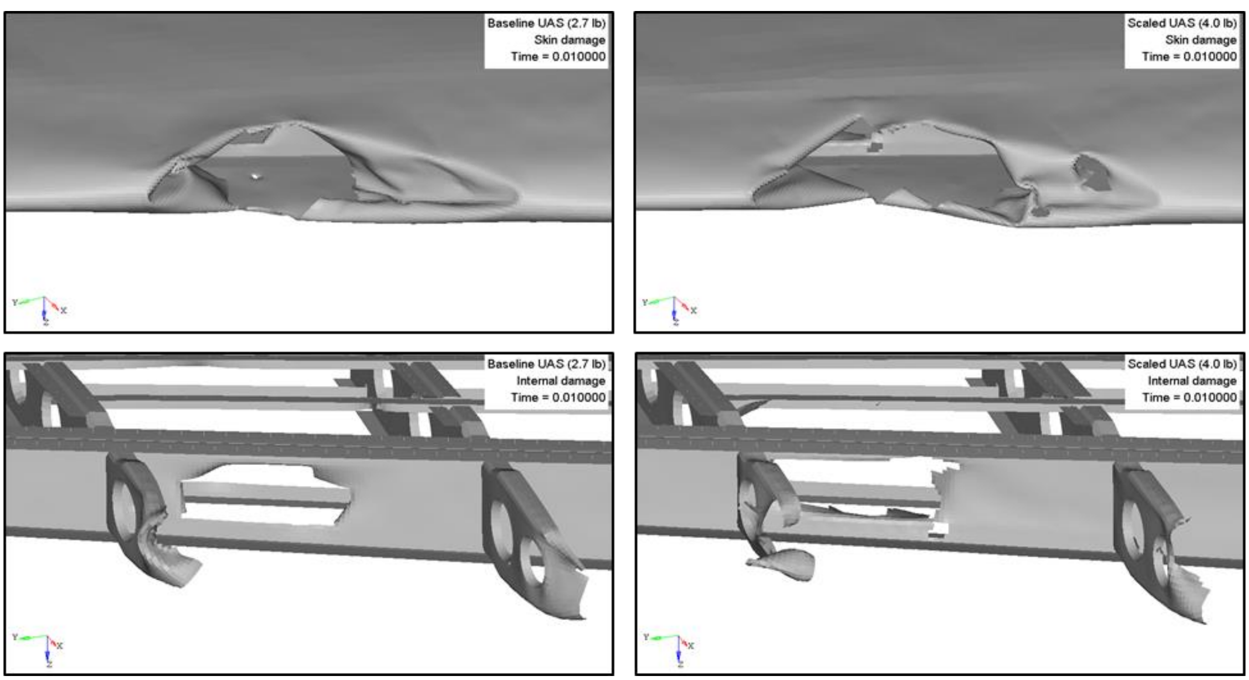

Figure 379. Comparison of external/internal damage sustained by a business jet horizontal stabilizer impacted with a 1.2/1.8 kg (2.7/4.0 lb) UAS at 128.6 m/s (250 knots)

Both 1.2 kg (2.7 lb) and 1.8 kg (4.0 lb) UAS damaged the skin, the nose ribs, and the front spar. It can also be perceived in Figure 379 that the damage introduced into the skin and front spar was considerably greater for the case of 1.8 kg (4.0 lb) UAS than of the 1.2 kg (2.7 lb) UAS.

The damage introduced by the 1.2 kg (2.7 lb) UAS as well as by the 1.8 kg (4.0 lb) UAS are classified as Level 4. In terms of damage, the 1.8 kg (4.0 lb) UAS can be considered slightly more severe than the 1.2 kg (2.7 lb) UAS due to the increase in the size of the damage.

Figure 380 shows the comparison for the contact force and impulse between the 1.2/1.8 kg (2.7/4.0 lb) UAS and horizontal stabilizer. Figure 381 shows the energy balance, normalized with the initial kinetic energy, for the impact comparison.

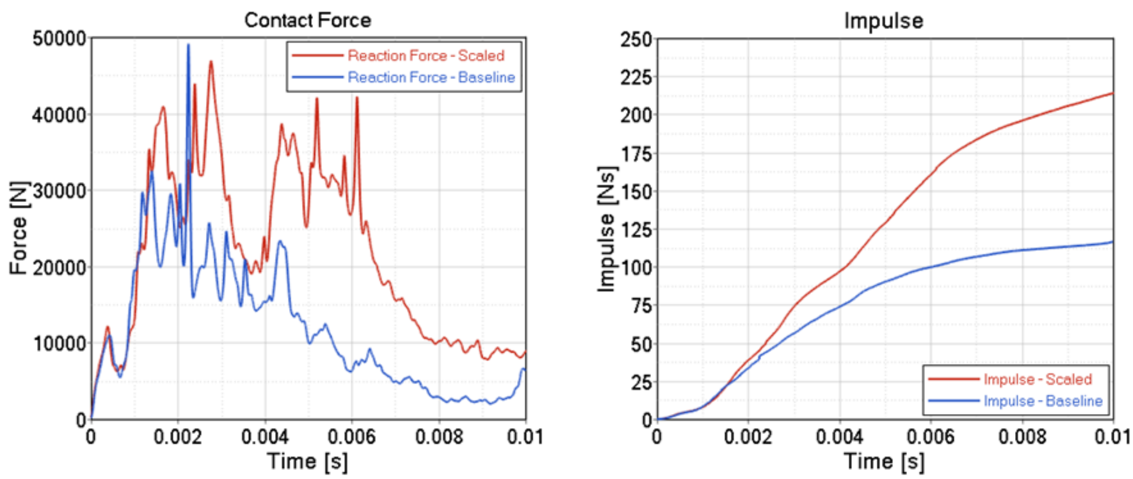

Figure 380. Comparison of the contact force and impulse of the impact between a business jet horizontal stabilizer and a 1.2/1.8 kg (2.7/4.0 lb) UAS at 128.6 m/s (250 knots)

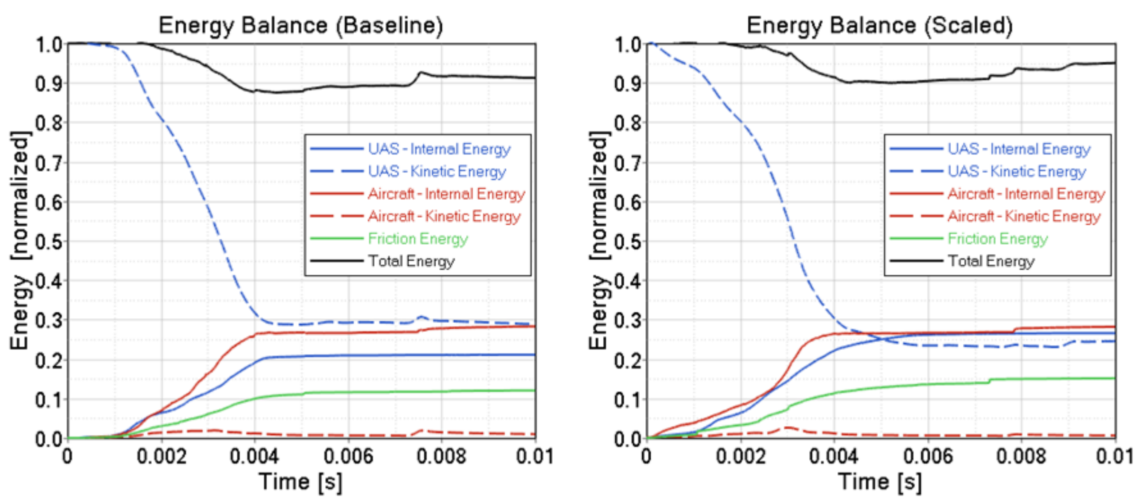

Figure 381. Comparison of the energy balance of the impact between a business jet horizontal stabilizer and a 1.2/1.8 kg (2.7/4.0 lb) UAS at 128.6 m/s (250 knots)

The impulse for the 1.8 kg (4.0 lb) UAS was greater than for the 1.2 kg (2.7 lb) UAS. From the energy balance comparison, it can be observed that the 1.8 kg (4.0 lb) UAS absorbed a similar ratio of internal energy than the 1.2 kg (2.7 lb) UAS. In addition, it is apparent that the residual kinetic energy of the 1.8 kg (4.0 lb) UAS after impact was smaller relatively than the 1.2 kg (2.7 lb) UAS. However, it can be seen that the higher mass UAS absorbed about a 6% more energy than the lower mass UAS, relatively to the impact energy.

C.2.3 Wing Leading Edge

Impact simulations of a 1.2 kg (2.7 lb) UAS (case BQW1) and 1.8 kg (4 lb) UAS (case BQsW1) against a wing leading edge are compared in terms of damage severity and kinematics. The initial conditions for both cases were based on BQW1, which was identified as the most critical case in the baseline simulations (see Section 4.4.3.1). Figure 382 depicts the comparison of the kinematics of the event. Figure 383 shows the comparison of the damage caused to the skin and the inner structure of the wing.

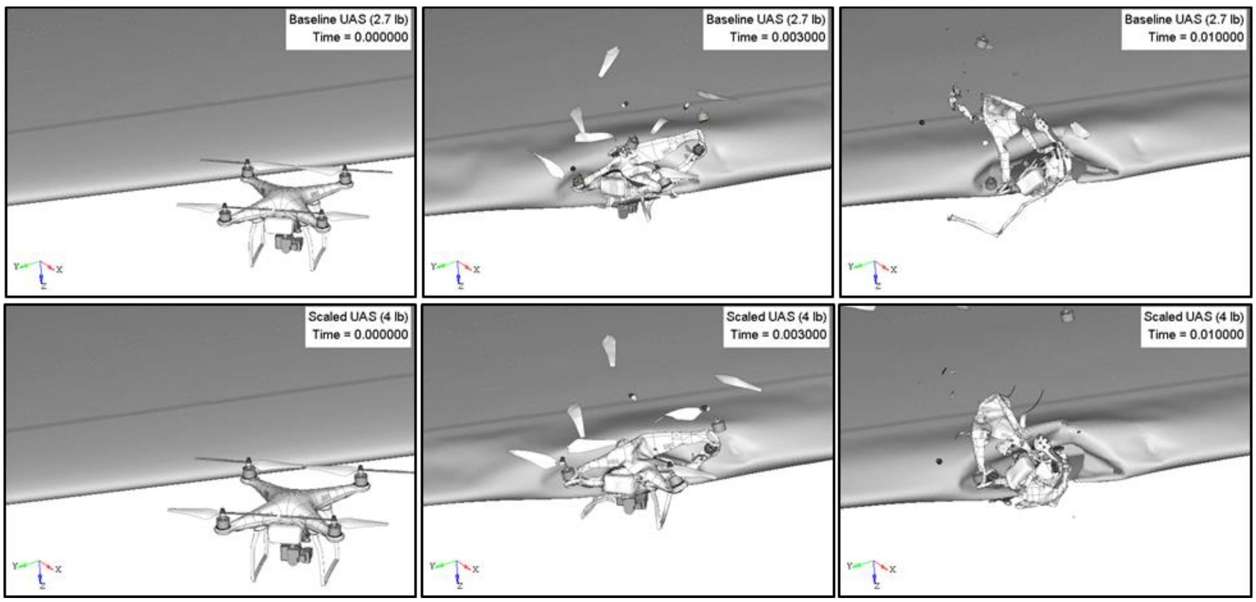

Figure 382. Comparison of the kinematics of impact between a business jet wing and a 1.2/1.8 kg (2.7/4.0 lb) UAS at 128.6 m/s (250 knots)

Both the UAS damaged the skin and the anti-ice tube with no visible deformation in the front spar. It can also be perceived in Figure 383 that the damage introduced into the skin and the anti-ice tube was considerably greater for the case of 1.8 kg (4.0 lb) UAS than of the 1.2 kg (2.7 lb) UAS.

The damage introduced by both the UAS is classified as Level 3 with risk of fire due to battery damage. Even with the same level, in terms of damage, the 1.8 kg (4.0 lb) UAS can be considered as more severe than the 1.2 kg (2.7 lb) UAS.

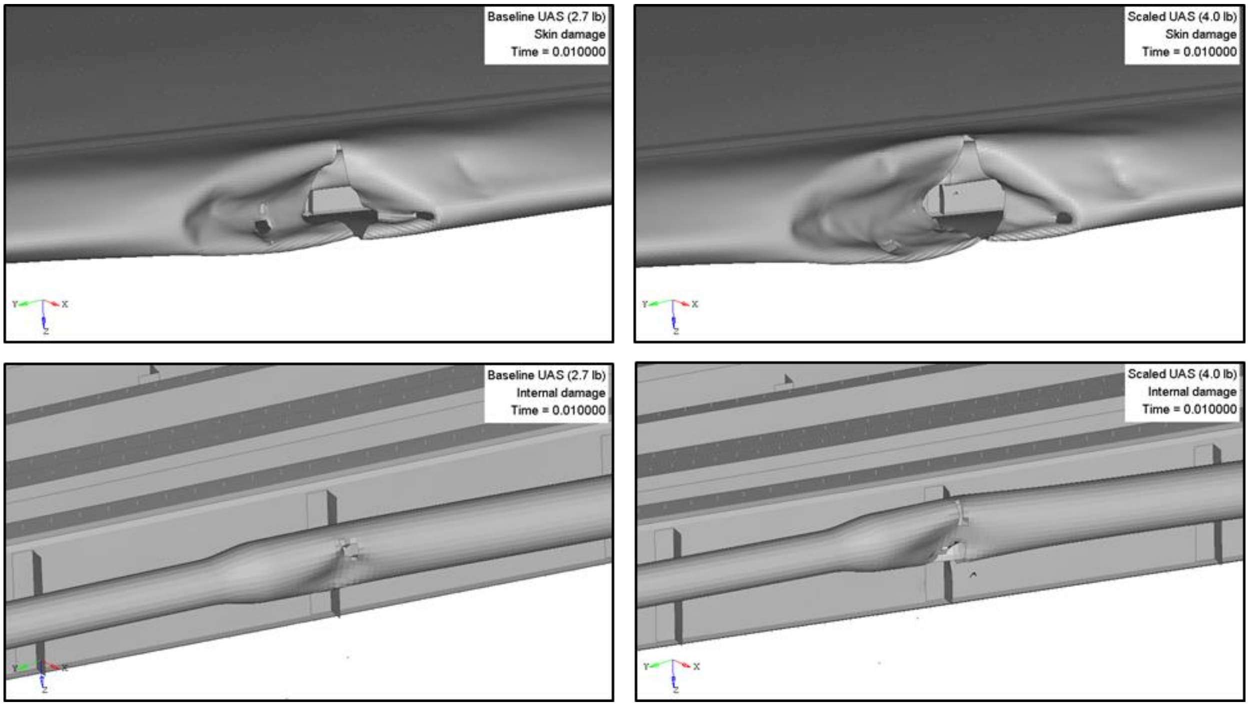

Figure 383. Comparison of external/internal damage sustained by a business jet wing impacted with a 1.2/1.8 kg (2.7/4.0 lb) UAS at 128.6 m/s (250 knots)

Figure 384 shows the comparison for the contact force and impulse between the 1.2/1.8 kg (2.7/4.0 lb) UAS and wing. Figure 385 shows the energy balance, normalized with the initial kinetic energy, for the impact comparison.

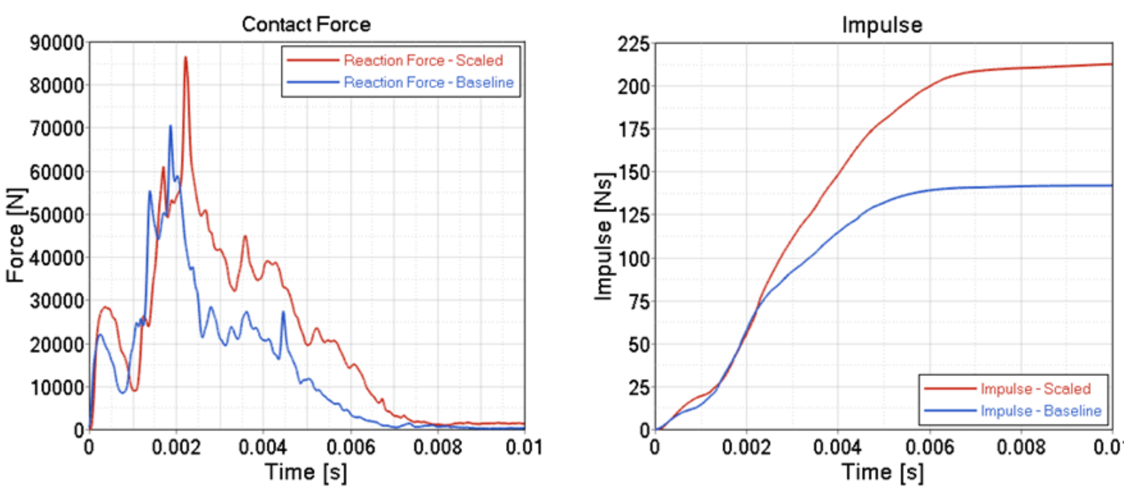

Figure 384. Comparison of the contact force and impulse of the impact between a business jet wing and a 1.2/1.8 kg (2.7/4.0 lb) UAS at 128.6 m/s (250 knots)

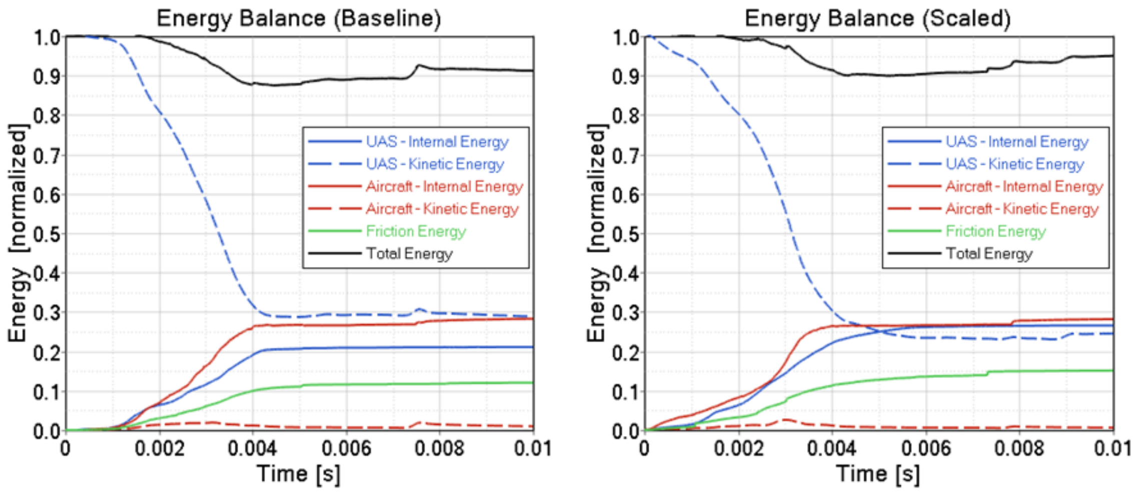

Figure 385. Comparison of the energy balance of the impact between a business jet wing and a 1.2/1.8 kg (2.7/4.0 lb) UAS at 128.6 m/s (250 knots)

The impulse for the 1.8 kg (4.0 lb) UAS was greater than for the 1.2 kg (2.7 lb) UAS. From the energy balance comparison, it can be observed that the 1.8 kg (4.0 lb) UAS absorbed a similar ratio of internal energy than the 1.2 kg (2.7 lb) UAS. In addition, it is apparent that the residual kinetic energy of the 1.8 kg (4.0 lb) UAS after impact was smaller relatively than the 1.2 kg (2.7 lb) UAS. However, it can be seen that the higher mass UAS absorbed about a 7% more energy than the lower mass UAS, relatively to the impact energy.

C.2.4 Windshield

Impact simulations of a 1.2 kg (2.7 lb) UAS (case BQC1) and 1.8 kg (4 lb) UAS (case BQsC1) against a windshield are compared in terms of damage severity and kinematics. The initial conditions for both cases were based on BQC1, which was identified as the most critical case in the baseline simulations (see Section 4.4.4.1). Figure 386 depicts the comparison of the kinematics of the event. Figure 387 shows the comparison of the damage caused to the windshield and surrounding structure.

Both UAS impacted the windshield and slid over because of the windshield deflection. The 1.2 kg (2.7 lb) UAS did not cause any damage to the windshield while the 1.8 kg (4.0 lb) UAS slightly damaged the windshield anti-ice shell. It can also be perceived in Figure 387 that there is no internal damage for both cases.

The damage introduced by both the 1.2 kg (2.7 lb) and the 1.8 kg (4.0 lb) UAS are classified as Level 2.

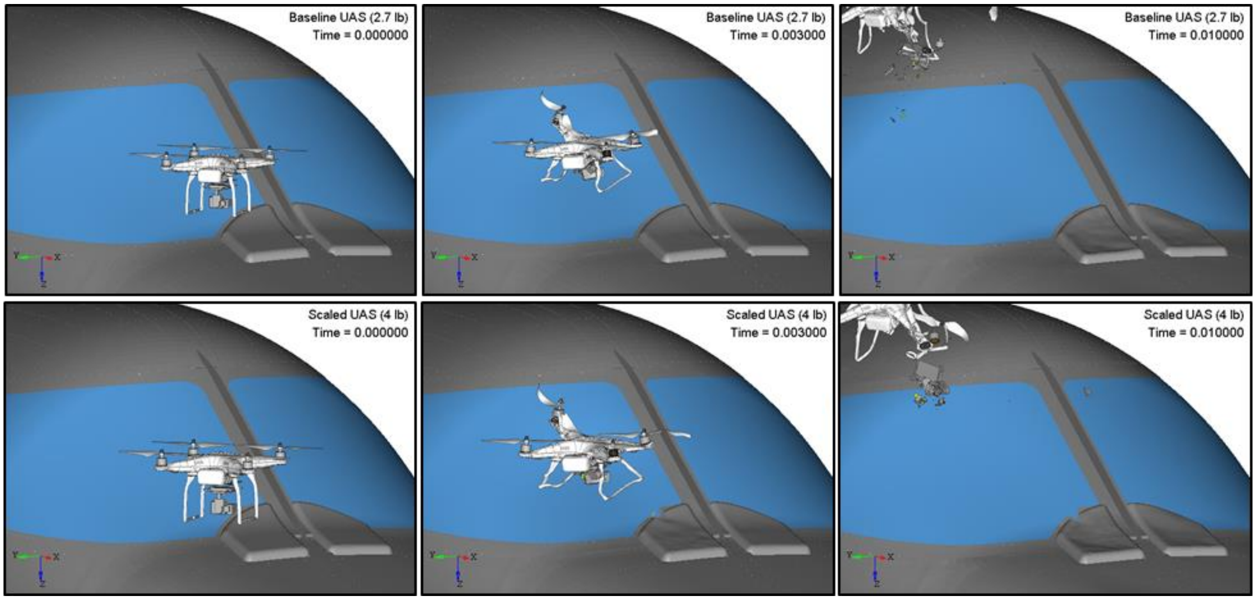

Figure 386. Comparison of the kinematics of impact between a business jet windshield and a 1.2/1.8 kg (2.7/4.0 lb) UAS at 128.6 m/s (250 knots)

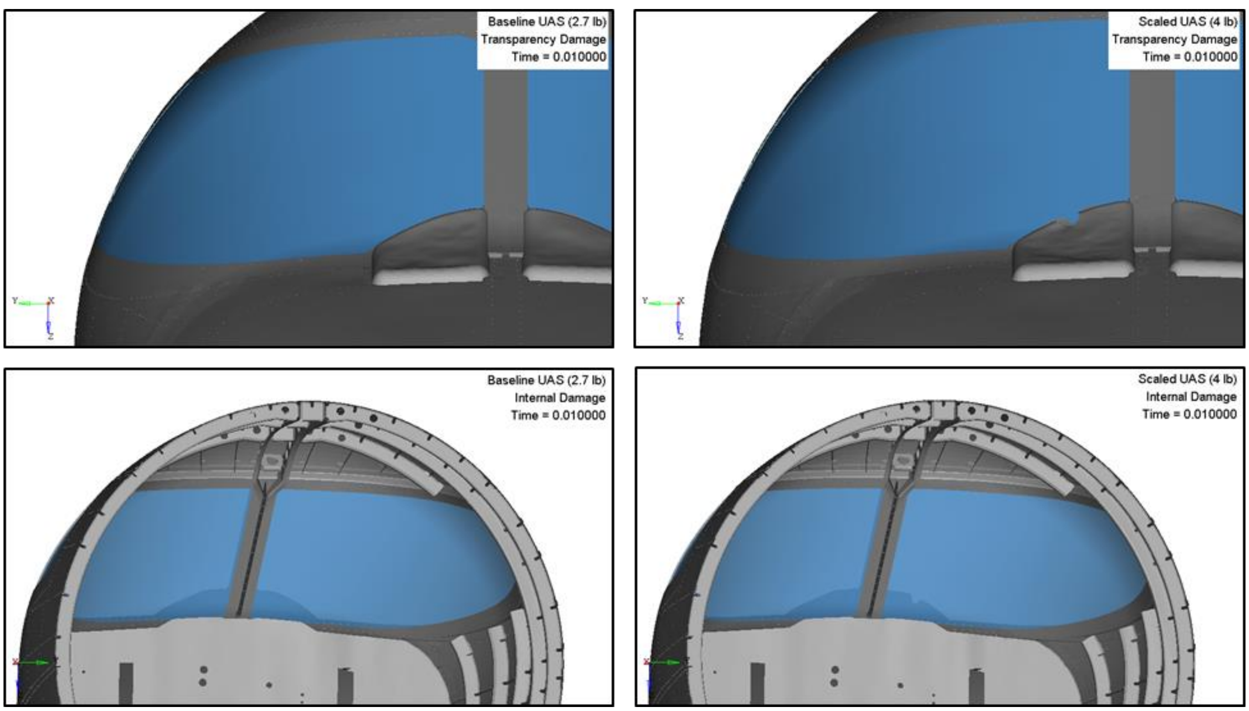

Figure 387. Comparison of external/internal damage sustained by a business jet windshield impacted with a 1.2/1.8 kg (2.7/4.0 lb) UAS at 128.6 m/s (250 knots)

Figure 388 shows the comparison for the contact force and impulse between the 1.2/1.8 kg (2.7/4.0 lb) UAS and windshield. Figure 389 shows the energy balance, normalized with the initial kinetic energy, for the impact comparison.

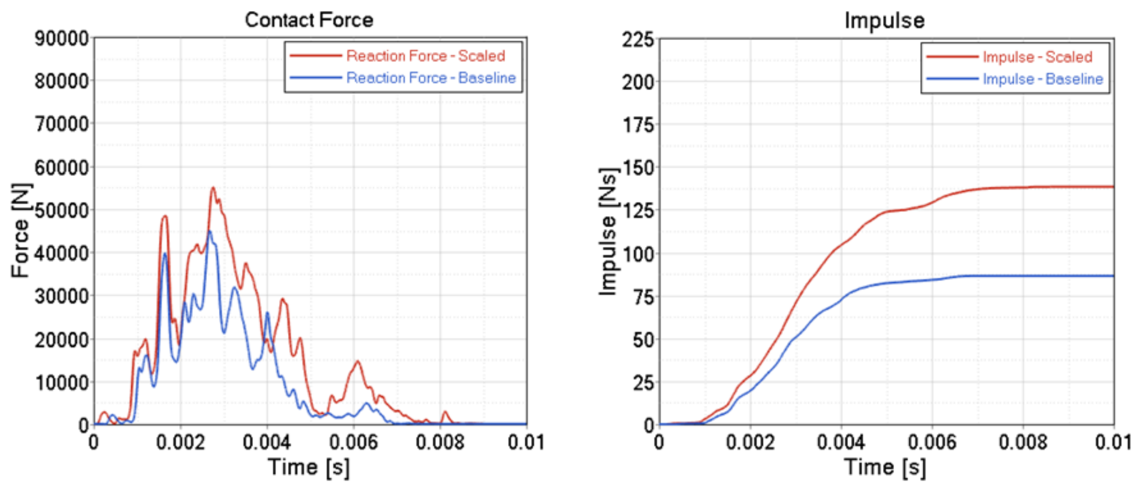

Figure 388. Comparison of the contact force and impulse of the impact between a business jet windshield and a 1.2/1.8 kg (2.7/4.0 lb) UAS at 128.6 m/s (250 knots)

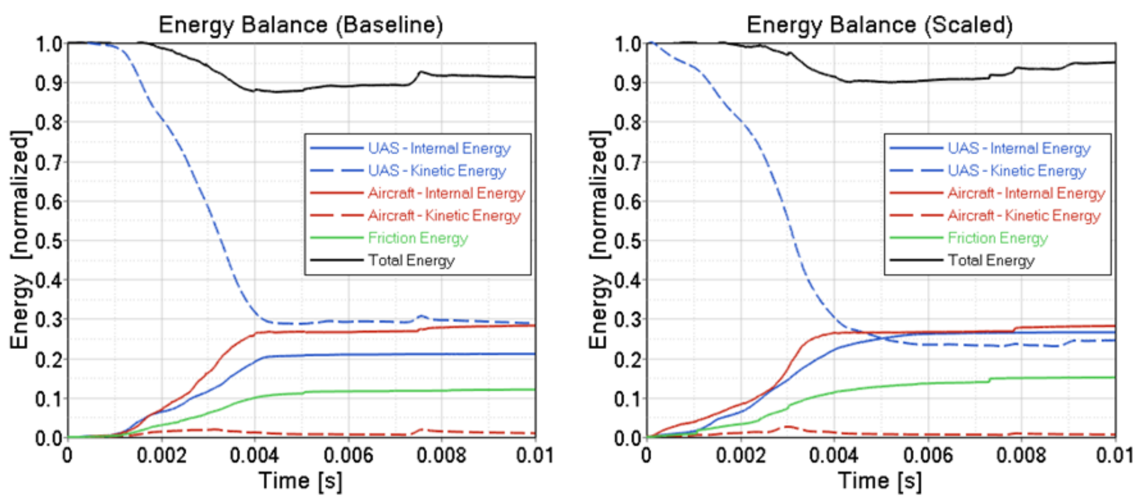

Figure 389. Comparison of the energy balance of the impact between a business jet windshield and a 1.2/1.8 kg (2.7/4.0 lb) UAS at 128.6 m/s (250 knots)

The impulse for the 1.8 kg (4.0 lb) UAS was greater than for the 1.2 kg (2.7 lb) UAS. From the energy balance comparison, it can be observed that the 1.8 kg (4.0 lb) UAS absorbed a similar ratio of internal energy than the 1.2 kg (2.7 lb) UAS. In addition, it is apparent that the residual kinetic energy of the 1.8 kg (4.0 lb) UAS after impact was smaller relatively than the 1.2 kg (2.7 lb) UAS. However, it can be seen that the higher mass UAS absorbed about a 4% more energy than the lower mass UAS, relatively to the impact energy.

APPENDIX D – VELOCITY SENSITIVITY STUDY

D.1 COMMERCIAL TRANSPORT JET

D.1.1 Vertical Stabilizer

Impact simulations of a 1.2 kg (2.7 lb) UAS (case CQV3) with three different velocities (56.7, 128.6, 187.8 m/s; or 110, 250, 365 knots) against a vertical stabilizer are compared in terms of damage severity and kinematics. The initial conditions for all the above cases except for the velocity were based on CQV3, which was identified as the most critical case in the baseline simulations (see Section 4.3.1.1). Figure 358 depicts the comparison of the kinematics of the event. Figure 359 shows the comparison of the damage caused to the skin and the inner structure of the vertical stabilizer.

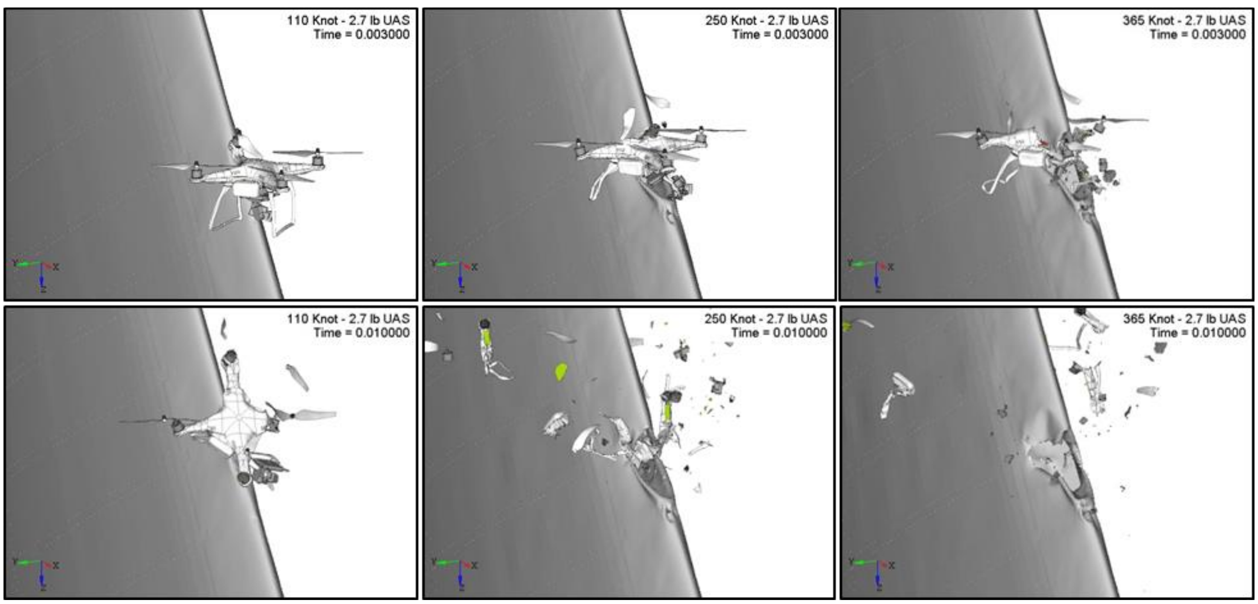

Figure 390. Comparison of the kinematics of impact between a commercial transport jet vertical stabilizer and a 1.2 kg UAS at 56.7/128.6/187.8 m/s (110/250/365 knots)

The UAS at 56.7 m/s (110 knots) deformed slightly the skin with no visible internal damage. On the other hand, the UAS at 128.6 m/s (250 knots) damaged the skin, the upper and lower ribs, and front spar while the UAS at 187.8 m/s (365 knots) damaged the skin, upper and lower ribs and the front spar to a greater degree. It can also be perceived in Figure 359 that the damage severity increases with respect to the increase in velocity.

The damage introduced by UAS at 56.7 m/s (110 knots) is classified as level 2, at 128.6 m/s (250 knots) as level 3 and at 187.8 m/s (365 knots) as level 4. It is evident that higher velocity results in greater damage.

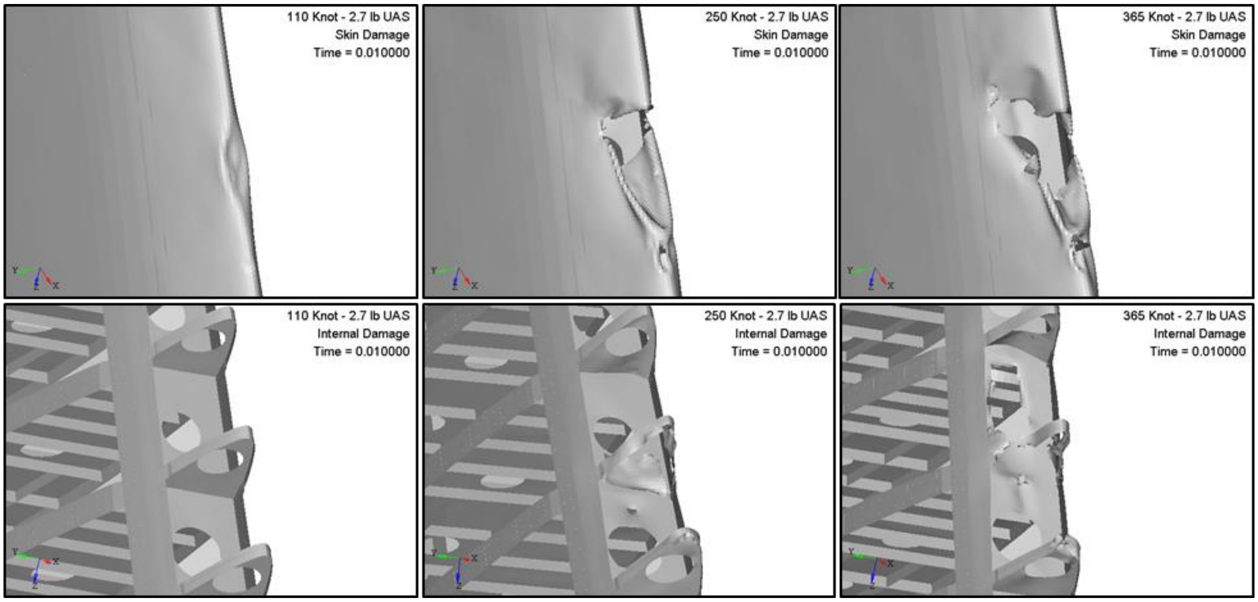

Figure 391. Comparison of external/internal damage sustained by a commercial transport jet vertical stabilizer impacted with a 1.2 kg UAS at 56.7/128.6/187.8 m/s (110/250/365 knots)

Figure 360 shows the comparison for the contact force and impulse between the UAS and vertical stabilizer for three different velocities. Figure 361 shows the normalized energy balance for the impact comparison.

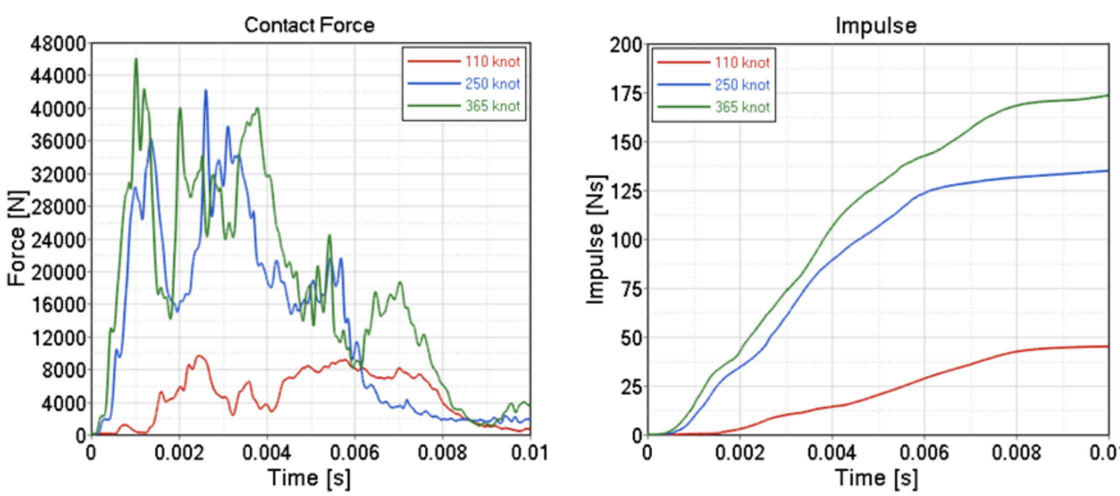

Figure 392. Comparison of the contact force and impulse of the impact between a commercial transport jet vertical stabilizer and a 1.2 kg UAS at 56.7/128.6/187.8 m/s (110/250/365 knots)

The impulse increases with higher velocities. From the energy balance comparison, it can be observed that the UAS absorbed greater internal energy at lower velocity than the UAS at higher velocity. The kinetic energy ratios do not appear to have specific trends related to the impact velocity; therefore, the visible damage and kinematics are used to draw conclusions.

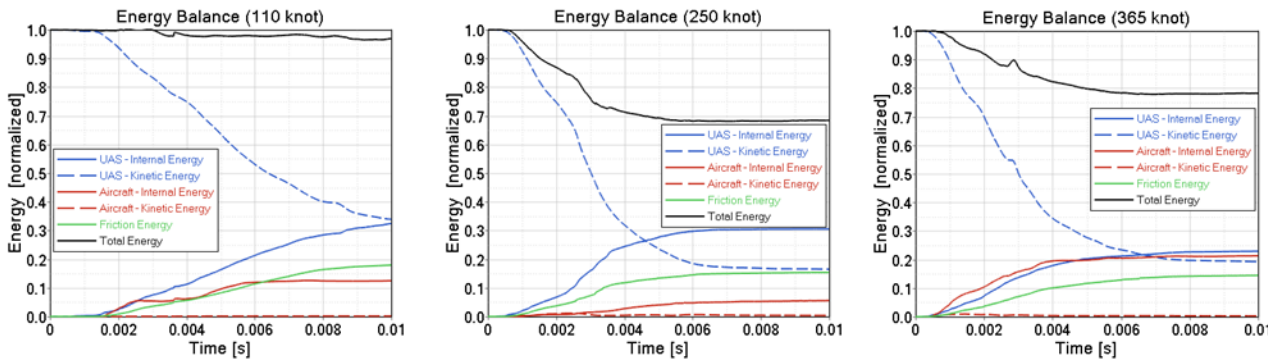

Figure 393. Comparison of the normalized energy balance of the impact between a commercial transport jet vertical stabilizer and a 1.2 kg UAS at 56.7/128.6/187.8 m/s (110/250/365 knots)

D.1.2 Horizontal Stabilizer

Impact simulations of a 1.2 kg (2.7 lb) UAS (case CQH3) with three different velocities (56.7, 128.6, 187.8 m/s; or 110, 250, 365 knots) against a horizontal stabilizer are compared in terms of damage severity and kinematics. The initial conditions for all the above cases except for the velocity were based on CQH3, which was identified as the most critical case in the baseline simulations (see Section 4.3.2.1). Figure 394 depicts the comparison of the kinematics of the event. Figure 395 shows the comparison of the damage caused to the skin and the inner structure of the horizontal stabilizer.

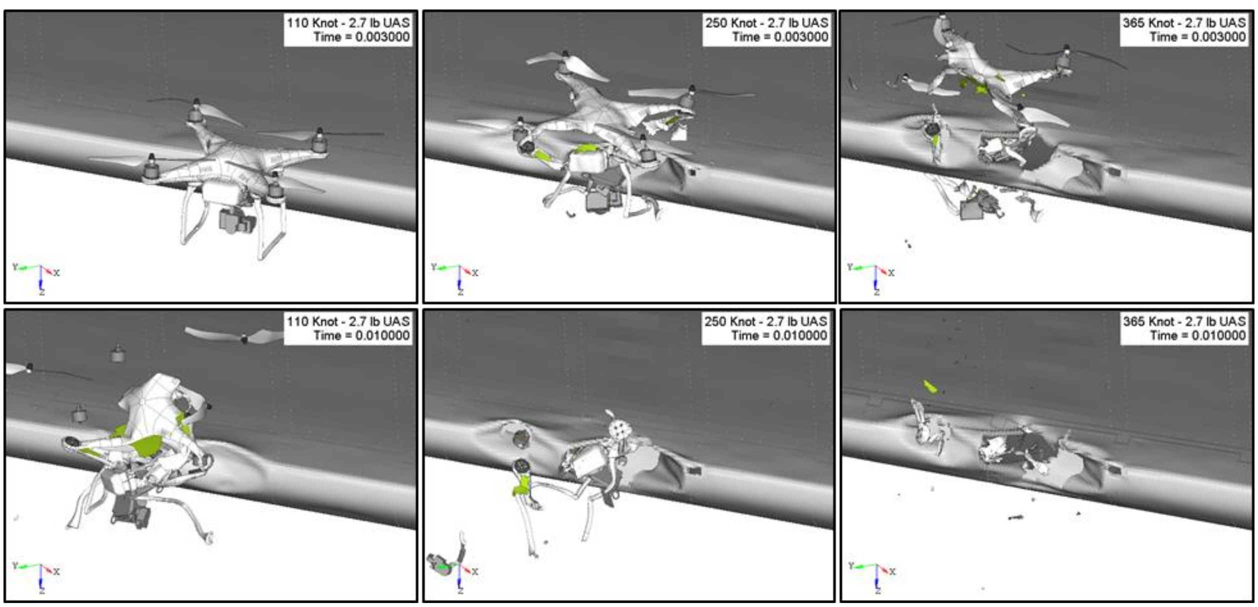

Figure 394. Comparison of the kinematics of impact between a commercial transport jet horizontal stabilizer and a 1.2 kg UAS at 56.7/128.6/187.8 m/s (110/250/365 knots)

The UAS at 56.7 m/s (110 knots) deformed slightly the skin and the nose rib with no other visible internal damage. On the other hand, the UAS at 128.6 m/s (250 knots) damaged the skin, the nose ribs, and front spar while the UAS at 187.8 m/s (365 knots) damaged the skin, the nose ribs, and the front spar to a greater degree. It can also be perceived in Figure 395 that the damage severity increases with respect to the increase in velocity.

The damage introduced by UAS at 56.7 m/s (110 knots) is classified as level 2 whereas the damage introduced by both UAS at 128.6 m/s (250 knots) and 187.8 m/s (365 knots) is classified as level 4. In addition, the risk of fire due to the battery is present only for the impacts of UAS at 56.7 and 128.6 m/s (110 and 250 knots). It is evident that higher velocity results in greater damage.

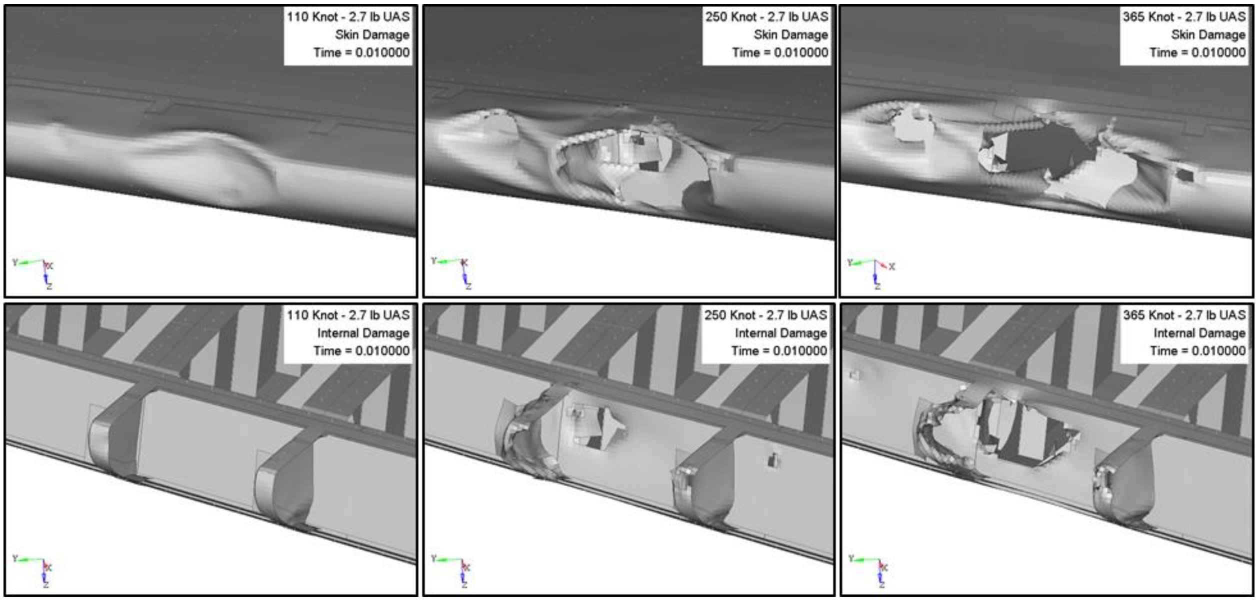

Figure 395. Comparison of external/internal damage sustained by a commercial transport jet horizontal stabilizer impacted with a 1.2 kg UAS at 56.7/128.6/187.8 m/s (110/250/365 knots)

Figure 396 shows the comparison for the contact force and impulse between the UAS and horizontal stabilizer for three different velocities. Figure 397 shows the normalized energy balance for the impact comparison.

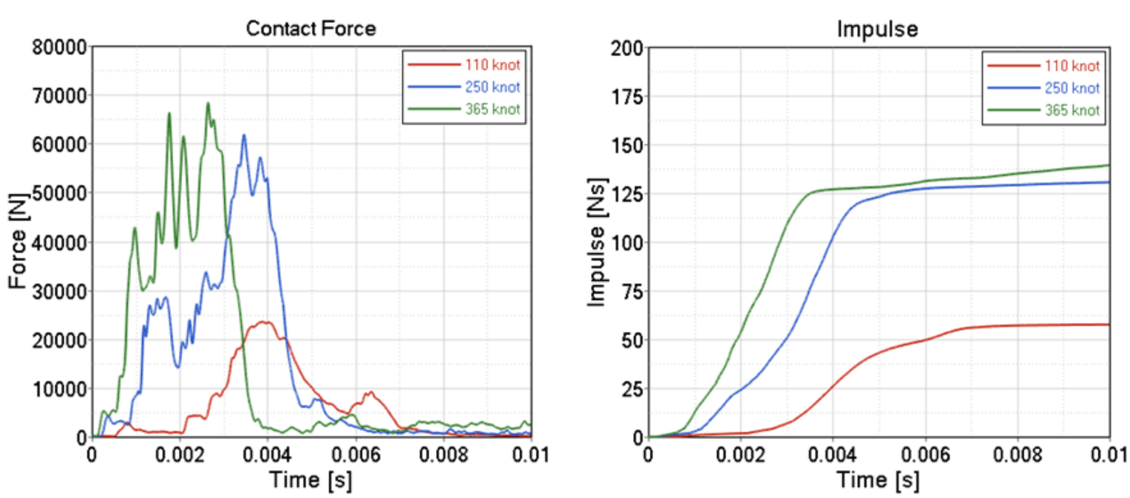

Figure 396. Comparison of the contact force and impulse of the impact between a commercial transport jet horizontal stabilizer and a 1.2 kg UAS at 56.7/128.6/187.8 m/s (110/250/365 knots)

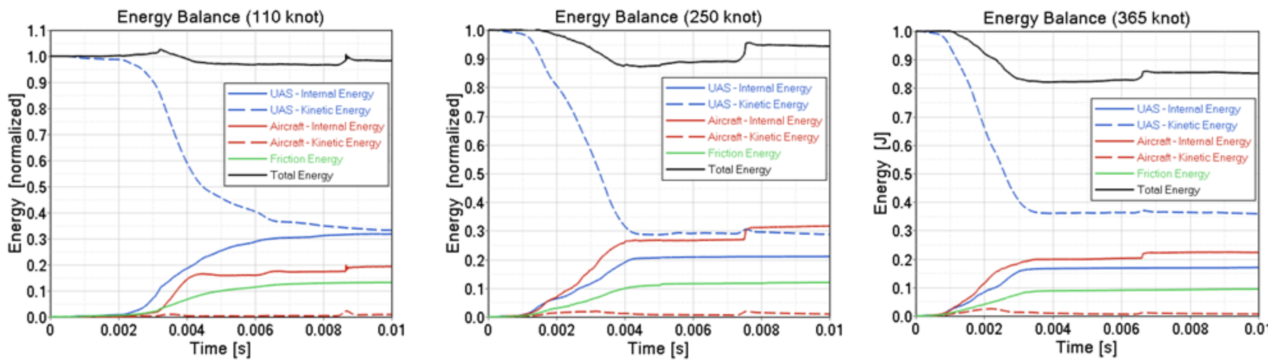

Figure 397. Comparison of the normalized energy balance of the impact between a commercial transport jet horizontal stabilizer and a 1.2 kg UAS at 56.7/128.6/187.8 m/s (110/250/365 knots)

The impulse increases with higher velocities. From the energy balance comparison, it can be observed that the UAS absorbed greater internal energy at lower velocity than the UAS at higher velocity. The kinetic energy ratios do not appear to have specific trends related to the impact velocity; therefore, the visible damage and kinematics are used to draw conclusions.

D.1.3 Wing Leading Edge

Impact simulations of a 1.2 kg (2.7 lb) UAS (case CQW1) with three different velocities (56.7, 128.6, 187.8 m/s; or 110, 250, 365 knots) against a wing leading edge are compared in terms of damage severity and kinematics. The initial conditions for all the above cases except for the velocity were based on CQW1, which was identified as the most critical case in the baseline simulations (see Section 4.3.3.1). Figure 398 depicts the comparison of the kinematics of the event. Figure 399 shows the comparison of the damage caused to the skin and the inner structure of the wing.

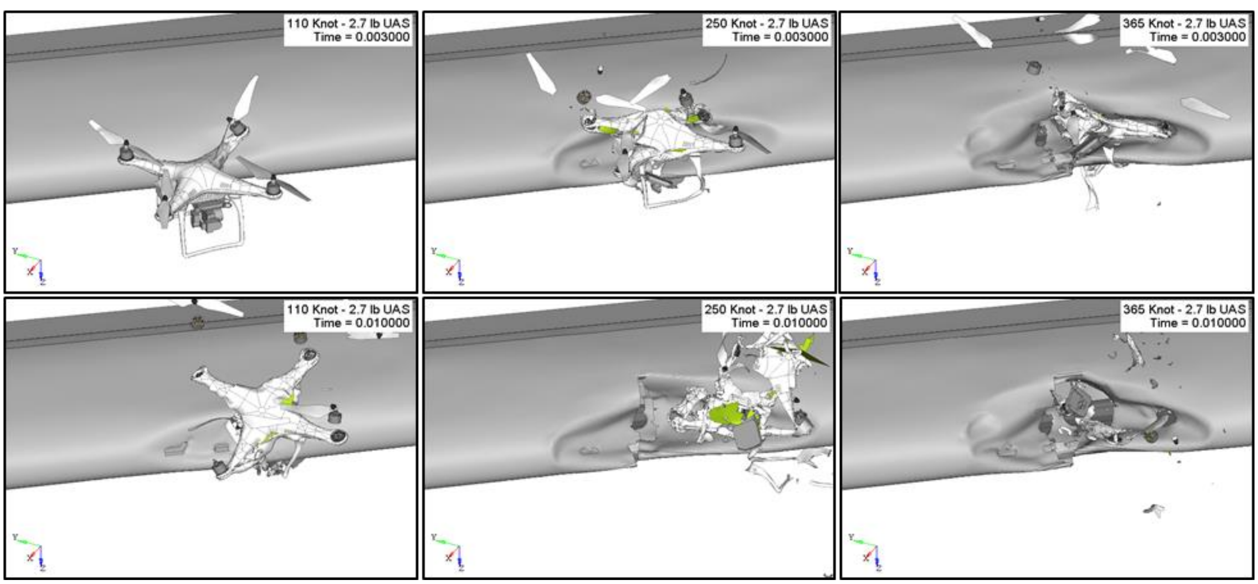

Figure 398. Comparison of the kinematics of impact between a commercial transport jet wing and a 1.2 kg UAS at 56.7/128.6/187.8 m/s (110/250/365 knots)

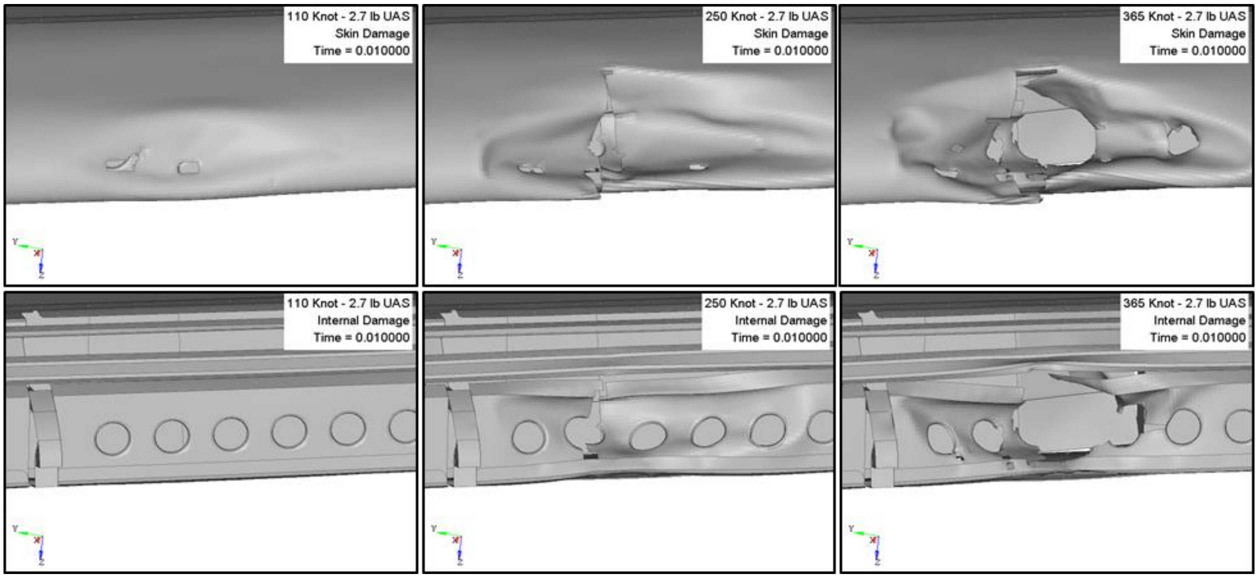

Figure 399. Comparison of external/internal damage sustained by a commercial transport jet wing impacted with a 1.2 kg UAS at 56.7/128.6/187.8 m/s (110/250/365 knots)

The UAS at 56.7 m/s (110 knots) damaged slightly the skin with no visible internal deformation. On the other hand, the UAS at 128.6 m/s (250 knots) damaged the skin and sub spar while the UAS at 187.8 m/s (365 knots) damaged the skin and the sub spar to a greater degree. It can also be perceived in Figure 399 that the damage severity increases with respect to the increase in velocity.

The damage introduced by UAS at 56.7 m/s (110 knots) is classified as level 2, at 128.6 m/s (250 knots) as level 3 and at 187.8 m/s (365 knots) as level 4. In addition, the risk of fire due to the battery is only present for the impact of UAS at 187.8 m/s (365 knots). It is evident that higher velocity results in greater damage.

Figure 400 shows the comparison for the contact force and impulse between the UAS and wing for three different velocities. Figure 401 shows the normalized energy balance for the impact comparison.

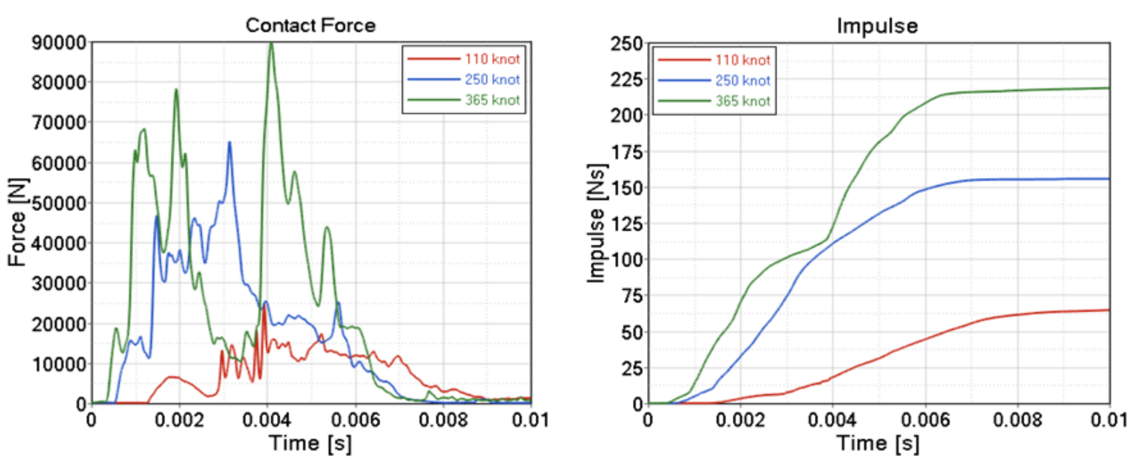

Figure 400. Comparison of the contact force and impulse of the impact between a commercial transport jet wing and a 1.2 kg UAS at 56.7/128.6/187.8 m/s (110/250/365 knots)

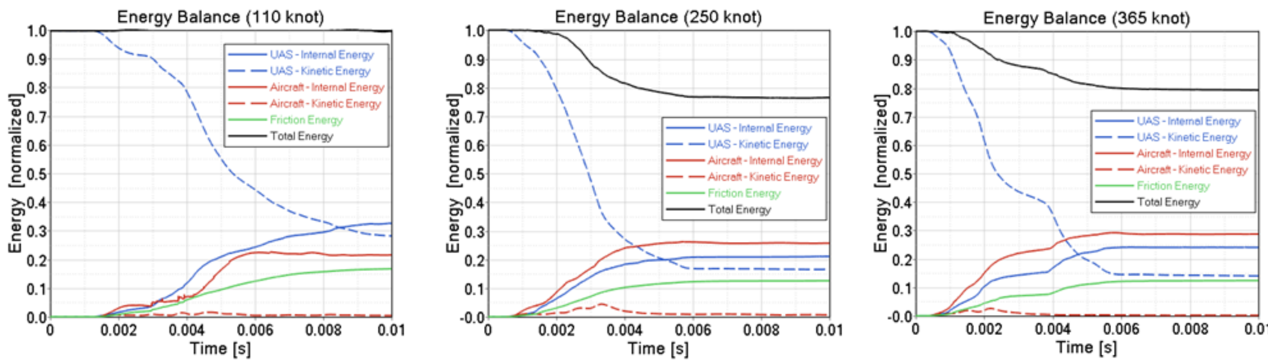

Figure 401. Comparison of the normalized energy balance of the impact between a commercial transport jet wing and a 1.2 kg UAS at 56.7/128.6/187.8 m/s (110/250/365 knots)

The impulse increases with higher velocities. From the energy balance comparison, it can be observed that the internal energy ratios do not appear to have specific trends related to the impact velocity. In addition, the residual kinetic energy after the impact was greater for UAS at lower velocities than for the UAS at higher velocities. This is an indication that the kinetic energy of the UAS at lower velocities was deflected more efficiently than that of the UAS at higher velocities, for which most of the energy was absorbed in the impact.

D.1.4 Windshield

Impact simulations of a 1.2 kg (2.7 lb) UAS (case CQC1) with three different velocities (56.7, 128.6, 187.8 m/s; or 110, 250, 365 knots) against a windshield are compared in terms of damage severity and kinematics. The initial conditions for all the above cases except for the velocity were based on CQC1, which was identified as the most critical case in the baseline simulations (see Section 4.3.4.1). Figure 402 depicts the comparison of the kinematics of the event. Figure 403 shows the comparison of the damage caused to the windshield and surrounding structure.

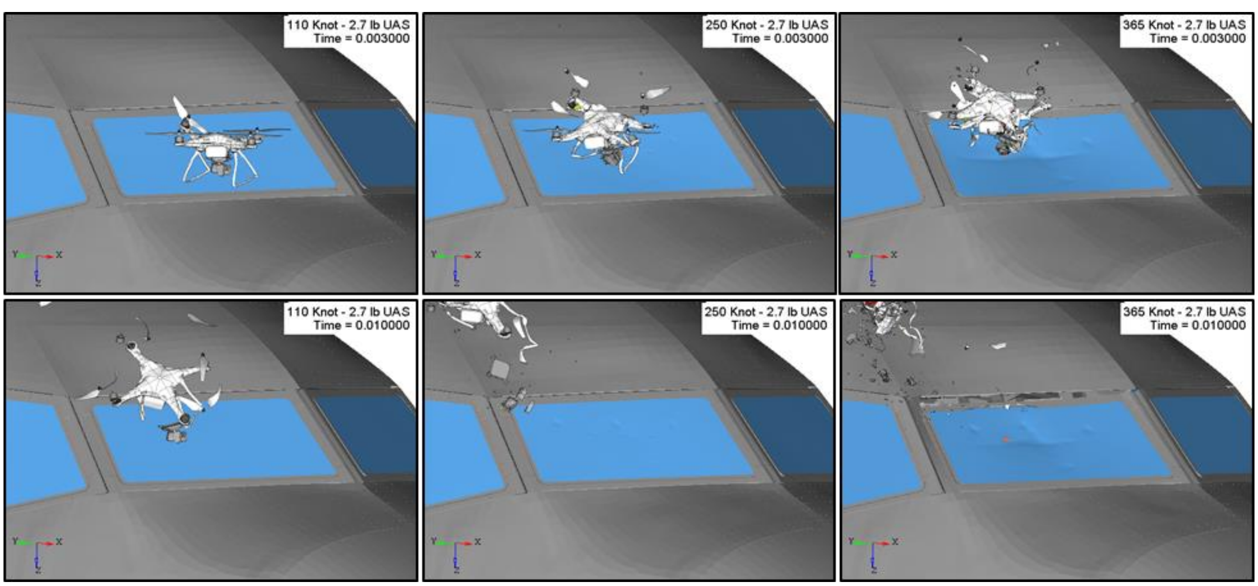

Figure 402. Comparison of the kinematics of impact between a commercial transport jet windshield and a 1.2 kg UAS at 56.7/128.6/187.8 m/s (110/250/365 knots)

All the UAS impacted the windshield and slid over it due to the small windshield angle. The UAS at 56.7 m/s (110 knots) did not damage the windshield. On the other hand, the UAS at 128.6 m/s (250 knots) slightly deformed the windshield while the UAS at 187.8 m/s (365 knots) damaged the windshield to a greater degree. It can also be perceived in Figure 403 that the damage severity increases with respect to the increase in velocity.

The damage introduced by UAS at 56.7, 128.6, and 187.8 m/s (110, 250 and 365 knots) is classified as Level 1, 2, and 4 respectively. It is evident that higher velocity results in greater damage.

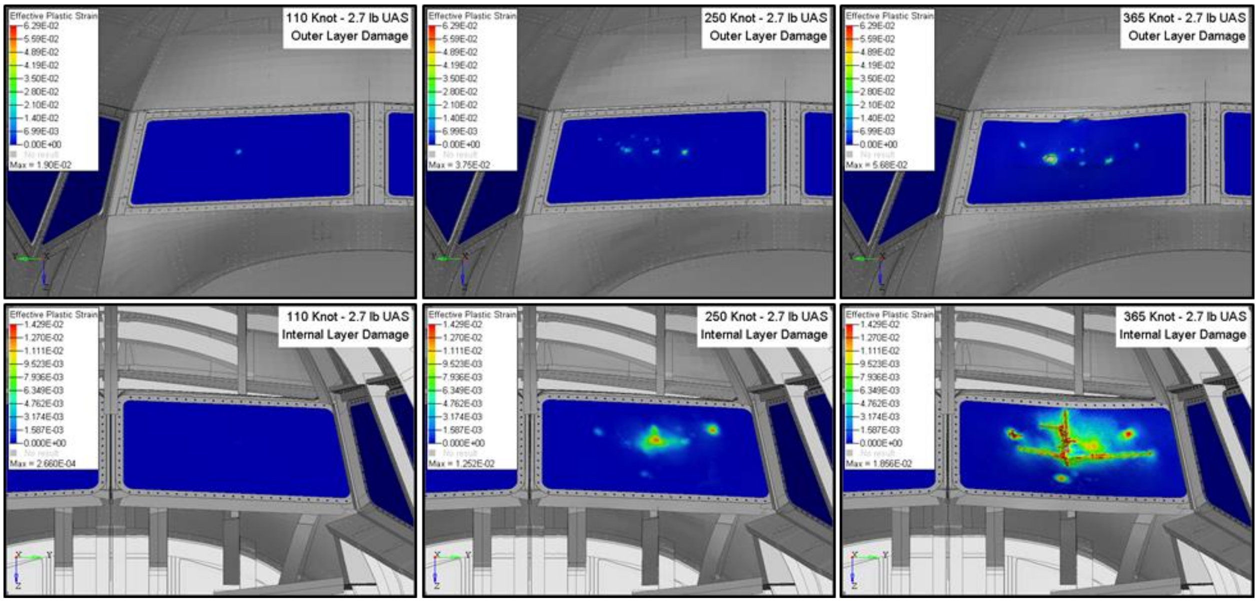

Figure 403. Comparison of external/internal damage sustained by a commercial transport jet windshield impacted with a 1.2 kg UAS at 56.7/128.6/187.8 m/s (110/250/365 knots)

Figure 404 shows the comparison for the contact force and impulse between the UAS and windshield for three different velocities. Figure 405 shows the normalized energy balance for the impact comparison.

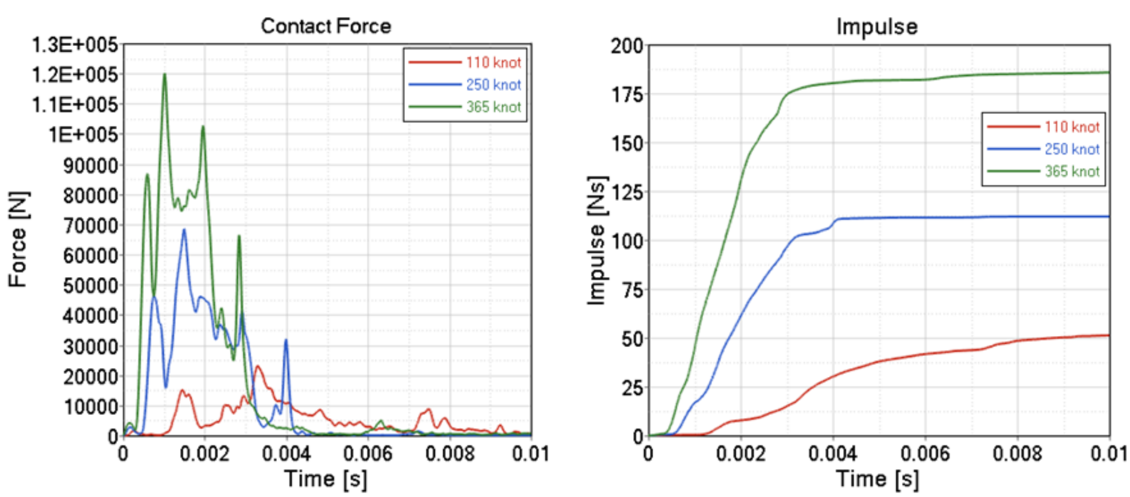

Figure 404. Comparison of the contact force and impulse of the impact between a commercial transport jet windshield and a 1.2 kg UAS at 56.7/128.6/187.8 m/s (110/250/365 knots)

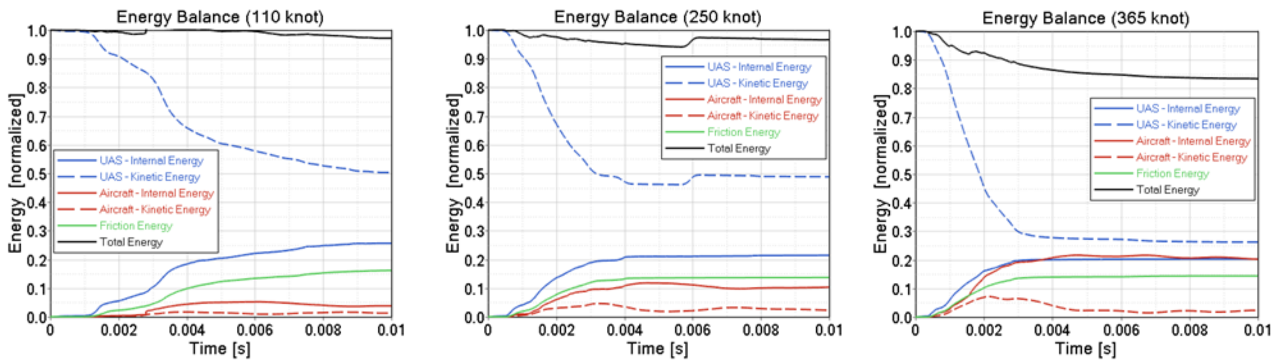

Figure 405. Comparison of the normalized energy balance of the impact between a commercial transport jet windshield and a 1.2 kg UAS at 56.7/128.6/187.8 m/s (110/250/365 knots)

The impulse increases with higher velocities. From the energy balance comparison, it can be observed that the UAS absorbed greater internal energy at lower velocity than the UAS at higher velocity. In addition, the residual kinetic energy after impact was greater for the UAS at lower velocities than for the UAS at higher velocities. This is an indication that the kinetic energy of the UAS at lower velocities was deflected more efficiently than that of the UAS at higher velocities, for which most of the energy was absorbed in the impact.

D.2 BUSINESS JET

D.2.1 Vertical Stabilizer

Impact simulations of a 1.2 kg (2.7 lb) UAS (case BQV2) with three different velocities (44.7, 128.6, 167.2 m/s; or 87, 250, 325 knots) against a vertical stabilizer are compared in terms of damage severity and kinematics. The initial conditions for all the above cases except for the velocity were based on BQV2, which was identified as the most critical case in the baseline simulations (see Section 4.4.1.1). Figure 406 depicts the comparison of the kinematics of the event. Figure 407 shows the comparison of the damage caused to the skin and the inner structure of the vertical stabilizer.

The UAS at 44.7 m/s (87 knots) deformed slightly the skin with no visible internal damage. On the other hand, the UAS at 128.6 m/s (250 knots) damaged the skin, the upper and lower ribs while the UAS at 167.2 m/s (325 knots) damaged the skin, upper and lower ribs to a greater degree, and the front spar. It can also be perceived in Figure 407 that the damage severity increases with respect to the increase in velocity.

The damage introduced by UAS at 44.7, 128.6 and 167.2 m/s (87, 250, and 325 knots) is classified as level 2, 3, and 4 respectively. It is evident that higher velocity results in greater damage.

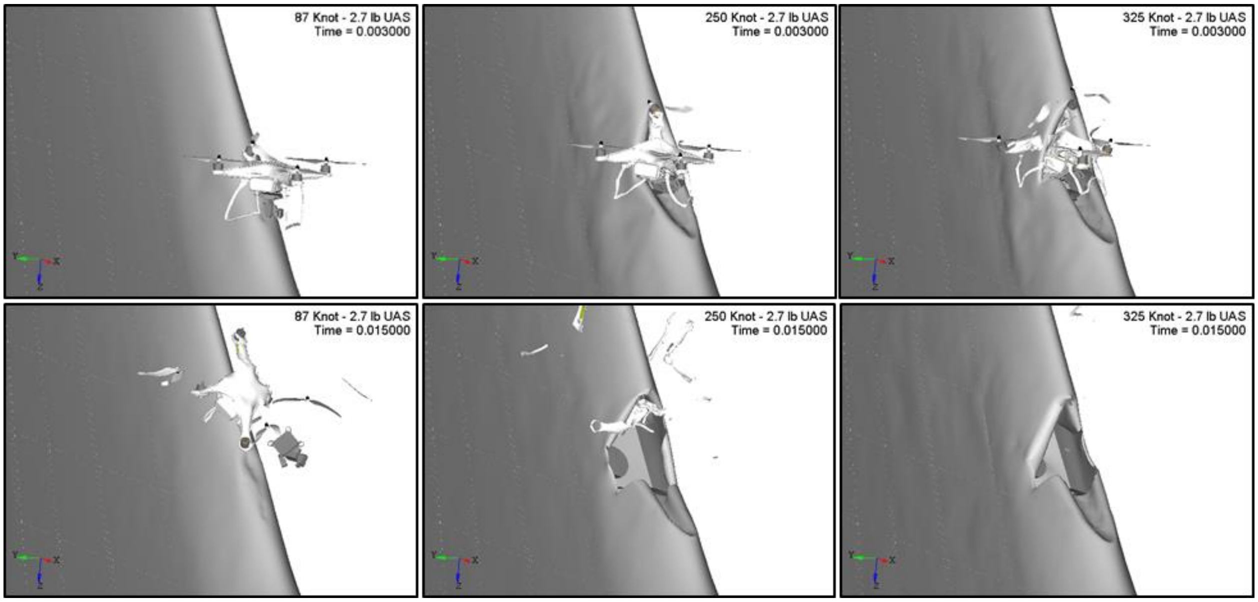

Figure 406. Comparison of the kinematics of impact between a business jet vertical stabilizer and a 1.2 kg UAS at 44.7/128.6/167.2 m/s (87/250/325 knots)

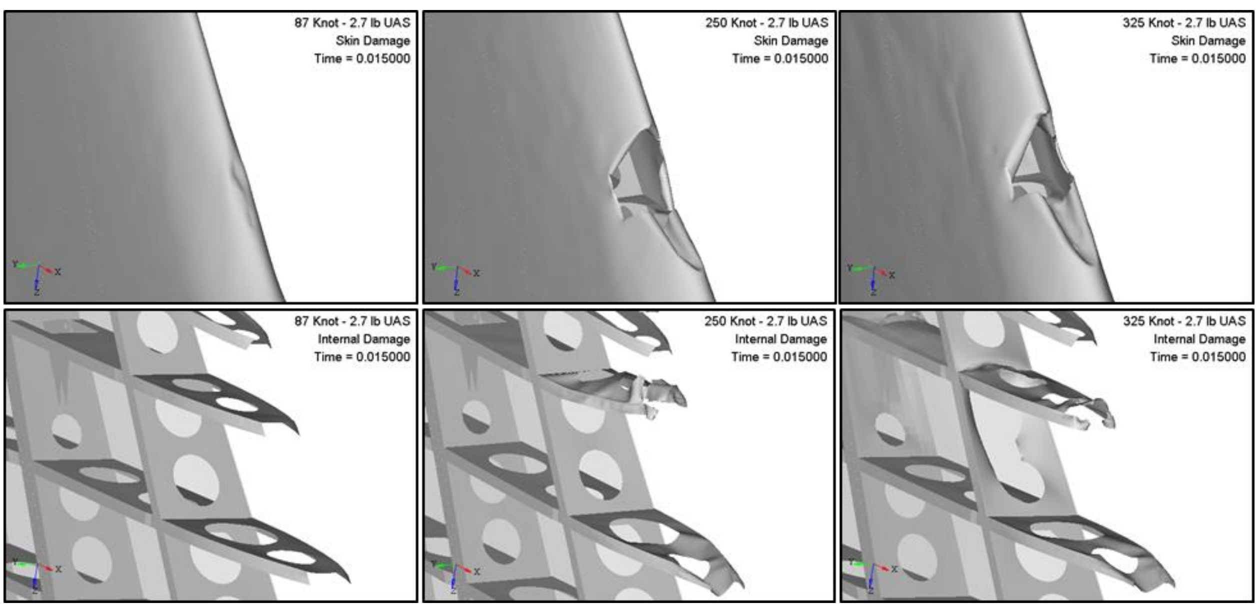

Figure 407. Comparison of external/internal damage sustained by a business jet vertical stabilizer impacted with a 1.2 kg UAS at 44.7/128.6/167.2 m/s (87/250/325 knots)

Figure 408 shows the comparison for the contact force and impulse between the UAS and vertical stabilizer for three different velocities. Figure 409 shows the normalized energy balance for the impact comparison.

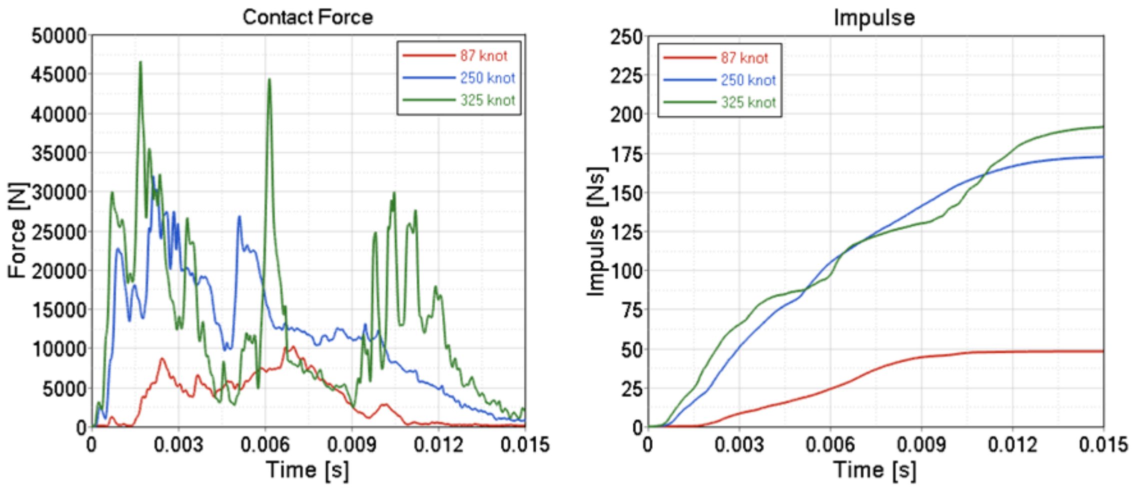

Figure 408. Comparison of the contact force and impulse of the impact between a business jet vertical stabilizer and a 1.2 kg UAS at 44.7/128.6/167.2 m/s (87/250/325 knots)

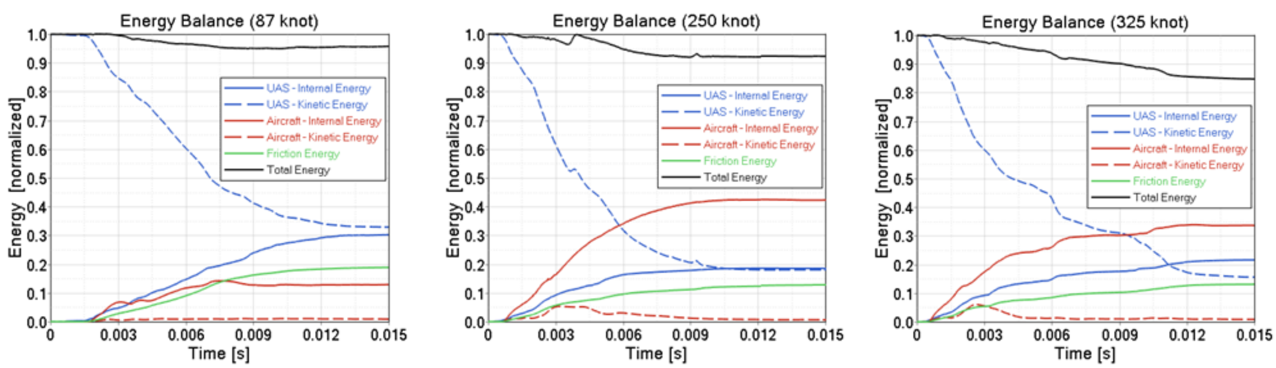

Figure 409. Comparison of the normalized energy balance of the impact between a business jet vertical stabilizer and a 1.2 kg UAS at 44.7/128.6/167.2 m/s (87/250/325 knots)

The impulse increases with higher velocities. From the energy balance comparison, it can be observed that the internal energy ratios do not appear to have specific trends related to the impact velocity. In addition, it is apparent that the residual kinetic energy after the impact was greater for UAS at lower velocities than for the UAS at higher velocities. This is an indication that the kinetic energy of the UAS at lower velocities was deflected more efficiently than that of the UAS at higher velocities, for which most of the energy was absorbed in the impact.

D.2.2 Horizontal Stabilizer

Impact simulations of a 1.2 kg (2.7 lb) UAS (case BQH2) with three different velocities (44.7, 128.6, 167.2 m/s; or 87, 250, 325 knots) against a horizontal stabilizer are compared in terms of damage severity and kinematics. The initial conditions for all the above cases except for the velocity were based on BQH2, which was identified as the most critical case in the baseline simulations (see Section 4.4.2.1). Figure 410 depicts the comparison of the kinematics of the event. Figure 411 shows the comparison of the damage caused to the skin and the inner structure of the horizontal stabilizer.

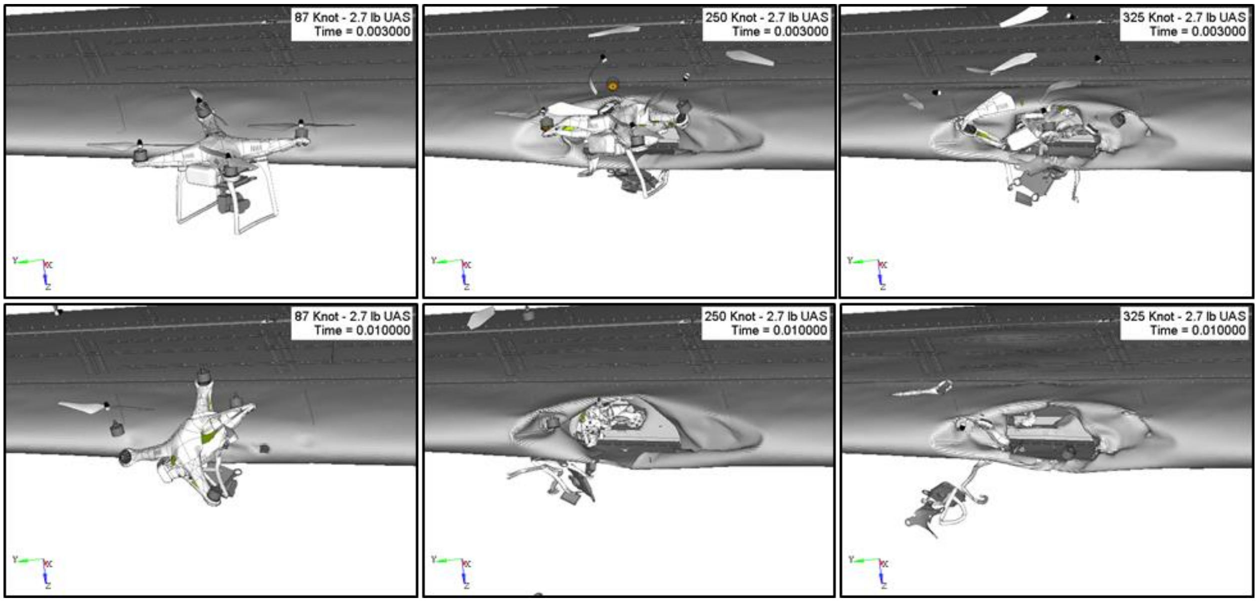

Figure 410. Comparison of the kinematics of impact between a business jet horizontal stabilizer and a 1.2 kg UAS at 44.7/128.6/167.2 m/s (87/250/325 knots)

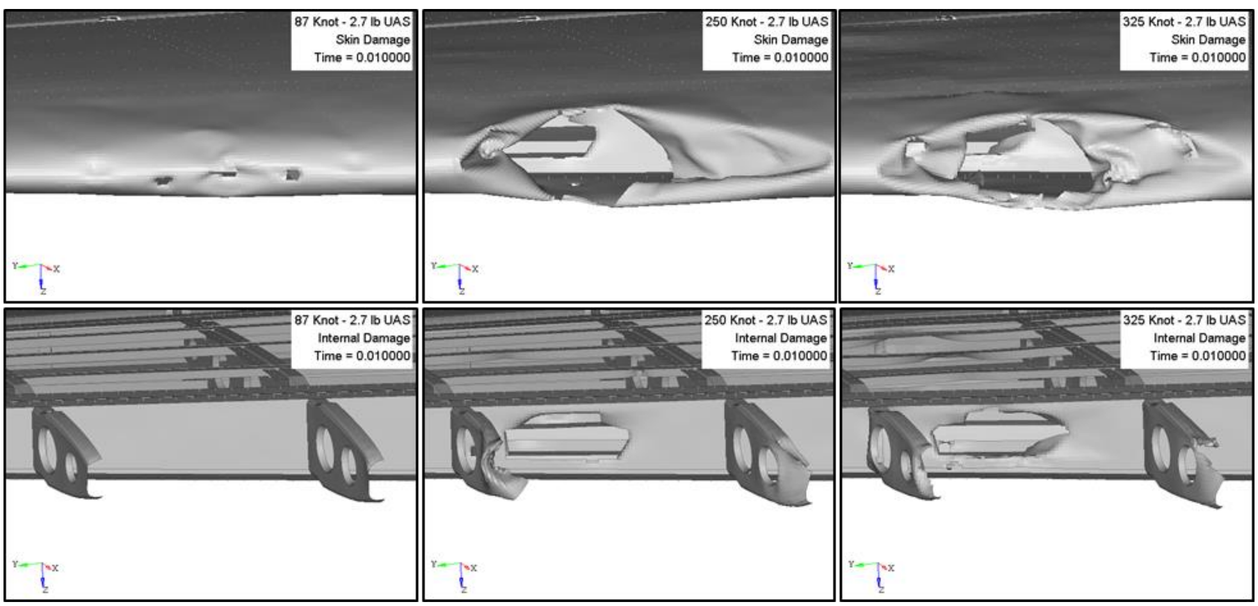

Figure 411. Comparison of external/internal damage sustained by a business jet horizontal stabilizer impacted with a 1.2 kg UAS at 44.7/128.6/167.2 m/s (87/250/325 knots)

The UAS at 44.7 m/s (87 knots) deformed slightly the skin and the nose ribs with no other visible internal damage. On the other hand, the UAS at 128.6 m/s (250 knots) damaged the skin, the nose ribs, and the front spar while the UAS at 167.2 m/s (325 knots) damaged the skin, the nose ribs, and the front spar to a greater degree. It can also be perceived in Figure 411 that the damage severity increases with respect to the increase in velocity.

The damage introduced by UAS at 44.7 m/s (87 knots) is classified as level 2 whereas the damage introduced by both UAS at 128.6 m/s (250 knots) and 167.2 m/s (325 knots) is classified as level 4 with risk of fire due to the battery. It is evident that higher velocity results in greater damage.

Figure 412 shows the comparison for the contact force and impulse between the UAS and horizontal stabilizer for three different velocities. Figure 413 shows the normalized energy balance for the impact comparison.

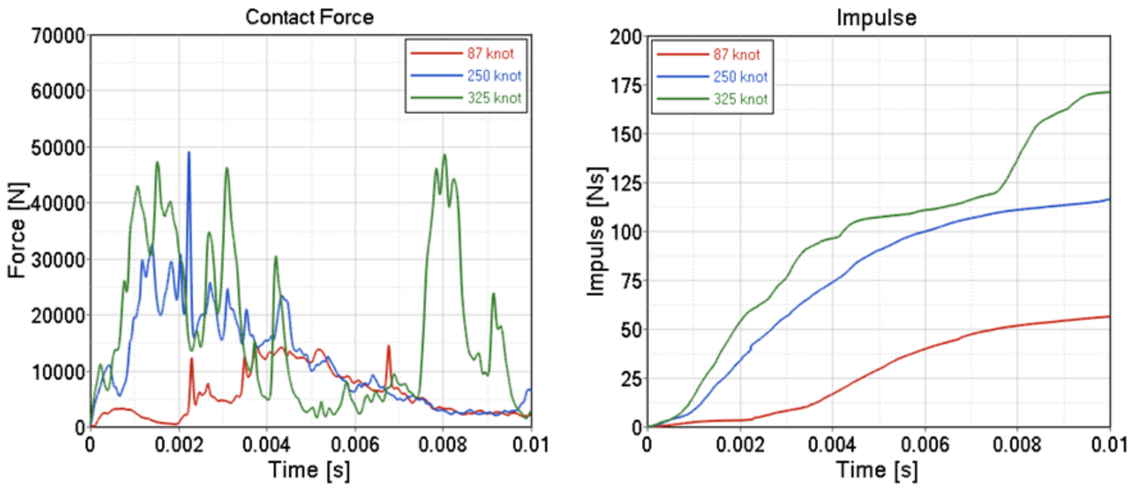

Figure 412. Comparison of the contact force and impulse of the impact between a business jet horizontal stabilizer and a 1.2 kg UAS at 44.7/128.6/167.2 m/s (87/250/325 knots)

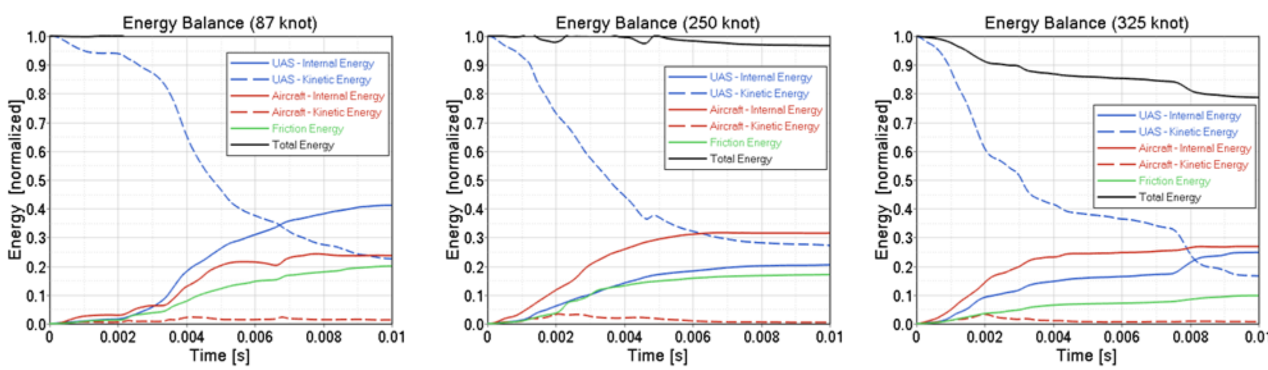

Figure 413. Comparison of the normalized energy balance of the impact between a business jet horizontal stabilizer and a 1.2 kg UAS at 44.7/128.6/167.2 m/s (87/250/325 knots)

The impulse increases with higher velocities. From the energy balance comparison, it can be observed that the internal energy ratios do not appear to have specific trends related to the impact velocity. In addition, the residual kinetic energy after the impact was greater for UAS at lower velocities than for the UAS at higher velocities. This is an indication that the kinetic energy of the UAS at lower velocities was deflected more efficiently than that of the UAS at higher velocities, for which most of the energy was absorbed in the impact.

D.2.3 Wing Leading Edge

Impact simulations of a 1.2 kg (2.7 lb) UAS (case BQW1) with three different velocities (44.7, 128.6, 167.2 m/s; or 87, 250, 325 knots) against a wing leading edge are compared in terms of damage severity and kinematics. The initial conditions for all the above cases except for the velocity were based on BQW1, which was identified as the most critical case in the baseline simulations (see Section 4.4.3.1). Figure 414 depicts the comparison of the kinematics of the event. Figure 415 shows the comparison of the damage caused to the skin and the inner structure of the wing.

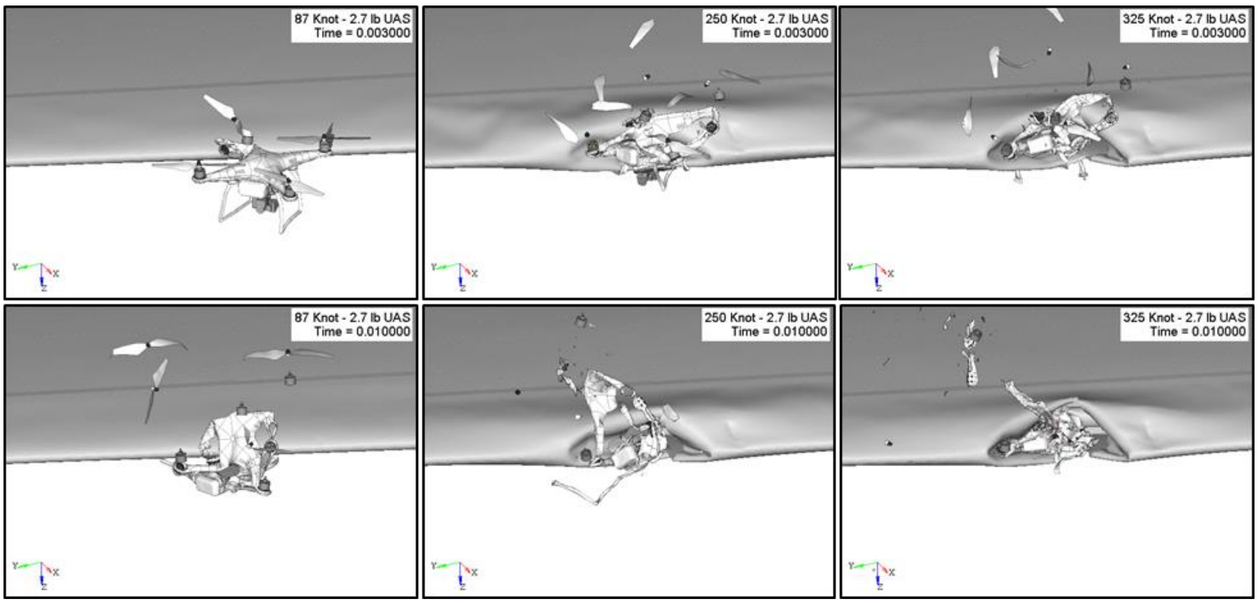

Figure 414. Comparison of the kinematics of impact between a business jet wing and a 1.2 kg UAS at 44.7/128.6/167.2 m/s (87/250/325 knots)

The UAS at 44.7 m/s (87 knots) deformed slightly the skin with no visible internal damage. On the other hand, the UAS at 128.6 m/s (250 knots) damaged the skin and the anti-ice tube while the UAS at 167.2 m/s (325 knots) damaged the skin and the anti-ice tube to a greater degree, and the front spar. It can also be perceived in Figure 415 that the damage severity increases with respect to the increase in velocity.

The damage introduced by UAS at 44.7 m/s (87 knots) is classified as level 2 whereas the damage introduced by UAS at 128.6 m/s (250 knots) and 167.2 m/s (325 knots) are classified as level 3. In addition, the risk of fire due to the battery is only present for the impacts of UAS at 128.6 and 167.2 m/s (250 and 325 knots). It is evident that higher velocity results in greater damage.

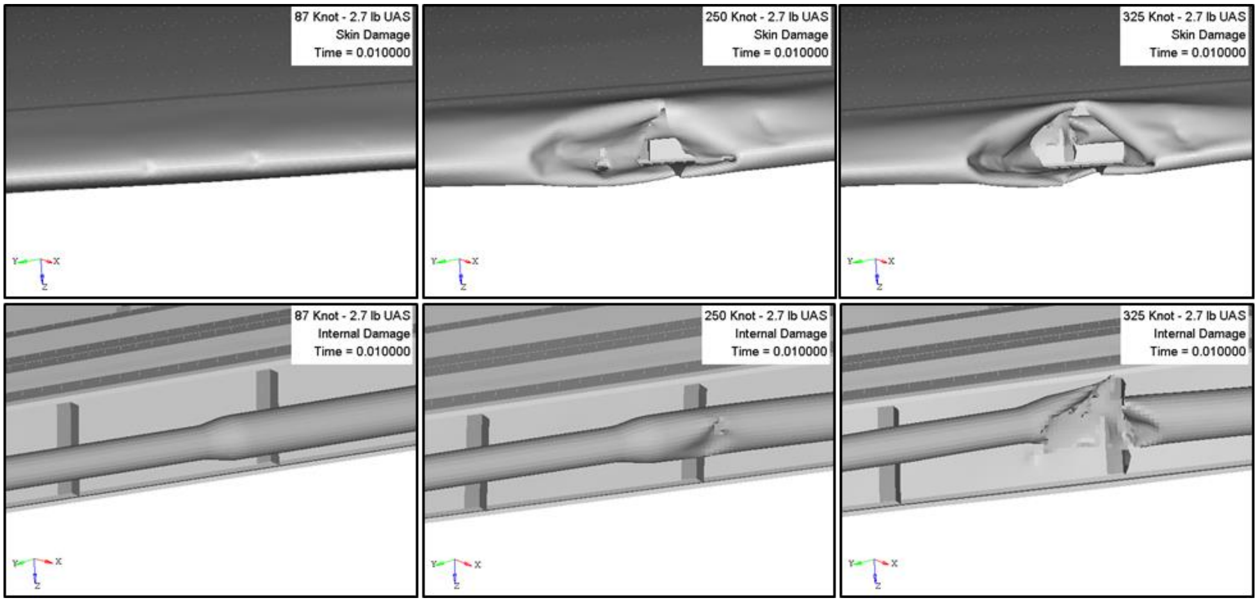

Figure 415. Comparison of external/internal damage sustained by a business jet wing impacted with a 1.2 kg UAS at 44.7/128.6/167.2 m/s (87/250/325 knots)

Figure 416 shows the comparison for the contact force and impulse between the UAS and wing for three different velocities. Figure 417 shows the normalized energy balance for the impact comparison.

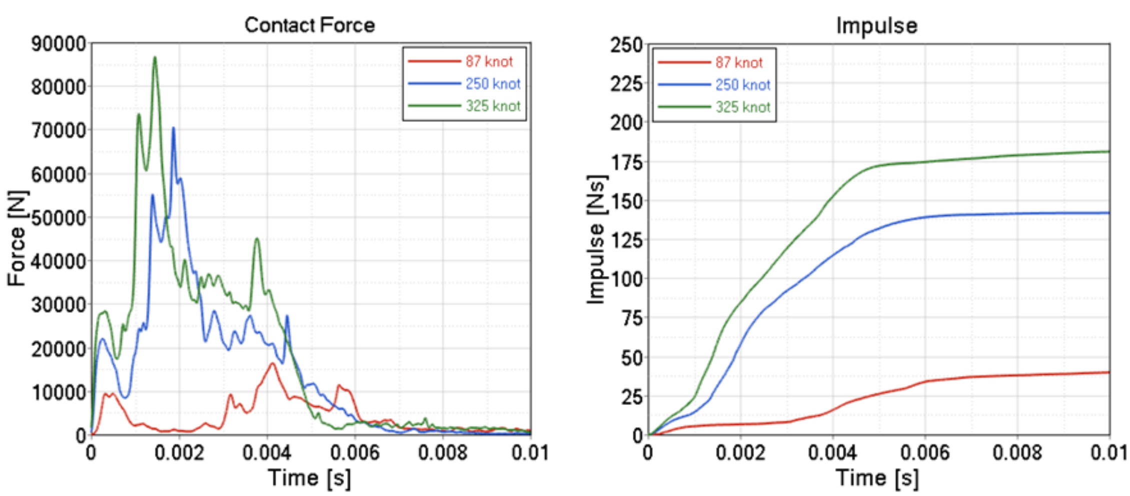

Figure 416. Comparison of the contact force and impulse of the impact between a business jet wing and a 1.2 kg UAS at 44.7/128.6/167.2 m/s (87/250/325 knots)

The impulse increases with higher velocities. From the energy balance comparison, it can be observed that the UAS absorbed greater internal energy at lower velocity than the UAS at higher velocity. The kinetic energy ratios do not appear to have specific trends related to the impact velocity; therefore, the visible damage and kinematics are used to draw conclusions.

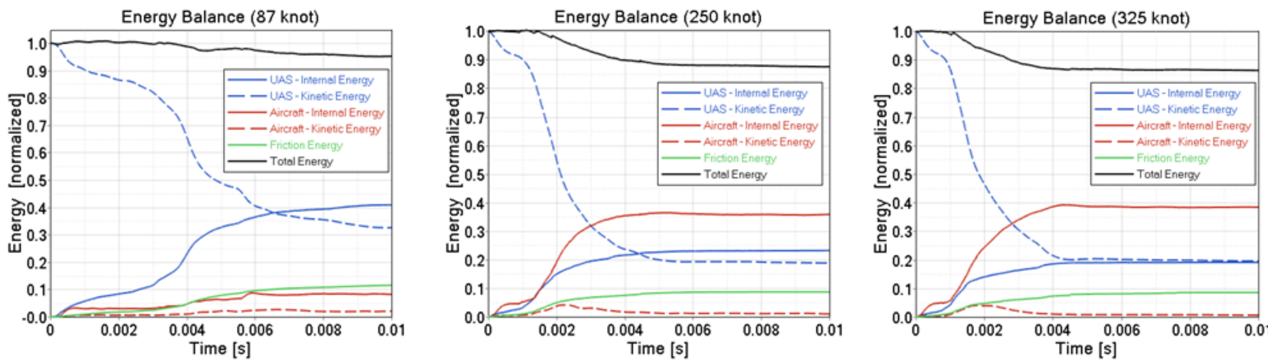

Figure 417. Comparison of the normalized energy balance of the impact between a business jet wing and a 1.2 kg UAS at 44.7/128.6/167.2 m/s (87/250/325 knots)

D.2.4 Windshield

Impact simulations of a 1.2 kg (2.7 lb) UAS (case BQC1) with three different velocities (44.7, 128.6, 167.2 m/s; or 87, 250, 325 knots) against a windshield are compared in terms of damage severity and kinematics. The initial conditions for all the above cases except for the velocity were based on BQC1, which was identified as the most critical case in the baseline simulations (see Section 4.4.4.1). Figure 418 depicts the comparison of the kinematics of the event. Figure 419 shows the comparison of the damage caused to the windshield and surrounding structure.

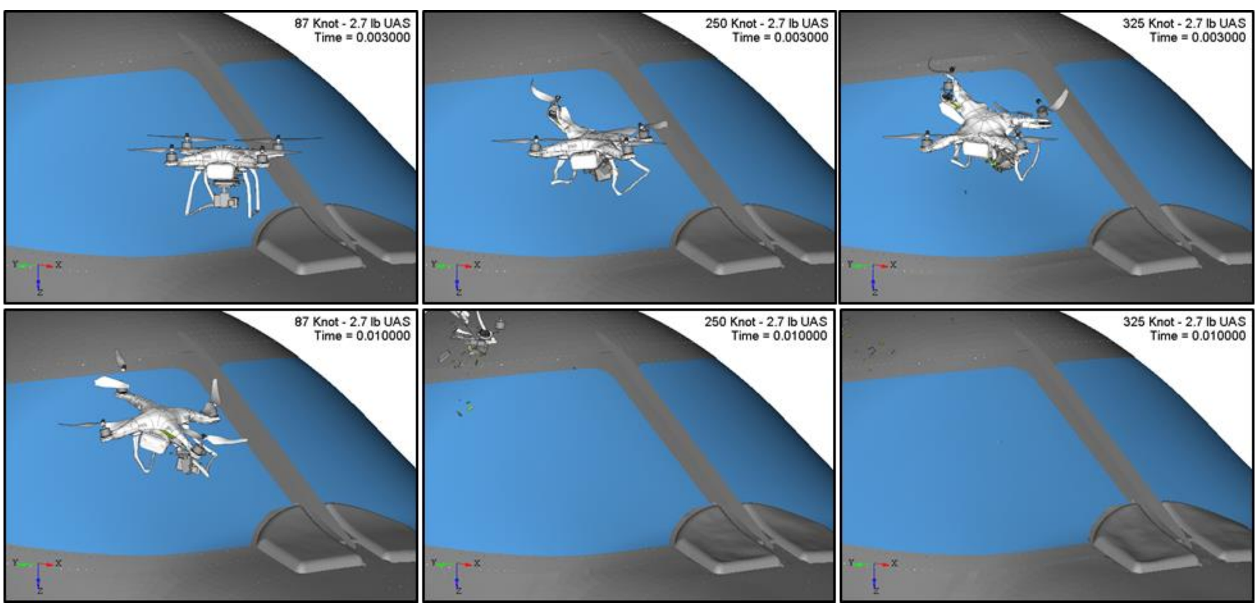

Figure 418. Comparison of the kinematics of impact between a business jet windshield and a 1.2 kg UAS at 44.7/128.6/167.2 m/s (87/250/325 knots)

All the UAS impacted the windshield and slid over it due to the small windshield angle. The UAS at 44.8, 128.6 and 167.12 m/s (87, 250, and 325 knots) did not cause any visible damage to the windshield and internal structure. It can also be perceived in Figure 419 that the damage severity increases with respect to the increase in velocity.

The damage introduced by UAS at 44.8 and 128.6 m/s (87 and 250 knots) is classified as Level 1 and Level 2 respectively, whereas the damage introduced by UAS at 167.2 m/s (325 knots) is classified as Level 3. It is evident that higher velocity results in greater damage.

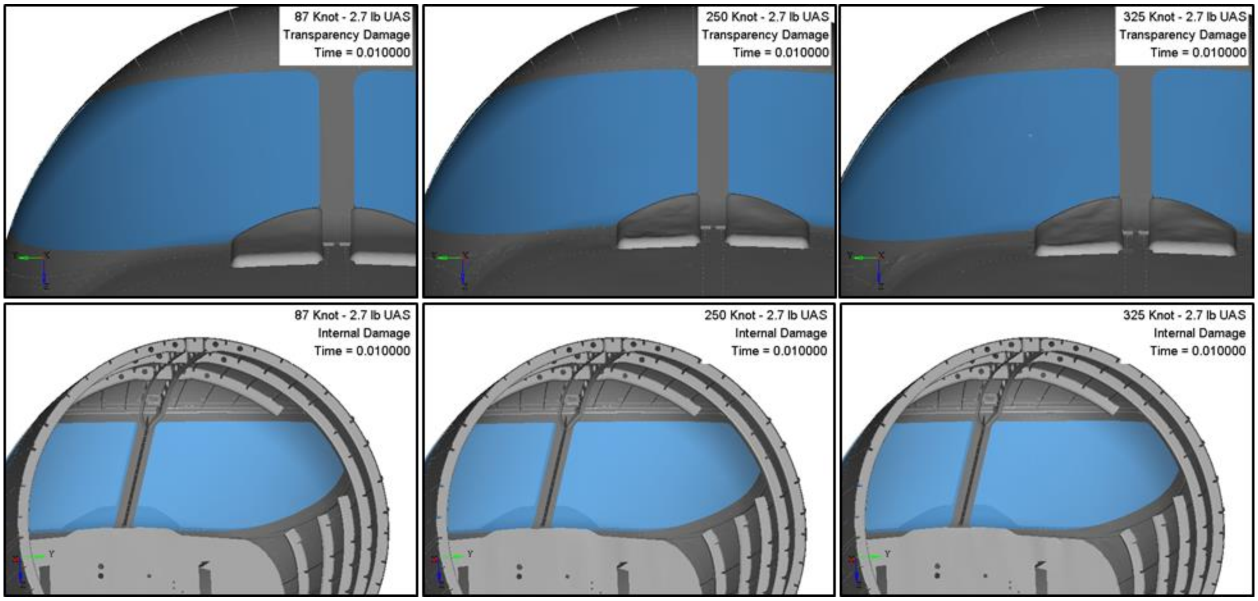

Figure 419. Comparison of external/internal damage sustained by a business jet windshield impacted with a 1.2 kg UAS at 44.7/128.6/167.2 m/s (87/250/325 knots)

Figure 420 shows the comparison for the contact force and impulse between the UAS and windshield for three different velocities. Figure 421 shows the normalized energy balance for the impact comparison.

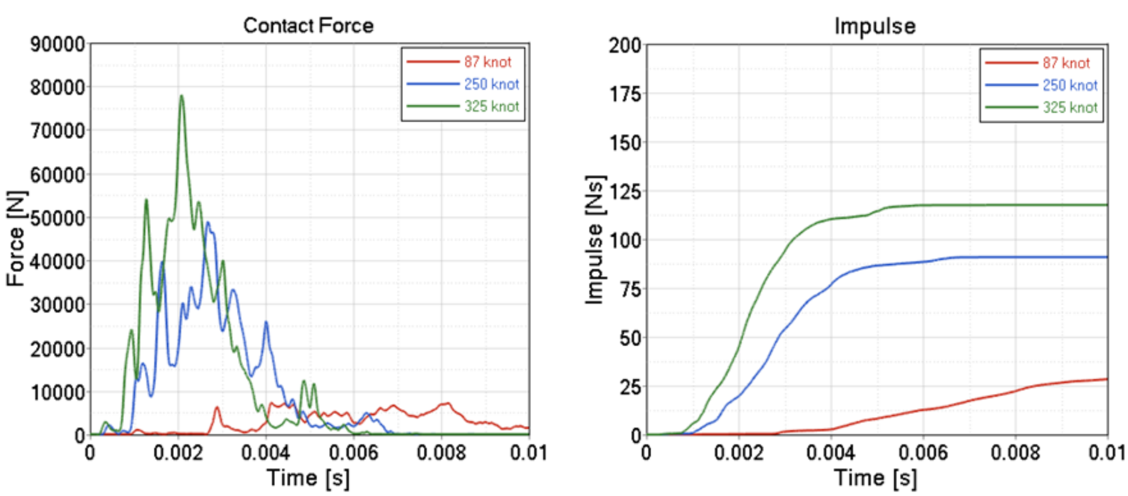

Figure 420. Comparison of the contact force and impulse of the impact between a business jet windshield and a 1.2 kg UAS at 44.7/128.6/167.2 m/s (87/250/325 knots)

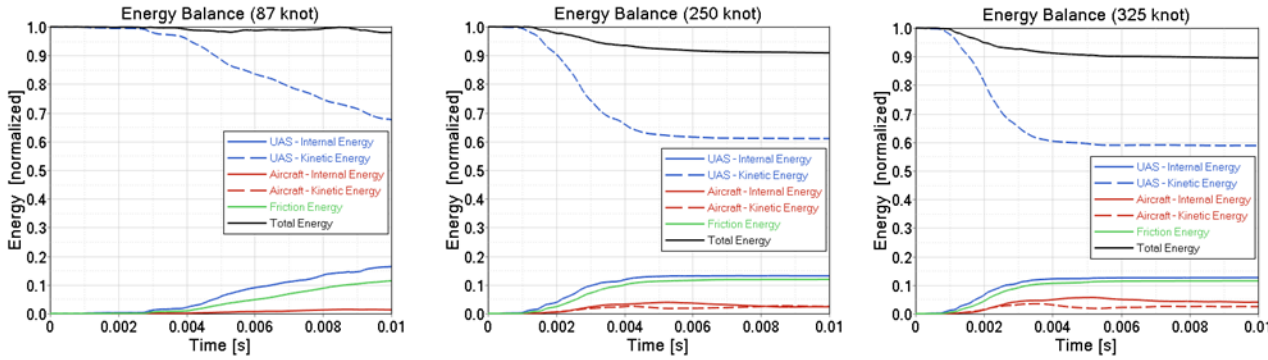

Figure 421. Comparison of the normalized energy balance of the impact between a business jet windshield and a 1.2 kg UAS at 44.7/128.6/167.2 m/s (87/250/325 knots)

The impulse increases with higher velocities. From the energy balance comparison, it can be observed that the internal energy ratios do not appear to have specific trends related to the impact velocity. In addition, the residual kinetic energy after impact was greater for the UAS at lower velocities than for the UAS at higher velocities. This is an indication that the kinetic energy of the UAS at lower velocities was deflected more efficiently than that of the UAS at higher velocities, for which most of the energy was absorbed in the impact.

APPENDIX E – BIRD STRIKE COMPARISON

E.1 TRANSPORT JET – UAS VS. BIRD (2.7 LB)

E.1.1 Vertical Stabilizer

Impact simulations of a 1.2 kg (2.7 lb) UAS (case CQV3) and a 1.2 kg (2.7 lb) bird (case CB2V3) against a vertical stabilizer are compared in terms of damage severity and kinematics. The initial conditions were based on the above UAS case, which was identified as the most critical in the baseline simulations (see Section 4.3.1.1). Figure 358 depicts the comparison of the kinematics of the event. Figure 359 shows the comparison of the damage caused to the skin and the inner structure of the vertical stabilizer.

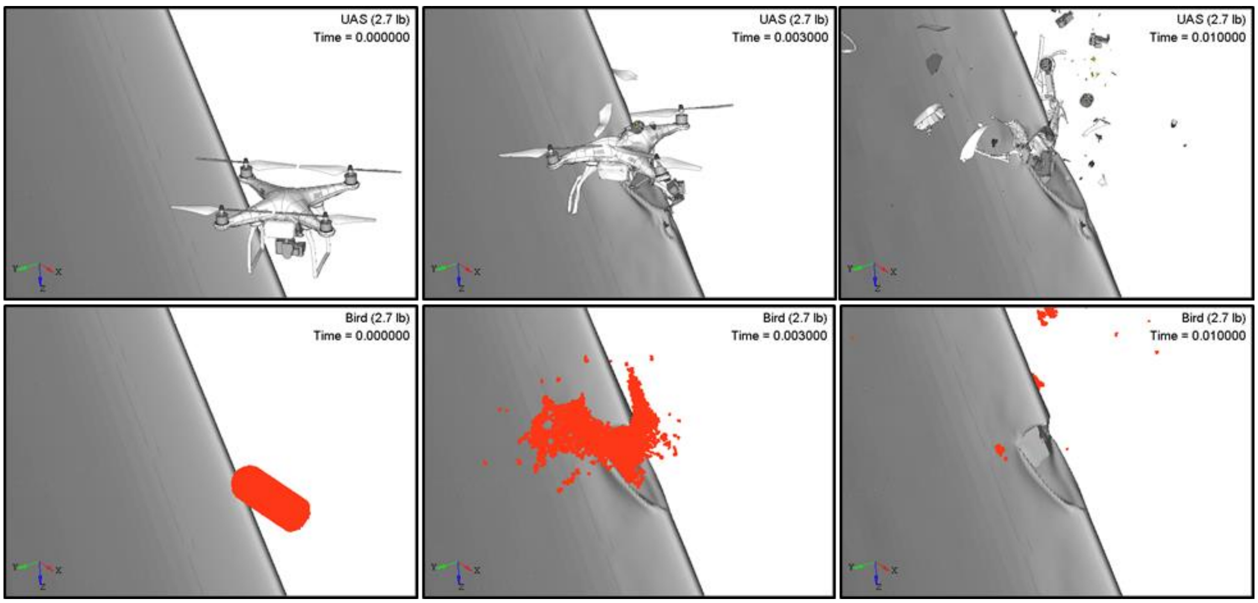

Figure 422.Comparison of the kinematics of impact between a commercial transport jet vertical stabilizer and a 1.2 kg (2.7 lb) UAS/Bird at 128.6 m/s (250 knots)

The UAS damaged the skin, the upper and lower ribs, and the lightening hole above the impact location in the front spar while the bird damaged the skin and forward spar to a lesser degree and just the upper rib. It can also be seen in Figure 359 that amount of damage introduced into the skin was considerably smaller for the case of bird than the UAS.

The damage introduced by both the bird and the UAS is classified as Level 3. Even with the same level, the UAS can be considered as slightly more severe than the bird in terms of damage.

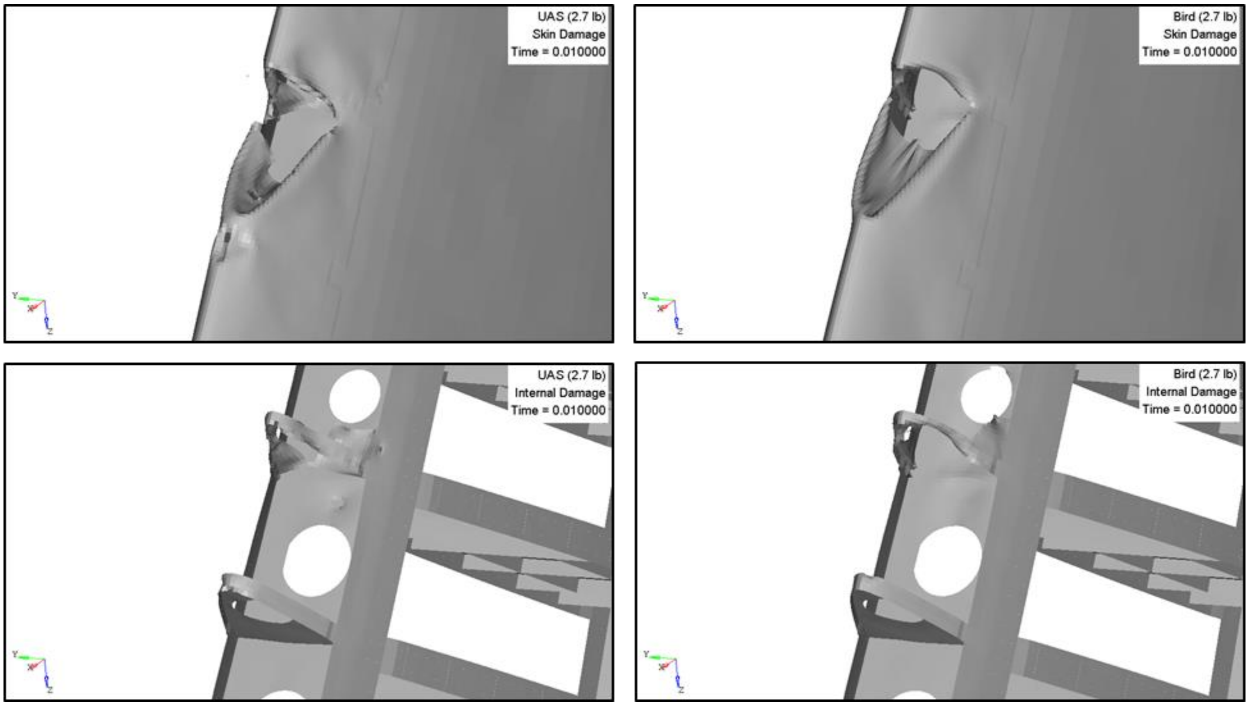

Figure 423 Comparison of external/internal damage sustained by a commercial transport jet vertical stabilizer impacted with a 1.2 kg (2.7 lb) UAS/Bird at 128.6 m/s (250 knots)

Figure 360 shows the comparison for the contact force and impulse between the UAS/bird and vertical stabilizer. Figure 361 shows the energy balance for the impact comparison.

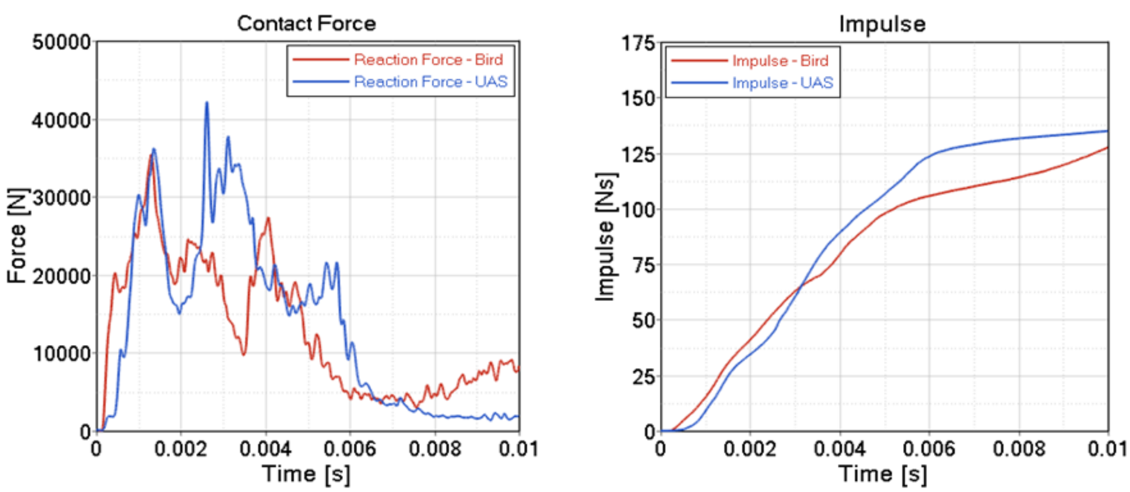

Figure 424 Comparison of the contact force and impulse of the impact between a commercial transport jet vertical stabilizer and a 1.2 kg (2.7 lb) UAS/bird at 128.6 m/s (250 knots)

The impulse for the UAS was higher than that of the bird. From the energy balance comparison, it can be observed that the UAS absorbed considerably greater internal energy than the bird. In addition, it is apparent that the residual kinetic energy of the bird after impact was greater than that of the UAS. This is an indication that the kinetic energy of the bird was deflected more efficiently than that of the UAS, for which most of the energy was absorbed in the impact.

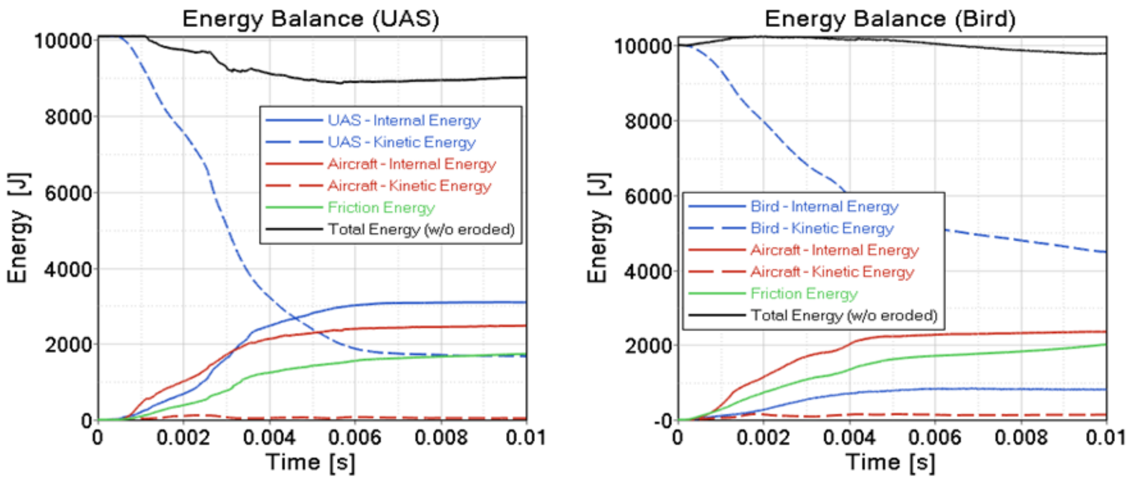

Figure 425 Comparison of the energy balance of the impact between a commercial transport jet vertical stabilizer and a 1.2 kg (2.7 lb) UAS/bird at 128.6 m/s (250 knots)

E.1.2 Horizontal Stabilizer

Impact simulations of a 1.2 kg (2.7 lb) UAS (case CQH3) and a 1.2 kg (2.7 lb) bird (case CB2H3) against a horizontal stabilizer are compared in terms of damage severity and kinematics. The initial conditions were based on the above UAS case, which was identified as the most critical in the baseline simulations (see Section 4.3.2.1). Figure 426 depicts the comparison of the kinematics of the event. Figure 427 shows the comparison of the damage caused to the skin and the inner structure of the horizontal stabilizer.

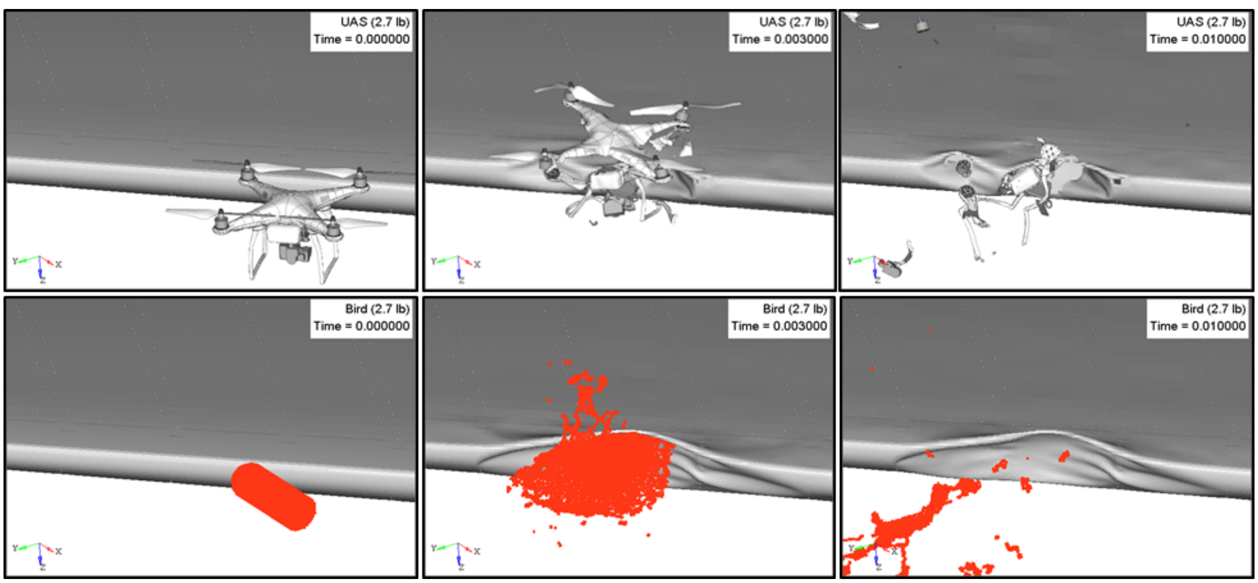

Figure 426.Comparison of the kinematics of impact between a commercial transport jet horizontal stabilizer and a 1.2 kg (2.7 lb) UAS/Bird at 128.6 m/s (250 knots)

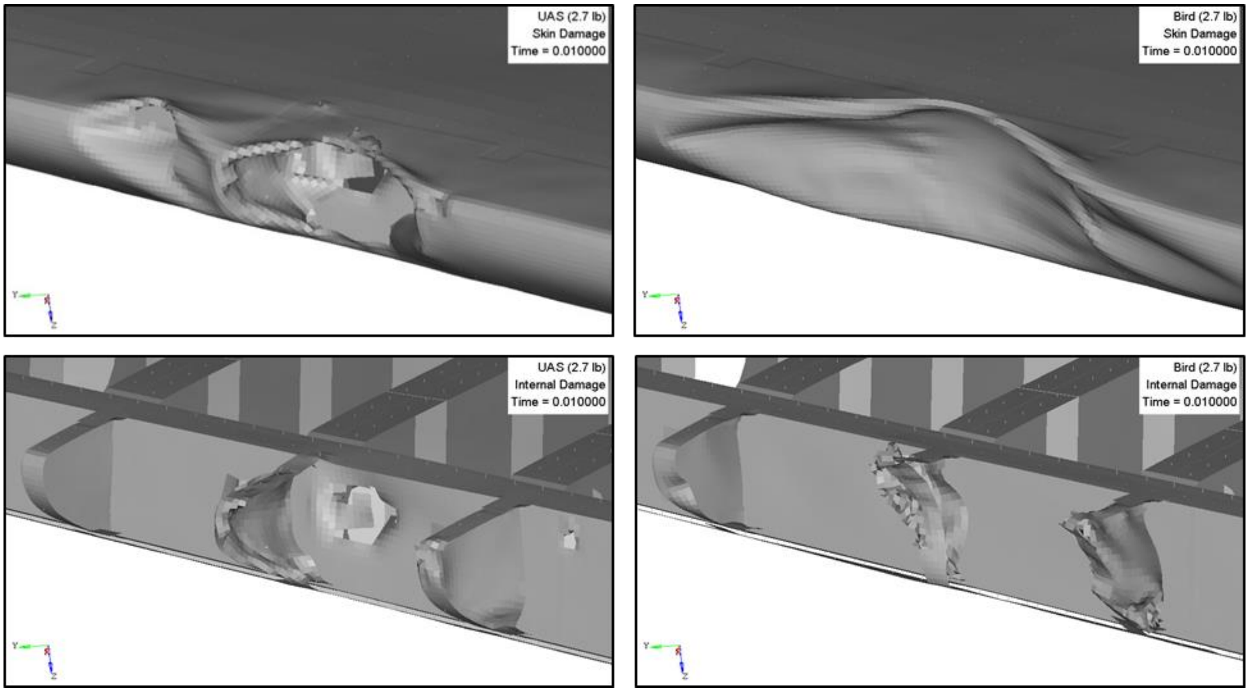

Figure 427 Comparison of external/internal damage sustained by a commercial transport jet horizontal stabilizer impacted with a 1.2 kg (2.7 lb) UAS/Bird at 128.6 m/s (250 knots)

The UAS damaged the skin, both the nose ribs and the sub spar while the bird damaged the skin to a lesser degree and both the nose ribs. It can also be seen in Figure 427 that amount of damage introduced into the skin was considerably smaller for the case of bird than the UAS.

The damage introduced by the UAS is classified as Level 4 with a risk of fire due to the battery, whereas the damage introduced by the bird is classified as Level 2. For this case, the UAS impact can be considered as more severe than the equivalent bird strike in terms of damage.

Figure 428 shows the comparison for the contact force and impulse between the UAS/bird and horizontal stabilizer. Figure 429 shows the energy balance for the impact comparison.

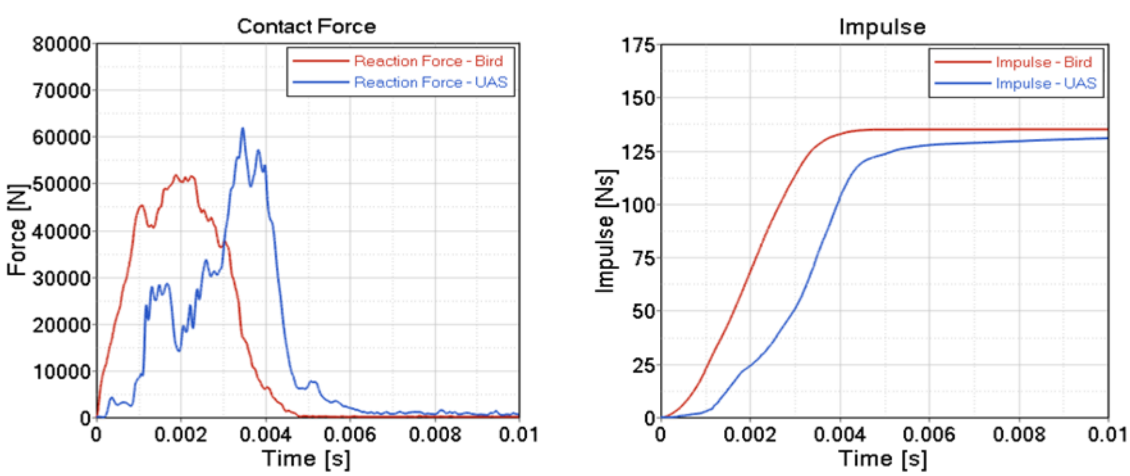

Figure 428 Comparison of the contact force and impulse of the impact between a commercial transport jet horizontal stabilizer and a 1.2 kg (2.7 lb) UAS/bird at 128.6 m/s (250 knots)

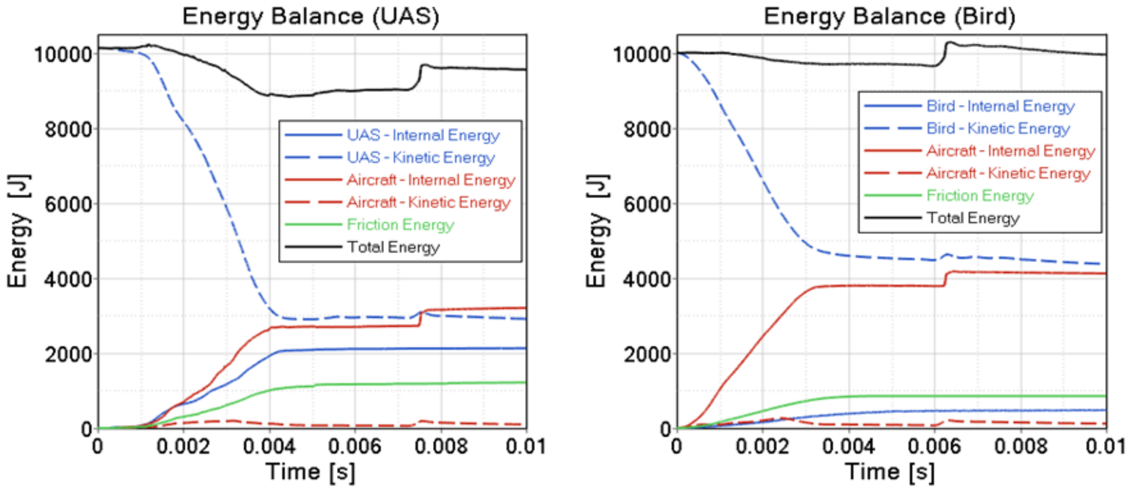

Figure 429. Comparison of the energy balance of the impact between a commercial transport jet horizontal stabilizer and a 1.2 kg (2.7 lb) UAS/bird at 128.6 m/s (250 knots)

The impulse for the bird was slightly higher than that of the UAS. From the energy balance comparison, it can be observed that the UAS absorbed considerably greater internal energy than the bird. In addition, it is apparent that the residual kinetic energy of the bird after impact was greater than that of the UAS. This is an indication that the kinetic energy of the bird was deflected more efficiently than that of the UAS, for which most of the energy was absorbed in the impact.

E.1.3 Wing Leading Edge

Impact simulations of a 1.2 kg (2.7 lb) UAS (case CQW1) and a 1.2 kg (2.7 lb) bird (case CB2W1) against the leading edge of a wing are compared in terms of damage severity and kinematics. The initial conditions were based on the above UAS case, which was identified as the most critical in the baseline simulations (see Section 4.3.3.1). Figure 430 depicts the comparison of the kinematics of the event. Figure 431 shows the comparison of the damage caused to the skin and the inner structure of the wing.

The UAS damaged the skin and the front spar while the bird damaged the skin and the front spar to a lesser degree. It can also be seen in Figure 431 that amount of damage introduced into the skin was considerably smaller for the case of bird than the UAS.

The damage introduced by the UAS is classified as Level 3, whereas the damage introduced by the bird is classified as Level 2. For this case, the UAS impact can be considered as more severe than the equivalent bird strike in terms of damage.

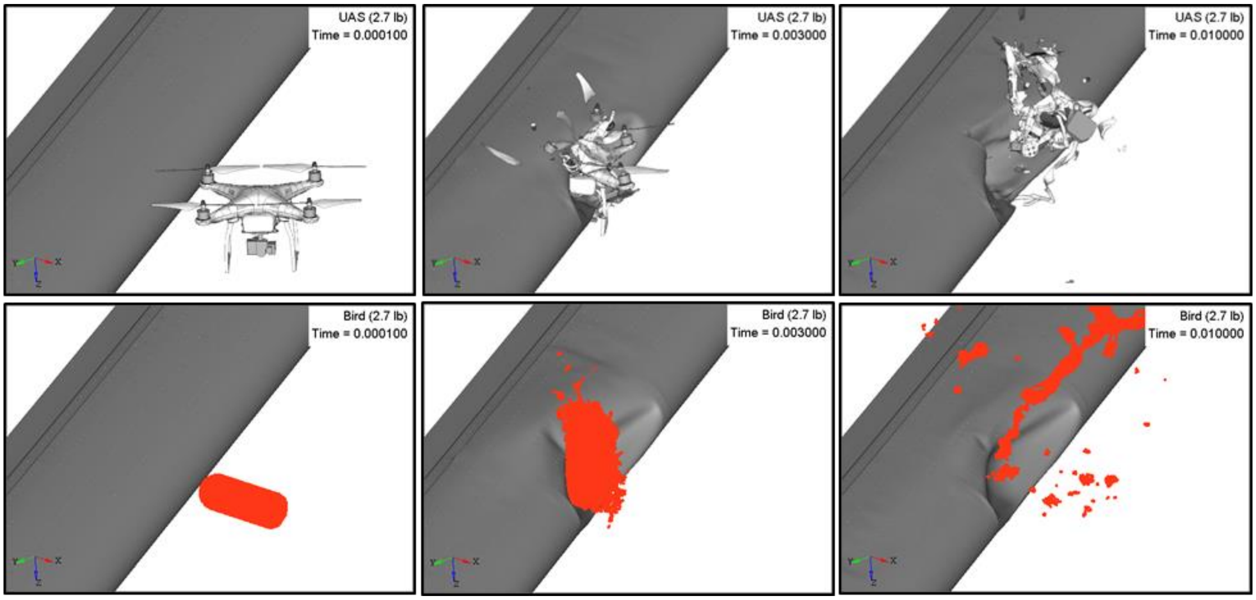

Figure 430. Comparison of the kinematics of impact between a commercial transport jet wing and a 1.2 kg (2.7 lb) UAS/Bird at 128.6 m/s (250 knots)

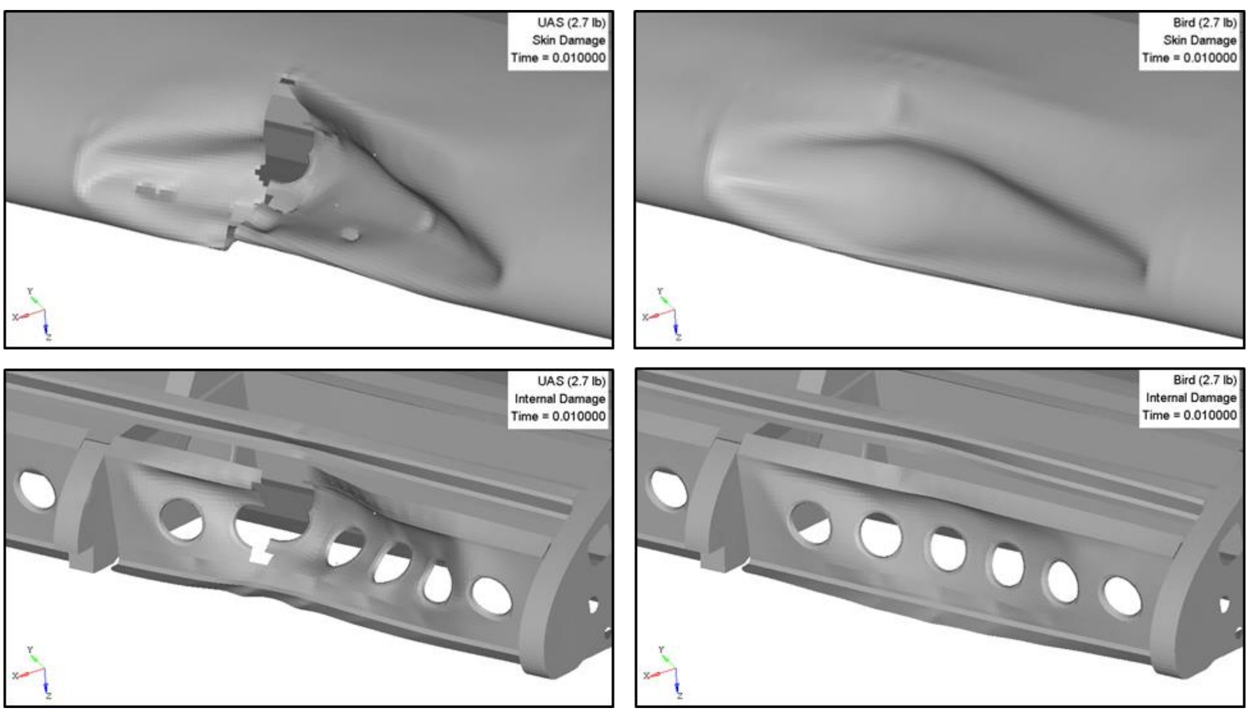

Figure 431. Comparison of external/internal damage sustained by a commercial transport jet wing impacted with a 1.2 kg (2.7 lb) UAS/Bird at 128.6 m/s (250 knots)

Figure 432 shows the comparison for the contact force and impulse between the UAS/bird and wing. Figure 433 shows the energy balance for the impact comparison.

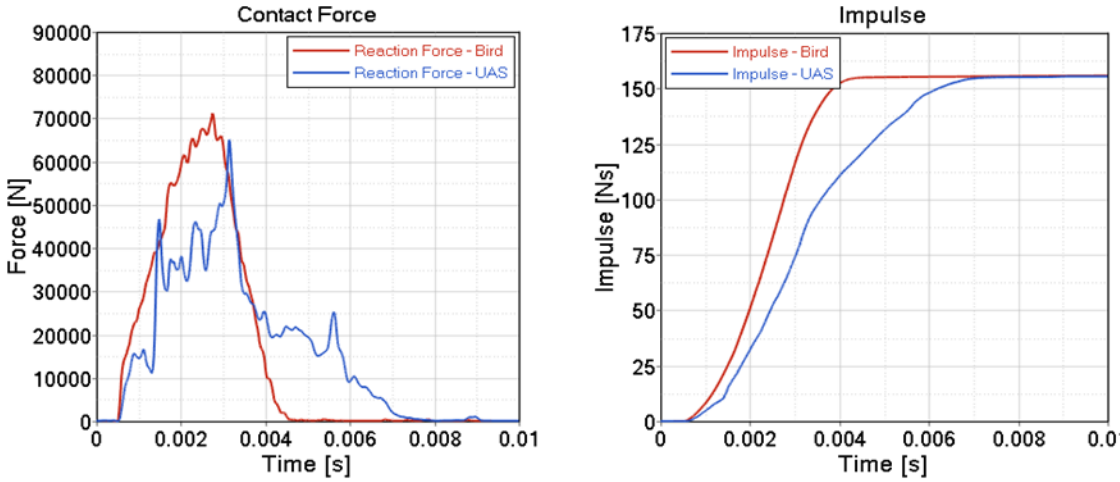

Figure 432 Comparison of the contact force and impulse of the impact between a commercial transport jet wing and a 1.2 kg (2.7 lb) UAS/bird at 128.6 m/s (250 knots)

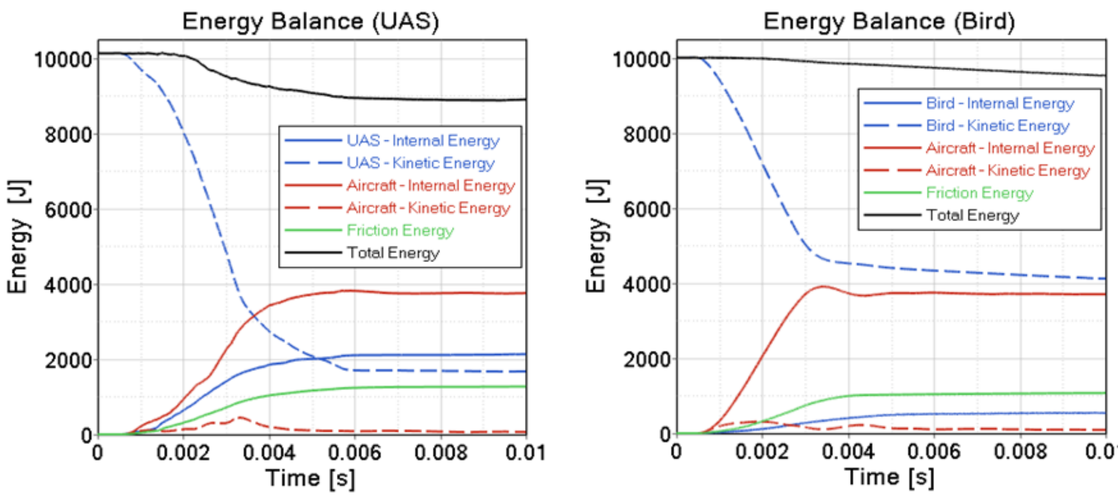

Figure 433 Comparison of the energy balance of the impact between a commercial transport jet wing and a 1.2 kg (2.7 lb) UAS/bird at 128.6 m/s (250 knots)

The impulse for both UAS and bird appear to be of similar magnitude. From the energy balance comparison, it can be observed that the UAS absorbed considerably greater internal energy than the bird. In addition, it is apparent that the residual kinetic energy of the bird after impact was greater than that of the UAS. This is an indication that the kinetic energy of the bird was deflected more efficiently than that of the UAS, for which most of the energy was absorbed in the impact.

E.1.4 Windshield

Impact simulations of a 1.2 kg (2.7 lb) UAS (case CQC1) and a 1.2 kg (2.7 lb) bird (case CB2C1) against a windshield are compared in terms of damage severity and kinematics. The initial conditions were based on the above UAS case, which was identified as the most critical in the baseline simulations (see Section 4.3.4.1). Figure 434 depicts the comparison of the kinematics of the event. Figure 435 shows the comparison of the damage caused to the windshield and surrounding structure.

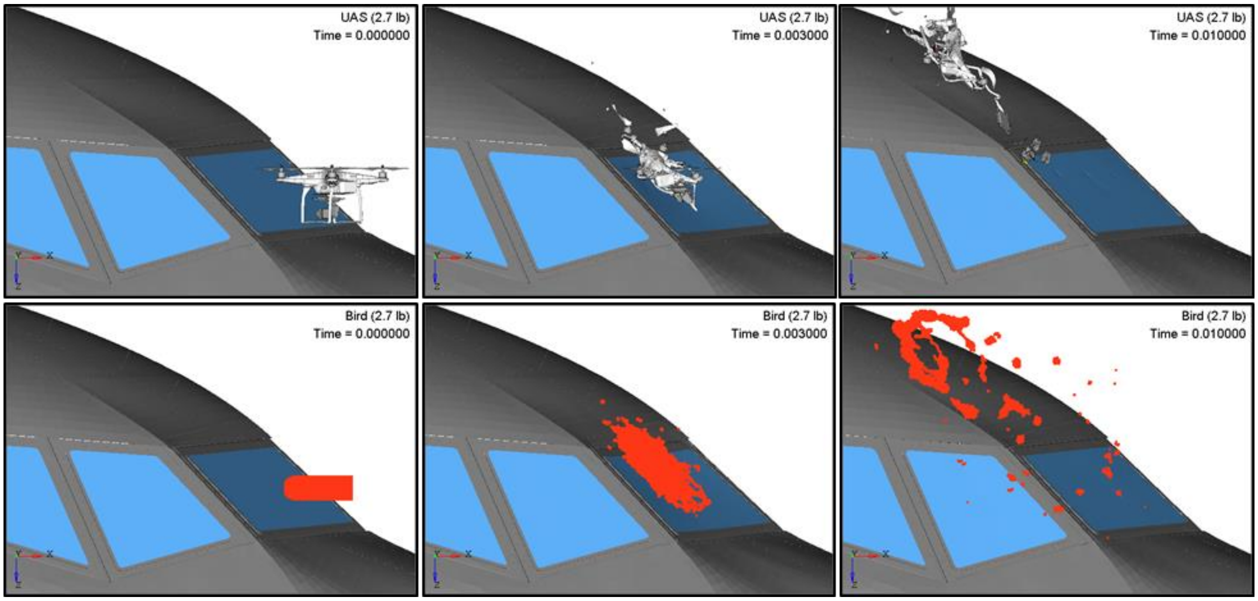

Figure 434.Comparison of the kinematics of impact between a commercial transport jet windshield and a 1.2 kg (2.7 lb) UAS/Bird at 128.6 m/s (250 knots)

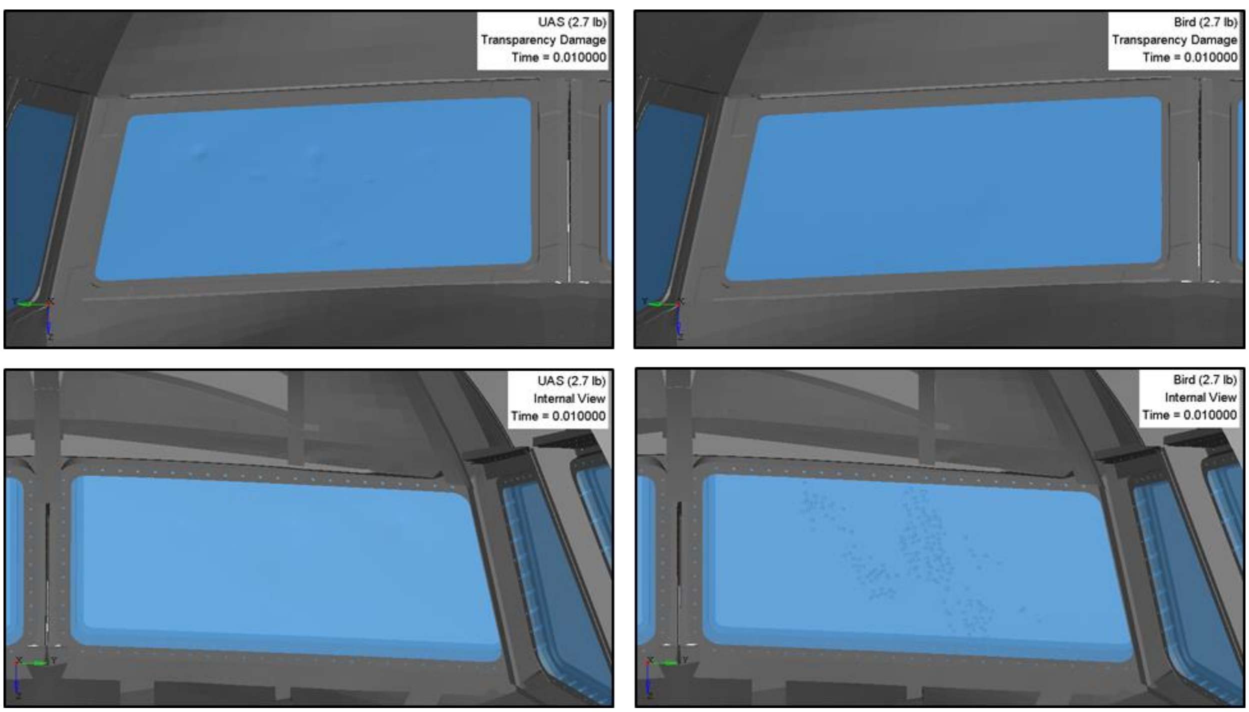

Figure 435 Comparison of external/internal damage sustained by a commercial transport jet windshield impacted with a 1.2 kg (2.7 lb) UAS/Bird at 128.6 m/s (250 knots)

The UAS impacted the windshield, causing noticeable permanent deformations on the transparency and slid over it due to the small windshield angle, whereas the bird also slid over the windshield but without causing any noticeable damage to the transparency. It can also be seen in Figure 435 that amount of damage introduced into the windshield was considerably smaller for the case of bird than the UAS.

The damage introduced by both the UAS and the bird are classified as Level 2. For this case, the UAS impact can be considered of similar severity than the equivalent bird strike in terms of damage.

Figure 436 shows the comparison for the contact force and impulse between the UAS/bird and windshield. Figure 437 shows the energy balance for the impact comparison.

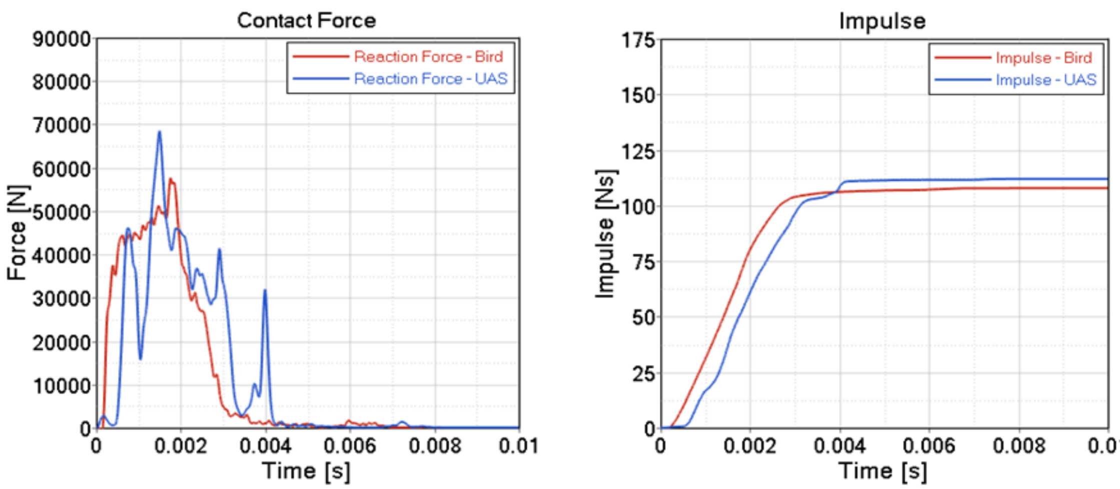

Figure 436 Comparison of the contact force and impulse of the impact between a commercial transport jet windshield and a 1.2 kg (2.7 lb) UAS/bird at 128.6 m/s (250 knots)

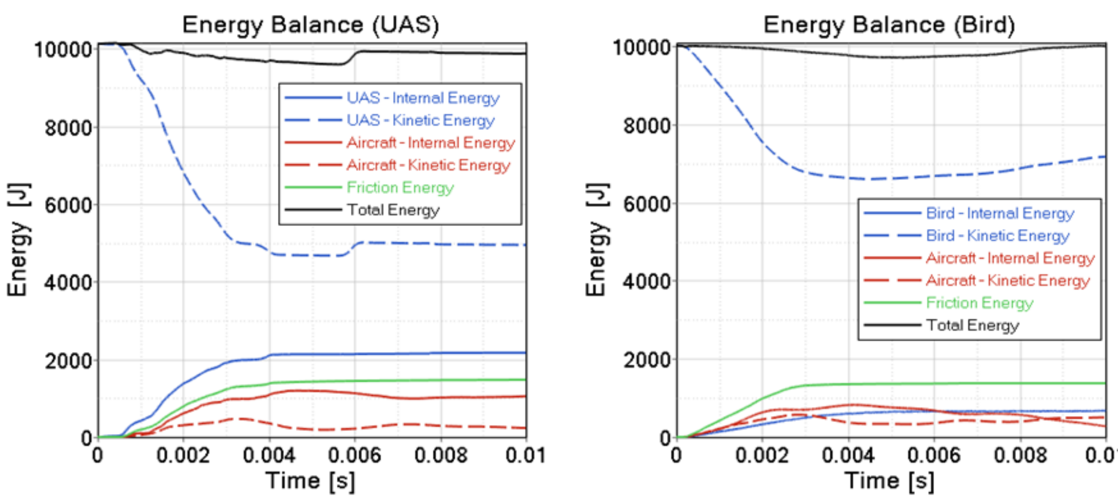

Figure 437 Comparison of the energy balance of the impact between a commercial transport jet windshield and a 1.2 kg (2.7 lb) UAS/bird at 128.6 m/s (250 knots)

The impulse for the UAS was slightly higher than that of the bird. From the energy balance comparison, it can be observed that the UAS absorbed considerably greater internal energy than the bird. In addition, it is apparent that the residual kinetic energy of the bird after impact was greater than that of the UAS. This is an indication that the kinetic energy of the bird was deflected more efficiently than that of the UAS, for which most of the energy was absorbed in the impact.

E.2 BUSINESS JET – UAS VS. BIRD (1.2 KG (2.7 LB))

E.2.1 Vertical Stabilizer

Impact simulations of a 1.2 kg (2.7 lb) UAS (case BQV2) and a 1.2 kg (2.7 lb) bird (case BB2V2) against a vertical stabilizer are compared in terms of damage severity and kinematics. The initial conditions were based on the above UAS case, which was identified as the most critical in the baseline simulations (see Section 4.4.1.1). Figure 438 depicts the comparison of the kinematics of the event. Figure 439 shows the comparison of the damage caused to the skin and the inner structure of the vertical stabilizer.

The UAS damaged the skin, the upper and lower ribs, while the bird damaged the skin to a lesser degree and the upper and lower ribs. It can also be seen in Figure 439 that amount of damage introduced into the skin was considerably smaller for the case of bird than the UAS.

The damage introduced by the UAS is classified as Level 3, whereas the damage introduced by the bird is classified as Level 2. For this case, the UAS impact can be considered as more severe than the equivalent bird strike in terms of damage.

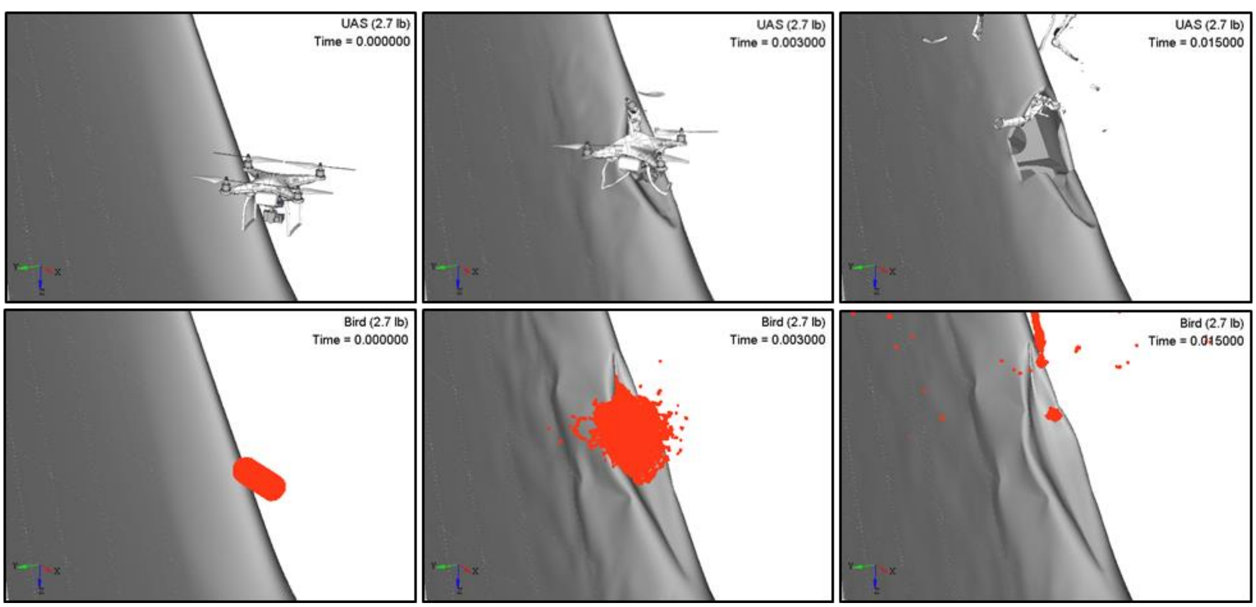

Figure 438.Comparison of the kinematics of impact between a business jet vertical stabilizer and a 1.2 kg (2.7 lb) UAS/Bird at 128.6 m/s (250 knots)

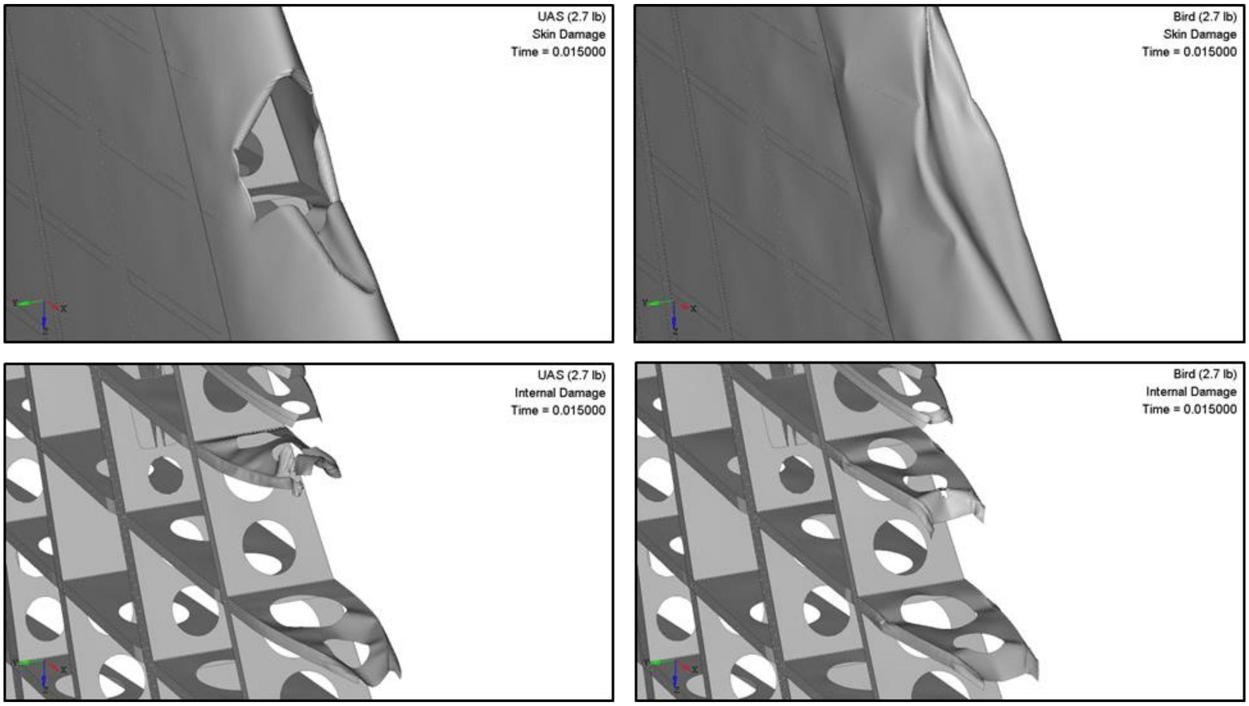

Figure 439 Comparison of external/internal damage sustained by a business jet vertical stabilizer impacted with a 1.2 kg (2.7 lb) UAS/Bird at 128.6 m/s (250 knots)

Figure 440 shows the comparison for the contact force and impulse between the UAS/bird and vertical stabilizer. Figure 441 shows the energy balance for the impact comparison.

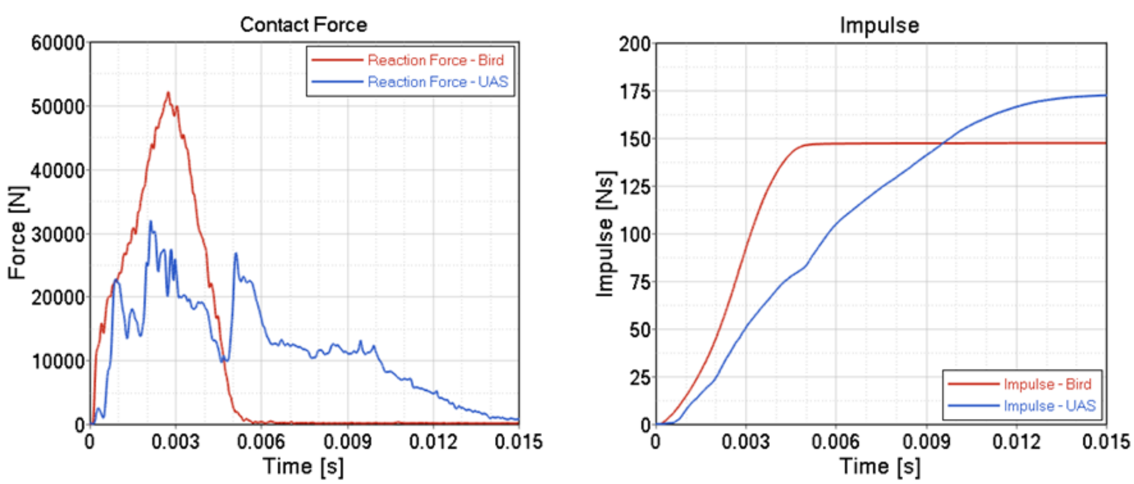

Figure 440 Comparison of the contact force and impulse of the impact between a business jet vertical stabilizer and a 1.2 kg (2.7 lb) UAS/bird at 128.6 m/s (250 knots)

The impulse for the UAS was higher than that of the bird. From the energy balance comparison, it can be observed that the UAS absorbed considerably greater internal energy than the bird. In addition, it is apparent that the residual kinetic energy of the bird after impact was greater than that of the UAS. This is an indication that the kinetic energy of the bird was deflected more efficiently than that of the UAS, for which most of the energy was absorbed in the impact.

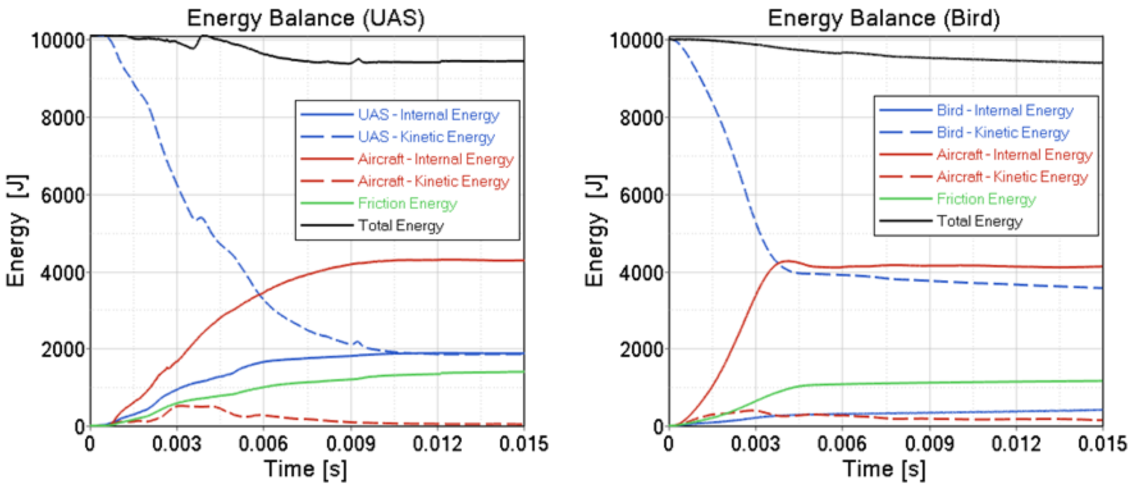

Figure 441 Comparison of the energy balance of the impact between a business jet vertical stabilizer and a 1.2 kg (2.7 lb) UAS/bird at 128.6 m/s (250 knots)

<u>E.2.2 Horizontal Stabilizer</u>

Impact simulations of a 1.2 kg (2.7 lb) UAS (case BQH2) and a 1.2 kg (2.7 lb) bird (case BB2H2) against a horizontal stabilizer are compared in terms of damage severity and kinematics. The initial conditions were based on the above UAS case, which was identified as the most critical in the baseline simulations (see Section 4.4.2.1). Figure 442 depicts the comparison of the kinematics of the event. Figure 443 shows the comparison of the damage caused to the skin and the inner structure of the horizontal stabilizer.

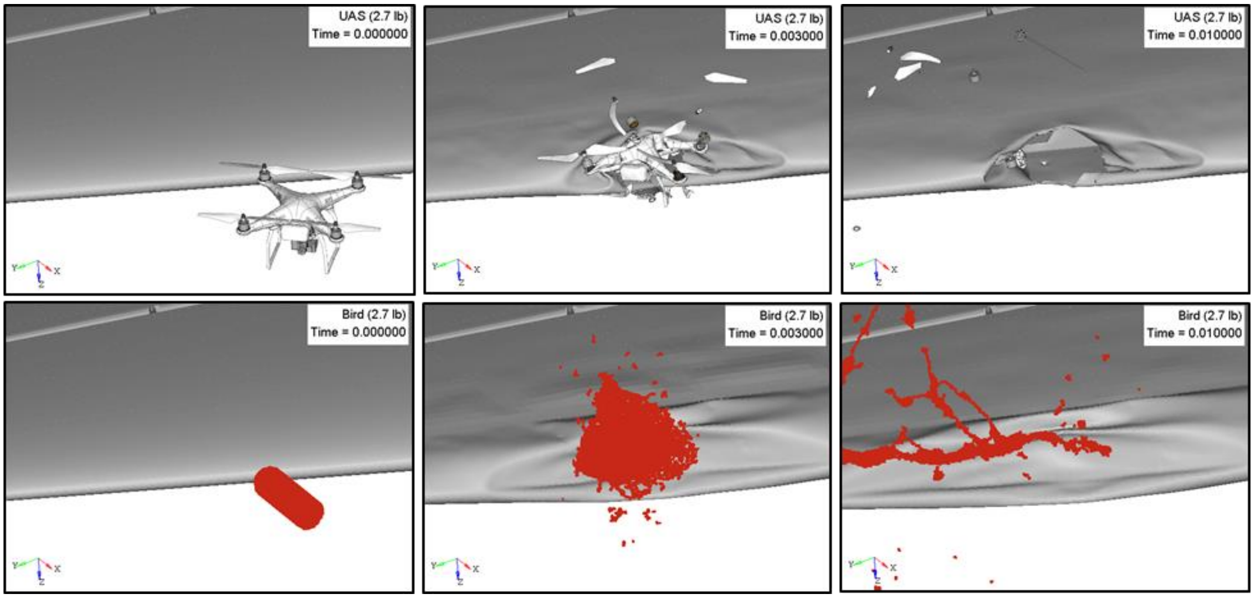

Figure 442.Comparison of the kinematics of impact between a business jet horizontal stabilizer and a 1.2 kg (2.7 lb) UAS/Bird at 128.6 m/s (250 knots)

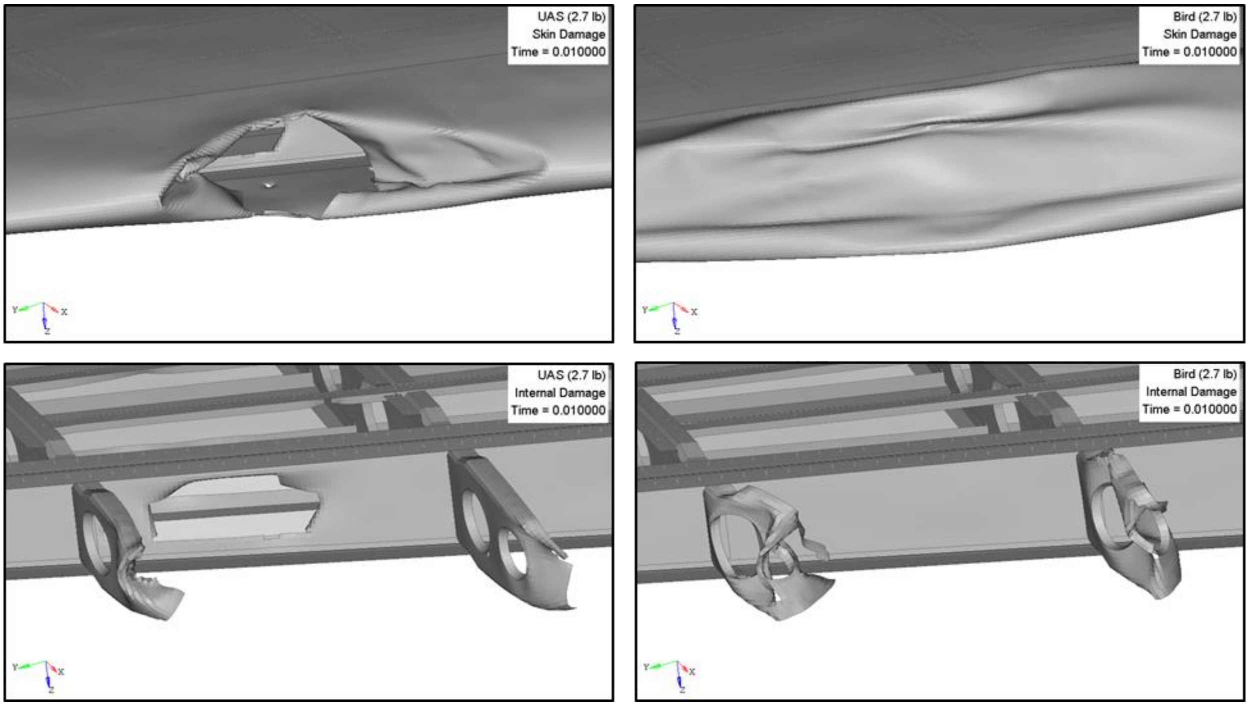

Figure 443 Comparison of external/internal damage sustained by a business jet horizontal stabilizer impacted with a 1.2 kg (2.7 lb) UAS/Bird at 128.6 m/s (250 knots)

Both the UAS and the bird deformed the skin. However, only the UAS penetrates the skin and damages and penetrates the front spar’s web. It can also be seen in Figure 443 that amount of damage introduced into the skin by the bird is more extent in terms of deformed surface.

The damage introduced by the UAS is classified as Level 4, whereas the damage introduced by the bird is classified as Level 2. For this case, the UAS impact can be considered as much more severe than the equivalent bird strike in terms of damage.

Figure 444 shows the comparison for the contact force and impulse between the UAS/bird and horizontal stabilizer. Figure 445 shows the energy balance for the impact comparison.

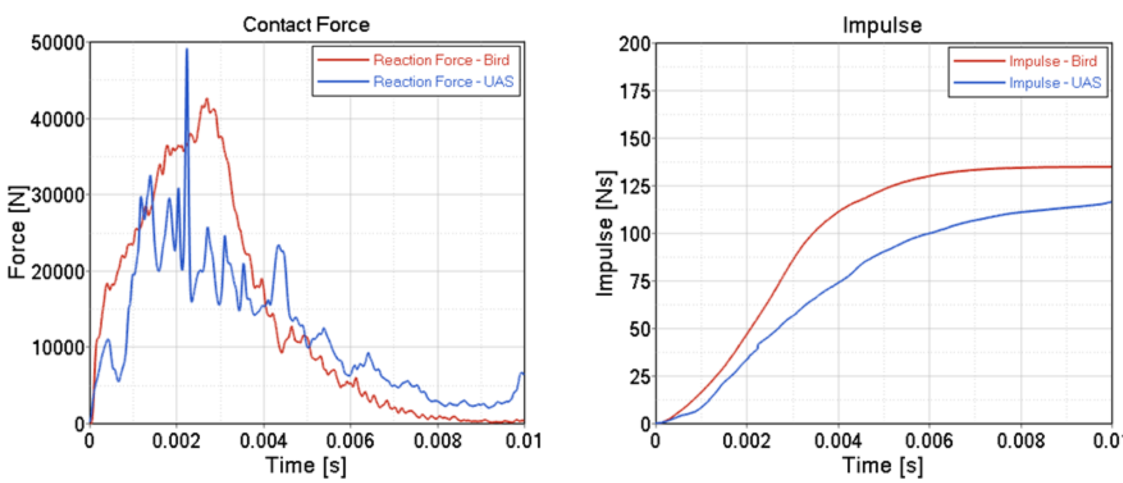

Figure 444 Comparison of the contact force and impulse of the impact between a business jet horizontal stabilizer and a 1.2 kg (2.7 lb) UAS/bird at 128.6 m/s (250 knots)

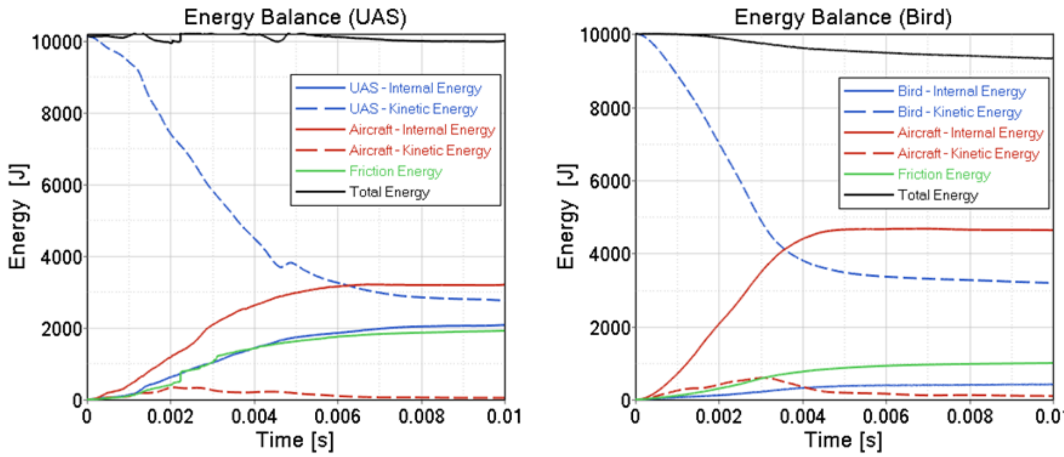

Figure 445. Comparison of the energy balance of the impact between a business jet horizontal stabilizer and a 1.2 kg (2.7 lb) UAS/bird at 128.6 m/s (250 knots)

The impulse for the bird was higher than that of the UAS. From the energy balance comparison, it can be observed that the UAS absorbed considerably greater internal energy than the bird. In addition, it is apparent that the residual kinetic energy of both the UAS and the bird after impact were of similar magnitude.

E.2.3 Wing Leading Edge

Impact simulations of a 1.2 kg (2.7 lb) UAS (case BQW1) and a 1.2 kg (2.7 lb) bird (case BB2W1) against the leading edge of a wing are compared in terms of damage severity and kinematics. The initial conditions were based on the above UAS case, which was identified as the most critical in the baseline simulations (see Section 4.4.3.1). Figure 446 depicts the comparison of the kinematics of the event. Figure 447 shows the comparison of the damage caused to the skin and the inner structure of the wing.

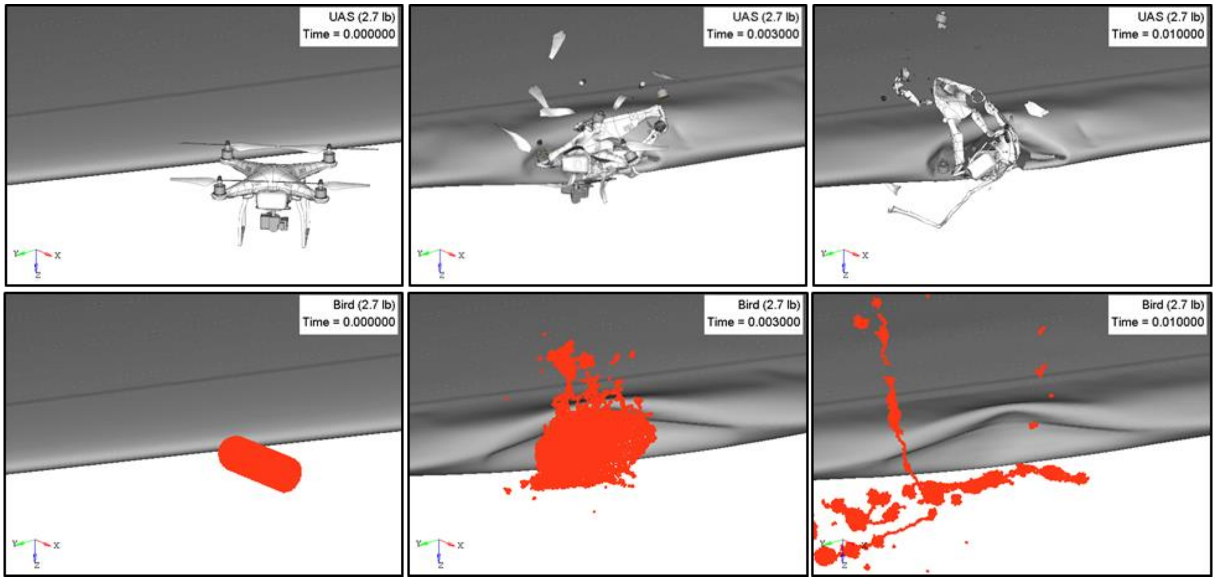

Figure 446. Comparison of the kinematics of impact between a business jet wing and a 1.2 kg (2.7 lb) UAS/Bird at 128.6 m/s (250 knots)

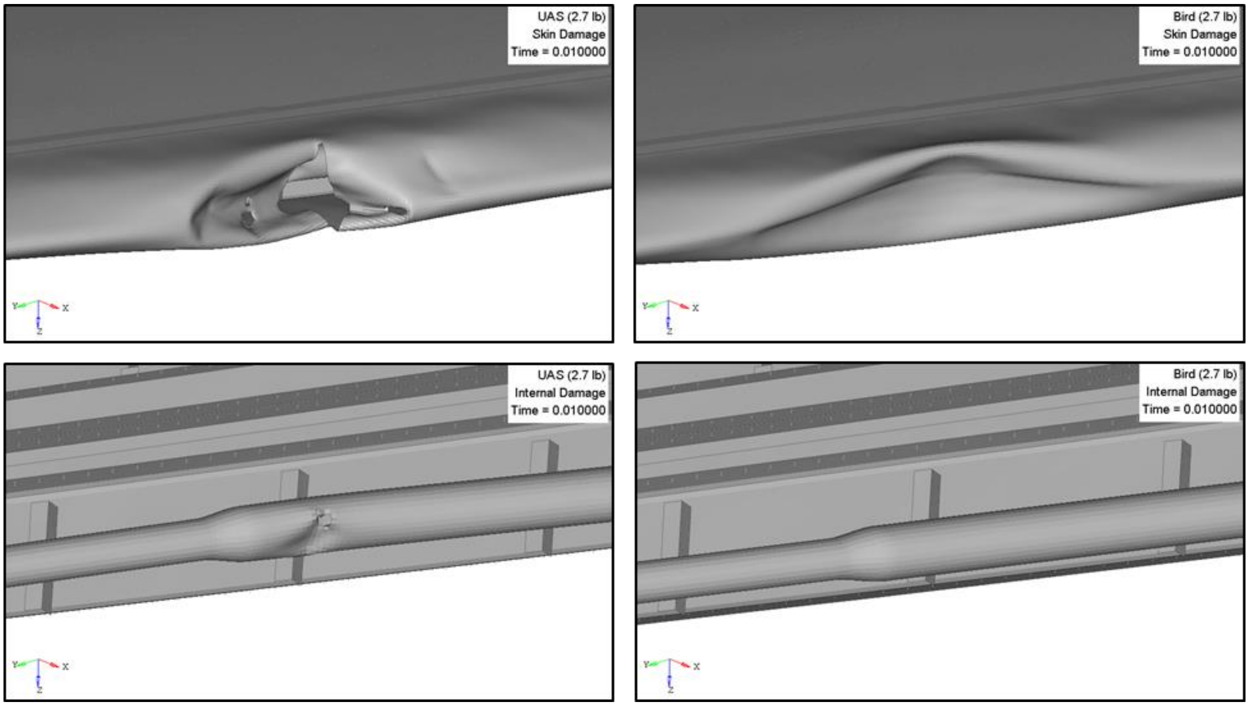

Figure 447. Comparison of external/internal damage sustained by a business jet wing impacted with a 1.2 kg (2.7 lb) UAS/Bird at 128.6 m/s (250 knots)

The UAS damaged the skin and the anti-ice tube while the bird damaged just the skin to a lesser degree. It can also be seen in Figure 447 that amount of damage introduced into the skin was considerably smaller for the case of bird than the UAS. The damage introduced by the UAS is classified as Level 3 with a risk of fire due to the battery, whereas the damage introduced by the bird is classified as Level 2. For this case, the UAS impact can be considered as more severe than the equivalent bird strike in terms of damage.

Figure 448 shows the comparison for the contact force and impulse between the UAS/bird and wing. Figure 449 shows the energy balance for the impact comparison. The impulse for the UAS was slightly higher than that of the bird.

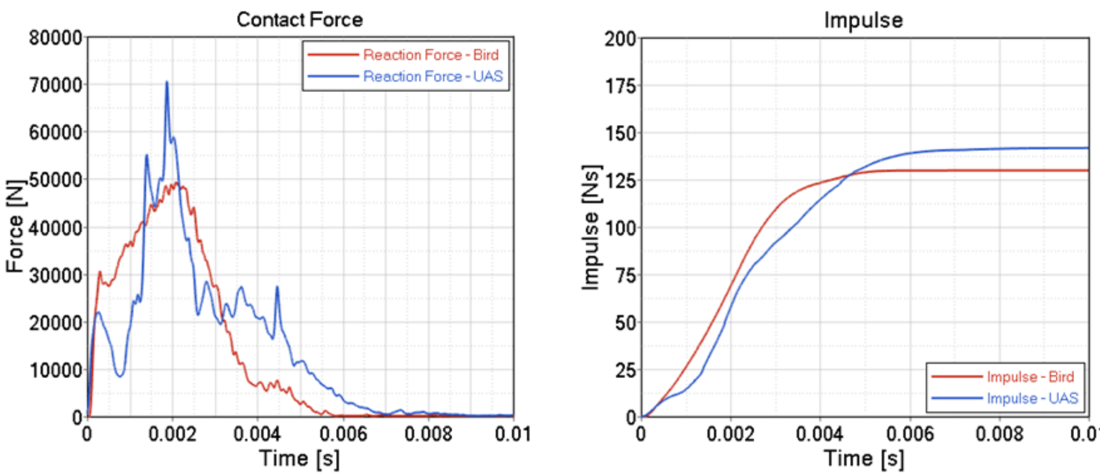

Figure 448 Comparison of the contact force and impulse of the impact between a business jet wing and a 1.2 kg (2.7 lb) UAS/bird at 128.6 m/s (250 knots)

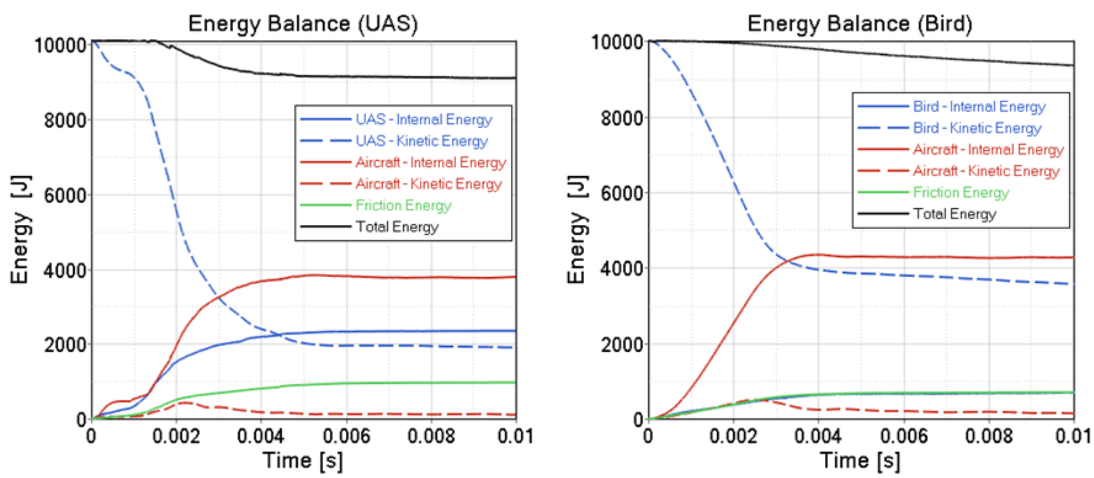

Figure 449 Comparison of the energy balance of the impact between a business jet wing and a 1.2 kg (2.7 lb) UAS/bird at 128.6 m/s (250 knots)

From the energy balance comparison, it can be observed that the UAS absorbed considerably greater internal energy than the bird. In addition, it is apparent that the residual kinetic energy of the bird after impact was greater than that of the UAS. This is an indication that the kinetic energy of the bird was deflected more efficiently than that of the UAS, for which most of the energy was absorbed in the impact.

E.2.4 Windshield

Impact simulations of a 1.2 kg (2.7 lb) UAS (case BQC1) and a 1.2 kg (2.7 lb) bird (case BB2C1) against a windshield are compared in terms of damage severity and kinematics. The initial conditions were based on the above UAS case, which was identified as the most critical in the baseline simulations (see Section 4.4.4.1). Figure 450 depicts the comparison of the kinematics of the event. Figure 451 shows the comparison of the damage caused to the windshield sub-assembly.

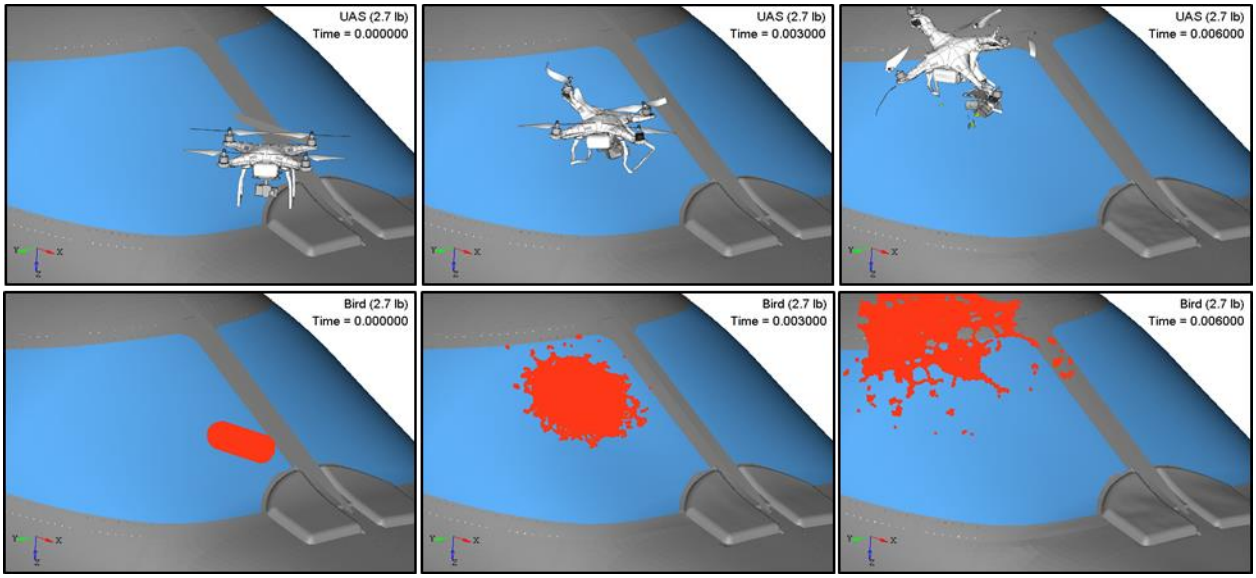

Figure 450.Comparison of the kinematics of impact between a business jet windshield and a 1.2 kg (2.7 lb) UAS/Bird at 128.6 m/s (250 knots)

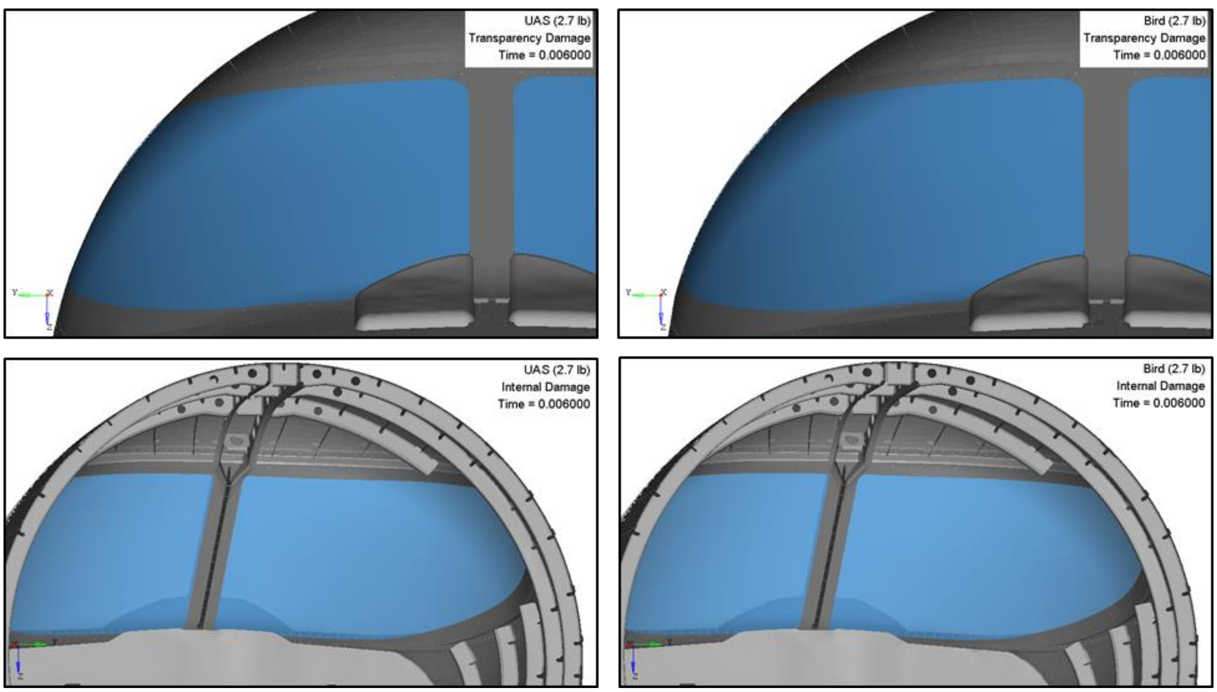

Figure 451 Comparison of external/internal damage sustained by a business jet windshield impacted with a 1.2 kg (2.7 lb) UAS/Bird at 128.6 m/s (250 knots)

Both the UAS and the bird impacted the windshield on the transparency and slid over it without causing noticeable permanent deformations to the transparency. It can also be seen in Figure 451 that amount of damage introduced into the windshield was negligible for both the bird and the UAS. The damage introduced by the UAS is classified as Level 2, while the bird is classified as Level 1. For this case, the UAS impact can be considered as more severe than the bird strike in terms of damage.

Figure 452 shows the comparison for the contact force and impulse between the UAS/bird and windshield. Figure 453 shows the energy balance for the impact comparison.

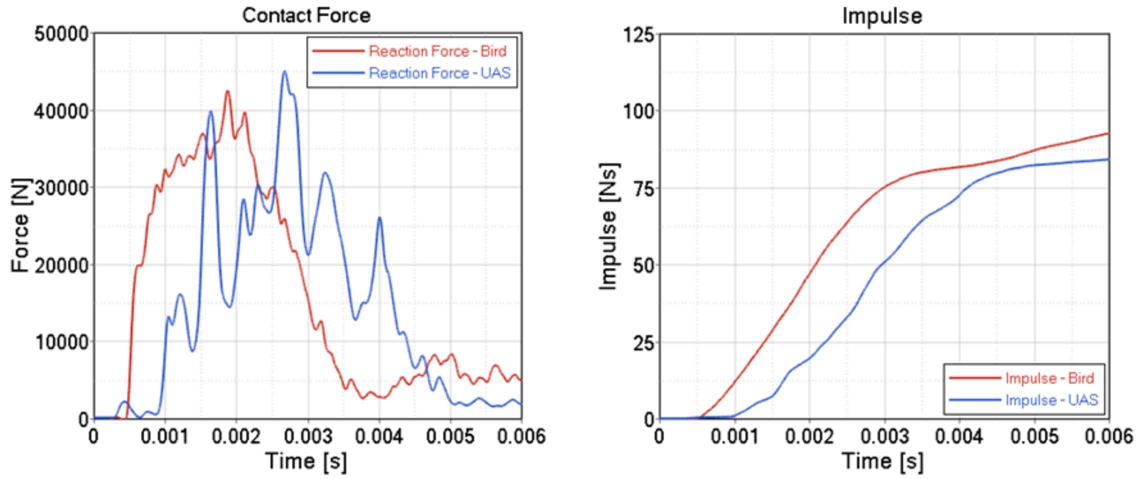

Figure 452 Comparison of the contact force and impulse of the impact between a business jet windshield and a 1.2 kg (2.7 lb) UAS/bird at 128.6 m/s (250 knots)

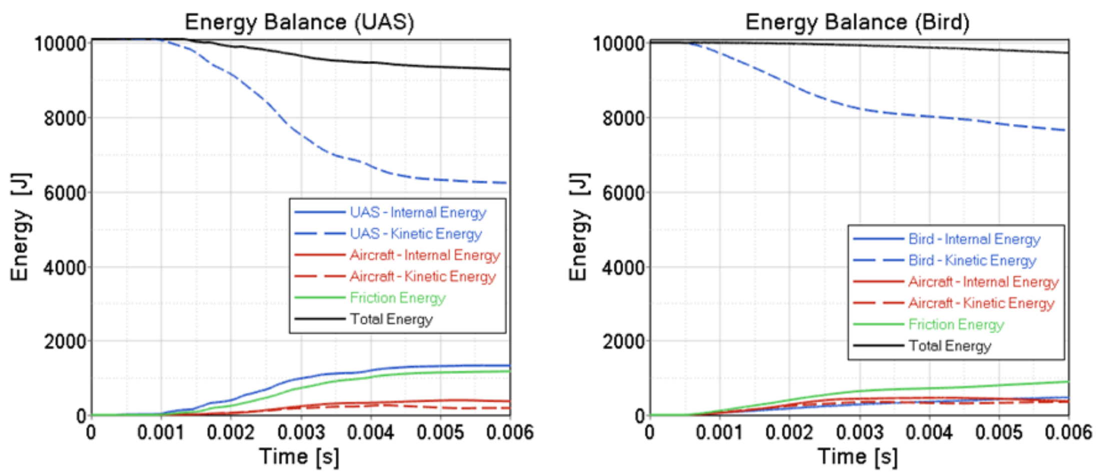

Figure 453 Comparison of the energy balance of the impact between a business jet windshield and a 1.2 kg (2.7 lb) UAS/bird at 128.6 m/s (250 knots)

The impulse for the bird was higher than that of the UAS. From the energy balance comparison, it can be observed that the UAS absorbed considerably greater internal energy than the bird. In addition, it is apparent that the residual kinetic energy of the bird after impact was greater than that of the UAS. This is an indication that the kinetic energy of the bird was deflected more efficiently than that of the UAS, for which most of the energy was absorbed in the impact.

E.3 TRANSPORT JET – UAS VS. BIRD (4.0 LB)

E.3.1 Vertical Stabilizer

Impact simulations of a 1.8 kg (4.0 lb) UAS (case CQsV3) and a 1.8 kg (4.0 lb) bird (case CB4V3) against a vertical stabilizer are compared in terms of damage severity and kinematics. The initial conditions were based on the most critical case (CQV3) identified in the baseline simulations (see

Section 4.3.1.1). Figure 454 depicts the comparison of the kinematics of the event. Figure 455 shows the comparison of the damage caused to the skin and inner structure of the vertical stabilizer.

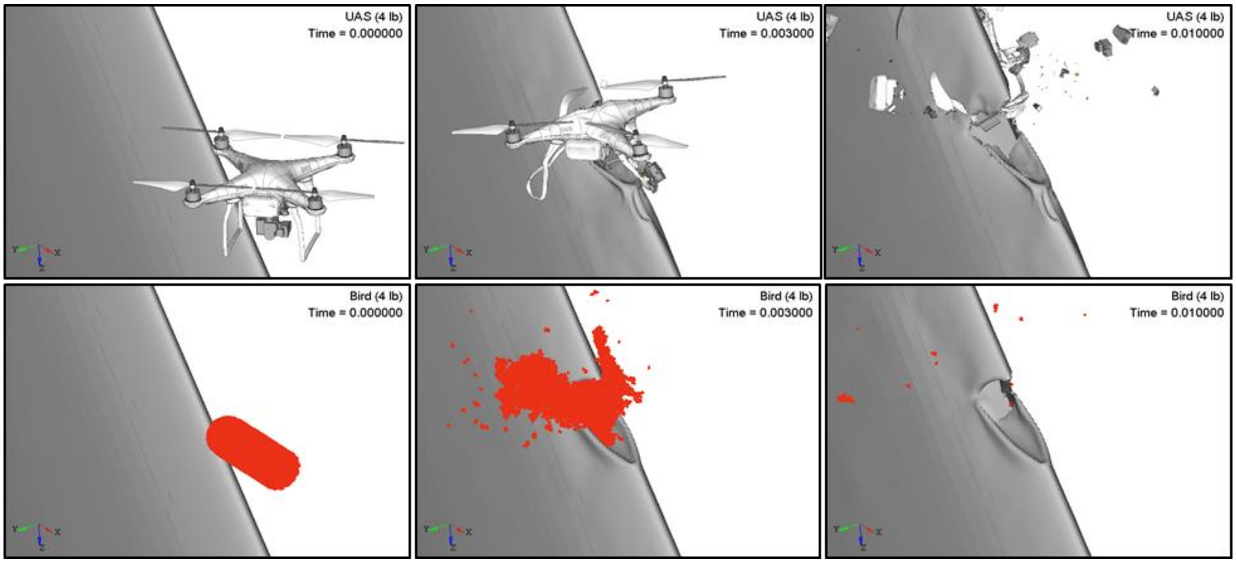

Figure 454.Comparison of the kinematics of impact between a commercial transport jet vertical stabilizer and a 1.8 kg (4.0 lb) UAS/Bird at 128.6 m/s (250 knots)

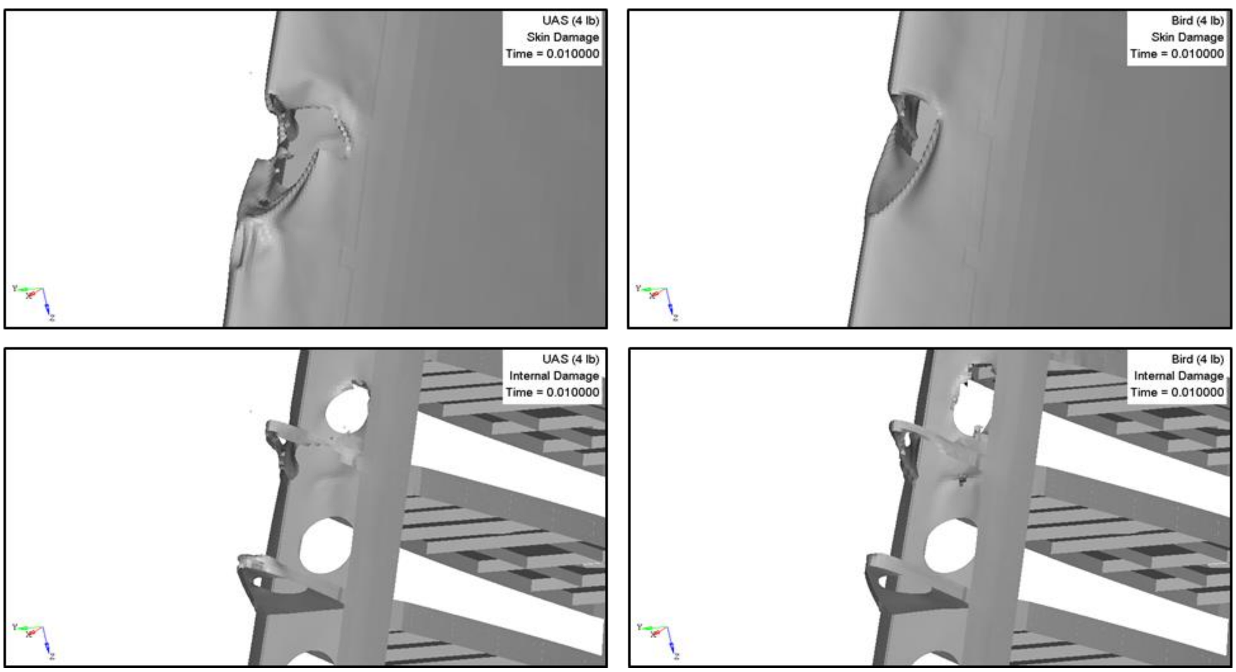

Figure 455 Comparison of external/internal damage sustained by a commercial transport jet vertical stabilizer impacted with a 1.8 kg (4.0 lb) UAS/Bird at 128.6 m/s (250 knots)

The UAS damaged the skin, the upper and lower ribs, and the lightening hole above the impact location in the forward spar while the bird damaged the skin and forward spar to a lesser degree and just the upper rib. It can also be seen in Figure 455 that amount of damage introduced into the skin was considerably smaller for the case of bird than the UAS. The damage introduced by the UAS is classified as Level 3, whereas the damage introduced by the bird is classified as Level 3.

For this case, the UAS impact can be considered as more severe than the equivalent bird strike in terms of damage.

Figure 456 shows the comparison for the contact force and impulse between the UAS/bird and vertical stabilizer. Figure 457 shows the energy balance for the impact comparison.

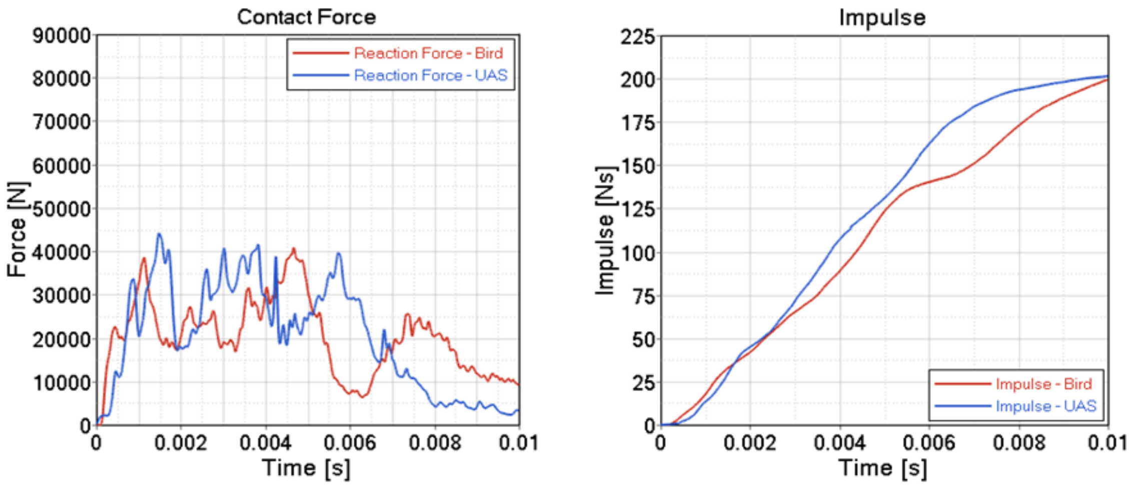

Figure 456 Comparison of the contact force and impulse of the impact between a commercial transport jet vertical stabilizer and a 1.8 kg (4.0 lb) UAS/bird at 128.6 m/s (250 knots)

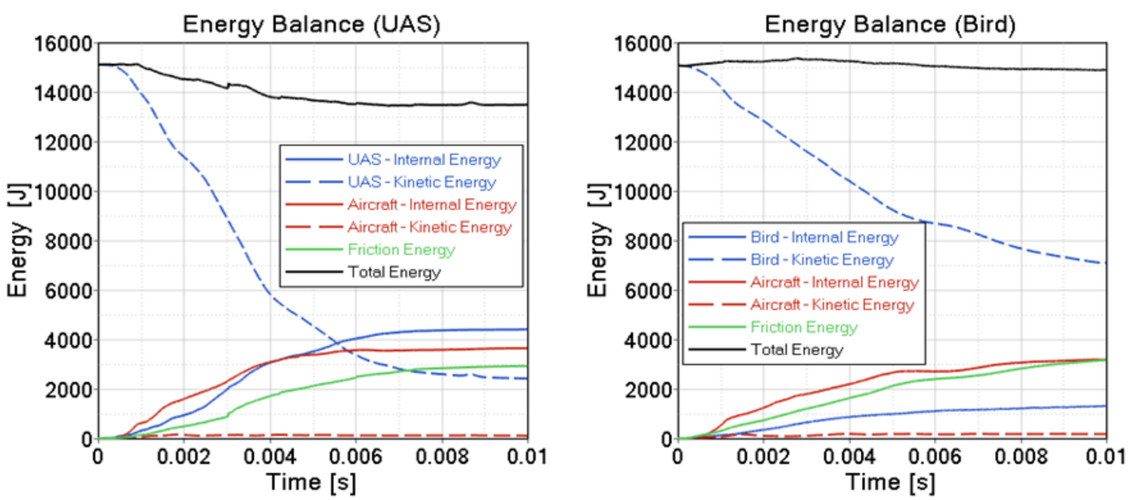

Figure 457 Comparison of the energy balance of the impact between a commercial transport jet vertical stabilizer and a 1.8 kg (4.0 lb) UAS/bird at 128.6 m/s (250 knots)

The impulse for both UAS and bird appear to be of similar magnitude. From the energy balance comparison, it can be observed that the UAS absorbed considerably greater internal energy than the bird. In addition, it is apparent that the residual kinetic energy of the bird after impact was greater than that of the UAS. This is an indication that the kinetic energy of the bird was deflected more efficiently than that of the UAS, for which most of the energy was absorbed in the impact.

E.3.2 Horizontal Stabilizer

Impact simulations of a 1.8 kg (4.0 lb) UAS (case CQsH3) and a 1.8 kg (4.0 lb) bird (case CB4H3) against a horizontal stabilizer are compared in terms of damage severity and kinematics. The initial conditions were based on the most critical case (CQH3) identified in the baseline simulations (see Section 4.3.2.1). Figure 458 depicts the comparison of the kinematics of the event. Figure 459 shows the comparison of the damage caused to the skin and the inner structure of the horizontal stabilizer.

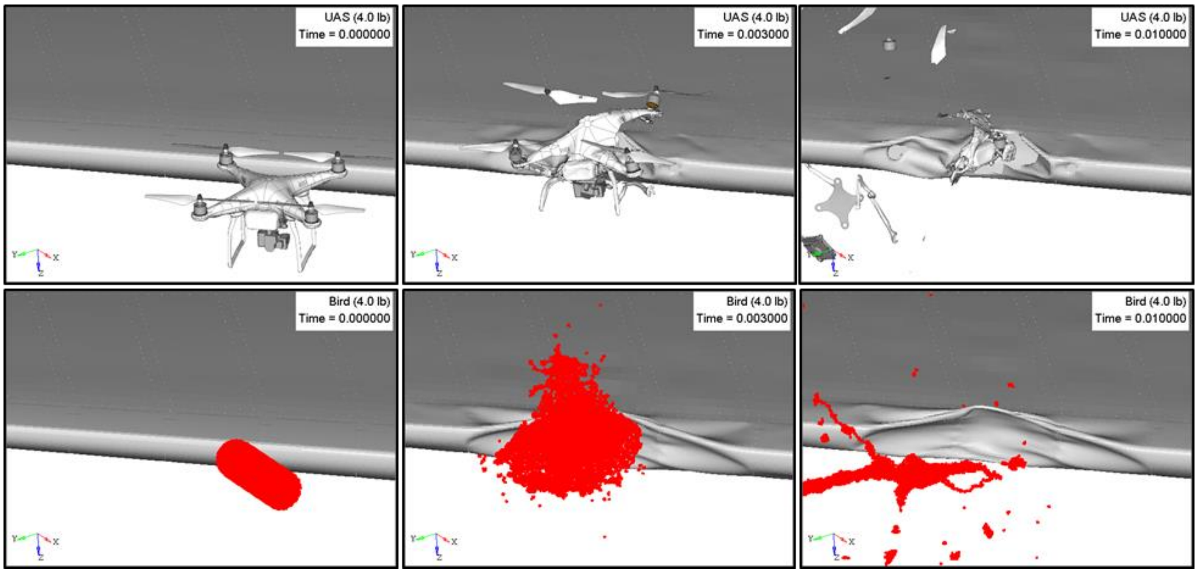

Figure 458.Comparison of the kinematics of impact between a commercial transport jet horizontal stabilizer and a 1.8 kg (4.0 lb) UAS/Bird at 128.6 m/s (250 knots)

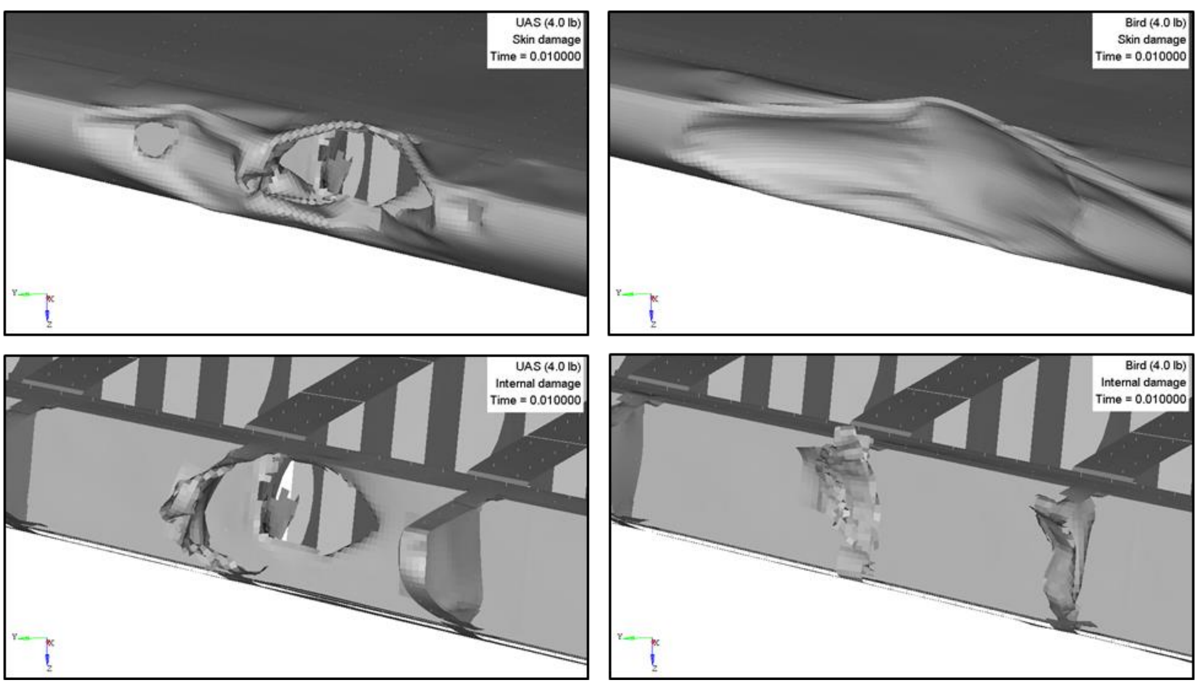

Figure 459 Comparison of external/internal damage sustained by a commercial transport jet horizontal stabilizer impacted with a 1.8 kg (4.0 lb) UAS/Bird at 128.6 m/s (250 knots)

The UAS damaged the skin, the left nose rib, and the sub spar while the bird damaged the skin to a lesser degree and both the nose ribs. It can also be seen in Figure 459 that amount of damage introduced into the skin was considerably smaller for the case of bird than the UAS. The damage introduced by the UAS is classified as Level 4 with a risk of fire due to the battery, whereas the damage introduced by the bird is classified as Level 2. For this case, the UAS impact can be considered as more severe than the equivalent bird strike in terms of damage.

Figure 460 shows the comparison for the contact force and impulse between the UAS/bird and horizontal stabilizer. Figure 461 shows the energy balance for the impact comparison.

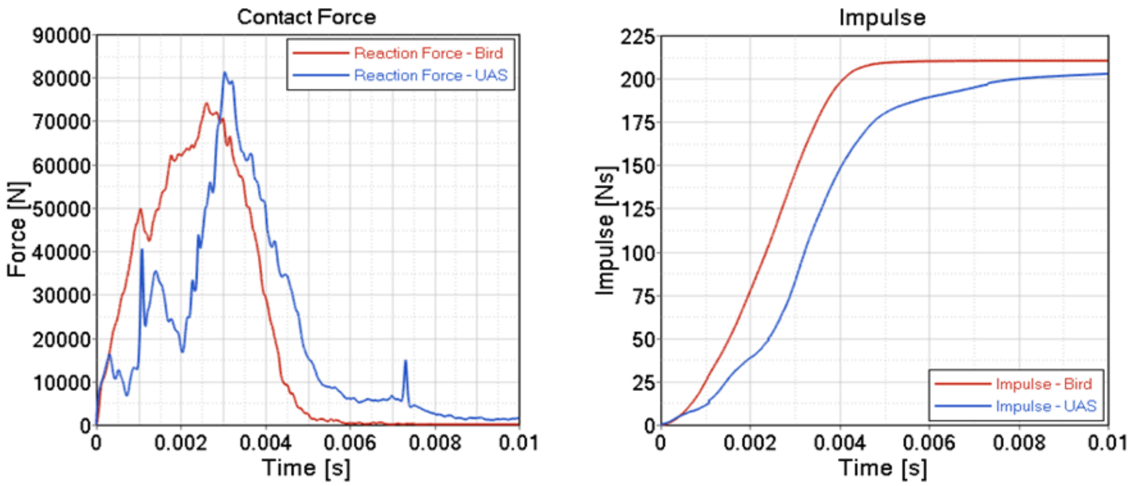

Figure 460 Comparison of the contact force and impulse of the impact between a commercial transport jet horizontal stabilizer and a 1.8 kg (4.0 lb) UAS/bird at 128.6 m/s (250 knots)

The impulse for the bird was slightly higher than that of the UAS. From the energy balance comparison, it can be observed that the UAS absorbed considerably greater internal energy than the bird. In addition, it is apparent that the residual kinetic energy of the bird after impact was greater than that of the UAS. This is an indication that the kinetic energy of the bird was deflected more efficiently than that of the UAS.

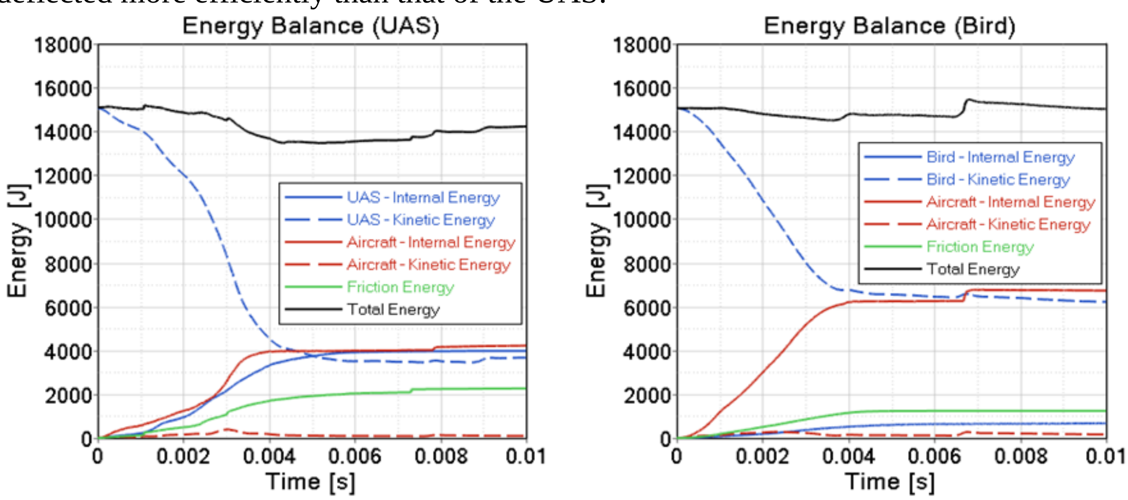

Figure 461. Comparison of the energy balance of the impact between a commercial transport jet horizontal stabilizer and a 1.8 kg (4.0 lb) UAS/bird at 128.6 m/s (250 knots)

E.3.3 Wing Leading Edge

Impact simulations of 1.8 kg (4.0 lb) UAS (case CQsW1) and bird (case CB4W1) against the leading edge of a wing are compared in terms of damage severity and kinematics. The initial conditions were based on the most critical case (CQW1) identified in the baseline simulations (see Section 4.3.3.1). Figure 462 depicts the comparison of the kinematics of the event. Figure 463 shows the comparison of the damage caused to the skin and inner structure of the wing.

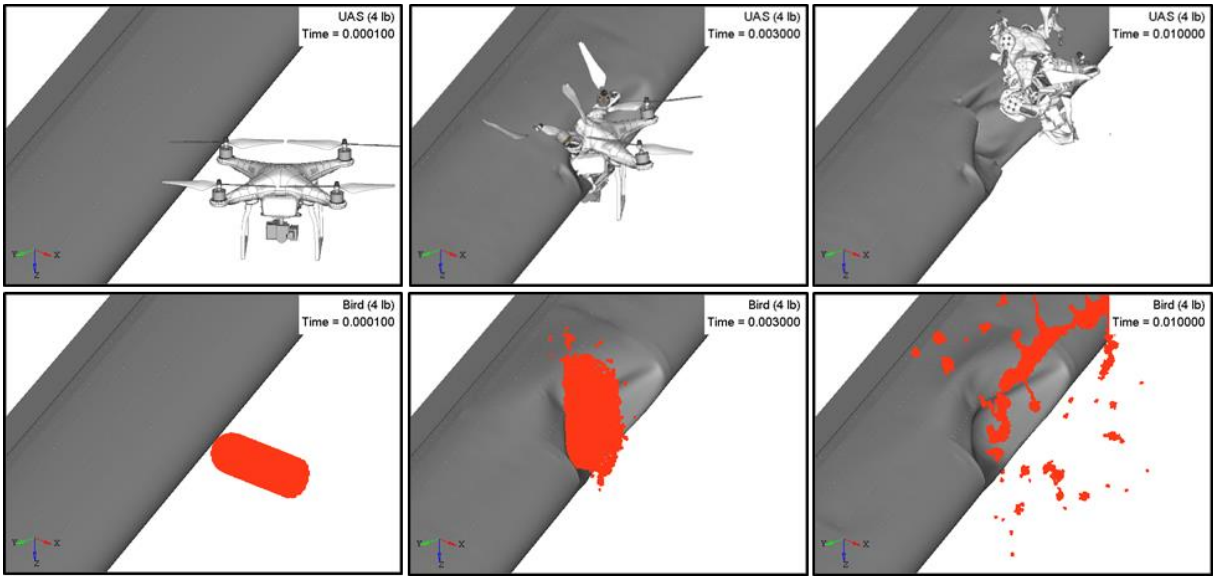

Figure 462. Comparison of the kinematics of impact between a commercial transport jet wing and a 1.8 kg (4.0 lb) UAS/Bird at 128.6 m/s (250 knots)

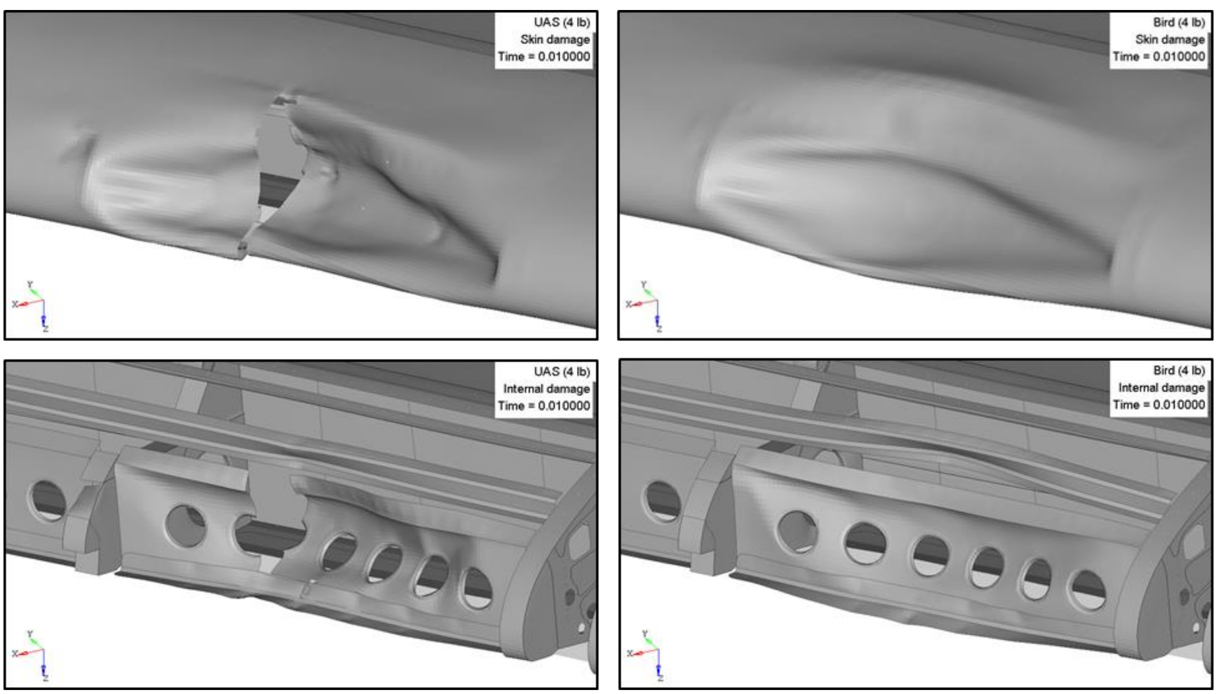

Figure 463. Comparison of external/internal damage sustained by a commercial transport jet wing impacted with a 1.8 kg (4.0 lb) UAS/Bird at 128.6 m/s (250 knots)

The UAS damaged the skin and the front spar while the bird damaged the skin to a lesser degree. It can also be seen in Figure 463 that amount of damage introduced into the skin was considerably smaller for the case of bird than the UAS. The damage introduced by the UAS is classified as Level 3 with a risk of fire due to the battery, whereas the damage introduced by the bird is classified as Level 2. For this case, the UAS impact can be considered as more severe than the equivalent bird strike in terms of damage.

Figure 464 shows the comparison for the contact force and impulse between the UAS/bird and wing. Figure 465 shows the energy balance for the impact comparison.

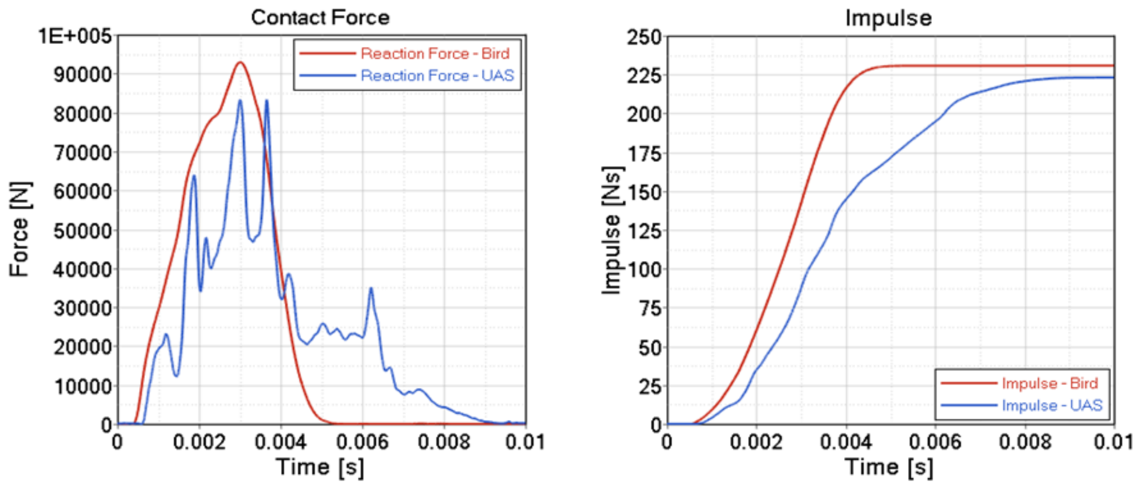

Figure 464 Comparison of the contact force and impulse of the impact between a commercial transport jet wing and a 1.8 kg (4.0 lb) UAS/bird at 128.6 m/s (250 knots)

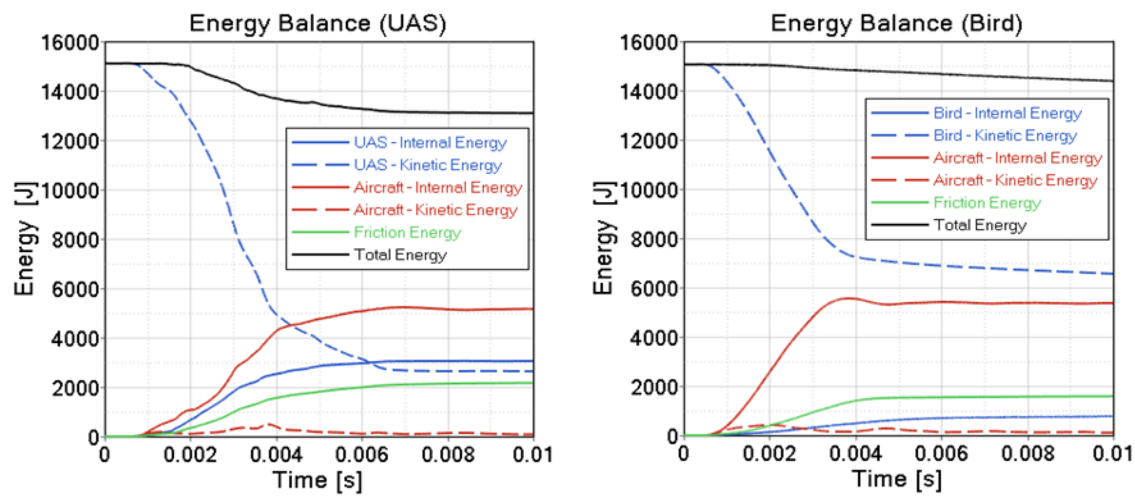

Figure 465 Comparison of the energy balance of the impact between a commercial transport jet wing and a 1.8 kg (4.0 lb) UAS/bird at 128.6 m/s (250 knots)

The impulse for the bird was slightly higher than that of the UAS. From the energy balance comparison, it can be observed that the UAS absorbed considerably greater internal energy than the bird. In addition, it is apparent that the residual kinetic energy of the bird after impact was greater than that of the UAS. This is an indication that the kinetic energy of the bird was deflected more efficiently than that of the UAS.

E.3.4 Windshield

Impact simulations of a 1.8 kg (4.0 lb) UAS (case CQsC1) and a 1.8 kg (4.0 lb) bird (case CB4C1) against a windshield are compared in terms of damage severity and kinematics. The initial conditions were based on the most critical case (CQC1) identified in the baseline simulations (see Section 4.3.4.1). Figure 466 depicts the comparison of the kinematics of the event. Figure 467 shows the comparison of the damage caused to the windshield and surrounding structure.

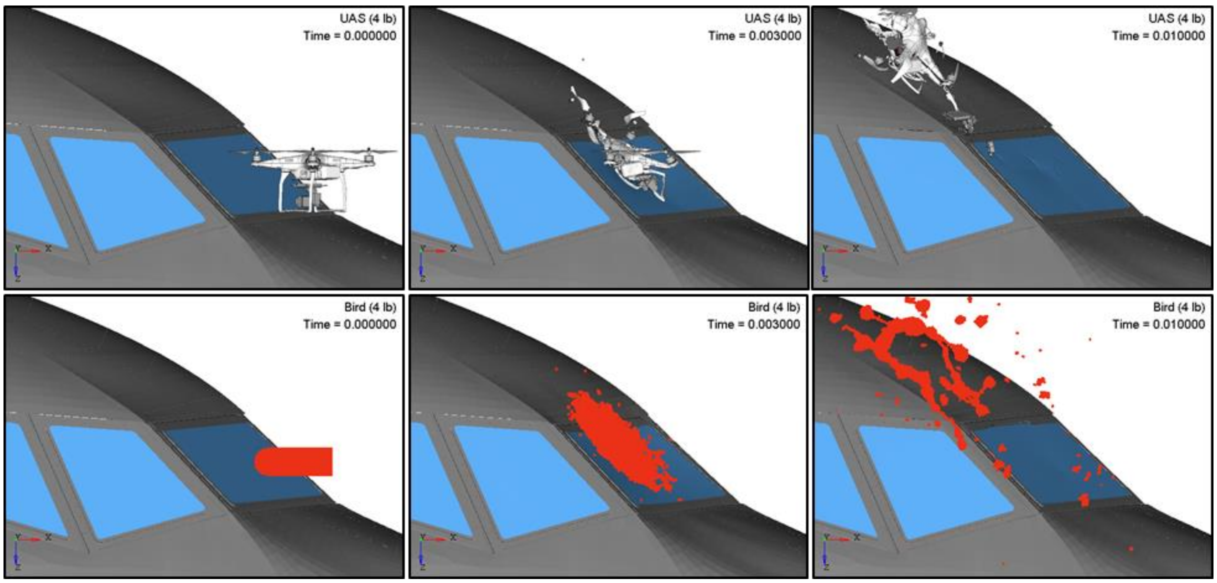

Figure 466.Comparison of the kinematics of impact between a commercial transport jet windshield and a 1.8 kg (4.0 lb) UAS/Bird at 128.6 m/s (250 knots)

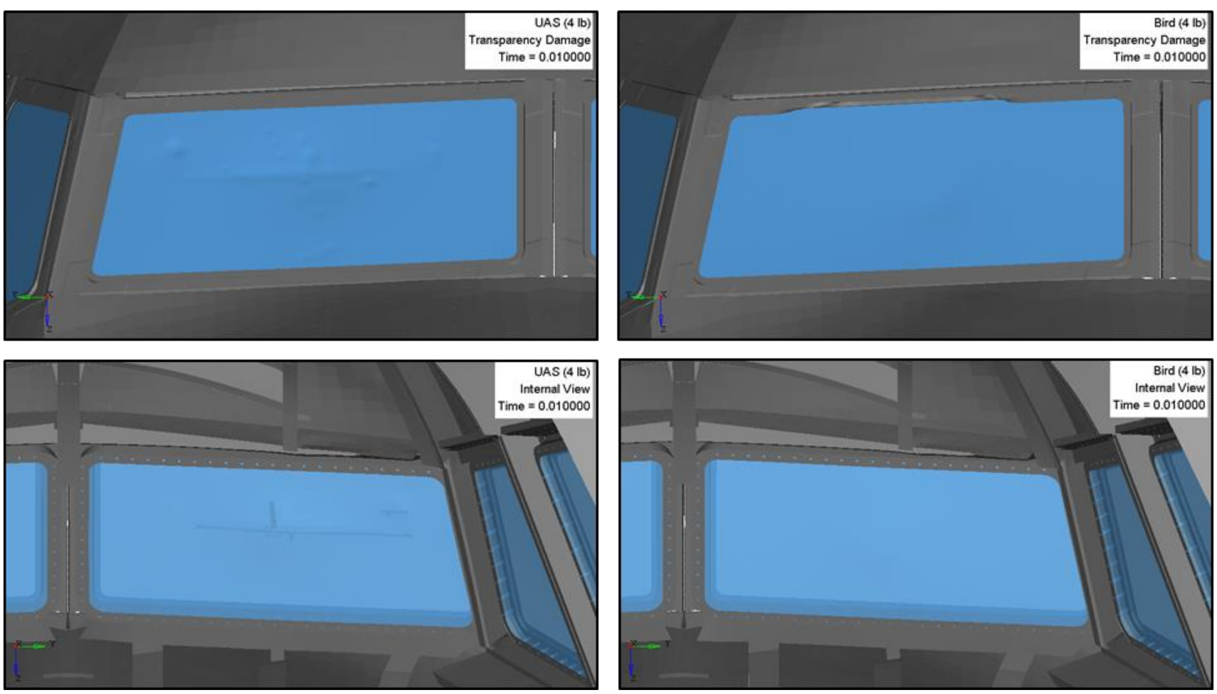

Figure 467 Comparison of external/internal damage sustained by a commercial transport jet windshield impacted with a 1.8 kg (4.0 lb) UAS/Bird at 128.6 m/s (250 knots)

The UAS impacted the windshield, causing noticeable permanent deformations on the transparency and slid over it due to the small windshield angle, whereas the bird also slid over the windshield but without causing any noticeable damage to the transparency. It can also be seen in Figure 467 that amount of damage introduced into the windshield was considerably smaller for the case of bird than the UAS. The damage introduced by the UAS is classified as Level 3, whereas the damage introduced by the bird is classified as Level 2. For this case, the UAS impact can be considered as more severe than the equivalent bird strike in terms of damage.

Figure 468 shows the comparison for the contact force and impulse between the UAS/bird and windshield. Figure 469 shows the energy balance for the impact comparison.

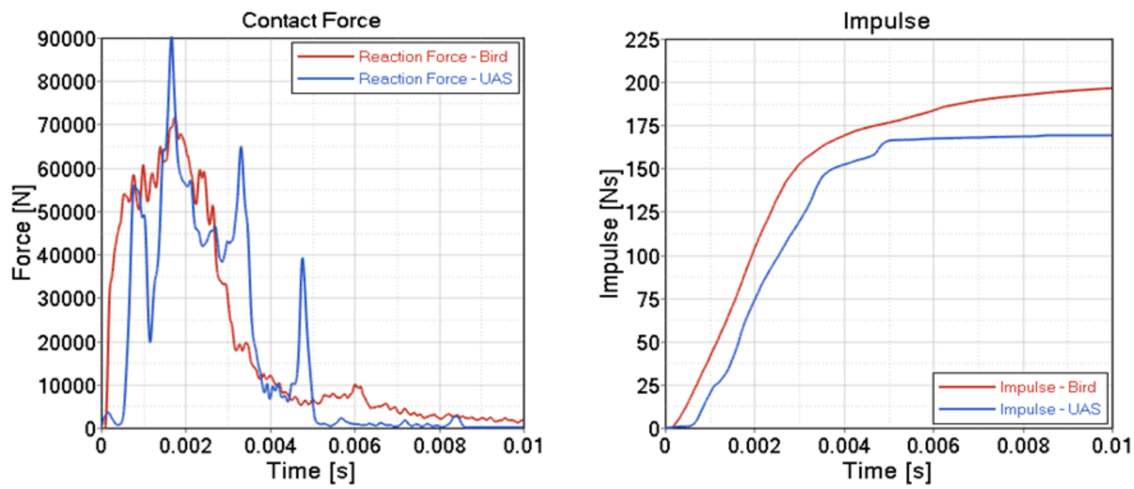

Figure 468 Comparison of the contact force and impulse of the impact between a commercial transport jet windshield and a 1.8 kg (4.0 lb) UAS/bird at 128.6 m/s (250 knots)

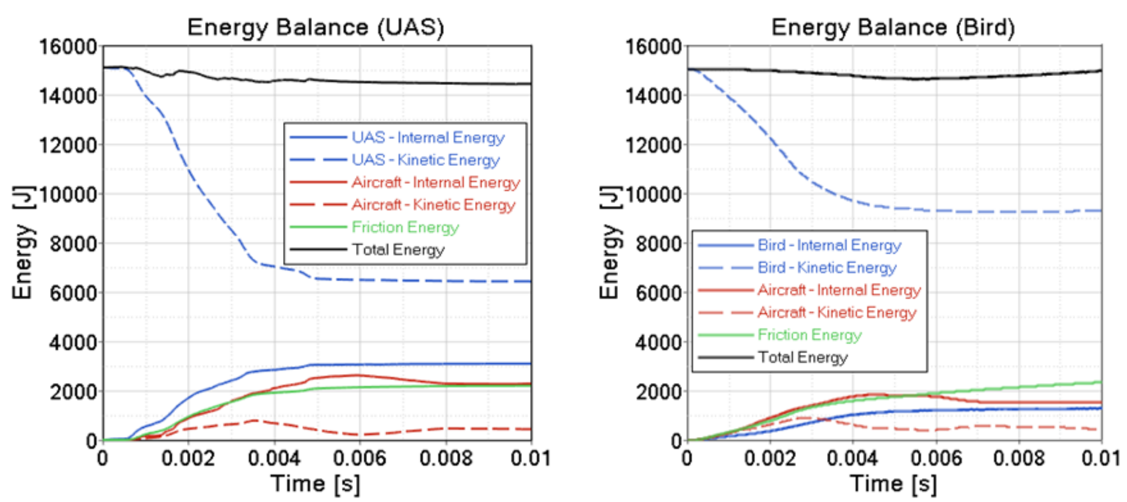

Figure 469 Comparison of the energy balance of the impact between a commercial transport jet windshield and a 1.8 kg (4.0 lb) UAS/bird at 128.6 m/s (250 knots)

The impulse for the bird was slightly higher than that of the UAS. From the energy balance comparison, it can be observed that the UAS absorbed considerably greater internal energy than the bird. In addition, it is apparent that the residual kinetic energy of the bird after impact was greater than that of the UAS. This is an indication that the kinetic energy of the bird was deflected more efficiently than that of the UAS, for which most of the energy was absorbed in the impact.

E.4 BUSINESS JET – UAS VS. BIRD (1.8 KG (4.0 LB))

E.4.1 Vertical Stabilizer

Impact simulations of a 1.8 kg (4.0 lb) UAS (case BQsV2) and a 1.8 kg (4.0 lb) bird (case BB4V2) against a vertical stabilizer are compared in terms of damage severity and kinematics. The initial conditions were based on the most critical case (BQV2) identified in the baseline simulations (see Section 4.4.1.1). Figure 470 depicts the comparison of the kinematics of the event. Figure 471 shows the comparison of the damage caused to the skin and the inner structure of the vertical stabilizer.

The UAS damaged the skin, the upper and lower ribs, and the lightening hole behind the impact location in the front spar while the bird damaged the skin to a lesser degree and the upper and lower ribs. It can also be seen in Figure 471 that amount of damage introduced into the skin was considerably smaller for the case of bird than the UAS.

The damage introduced by the UAS is classified as Level 4, whereas the damage introduced by the bird is classified as Level 2. For this case, the UAS impact can be considered as more severe than the equivalent bird strike in terms of damage.

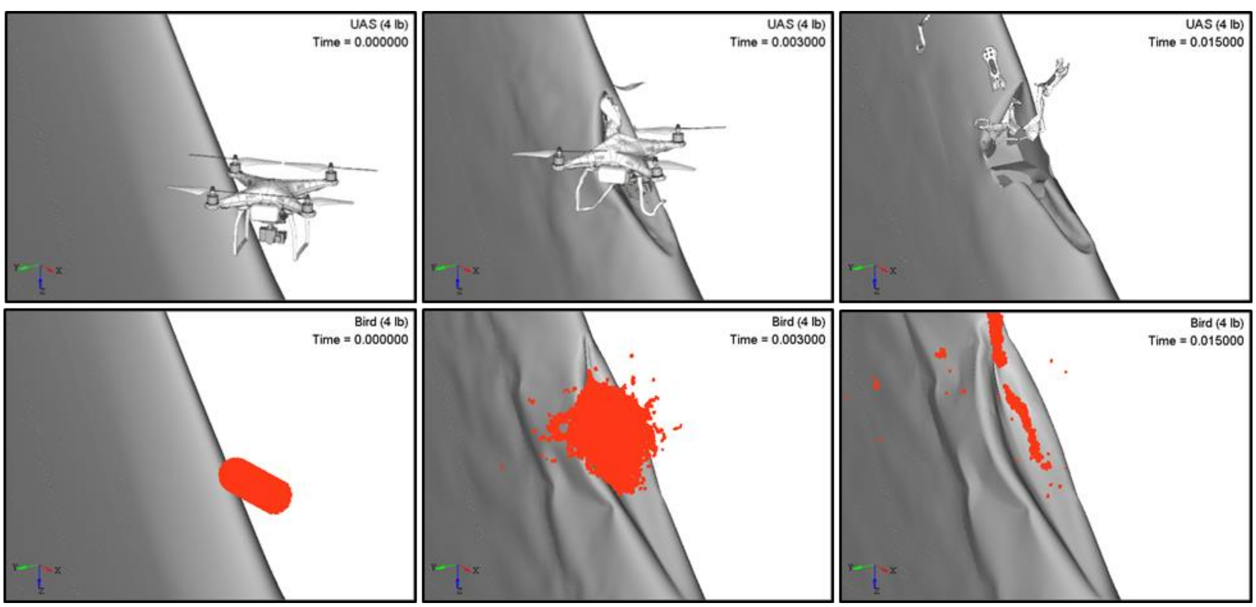

Figure 470.Comparison of the kinematics of impact between a business jet vertical stabilizer and a 1.8 kg (4.0 lb) UAS/Bird at 128.6 m/s (250 knots)

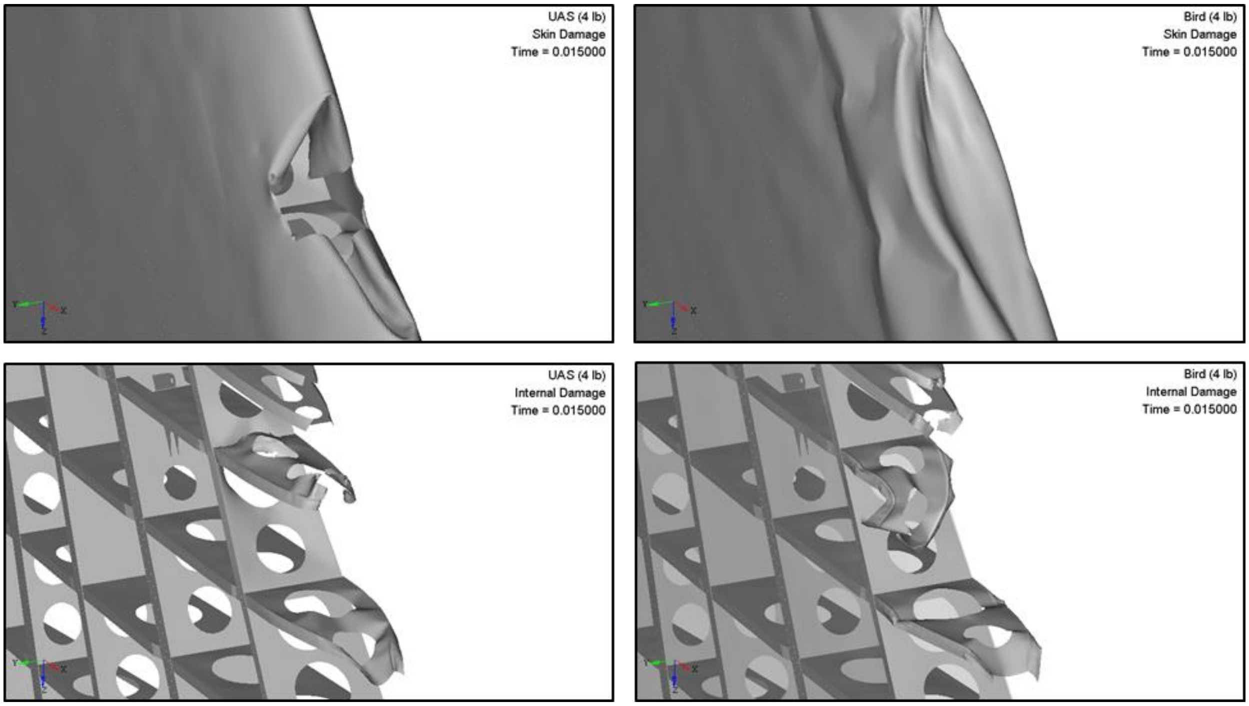

Figure 471 Comparison of external/internal damage sustained by a business jet vertical stabilizer impacted with a 1.8 kg (4.0 lb) UAS/Bird at 128.6 m/s (250 knots)

Figure 472 shows the comparison for the contact force and impulse between the UAS/bird and vertical stabilizer. Figure 473 shows the energy balance for the impact comparison. The impulse for the UAS was slightly higher than that of the bird. From the energy balance comparison, it can be observed that the UAS absorbed considerably greater internal energy than the bird. In addition, it is apparent that the residual kinetic energy of the bird after impact was greater than that of the UAS. This is an indication that the kinetic energy of the bird was deflected more efficiently than that of the UAS, for which most of the energy was absorbed in the impact.

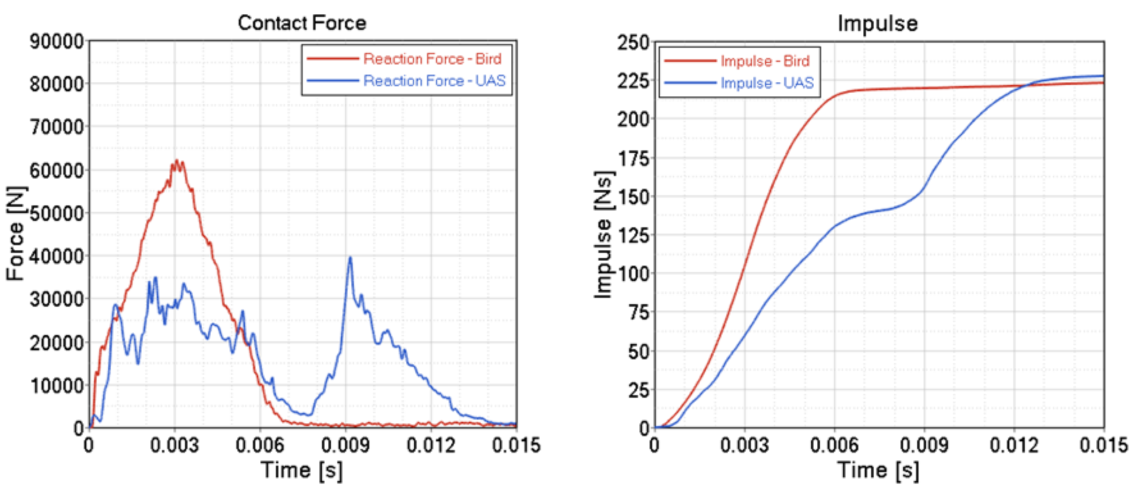

Figure 472 Comparison of the contact force and impulse of the impact between a business jet vertical stabilizer and a 1.8 kg (4.0 lb) UAS/bird at 128.6 m/s (250 knots)

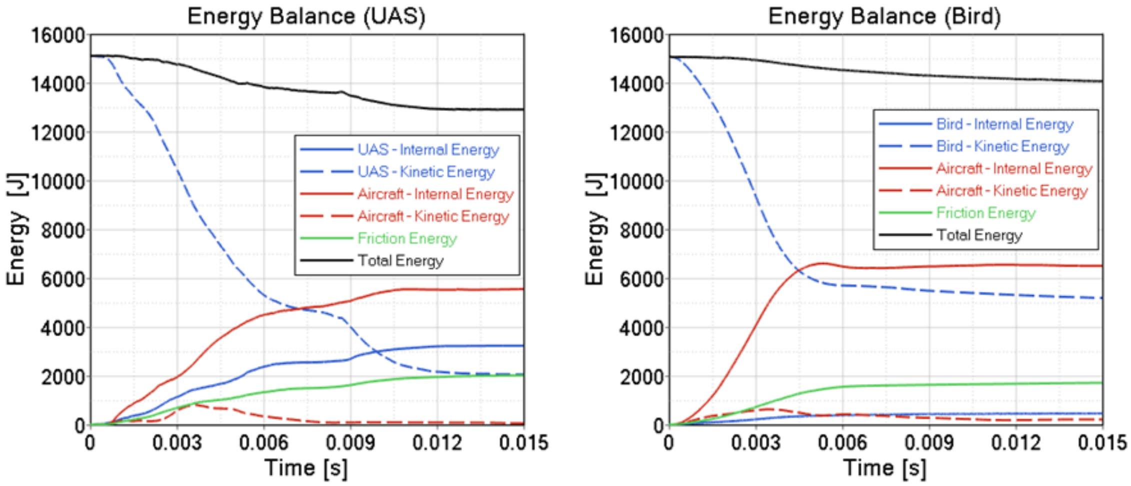

Figure 473 Comparison of the energy balance of the impact between a business jet vertical stabilizer and a 1.8 kg (4.0 lb) UAS/bird at 128.6 m/s (250 knots)

E.4.2 Horizontal Stabilizer

Impact simulations of a 1.8 kg (4.0 lb) UAS (case BQsH1) and a 1.8 kg (4.0 lb) bird (case BB4H1) against a horizontal stabilizer are compared in terms of damage severity and kinematics. The initial conditions were based on the most critical case (BQH1) identified in the baseline simulations (see Section 4.4.2.1). Figure 474 depicts the comparison of the kinematics of the event. Figure 475 shows the comparison of the damage caused to the skin and the inner structure of the horizontal stabilizer.

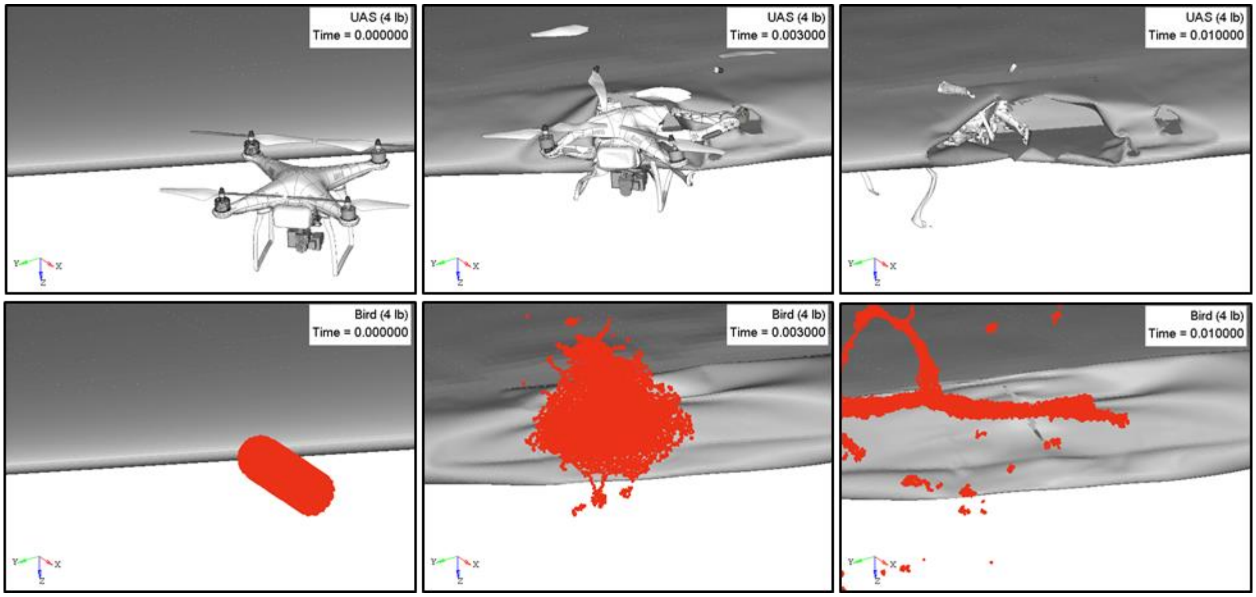

Figure 474.Comparison of the kinematics of impact between a business jet horizontal stabilizer and a 1.8 kg (4.0 lb) UAS/Bird at 128.6 m/s (250 knots)

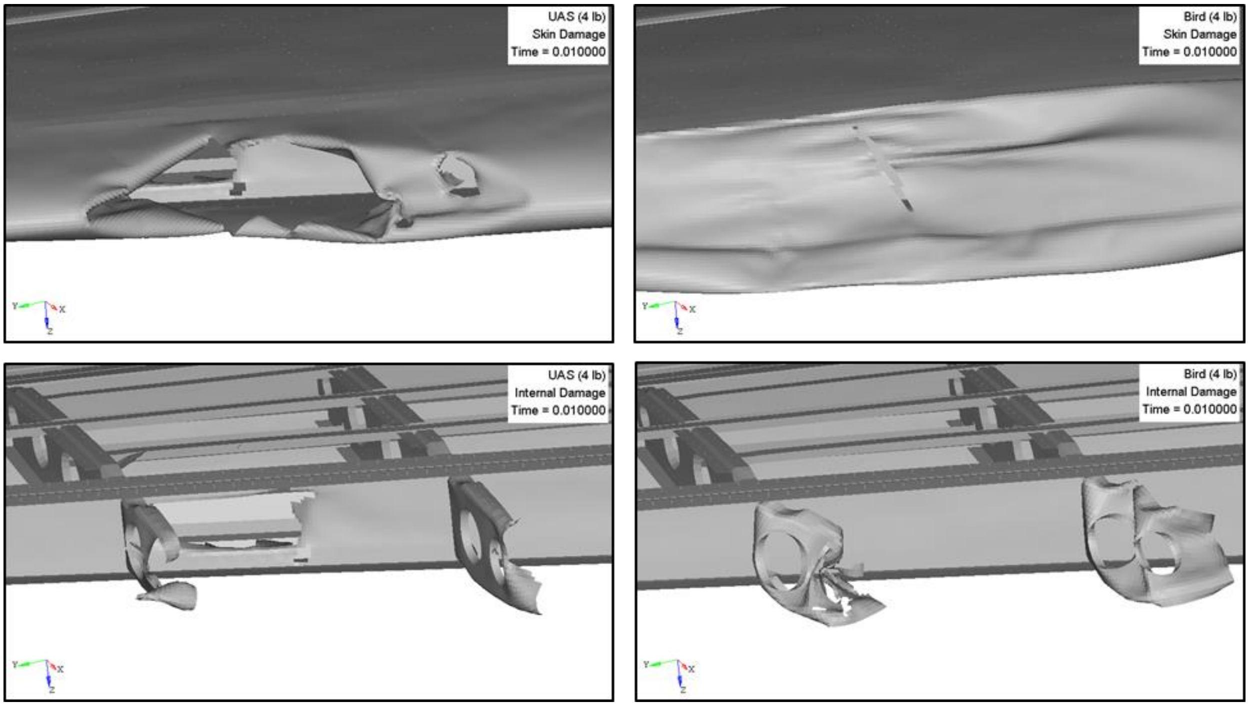

Figure 475 Comparison of external/internal damage sustained by a business jet horizontal stabilizer impacted with a 1.8 kg (4.0 lb) UAS/Bird at 128.6 m/s (250 knots)

The UAS damaged the skin, both the nose ribs and the front spar while the bird only deformed the skin without penetration. It can also be seen in Figure 475 that amount of damage introduced into the skin was of much greater magnitude for the UAS. However, the bird strike processes a more extent deformation of the skin in terms of area. The damage introduced by the UAS is classified as Level 4, whereas the damage introduced by the bird is classified as Level 2. For this case, the UAS impact can be considered as more severe than the equivalent bird strike in terms of damage.

Figure 476 shows the comparison for the contact force and impulse between the UAS/bird and horizontal stabilizer. Figure 477 shows the energy balance for the impact comparison.

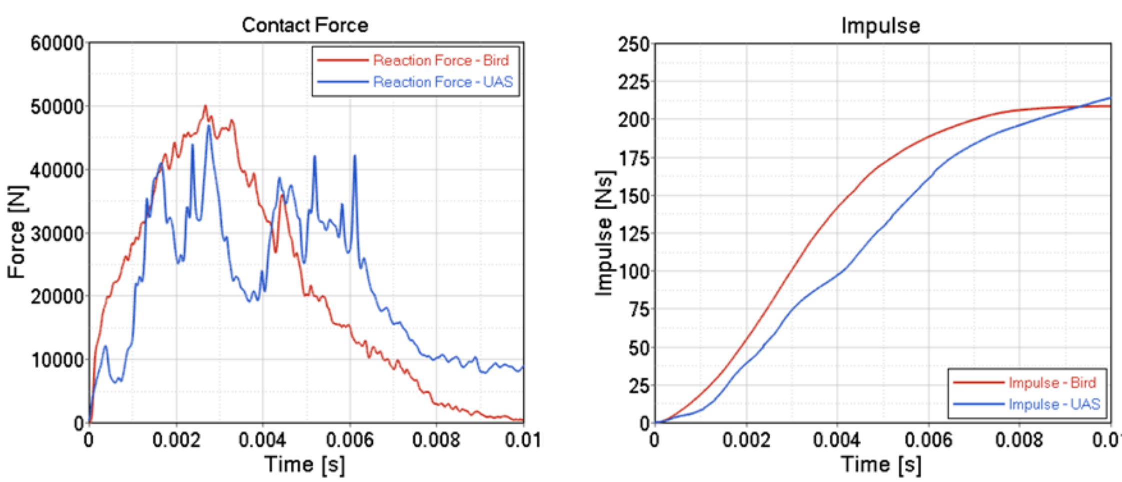

Figure 476 Comparison of the contact force and impulse of the impact between a business jet horizontal stabilizer and a 1.8 kg (4.0 lb) UAS/bird at 128.6 m/s (250 knots)

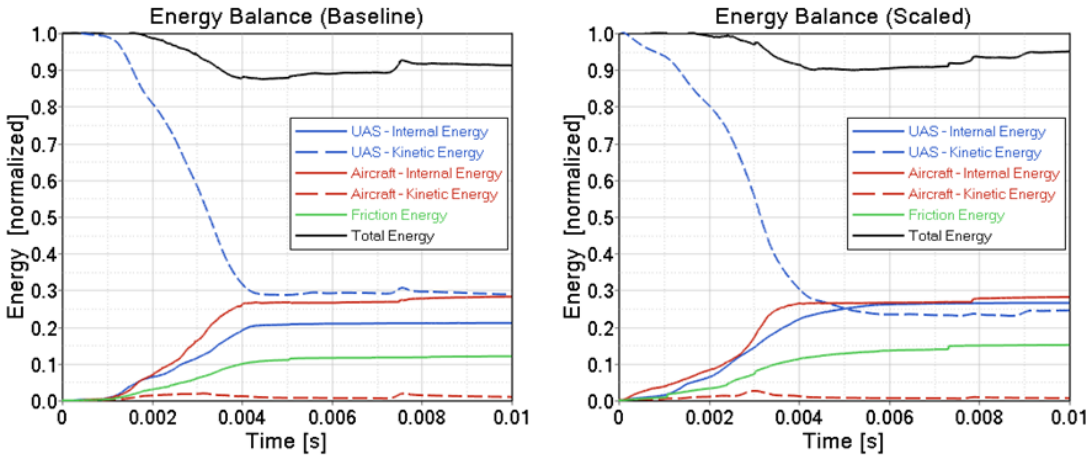

Figure 477. Comparison of the energy balance of the impact between a business jet horizontal stabilizer and a 1.8 kg (4.0 lb) UAS/bird at 128.6 m/s (250 knots)

The impulse for the bird was higher than that of the UAS. From the energy balance comparison, it can be observed that the UAS absorbed considerably greater internal energy than the bird. In addition, it is apparent that the residual kinetic energy of both the UAS and the bird after impact were of similar magnitude. This is an indication that the kinetic energy of both the UAS and the bird were deflected to an equal extent.

E.4.3 Wing Leading Edge

Impact simulations of a 1.8 kg (4.0 lb) UAS (case BQsW1) and a 1.8 kg (4.0 lb) bird (case BB4W1) against the leading edge of a wing are compared in terms of damage severity and kinematics. The initial conditions were based on the most critical case (BQW1) identified in the baseline simulations (see Section 4.4.3.1). Figure 478 depicts the comparison of the kinematics of the event. Figure 479 shows the comparison of the damage caused to the skin and the inner structure of the wing.

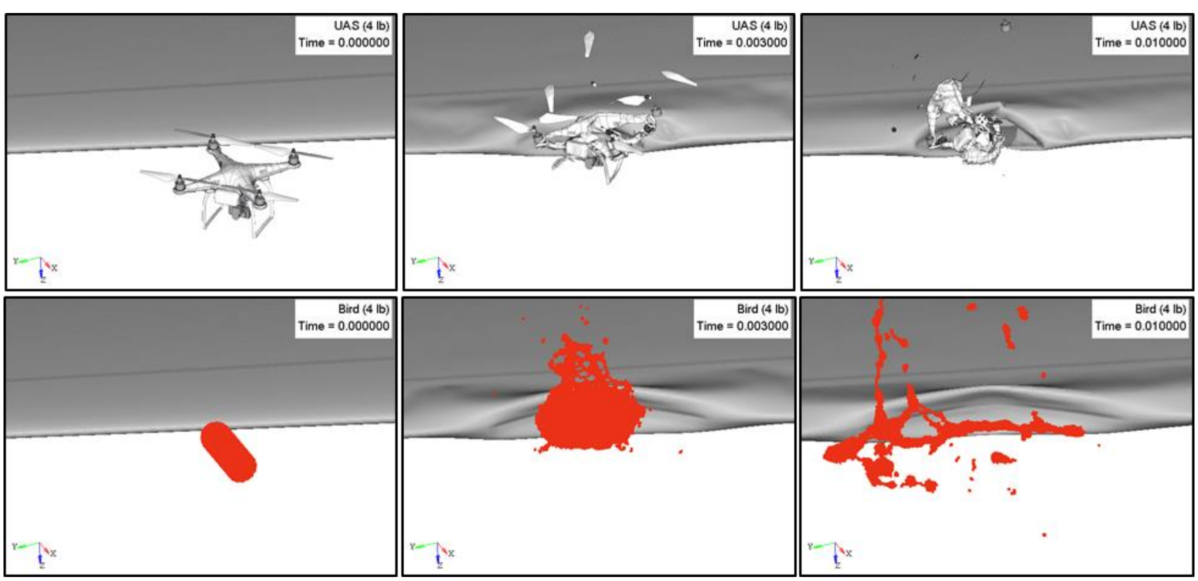

Figure 478. Comparison of the kinematics of impact between a business jet wing and a 1.8 kg (4.0 lb) UAS/Bird at 128.6 m/s (250 knots)

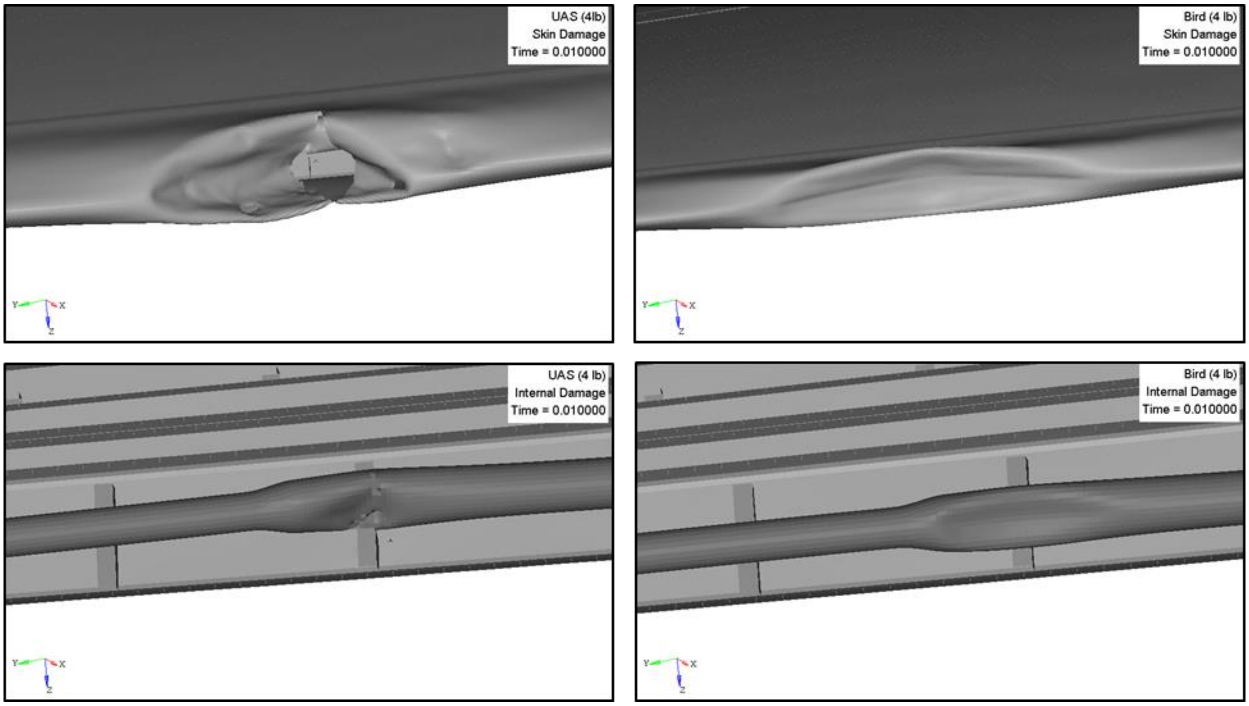

Figure 479. Comparison of external/internal damage sustained by a business jet wing impacted with a 1.8 kg (4.0 lb) UAS/Bird at 128.6 m/s (250 knots)

The UAS damaged the skin and the anti-ice tube while the bird also damaged the skin and the anti-ice tube but to a lesser degree. It can also be seen in Figure 479 that amount of damage introduced into the skin was considerably smaller for the case of bird than the UAS. The damage introduced by the UAS is classified as Level 3 with a risk of fire due to the battery, whereas the damage introduced by the bird is classified as Level 2. For this case, the UAS impact can be considered as more severe than the equivalent bird strike in terms of damage.

Figure 480 shows the comparison for the contact force and impulse between the UAS/bird and wing. Figure 481 shows the energy balance for the impact comparison.

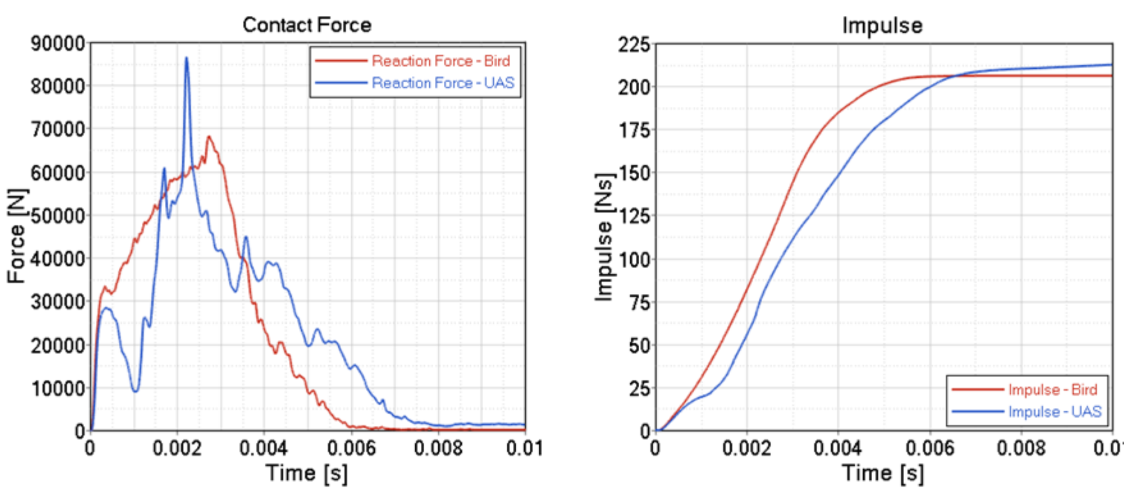

Figure 480 Comparison of the contact force and impulse of the impact between a business jet wing and a 1.8 kg (4.0 lb) UAS/bird at 128.6 m/s (250 knots)

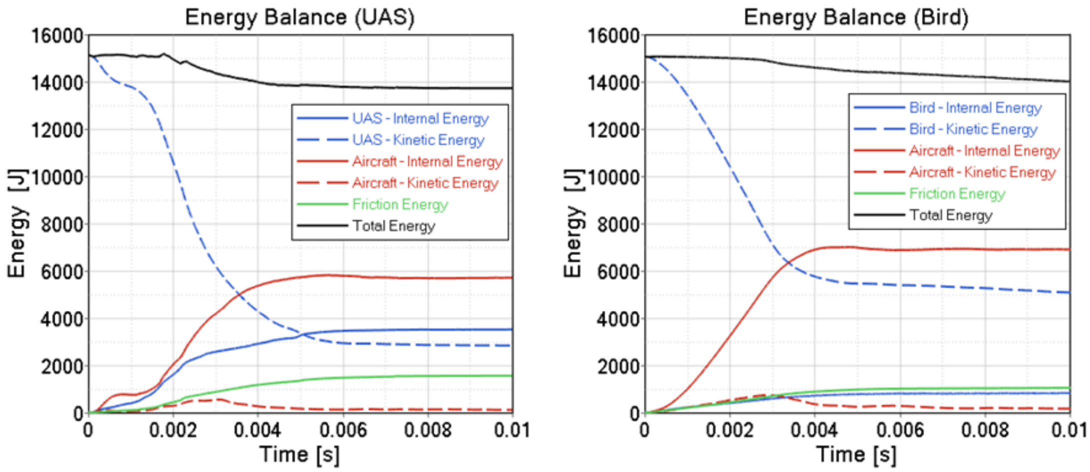

Figure 481 Comparison of the energy balance of the impact between a business jet wing and a 1.8 kg (4.0 lb) UAS/bird at 128.6 m/s (250 knots)

The impulse for the UAS was slightly higher than that of the bird. From the energy balance comparison, it can be observed that the UAS absorbed considerably greater internal energy than the bird. In addition, it is apparent that the residual kinetic energy of the bird after impact was greater than that of the UAS. This is an indication that the kinetic energy of the bird was deflected more efficiently than that of the UAS.

E.4.4 Windshield

Impact simulations of a 1.8 kg (4.0 lb) UAS (case BQsC1) and a 1.8 kg (4.0 lb) bird (case BB4C1) against a windshield are compared in terms of damage severity and kinematics. The initial conditions were based on the most critical case (BQC1) identified in the baseline simulations (see Section 4.4.4.1). Figure 482 depicts the comparison of the kinematics of the event. Figure 483 shows the comparison of the damage caused to the windshield and surrounding structure.

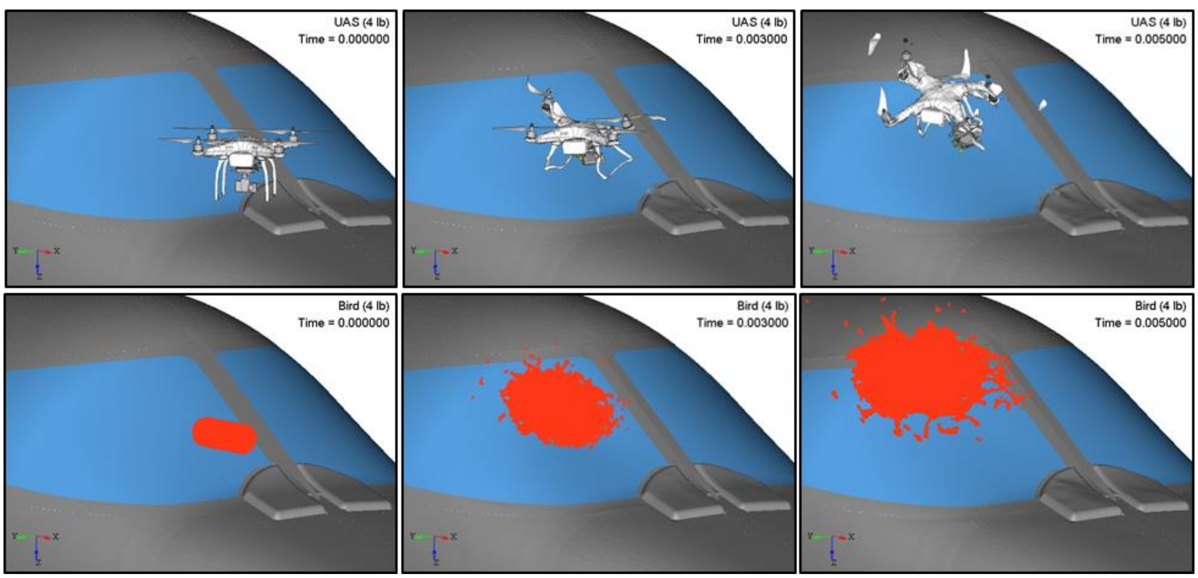

Figure 482.Comparison of the kinematics of impact between a business jet windshield and a 1.8 kg (4.0 lb) UAS/Bird at 128.6 m/s (250 knots)

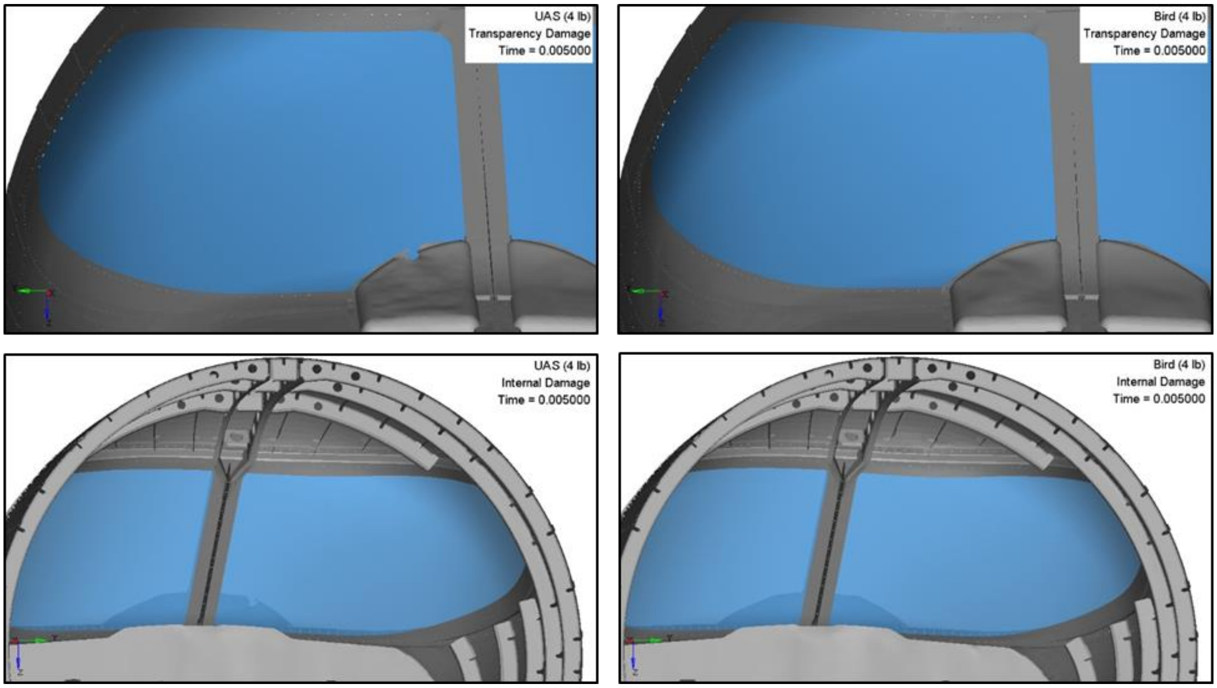

Figure 483 Comparison of external/internal damage sustained by a business jet windshield impacted with a 1.8 kg (4.0 lb) UAS/Bird at 128.6 m/s (250 knots)

Both the UAS and the bird impacted the windshield on the transparency and slid over it without causing noticeable permanent deformations to the transparency. The UAS damages the windshield anti-ice shell at the base of the transparency. It can also be seen in Figure 483 that amount of damage introduced into the windshield was smaller for the case of bird than the UAS. The damage introduced by the UAS is classified as Level 2, whereas the damage introduced by the bird is classified as Level 1. For this case, the UAS impact can be considered as more severe than the equivalent bird strike in terms of damage.

Figure 484 shows the comparison for the contact force and impulse between the UAS/bird and windshield. Figure 485 shows the energy balance for the impact comparison.

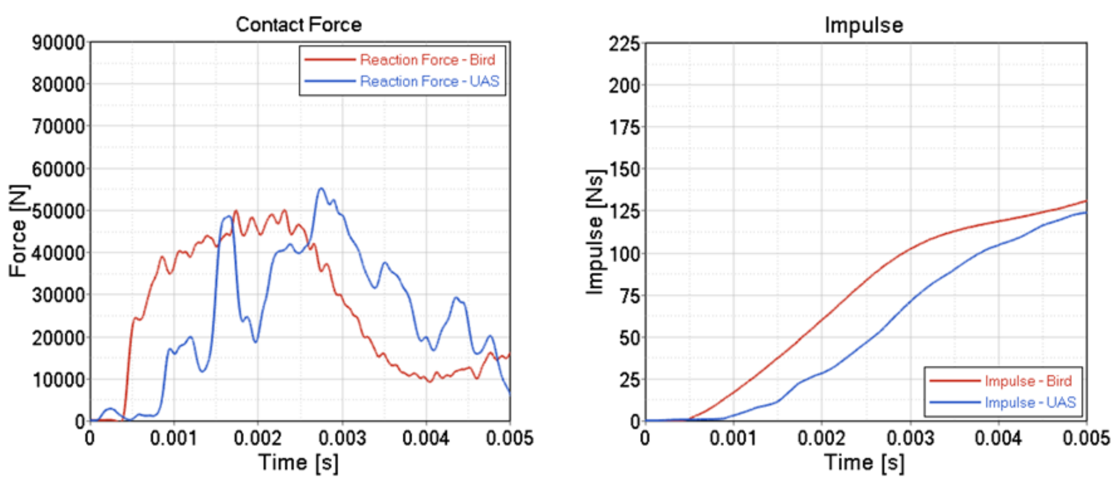

Figure 484 Comparison of the contact force and impulse of the impact between a business jet windshield and a 1.8 kg (4.0 lb) UAS/bird at 128.6 m/s (250 knots)

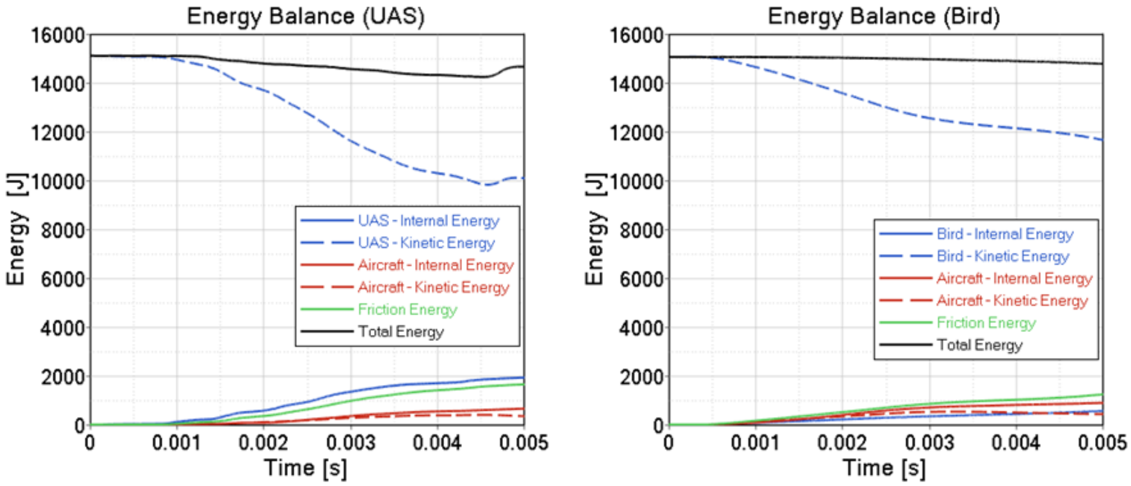

Figure 485 Comparison of the energy balance of the impact between a business jet windshield and a 1.8 kg (4.0 lb) UAS/bird at 128.6 m/s (250 knots)

The impulse for the bird was slightly higher than that of the UAS. From the energy balance comparison, it can be observed that the UAS absorbed considerably greater internal energy than the bird. In addition, it is apparent that the residual kinetic energy of the bird after impact was greater than that of the UAS. This is an indication that the kinetic energy of the bird was deflected more efficiently than that of the UAS, for which most of the energy was absorbed in the impact.

APPENDIX F– DATA PROCESSING METHODS

This appendix presents the methodology followed for the data processing of both physical testing and simulation for the test cases presented in Chapter 2. The procedure is presented with an example of how filtering was applied for a specific case. This same procedure was followed for all the plots in Chapter 2 in which it was indicated that the data had been filtered.

F.1 DATA PROCESSING EXAMPLE: COMPONENT LEVEL TEST 1

This section presents a sample case for the strain gage channel 4 of battery test 1, see section 2.4.4.6. The strain data acquired from the strain gages was sampled at 1 MHz. Similarly, the simulation set up to virtually replicate the test was also sampled at 1 MHz. Figure 486 shows a comparison of the raw data acquired for strain gage 4 during the simulation, and tests 5660, 5669, and 5670, respectively. It can be seen that for some cases the signal obtained became considerably noisy, therefore filtering was required to perceive a cleaner plot for comparison.

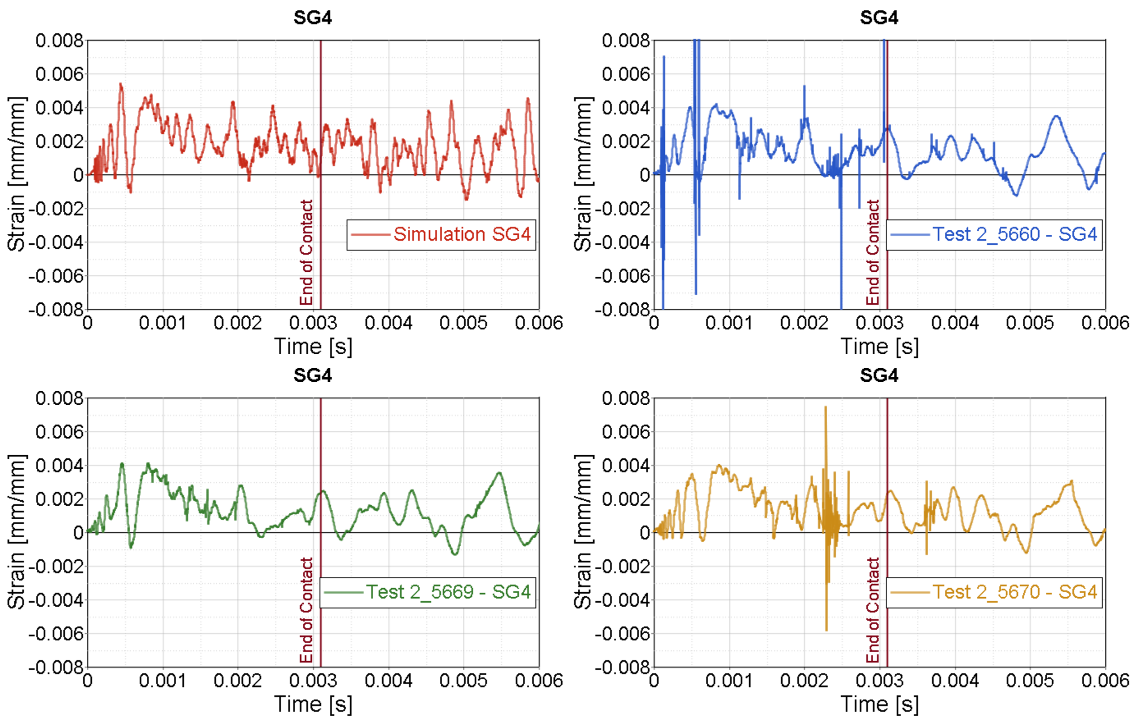

Figure 486. Component level test 1, strain gage 4, raw data.

To each of these signals, a low-pass filter of 15 kHz was applied to remove the high frequency noise present in the plots, without interfering with the strain oscillations. Altair Hypergraph software was used to process and filter the data. The filtered function selected was available in the software as an 'ideal low-pass' filter. More information about this filter can be found in the software's manual. [64]

Figure 487 presents the results of applying the filter to the noisy signal from Test 5660. Similarly, Figure 488 shows the results of filtering a not so noisy signal.

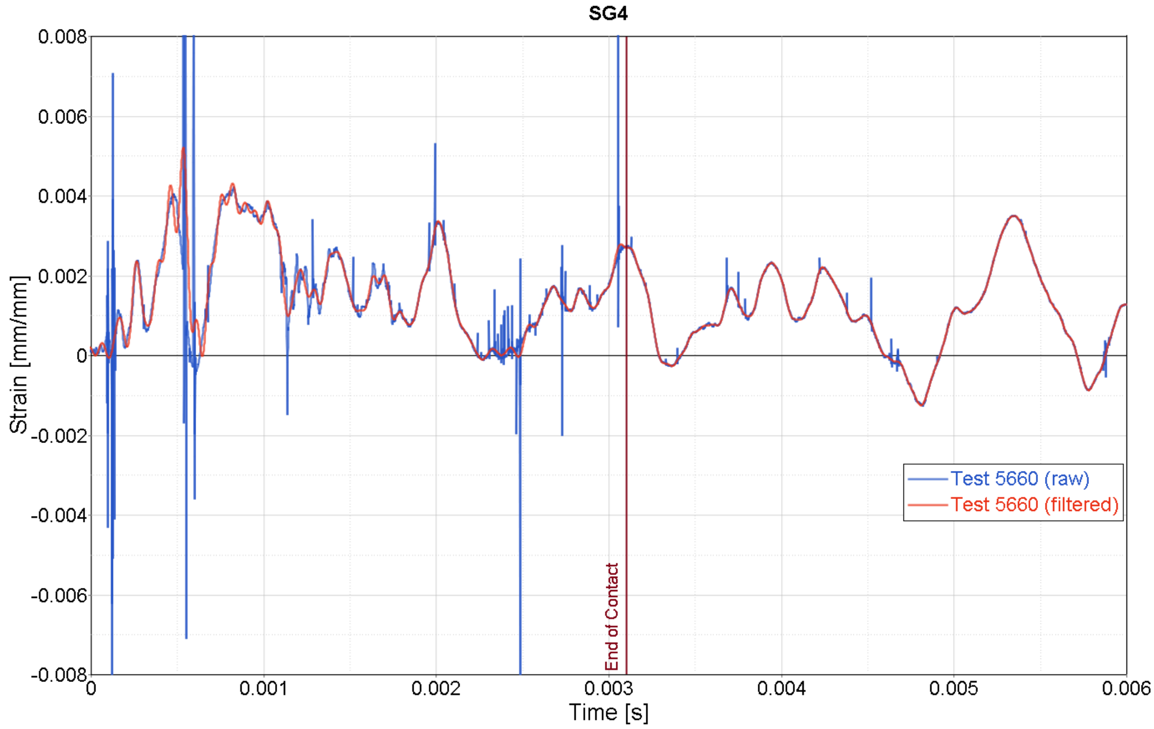

Figure 487. Component level test 1-5660, strain gage 4, comparison filtered/unfiltered.

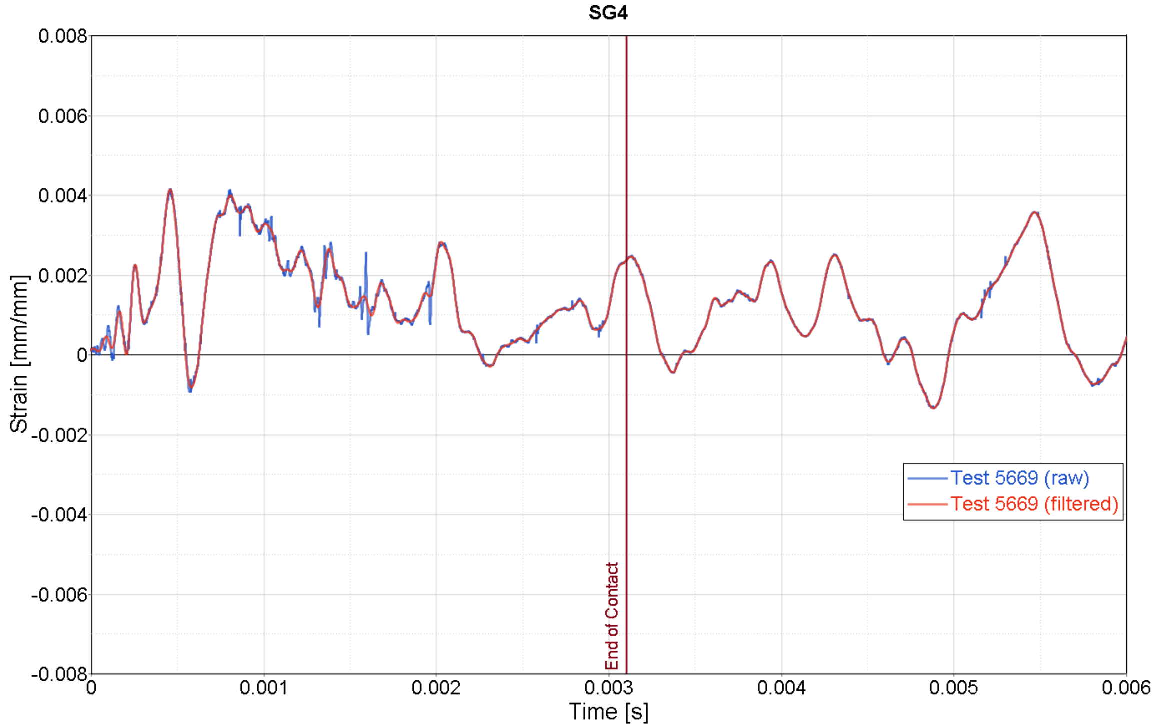

Figure 488. Component level test 1-5669, strain gage 4, comparison filtered/unfiltered.

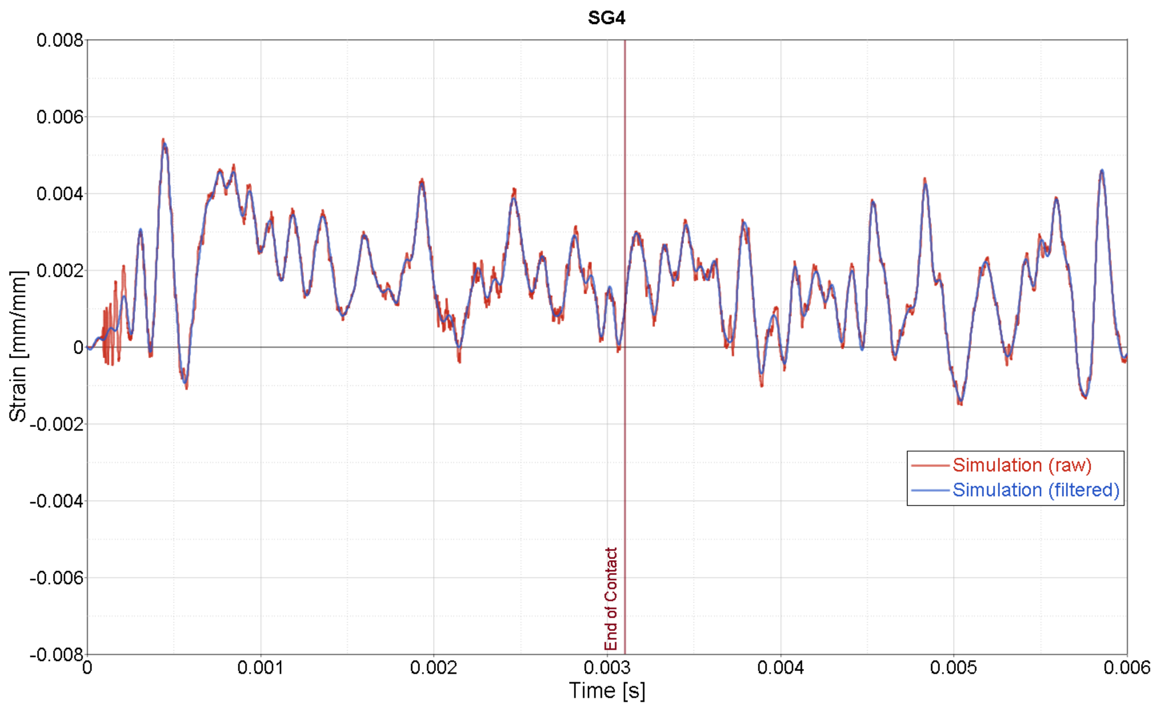

Figure 489. Component level test 1 simulation, strain gage 4, comparison filtered/unfiltered.